

ISSN 1822-5721

**KAUNAS UNIVERSITY OF TECHNOLOGY**

**MEDICAL PHYSICS IN THE BALTIC STATES**

**Proceedings of the 15<sup>th</sup> International Conference on Medical Physics**

**Kaunas, Lithuania  
4 – 6 November, 2021**

Executive editor **Diana Adlienė**

***CONFERENCE IS ORGANIZED BY:***

Kaunas University of Technology  
Skåne University Hospital, Lund University  
Medical Physicists Society  
University Hospital of Lithuanian University of Health Sciences „Kauno klinikos“

***PROGRAM COMMITTEE***

Diana ADLIENĖ - Kaunas University of Technology (Lithuania)  
Sören MATTSSON - Lund University, Skåne University Hospital (Sweden)  
Marius LAURIKAITIS - Medical Physicists Society (Lithuania)  
Birutė GRICIENĖ – Vilnius University Hospital „Santaros klinikos“ (Lithuania)  
Viktoras RUDŽIANSKAS - Hospital of Lithuanian University of Health Sciences „Kauno klinikos“ (Lithuania)  
Jurgita LAURIKAITIENĖ – Kaunas University of Technology (Lithuania)  
Kalle KEPLER - Radexpert OÜ (Estonia)  
Maksims POLAKOVŠ - Institute of Solid State Physics, University of Latvia (Latvia)  
Reda ČERAPAITĖ – TRUŠINSKIENĖ - Lithuanian University of Health Sciences (Lithuania)  
Saulius MICKEVIČIUS - Vytautas Magnus University (Lithuania)

***ORGANISING COMMITTEE***

Benas Gabrielis URBONAVIČIUS - Kaunas University of Technology (Lithuania)  
Lena CIBULSKYTĖ - Kaunas University of Technology (Lithuania)  
Judita PUIŠO - Kaunas University of Technology (Lithuania)  
Dalia BAREIŠIENĖ - Kaunas University of Technology (Lithuania)  
Mantvydas MERKIS - Kaunas University of Technology (Lithuania)  
Lijana LILEIKYTĖ - Kaunas University of Technology (Lithuania)

***CONFERENCE IS SUPPORTED BY:***

Kaunas University of Technology  
Lund University Skåne University Hospital  
Medical Physicists Society

Papers included in the Proceedings were reviewed by independent peer reviewers

©Kaunas University of Technology 2021

## **REFLECTIONS ON 60 YEARS OF DEVELOPMENT IN MEDICAL PHYSICS AND THOUGHTS ABOUT THE FUTURE**

Sören MATTSSON

Medical Radiation Physics Malmö, Lund University, Skåne University Hospital, SE-205 02 MALMÖ, Sweden  
Department of Physics, Kaunas University of Technology, Kaunas, Lithuania  
soren.mattsson@med.lu.se

**Abstract:** The paper deals with advances in medical physics during the last 60 years and share some thoughts on the future. Some of today's advances and challenges in medical physics applied to radiation therapy, diagnostic radiology, nuclear medicine, MR-imaging and radiation safety will be discussed. To be prepared for the future, we need continued good undergraduate education, advanced postgraduate courses as well as active research in the different fields of medical physics.

**Keywords:** Medical physics, radiotherapy, medical imaging, radiation safety.

### **1. Introduction**

Medical physics is the application of physics concepts, theories, and methods to medicine and healthcare. The International Organisation for Medical Physics (IOMP) describes the field in the following way: “Medical physics is a branch of applied physics, pursued by medical physicists, that uses physics principles, methods and techniques in practice and research for the prevention, diagnosis and treatment of human diseases with a specific goal of improving human health and well-being. Medical physics may further be classified into a number of sub-fields (specialties), including Radiation oncology physics, Medical imaging physics, Nuclear medicine physics, Medical health physics (Radiation protection in medicine), Non-ionizing medical radiation physics, and Physiological measurement. It is also closely linked to neighboring sciences such as Biophysics, Biological physics, and Health physics” (<https://www.iomp.org/medical-physics/>).

### **2. Development**

Figure 1 schematically describes 60 years of development in medical physics from 1960 until now and will be discussed in more details below.

Medical physics has taken advantage of the rapid technological developments in the society, especially of computers, computer programs and IT. Manual calculations and calculations using slide-rulers and pocket calculators have been replaced by calculations based on self-designed or commercially available software programs for e.g. dose planning and image reconstruction. Information, data and images are sent over the www. Developments of detectors and electronics in high-energy physics have been adopted and utilized in medical physics resulting in improved measuring possibilities and dosimetry. The increased collaboration with industry has achieved better accelerators for radiation therapy and production of radioactive trace elements. A similar cooperation has taken place with regard to imaging equipment.

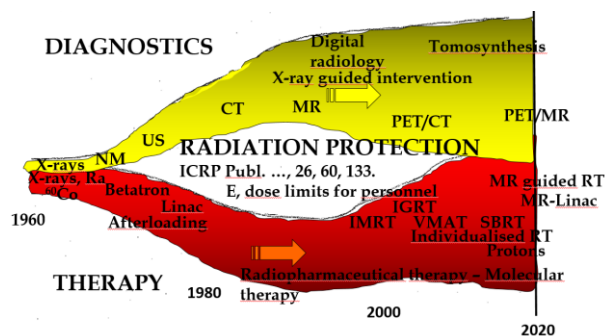


**Fig 1.** Schematic description of developments in medical physics 1960-2020. For abbreviations, please see the text.

### **2.1. Radiation therapy technologies**

In 1960, radiation therapy dominated the field of medical physics. Most treatments were based on x-ray therapy and the use of radium sources. The first  $^{60}\text{Co}$  units had been installed. Then radiation therapy has undergone a dramatic development. New radiation sources have been introduced, first betatrons, and then mostly linear accelerators. Dose planning for external radiotherapy has been much improved and based on CT images. The development of the multi-leaf collimator,

the inverse dose planning and thus the possibility of intensity modulated radiation therapy (IMRT) has been of crucial importance here [1,2]. Volumetric modulated arc therapy (VMAT), breath-controlled treatments, stereotactic methods, proton therapy and “MR-only” radiation therapy have been invented. In parallel, brachytherapy and after-loading technology, have been developed and improved. Radiopharmaceutical therapy was long dominated by the treatment of thyroid diseases and has now developed in parallel to the diagnostic nuclear medicine and includes treatments of neuroendocrine tumours, lymphoma and prostate cancer.

## 2.2. Imaging technologies

With the growth of nuclear medicine after the 2<sup>nd</sup> world war, medical physicists to a greater extent entered also the diagnostic applications of ionising radiation. Since then, the diagnostic applications of ionizing radiation have undergone an equally dramatic development as the therapeutic applications [3].

### 2.2.1 X-ray imaging and CT

In the 1960's, the radiation physics efforts on the x-ray side were quite modest. In some countries, gonad doses were measured [4,5] and the forerunners of the DAP or KAP meters that are currently available on most x-ray equipment for controlling the patient radiation dose were developed and introduced in the clinic [6,7,8].

Much work was later done in relation to optimisation of imaging and to patient dose estimates and radiation protection in planar x-ray imaging using various film-screen combinations [9,10,11]. The development of CT was a revolutionary contribution of physics and technology to medicine [12]. CT imaging has broad diagnostic applications and is the “gold standard” for many clinical indications. The patient doses are however higher than for many other x-ray investigations. In the late 2000's iterative image reconstruction methods brought the doses down. Now, new AI-based deep learning reconstruction and post-processing techniques have been shown to improve the diagnostic imaging quality for doses far beyond what is possible with current reconstruction techniques.

Digital x-ray imaging begun in the 1980's and over a period of 30 years it has eliminated the analogue film/screen technology, now using flat panel detectors with digital detector arrays. These developments have needed increased medical physics input.

### 2.2.2 Nuclear medicine imaging

The earliest nuclear medicine studies were performed without imaging, just using blood or urine samples or external counting, initially with Geiger counters and later with scintillation detectors. Automation of the external measurements led to development of the rectilinear scanner, which was frequently used in the 1960's and 1970's. The first Anger gamma-cameras [13] appeared in the late 1960's and the <sup>99m</sup>Tc-generator was invented in 1957 by the three Brookhaven chemists Walt Tucker, Powell Richards, and Margaret Greene

(and became in more frequent use in the middle of the 1960's). The combination of technetium <sup>99m</sup>Tc and the gamma camera was a success – a combination which still retains its position, and has been supplemented with single photon emission computed tomography (SPECT) [14] and positron emission tomography (PET) [15] and a number of new radionuclides and radiopharmaceuticals.

### 2.2.3 Ultrasound

Ultrasound imaging uses high-frequency sound waves to view inside the body. The ultrasound image is produced based on the reflection of the waves off of the body structures. The strength (amplitude) of the sound signal and the time it takes for the wave to travel through the body provide the information necessary to produce an image. Because ultrasound images are captured in real-time, they can also show movement of the body's internal organs as well as blood flow. Compared with other medical imaging modalities, such as CT and MRI, ultrasound is a low-cost modality and, most importantly, allows real time bedside imaging. Conventional ultrasound imaging techniques, however, have lower specificity and lower spatial resolutions compared with CT and MRI.

In most hospitals, biomedical engineers and not medical physicists, are responsible for the control, optimization and development of ultrasound imaging technology.

### 2.2.4. Magnetic resonance imaging (MRI)

MRI scanners use strong magnetic fields and radio waves to make images [16]. The signal in an MR image comes mainly from the protons in water and fat molecules in the body. During an MRI examination, an electric current is passed through coiled wires to create a temporary magnetic field in a patient's body. Radio waves are sent from and received by a transmitter/receiver in the machine, and these signals are used to make digital images of the scanned area of the body. A typical MRI scan last from 20 - 90 minutes, depending on which part of the body being imaged. MRI provides better soft tissue contrast than CT and can differentiate better between muscle, fat and other soft tissue than CT, which is usually better at imaging bones. For some MRI exams, intravenous drugs, such as gadolinium-based contrast agents are used to improve the contrast of the MR image. MRI takes now over some CT examinations (prostate cancer, uterine cancer, certain liver cancers, metastases in the skeleton and brain).

### 2.2.5. Hybrid imaging

By using the combined-modalities PET/CT and SPECT/CT, functional processes can be localized within the body to an anatomically identified or, in some instances, as yet unidentifiable structural alteration. In this way, the accuracy with which a disease can be detected and described in terms of extent and severity is increased. The hybrid techniques PET/CT and SPECT/CT have later been expanded with PET/MR [17].



### 2.2.6, Artificial intelligence

The large amounts of data that are produced is now analyzed with the help of artificial intelligence (AI) technology. Machine learning is a branch of AI based on the idea that systems can learn from data, identify patterns and make decisions with minimal human support. We have already seen that AI technology can achieve the same image quality as standard imaging with less data, or alternatively shorter examination times.

### 2.3. Radiation protection

The primary aim of radiological protection is to contribute to an appropriate level of protection for people and the environment without unduly limiting the desirable human activities that may be associated with radiation [18]. ICRP has published General Recommendations which set out the entire System of Radiological Protection. In the period 1960-2020 such recommendations were issued in *Publications 1* [19], 6 [20], 9 [21], 26 [22], 60 [23], and 103 [18]. There are some unique aspects of radiological protection for patients: Exposure is conscious and voluntary. The same individual is subject to both benefits and risks. There are no dose limits for medical exposure of patients. The exposure is considered justified if it does more good than harm. There are three eligibility levels to apply: general, procedure, and individual patient.

In addition to being justified, imaging and therapy must be optimized. Optimization means that the radiation dose should be "as low as readily available or ALARA". In diagnostic and interventional medical exposure, it means, keeping the exposure of patients to the minimum necessary to achieve the required diagnostic or interventional objective. In therapeutic medical exposure, it means keeping the exposure of normal tissue as low as reasonably achievable consistent with delivering the required dose to the planning target volume.

ALARA is the management of the radiation dose to the patient in accordance with the medical purpose and does. ALARA does not necessarily mean the lowest radiation dose.

In diagnostics, use of diagnostic reference levels, (DRL) [24] is a way towards optimization. A diagnostic reference level (DRL) is a specified radiation dose for a given imaging study that is not expected to be exceeded. If a radiation dose does exceed the DRL for a particular study, this should prompt an investigation into radiographic technique or equipment performance.

For the personnel there are also dose limits, which have been subject to changes during the period. From 1957, corresponding to an average annual occupational effective dose of 50 mSv. For individual members of the public, the dose limit was set at 5 mSv/year and, in addition, a genetic dose limit of 50 mSv/generation was suggested. From 1991, the dose limit is a maximum of 50 mSv in an individual year, or 20 mSv on average per year over a period of five years. In 2011, ICRP made a substantial revision to the equivalent dose to the lens of the eye and reduced it from 150 mSv per year to 20 mSv

per year averaged over 5 years, with no single year exceeding 50 mSv.

## 3. Current situation and trends for the future

### 3.1. X-ray imaging, CT

Today's trends are that the fraction of regular planar x-rays decrease, CT and MRI increase, while ultrasound and nuclear medicine retain their share of the examination panorama [25].

The effective dose per capita from CT, other x-ray imaging and nuclear medicine diagnostics in Sweden during 2018 has been estimated to 0.7 mSv [25].

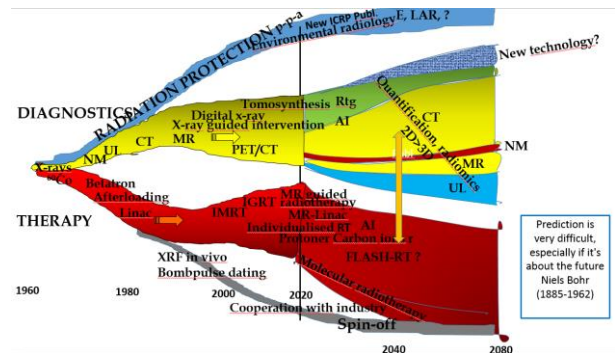


**Fig 2.** Figure 1 has been expanded to include also the time period 2020-2060

Recent developments include dual-energy-CT to exploit differences in the energy dependency of the attenuation coefficients and give a possibility to selectively display materials that have the same CT-value in single energy CT. Another development is photon-counting CT. Photon-counting CT detectors count the number of incoming photons and measure photon energy. This technique results in higher contrast-to-noise ratio, improved spatial resolution, and optimized spectral imaging. Compared with current CT technology, photon-counting CT will allow for reduced radiation exposure, increased spatial resolution, correction of beam-hardening artifacts, and alternative contrast agent protocols while creating opportunities for quantitative imaging [26].

Tomosynthesis or digital tomosynthesis is a limited angle tomography at absorbed doses similar to planar projection radiography. It is frequently applied for mammographic screening and for chest imaging

### 3.2. Nuclear medicine

Nuclear medicine includes both the use of radiopharmaceuticals to track physiological processes and to deliver therapeutic absorbed doses to specific targets. The development in both these areas is illustrated in Figure 3 showing radiopharmaceuticals/radionuclides used and associated equipment and substance used for therapy and treated organs and tissues.

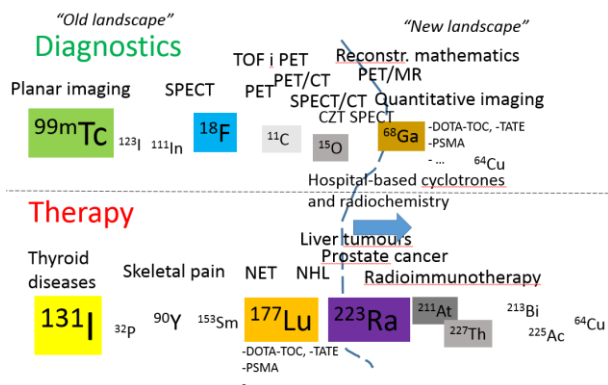


**Fig. 3.** Radiopharmaceuticals/radionuclides and associated methods and equipment used for diagnostics and therapy of various organs and tissues.

### 3.3 Ultrasound

Over the last decade, ultrasound imaging technology has improved dramatically, creating clearer and more defined pictures. Real-time computer imaging has helped increase processing speeds, which in turn produces better images. New contrast enhancing agents have been introduced as well as therapeutic use of high-intensity focused ultrasound. Integration of ultrasound with other diagnostic or therapeutic modalities have been done.

### 3.4. MRI

Magnetic resonance imaging shows a strong expansion. MRI takes over some CT examinations (prostate cancer, uterine cancer, certain liver cancers, metastases in the skeleton and brain). Breast cancer screening MRI may be of value to women with unclear findings and dense breasts. The slowness is however the Achilles' heel of the MRI technology. Therefore, so called super-fast MRI protocols are developed. MRI is used for morphological imaging, MR angiography, diffusion-perfusion measurements, functional MRI (fMRI) and MRI spectroscopy.

### 3.5 Hybrid imaging

#### PET / MR

By replacing the vacuum PM tubes in PET (which is disturbed by the magnetic fields from the MR camera) with avalanche photodiodes (SiPM) [27], it has been possible to integrate the PET and MR equipment. Such cameras are currently available in a limited number of hospitals/research centers.

### 3.6. Radiation therapy

MR-Linac combines a linear accelerator with a MRI scanner [28]. This enables tracking of breathing-induced and other movements and adapts the specific therapy delivery. It also registers any change in position and volume of the tumour during the weeks of therapy. It increases the chance of better tumor control and reduces the risk of damage to surrounding healthy tissue.

Proton therapy is a promising treatment technique especially for patients whose tumors are close to sensitive organs in the head, chest, or abdominal cavity.

A proton beam can be controlled more precisely than traditional photon radiation, which can reduce the risk of side effects. The energy in a proton beam can be varied so that the radiation dose almost entirely ends up at a certain predetermined depth.

Therefore, radiation with proton therapy can be almost completely concentrated on the tumor itself, thus the radiation absorbed dose can be increased, while maintaining a low dose to the surrounding normal tissues. Proton therapy is particularly suitable for children and adolescents since fewer long-term side effects are expected than from conventional therapy. In a few places in the world, therapy is also done with heavier ions, usually carbon ions. Compared to protons, the carbon ion beams add to the geographical precision also a higher biological effectiveness for treatment of some specific types of cancer.

## 4. Outlook

### 4.1. X-rays, CT

CT stands for a majority of the dose contribution in today's radiology. There is a need to improve the dosimetry at CT investigations. To continue to rely on only CTDI, DLP and effective dose is not enough. We urgently need to decrease the uncertainties in the dose estimates for assessment of the risk of cancer and non-cancer effects. This is of special importance for a number of patients undergoing multiple CT scans, for pregnant women who need a CT scan, and in case of accidents. In fact, every discussion about justification and optimization needs accurate dose estimates.

A first step is to implement the joint recommendations from the American Association of Physicists in Medicine (AAPM) and the European Federation of Organisations for Medical Physics (EFOMP) in their AAPM Report 246 [29]. A very valuable review of the field is given in a new book entitled "The physics of CT dosimetry. CTDI and beyond" by Robert Dixon [30].

### 4.2. Nuclear medicine

Today, many nuclear research reactors are being shut down. One immediate consequence is the shortage of medical radionuclides, such as  $^{99m}\text{Tc}$ . It is therefore important to investigate alternative technologies to produce a sustainable supply of  $^{99m}\text{Tc}$  [31].

In positron emission tomography, as much as 40% of positron annihilation occurs through the production of positronium atoms inside the patient's body. The decay of these is sensitive to metabolism and could provide information about disease progression. New research is needed to take full advantage of what positronium decays reveal [32].

### 4.3 MRI

Today, hospitals routinely use machines with field strengths of 1.5 T or 3 T but ultra-high-field scanners are on the rise. There are already dozens of 7 T machines in research labs around the world, and 2017, the first 7 T model was cleared for clinical use in both the United States and Europe. At the extreme end are scanners designed for humans that reach beyond 10 T

having a potential for imaging with greater spatial resolution, or at the same resolution, but faster. Still, at some point there will be a limit to field strength beyond which one can't go without damaging the body

#### 4.4 Radiation therapy

FLASH radiotherapy (FLASH-RT) is a novel radiotherapy technology defined as a single ultra-high dose-rate ( $\geq 40$  Gy/s) radiotherapy [33]. Compared with conventional dose-rate irradiation, FLASH irradiation is 400-fold more rapid than conventional irradiation. Recent animal experiments have shown that FLASH-RT can reduce radiation-induced damage in healthy tissues. In the first patient with T-cell cutaneous lymphoma who received FLASH-RT, the anti-tumor effect was rapid and long-lasting; moreover, only grade 1 epithelitis and grade 1 edema occurred in the soft tissues surrounding the tumor. In this first clinical use of FLASH-RT, the treatment time was only 90 ms. Compared with conventional dose-rate radiotherapy, the very short radiotherapy time is another advantage of FLASH-RT. Considering that FLASH-RT can reduce the damage to healthy tissue and the advantages of the short treatment time, we have reason to predict that FLASH radiotherapy may become one of the main radiotherapy technologies in clinical practice in the future.

#### 4.5 Radiological protection

In the coming 4-8 years, the ICRP will update its general recommendations on radiation protection for humans and the environment [18]. This may affect the work in medical physics. A recent article outlines what is considered to be needed [34]. Many areas are identified for potential review and include classification of effects. Examples are tissue reactions; reformulation of detriment, potentially including non-cancer diseases; re-evaluation of the relationship between detriment and effective dose, and the possibility of defining detriments for males and females of different ages as well as of patients with different diagnoses [35], individual variation in the response to radiation exposure; heritable effects; and effects and risks in non-human biota and ecosystems. Some of the basic concepts are also being considered, including the framework for bringing together protection of people and the environment, incremental improvements to the fundamental principles of justification and optimisation, a broader approach to protection of individuals, and clarification of the exposure situations introduced in 2007.

#### 4.6. Artificial intelligence

The different techniques used in AI, i.e., mainly machine learning and deep learning algorithms, are especially useful when it comes to the emerging field of "big data". Artificially intelligence is increasingly used in healthcare. It has already positively affected several imaging applications (e.g. deep learning based attenuation correction, and image enhancement). There is now even a special concept - radiomics – introduced for this [36].

### 5. Some final remarks

In the future, we can expect a continued dramatic development in medical physics for both diagnostics and therapy. There are however a number of challenges: Medical physicists work in a fragmented, commercialized and often underfinanced healthcare system. In recent years there has also been a trend to separate clinical work and research. In the long run, it is dangerous and results in poorer healthcare as well as poorer research. This has received attention in radiation therapy [37] but is equally important in diagnostic applications. Clinic and research are Siamese twins and not just temporary acquaintances. This is an important message to our university hospitals with strong central control of healthcare and research, usually with managers (economists, administrators) without detailed subject knowledge.

To be able to apply physics in healthcare also in the future, the medical physicists have both to be fully integrated in the multidisciplinary clinical team responsible for the patient (as illustrated for radiation oncology by Fiorino *et al.* [38]) and continuously increase our knowledge of fundamental radiation physics including the interaction of radiation with the body and the changes it creates to make the most effective and safe use of the radiation.

To be prepared for the future, we need continued good under-graduate education, advanced postgraduate courses as well as active research in the different fields of medical physics.

### 6. Information

This article is based on a lecture that the author gave in connection with his honorary assignment to hold the Kalle Vikterlöf lecture at the Swedish Association for Radiation Physics meeting on 19 November 2020. Kalle Vikterlöf, former chief medical physicist in Örebro was a pioneer in medical physics and an important mentor for many younger colleagues. Thanks are due to prof. Tommy Knöös for comments on the manuscript.

### 7. References

1. Brahme A., Roos J.E., and Lax I. Solution of an integral equation encountered in rotation therapy. *Phys Med Biol* 27(10), 1221-1229, 1982.
2. Brahme A. Optimization of stationary and moving beam radiation therapy techniques. *Radiother Oncol* 12(2), 129-140, 1988.
3. Beyer T., Bailey D.L., Birk U.J., Buvat I., Catana C., Cheng Z., *et al.* Medical physics and imaging—A timely perspective. *Front Phys* 9,634693, 2021. doi: 10.3389/fphy.2021.634693.
4. Koren K., Maudal S. Gonad doses received during the medical application of roentgen radiation. *Acta Radiol* 48(4), 272-279, 1957.
5. Larsson L.-E. Radiation doses to the gonads of patients in Swedish roentgen diagnostics: studies on magnitude and variation of the gonad doses together with dose reducing measures. *Acta Radiol Suppl* 157, 1-127, 1958.
6. Carlsson, C. Determination of integral absorbed dose from exposure measurements *Acta Radiol Ther Phys Biol* 1, 433-458, 1963.

7. Carlsson, C.A., Integral absorbed doses in roentgen diagnostic procedures, I: The dosimeter, *Acta Radiol* 3, 310–326, 1965.
8. Pychlau H. and Pychlau P. Ein Diagnostik-Dosimeter-Grundform und Abwandlung Deutsch Röntgenkongr, 1963, Beiheft Fortschr Röntgenstr 100, 177-180.
9. European Commission. European guidelines on quality criteria for diagnostic radiographic images. EUR 16260, 1996, 80 pp.
10. Moores B.M., Mattsson S., Månsson L.G., Panzer W., Regulla D., Dance D., *et al.* RADIUS - closing the circle on the assessment of imaging performance. *Radiat Prot Dosim* 114(1-3), 450-457, 2005.
11. IAEA. Dosimetry in diagnostic radio logy: an international code of practice. Technical Reports Series No. 457, 2007.
12. Hounsfield G.N. Computerized transverse axial scanning (tomography): Part 1, description of system. *Brit J Radiol* 46(552), 1016-1022, 1973.
13. Anger H.O. Scintillation camera. *Rev Sci Instrum* 29, 27, 1958.
14. Kuhl D.E., and Edwards R.Q. Image separation radioisotope scanning. *Radiology* 80, 653–662, 1963.
15. Hoffman E.J. and Phelps M.E. Positron emission tomography. *Medical Instrumentation* 13, 147-151.
16. Lauterbur P.C. Image formation by induced local interactions: examples employing nuclear magnetic resonance. *Nature* 242, 190–191, 1973.
17. Cal-Gonzalez J., Rausch I., Shivam Sundar L.K., Lassen M.L., Muzik O., Moser E, *et al.* Hybrid imaging: Instrumentation and data processing. *Front Phys*, 6, 47, 2018.  
[doi.org/10.3389/fphy.2018.00047](https://doi.org/10.3389/fphy.2018.00047)
18. ICRP. The 2007 Recommendations of the International Commission on Radiological Protection. ICRP Publication 103. *Ann ICRP* 37(2–4), 2007.
19. ICRP. Recommendations of the International Commission on Radiological Protection. Now known as ICRP Publication 1. Pergamon Press, London, 1959.
20. ICRP. Recommendations of the International Commission on Radiological Protection. ICRP Publication 6. Pergamon Press, Oxford, 1964.
21. ICRP. Recommendations of the International Commission on Radiological Protection. ICRP Publication 9. Pergamon Press, Oxford, 1966.
22. ICRP. Recommendations of the ICRP. ICRP Publication 26. *Ann ICRP* 1(3), 1977.
23. ICRP. 1990 Recommendations of the International Commission on Radiological Protection. ICRP Publication 60. *Ann ICRP* 21(1–3), 1991.
24. ICRP. Diagnostic reference levels in medical imaging. ICRP Publication 135. *Ann ICRP* 46 (1), 2017.
25. Almén A. and Jangland L. Radiologiska undersökningar i Sverige under 2018. Report SSM 2020:14 (In Swedish).
26. Willemink M.J., Persson M., Pourmorteza A., Pelc N.J., and Fleischmann D. Photon-counting CT: Technical principles and clinical prospects. *Radiology* 289, 293–312, 2018.
27. Herrnsdorf L., Caccia M., and Mattsson S. Silicon photomultiplier for medical imaging and dosimetry-An overview. *Radiat Prot Dosim* 169(1-4), 430-435, 2016.
28. Raaymakers B.W., Lagendijk J.J.W., Overweg J., Kok J.G.M., Raaijmakers A.J.E., Kerkhof E.M., *et al.* Integrating a 1.5 T MRI scanner with a 6 MV accelerator: proof of concept. *Phys Med Biol* 54(12), N229-237, 2009.
29. Andersson J., Pavlicek W., Al-Senan R., Bolch W., Bosmans H., Cody D., *et al.* Estimating patient organ dose with computed tomography: A review of present methodology and required DICOM information. A Joint Report of AAPM Task Group 246 and the European Federation of Organizations for Medical Physics (EFOMP). AAPM Report No 246, 2019.
30. Dixon R.L. The physics of CT dosimetry. CTDI and beyond. Series in Medical Physics and Biomedical Engineering, 1st Edition, CRC Press, 2021, 232 p.
31. Charlton K. A sustainable future for nuclear Imaging. *Nature Rev Phys* 1, 530-532, 2019.
32. Moskal P., Jasińska B., Stępień E.L., and Bass S.D. Positronium in medicine and biology. *Nature Rev Phys* 1, 527-529, 2019.
33. Lin B., Gao F., Yang Y., Wu D., Zhang Y., Feng G., *et al.* FLASH radiotherapy: History and future. Review article. *Front Oncol*, 25 May 2021, [doi.org/10.3389/fonc.2021.644400](https://doi.org/10.3389/fonc.2021.644400)
34. Clement C., Rühm W., Harrison J., Applegate K., Cool D., Larsson C.-M., *et al.* Keeping the ICRP recommendations fit for purpose. *J Radiol Prot* (in press), 2021.  
[doi.org/10.1088/1361-6498/ac1611](https://doi.org/10.1088/1361-6498/ac1611)
35. Andersson M., Eckerman K., Pawel D., Almén A., and Mattsson S. Improved radiation risk models applied to different patient groups in Sweden. *Radiation Hygiene (Radiatsionnaya Gygiena)* 12(2), 44-54, 2019
36. van Timmeren J.E., Cester D., Tanadini-Lang S., Alkadhi H., and Baessler B. Radiomics in medical imaging—“how-to” guide and critical reflection. *Insights into Imaging* 11, 91, 2020.  
[doi.org/10.1186/s13244-020-00887-2](https://doi.org/10.1186/s13244-020-00887-2)
37. Bortfeld T., Torresin A., Fiorino C., Andreo P., Gagliardi G., Jeraj R., *et al.* The research versus clinical service role of medical physics. *Radiother Oncol* 114, 285-288, 2015.
38. Fiorino C., Jeraj R., Clark C.H., Garibaldi C., Georg D., Muren L., *et al.* Grand challenges for medical physics in radiation oncology. *Radiother Oncol* 153, 7-14, 2020.

## **DEVELOPING STRATEGIC LEADERSHIP SKILLS IS CRUCIAL FOR THE FUTURE OF MEDICAL PHYSICS**

Carmel J. CARUANA

Medical Physics, Faculty of Health Sciences, University of Malta  
carmel.j.caruana@um.edu.mt

**Abstract:** In times of rapid change, inter-professional competition, austerity economics and commoditization, strategic leadership is critical for all professions; more so for small professions such as Medical Physics. Notwithstanding this, a comprehensive search regarding leadership in Pubmed resulted in only 3 relevant hits for Medical Physics as opposed to 2590 for the Medical profession. Medical Physicists give little attention to strategic leadership and this needs to change if the profession is to move forward – indeed survive.

**Keywords:** strategic leadership, medical physics, leadership roles.

### **1. Introduction**

In a world of rapid change, inter-professional competition, austerity economics and sometimes unbridled commoditization, strategic leadership has become crucial for all professions and even more for small professions such as Medical Physics.

### **2. Literature review**

A comprehensive search regarding medical physics leadership carried out via Pubmed and Google in November 2020 led to the conclusion that Medical Physicists give too little attention to leadership when compared to the Medical profession. Indeed using the searchwords ‘leadership medical physics’ vs ‘leadership medical’ in title in Pubmed resulted in only 7 hits for Medical Physics (3 relevant) as opposed to 2590 for Medical. Using ‘strategic planning medical physics’ vs ‘strategic planning medical’ resulted in only 1 hit for Medical Physics and 232 for Medical. Total number of relevant articles for Medical Physics leadership in Pubmed were only four[1-4]. The first article discussed whether an MBA is needed for Medical Physics leadership roles; the second described an international online medical physics mentoring programme; the third discussed leadership in the ambit of redefining and reinvigorating the role of physics in clinical medicine in

the US whilst the last was a point-counterpoint discussion for and against the introduction of subjects such as strategic planning, extra-disciplinary communication, and management in the medical physics curriculum. A book on strategic leadership for Medical Physicists was published in 2020 Fig. 1 [5]. A comprehensive module on leadership has been offered biannually by the EUTEMPE consortium in Europe (Fig. 2) over the last 6 years and is based on real world leadership case studies[6]. The AAPM organizes an annual meeting and sometimes a summer school through its leadership academy[7]. Using the searchword ‘leadership’ in the AAPM Virtual Library again in November 2020 led to 47 presentations but few were relevant to strategic leadership. However, it is very significant to note that the AAPM leadership academy has since taken proactive steps to raise its profile and also promote the use of real world case studies as in the case of the EFOMP-EUTEMPE module mentioned earlier [8-12]. The Medical Physics Leadership and Mentoring group has developed some resources [13].

### **3. Effects of absence of strategic leadership**

The lack of attention to strategic leadership over the past years have had their undesirable effects. Other professions have sought to expand their own role at the expense of ours. A case in point is the role of Radiation Protection Expert which in some countries is being lost to other professions which are much less competent than we are in the subject and who have qualifications lower than those recommended by ENETRAP [14] and IRPA [15] (which both insist on Radiation Protection Experts having a first degree in either radiation protection or physics/engineering/mathematics). However, all is not lost provided we move fast and take the necessary actions *in a proactive manner as opposed to reacting to events as they unfold*.

### **4. Conclusions**

Medical Physicists give little attention to strategic leadership and this needs to change if the profession is to



move forward - indeed survive. We need to ensure that both the present generation of Medical Physics leaders as well as the next generation of young leaders are *intrinsically both scientific and strategic leaders*. We need to include leadership in our curricula starting at an early level. The profession also needs to invest time in developing learning resources in strategic leadership specifically targeted to Medical Physicists.

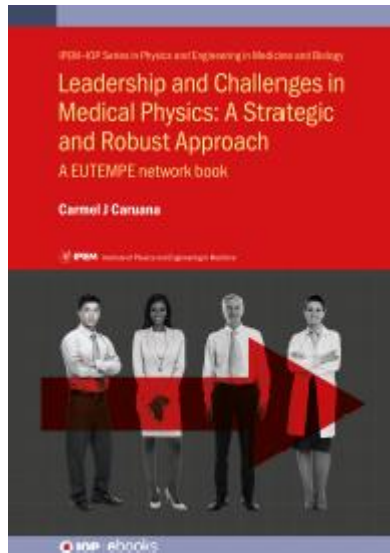


**Fig. 1.** Cover of the only book in strategic leadership for Medical Physicists



**Fig. 2.** The EFOMP-EUTEMPE module in leadership for Medical Physicists. The next run of the module which will be held in Oct 2022 – Feb 2023 will include leadership for all specialties of Medical Physics.

## 5. References

- Burinskiene Gutierrez AN et al. MBA degree is needed for leadership roles in Medical Physics profession. J Appl Clin Med Phys. 2017;6:6-9.
- Santos JC et al. Leadership and mentoring in medical physics: The experience of a medical physics international mentoring program. Phys Med. 2020;76:337-344.
- Samei E et al. Redefining and reinvigorating the role of physics in clinical medicine: A Report from the AAPM Medical Physics 3.0 Ad Hoc Committee. Med Phys. 2018 Jul 10.
- Caruana CJ et al. Subjects such as strategic planning, extra-disciplinary communication, and management have become crucial to medical physics clinical practice and should become an integral part of the medical physics curriculum. Med Phys. 2017;44:3885-3887.
- Caruana CJ. Leadership and Challenges in Medical Physics: A Strategic and Robust Approach. A EUTEMPE network book. IOP Publishing 2020. <https://iopscience.iop.org/book/978-0-7503-1395-7>
- EUTEMPE consortium: Module MPE01 Leadership in Medical Physics, development of the professions and the challenges for the Medical Physics Expert <http://eutempe-net.eu/mpe01/>
- AAPM Medical Physics Leadership Academy [https://www.aapm.org/org/structure/?committee\\_code=MPLAWG](https://www.aapm.org/org/structure/?committee_code=MPLAWG)
- Gronberg M and Wang D. Introduction of Medical Physics Leadership Academy (MPLA) case studies. J Appl Clin Med Phys 2021; 22:3:287.
- Wang D, Kim L, Gronberg M, Stambaugh C. A brief guide to writing a medical physics leadership case. J Appl Clin Med Phys 2021; 22:3:285–286.
- Wang D, Meis G, Ellet W, Kim L. Stambaugh C, Gronberg M, Johnson J. MPLA Case 1: Implementing Cone-Beam CT in a Community Hospital. J Appl Clin Med Phys 2021; 22:3:246–250.
- Wang D, Meis G, Gronberg M, Stambaugh C, Kim L. MPLA Case 2: A junior physicist attempts to improve radiotherapy workflow. J Appl Clin Med Phys 2021; 22:3:251–253.
- Hendrickson K, Kim S, Stambaugh C, Gronberg M, Kim L, Wang D. MPLA Case 3: Don't criticize me in public! J Appl Clin M wileyonlinelibrary.com/journal/acm2 ed Phys. 2021;22:280–283.
- Medical Physics Leadership and Mentoring group. <https://medphysmentoring.wixsite.com/medphys-mentoring>  
[https://www.youtube.com/channel/UCPZJeXW-\\_pFfY-khOog3W3w](https://www.youtube.com/channel/UCPZJeXW-_pFfY-khOog3W3w)
- ENETRAP (2016). European Guidance on the Implementation of the Requirements of the Euratom BSS with respect to the Radiation Protection Expert and the Radiation Protection Officer. <http://euterp.eu/uploaditems/ENETRAPIII/ENETRAP-III-European-Guidance-Document-01-03-2016.pdf>
- IRPA guidance on certification of a Radiation Protection Expert (2016) [www.irpa.net/docs/IRPA%20Guidance%20on%20Certification%20of%20a%20RP%20Expert%20\(2016\).pdf](http://www.irpa.net/docs/IRPA%20Guidance%20on%20Certification%20of%20a%20RP%20Expert%20(2016).pdf)

## THE ADJUSTED EFFECTIVE DOSE ASSESSMENT FROM CT OF THE CHEST FOR PEDIATRIC PATIENTS: A HOSPITAL BASED STUDY

P.S. Druzhinina<sup>1</sup>, L.A. Chipiga<sup>1,2,3</sup>, A.V. Vodovatov<sup>1,4</sup>, A.V. Pozdnyakov<sup>4</sup>, Yu. N. Kapyrina<sup>4</sup>, D.O. Ivanov<sup>4</sup>, Yu. V. Petrenko<sup>4</sup>, V.G. Puzyrev<sup>4</sup>

<sup>1</sup>St-Petersburg Research Institute of Radiation Hygiene after professor P.V. Ramzaev, St-Petersburg, Russia; <sup>2</sup>A. Granov Russian Scientific Center of Radiology and Surgical Technologies, Saint-Petersburg, Russia; <sup>3</sup>V. Almazov National Medical Research Center, Saint-Petersburg, Russia; <sup>4</sup>St. Petersburg State Pediatric Medical University, St-Petersburg, Russia

<sup>1</sup>Corresponding author: druzhininapauline@gmail.com

**Abstract:** Computed tomography is associated with high patient doses. CT is actively used in pediatric diagnostics, however, currently, there is no reliable data on the pediatric patient doses in the Russian Federation. The current study presents the data on the assessment of the effective doses for 5, 10, and 15-year-old pediatric patients from CT examinations of the chest. Data was collected in a major university hospital in St. Petersburg.

**Keywords:** computed tomography, pediatric patients, effective dose

### 1. Introduction

Today, computed tomography (CT) is one of the most informative methods of X-ray diagnostics, generally used for diagnostic of both adult and pediatric patients. CT is associated with significant individual patient doses [1]. In the Russian Federation, the number of CT-examinations increases every year, with a proportional increase in the collective dose.

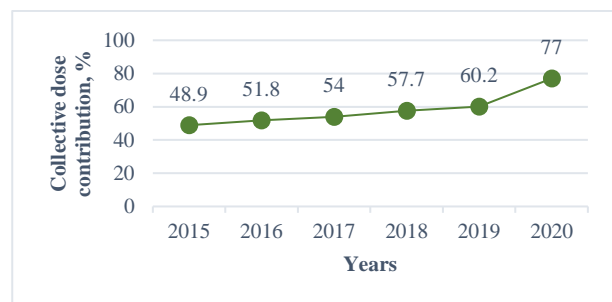


**Fig. 1.** Contribution of CT to the collective dose of the population of the Russian Federation from all types of medical exposure according to the 3-DOZ form

In addition, in the context of a pandemic of a novel coronavirus infection (COVID-19), due to insufficient sensitivity of laboratory diagnostic methods, computed

tomography became the main method of early and primary diagnosis of COVID-19 in the Russian Federation, including pediatrics.

At the same time, there is no reliable information on the exposure levels of pediatric patients in the Russian Federation. In the 3-DOZ form of the ESKID system, which is the only centralized source of information on patient doses, it does not specifically account for the X-ray examinations of children [2]. There are almost no publications focused on the evaluation of the Russian doses in pediatric radiology, including CT.

In the international practice, special attention is focused on the radiation protection of pediatric patients during CT examinations, including the collection and analysis of data on the levels of exposure, the assessment of typical doses of pediatric patients, the establishment and the use of reference diagnostic levels as an optimization tool [3-8, 14-18]. This attention is explained by the fact that children are the most sensitive group to the effects of ionizing radiation [5].

Despite the fact that in international practice it is CTDI<sub>vol</sub> and DLP values that are commonly used for the assessment of the patient dose, in this study, the effective doses were calculated, since in the Russian Federation the patient doses are expressed in this value. Modern CT scanners are equipped with automatic tube current modulation programs. These programs determine the tube current and, as a result, the patient dose, depending on the thickness and density of the scanned area. One of the features of the assessment of pediatric doses is a wide range of their anthropometric characteristics (height, body mass, physique, and other derived indicators), which determine the variability of doses for individual patients.

The aim of the study was to evaluate the effective doses of 5-, 10- and 15-year-old children, considering their anthropometric characteristics, during chest CT examinations for the period from January to December



2020 on the base of the major St. Petersburg university hospital.

## 2. Materials and methods

The data for the study was collected on the base of the CT department of the St. Petersburg State Pediatric Medical University.

For the period from January to December 2020 data was collected on 79 CT-examinations of the chest without contrast, performed for three groups of children with an average age: 5, 10, and 15 years. This sample was randomly selected from the general array of children who underwent CT-examinations during this period. The distribution of the sample of patients by age is presented in Table 1.

**Table 1.** The number of patients participating in the study

Age range	Age group	The number of patients
2-6	5	19
7-11	10	34
12-16	15	26

All examinations were performed on a Brilliance eCT System computed tomograph (Philips Medical Systems, USA, year of manufacture – 2011).

The following characteristics were collected for each patient: age (years), height (cm), body mass (kg). Additionally, the anterior-posterior and lateral body dimensions were determined. The calculation of the effective diameters of the patients was performed using the expression 1.

$$d_{eff} = \sqrt{AP \times LAT}, \text{ cm (1)}$$

where, AP - anterior-posterior patient body size, cm; LAT - lateral patient body size, cm [4].

Anterior-posterior and lateral patient body size measurements were performed using the Philips CT workstation software. Body dimensions were measured on a slice corresponding to the middle part of the sternum by analyzing the patient medical records.

The parameters of the CT examinations were collected by direct registration from the CT console, as well as by the data extracted from DICOM images with preliminary anonymization. For each CT examination, the following parameters were collected: scan length (cm), and volume computed tomographic dose index (CTDI<sub>vol</sub>, mGy) considering tube current modulation for each patient.

Several protocols were used for chest scans in the CT department. The standard parameters of the protocols are presented in Table 2.

Calculation of the adjusted effective doses of pediatric patients considered body mass and height using the specialized software NCICT 3.0 [11-13].

This software allows calculating the absorbed doses in organs and the effective dose, considering the specifics of the CT scanner model based on the examination parameters. It should be noted that this effective dose does not correspond to the ICRP definition and is a

value that depends on the gender, body mass and height of the patient [11-13]. Moreover, this software does not consider the dose to the lymphatic system.

**Table 2.** Standard CT scan protocol parameters

Protocol	Chest Low Dose	Child Chest 20-30kg	Chest Standard	Child Chest 40-50kg	Child Chest 30-40kg
Scan type	Helical	Helical	Helical	Helical	Helical
Collimation n, mm	64x0, 625	64x0, 625	64x0, 625	64x0, 625	64x0, 625
Pitch, rel.un.	1,49	1,575	0,797	1,49	1
Rotation time, s	0,4	0,4	0,75	0,4	0,4
Scan time, s	3	1,6	9,8	1,7	2,5
Voltage, kV	120	100	120	120	100
Exposition, mAs	64	84	159	104	158

To calculate the adjusted individual effective doses, a phantom was selected for each patient that corresponded to his gender and was the closest to his anthropometric data; the model of the computed tomography scanner and such parameters of the examination as CTDI<sub>vol</sub> and scan length were also considered.

Statistical data processing was performed using Statistica 12.0 and Microsoft Excel software.

## 3. Results

The results of the calculated effective diameter distribution of the surveyed age groups are presented in Figure 1.

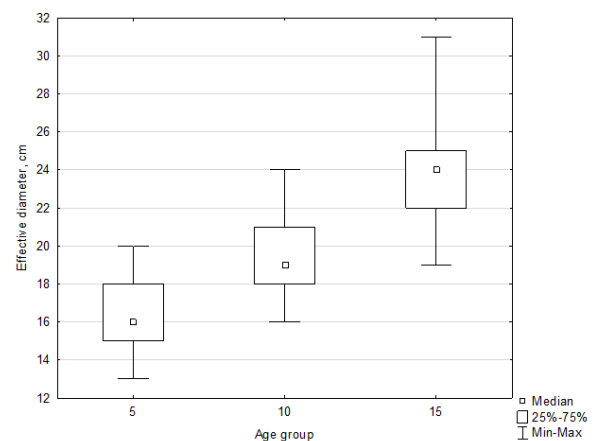


**Fig. 1.** Distribution of calculated effective diameters in the studied age groups. Results are presented in the format: median ± 25% -75%-percentiles (minimum-maximum)

The distribution of parameters of effective doses of chest CT examination is presented in table 2. The results of the study show that for 5-year-old children the effective doses are minimal and are lower than the effective doses for other age categories (10-year-old up to a factor of 1,5 and 15-year-old up to a factor of 2).

Effective doses for 10- and 15-year-old children differ for 22%.

**Table 2.** Distribution of parameters of effective doses of chest CT examination. Descriptive statistics are presented in the format: median  $\pm$  standard deviation, (minimum-maximum)

Age group	$E_{NCICT}$ , mSv
5-year-old	2,8 $\pm$ 1,3 (0,8-5,6)
10-year-old	5,1 $\pm$ 1,2 (2,1-7,4)
15-year-old	6,3 $\pm$ 1,8 (1,7-10,4)

#### 4. Discussion

The typical (median) local doses in a facility for chest CT-examinations were: 5-year old – 2,8 mSv; 10-year old – 5,1 mSv; 15-year-old – 6,3 mSv.

The results show that the effective dose depends on the patient age - the lowest is observed in children with an average age of 5- years, the highest is observed in children with an average age of 15-years. This is due to the fact that children in each age group differ in chest thickness. Figure 1 shows that the effective diameter is directly proportional to the age group. Thus, an increase in the thickness and density of the scanned area leads to an increase in tube current and an increase in  $CTDI_{vol}$  and patient effective dose.

A comparison of the typical effective doses of CT examination of chest with data from foreign sources was carried out. The comparison results are presented in the table 3.

**Table 3.** The comparison of the typical effective dose values with foreign data of chest CT examinations

Age	Foreign data					Collected data*
	[21] 2017	[22]** 2012	[17]* 2016	[18] 2017	[20] 2014	$E_{NCICT}$ , mSv
5	0,8 $\pm$ 0,4	1,8-13,0	6,4	1,0	128-slices: 0,61 $\pm$ 0,32 64-slices: 1,24 $\pm$ 0,97 Others: 2,56 $\pm$ 1,98	2,8
10	-		-	1,0	-	5,1
15	-		-	3,3	-	6,3

\*For western CT manufacturer

\*\*There was no information about division by age

The comparison of the results shows that in foreign practice there are no differences between the effective doses for different age categories of children. At the same time, there are significant (up to a factor of 7) differences between the effective doses for the same age category between different sources, which indicates the use of different CT scanning protocols and the lack of harmonization of practices.

Comparing patient doses between different CT departments and medical facilities, it is necessary to consider the differences in medical practices - different models and year of manufacture of computed tomographs, different parameters of the scanning

protocols, the use of programs for automatic modulation of the tube current. In addition, it is also necessary to consider the differences in the body size of the patients. All of these factors affect the patient dose.

Difficulties in assessing the children doses can also be associated with the large number of scanning protocols with different parameters and, simultaneously, lack of standardization of their use in specific clinical cases. For example, children with similar anthropometric characteristics and similar clinical cases can be scanned on different protocols, and as a result, the doses can vary.

To ensure the radiation protection of pediatric patients, it is necessary to use the principle of optimization of CT examinations. It requires a revision of all CT scan protocols. It is important to determine the specific parameters for a particular tomography scanner, which provide the minimum dose to the patient and required quality of the CT image. Moreover, over time, more and more modern scanning protocols appear (including for children) which allow reducing the patient dose.

#### 5. Conclusions

1. The typical local doses in a facility for chest CT-examinations without contrast are: 5-year old – 2,8 mSv; 10-year old – 5,1 mSv; 15-year-old – 6,3 mSv.

2. The patient dose depends both on the physical and technical characteristics of the equipment (CT model, parameters of the scanning protocols, the availability of programs for automatic modulation tube current), and on the anthropometric characteristics of the patients (the thickness of the scanned area). All of these parameters must be considered for calculating doses for pediatric patients.

3. To ensure the radiation protection of pediatric patients, it is necessary to use the principle of optimization of CT examinations. It requires a revision of all CT scan protocols. It is important to determine the specific parameters for a particular tomography scanner, which provide the minimum dose to the patient and required quality of the CT image.

#### Acknowledgements

The authors would like to thank the medical staff of the CT department of the St. Petersburg State Pediatric Medical University for the support in the data collection.

#### 6. References

1. Druzhinina P.S. Proposals for the Russian quality assurance program in computed tomography/Druzhinina P.S., Chipiga L.A., Ryzhov S.A., Vodovatov A.V., Berkovich G.V., Smirnov A.V., Yaryna D.V., Ermolina E.P., Druzhinina U.V.// Radiatsionnaya Gygiena = Radiation Hygiene.
2. Filling of the Federal state statistical surveillance form No. 3-DOZ. Methodical recommendations the provision of the radiation safety. Approved by the Federal Service for Surveillance on Human Well-being and Consumer Rights Protection on February 16, 2007, No. 0100 / 1659-07-26 (In Russ.)
3. Ranish Deedar Ali Khawaja. Simplifying Size-Specific Radiation Dose Estimates in Pediatric CT/ Ranish Deedar

- Ali Khawaja, Sarabjeet Singh, Beth Vettiyl, Ruth Lim, Michael Gee, Sjirk Westra, Mannudeep K. Kalra//AJR – 2015. – V.204. – 167-177p.
4. The American Association of Physicists in Medicine. Size-Specific Dose Estimates (SSDE) in Pediatric and Adult Body CT Examinations/ American Association of Physicists in Medicine//AAPM Report No 204. – 2011. – 30p.
5. The International Commission on Radiological Protection. Diagnostic Reference Levels in Medical Imaging/ICRP/ICRP PUBLICATION 135. Ann. ICRP 46(1). – 2017. – 140p.
6. Neige M Y Journy. Individual radiation exposure from computed tomography: a survey of paediatric practice in French university hospitals, 2010-2013/Neige M Y Journy , Serge Dreuil , Nathalie Boddaert , Jean-François Chateil, Didier Defez, Hubert Ducou-le-Pointe , Jean-Marc Garcier, Joël Guersen , Bouchra Habib Geryes , Andreas Jahnen , Choonsik Lee , Jacqueline Payen-de-la-Garanderie , Jean-Pierre Pracros , Dominique Sirinelli, Isabelle Thierry-Chef , Marie-Odile Bernier// Eur Radiol. - 2018 Feb;28(2):630-641. Doi: 10.1007/s00330-017-5001-y.
7. David Célier. Multicentre survey on patient dose in paediatric imaging and proposal for updated diagnostic reference levels for France. Part 1: computed tomography/David Célier, Patrice Roch , Cécile Etard , Hubert Ducou Le Pointe, Hervé J Brisse// Eur Radiol. - 2020 Feb;30(2):1156-1165. Doi: 10.1007/s00330-019-06405-3.
8. J Vassileva. A study to establish international diagnostic reference levels for paediatric computed tomography/J Vassileva, M Rehani , D Kostova-Lefterova , H M Al-Naemi , J S Al Suwaidi, D Arandjic, E H O Bashier, S Kodlulovich Renha, L El-Nachef , J G Aguilar, V Gershan , E Gershkevitch, E Gruppeta , A Hustuc , A Jauhari , Mohammad Hassan Kharita , N Khelassi-Toutaoui , H R Khosravi, H Khoury, I Kralik , S Mahere, J Mazuoliene, P Mora, W Muhogora , P Muthuvelu, D Nikodemova, L Novak, A Pallewatte, D Pekarović , M Shaaban, E Shelly , K Stepanyan , N Thelsy , P Visrutaratna , A Zaman// Radiat Prot Dosimetry - 2015 Jul;165(1-4):70-80. Doi: 10.1093/rpd/ncv116.
9. Keith J Strauss. Radiation Dose for Pediatric CT: Comparison of Pediatric versus Adult Imaging Facilities/Keith J Strauss, Elanchezhian Somasundaram, Debapriya Sengupta , Jennifer R Marin , Samuel L Brady// Radiology - 2019 Apr;291(1):158-167. Doi: 10.1148/radiol.2019181753.
10. D Jackson. Paediatric CT dose: a multicentre audit of subspecialty practice in Australia and New Zealand/D Jackson, K Atkin, F Bettenay, J Clark, M R Ditchfield , J E Grimm, R Linke, G Long, E Onikul, J Pereira, M Phillips, F Wilson , E Paul , S K Goergen// Eur Radiol. - 2015 Nov;25(11):3109-22. Doi: 10.1007/s00330-015-3727-y.
11. Choonsik Lee. NCICT: a computational solution to estimate organ doses for pediatric and adult patients undergoing CT scans/Choonsik Lee, Kwang Pyo Kim, Wesley E Bolch, Brian E Moroz, Les Folio// J Radiol Prot - 2015 Dec;35(4):891-909. Doi: 10.1088/0952-4746/35/4/891
12. Choonsik Lee. NCICT: user manual – 6p.
13. National Cancer Institute - [On-line resource]: - Available from: <https://ncidose.cancer.gov> Last accessed: 26.07.2021
14. Yuta Matsunaga. Effective radiation doses of CT examinations in Japan: a nationwide questionnaire-based study/Yuta Matsunaga, Ai Kawaguchi, Kenichi Kobayashi, Masanao Kobayashi, Yasuki Asada , Kazuyuki Minami, Shoichi Suzuki, Koichi Chida// Br J Radiol. - 2016. - ;89(1058):20150671 Doi: 10.1259/bjr.20150671
15. Jonina Gudjonsdottir . Effective dose from pediatric CT in Iceland/Jonina Gudjonsdottir, Arna Bjork Jonsdottir// Laeknabladid - 2017 Nov;103(11):489-492. Doi: 10.17992/lbl.2017.11.160.
16. C. Mordacq. Chest computed tomography in children: indications, efficiency and effective dose/C Mordacq, A Deschildre, L Petyt, T Santangelo, C Delvart, C Doan, C Thumerelle// Arch Pediatr. - 2014 Mar;21(3):279-86. Doi: 10.1016/j.arcped.2013.12.021.
17. Hideki Obara, Midori Takahashi, Kazuya Kudou, Yasushi Mariya, Yoshihiro Takai, Ikuo Kashiwakura. Estimation of effective doses in pediatric X-ray computed tomography examination// Exp Ther Med – 2017 Nov;14(5):4515-4520. doi:10.3892/etm.2017.5102
18. Z. Brady. Assessment of paediatric CT dose indicators for the purpose of optimization/Z Brady, F Ramanauskas, T M Cain, P N Johnston//Br J Radiol. – 2012. - Nov;85(1019):1488-98. Doi: 10.1259/bjr/28015185.

**ASSESSMENT OF THE CHANGES IN STRUCTURE OF X-RAY  
DIAGNOSTICS AND COLLECTIVE DOSE FROM CT EXAMINATIONS  
RELATED TO COVID-19 IN THE RUSSIAN FEDERATION IN 2020**

Aleksandr VODOVATOV<sup>1,2</sup>, Ivan ROMANOVICH<sup>1</sup>, Sergey RYZHOV<sup>3,4</sup>, Larisa CHIPIGA<sup>1,5,6</sup>, Gleb  
BERKOVICH<sup>5</sup>, Artem BIBLIN<sup>1</sup>

<sup>1</sup>St-Petersburg Research Institute of Radiation Hygiene after prof. P.V. Ramzaev; <sup>2</sup>St-Petersburg State Pediatric  
Medical University; <sup>3</sup>Dmitry Rogachev National Medical Research Center of Pediatric  
Hematology, Oncology, and Immunology, <sup>4</sup>Research and Practice Center of Diagnostics and Telemedicine  
Technologies, <sup>5</sup>V. Almazov National Medical Research Center, <sup>6</sup>A. Granov Russian Scientific Center of Radiology and  
Surgical Technologies  
<sup>1</sup>vodovattoff@gmail.com

**Abstract:** The pandemic of COVID-19 and the corresponding transformation of the Russian healthcare system had a significant impact on X-ray and nuclear medicine diagnostics in 2020. A reduction of 10-30% could be observed for all imaging modalities, both in the number of examinations and corresponding collective dose. Computed tomography is an exception, increasing by 60% in number and by 81% in collective dose. The previous estimates of the changes in the collective dose from CT examinations correlate well with the results.

**Keywords:** COVID-19, medical exposure, X-ray diagnostics, collective dose, computed tomography

### **1. Introduction**

The novel coronavirus infection (COVID-19) is an infectious disease caused by the SARS-CoV-2 virus [1]. At the current moment, the virus has spread to almost all countries of the world. As of August 22, 2021, in the Russian Federation, the coronavirus infection has been detected in more than 6.7 million people, more than 176 thousand people have died already [1].

The use of computed tomography (CT) for the diagnostics of COVID-19 has been widely discussed within the medical community. Initially, there were several points of view on the applicability of diagnostic imaging modalities, ranging from the use of CT scan for screening of the disease to the use of CT only for confirmed cases of COVID-19 [2]. However, due to the availability, high diagnostic informativity, non-invasiveness, and fast speed, CT scan became the indispensable diagnostic method for the early and initial diagnosis of COVID-19 in the Russian Federation.

The widespread application of CT for COVID-19 diagnostics was associated with various issues connected to radiation protection and risk communication. Rapidly increasing number of CT examinations in hospitals and even in outpatient facilities, lack of general opinion on the frequency of CT scans during the treatment period, referral of CT scans of the chest even for the representatives of risk groups (i.e. pregnant women) lead to the increased public anxiety. Unfortunately, no data on patient doses was available from the hospitals, leading to the overestimation of the radiation risks from CT by the public.

The patient dose data collection in the Russian Federation is performed on an annual basis using state statistical data collection systems, using statistical form №3-DOZ [3] (a part of Joint governmental system of control and accounting of the individual doses of the citizens) and radiation-hygienic passports [4]. However, these forms are filled in and collected on an annual basis, hence not allowing operative patient dose data acquisition. Additionally, doses are averaged per medical facility, and the data on typical patient doses is unavailable.

Considering the lack of reliable information on the changes in the structure of X-ray diagnostics and collective doses from medical exposure, in the summer of 2020, the Institute of Radiation Hygiene in collaboration with local radiation protection and healthcare authorities as well as with several major hospitals. The results were published as a preprint [5].

At the current time, all the statistics on the structure and collective doses from medical exposure for 2020 have been collected. Hence it is important to assess the changes between these indicators between 2019 and

2020, considering the overall trends of the development of radiology in the Russian Federation.

The aim of the current study was to perform the assessment of changes in the structure of the X-ray diagnostics and collective dose from medical exposure in the Russian Federation in 2019-2020 (during the COVID pandemic).

## 2. Materials and methods

The study was based on the data from state statistical dose data collection form: №3-DOZ "Data on the patient doses from X-ray examinations. Form №3-DOZ contains the data on the collective doses from medical exposure and number of the examinations for the following imaging modalities: fluorography (chest screening), radiography, fluoroscopy, computed tomography, interventional examinations, diagnostic nuclear medicine examinations and "other" (everything that did not fit into other categories, i.e. bone densitometry). Data was taken from the federal dose databank of the Joint system of the control and accounting of the individual doses of the citizens hosted by the Institute of Radiation Hygiene for the 2015-2020 period for all 85 regions of the Russian Federation [3,4]. For the simplicity of the data processing, digital and analogue fluorography and radiography examinations were merged.

To assess the changes in the structure of the X-ray diagnostics and collective dose from medical exposure in each of the regions of the Russian Federation, data from Form #3-DOZ was processed using the following steps:

- Estimation of the number of X-ray and nuclear medicine examinations in each of 85 regions of the Russian Federation for each year for each imaging modality;
- Estimation of the collective dose from X-ray and nuclear medicine examinations in each of 85 regions of the Russian Federation for each year for each imaging modality;
- Calculation of the increment rates for the number and collective dose from X-ray and nuclear medicine examinations for each region of the Russian Federation for each year for each imaging modality using Equations 1 and 2 respectively:

$$\Delta_{N,i,k} = \frac{N_{i,k} - N_{i,k-1}}{N_{i,k-1}} \times 100\% \quad (1)$$

$$\Delta_{E,i,k} = \frac{E_{i,k} - E_{i,k-1}}{E_{i,k-1}} \times 100\% \quad (2)$$

where:

N – total number of X-ray or nuclear medicine examinations from the imaging modality I for the year k (2016, 2017, 2018, 2019 and 2020), examinations;

E – total collective dose from X-ray or nuclear medicine examinations from the imaging modality I for the year k (2016, 2017, 2018, 2019 and 2020), man -Sv;

$\Delta_{N,i,k}$  – increment rate of the number of examinations for imaging modality I for the year k (2016, 2017, 2018, 2019 and 2020), %;

$\Delta_{E,i,k}$  – increment rate of the collective dose for imaging modality I for the year k (2016, 2017, 2018, 2019 and 2020), %.

- Calculation of the average increment rate for the number and collective dose from X-ray and nuclear medicine examinations for each region of the Russian Federation for 2015-2019 for each imaging modality using Equations 3 and 4 respectively:

$$\Delta_{N,avg,i} = \frac{\sum_{2016}^{2019} \Delta_{N,i,k}}{4} \quad (3)$$

$$\Delta_{E,avg,i} = \frac{\sum_{2016}^{2019} \Delta_{E,i,k}}{4} \quad (4)$$

where:

$\Delta_{N,avg,i}$  – average increment rate of the number of examinations for imaging modality I for the four time intervals (2015/2016, 2016/2017, 2017/2018 and 2018/2019), %

$\Delta_{E,avg,i}$  – average increment rate of the collective dose for imaging modality I for the four time intervals (2015/2016, 2016/2017, 2017/2018 and 2018/2019), %

- Correction of the changes in the number and collective doses from X-ray and nuclear medicine examinations for each imaging modality for each of 85 regions of the Russian Federation for the 2019/2020 period considering average increment rate for the last four years using Equations 5 and 6 respectively:

$$\Delta_{N,i,adj}^{2020} = \Delta_{N,i,2020} - \Delta_{N,avg,i} \quad (5)$$

$$\Delta_{E,i,adj}^{2020} = \Delta_{E,i,2020} - \Delta_{E,avg,i} \quad (6)$$

where:

$\Delta_{N,i,adj}^{2020}$  – change in the number of the examinations from imaging modality I in 2020 compared to 2019, adjusted considering the average increment rate in 2015-2019, %;

$\Delta_{E,i,adj}^{2020}$  – change in the collective dose from imaging modality I in 2020 compared to 2019, adjusted considering the average increment rate in 2015-2019, %;

All results were processed to exclude missing or biased data. The following exclusion criteria for the biased data were established:

- Lack of data on the number of examinations or collective dose for the selected imaging modality for one of the surveyed years;
- Increase or decrease in the number of examinations or collective dose from the selected imaging modalities exceeding 500% for one of the surveyed years;

Changes in the number of examinations and collective dose from the selected imaging modalities for the Russian Federation were calculated as mean values for the sample of 85 regions for each parameter.

Descriptive statistics were generated using Statistica 10 software. Comparison between samples was performed using the Mann-Whitney test. Relations between the assessed parameters were estimated using regression analysis. Results were considered significant with  $p < 0.05$ .

### 3. Results and discussion

Data on the changes in the number of the X-ray and nuclear medicine examinations and collective dose from medical exposure as well as the increment rates for the selected imaging modalities are presented in tables 1-2 and 3-4, respectively.

**Table 1.** Changes in the number of X-ray and nuclear medicine examinations in the 2019/2020 period

Imaging modality	Number of X-ray and nuclear medicine examinations, thousands	
	2020	2019
Fluorography	72367	85706
Radiography	161861	190752
Fluoroscopy	999	1548
Computed tomography	2929	1724
Interventional examinations	1327	2291
Nuclear medicine	549	583
Other	247	183
Total	240280	282787

**Table 2.** Increment rates for X-ray and nuclear medicine examinations in the 2019/2020 period

Imaging modality	Increment rate, %	Increment rate adjusted by the 2015-2019 trends, %
Fluorography	-17.2	-18.0
Radiography	-15.5	-18.5
Fluoroscopy	-32.4	-28.5
Computed tomography	+60.5	+43.0
Interventional examinations	-23.9	-34.5
Nuclear medicine	-9.5	-16.3
Other	-2.5	+11.3
Total	-12.9	-15.4

**Table 3.** Changes in the collective dose from medical exposure in the 2019/2020 period

Imaging modality	Collective dose, man - Sv	
	2020	2019
Fluorography	4298	5318
Radiography	12106	16677
Fluoroscopy	2690	4069
Computed tomography	85075	49766
Interventional examinations	6847	8584
Nuclear medicine	3666	288
Other	183	3083
Total	114865	87785

**Table 4.** Increment rates for collective dose from medical exposure for the 2019/2020 period

Imaging modality	Increment rate, %	Increment rate adjusted by the 2015-2019 trends, %
Fluorography	-18.7	-15.6
Radiography	-28.1	-25.8
Fluoroscopy	-31.7	-28.4
Computed tomography	+81.0	+63.5
Interventional examinations	-18.3	-35.4
Nuclear medicine	11.4	-10.4
Other	-32.8	-27.6
Total	+37.1	+31.0

It is visible from tables 1-4 that during the pandemic of COVID-19 both structure of X-ray diagnostics and collective dose from medical exposure has undergone significant changes. The number of all X-ray examinations has decreased by 20% on average, varying from 10% for nuclear medicine, to almost 30% for fluoroscopy. Only computed tomography has undergone a significant boost, increasing up to 60%. That can be explained by several factors:

- Transformation of general practice hospitals into COVID hospitals;
- Reduction of diagnostics, including radiology, during the lockdown periods;
- Increase in the number of operating CT units and departments.

First two factors were deciding for the first wave (March-July) of coronavirus, when the healthcare system was 'mobilized' for the COVID epidemics, with the subsequent negative impact on the provision of healthcare for non-infected patients. The majority of the hospitals were closed down for the quarantine, accepting only emergency patients, or transformed into COVID treatment centers. All planned treatment was postponed. Later, during the second wave, a more balanced approach was applied, with the establishment of dedicated COVID treatment centers and/or departments. Hence, major hospitals returned to normal functioning, but the number of X-ray examinations nevertheless has decreased.

It should be noted that the lowest reduction in number was observed for nuclear medicine examinations. That can be explained by the fact that in the Russian Federation they are mainly performed for oncology patients. Diagnostics and treatment of such patients received the least impact from COVID pandemics.

Correction of the changes in the number of X-ray examinations by the 2015-2019 trends does not significantly change the results, except for CT. Increase in the number of CT examinations becomes less pronounced (43% compared to 60%). The changes in the total number of X-ray and nuclear medicine examinations are equal to -15% (from 283 million

examinations in 2019 to 240 million examinations in 2020).

The similar situation can be observed for the collective dose from medical exposure. However, the increase of the collective dose from CT examinations is more significant (81% unadjusted, 64% adjusted by the 2015-2019 trends). It should be noted that the decrease in the number of nuclear medicine examinations is accompanied by the increase in the collective dose (11%), indicating the increasing contribution of high dose procedures, mainly PET/CT. Total increase of the collective dose from medical exposure is equal to 37%, mainly due to the increased contribution of CT examinations.

It is interesting to compare the actual changes in the collective dose from CT examinations with the estimates, calculated by the Institute of Radiation Hygiene in August 2020, based on the data collection in several representative hospitals and regions [5]. These estimates considered three basic scenarios for the Russian hospitals:

**Scenario 1. "Covid-19 hospital".** It corresponds to the transformation of general practice regional hospitals into hospitals for COVID-19 patients and emergency patients with various pathologies. In this scenario, it was assumed that the total number of CT examinations in the region has not been changed; the number of CT exams of all other anatomical areas (except for the chest) decreased by 80%. The released capacities were used for chest CT scans.

**Scenario 2. "Intense activity".** Corresponds to the medical facilities operating after the peak of COVID-19: the number of examinations remains the same as in 2019, except for chest CT scans. It was assumed that prior to each admission to the hospital or planned X-ray examination, a patient undergoes chest CT examination. The number of CT studies increases by the sum of all other CT exams.

**Scenario 3. "Combined".** A combination of scenario "Covid-19 hospital" for three quarters of the time with the scenario "Intensive activity" for one quarter. Comparison between these scenarios and the real data for the collective dose from CT examinations is presented on figure 1.

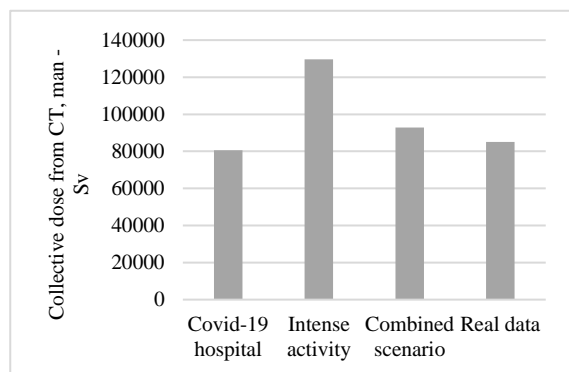


**Fig. 1.** Comparison between the estimated collective dose from CT examinations for three scenarios and real data.

It is visible from Figure 1 that the real collective dose from CT examinations is comparable with scenarios 1

and 3. Scenario 2, as it was mentioned before, is ultra-conservative and differs from the real data by 20%.

#### 4. Conclusions

The pandemic of COVID-19 and the corresponding transformation of the Russian healthcare system had a significant impact on X-ray and nuclear medicine diagnostics in 2020. A reduction of 10-30% can be observed for all imaging modalities, both in the number of examinations and corresponding collective dose. Computed tomography is an exception, increasing by 60% in number and by 81% in collective dose. The changes in the structure of X-ray and nuclear medicine diagnostics follow the trends for the last four years, however, these trends become more pronounced in the year of the pandemic. The results of the study indicate that the previous rough estimates of the changes in the collective dose from CT examinations were mostly accurate, allowing using the methods for such estimates in the future. The limitation of the current study is that it presents only general data, without a detailed evaluation of the changes in the structure of each imaging modality or dosimetry data. Such data will be processed and presented in future studies.

#### 5. References

1. Stopcoronavirus.RF. [On-line resource]: - Available from: <https://xn80aesfpebagmfbcl0a.xn-p1ai/> Last accessed: 07.09.2021
2. Interim guidelines for the prevention, diagnosis, and treatment of a new coronavirus infection (covid-19) Version 11 (07/05/2021) Ministry of Health of the Russian Federation [https://spbmia.ru/wp-content/uploads/2021/05/B%D0%9C%D0%A0\\_COVID-19.pdf](https://spbmia.ru/wp-content/uploads/2021/05/B%D0%9C%D0%A0_COVID-19.pdf) Last accessed: 07.09.2021
3. Methodical guidelines "Completion of the federal statistical surveillance form 3-DOZ". M., Rospotrebnadzor, 2014. 34 p.
4. Order of the Ministry of healthcare of the Russian Federation №298 "On the establishment of the Provision on the joint state system of the control and accounting of the individual doses of citizens". <https://docs.cntd.ru/document/901766853> Last accessed 07.09.2021
5. A.V. Vodovatov et.al. Preliminary assessment of structure and collective dose from CT examinations related to COVID-19 diagnostics in the Russian Federation in March - June 2020. medRxiv 2020.08.25.20181396; doi: <https://doi.org/10.1101/2020.08.25.20181396>



## **APPLICATION OF SUMMARY MEASURES OF POPULATION HEALTH TO RADIATION RISKS ASSESSMENT**

Leonid REPIN, Rustam AKHMATDINOV, Artem BIBLIN

St-Petersburg Research Institute of Radiation Hygiene after Professor P.V. Ramzaev, Mira st.8, 197101, St-Petersburg  
l.repin@niirg.ru

**Abstract:** The authors made an attempt to analyze the possibilities of using some generalized measures of public health for calculating radiation detriment, different from those used by the International Commission on Radiological Protection. The most promising approach is to use the Disability-Adjusted Life Years measure in calculating sex- and age-dependent measures of radiation detriment.

**Keywords:** radiation risk, detriment, DALY, Global Burden of Disease

### **1. Introduction**

One of the definitions of “risk” describes this concept as a combination of the probability and severity of a negative outcome. With regard to assessing the health risk associated with exposure to harmful environmental factors, this definition is transformed into “a combination of the probability of negative health consequences of exposure to a harmful factor, consider the severity of these consequences”. This understanding of risk is embedded in the radiation detriment measure developed by the International Commission on Radiological Protection (ICRP). However, the methodology used by the ICRP in calculating the severity of various diseases caused by exposure has a number of disadvantages, some of which are even pointed out by the authors of the methodology. One of the most significant limitations for the possibilities of wider application of radiation detriment is its unsuitability for solving the problems of comparative analysis of risks from various harmful environmental factors.

The use of integrated measures to quantify the negative impact of various environmental factors on the health of the population is important for solving many applied tasks in the field of ensuring life safety. Such tasks include, for example, justification of the levels of permissible exposure to harmful factors, solving problems of optimizing costs to ensure protection from the effects of such factors or minimizing the consequences of exposure, etc.

In the field of radiation protection, the value of radiation detriment developed by the International Commission on Radiological Protection [1-3] has been used as one of the main integrated measures for more than 30 years. Radiation detriment includes the total lifetime risk of oncological diseases of various localization and hereditary effects caused by exposure to ionizing radiation (in low doses and/or at low dose rates), while different weighting factors are used for different diseases, reflecting the “severity” of a given disease. The unit of detriment measure, to which all known possible negative consequences of radiation exposure for human health are given, is a fatal case of radiation-induced malignant neoplasm (MN), adjusted for an average reduction in life expectancy. Detriment per unit of radiation dose is calculated by the equation:

$$D_T = (R_{F,T} + q_T \times R_{NF,T}) \times L_T/L_C = \dots \\ \dots = (R_I \times k_T + q_T \times R_I \times (1 - k_T)) \times L_T/L_C \quad (1)$$

where the T indicates the localization of the MN (organ or tissue);  $D_T$  - radiation detriment to organ or tissue T;  $R_{F,T}$  is the probability of fatal radiation-induced cancer of localization T;  $R_{NF,T}$  - the probability of non-fatal radiation-induced cancer of localization T;  $R_I$  - the probability of morbidity to radiation-induced cancer of localization T;  $k_T$  is the mortality rate of MN of localization T;  $q_T$  is a weighting factor reflecting a reduced quality of life due to the occurrence of a non-fatal MN of localization T;  $L_T$  is the average number of years of life lost due to a malignant neoplasm of localization T;  $L_C$  is the average number of years of life lost due to the occurrence of radiation-induced MN of any location.

As can be seen from equation 1, one should not literally take a unit of detriment as one expected death from radiation-induced cancer.

The concept of “severity of the disease” usually implies an assessment of three components: the lethality fraction of disease, a reduction in life expectancy due to disease and reduced quality of life due to the presence of disease.

All three components of the concept of “severity” of a disease are not objectively determined universal constants - they can change over time and vary for different populations. This is primarily due to the improvement of diagnostic and treatment methods. In addition, this is due to an increasing average life expectancy of the population in developed countries. The magnitude of the radiation detriment of the ICRP is used primarily to substantiate the internationally recommended universal dose limits for exposure of the population and workers in various exposure situations and under various exposure scenarios.

When calculating the values of so-called “nominal risk coefficients” [4], medical and demographic data of various populations (including artificial “nominal population”) was used, and authors of some scientific publications periodically make attempts to apply the ICRP methodology to calculate risk coefficients using medical and demographic data of specific populations, including gender- and age-dependent radiation detriment coefficients. Much less frequent are publications devoted to the detriment assessment methodology itself [5-7].

One of the most difficult, controversial and of the greatest methodological interest is, from our point of view, the issue of assessing the “reduced quality of life” due to the occurrence of various diseases caused by the influence of a harmful factor.

The Research Institute of Radiation Hygiene currently solves the scientific task of the development of methodological approaches to assessing radiation detriment based on modern approaches to quantifying the severity of cancer<sup>1</sup>.

## 2. The ICRP approach to assessing quality of life reduction

The main approaches to the development of integral measures of health in relation to radiation exposure were formed in the 1970s and 1980s [1]. The methodology of calculation of weighting factors to consider the reduced quality of life because of the disease was developed at the same time and is now used by the ICRP in a slightly modified form:

$$q_T = q_{\min} + k_T \times (1 - q_{\min}), \quad (2)$$

where T indicates the localization of MN (organ or tissue);  $q_T$  is a weighting factor characterizing the reduction in quality of life due to the occurrence of a non-fatal MN of T localization;  $k_T$  is the fatality rate of a MN of T localization;  $q_{\min}$  is the minimum weighting factor for non-fatal cancers, whose value was expertly determined to be 0,1 for the vast majority of MN<sup>2</sup>. At the same time, the ICRP itself pointed out the fact that for all cancers, except breast and thyroid cancers, the

methodology is not sensitive even to a significant change in the  $q_{\min}$ .

As can be seen from the formula, the assessment of the “reduced quality of life” depends only on the mortality rate and the choice of the  $q_{\min}$  value.

That is, in fact, a reduction in the quality of life in connection with the disease essentially depends only on its mortality.

## 3. The World Health Organization approaches to assessing disease severity based on the Health-Related Quality of Life

Using the approach described above to assess impairment in disease-related quality of life, which did not involve a detailed consideration of the concept of “disease severity”, was justified in those years. However, actual scientific (medical, social, economic, etc.) understanding of the concept of “severity of the disease” and the huge amount of data accumulated to date in the framework of the Global Burden of Disease (GBD) project of the World Health Organization (WHO) [8], allows us to take a fresh look at the possibilities of a quantitative assessment of health detriment associated with exposure to harmful environmental factors.

Assessment of the severity of various diseases in estimating integral measures of population health has been used quite extensively in recent years. The sequential replacement of mortality-based measures by more informative that consider the years of healthy life lost in the population has provided an important opportunity to review and develop approaches to assessing radiation detriment (as well as the health harms associated with exposure to other environmental hazards) [4], [9].

One of the integral measures of population health that have become most widely used in recent years in various public health management tasks is the DALY<sup>3</sup> [10-13]. The general equation for calculating DALY is shown below:

$$DALY = YLL + YLD, \quad (3)$$

where:

YLL<sup>4</sup> – the number of years of life lost due to premature mortality, i.e. the number of years a person does not live to the age of life expectancy due to premature death caused by a disease; YLD<sup>5</sup> – number of years lived with a disability.

$$YLL = M \times LE, \quad (4)$$

where:

M – number of deaths due to disease;

LE – standard life expectancy at the age of death. The YLD is calculated using a formula with a weighting

<sup>1</sup> As models emerge that describe the probability of other diseases depending on the radiation dose (for example, diseases of the cardiovascular system), detriment can be easily modified to consider the severity of such diseases.

<sup>2</sup> This weighting factor is not used for skin cancer, because “radiogenic skin cancer is almost exclusively of the basal cell type which is usually associated with very little pain, suffering or treatment sequelae” [3]. For thyroid cancer the  $q_{\min}$  is set to 0,2.

<sup>3</sup> Disability-Adjusted Life Years

<sup>4</sup> Years of Life Lost

<sup>5</sup> Years Lived with Disability

factor that reflects the reduction in quality of life depending on the disease:

$$YLD = DW \times I \times DD, \quad (5)$$

where:

I – number of cases;

DD – the average length of disability due to the disease;

DW – the weighting factor attributed to the disease, reflecting the reduction in quality of life due to the disease.

The GBD project regularly publishes estimates of DALYs and DW rates for various diseases from national registers of almost two hundred WHO Member States [14-17].

The equation is not a strict mathematical formula and reflects only the concept of estimating an integral quantitative measure of disease severity. This is one of the advantages of using DALYs as an integral measure of radiation detriment. The DALY itself, or another measure estimated from it, is very convenient for comparative analysis of risks of different nature and lacks more of the limitations of the ICRP radiation detriment measure currently in use.

#### 4. Development of approaches to assessing radiation detriment

The international system for ensuring radiation protection is rather inert because any proposed changes and improvements should be the result of careful analysis. Their implementation should be justified from a practical point of view since any significant changes will inevitably require the retraining of a very large number of specialists around the world. In this regard, special attention should be paid to the possibility of a smooth and gradual introduction of any innovations. On the way from one measure to another, it is important to ensure the comparability of related measures.

Just one of the possible ways of developing the system of risk measures used in the field of radiation protection is discussed below.

With regard to the magnitude of radiation detriment, one of the possible approaches in the transition from the number of deaths in the population, as a unit of radiation detriment, to the number of healthy life years lost in the population, is to gradually change the methodology for assessing detriment.

For example, at the first stage, it is possible to replace the  $L_T$ ,  $L_C$  and  $k_T$  with estimates made on the basis of modern medical and demographic data, and use modern DW estimates instead of the  $q_T$ .

In parallel with the change of the nominal detriment coefficients, it is possible to revise the weighting factors for organs and tissues.

Preliminary calculations show that, if only  $q_T$  is changed to DW in the ICRP formula for the assessment of radiation detriment, the detriment thus calculated for the all population group would decrease from  $5,7 \cdot 10^{-2} \cdot Sv^{-1}$  to  $4,1 \cdot 10^{-2} \cdot Sv^{-1}$ . Weighting factors for organs and tissues would need to be revised.

When detriment is calculated using DW coefficients and up-to-date medical and demographic data for the

Russian population, the value of detriment would increase to  $6,1 \cdot 10^{-2} \cdot Sv^{-1}$ , but the weighting factors can remain unchanged.

The preliminary results obtained in the course of the study, as well as an analysis of the modern scientific publications literature, show the promise of research in the field of radiation detriment assessment, given the huge body of data accumulated over the last 25 years.

#### 5. Conclusions

As a part of a study currently being conducted at the St. Petersburg Research Institute of Radiation Hygiene, a methodology for calculating a new integral measure of radiation detriment is being developed. It is planned to assess the informativeness of the developed measure and its suitability for assessing risk in various exposure situations and under various exposure scenarios, including consider national medical and demographic data and with the possibility of calculating risk coefficients for different age and gender groups of the population.

#### 6. References

1. ICRP. Problems Involved in Developing an Index of Harm. ICRP Publication 27. Ann. ICRP 1 (4), 1977.
2. ICRP. Recommendations of the International Commission on Radiological Protection. ICRP Publication 60. Ann. ICRP 21(1-3), 1990
3. ICRP. The 2007 recommendations of the International Commission on Radiological Protection. ICRP Publication 103. Ann. ICRP 37 (2-4), 2007
4. Cléro E., Vaillant L., Hamada N., Zhang W., Preston D., Laurier D., Ban N., 2019. History of radiation detriment and its calculation methodology used in ICRP Publication 103. J. Radiol. Prot. 39 (3), R19–R36. doi:10.1088/1361-6498/ab294a.
5. Zhang W., Laurier D., Cléro E., Hamada N., Preston D., Vaillant L. & Ban N. Sensitivity analysis of parameters and methodological choices used in calculation of radiation detriment for solid cancer. International Journal of Radiation Biology, 2020. 96(5), 596-605.
6. Breckow J. Do we really need the “detriment” for radiation protection? Radiation and Environmental Biophysics, 2020. 59(3), 343-348.
7. Breckow J., Emami S., Amalhaf S., Beshgard A., Buermeyer J., Spruck K. Impact of updating the non-radiation parameters in the ICRP 103 detriment model. Radiation and environmental biophysics, 2018. 57(2), 89-98.
8. WHO. The Global Burden of Disease concept. [https://www.who.int/quantifying\\_ehimpacts/publications/en/9241546204chap3.pdf](https://www.who.int/quantifying_ehimpacts/publications/en/9241546204chap3.pdf)
9. Shimada K., Kai M. Calculating disability-adjusted life years (DALY) as a measure of excess cancer risk following radiation exposure. 2015. J Radiol Prot. 35 (4) 763–775
10. Gold M. R., Stevenson D., Fryback, D. G. (2002). HALYS and QALYS and DALYS, Oh My: similarities and differences in summary measures of population Health. Annual review of public health, 23(1), 115-134. doi: 10.1146/annurev.publhealth.23.100901.140513
11. Devleeschauwer B., Havelaar A. H., De Noordhout et al. DALY calculation in practice: a stepwise approach. 2014. International Journal of Public Health, 59(3), 571-574. doi: 10.1146/annurev.publhealth.23.100901.140513

12. Lajoie J. Understanding the Measurement of Global Burden of Disease, Prepared for the National Collaborating Centre for Infectious Diseases. (2015). [https://nccid.ca/wp-content/uploads/sites/2/2015/03/Global\\_Burden\\_Disease\\_Influenza\\_ENG.pdf](https://nccid.ca/wp-content/uploads/sites/2/2015/03/Global_Burden_Disease_Influenza_ENG.pdf)
13. David Kim, J.E., Disability Adjusted Life Years (DALY) Calculator: Methodology. 2018, Center for the Evaluation of Value and Risk in Health, Tufts Medical Center. [http://ghcearegistry.org/ghcearegistry/Calculator\\_Methodology.pdf](http://ghcearegistry.org/ghcearegistry/Calculator_Methodology.pdf)
14. WHO. The global burden of disease: 2004 update. 2008. [https://www.who.int/quantifying\\_ehimpacts/publications/en/9241546204chap3.pdf](https://www.who.int/quantifying_ehimpacts/publications/en/9241546204chap3.pdf)
15. Global Burden of Disease Cancer Collaboration. Global, Regional, and National Cancer Incidence, Mortality, Years of Life Lost, Years Lived With Disability, and Disability-Adjusted Life-years for 32 Cancer Groups, 1990 to 2015: A Systematic Analysis for the Global Burden of Disease Study. *JAMA Oncol.* 2017;3(4):524–548. doi:10.1001/jamaoncol.2016.5688
16. Salomon J.A., Haagsma J.A., Davis A. et al. Disability weights for the Global Burden of Disease 2013 study. 2015. *The Lancet Global Health*, 3(11), e712-e723. doi: 10.1016/S2214-109X(15)00069-8
17. Vos T., Lim S. S., Abbafati C. et al. Global burden of 369 diseases and injuries in 204 countries and territories, 1990–2019: a systematic analysis for the Global Burden of Disease Study 2019. 2020. *The Lancet*, 396(10258), 1204-1222. doi: 10.1016/S0140-6736(20)30925-9

## TOWARDS HARMONIZATION OF CLINICAL BONE SCINTIGRAPHY PROTOCOL BETWEEN THREE DIFFERENT SPECT/CT SYSTEMS IN LITHUANIA

Kirill SKOVORODKO<sup>1,2</sup>, Mažena MACIUSOVIČ<sup>3</sup>, Marius BURKANAS<sup>3</sup>, Sigita TIŠKEVIČIUS<sup>3</sup>, Laurynas GILYS<sup>4</sup>, Renata KOMIAGIENĖ<sup>1,5</sup>, Jonas VENIUS<sup>3,6</sup>

<sup>1</sup>Vilnius University Hospital Santaros Klinikos, Vilnius, Lithuania; <sup>2</sup>Center for Physical Sciences and Technology (FTMC), Vilnius, Lithuania; <sup>3</sup>National Cancer Institute, Medical physics department, Vilnius, Lithuania; <sup>4</sup>The Hospital of Lithuanian University of Health Sciences, Kaunas, Lithuania; <sup>5</sup>Vilnius University, Faculty of Medicine, Institute of Biomedical Sciences, Vilnius, Lithuania; <sup>6</sup>National Cancer Institute, Biomedical physics laboratory, Vilnius, Lithuania.

<sup>1</sup>kirill.skov@gmail.com; <sup>3</sup>mazena.maciusovic@nvi.lt; <sup>3</sup>marius.burkanas@nvi.lt; <sup>3</sup>sigita.tiskevicius@nvi.lt

<sup>4</sup>gilys.laurynas@gmail.com; <sup>5</sup>renata.komiagiene@santa.lt; <sup>3</sup>jonas.venius@nvi.lt

**Abstract:** In the past few years the main Lithuanian hospitals that provide nuclear medicine services have updated their SPECT/CT systems. The novel SPECT/CT systems allow us to acquire improved image quality, shorter acquisition and new reconstruction algorithms. Systems with CZT detectors provide higher sensitivity, better energy resolution and image contrast. However, due to the different technical approaches used by vendors, image quality may vary, thus the comparison of diagnostic information between the systems is not straightforward. Harmonization of the clinical protocols would allow to minimize an equipment-based images differences and help uniform the follow-up assessments.

The purpose of this work was to acquire scintigraphic images of the phantoms with the different manufacturers systems and compare images using the clinical bone scintigraphy protocol reconstructions and identify parameters for scanning protocol harmonization. Images were obtained and reconstructed by three SPECT/CT systems: GE NM/CT 870 CZT, SIEMENS Symbia Intevo Excel, Mediso AnyScan SC. For the evaluation of the different parameters Jaszcak, NEMA IQ phantom and capillary point sources were used. The phantoms were filled with the same activity of <sup>99m</sup>Tc solution. SPECT and CT scans were acquired for the standard bone SPECT/CT protocol and for unify protocol. Reconstructions of the images were performed using site approved standard parameters, while using various filters and reconstructions algorithms. Investigation of the phantoms revealed the main differences of SPECT/CT systems. Different detection technologies, reconstructions algorithms and concepts of the equipment add some limitations to the harmonization. Nevertheless, new technologies and

image post processing algorithms used in all systems allow to decrease acquisition time and administered activity to the patients almost without losing image quality. Subsequently this results in reduced exposure of ionizing radiation to the patients and medical staff.

**Keywords:** bone scintigraphy SPECT/CT, nuclear medicine, molecular imaging, harmonization, medical imaging.

### 1. Introduction

Bone scintigraphy is one the most common and highly sensitive functional imaging procedures performed in a nuclear medicine department. The radioactive (<sup>99m</sup>Tc-MDP, methylene diphosphonate) tracer is used to detect distribution of osseous abnormalities related to benign and malignant diseases, Paget's disease, infections, avascular necrosis, loosening of joint prostheses as well as physiological processes [1, 3, 6, 7]. Bone scintigraphy scans can detect metabolic activity earlier than structural changes appear on conventional radiological scans [2]. The accumulation of injected radiopharmaceutical tracer depends upon blood flow and osteoblastic activity [2, 3]. In most malignant and benign conditions increased tracer uptake may be seen on bone scans due to the increased vascularity and bone remodeling. About four hours after injection, approximately 50 - 60 % of the injected radiopharmaceutical is fixed in the patient body, about 34 % is excreted with the urine, 6 % remains in the other organism locations [3], however, uptake of the tracer depends on individual local blood flow. Thus, in order to correctly simulate human scanning using phantoms, it is necessary to correctly assess the

accumulated part of the activity at a certain time in the human body and link it to the filled activity in the phantoms.

Modern SPECT systems with digital solid-state cadmium zinc telluride (CZT) detectors and tungsten collimators provide improved images when compared to those produced by conventional analog cameras, fitted with thallium-doped sodium iodine (NaI(Tl)) detectors and lead collimators [4,5,8]. Systems with CZT detectors provide higher sensitivity, better energy resolution and image contrast [4]. However, due to the different technical approaches used by vendors, image quality may vary, thus the comparison of diagnostic information between the systems is not straightforward.

It is important to assure the performance of the systems, because the accuracy of clinical SPECT depends on the acquisition and processing parameters which are selected and may differ according to the clinical task [3, 8]. Selection of the parameters by user may result in errors, though manufacturers offer clinical protocols for certain examinations without changing any acquisition parameters. These parameters are usually set within the protocols and help to speed up clinic routine and provide good standardization for patient studies [3].

In order to evaluate patients' images acquired at different centers as accurately as possible, it is necessary to evaluate the quantitative accuracy of the systems.

The aim of this study is to harmonize the protocol for bone scan between different vendors in order to have unified follow up of the imaging.

## 2. Materials and Methods

### 2.1 SPECT/CT systems

The SPECT/CT acquisition was performed using three different systems. The characteristics of the systems are shown in Table 1.

**Table 1.** SPECT/CT systems information.

Manufacturer	Model	Installation year
GE	NM/CT 870 CZT SPECT/CT	2021
SIEMENS	Symbia Intevo Excel SPECT/CT	2019
Mediso	AnyScan SC SPECT/CT	2021

### 2.2. Phantom design and preparation

The same phantoms (Jaszczak, NEMA-IEC and capillary) were used with all SPECT/CT systems for image acquisitions.

#### 2.2.1. The Jaszczak phantom

The Jaszczak phantom manufactured by Pro-Project was used for SPECT systems performance evaluation (Fig. 1.). The acrylic, cylindrical Jaszczak phantom included three parts: the sectors of rods with diameters of 1.6, 1.8, 2.0, 2.2, 2.4, 2.6 mm, five spheres with diameters of 9.1, 7.8, 6.5, 5.2, 3.9, 3.25 mm and a uniformity region. The phantom was filled with  $\sim 400$  MBq of  $^{99m}\text{Tc}$  solution and was well mixed.



**Fig. 1.** Jaszczak phantom with inner structures.

#### 2.2.2. The NEMA-IEC phantom

NEMA-IEC phantom manufactured by Pro-Project was used for quantification. Phantom consists of 6 fillable spheres with inner diameter: 10 mm, 13 mm, 17 mm, 22 mm, 28 mm and 37 mm (Fig. 2.). The phantom was filled to an  $\sim 6:1$  insert-background concentration ratio. The phantom cavity was filled with  $\sim 68.2$  MBq of  $^{99m}\text{Tc}$  solution and was well mixed, the spheres were filled with 3.78 MBq to 100 mL concentration.



**Fig. 2.** NEMA-IEC phantom design.

#### 2.2.3. Phantom for spatial resolution

Spatial resolution was evaluated using homemade longitudinal source – 1 mm diameter capillary filled with 50 MBq of  $^{99m}\text{Tc}$  solution.

### 2.3. Metrological traceability of activity meters

The readings of activity meters that were used for preparation of activity ( $< 3\%$  deviation) were verified by the secondary standard chamber Capintec CRC-15R, No. 158488 ( $4\pi$   $\gamma$  ionization chamber) brought to hospitals by the Ionizing Radiation Metrology Laboratory of the FTMC that is the National Metrology Institute (NMI) in Lithuania.

### 2.4. Image acquisition parameters

The phantoms were scanned positioning at isocentre on each camera to evaluate general image quality, lesion detectability and uniformity of the reconstructed slice [3].

The NEMA-IEC phantom was scanned with the same protocol at each site. SPECT/CT acquisition of the bone SPECT protocols were acquired at each site using autocontour mode and noncircular orbit. The following default parameters described in Table 2 were used for the acquisition.

The second part of this work was performed to investigate how scanning parameters (counts per projection) affect image quality. Jaszczak phantom was scanned using 100, 200, 300, 400, 500 kcounts per projection as stop condition.

**Table 2.** Parameters used for standard clinical bone SPECT/CT acquisition protocol on different systems.

Parameters	NM/CT 870 CZT	Symbia Intevo Excel	AnyScan
Collimator	WEHR45	LEHR	LEGP
Matrix size	256x256	256x256	128x128
Zoom	1	1	1.14286
Detectors and configuration	Both, H	Both, H	Both, H
Mode	step and shoot, acquire during motion	continuous	continuous
No of projection	60	120	120
kcounts per projection	180	160	190
Total scanning time, min	7	11	15
Energy window	±7.5 %	±15%	±20 %
Reconstruction algorithm	OSEM, 4 iterations 10 subsets	XSPECT	OSEM, 48 iterations, 4 subsets

### 2.5. Image reconstruction parameters

The third part of this work was performed to investigate how reconstruction algorithm types affect image quality. The acquired phantom raw data were reconstructed using OSEM, Flash3D, FB, Wallis, XSPECT algorithms. Additionally, the effect of attenuation correction (AC) on image quality was evaluated.

### 2.6. Analysis

To easily compare the SPECT performance between different cameras, image quality was quantitatively assessed by computing contrast, uniformity noise index values and spatial resolution as proposed by the American Association of Physicists in Medicine (AAPM). [4]

Quantitative assessment of image quality was performed using a Web-based image-processing software program ImageJ and developed by the International Atomic Energy Agency the Nuclear Medicine Quality Control (IAEA-NMQC) Toolkit for image evaluation. The Toolkit is a set of ImageJ based codes that allow to process and analyse nuclear medicine images of gamma cameras and SPECT systems. Spatial resolution, integral and differential uniformity, signal-to-noise ratio (SNR) and contrast were estimated.

## 3. Results

The images were captured using clinical protocols that are used for routine patient bone scintigraphy scanning

(Table 2). The results of image quality (contrast, SNR, integral uniformity, differential uniformity and spatial resolution) of three SPECT systems (GE, Siemens and Mediso) are presented in Table 3.

**Table 3.** Results of image quality analysis.

	Contrast	SNR	Integral Uniformity, %	Differential Uniformity, %	Spatial Resolution, mm
NM/CT 870 CZT	26.4	12	15.6	13	6
Symbia Intevo Excel	38.3	10.6	8.4	7.3	7.4
Any Scan	29.3	24.5	9.8	5.9	7

The contrast, shown in Table 3, is calculated from the biggest sphere of Jaszczak phantom.

As shown in Table 3, all image quality parameters are quite scattered. This is the result of usage of different scanning hardware as well as reconstruction algorithms and scanning parameters in standard clinical protocols. Siemens SPECT system demonstrate the highest contrast and best integral uniformity. Mediso SPECT system demonstrate highest SNR and the best differential uniformity. GE demonstrate the highest spatial resolution.

To harmonize imaging protocols particular image quality parameters from different vendors should be as close as possible to each other. Harmonization could be performed by adapting scanning parameters and/or reconstruction algorithms. One of the main scanning parameters impacting SPECT image quality is counts per projection that is determined by scanning time and administered activity. However, these two parameters are dependent and can compensate each other. Image quality dependency from counts per projection is present in Table 4.

**Table 4.** Image quality dependency from counts per projection.

kcounts per projection	Contrast	SNR	Integral Uniformity	Differential Uniformity	Spatial Resolution, mm
100	37,5	7,45	15,6	10,9	7,4
200	36,2	11,7	10,1	8,1	7,3
300	37,3	13,76	6,1	4,6	7,2
400	36,8	17,06	6,2	5,2	7,4
500	37,2	20,06	6,6	5,9	7,3

The results of counts per projection registered with Symbia Intevo Excel system (Fig.3. and Fig. 4.) showed that this parameter did not impact contrast and spatial resolution, however, SNR and image uniformity can be increased.

SNR dependency on counts per projection is presented in Fig. 3.



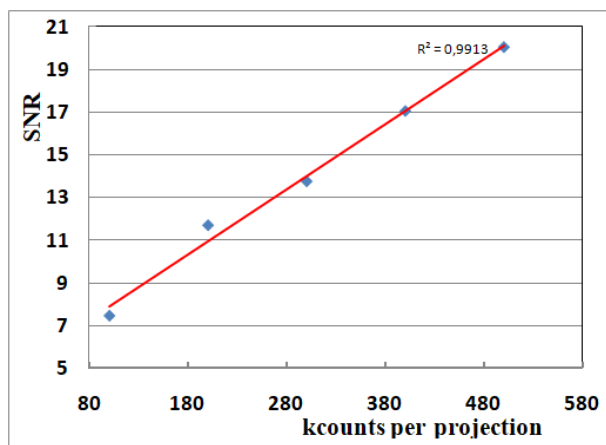


Fig. 3. SNR dependency on kcounts per projection.

SNR has linear dependency and can be directly increased by increasing scanning time or administrated activity. However, administered activity can be decreased just to a certain level to avoid very long scanning times that could be unacceptable for the patient and examination quality.

Integral uniformity also has linear dependency at a low number of counts per projection, however from a certain count level it stops decreasing (Fig. 4).

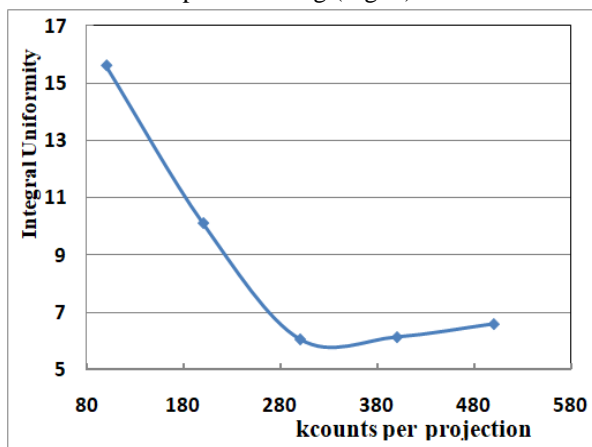


Fig. 4. Integral Uniformity dependency on kcounts per projection

Differential uniformity changes in a similar manner, therefore image uniformity in general can be improved only to a certain level.

The analysis performed above suggests that quality of images obtained from different SPECT systems cannot be unified only by changing scanning time and/or administered activity. Greater impact on image quality has reconstruction algorithms, prefiltering, postfiltering and attenuation correction.

Image quality parameters dependency on reconstruction and attenuation correction is presented in Table 5.

As it is seen from table 5, images, obtained using different reconstruction algorithms, have very varying characteristics. Even the same type of reconstruction algorithm, used by different vendor, generates images with different quality.

Table 5. Image quality parameters dependency on reconstruction and attenuation correction.

	Contrast	SNR	Integral Uniformity	Differential Uniformity	Spatial Resolution, mm
Symbia Intevo Excel					
OSEM	24,23	19,6	14,86	7,16	10,4
Flash3D	28,65	13,21	17,99	10,3	10,3
FBP	26,82	5,1	20,9	13,4	12,8
Wallis	33,73	3,9	28,2	20,1	11,7
AC	38,29	10,6	8,421	7,314	7,4
XSPECT					
NM/CT 870 CZT					
OSEM	28,34	13,6	21,5	13,1	7,7
AC	26,4	12	15,6	13	6
OSEM					
FBP	31,5	10,6	23,1	14,6	9,7
AnyScan					
OSEM	11,97	24	13,6	7,9	8,2
AC	29,3	24,5	9,8	5,9	7
OSEM					

Reconstruction algorithms used in this study did not change all image quality parameters equally, moreover increasing one parameter another image quality parameter could decrease. In such case changing the reconstruction algorithm did not result in better image quality in general.

Use of attenuation correction improves image uniformity and spatial resolution. Moreover, attenuation correction greatly improved contrast for Mediso SPECT system.

#### 4. Discussion

The performance check of SPECT equipment using NEMA, Jaszczak and capillary quality control systems gave valuable information about systems design, reconstruction algorithms and its settings, allowed to compare clinical protocols and evaluate possible causes of performance differences.

Due to unique software and hardware used in different SPECT systems, some parameters could not be harmonized and protocols resulting in identical image quality could not be created. For instance, a specialized bone scanning reconstruction algorithm developed by Siemens gives the highest image quality parameters that could be difficult to achieve using standard reconstruction algorithms. GE uses the FAME post-processing algorithm, which integrates the CT anatomical bone information into the SPECT bone image processing [9].

It should be noted that all SPECT systems produce images with quality suitable for diagnosis. However, some of the image quality parameters (SNR and image uniformity) could be improved by changing scanning parameters, such as scanning time. One of the SPECT/CT systems equipped with a tungsten collimator.

The change of reconstruction algorithms allowed to increase separate image quality parameters, however did not result in better image quality in general. The reason is, that each reconstruction algorithm for its best

performance needs specific scanning parameters and the adjustment of reconstruction settings. This suggests that there is still some “space” for image quality improvement. For that, optimization strategies should be implemented in daily practice in order to minimize differences in image quality registered with different SPECT systems.

In order to create a harmonized protocol, optimization should be performed individually for each particular SPECT/CT modality considering the clinical setting time of scan (time between injection and acquisition), administered activity, scanning and reconstruction parameters.

The results and knowledge gained in this work will allow to optimize scanning protocols and proceed further with the harmonizing of the bone scanning protocol, moreover it will serve as a good start for harmonization of other scanning protocols.

### 5. Conclusions

Quality of images, obtained with clinical protocols used for the same purpose, are different.

Changing of the main scanning parameters (scanning time and/or administered activity) did not allow to unify image quality of different vendors.

The same reconstruction algorithm used by different vendors produces images of different quality.

Because of intelligent (dedicated) reconstruction algorithms used by vendors it could be impossible to achieve the highest quality images for all SPECT systems.

To harmonize imaging protocols the adaptation of scanning parameters together with reconstruction algorithm type and its settings should be performed.

### 6. References

1. Takayuki Shibutani, Masahisa Onoguchi, Yuka Naoi et al. The usefulness of SwiftScan technology for bone scintigraphy. *Nature Scientific Reports*, 2021. 11:2644. doi.org/10.1038/s41598-021-82082-x
2. Bartel TB., Kuruva M., Gnanasegaran G., Beheshti M, Cohen EJ, Weissman AF, Yarbrough TL. SNMMI Procedure Standard for Bone Scintigraphy 4.0. *J Nucl Med Technol*. 2018 Dec;46(4):398-404. PMID: 30518604.
3. Wyngaert T. Van Den., Strobel K., Kampen W. U., et al. The EANM practice guidelines for bone scintigraphy *Eur J Nucl Med Mol Imaging*, 2016 43:1723–1738.
4. Desmots C, Bouthiba MA, Enilorac B et al. Evaluation of a new multipurpose whole-body CZT-based camera: comparison with a dual-head Anger camera and first clinical images. *EJNMMI Physics*, 2020. 7:18 doi.org/10.1186/s40658-020-0284-5
5. Goshen E, Beilin L, Stern E et al. Feasibility study of a novel general purpose CZT-based digital SPECT camera: initial clinical results. *EJNMMI Physics*, 2018. 5:6 doi.org/10.1186/s40658-018-0205-z
6. Kurt A., Bor D., Tastan S. et al. Accuracy of Clinical Protocols in SPECT. *J Nucl Med Technol*, 2012. 40:259-264 doi:10.2967/jnmt.111.098715
7. Ghosh P. White Paper xSPECT Bone: a clinical overview. Siemens Healthineers Headquarters, 2018. MI-3878.DD.JV.
8. International Atomic Energy Agency. SPECT/CT Atlas of Quality Control and Image Artefacts. Human Health Series No. 36. 2019.
9. <https://www.gehealthcare.co.uk/products/molecular-imaging/starguide> (Accessed: 9<sup>th</sup> September 2021)

## **DOSIMETRY CONCEPTS FOR QUALITY ASSURANCE IN $\mu$ CT**

Richard DEYHLE JR.<sup>1</sup>, Christian BERNHARDSSON<sup>1</sup>, Lovisa WALDNER<sup>1</sup>, Lars E. OLSSON<sup>1</sup>, Marie SYDOFF<sup>2</sup>

<sup>1</sup>Medical Radiation Physics, Department of Translational Medicine, Lund University, Skåne University Hospital Malmö, Inga-Marie Nilssons gata 49, 205 02 Malmö, Sweden; <sup>2</sup>Lund University Bio-Imaging Centre (LBIC), Faculty of Medicine, Biomedical Center (BMC) D11 Klinikgatan 32, 221 84 Lund, Sweden

<sup>1</sup>richard.deyhle\_jr@med.lu.se; lovisa.waldner@med.lu.se; christian.bernhardsson@med.lu.se; lars\_e.olsson@med.lu.se;

<sup>2</sup>marie.sydooff@med.lu.se

**Abstract:** The aim of this paper was to suggest a low-cost phantom for verifying reproducible dosimetric assessment using a pre-clinical micro-computed tomography ( $\mu$ CT) scanner. The suggested phantom is made from Polymethyl methacrylate (PMMA). The absorbed dose at different positions within the phantom was measured using two techniques: thermoluminescent dosimeter of LiF (TLD) chips and salt (NaCl) pellets, the latter being a proof of concept as a potential optically stimulated luminescent (OSL) dosimeter.

**Keywords:** OSL, TL, radiation dosimetry, luminescence dosimetry, x-ray micro-computed tomography.

### **1. Introduction**

Small animal imaging (SAI) has gained considerable importance as a method for preclinical studies during the last decade. With its capability to provide cost-effective and fast 3D imaging at high resolution, micro computed tomography ( $\mu$ CT) has proven to be a valuable tool in the assessment of a wide variety of preclinical disease models using small animals such as mice and rats. For *in-vivo* preclinical applications, biological response rarely happens in three dimensions only. The addition of time is necessary to perform longitudinal imaging, allowing researchers to study morphological and physiological alterations over several weeks to months. The radiation dose must be taken into consideration for *in-vivo* applications as biological damage caused from ionizing radiation may affect the biological system, which may confound the results.

In order to achieve a sufficient signal-to-noise ratio in conjunction with the high resolution (50 – 100  $\mu$ m) needed when imaging small animals, the radiation dose for  $\mu$ CT is higher than for clinical CT. Opposite to clinical CT, no standardization has been established for dosimetry and quality assurance purposes for *in-vivo* pre-clinical  $\mu$ CT [1]. However, current commercial  $\mu$ CT systems provide users with a set of scanning protocols

designed to meet the image quality requirements, for a variety of applications, at a reasonably low animal exposure.

Hence, the aim of this study was to investigate practical and feasible methods for  $\mu$ CT dosimetry regarding radiation dose verification. The initial concept of a phantom designed for dosimetry purposes is based on a cylinder made of polymethyl methacrylate (PMMA). PMMA has an atomic density mimicking water, it is cheap, easily accessible and easily reproducible for validation between laboratories. The physical dimensions of the PMMA phantom was designed to approximately mimic the thickness of a adult rat.

### **2. Material and Methods**

All radiation exposures were made at the Lund Biomedical Imaging Center (LBIC), Lund University, Lund, Sweden, using MILabs xuhr- $\mu$ CT, Milabs, Utrecht, Netherlands. The polymethyl methacrylate (PMMA) phantom was constructed by Promech Lab, Malmö, Sweden. The NaCl pellets were made in-house at the department of Medical Radiation Physics, Lund University, Skåne University Hospital, Malmö, Sweden, using ordinary household salt that can be purchased in Swedish supermarkets. The used TLDs were of the type MCP-N chips (LiF:Mg,Cu,P) from Mikrolab, Poland. The signals from both the MCP-N chips and the NaCl pellets were read-out using Risö TL/OSL readers, DTU Physics, Technical University of Denmark (DTU), Nutech, Denmark. The signal measured in the reader was converted to an absorbed dose for each chip or pellet. Further description of the experimental setup and methodology will be provided.

The suggested PMMA phantom has the following dimensions: 49 mm in diameter and 54 mm in length (Fig. 2). The phantom has four separate boreholes, with varying depths, to quantify the radiation dose at each position. The boreholes were filled with either LiF chips for thermoluminescent dosimetry (TLD), the gold standard in many dosimetry applications, or NaCl pellets

(made from ordinary household salt) which have proven to be a potential dosimeter for optically stimulated luminescence dosimetry (OSLD). Previous similar studies have utilized other OSL materials but none have attempted using NaCl as an OSL material [2, 3] in  $\mu$ CT dosimetry studies. Repeated measurements were made for various *in-vivo* imaging protocols frequently used on a MILabs Extra Ultra High Resolution (xuhr- $\mu$ CT) scanner. The PMMA phantom is low-cost and easily reproducible but lacks tissue inhomogeneity as in a real mouse or rat.

### 2.1 *In-vivo* preclinical $\mu$ CT scanner

MILabs xuhr- $\mu$ CT scanner has many features that make it a competitive  $\mu$ CT scanner on the market (<https://www.milabs.com/u-ct/>). A list of features of the  $\mu$ CT scanner used at LBIC is provided in Table 1.

**Table 1.** Properties of MILabs xuhr- $\mu$ CT scanner at LBIC

MILabs xuhr- $\mu$ CT scanner	
Type	<i>In-vivo</i> and <i>ex-vivo</i>
Diameter FOV (mm)	Up to 130 mm
Length (mm)	Up to 712 mm
Voxel Resolution	Max 2.4 $\mu$ m voxel size
Kilovoltage peak (kVp)	65 kVp (80 kVp optional)
Milliamperage	Max 0.26 mA
Scanning time	Down to 5 sec for total body mouse
Gating	Sensor free and sensor based respiratory and cardiac gating
Other Characteristics	Dual-energy $\mu$ CT High, medium and low energy filter options

The MILabs xuhr- $\mu$ CT scanner has three default protocols with settings that user can choose to either use per default or optimize to improve the desired need of the specific measurement, *i.e.* improve image quality, dose reduction, high-throughput demand. The protocols are titled „normal“, „accurate“ and „gated“. When performing *ex-vivo* scans, the normal and accurate protocols are recommended. When performing *in-vivo* imaging, and if the reduction of motion artifacts is required for the application, then the Gating mode must be selected. This allows the user to acquire physiological information and record it with each projection in order to retrospectively correlate each projection with a specific phase of the motion.

In this paper, only one protocol have been investigated, Normal acquisition protocol. Listed in Table 2 are the settings for the default imaging protocol.

In the normal, accurate and gated protocols the gantry rotates 360° around the sample (*i.e.* mouse or rat). By lowering the step angle, a larger number of projections are acquired, increasing the radiation dose. The Normal imaging protocol allows users to gain a high resolution image with a radiation dose of 162 mGy (as stated by the vendor that supplies an estimate of air kerma for the default setting).

**Table 2.** Protocol settings for the various standard imaging protocols of the MILabs xuhr- $\mu$ CT scanner

Protocol Settings	Normal	Accurate	Gated
Kilovoltage peak (kVp)	55	55	55
Milliamperage (mA)	0.19	0.19	0.19
Exposure time (milliseconds)	75	75	20
Number of projections	960	1440	7680
Total scan time (minute:second)	3:49	5:23	8:28

The Accurate imaging protocol increases the image quality and also increases the radiation exposure, corresponding to an estimated air kerma of 228 mGy as reported from the vendor for the default setting. To reduce motion artifacts caused by natural physiological processes such as respiration and cardiac motions, so-called Gating is used. When using the gated protocol, a time stamp is recorded with each projection. That is used to correlate each projection to the recorded cardiac and/or respiratory signal. This signal can be reconstructed into a dynamic image series derived from, for example a rodent. For the default gated acquisition protocol, the estimated air kerma is 362 mGy, as reported from MILabs.

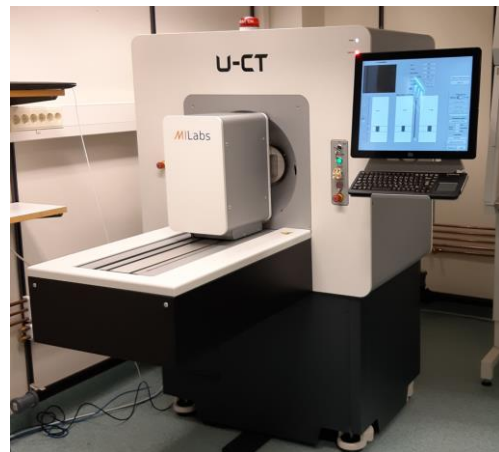


**Fig. 1.** MILabs xuhr- $\mu$ CT scanner at LBIC, Lund University, Lund, Sweden.

### 2.2 PMMA phantom

The PMMA phantom was designed with the following dimensions: 49 mm diameter and 54 mm length with four boreholes with different depths;  $24.5 \pm 0.05$  mm from the surface of the phantom to the first borehole, with a difference in depth between the following holes of  $6.13 \pm 0.05$  mm (Fig. 2), towards the center of the phantom. Validity of physical dimensions was confirmed using a „Tolerator“ from Ultra Prazison Messege GMBH ULTRA, Glattbach, Germany. In addition, a 1 mm extra

depth of each borehole was used to allow for positioning of TL chips or OSL pellets. This allows four detectors to be used simultaneously in one scan. The phantom was placed in the animal bed as shown in Fig. 3.

Fig. 4 shows a side view, along the Z-axis, of the phantom where each position in the phantom is denoted with an associated number 1-4.

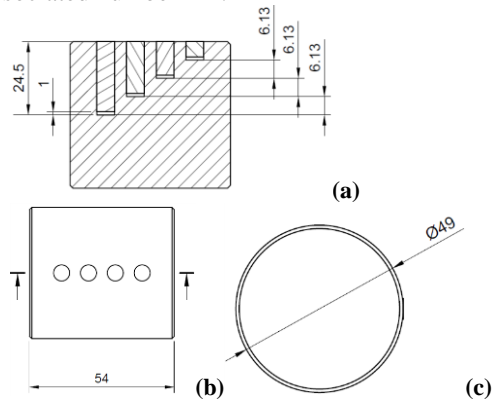


**Fig. 2.** Schematic outline of the PMMA phantom. (a) represents the y-axis angle with the depths of the four boreholes each spaced 6.13 mm apart; (b) top view angle with total length of 54 mm; (c) z-axis (in-plane) angle with 49 mm diameter.

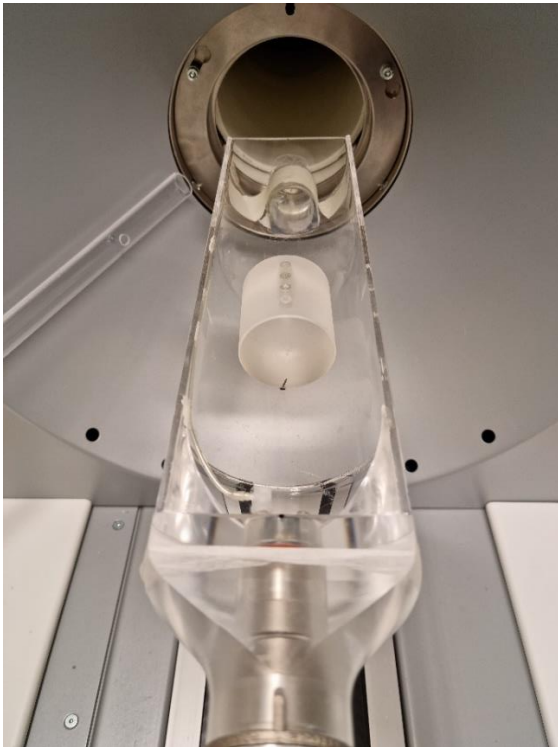


**Fig. 3.** PMMA phantom placed in the iso-center of the animal bed

### 2.3. Production, irradiation and read-outs of TLD and NaCl pellets

The NaCl pellets were produced in-house at Lund University [4, 5]. For both the TL and the OSL readouts, two different Risø TL/OSL readers (TL/OSL-DA-15 and DA-20, DTU Physics, Nutech, Denmark) [6] were used.

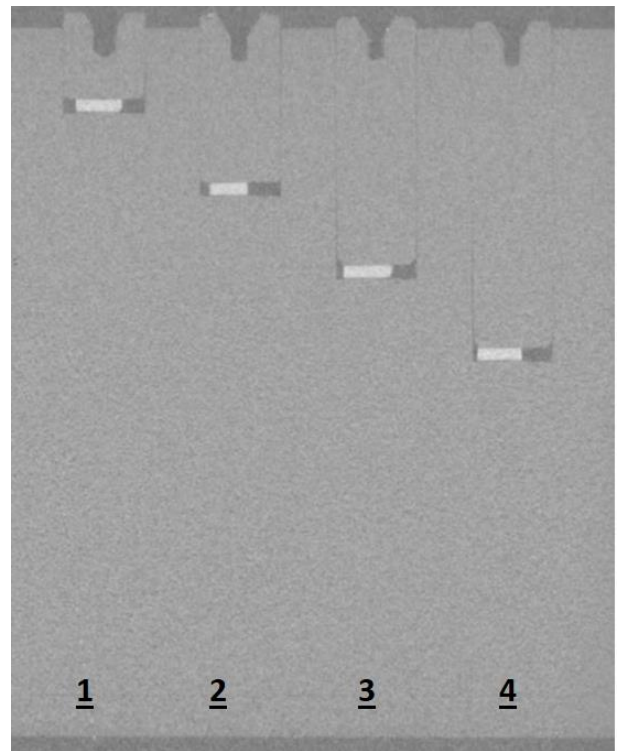


**Fig. 4.** A reconstructed  $\mu$ CT image of the phantom, cropped to focus on the placement of each borehole within the phantom. Position 1-4 are listed below the respective borehole, each being 24.5 mm apart.

The readers are equipped with internal  $^{90}\text{Sr}/^{90}\text{Y}$  radiation sources (20 MBq as of 9th of April 2009 and 100 MBq as of 22nd of October 2010) with absorbed dose rates of  $0.58 \pm 0.01 \text{ mGy s}^{-1}$  (as of 23rd of April 2021) and  $5.03 \pm 0.1 \text{ mGy s}^{-1}$  (as of 21st of June 2021) to quartz (calibration quartz, DTU Nutech, Batch 123), respectively. The dose rate to the NaCl pellets is calculated using a stopping power ratio of 0.938 between NaCl and quartz ( $\text{SiO}_2$ ) [7, 8]. The readouts were performed using a continuous wave stimulation mode by means of blue ( $\lambda=470 \text{ nm}$ ) LEDs according to [4]. The TLDs used were MCP-N chips ( $\text{LiF:Mg,Cu,P}$ ) from Mikrolab, Poland. The chips were calibrated in an external  $^{60}\text{Co}$  beam and readout were made with the Risø TL/OSL readers using annealing conditions as stated by the manufacturer (pre-irradiation:  $240^\circ\text{C}$  for 10 min; post-irradiation:  $100^\circ\text{C}$  for 10 min.). The TL signals were acquired by linearly heating ( $10^\circ\text{C/s}$ ) the MCP-N chips to  $240^\circ\text{C}$  and holding that temperature for 20 s.

### 3. Results and discussion

Reported here is the dose values from the scan mode titled „Normal“. Choosing position one to represent the position closest to the surface of the phantom, separated by a distance of 6.13 mm between each of the following positions two, three and four. All reported absorbed dose values are measured in milligray (mGy). Included in the total absorbed doses reported is the dose from an X-ray scout view that is always performed prior to irradiation with any of the selected imaging protocols.

The number of individual dose measurements ( $n$ ) is listed along with the arithmetic mean dose value and the



variation of dose per dosimeter per position among the  $n$  chips or pellets at each position.

As measured by the TLDs (LiF), in normal scan mode, the absorbed dose at position one was:  $115.2 \pm 9.8$  mGy ( $n=12$ ), position two:  $104.2 \pm 10.2$  mGy ( $n=11$ ), position three:  $96.5 \pm 9.8$  mGy ( $n=12$ ), and position four:  $90.1 \pm 9.5$  mGy ( $n=11$ ), respectively. A sensitivity correction was applied to each TLD by considering the coefficient of variance of the mean in the measurement.

As measured by the OSLDs (NaCl), in normal scan mode, for position one the corresponding absorbed dose was  $122.6 \pm 10.9$  mGy ( $n=12$ ), position two:  $114.5 \pm 10.4$  mGy ( $n=12$ ), position three:  $105.1 \pm 9.8$  mGy ( $n=12$ ), and position four:  $97.5 \pm 8.5$  mGy ( $n=12$ ), respectively. A sensitivity correction was applied to each NaCl pellet as described by [5].

Throughout the homogeneous PMMA phantom, the TLDs had a reduction of approximately 10% in the dose between each position ( $6.13 \pm 0.05$  mm of PMMA). For the NaCl pellets, the corresponding reduction was observed to be approximately 8%. This indicates a strong agreement between the two dosimeter materials and the possibility to resolve doses, at least, down to 10 mGy for this X-ray energy range. With the suggested phantom, the next step in verifying this method is to measure the radiation absorbed dose for all default imaging protocols using the same type of dosimeters and an ionization chamber.

#### 4. Conclusion

In order to optimize the dose delivered during longitudinal studies, scan parameters should be optimized; this can be accomplished using the phantom and method suggested in this work. In longitudinal small animal studies, the dose delivered by  $\mu$ CT protocols should be a consideration when evaluating results. In all CT studies, the primary limiting factor is the exposure, indeed also for  $\mu$ CT [9]. The suggested methodology is a low-cost, simple way to assess the dose delivered by any future protocols as well as for comparisons with other similar scanners. The results have established the use of TLD of LiF chips and OSLD of NaCl pellets to measure the absorbed dose with a similar reduction in dose per position of about 8-10%. This confirms the use of the NaCl pellets as an alternative for preclinical dosimetry in combination with the suggested PMMA phantom. The prototype PMMA phantom built for this study, in

combination with the NaCl pellets, is easily reproducible and suggests a robust and simple method for future dose assessment of  $\mu$ CT protocols. The method presented here is a first attempt to provide an accurate and practical way of assessing dose and evaluating protocol parameters in terms of dose and could be used for routine quality control of current and future  $\mu$ CTs scanners.

#### Acknowledgement

The authors are grateful to Promech Lab (Malmö) for help with manufacturing and developing the PMMA phantom and to Lund Biomedical Imaging Center for providing access to MILabs xuhr- $\mu$ CT for dose measurements.

#### 5. References

1. Hupfer, M., et al., Dosimetry concepts for scanner quality assurance and tissue dose assessment in micro-CT. *Medical physics*, 2012. 39(2): p. 658-670.
2. Vrigneaud, J.M., et al., Application of the optically stimulated luminescence (OSL) technique for mouse dosimetry in micro-CT imaging. *Medical physics*, 2013. 40(12): p. 122102.
3. Mendez, C., et al., Development of a phantom for dosimetric comparison of murine micro-CT protocols with optically stimulated luminescent dosimeters. *Medical physics*, 2018. 45(8): p. 3974-3979.
4. Waldner, L., Optically stimulated luminescence dosimetry with NaCl pellets. *Dosimetry for prospective applications*. 2021, Lund University.
5. Waldner, L. and C. Bernhardsson, Physical and dosimetric properties of NaCl pellets made in-house for the use in prospective optically stimulated luminescence dosimetry applications. *Radiation Measurements*, 2018. 119: p. 52-57.
6. Berger, M., et al., Stopping-power and range tables for electrons, protons, and helium ions, NIST Standard Reference Database 124. National Institute of Standards and Technology (NIST), Physical Measurement Laboratory (PML), 2017.
7. Bøtter-Jensen, L., et al., Developments in radiation, stimulation and observation facilities in luminescence measurements. *Radiation Measurements*, 2003. 37(4-5): p. 535-541.
8. Bøtter-Jensen, L., K.J. Thomsen, and M. Jain, Review of optically stimulated luminescence (OSL) instrumental developments for retrospective dosimetry. *Radiation Measurements*, 2010. 45(3-6): p. 253-257.
9. Clark, D.P. and C. Badea, Micro-CT of rodents: state-of-the-art and future perspectives. *Physica medica*, 2014. 30(6): p. 619-634.

## PERCEPTION OF MEDICAL RISKS AND SOCIODEMOGRAPHIC CHARACTERISTICS OF RESPONDENTS

Artem DAVYDOV<sup>1</sup>, Dmitri KONONENKO<sup>2</sup>, Artem BIBLIN<sup>3</sup>, Alexander VODOVATOV<sup>4</sup>

Research Institute of Radiation Hygiene after P.V. Ramzaev, Saint-Petersburg, Russia

<sup>1</sup>a.davidov@niirg.ru, <sup>2</sup>d.kononenko@niirg.ru, <sup>3</sup>a.biblin@niirg.ru, <sup>4</sup>a.vodovatov@niirg.ru

**Abstract:** this article presents the results of a social survey of the population of the Russian Federation in 2019. The results show that the risk from diagnostic medical use of radiation is perceived as one of the lowest among other radiation risks. This contradicts the warnings of experts predicting an increase in the dose burden on the population as a result of increased frequency of high-dose examinations. Socio-demographic differences in public perception of risk from diagnostic medical uses of radiation were also examined. The results of the study may be useful in informing patients about the risk of diagnostic medical use of radiation compared to other risks.

**Keywords:** risk perception, radiation, risk communication

### 1. Introduction

With the introduction of high-dose radiodiagnostic tests into medical practice, the collective dose per population is increasing [1-3]. In the United States, it is estimated that in the 20-30 years following 2007, approximately 29,000 cancer cases will be induced as a result of the use of CT in diagnosis [2,4]. However, the use of radiodiagnostic techniques remains justified because the benefits outweigh the risks [5]. The ALARA principle must be respected [5] and patients have the right to be informed of the risks, which is enshrined in the legislation of many countries. This makes communication about radiation risks in medicine relevant. A recent review of informing practices in medical examinations has shown that the most successful method is visual, namely pictographs [6]. Comparisons with other radiation risks, including airplane flight, risks from medical exposure are no longer as strong, but still relevant. It is known [7,8] that ordinary people perceive radiation risks differently - worse if they are related to the MIC and someone's interests, the benefit of corporations (the difference in the perception of nuclear power plants in the United States and France [9]), better if it benefits them (airplane flight, medicine) or related to a natural source, besides, the history of accidents, media attention,

representation of technology, information source, influence the perception of the society.

The use of radiodiagnostics in medicine is beneficial to patients and does not significantly benefit physicians - it allows for a more accurate diagnosis and does not bring super-profits to medical organizations, so their perception should be rather positive. However, there is the question of comparing the risks of medical exposure to other types of radiation risks that medical exposure can exceed. For example, is it reasonable to compare medical risks to the risks of living near a nuclear power plant or natural radioactive areas? Are medical radiation risks perceived more acutely than airplane travel or naturally occurring radioactivity in water and food? Are there socio-demographic differences in the perception of medical radiation risks? These questions were addressed in this article. Similar studies have already been conducted in the West, but the specifics of risk perception are highly dependent on the cultural environment and may differ from country to country. For example, in America the image of radiation is strongly associated with comic book characters [10], radiation does not contaminate but "infects" [11], but in other cultures perception of radiation risks may be different, which may be related to other modes of transmission and other images of radiation.

### 2. Methods

The paper presents the results of a social survey of the population of the Russian Federation in 2019. Among other things, the questionnaire included questions about the perception of radiation risks. The position of risk from diagnostic medical uses of radiation in the structure of public perception of radiation risks from other sources, such as high background radiation areas, nuclear power plants, radon, cosmic rays during plane trips, X-ray security scanners, radioactivity in food and drinking water, was determined.

The survey represented the population of Russia by gender, age, and region of residence. The random sampling error does not exceed 2.5% for a 95% confidence level. The survey was conducted within the



framework of the IAEA technical cooperation project RER9153 "Development of Regional Capabilities to Control Long-Term Risks to Population Due to Radon Exposure in Households and Workplaces".

In addition to socio-demographic characteristics such as sex, education, income, age, respondents were asked to indicate the level of risk that they considered relevant for them personally (personal level) and for the population of the country as a whole (societal level). The following options were available 1 - low, 2 - rather low, 3 - moderate, 4 - rather high, 5 - very high, 6,7 - don't know, I prefer not to answer. The logistic model with the dependent variable of perception of medical risks was used in the analysis of the results. The model was dichotomized in advance: the answer options "high" and "very high" were taken as 1, other options - as 0. Besides, to rank the radiation risks, the method of arithmetic mean calculation was used, for which the scale was transformed into a numeric one, the answer options 6,7 - "don't know" and "I prefer not to answer" were removed from the analysis. To compare the researched by socio-demographic groups the method of calculation of chi-square values was applied.

### 3. Results and discussion

Studies of risk perception have found a distinction in the perception of personal risks and generalized (societal) risks [12]. In our study, no differences were found in the perception of medical radiation risks at the personal and generalized (societal) level (Table 1).

**Table 1.** Personal and societal perception of radiation risks

	Personal, % high and very high	Personal average (max 5 points)	Societal, % high and very high	Average societal (max 5 points)
Areas with high natural radioactivity (e.g., the vicinity of uranium mines)	66.7	3.88	66.8	3.98
Nuclear power plants	38.9	3.09	43.6	3.29
Radon at home and in the workplace	30.6	3.06	33.7	3.22
Natural radioactivity of drinking water and food	25.4	2.86	28.2	3.00
Medical exposure (X-rays, CT scans, etc.)	17.5	2.76	16.9	2.76
Inspection units (security frames)	8.5	2.27	8.5	2.33
A two-hour airplane flight	5.9	2.23	6.9	2.30

The problem of medical risks among other radiation risks is one of the least acutely perceived - the respondents are more seriously concerned about the risks of living in areas with high natural radioactivity, nuclear power plants, natural radioactivity of drinking water and food products, less concerned about safety inspection frames and airplane flights.

The socio-demographic differences in the public perception of risk from diagnostic medical uses of radiation were also investigated. It was found that women

were more inclined to assess societal risk as high (20.6% vs. 12.4% among men,  $\chi^2=17.883$ ,  $df=1$ ,  $P\text{-value}<0.001$ ). The respondents with the lowest income (below the minimum wage) tend to assess this risk for the entire Russian

population higher than respondents with income above the minimum wage (22.5% vs. 16.0%,  $\chi^2=4.33$ ,  $df=1$ ,  $P\text{-value}<0.05$ ). The respondents in the 25-54 age group perceive personal risk more acutely (from 19.5% to 20.3% assess this risk as high) than the respondents of younger and older ages (11.5% and 13.3% respectively,  $\chi^2=12.106$ ,  $df=3$ ,  $P\text{-value}<0.01$ ) and a similar pattern is observed for societal risk.

The data are confirmed by logistic models (see Tables 2 and 3). The perception of medical radiation risks depends on the income, age, gender of the respondent. No connection with the level of education was found, as in the case of the chi-square method. In general, it can be argued that more privileged members of society perceive risk more calmly, in America this is called "white male effects" [13, 14]. The small values of the pseudo-P squares showed that the sociodemographic characteristics of the respondents play a secondary role in the difference in radiodiagnostic risk perception.

**Table 2.** Dependent variable - perception of medical risks, personal level

	B	Significance
Income, above minimum wage*	-,436	,037
Education, higher**	,189	,238
Gender, female***	,114	,455
Age_25-39****	,174	,572
Age_40-54****	-,399	,049
Age_55 and older****	-,460	,031
Constant	1,779	,000
* - reference category "below minimum wage", ** - reference category "without higher education", *** - reference category "male", **** - reference category "under 24 years"		
Cox and Snell R-squared 0.012, Nagelkerk R-squared 0.020		

**Table 3.** Dependent variable - perception of medical risks, societal level

	B	Significance
Income, above minimum wage*	-,439	,039
Education, higher**	,295	,076
Gender, female***	,339	,031
Age_25-39****	-,418	,177
Age_40-54****	-,830	,000
Age_55 and older****	-,618	,010
Constant	2,009	,000
* - reference category "below minimum wage", ** - reference category "without higher education", *** - reference category "male", **** - reference category "under 24 years"		
R-squared Cox and Snell 0.026, R-squared Nagelkerk 0,044		

#### 4. Conclusion

In general, medical risks are not perceived as acutely as risks from nuclear power plants and uranium mine surroundings, but more acutely than from inspection frames or airplane flights. When communicating the risks to the most vulnerable populations - low-income, women - it should be borne in mind that they feel the least protected and perceive medical radiation risks most acutely. Presenting the risk information in the form of a graph is the best strategy in order to convince the patient of the radiodiagnostics benefit (alternative risks of poor diagnosis) [15, 16] and the lack of significant financial benefit to the medical institution.

#### 5. References

- Hall, E. J., & Brenner, D. J. (2008). Cancer risks from diagnostic radiology. *The British journal of radiology*, 81(965), 362-378
- Brenner, D. J., & Hall, E. J. (2007). Computed tomography—an increasing source of radiation exposure. *New England journal of medicine*, 357(22), 2277-2284.
- Onischenko G.G., Popova A.Yu., Romanovich I.K., Vodovatov A.V., Bashketova N.S., Istorik O.A., Chipiga L.A., Shatsky I.G., Sarycheva S.S., Biblin A.M., Repin L.V. Modern principles of the radiation protection from sources of ionizing radiation in medicine. Part 2: radiation risks and development of the system of radiation protection. *Radiatsionnaya Gygiena = Radiation Hygiene*. 2019;12(2):6-24. (In Russ.) <https://doi.org/10.21514/1998-426X-2019-12-2-6-24>
- Berrington Gonzalez A de, Mahesh M, Kim KP et al (2009) Projected cancer risks from computed tomographic scans performed in the United States in 2007. *Arch Intern Med* 169:2071–2077
- Schindera, S. T., Nauer, C., Treier, R., Trueb, P., Von Allmen, G., Vock, P., & Szűcs Farkas, Z. (2010). Strategies for reducing the CT radiation dose. *Radiologie*, 50(12), 1120-1122.
- Younger, C. W. E., Wagner, M. J., Douglas, C., & Warren-Forward, H. (2019). Describing ionising radiation risk in the clinical setting: a systematic review. *Radiography*, 25(1), 83-90.
- Slovic, P. (1996). Perception of risk from radiation. *Radiation protection dosimetry*, 68(3-4), 165-180.
- Sjöberg, L. (2000). Specifying factors in radiation risk perception1. *Scandinavian Journal of Psychology*, 41(2), 169-174.
- Slovic, P., Flynn, J., Mertz, C. K., Poumadere, M., & Mays, C. (2000). Nuclear power and the public. In *Cross-cultural risk perception* (pp. 55-102). Springer, Boston, MA.
- Hendee, W. R. (1991). Personal and public perceptions of radiation risks. *RadioGraphics*, 11(6), 1109–1119. doi:10.1148/radiographics.11.6
- Erikson, K. (1990). Toxic reckoning: business faces a new kind of fear. *Harvard Business Review*, 68(1), 118-126.
- Coleman, C. L. (1993). The influence of mass media and interpersonal communication on societal and personal risk judgments. *Communication research*, 20(4), 611-628
- Kahan, D. M., Braman, D., Gastil, J., Slovic, P., & Mertz, C. K. (2007). Culture and identity-protective cognition: Explaining the white-male effect in risk perception. *Journal of Empirical Legal Studies*, 4(3), 465-505.
- Finucane, M. L., Slovic, P., Mertz, C. K., Flynn, J., & Satterfield, T. A. (2000). Gender, race, and perceived risk: The 'white male' effect. *Health, risk & society*, 2(2), 159-172.
- Freudenberg LS, Müller SP, Beyer T, Bockisch A. Subjective perception of radioactivity: no change after successful treatment with radioiodine [in German]. *Nuklearmedizin*. 2009;48:84–88.
- Erikson, K. (1991). Radiation's lingering dread. *Bulletin of the Atomic Scientists*, 47(2), 34-39.

## **ESTIMATION METHOD OF BREAST ABSORBED RADIATION DOSE DURING CORONARY ANGIOGRAPHY**

Tatjana VIGOVSKA<sup>1</sup>, Katrina CAIKOVSKA<sup>2</sup>, Mara EPERMANE<sup>3</sup>

<sup>1</sup>Riga Technical University; <sup>2</sup>Riga East university hospital; <sup>3</sup>Riga East university hospital  
<sup>1</sup>vigovska.t.n@gmail.com; <sup>2</sup>katrina.caikovska@gmail.com; <sup>3</sup>mara.epermane@aslimnica.lv

**Abstract:** Due to the growing number and complexity of coronary angiography examinations, it is highly important to estimate absorbed radiation dose for breast tissue. The aim of this study was to develop an estimation method of breast dose during coronary angiography. During the study breast dose was measured for 15 adult female patients who underwent percutaneous coronary intervention. Gafchromic RTQA2 film was used to estimate breast dose and correlation factor was found between breast dose and cumulative dose.

**Keywords:** Coronary angiography; Percutaneous coronary intervention; Gafchromic film; Breast absorbed radiation dose; Estimation method

### **1. Introduction**

Coronary angiography is one of the high-dose and long exposure time interventional radiology examinations and it is performed using an angiography equipment. During coronary angiography, various radiosensitive organs, such as breast tissue, are exposed to ionizing radiation. The breast tissues are exposed to direct x-ray beam and have a low recovery rate, therefore it is important to evaluate dose to breast tissue during coronary angiography procedures [1]. During the examination, the angiography system registers various radiation parameters such as kerma area product (KAP) and cumulative dose [2]. To estimate the breast dose to individual patient in vivo measurements were performed. Results from the measurements were used to find correlation between breast dose and data provided by angiography system. The aim of this study was to develop an estimation method of breast dose during coronary angiography using the data provided by the angiography system.

### **2. Materials and methods**

In this study, doses to breast tissue were determined using gafchromic RTQA2 films (size 1x12.7 cm, dynamic range 0.02 Gy to 8 Gy) for 15 female patients

during percutaneous coronary intervention (PCI) with and without stenting between March and May 2021. Percutaneous coronary intervention procedures were chosen for this study due to the long exposure times and high patient doses based on previous literature [3, 4]. The research was carried out in Riga East University Hospital, Latvia, using *GE healthcare Innova 2100* angiography equipment. This study was approved by the local esthetic committee and can be tracked under 6-1/12/45. All patients signed confirmation to participate in this study.

Before the study, film calibration was done in X-ray beam at dose range 0-2Gy. The film was placed side by side with solid state detector *MagicMaX* on the surface of polymethyl methacrylate (PMMA) plate with thickness 70 mm. The X-ray tube was positioned under the table (180°) and the film was irradiated using a tube voltage of 120 kV and 32 mA current. Gafchromic films were scanned and digitized at least 12 hours after irradiation using Epson 1200XL scanner in 48-bit color, 75 dpi resolution and no color correction [5]. The mean pixel values for films (using red channel) were extracted using *ImageJ* program [6]. 4th polynomial function was used to determine calibration equation (1) (coefficient of determinisms is 0.997) [7].

$$D = (0.019 \cdot 10^{12} x^4 - 2.7338 \cdot 10^9 x^3 + 1.478 \cdot 10^4 x^2 - 3.5468 x + 31\,954.6118) \cdot 1000 \quad (1)$$

To determine absorbed dose by breast tissue, two gafchromic film strips with the size 1x12.7 cm (area used for measurements – 0.6x12.1 cm) were placed on each patient as shown in figure 1. Film Nr.1 was placed in the middle of left breast and film Nr.2 was placed in center of the patient – between the breasts. Both films were secured with tape. The position of film strips was chosen based on information from previous literature, where using phantom the measured dose for left breast was 2.3 mGy and for right breast 1.17 mGy [8]. During the procedure the X-ray tube may be in varies positions, but mainly the position is under the table, the distance between the table and the tube varies from 50 to 110

cm. Standard protocols with automatic exposure control were used for all patients, a catheter was inserted through the right wrist arteries.

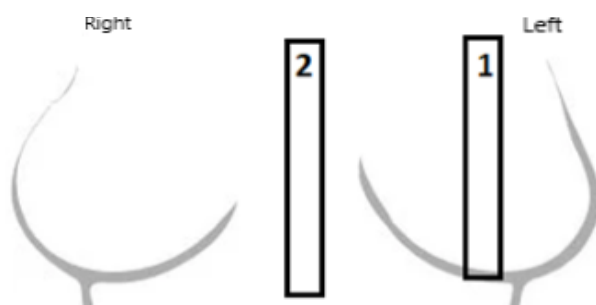


**Fig 1.** Gafchromic film position over breasts.

Patients' parameters were recorded before examination - weight, chest circumference and over-bust chest circumference are shown in Table 1.

**Table 1.** Patients' anatomical parameters

n=15	Minimum value	Median value	Maximum value
Weight (kg)	48	80	116
Chest circumference (cm)	80	95	115
Circumference over bust (cm)	98	114	132

Patient weight varied in range of 68 kg with median value – 80 kg. Chest circumference varied in range of 35 cm with median value 95 cm and circumference over bust varied in range of 34 cm with median value of 114 cm.

### 3. Results and discussion

From the data provided by angiography system, median KAP value and median cumulated dose for 15 patients was calculated using *Excel* formula MEDIAN. Table 2 includes median exposure parameters registered by angiography system – KAP and cumulated dose. 8 patients underwent PCI with stenting and 7 patients without stenting.

**Table 2.** Median exposure parameters

Stenting	Median KAP value (mGy*cm <sup>2</sup> )	Median cumulated dose (mGy)
With	21725,0	560,5
Without	24020,0	588,0
Total for 15 patients	23985,0	588,0

As shown in table 2, there was an insignificant difference between median KAP value and median cumulated dose value for PCI procedures with and without stenting (deviation 0% - 9.4% from total median values). Therefore all data from 15 patients

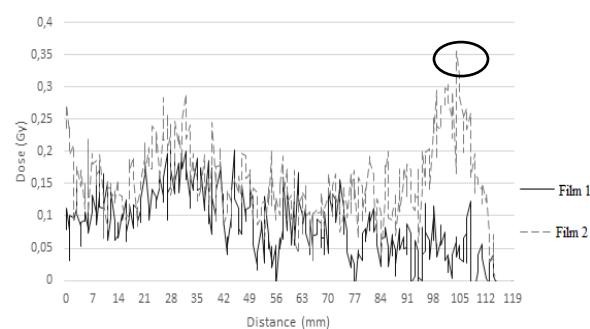
(with and without stenting) were used to develop an estimation method of breast dose.

Table 3 contains data for absorbed dose for each film and breast tissue.

**Table 3.** Absorbed dose for 15 patients

Patient nr.	Film 1 (mGy)	Film 2 (mGy)	Absorbed dose by breast (mGy)
1	205±12	355±12	280±12
2	312±12	352±12	332±12
3	199±12	308±12	253±12
4	101±12	104±12	103±12
5	138±12	223±12	181±12
6	110±12	141±12	125±12
7	56±12	262±12	159±12
8	124±12	285±12	205±12
9	150±12	194±12	172±12
10	347±12	119±12	233±12
11	163±12	283±12	223±12
12	240±12	132±12	186±12
13	261±12	158±12	209±12
14	169±12	159±12	164±12
15	120±12	276±12	198±12

Absorbed dose for the film 1 and film 2 was found by plotting a dose profile in *ImageJ* software and selecting a maximal dose value as shown in figure 2. Figure 2 contains absorbed dose data along the film strip - x-axis represents the location of the dose value on the film strip (point 0 on x-axis corresponds to a point at the top of the film).



**Fig 2.** Example of dose profiles for patient 1

Selected maximal dose values from film strips for each patient are included in table 3. Breast tissue dose was estimated by calculating the average dose value for maximal dose point on the film 1 and film 2. Median breast dose to 15 patients for the film strip placed in the middle of the left breast was  $180 \pm 12$  mGy (max  $347 \pm 12$  mGy), and for the film strip placed between patient's breasts was  $223 \pm 12$  mGy (max  $355 \pm 12$  mGy). Film 2 placed on the skin between breasts, absorbed higher dose.

To evaluate the dose distribution on patient's skin, averaged dose profiles were created using *ImageJ* and

*Excel*. From averaged dose profiles a schematic illustration for dose distribution was created and included as figure 3. Dark grey lines illustrate higher doses (0.12 Gy) and light grey lines – low doses (<0.02 Gy). As shown in figure 3 – film 2 absorbs higher doses, as well the maximum absorbed dose is located between the breasts.

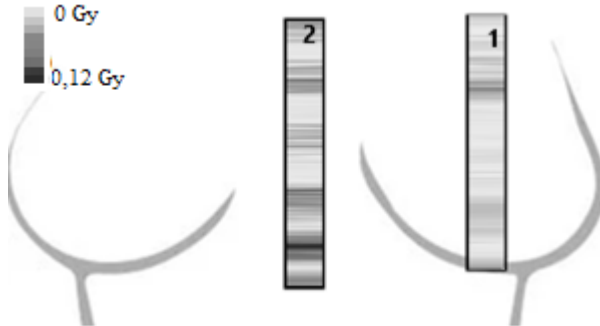


**Fig 3.** Averaged dose profile for gafchromic films

To develop an estimation method for breast dose using parameters from angiography system, correlation between absorbed dose and KAP and correlation between cumulated dose and absorbed breast dose was determined by plotting a graph. From the graph correlation factor was found.

Correlation coefficient between cumulative dose and absorbed breast dose is 0.79 (coefficient of determinism – 0.91) as shown in figure 4. Correlation coefficient was calculated using *Excel* equation *CORREL*.

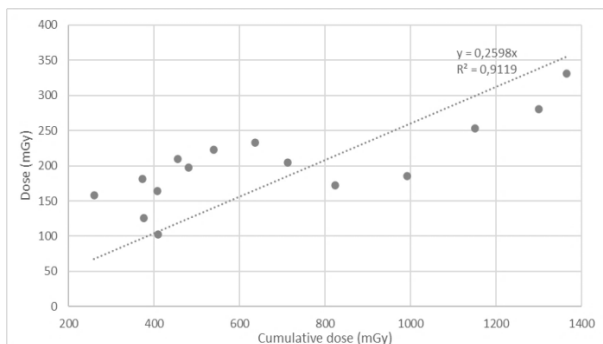


**Fig 4.** Absorbed dose by breast tissue depending on cumulative dose

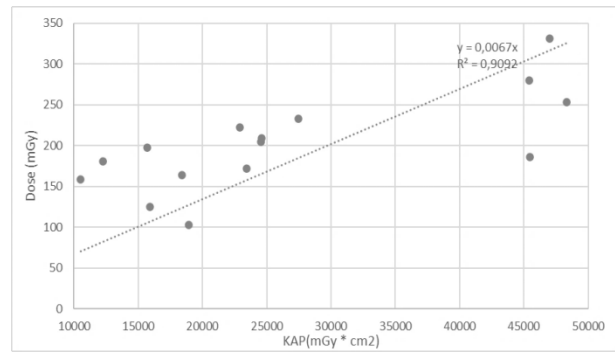
To estimate breast absorbed dose (D) during PCI, the following formula must be used:

$$D = 0,2598 * (\text{cumulative dose}) \quad (2)$$

Correlation coefficient between KAP and absorbed dose is 0.73 (coefficient of determinism – 0.91) as shown in figure 5.

To estimate breast absorbed dose during PCI, the following formula must be used:

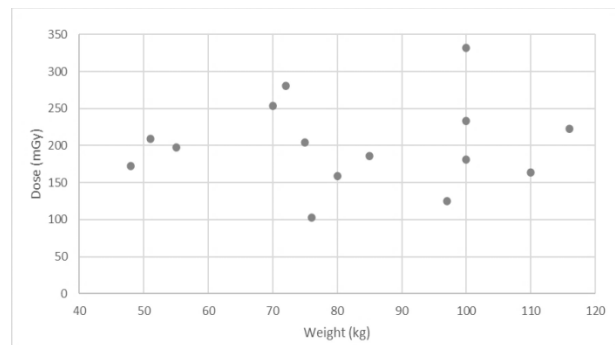
$$D = 0,0067 * \text{KAP} \quad (3)$$



**Fig 5.** Absorbed dose by breast tissue depending on KAP

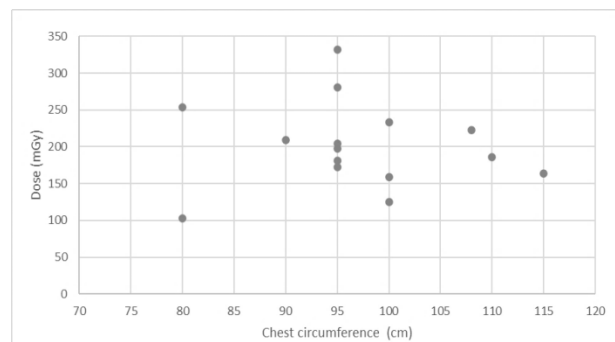
Higher accuracy for absorbed dose calculation will be reached using cumulative dose (2), nonetheless it is possible to use KAP values (3).

To evaluate breast dose dependence on patient's anatomical parameters, dose dependence graphs were created. Figure 6 shows that there is no correlation between patient's weight and breast dose (correlation coefficient 0.06).



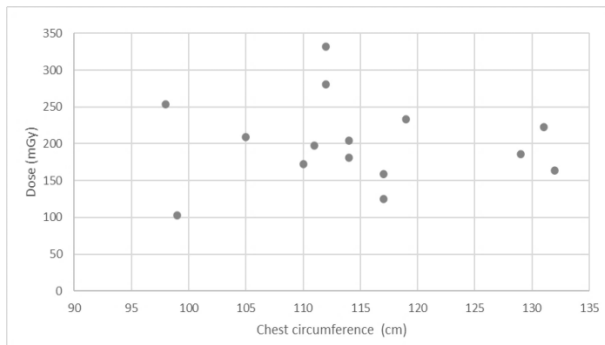
**Fig 6.** Absorbed dose by breast tissue depending on patients' weight

Figure 7 shows that there is no correlation between patient's chest circumference and breast dose (correlation coefficient -0.06).



**Fig 7.** Absorbed dose by breast tissue depending on patients' chest circumference

Figure 8 shows that there is no correlation between patient's circumference over bust and breast dose (correlation coefficient -0.05).



**Figure 8.** Absorbed dose by breast tissue depending on patients' circumference over bust

The correlation between patient's anatomical parameters and absorbed dose by breast tissue was not found. Therefore, developed estimation method does not depend on patient's anatomical parameters and this method can be used for any patient that underwent percutaneous coronary intervention with or without stenting regardless of their weight, chest circumference, cup size.

#### 4. Conclusions

The results of this study show that:

- 1) To estimate the breast dose for patients that underwent PCI procedures, cumulated dose displayed by angiography system should be multiplied by factor 0.2598.
- 2) Higher accuracy for absorbed dose calculation will be reached by using cumulative dose data, nonetheless is possible to use KAP values and multiply them with factor 0.0067.
- 3) Multiplying factors developed in this study can be used for every patient regardless of their anatomical parameters.
- 4) Largest dose is absorbed by the breast tissues located closer to patient's center.

5) The developed method for breast dose estimation is limited for PCI procedures using angiography system.

#### 5. References

1. Engel, C. L., Sharima Rasanayagam, M., Gray, J. M., & Rizzo, J.. Work and female breast Cancer: the state of the evidence, 2002–2017. *NEW SOLUTIONS: A Journal of Environmental and Occupational Health Policy*, 2018. P. 55-78.
2. Writing committee members, Hirshfeld Jr, J. W., Balter, S., Brinker, J. A., Kern, M. J., Klein, L. W., Weitz, H. H. ACCF/AHA/HRS/SCAI clinical competence statement on physician knowledge to optimize patient safety and image quality in fluoroscopically guided invasive cardiovascular procedures: a report of the American College of Cardiology Foundation/American Heart Association/American College of Physicians Task Force on Clinical Competence and Training. *Circulation*. 205. p. 511-532.
3. Betsou, S., Efstathiopoulos, E. P., Katritsis, D., Faulkner, K., & Panayiotakis, G. Patient radiation doses during cardiac catheterization procedures. *The British journal of radiology*. 1998. p. 634-639.
4. Crowhurst, J. A., Whitby, M., Thiele, D., Halligan, T., Westerink, A., Crown, S., & Milne, J. Radiation dose in coronary angiography and intervention: initial results from the establishment of a multi-centre diagnostic reference level in Queensland public hospitals. *Journal of medical radiation sciences*. 2014. p. 135-141.
5. Reinstein, L. E., Gluckman, G. R., & Meek, A. G. A rapid colour stabilization technique for radiochromic film dosimetry. *Physics in Medicine & Biology*. 1998. p. 2703.
6. Devic, S., Seuntjens, J., Hegyi, G., Podgorsak, E. B., Soares, C. G., Kirov, A. S., ... & Elizondo, A. Dosimetric properties of improved GafChromic films for seven different digitizers. *Medical physics*. 2004. p. 2392-2401.
7. Mong, K. S., Wallace, A. B., & Franich, R. D. Asymmetric breast dose in coronary angiography. *Journal of applied clinical medical physics*, 2016. p. 532-541.
8. Ратнер, Т. Г., & Лебеденко, И. М. Клиническая дозиметрия. Физико-технические основы. 2017. 259 p.

## **RADIATION DOSE FOLLOW-UP FOR COMMON INTERVENTIONAL CARDIOLOGY AND RADIOLOGY PROCEDURES**

Leonid KRYNKE<sup>1</sup>, Birutė GRICIENĖ<sup>1,3</sup>, Antonio JREIJE<sup>1,2</sup>, Laura BILOTAITĖ<sup>3</sup>

<sup>1</sup>Vilnius University Hospital Santaros Klinikos, Vilnius, Lithuania; <sup>2</sup>Department of Physics, Kaunas University of Technology, Kaunas, Lithuania; <sup>3</sup>Vilnius University, Faculty of Medicine, Vilnius, Lithuania  
leonid.krynke@santa.lt; birute.griciene@santa.lt; antonio.jreije@santa.lt; laura.bilotaite@mf.vu.lt

**Abstract:** Radiation dose delivered to patients undergoing invasive angiography and interventional radiography procedures remains relatively high. International guidelines suggest that local benchmarks should be established for these procedures. The purpose of this study was to establish local diagnostic reference levels (DRLs) for common interventional radiology and cardiology procedures and to compare them with local DRLs set in 2015 and National DRLs. The six-month investigation covered six fluoroscopy units and focused on seven interventional radiology examination types. DRLs were set as the 3rd quartile of the dose area product (DAP), surface entrance dose (ESD) and fluoroscopy time (FT) values. This work indicated that preliminary local DRLs can provide an adequate reference tool for patient dose optimization and a reflection on clinical practices.

**Keywords:** Interventional radiology, Radiation protection, Diagnostic reference level, Patient dose

### **1. Introduction**

Interventional radiology guides different critical procedures including stent placement, angioplasty, embolization, radiofrequency ablation, taking biopsies and treating tumors. The use of examinations involving fluoroscopy, especially in interventional cardiology procedures is rapidly increasing due to substantial decrease in associated risks, pain, expenses as well as improved recovery when compared to invasive procedures [1]. However, these types of examinations are associated with longer exposure time and higher effective doses up to 100 mSv as opposed to regular diagnostic examinations. Consequently, this result in a significant risk of health effects, notably to the skin, including several reported cases of skin erythema, dermal atrophy and ulcerations [2].

In this context, different radiation protection bodies such as the ICRP and IAEA recommend maintaining radiation exposure from radiological procedures as low

as possible and monitoring patient doses closely at a local, regional and national level. This can be achieved successfully by implementing a system of dose reference levels, which was formulated by the ICRP as a tool for dose optimization in diagnostic and interventional medical imaging [3, 4]. Setting up DRLs for examinations involving fluoroscopy could be a challenging task due to the large difference in the exposure time and the number of acquired images between patients resulting in a large variability of patient dose observed for the same fluoroscopic procedure. This is attributed to the lack of well-established definition of the performed examination, differences in the used techniques and protocol parameters, complexity of each case and the experience of the radiologist [5].

The most important aspect of quality assurance in interventional radiology should be the regular assembly of patient doses and the comparison of the median values with existing local and national DRLs in order to decide if any further correction action is necessary to optimize patient exposure.

Due to the complexity of fluoroscopic exposures, national DRLs for common interventional radiology procedures are, until present, not established in most countries. In Lithuania, national DRLs were set in 2018 for two interventional radiology examinations (coronary angiography and coronary intervention) [6], despite the fact that this radiographic technique is used to conduct additional procedures such as transcatheter aortic valve implantation, pacemaker implantation/replacement, chemoembolization, etc. The aim of this work was to assess the local diagnostic reference levels (DRLs) for most common interventional radiology procedures and to compare the new DRLs with previously evaluated local DRLs as well as National DRLs when available.

### **2. Materials and Methods**

Data collection was carried for seven interventional procedures performed on six angiography systems at



Vilnius University Hospital Santaros Klinikos from January until June 2021 (Fig. 1).

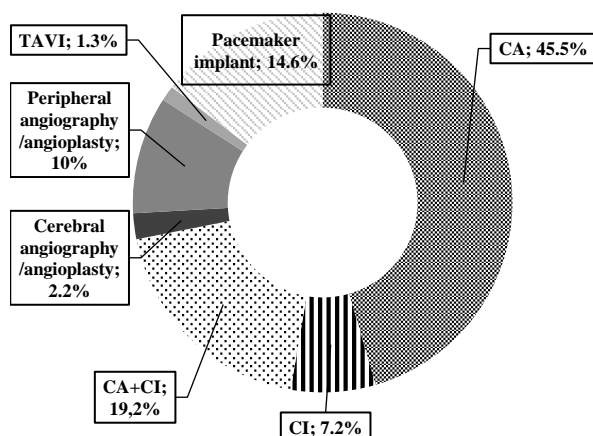


**Fig. 1.** Distribution of Interventional exams carried out over a six-month period.

Information about fluoroscopy equipment in use at the hospital including manufacturer, model and year of installation are presented in Table 1.

**Table 1.** Fluoroscopy equipment information

OR	Model	Manufacturer	Installation year
1	C-arm, OEC Elite	GE	2021
2	Innova IGS 520	GE	2019
4	Azurion 7	Philips	2020
5	Trinias B12	Shimadzu	2017
7	Innova 2100	GE	2009
8	Allura Xper FD20	Philips	2015

For each examination, patient-related and dosimetry-related data were collected: procedure type, performing physician, dose area product (DAP), entrance surface dose (ESD), fluoroscopy time (FT) as well as patient height and weight (if available in the report book). Local DRLs were established for the following procedures: coronary angiography (CA), coronary intervention (CI), transcatheter aortic valve implantation (TAVI), cerebral angiography and/or angioplasty (Cerebral ANG/PTA), peripheral angiography and/or angioplasty (Peripheral ANG/PTA) and pacemaker implantation/replacement (Pacemaker). Local DRL were set as the 75<sup>th</sup> percentile of the distribution of DAP, ESD and FT as recommended by the European commission (Council Directive 2013/59/EURATOM) [7] and Radiation Protection Centre in Lithuania (methodical guidelines for patients dose estimation in diagnostic radiology) [8].

Statistical analysis was performed using “SPSS Statistics” in order to compare exposure dose and time between fluoroscopy equipment for angiography and angioplasty procedures. Differences between medians were estimated using Kruskal-Wallis non-parametric test with follow-up pair wise comparison with Mann-Whitney test. Differences were considered statistically significant for  $p$ -value  $<0.05$ .

### 3. Results and discussion

A total of 2186 collected examinations between January and June 2021 was included in this study. The most performed procedures at hospital were coronary angiography and angioplasty (995 CA; 420 CA & CI). These cardiovascular (CV) procedures were performed in 4,7,8 operation rooms (OR). Results of DAP and FT for different CV interventional procedures along with comparison with Lithuanian DRLs are presented in Fig. 2 and Fig. 3 respectively. Direct comparison of the three operation rooms indicated a statistically significant difference in patient doses delivered during CA and CI (Kruskal-Wallis test,  $p$ -value  $<0.05$ ). In the case of combined CA & CI procedures, follow up Mann-Whitney test revealed no significant difference between OR 1 & 3 ( $p$ -value = 0.539). Similarly, registered exposure times were different between the three-operation room for CA (difference not significant between OR 1 & 2; Mann-Whitney test  $p$ -value = 0.115). Nevertheless, no significant difference between ORs was found in case of CI ( $p$ -value = 0.705) and CA & CI ( $p$ -value = 0.286). These differences can be attributed to several factors such as difference in the used equipment in each operation room, experience of the practitioner (10 physicians were involved in performing CV procedures) and the degree of complexity of each examination.

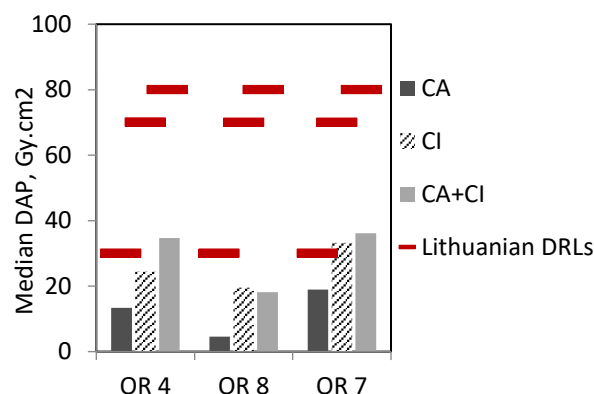


**Fig. 2.** Median dose area product (DAP) for cardiovascular interventional procedures in three different operation rooms compared with Lithuanian DRLs.

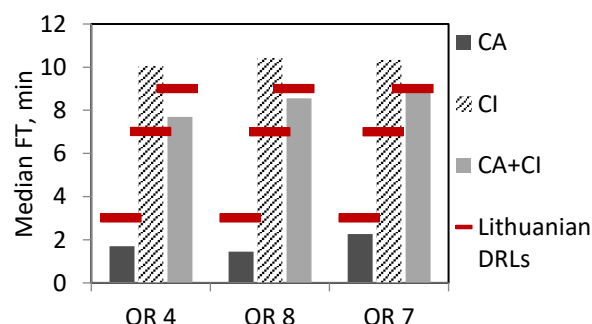


**Fig. 3.** Median fluoroscopy time (FT) for cardiovascular interventional procedures in three different operation rooms compared with Lithuanian DRLs.

Median dose (DAPs) were compared with national DRLs and with data collected at hospital in 2015 for few interventional procedures as part of work done on patient protecting against ionizing radiation. Median DAPs for all interventional procedures were



significantly lower than national DRL. When compared with data from 2015, dose delivered to patients undergoing interventional procedures in general decreased (from 51% for CA&CI and up to 74% for TAVI). The median time taken to perform interventional procedures in general decreased (table 4). Since physicians at hospital undergoes trainings on the aspects of radiation protection, they are aware of exposure time-dose relationship and seek to limit exposure time whenever possible.

Additional factor that could contribute to this notable change in patient doses include the size of data used in setting median dose values (i.e. data from 2015 was based on a smaller sample size of 761 procedures). Therefore, DRL should be updated frequently in order to account for all previously mentioned factors.

In this work, local DRLs were only established for CA (DAP 23 Gy.cm<sup>2</sup>, Dose 292 mGy) and CA+CI (DAP 56 Gy.cm<sup>2</sup>, Dose 785 mGy). Setting DRL for other procedures need additional data collection and investigation.

Finally, it should be mentioned that some difficulties were faced when establishing local DRLs at hospital. A major limitation of this study was unregistered patient weight and height for most procedures which prompted

setting DRLs without any size correction factor. This issue will be addressed when updating local DRLs in the near future. Moreover, data processing was a challenging task, thus suggesting that a better definition of the procedures is required.

**Table 2.** Entrance surface dose for interventional procedures.

Procedure/Number		Dose, mGy (2021)		Dose, mGy (2015)	
		Median	75 <sup>th</sup>	Median	75 <sup>th</sup>
CA	995	162	292	377	608
CI	157	429	750	-	-
CA+CI	420	470	785	916	1426
Cerebral ANG/PTA	47	225	393	450	896
Peripheral ANG/PTA	220	155	247	-	-
TAVI	29	252	320	1566	-
Pacemaker	318	7	16	-	-

**Table 3.** Dose area products (DAPs) for interventional procedures; \* Lithuania (2018); \*\* Germany (2019); \*\*\* Finland (2016)

Procedure	DAP, Gy.cm <sup>2</sup> (2021)		DAP, Gy.cm <sup>2</sup> (2015)		National DRLs
	Median	75 <sup>th</sup>	Median	75 <sup>th</sup>	
CA	12.3	22.5	30.4	48.2	30*
CI	26.7	46.5	-	-	70*
CA+CI	32.1	55.6	65.6	106.2	80*
Cerebral ANG/PTA	21.1	43.5	50.9	70.9	-
Peripheral ANG/PTA	19.6	31.0	-	-	25**
TAVI	23.1	33.2	91.0	-	80**
Pacemaker	0.9	2.3	-	-	3.5***

**Table 4.** Fluoroscopy times (FT) for interventional procedures; \* Lithuania (2018); \*\* Germany (2019); \*\*\* Finland (2016)

Procedure	FT, min (2021)		FT, min (2015)		National DRLs
	Median	75 <sup>th</sup>	Median	75 <sup>th</sup>	
CA	2.0	3.5	2.3	-	3*
CI	8.8	13.0	9.5	-	7*
CA+CI	10.4	16.2	-	-	9*
Cerebral ANG/PTA	6.1	11.0	11.2	-	-
Peripheral ANG/PTA	9.5	18.9	-	-	18**
TAVI	11.1	13.4	17.3	-	18**
Pacemaker	2.9	5.3	4.0	-	5***

#### 4. Conclusions

Statistical evaluation related to patient doses in interventional radiology and cardiology procedures, mainly performed at the hospital in 2021 was done. The results showed that median doses are smaller than national DRLs. In addition, follow-up with data collected in 2015, exposure dose and time decreased significantly for all procedures.

Local DRLs were established for 2 main interventional cardiology procedures (CA and CI+CA).

The established local DRLs will be further used for the patient dose optimization.

#### 5. References

1. Tsapaki V, Ahmed NA, AlSuwaidi JS, et al. Radiation exposure to patients during interventional procedures in 20 countries: initial IAEA project results. *AJR Am J Roentgenol* 2009; 193: 559–69.
2. Koenig TR, Wolff D, Mettler FA, et al. Skin injuries from fluoroscopically guided procedures: part 1, characteristics of radiation injury. *AJR Am J Roentgenol* 2001; 177: 3–11.
3. Committee 3 ICRP. Diagnostic reference Levels in medical imaging: Review and additional advice. 2012; 1–7. (accessed 04/08/2013). Available from: [http://www.icrp.org/docs/DRL\\_for\\_web.pdf](http://www.icrp.org/docs/DRL_for_web.pdf).
4. IAEA Safety Series No. 115: International basic safety standards for protection against ionizing radiation and for the safety of radiation sources. Vienna: International Commission on Radiological Protection; 1996.
5. Bartal G, Vano E, Paulo G, Miller DL (2014) Management of patient and staff radiation dose in interventional radiology: current concepts. *Cardiovasc Intervent Radiol* 37:289–298
6. Order No. V-952 “Approval of diagnostic reference levels applicable during radiation diagnostics and intervention radiology procedures” by the Lithuanian Minister of Health Care. 2018.
7. European Commission (2014) Council Directive 2013/59/EURATOM of 5 December 2013 laying down basic safety standards for protection against the dangers arising from exposure to ionising radiation. *Off J Eur Union* L31:1–73.
8. Radiation protection Centre in Lithuania. Methodical guidelines for patient radiation dose estimation in diagnostic radiology, (accessed 10/09/2021). Available from: [https:// www.rsc.lt/ index.php/ pageid/717](https://www.rsc.lt/index.php/pageid/717).

## **RELATION BETWEEN THE SEVERITY OF THE COURSE OF THE DISEASE AND DOSES AND RADIATION RISK OF THE CHEST X-RAY AND CT EXAMINATION OF CHILDREN WITH COVID-19**

Iliya SHATSKIY <sup>1</sup>, Dmitry IVANOV <sup>2</sup>, Vitaly REZNIK <sup>3</sup>, Aleksandr POZDNYAKOV <sup>4</sup>, Viktor PUZYREV <sup>5</sup>,  
Yuliya KAPYRINA <sup>6</sup>, Anna NABIEVA <sup>7</sup>, Karine PANUNTSEVA <sup>8</sup>, Svetlana BANNOVA <sup>9</sup>, Yury PETRENKO <sup>10</sup>  
<sup>1</sup>St-Petersburg Research Institute of Radiation Hygiene after Professor P.V. Ramzaev; <sup>2,3,4,5,6,7,8,9,10</sup>Saint-Petersburg  
State Pediatric Medical University, Russian Federation

<sup>1</sup>I.Shatskiy@niirg.ru; <sup>2</sup>spb@gpmu.org; <sup>3</sup>vitaliy-reznik@mail.ru; <sup>4</sup>pozdneyakovalex@yandex.ru;  
<sup>5</sup>vgpuzyrev@mail.ru; <sup>6</sup>kapyrina-yuliya@yandex.ru; <sup>7</sup>hamatum@bk.ru; <sup>8</sup>kpanuntseva@mail.ru; <sup>9</sup>svetlanalb81@mail.ru;  
<sup>10</sup>klinika.spb@gmail.com

**Abstract:** The effective doses and radiation risks of X-ray and CT examinations for children during the diagnosis and treatment of COVID-19 were assessed and the dependence of the number of examinations and the total radiation risk for one patient on the severity of the disease was analyzed. Sufficient grounds to assert if the severity of the course of the disease is associated with radiation risks from the performed CT examinations have not been received.

**Keywords:** chest imaging, computed tomography, radiation risk, children, COVID-19

### **1. Introduction**

Computed tomography (CT) is used to diagnose the coronavirus disease COVID-19 along with the reference standard analysis of respiratory tract samples using next-generation sequencing methods or reverse transcription polymerase chain reaction methods. In the early stages of the disease and with minimal clinical manifestations, on the chest X-ray, there may be no focal changes, and therefore, this method has low sensitivity. In addition, at the initial stages of the disease, lesions in the lungs appear as "ground glass", which is not sensitive for radiography [1]. At the same time, computed tomography is a more highly sensitive method of investigation for viral pneumonia. Although for the follow-up of the patient, chest x-ray may be recommended [2-4], in accordance with Russian guidelines [5, 6], to assess the dynamics of the process of lung damage, it is necessary to use only one type of examination. In addition, in critically ill patients, immediate CT may be mandatory for diagnosis and assessment of disease severity. Although COVID-19 usually causes more severe symptoms in older patients, the number of younger

patients may increase in the future. However, in children, the CT findings are generally mild and due to its high radiation burden, the exact role of early chest CT imaging remains unknown [7]. The risk of developing radiation-induced cancers is higher for children. Although repeat examinations are not required for most patients, patients with severe and progressive symptoms may have CT examinations repeatedly to monitor pulmonary changes. Consequently, there is a need to assess the radiation doses to children for the possibility of subsequent optimization of such examinations, as well as the assessment of radiation risks, especially for multiple examinations. The aim of the study was to assess the effective doses and radiation risks of X-ray and CT examinations for children during the diagnosis and treatment of COVID-19, as well as to analyze the dependence of the number of examinations and the total radiation risk for one patient on the severity of the disease.

### **2. Materials and methods**

The study used the data of X-ray studies of 71 children admitted to the clinic of the St-Petersburg State Pediatric Medical University with suspicions of COVID-19, 58 children of them underwent 104 X-ray examinations, and 30 CT scans were taken for 22 children. One patient could undergo both several of the same type, as well as a combination of X-ray and CT examinations. All patients were divided into five age groups of children: newborns (<0.5), 0.5-2, 3-7, 8-12 and 13-18 years old - with an average age of 0, 1, 5, 10 and 15 years respectively. Anthropometric data for each age group corresponded to mathematical anthropomorphic phantoms [8] and were taken as characteristics of a "standard patient" in each age group to collect typical treatment regimens and calculate doses.

The input physical parameters for calculating organ doses and effective dose of the patient for X-ray devices were radiation output of the device, filter thickness and material, voltage at the tube anode, exposure, distance from source to receiver, size of the irradiation field, geometry of irradiation, for CT – CTDI, tube anode voltage, exposure, pitch, collimation, DLP, effective diameter of the target area.

The absorbed doses in organs and effective doses were calculated for X-ray units using the PCXMC program for each patient, and for CT using NCICT 3.0 for typical study parameters. Both programs use the same mathematical anthropomorphic phantoms [8] to model the patient's body, which contain a set of 31 organs/tissues needed to calculate the effective dose using tissue weighting factors from ICRP Publication 103.

The subsequent calculation of lifetime attributive risks according to the model given in Publication 103 of the ICRP was carried out in accordance with the methodology published in the article by Ivanov et al. [9]. The absorbed doses in organ were interpolated to 5 y age bands corresponding to data available concerning the age dependence of radiation risk. The final lifetime detriment-weighted radiation risk  ${}^{\text{det}}R_p(A, G)$  was calculated using the ratio of radiogenic incidence  ${}^{\text{inc}}R_p(A, G)$  of organ O to detriment D from Table A.4.18 [10]

A detailed methodology and conditions for calculating doses and radiation risks are given in previous publications [11-13].

The assessment of the severity (volume, area, extent) of changes in the lungs in patients with suspected/known COVID-19 pneumonia was carried out using an "empirical" visual scale [6, 14]. It is based on a visual assessment of the approximate volume of compacted lung tissue in both lungs and consists of five groups:

1. Absence of characteristic manifestations (CT-0)
2. Minimum volume/prevalence <25% of lung volume (CT-1)
3. Mean volume/prevalence 25-50% of lung volume (CT-2)
4. Significant volume/prevalence of 50 - 75% of lung volume (CT-3)
5. Critical volume/prevalence > 75% of lung volume (CT-4)

### 3. Results and discussion

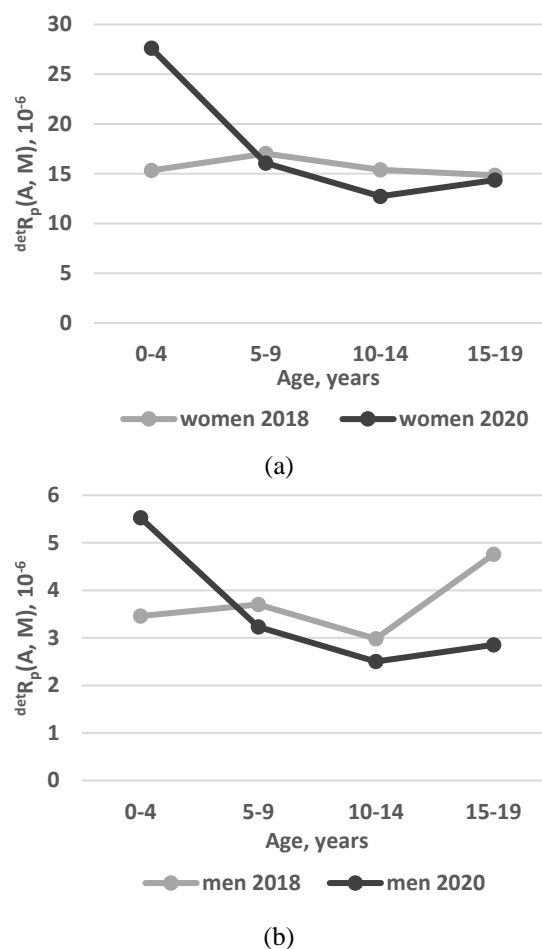
The median values of the effective dose for X-ray chest examinations for all age groups are in the range of 0.09-0.13 mSv (Table 1). The highest values are observed in the 0-4 age group. Effective doses for chest CT scan were 3.21 mSv and 4.68 mSv for groups 5-9 and 15-19 years old, respectively.

The radiation risk for all types of examination for female patients is several times greater than for male patients. For X-ray studies for women, it ranges from  $12.73 \cdot 10^{-6}$  to  $27.62 \cdot 10^{-6}$ , for men from  $2.5 \cdot 10^{-6}$  to  $5.52 \cdot 10^{-6}$ . The minimum corresponds to the age group 10-14 years old, and the maximum – to the group 0-4 years old. For CT, the risk increases with age from  $425.97 \cdot 10^{-6}$  for the 5-9-year group to  $434.37 \cdot 10^{-6}$  for 15-19 years.

**Table 1.** Effective doses (mSv) and radiation risks per examination.

Age group	Examination	Effective dose ICRP103 (mSv)	Radiation risk, men, $10^{-6}$	Radiation risk, women, $10^{-6}$
0-4	Chest X-ray	0.13	5.52	27.62
5-9	Chest X-ray	0.09	3.23	16.08
10-14	Chest X-ray	0.09	2.50	12.73
15-19	Chest X-ray	0.12	2.85	14.37
5-9	Chest CT	3.21	140.39	425.97
15-19	Chest CT	4.68	169.10	434.37

Comparison of the results with previous similar studies in St. Petersburg [11-13] are presented in Figure 1. In contrast to the practically unchanged risk values of X-ray examinations for women of all age groups in previous studies in St. Petersburg, in the current study, the risk decreases with increasing age with a minimum at the age group of 10-14 years. The largest difference between studies in 2018 and 2020 is observed for the younger age group 0-4, although the values for the other groups are approximately the same. For men, the dependences of risk on age are oppositely directed: in previous studies, the risk increased unevenly with age, and in the current one it decreases unevenly.



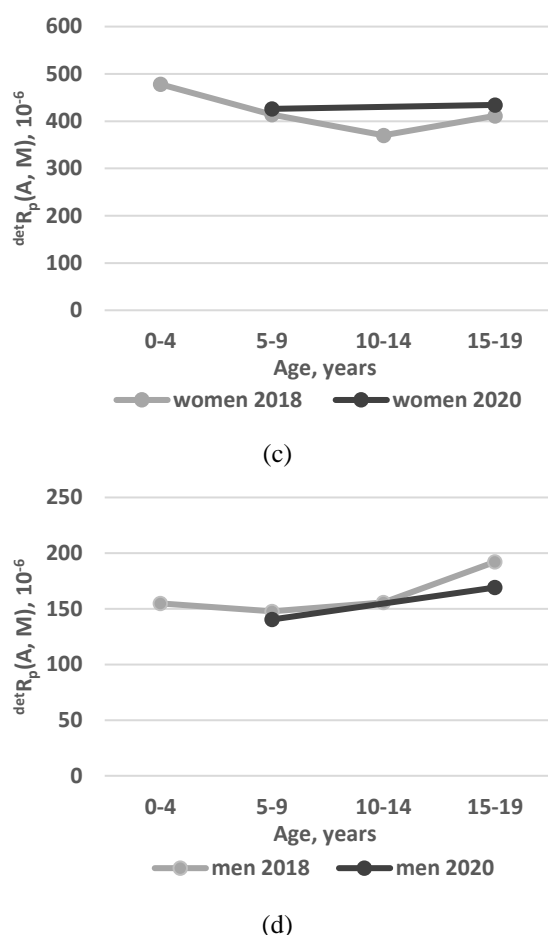


**Fig. 1.** Radiation risks of chest X-ray (a, b) and CT (c, d) examinations for children of both sexes in 2018 and 2020 in St. Petersburg

The current study has data for only two age groups, for CT examinations, so it is difficult to fully judge the relationship between risk and age. But the values for each of the groups for both sexes are quite similar to results from previous studies [15].

To determine the degree of influence of the severity of the course of the disease on the number of studies and, accordingly, radiation risks, a one-sided Kruskal-Wallis analysis of variance of the total radiation risks from CT examinations of the patient was carried out for the entire period of hospitalization for each degree of lung damage.

**Table 2.** Medians of the number of examinations and the total risks of a patient for CT scan, depending on age, gender and severity of the course of the disease.

Age group	Sex	severity of changes in the lungs			
		CT-0	CT-1	CT-2	CT-3
Number of examinations					
5-9	w		2.00	2.00	
5-9	m	1.00	2.00	2.00	2.00
15-19	w	1.00	2.00		
15-19	m		2.00	3.00	
Radiation risk. 10 <sup>-6</sup>					
5-9	w		851.94	851.94	
5-9	m	140.39	280.77	280.77	280.77
15-19	w	434.37	868.73		
15-19	m		338.19	507.29	

The medians of the number of studies and the total risks of a patient for CT scan depending on age and sex are shown in Table. 2.

The results of the analysis for the entire sample of patients ( $H = 9.7745$ ,  $p = 0.0206$ ) meet the criteria for statistically significant differences between the groups of lesions, and, consequently, the dependence of the number of CT examinations and radiation risks on the severity of the disease. But an additional multiple comparison of the average ranks of all groups showed significant differences only between CT-0 and CT-1. A more detailed analysis of each age-sex subgroup of patients did not reveal any statistically significant differences between the groups of lesions in any of them (Table 3).

**Table 3.** Results of Kruskal-Wallis analysis of variance of the total radiation risks from CT examinations for severity of lung damage for entire sample of patients and each age-sex subgroup.

severity of changes in the lungs	severity of changes in the lungs			
	CT-0	CT-1	CT-2	CT-3
Entire sample of patients $H = 9.7745$ $p = 0.0206$				
CT-0	-	0.0175	0.8283	1
CT-1	0.0175	-	1	0.7252
CT-2	0.8283	1	-	1
CT-3	1	0.7252	1	-
Age group 5-9, men $H = 5.0$ $p = 0.1718$				
CT-0	-	1	1	0.3350
CT-1	1	-	1	1
CT-2	1	1	-	1
CT-3	0.3350	1	1	-
Age group 5-9, women $H = 0.25$ $p = 0.6171$				
CT-0	-	-	-	-
CT-1	-	-	0.7237	-
CT-2	-	0.7237	-	-
CT-3	-	-	-	-
Age group 15-19, men $H = 2.0$ $p = 0.1573$				
CT-0	-	-	-	-
CT-1	-	-	0.2207	-
CT-2	-	0.2207	-	-
CT-3	-	-	-	-
Age group 15-19, women $H = 4.0$ $p = 0.0455$				
CT-0	-	0.1573	-	-
CT-1	0.1573	-	-	-
CT-2	-	-	-	-
CT-3	-	-	-	-

It is necessary to take into account the small size of the age-sex subgroups, which can affect the accuracy of the obtained results. Nevertheless, the current study has not received sufficient grounds to assert that the severity of the course of the disease is associated with radiation risks from the performed CT examinations. In a systematic review of the radiological characteristics of COVID-19 in pediatric population [7], it was found that most children with COVID-19 demonstrate similar radiological manifestations as in adults, except for a higher percentage of normal scans (26%). Pulmonary

findings on pediatric imaging studies were often milder compared to adults, probably indicating a milder inflammatory response induced by COVID-19 in this population. This may partly correlate with the results of this study on the absence of a relationship between dose and radiation risk of chest x-ray and CT examination and the severity of the course of the disease.

However, it should be noted that higher incidence of normal CT or frequent asymptomatic/oligosymptomatic pediatric COVID-19 cases might also underline the importance of early detection of the disease in this specific population [7]. The results obtained allow to conclude that it is necessary to take into account the dependence on age and sex when assessing radiation risks and especially the relationship between the severity of the disease and the levels of exposure and radiation risks.

Finally, the continuation of the study and an increase in patients sample will allow to clarify the results and draw more reliable conclusions.

#### 4. Conclusions

Radiation risk for X-ray studies ranges from  $12.73 \cdot 10^{-6}$  to  $27.62 \cdot 10^{-6}$  for women and from  $2.5 \cdot 10^{-6}$  to  $5.52 \cdot 10^{-6}$  for men. The minimum corresponds to the 10-14 years age group, and the maximum – to the group 0-4 years. For CT, the risk increases with age, from  $425.97 \cdot 10^{-6}$  for the 5-9-year group to  $434.37 \cdot 10^{-6}$  for 15-19 years. The age dependence of radiation risk for X-ray examinations differs from the results of previous studies. The values for each of the groups for both sexes for CT examinations coincide quite closely with results from previous studies. The current study has not received sufficient grounds to assert that the severity of the course of the disease is associated with radiation risks from the performed CT examinations. The continuation of the study and an increase in the sample of patients will allow to clarify the results and draw more reliable conclusions.

#### 5. References

1. Lee E, Yang J et al. Imaging profile of the COVID-19 infection: radiologic findings and literature review. *Radiol Cardiothorac Imaging* 2020; 2(1)
2. Revel M.P., Parkar A.P., Prosch H., Silva M., Sverzellati N., Gleeson F. European Society of Radiology (ESR) and the European Society of Thoracic Imaging (ESTI). COVID-19 patients and the radiology department - advice from the European Society of Radiology (ESR) and the European Society of Thoracic Imaging (ESTI) *Eur Radiol.* 2020 doi: 10.1007/s00330-020-06865-y.
3. Salehi S, Abedi A, Balakrishnan S and Gholamrezanezhad A 2020 Coronavirus disease 2019 (COVID-19): A systematic review of imaging findings in 919 patients *Am. J. Roentgenol.* 215 87-93.
4. Lippi G, Simundic A and Plebani M 2020 Potential preanalytical and analytical vulnerabilities in the laboratory diagnosis of coronavirus disease 2019 (COVID-19) *Clin. Chem. Lab. Med.* 58 1070–6.
5. Guidelines - features of clinical manifestations and treatment of a disease caused by a new coronavirus infection (COVID-19) in children. Version 2 (03.07.2020) Ministry of Health of the Russian Federation, Moscow, 2020. – 74 p.
6. Interim guidelines "Prevention, diagnosis and treatment of new coronavirus infection (COVID-19). Version 6 (approved by the Ministry of Health of the Russian Federation on April 28, 2020).
7. Katal S, Johnston SK, Johnston JH, Gholamrezanezhad A. Imaging Findings of SARS-CoV-2 Infection in Pediatrics: A Systematic Review of Coronavirus Disease 2019 (COVID-9) in 850 Patients. *Acad Radiol.* 2020 Nov;27(11):1608-1621. doi: 10.1016/j.acra.2020.07.031. Epub 2020 Jul 30. PMID: 32773328; PMCID: PMC7392075.
8. Cristy M., Mathematical phantoms representing children of various ages for use in estimates of internal dose. ORNL, NUREG/CR-1159, ORNL/NUREG/TM-367 (1980).
9. Ivanov, V., Tsyb, A., Mettler, F., Menyaylo, A. and Kashcheev, V. Methodology for estimating cancer risks of diagnostic medical exposure: with an example of the risks associated with computed tomography. *Health Phys.* 103 (6), 732-739 (2012).
10. International Commission on Radiological Protection. Recommendations of the International Commission on Radiological Protection. ICRP Publication 103. *Ann ICRP*, 37 (2-4) (2007).
11. Shatsky I.G. Risk assessment of medical exposure in X-ray examinations of children. *Radiatsionnaya Gygiena = Radiation Hygiene.* 2017;10(2):31-42. (In Russ.) <https://doi.org/10.21514/1998-426X-2017-10-2-31-42>.
12. Balonov M., I. Shatsky Evaluation of radiation risks from medical exposures: Organ dose approach versus effective dose approach. *J. Radiation Protection № 187*, European Commission Radiation Protection and nuclear Safety: 45-59 (2018).
13. Ilia Shatskii. Use of organ dose approach versus effective dose approach in risk assessment for the common radiographic X-ray examinations of children. Proceedings of the 13th international conference on Medical Physics in the Baltic States 2017. 9 – 11 November, 2017: 104 – 109.
14. Shohei Inui, Akira Fujikawa, Motoyuki Jitsu, Naoaki Kunishima, Sadahiro Watanabe, Yuhi Suzuki, Satoshi Umeda, and Yasuhide Uwabe Chest CT Findings in Cases from the Cruise Ship Diamond Princess with Coronavirus Disease (COVID-19) *Radiology: Cardiothoracic Imaging* 2020 2:2.
15. Federal Service for Supervision of Consumer Rights Protection and Human Welfare of the Russian Federation MR 2.6.1.0215-20. 2.6.1. Ionizing radiation, radiation safety. Assessment of radiation risk in patients during X-ray and radiological studies. Methodical recommendations.

## **GAMMA SPECTROSCOPIC ANALYSIS OF 18 MeV PHOTONS ACTIVATED RADIOISOTOPES IN SIEMENS ONCOR IMPRESSION 3D LINAC HEAD AND ITS DECOMMISSIONING EXPERIENCE**

Aurimas KRAULEIDIS<sup>1,2</sup>, Vanda ANDRIJAITIENĖ<sup>1</sup>

<sup>1</sup>Klaipėda University hospital <sup>2</sup>Department of Physics, Kaunas University of Technology  
aurimas.krauleidis@gmail.com; vanda.andrijaitiene@gmail.com

**Abstract:** Medical linear accelerators (linacs) are the most used technique to treat various forms of cancers in patient by different energies megavoltage photon beams. However, product of the high-energy photons (>8 MeV – 10 MeV) generated by a linear accelerator is activation of components within the machine itself. The activation products cause regulatory and radiological challenges during the operation of the accelerator as well as when it is time for final decommissioning. The responsible authorities for radioprotection require a measurement of the activity of the linacs, when hospital is dismantling and/or replacing their equipment.

The purpose of this work was to measure residual activity and to identify the remaining radioisotopes present in the Siemens Oncor Impression 3D linac components. Based on preliminary results decommissioning case was made.

**Keywords:** high-energy photons, spectroscopy, decommissioning.

### **1. Introduction**

The techniques and equipment used for radiation treatments of cancer have become increasingly sophisticated. The application of linear accelerator for cancer treatment has allowed for radiation to be delivered at higher energies and with greater penetration and accuracy than ever before. With the introduction of techniques such as IMRT and VMAT, the energy of the radiation produced by these machines can reach energies of 20 MeV [1,2].

In radiation therapy with photon beams ( $E > 10$  MeV), neutrons are generated thorough photonuclear reactions of photons with nuclei of high atomic number materials constituting the linac head and the beam collimation system. The most common photonuclear reaction is the  $(\gamma, n)$  in which a high energy photon will interact with the target nuclei resulting in the emission of a neutron [3]. This neutron will travel a distance and will lose energy through interaction with the surrounding material until it undergoes an  $(n, \gamma)$  interaction which results in the

activation of a material outside of the initial photon beam. This photoactivation include linac components, patient support systems, treatment accessories, building material, air and the patient [4,5]. The linear accelerator head components such as the target, primary collimators, flattening filter, secondary collimator, and multileaf collimators (MLCs) are made of high Z materials. When high energy photons interact with high Z material, the probability of production of activated nuclei is significant. These high Z materials (lead and tungsten) are found principally in the flattening filters and in the collimator system. Most of the activation products in tungsten will be short lived  $^{187}\text{W}$  ( $T_{1/2} = 23.7$  h) and  $^{181}\text{W}$  ( $T_{1/2} = 121.2$  d), while in lead alloys the content of antimony gives rise to  $^{121}\text{Sb}$  (short lived) and  $^{124}\text{Sb}$  ( $T_{1/2} = 60.2$  d). Gold may be present in foils or monitor chambers, leading to the production of  $^{198}\text{Au}$  ( $T_{1/2} = 2.7$  d) [6]. Activation of the chemical elements of these materials leads to unstable isotopes, decaying with very different half-lives. Most of the activated radioisotopes are decaying with short half-lives, in the range of hours or days, but some other radioisotopes have half-lives of several years [7].

In 2004, a study of the induced activity of various components of an 18 MV Siemens KDS linac was conducted [8]. Activation products were found in the target, window wave-guide, flattening filter, and wedge. Typical radionuclides produced by the photoactivation process in components are summarized in Table 1.

The activities found in Table 1. were estimated from the set of measurements the team made seven days after the accelerator's last clinical use. It was determined that the most activated component of the linear accelerator head was the target.

Other author analyzed the long term activation produced in the treatment head of a 15 MV Mevatron Siemens 77 medical linac one year after its last clinical use. Ten different components of the treatment head were analyzed for radionuclide activity including, accelerating waveguide terminal, two external shields, target sledge, scattering foil support, sledge stirrup, primary photon

collimator, flattening filter, and jaw. From these measurements it was shown that one year after the medical linacs last clinical use, the bulk of the material exhibited a specific activity of less than 1 Bq/g. Common radioisotopes found in the materials included  $^{54}\text{Mn}$ ,  $^{57}\text{Co}$ ,  $^{58}\text{Co}$ ,  $^{60}\text{Co}$ ,  $^{65}\text{Zn}$ ,  $^{181}\text{W}$  [9,10].

**Table 1.** Activation products found in an 18MV Siemens KDS linac

Linac components	Radionuclide	Half-life (days)	Energy (keV)	Estimated activities and uncertainty ( $k = 2$ ) (kBq)
Target	XR Au		65–77	
	$^{196}\text{Au}$	6.2	333.0	7100 $\pm$ 710
	$^{196}\text{Au}$		355.7	
	$^{196}\text{Au}$		426.1	
Window wave-guide	$^{54}\text{Mn}$	312	834.8	27 $\pm$ 8.1
	$^{57}\text{Co}$	272	122.0	16 $\pm$ 1.9
	$^{57}\text{Co}$		136.5	
	$^{51}\text{Cr}$	28	320	11 $\pm$ 1.8
	$^{196}\text{Au}$	6.2	333	18 $\pm$ 2.2
	$^{196}\text{Au}$		355.7	
	$^{196}\text{Au}$		426.1	
	$^{198}\text{Au}$	2.69	411	
	$^{58}\text{Co}$	70.86	810.7	3 $\pm$ 0.3
	$^{54}\text{Mn}$	312	834.8	3 $\pm$ 0.4
	$^{60}\text{Co}$	1925	1174	11 $\pm$ 1.1
	$^{60}\text{Co}$		1333	1 $\pm$ 0.2
Flattening filter	$^{57}\text{Co}$	272	122.0	45 $\pm$ 5.4
	$^{57}\text{Co}$		136.5	
	$^{51}\text{Cr}$	28	320.0	37 $\pm$ 17.4
	$^{54}\text{Mn}$	312	834.8	40 $\pm$ 5.2
Wedge	Only background peaks were identified			

Also a study was conducted into the undesirable photonuclear, electronuclear, and neutron capture reactions that take place after high energy therapeutic beam emission. A Varian Clinac-2300 and a Primus Siemens medical linear accelerator were measured and the following radioisotopes were found:  $^{187}\text{W}$ ,  $^{56}\text{Mn}$ ,  $^{28}\text{Al}$ ,  $^{57}\text{Ni}$ ,  $^{38}\text{Cl}$ ,  $^{57}\text{Co}$ ,  $^{196}\text{Au}$ , and the neutron activation of  $^1\text{H}$  [11,12,13].

There are a variety of positive and negative issues associated with the activation of materials through photonuclear reactions. Materials activated in a linear accelerator can cause issues to arise during decommissioning of the machine as workers may be exposed to radiation from the activation products and also can potentially contribute to additional dose to patients and staff [14,15]. A number of studies have identified various radioisotopes produced from photoactivation, but few studies have quantified the total activity from these activated isotopes.

Accelerators decommissioning projects started in technical literature and a few detailed decommissioning reports from 1980s were published. Over time, documentation on decommissioning planning, costs and lessons learned became available to the international community. In 1999, the European Commission issued the report Evaluation of the Radiological and Economic Consequences of Decommissioning Particle Accelerators is the first publication that systematically provides information and guidance on accelerator decommissioning that can be usefully applied worldwide [16].

In 2020 IAEA published Decommissioning of particle accelerators [17]. This information can be used as the basis of costing for waste and materials management, but

predicted activities need to be verified for each of the individual pieces by dismantling the equipment after they have been checked for activation. Suitable instrumentation for initial screening includes portable contamination monitors, and for more detailed assessment of materials high resolution portable gamma ray spectrometry hyper-pure germanium (HPGe) systems can greatly assist in accurately identifying and quantifying the radionuclides present. Dose and dose rate meters can be used to evaluate the emission from components and to assess the order of magnitude of activation, according to the gamma ray emission constant for the principal radionuclide identified [18].

The benefits of early planning for future decommissioning include the establishment of optimized procedures to minimize the exposure of workers and the public to radiation, the provision of maximum levels of protection of the environment necessitated by the decommissioning activities, the minimization of radioactive waste, and the timely release of the facility or site from regulatory control at the end of decommissioning activities. Other benefits of considering decommissioning of a particle accelerator at the early stage of operation arise from the establishment of suitable record keeping arrangements, knowledge retention to facilitate decommissioning and provision of both adequate financial and other necessary resources for when shutdown occurs [18].

The initial decommissioning plan needs to be reviewed and updated periodically during operation. Changes in the design of the facility, the introduction of different waste management arrangements or alternative disposal routes, changes in the overall financial status or specific modifications of the equipment or building that will impact the decommissioning plan. Revisions or amendments to the decommissioning plan need to also be made during the operational lifetime of the facility to reflect advances in operational experience, new safety requirements, or the introduction of improved technology, as well as changes to the decommissioning strategy and proposed end state that have been agreed with the regulatory body. Such revisions or amendments need to be comprehensively documented and then stored in a suitable record retrieval system so that they will be readily available to facilitate future decommissioning. The plan also needs to be reviewed and revised when significant accidents or incidents occur that could affect facility characteristics [19].

The final decommissioning plan need to be submitted to the regulatory body for approval prior to commencement of decommissioning. All applicable requirements for the accelerator need to be appropriately maintained unless approved by the regulatory body on the basis of reduced hazards. In preparation for decommissioning, all operational waste (e.g. used targets, components of the accelerator or radioactive materials for ion sources or guns) will need to be removed and properly managed. The main objectives of waste management within the context of decommissioning of accelerators are to:

1. Minimize the quantities of radioactive waste at all stages of decommissioning;



2. Prevent the combination of waste of different categories (e.g. radioactive waste, hazardous chemical waste);
3. Comply with all applicable regulations in the handling, storage, processing and disposal of the waste.

## 2. Methods and materials

Linear accelerator Siemens Oncor Impression 3D has been in operation at Klaipeda University Hospital from 2010. The accelerator was in regular use for cancer treatment until 6 April 2021, with just minor periods when it was not operational owing to shutdown and planned maintenance, upgrading or repairs. Photon beam energies used for cancer treatment were 6 and 18 MeV. At the beginning of operation, the machine had a high workload for cancer treatment, about 120 patient per day. On April 2021, the linac was shut down and decommissioned, because new technologies and methods of cancer treatment have become available and the existing machine cannot be adapted to incorporate them. The normal life time of a device of this kind is between 10 and 20 years.

Before linac decommissioning, the following was done:

1. Final decommissioning plan of the facility was prepared according to national legislation.
2. Radiation protection programme and physical security description were supplemented.
3. Assessment of the quality and effectiveness of the measure was reviewed to ensure the physical security system.
4. Linac dismantling plan was prepared.
5. A contract with the radioactive waste manager for radioactive material disposal was concluded.

All essential information and documents for the decommissioning were accepted by responsible authorities and permission was granted to carry out decommissioning.

The next stage was to instruct all personnel working within the area on the radiation protection measure and work safety procedures and confirmed in the protocol.

The dismantling of the accelerator started on 6 April 2021 and was finished on 8 April 2021. The qualified company engineers had permission granted under the Lithuania radiation protection center to work in facilities to dismantling linacs. First of all, they carried out the heavy duty dismantling and disposal of inactive waste. According to the radiation protection programme all engineers had digital personal radiation dosimeters PM1703MO-I BT to evaluate the received exposure dose. (fig. 1).



**Fig.1** Personal radiation detector

While dismantling the machine hospital medical physicist continuously measured radiation background in the working area and also separated the activated parts of the machine using different kind of measurement equipment. Dose rate limit to separate parts was 0,2  $\mu\text{Sv/h}$ . For the  $\gamma$  dose rate measurement, medical physicist used portable multifunction dosimeter Atomtex AT 1123. Surface contamination was measured with portable contamination monitor CoMo 170, and  $\beta$  radiation was measured with RadEye B20 dose rate meter (Fig. 2).



**Fig. 2**  $\gamma$  radiation dosimeter (a), multi-purpose survey meter (b) and portable contamination monitor CoMo 170 (c)

According to meter data, activated linac parts were identified including vacuum window of the accelerating wave-guide, bending magnet core, the target and the flattening filter (Fig. 3).



**Fig.3** Activated linac parts, vacuum window of the accelerating wave-guide, the target and the flattening filter (a), bending magnet core (b)

Target consist of  $^{196}\text{Au}$  and  $^{54}\text{Mn}$  alloy. Flattening filter is made of stainless steel. The chemical composition of the main elements is the following: Fe 67.8%, Cr 19.0%, Ni 8.0%, Mn 2.0%, S 2.0%, Si 1.0%, C 0.12%, P 0.05%. For example, multileaf collimator driving engines was not activated, dose rate was below natural background. Total mass of activated parts was 158 kg.

To ensure safety and security, activated linac head parts were packaged in two 3 mm thickness steel transport boxes, in compliance with the regulations, marked with a sign of ionizing radiation and temporary storage in the department specific room with a security alarm, video surveillance system and limited access. Additionally, dose rate measurements were performed on storage-assisted radioactive packages. Packages dimensions were 280 x 460 x 100 (mm) and 345 x 310 x 220 (mm) (Fig.4).



**Fig.4** Radioactive material transporting boxes

At the termination of dismantling activities, on 8 April 2021, accumulated dose to the engineers was confirmed to be consistent with the working protocol and was added to their occupational exposure protocol. The disassembled linac was taken over completely by hospital engineering division as confirmed in the written procedure. The identified inactive parts were placed for recycling.

A Canberra Falcon 5000 High Purity Germanium (HPGe) detector was used to detect isotopes by gamma rays emitted from the activated parts (Fig. 5). It is portable and contains an ultra-low noise pulse tube cooling system capable of electrical cooling to operating temperatures of approximately  $-170^{\circ}\text{C}$  [20]. Detector operation was conducted through wired communication with an external tablet running Windows XP with spectra analysis support of Canberra's Genie 2000 and Fitzpeaks spectroscopy software. Gamma spectroscopy was performed by regulator body according to the agreement.



**Fig.5** A Canberra Falcon 5000 (HPGe)

After the characterization of radionuclides, radioactive waste manager removed activated materials from the hospital to Ignalina nuclear power plant storage decay. The responsibility of the hospital for the decommissioning project ended with the settlement of the bill to the radioactive waste manager. The cost for the radioactive waste disposal depends on isotopes spectrum, activity of isotopes and total weight of activated materials.

### 3. Results and discussion

#### 3.1 Accumulated dose

Based on personal radiation dosimeters data, accumulated dose to engineers was not higher than background level. Table 1 summarizes measured cumulative equivalent dose.

According to our results, company engineers did not received increased radiation exposure dose from radioactive materials. Radiation safety was ensured and radiation protection requirements were complied with.

**Table 1.** Engineers cumulative equivalent dose

Engineer	Working time, h	Cumulative equivalent dose, $\mu\text{Sv}$
1	27	3,25
2	27	2,83
3	27	3,12
4	27	2,25

#### 3.2 $\gamma$ , $\beta$ dose rate and surface contamination measurements

Dose rate and surface contamination results are shown in table 2. All measurements were done by previously mentioned devices, which are calibrated and metrologically verified.

**Table 2.** Measurements results

Measured point	Dose rate, $\mu\text{Sv/h}$		Surface contamination, $\text{Bq/cm}^2$
	$\gamma$	$\beta$	
Linac gantry:	5 cm	1 m	5 cm
a) left side	0,12	0,1	-
b) right side	0,08	0,07	-
c) above	0,13	0,1	-
d) in front	0,14	0,1	-
e) below (field closed)	0,1	0,09	-
e) below (field open)	0,24	0,1	1,47
Background at room after dismantling	0,1	-	-
Bending magnet	1,85	-	0,4
Flattening filter with accelerating wave guide window	1,36	2,58	0,4
Target	6,1	-	0,4
Background at storage room	0,11	-	-
Activated parts packed in transporting box Nr.1	<0,1	-	<0,4
Activated parts packed in transporting box Nr.2	<0,1	-	<0,4



**Fig 6.** Measurements points of linac gantry

Dose rate emission levels from activated components have been measured and have been found to be in the range of 0,08–0,24  $\mu\text{Sv/h}$  at 5 cm from the linac head and in the range of 0,07–0,1  $\mu\text{Sv/h}$  at 100 cm after 3 days in operation. Dose rates measured after dismantling was higher owing to the lack of shielding provided by the head. The highest activation levels were found in target, flattening filter and bending magnet with dose rates up to 6,1 microsieverts per hour at a distance of 5 cm. Also,  $\beta$  dose rate up to 2,58  $\mu\text{Sv/h}$  were measured from accelerating wave guide window. Based on the results, no surface contamination were observed.

### 3.3 Gamma – ray spectroscopy

Two total measurements were conducted and the gamma spectra was analyzed. First, it was measured for the activated accelerating wave-guide vacuum window, the target and the flattening filter parts. The gamma spectrum measured by a spectrometer showed gamma peaks corresponding to several activation products (fig. 7).

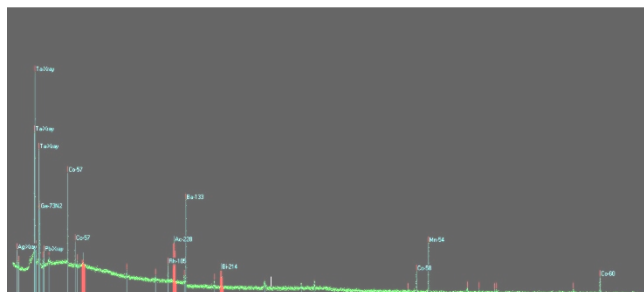


**Fig 7.** Gamma spectrum of the accelerating wave-guide vacuum window, the target and the flattening filter

Spectrum analysis revealed dominant radioisotopes  $^{51}\text{Cr}$ ,  $^{54}\text{Mn}$ ,  $^{57}\text{Co}$ ,  $^{58}\text{Co}$ ,  $^{60}\text{Co}$ ,  $^{181}\text{W}$ ,  $^{196}\text{Au}$  and  $^{198}\text{Au}$ , of which the highest peak of spectrum corresponded to  $^{181}\text{W}$  electron capture decay to  $^{181}\text{Ta}$  which results in x-ray photons. The spectrum showed the annihilation peak at 511 keV as a result of beta plus decay from  $^{54}\text{Mn}$ . The characteristics of each radioisotope are displayed in table 3.

**Table 3.** Radioisotopes measured in the accelerating wave-guide vacuum window, the target and the flattening filter

Radio isotope	Activity MBq	Uncertainty MBq	Peak energy keV	Half-life
$^{51}\text{Cr}$	0,11	0,02	320,1	27,7 d
$^{54}\text{Mn}$	0,1	0,01	835	312,3 d
$^{57}\text{Co}$	0,24	0,04	122,1	271,8 d
$^{58}\text{Co}$	0,021	0,002	811	70,8 d
$^{60}\text{Co}$	0,018	0,001	1173,5/1 332,8	5,3 y
$^{181}\text{W}$	9,8	1,2	EC (56,3 to 67,1)	121,2 d
$^{196}\text{Au}$	0,19	0,01	84,6	6,2 d
$^{198}\text{Au}$	0,0036	0,0001	411,9	2,7 d

The gamma spectrum of bending magnet core is shown in Figure 8. Table 4 summarizes the measured elements, essentially  $^{54}\text{Mn}$ ,  $^{57}\text{Co}$ ,  $^{58}\text{Co}$ ,  $^{60}\text{Co}$ ,  $^{124}\text{Sb}$  and  $^{59}\text{Fe}$ . The

results showed that the dominant activation products are  $^{54}\text{Mn}$ ,  $^{60}\text{Co}$  and  $^{59}\text{Fe}$  radioisotopes.

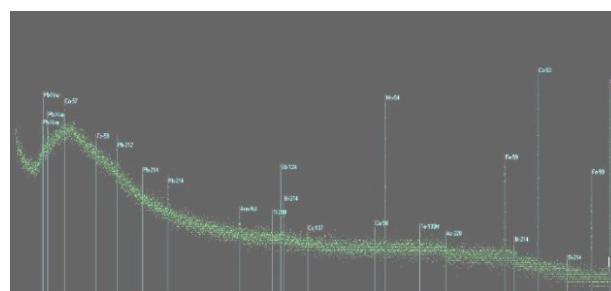


**Fig 8.** Gamma spectrum of bending magnet core

**Table 4.** Radioisotopes measured in bending magnet core

Radio isotope	Activity, MBq	Uncertainty, MBq	Peak energy, keV	Half-life
$^{54}\text{Mn}$	0,015	0,002	835	312,3 d
$^{57}\text{Co}$	0,002	0,001	122,1	271,8 d
$^{58}\text{Co}$	0,0011	0,0004	811	70,8 d
$^{60}\text{Co}$	0,031	0,002	1173,5/1 332,8	5,3 y
$^{124}\text{Sb}$	0,004	0,001	602,8	60,2 d
$^{59}\text{Fe}$	0,018	0,0001	1099/129 1,6	45 d

As already mentioned above, activation products are generated when the photoneutrons interact with the components of the linac head. The most probable reactions produced with a high energy photon beam are photonuclear ( $\gamma, n$ ) reactions. ( $\gamma, 2n$ ) reactions occur preferably at higher energies. When determining the activity of each radioisotope, it was found that dominant activation product were  $^{54}\text{Mn}$ ,  $^{181}\text{W}$  and cobalt isotopes. The highest observed radioactivity was 9,8 MBq of  $^{181}\text{W}$ . Based on spectrum analysis, almost all identified isotopes are long-lived, where half-life varies from few days to several years. For example, the natural Mn in the filters was activated through the reaction:  $n + ^{55}\text{Mn} \rightarrow ^{56}\text{Mn} + \gamma$ , but  $^{56}\text{Mn}$  half-time is 2,58 h and thus was not measured since the last operation of linear accelerator was 10 days before gamma spectroscopy measurement. Other studies analysis showed, that most dominant radioisotopes after irradiation are  $^{28}\text{Al}$  and  $^{24}\text{Na}$  with half-time 2,3 min and 15 hour respectively.

Based on previous studies, it has been shown that the treatment head parts and target are the primary source of induced activity.

### 4. Conclusions

In the current study, decommissioning of linear accelerator Siemens Oncor Impression 3D was carried out. It is necessary to mention that one of the most important steps was the decommissioning plan preparation to ensure smooth running of the process. Based on occupational doses, gamma and beta dose rate measurements we can assume that radiation protection was ensured. We have determined the spectra of activated linac parts and minimized the amount of low

activity radioactive materials to be stored in national facility. Dominant radioisotopes were  $^{54}\text{Mn}$ ,  $^{57}\text{Co}$ ,  $^{58}\text{Co}$ ,  $^{60}\text{Co}$ ,  $^{181}\text{W}$  which corresponded to the literature.

### Acknowledgements

The authors would like to thank the Radiation protection center specialists for their assistance with gamma spectroscopy data collection.

### 5. References

1. Fischer, H.W., Tabot, B.E., Poppe, B., Activation processes in a medical linear accelerator and spatial distribution of activation products, *Phys. Med. Biol.* 51 24, 2006.
2. Amgarou A., Lacoste V., Martin A., Experimental characterization of the neutron spectra generated by a high-energy clinical Linac. *Nuclear Instruments and Methods in Physics Research A* 629: 329-336, 2011.
3. Khan, F.M., Gibbons, J.P. Khan's The Physics of Radiation Therapy (5th ed.). Philadelphia, PA: Lippincott Williams & Wilkins, 2014.
4. Konefal A., Orlef A., Marcin D., Zbigniew M., Correlation between radioactivity induced inside the treatment room and the undesirable thermal/resonance neutron radiation produced by linac, 2008 *Physica Medica* 24(4):212-218.
5. Fujibuchi, T., Induced radioactive nuclides of 10-MeV radiotherapy accelerators detected by using a portable HP-Ge survey meter, *Radiat. Prot. Dosim.* 148 2, 2012, 168–173.
6. Garnett, R.W., Sheffield, R.L., Accelerator applications in energy and security, *Reviews of Accelerator Science and Technology*, Vol. 8 World Scientific Publishing Company, Singapore, 2015.
7. Wen-Shan L, Sheng-Pin Ch, Lung-Kwang P, Hsien-Chun T, Chien-Yi Ch. Thermal neutron fluence in a treatment room with a Varian linear accelerator at a medical university hospital. *Radiation Physics and Chemistry* 80: 917-922, 2011.
8. Roig M, Panettieri V, Ginjaume M, Sanchez-Reyes A. Photonuclear isotope characterization of a Siemens KDS 18 MV linac head, 2004, *Physics in Medicine and Biology* 49(14):N243-6.
9. Konefal A., Orlef A., Laciak M., Ciba A., Szewczuk M. Thermal and resonance neutrons generated by various electron and X-ray therapeutic beams from medical linacs installed in Polish oncological centers. *Reports of Practical Oncology and Radiotherapy*, 2012.
10. Brusa, A., Cesana, A., Stucchi, C., Terrani, M., & Zanellati, F. Long term activation in a 15 MeV radiotherapy accelerator. *Medical Physics*, 35(7), 2008 3049-3053.
11. Konefal, A., Orlef A., Bieniasiewicz M., Measurements of neutron radiation and induced radioactivity for the new medical linear accelerator, the Varian TrueBeam. *Radiation Measurements* Vol 86, 8-15, 2016.
12. Howard, S., Starovoitova, V.N. Target optimization for the photonuclear production of radioisotopes. *Applied Radiation and Isotopes*, 96, 2015, 162-167.
13. Fischer, H.W., Tabot, B., & Poppe, B. Comparison of activation products and induced dose rates in different high-energy medical linear accelerators. *Health Physics*, 2008, 94(3), 272-278.
14. Weber P., Vuilleumier J., Tamburella C., Linac activation of radioisotopes and underground gammaspectrometric analyses. *Materials Science, Medical Physics*, 2017.
15. Isra Israngkul-Na-Ayuthaya, Sivalee Suriyapee and Phongpheath Pengvanich, Evaluation of equivalent dose from neutrons and activation products from a 15-MV X-ray LINAC, *Journal of Radiation Research*, Vol. 56, No. 6, 2015, pp. 919–926.
16. International Atomic Energy Agency, Decommissioning of Facilities, IAEA Safety Standards Series No. GSR Part 6, IAEA, Vienna, 2014.
17. International Atomic Energy Agency. Decommissioning of particle accelerators, 2020. IAEA nuclear energy series, ISSN 1995–7807 ; no. NW-T-2.9
18. International Atomic Energy Agency, Safety Assessment for Facilities and Activities, IAEA Safety Standards Series No. GSR Part 4 (Rev. 1), IAEA, Vienna, 2016.
19. Krammar, M., The update of the European strategy for particle physics, *Physica Scripta*, 2013, T158.
20. Canberra Industries., Falcon 5000: User Manual. Meriden, CT: Canberra Industries and effects, 2011.

## A NEW MONTE CARLO ALGORITHM TO SIMULATE VIRTUAL SOURCE MODEL ON AN ELEKTA VERSAHD LINAC

Sumeyra CAN<sup>1</sup>, Didem KARACETIN<sup>2</sup>, Niyazi MERIC<sup>3</sup>

<sup>1</sup>Ankara University Institution of Nuclear Sciences; <sup>2</sup>Basaksehir Çam and Sakura City Hospital Radiation Oncology; <sup>3</sup>Ankara University Institution of Nuclear Sciences

<sup>1</sup>sumeyracn@gmail.com; <sup>2</sup>didemkaracetin@gmail.com; <sup>3</sup>niyazi.meric@ankara.edu.tr

**Abstract:** The aim is to develop a new Monte Carlo code namely MC-SCAN to simulate virtual source model. The dose calculation via MC-SCAN and experimental measurements were done. The difference between MC-SCAN and experimental measurement is 0.4% and 1.62% for absolute dose and TPR<sub>20/10</sub> respectively. For output factors, the difference between both approaches is < 4%. The MC-SCAN engine can be used to simulate virtual source model, however, further investigation needs to be done to develop this algorithm.

**Keywords:** Beam modelling, Elekta VersaHD, Monte Carlo simulation, Virtual Source Model

### 1. Introduction

The Monte Carlo simulation has been accepted as an accurate tool to calculate the radiation dose for radiation therapy. Knowing detailed phase space information including energy, type and angular distribution of particles provide to accurately predict radiation dose through Monte Carlo method for different geometry [1-3]. Additionally, direct measurement of PS information for clinic beam is not possible due to the high-level intensities of radiation at the medical linear accelerator (LINAC) exit window [4-6]. Moreover, some limiting factors - e.g. the availability of suitable detectors - prevent direct measurement of PS information; therefore, PS information which is mandatory for patient dose calculation is provided by Monte Carlo (MC) - based treatment planning system (TPS) such as Monaco TPS [7-10].

A Monaco beam model, i.e., a “Virtual Source Model (VSM),” includes beam components as primary beam photons, head scatter photons and electron contamination sources [11, 12]. In VSM, the particles coming from different parts of the accelerator are treated as if they were coming from these aforementioned virtual sources. To simulate full MC simulation of LINAC head information, dosimetric

measurements including square/rectangular open field data, percent depth dose, profiles and output factors should be provided [13]. The advantage of virtual source model-based MC simulation minimizes the difference between the calculated dose and the measured one [14-17].

In this study, it was aimed to develop a new Monte Carlo algorithm namely MC-SCAN as an alternative tool to simulate virtual source model on Elekta VersaHD LINAC.

### 2. Materials and Methods

#### 2.1. Experimental measurements for virtual source model

Before the experimental measurements, the absolute dose calibration was done per monitor unit (MU) for 10x10 cm<sup>2</sup> field size at 100 cm SSD and the depth of 10 cm. The geometry at which the absolute dose was calibrated turned to be 1 Gy/100 MU. Beam data collection to model virtual source model of Monaco TPS was done based on the manufacturer instructions and AAPM TG-106. A PTW BEAMSCAN (PTW, Freiburg, Germany) water phantom was used to perform all point dose, percent depth dose (PDD), tissue phantom ratio (TPR<sub>20/10</sub>), point dose measurements. All PDD measurements were acquired at 90 cm source to surface distance (SSD) for field size from 2x2 cm<sup>2</sup> to 40x40 cm<sup>2</sup>. Additionally, all point dose measurements in water were measured at 90 cm SSD and at the depth of 10 cm. A PTW PinPoint chamber (active volume = 0.016 cm<sup>3</sup>) was used for the field sizes ≤ 5x5 cm<sup>2</sup> whereas PTW Semiflex 3D chamber (active volume = 0.07 cm<sup>3</sup>) was used for the field sizes ≥ 5x5 cm<sup>2</sup>. For point dose measurements, an open field of 10x10 cm<sup>2</sup> at 90 cm SSD was created for testing purposes and the calculation was made with voxel-based Monte Carlo algorithm through Monaco TPS Version 5.51. Prescription dose was 200 cGy per fraction and 100 MU was delivered for the 6 MV photon energy. In order to represent the location of the ionization chamber, an



interest point was added in the Monaco plan. PTW Farmer type ionization chamber (active volume = 0.6 cm<sup>3</sup>) was utilized for point dose measurements along with PTW Unidose Weblin Electrometer.

## 2.2. Monte Carlo simulation (MC-SCAN code)

In Monte Carlo simulation, random number generator is the most crucial part. At this stage, the Mersenne Twister algorithm was implemented to generate large supplies of random number. The main reason to apply this algorithm is the random number period has  $2^{19937} - 1$  iteration and the generated random numbers repeat one time within this period. Since the source dimensions are very small compared to the source to surface distance (SSD), the source is modelled as a point source. The probability of a  $\gamma$ -ray from an isotropic point source is the same for all directions. The direction of a  $\gamma$ -ray emitted from the source is determined in spherical coordinates by the polar angle ( $\theta$ ) and the azimuth angle ( $\phi$ ). The polar angle of the direction of the  $\gamma$ -ray emitted from the point source varies in the range  $0 \leq \theta \leq \pi$ , and the azimuth angle varies in the range  $0 \leq \phi \leq 2\pi$ . In MC-SCAN dose engine, the  $\gamma$ -ray directions were determined randomly. The coordinates of the  $\gamma$ -rays, whose direction was determined, to the phantom surface were calculated with the following equation.

$$\alpha = \sin\theta x \cos\phi, \beta = \sin\theta x \sin\phi, \gamma = \cos\theta \quad (1)$$

$$x_0 = r\alpha, y_0 = r\beta, z_0 = r\gamma \quad (2)$$

where  $r = \text{SSD}/\cos\theta$ . If the calculated surface coordinates are in field size and provide the conditions that  $-A/2 \leq x_0 \leq A/2$  and  $-B/2 \leq y_0 \leq B/2$  where A and B field size, the photon was followed otherwise new photon which has a new energy and direction was sampled. After determining that the photon was in the water phantom, the atom photon interactions were modelled based on mean free path. If the interaction was photoelectric effect, it was accepted that the  $\gamma$ -ray transfers all its energy to the medium and a new photon tracking was started. When the interaction was Compton scattering, it was assumed that the  $\gamma$ -ray was scattered at  $\theta$  angle and the scattering angle was simulated with Klein-Nishina [18] given by the following equation.

$$\frac{d\sigma_{KN}}{d\Omega} = \frac{r_e^2}{2} [1 + k(1 - \cos\theta)]^{-2} [1 + \cos^2\theta + \frac{k^2(1 - \cos\theta)^2}{1 + k(1 - \cos\theta)}] \quad (3)$$

$$k = \frac{E}{mc^2} \quad (4)$$

where  $d\Omega$  is  $2\pi\sin\theta d\theta$  and  $r_e$  is electron radius. Although there is no energy transfer to the medium in Rayleigh scattering, it was also considered in MC-SCAN code to simulate all interactions. For Rayleigh differential scattering cross section, Thomson scattering was applied [19].

$$\frac{d\sigma_R}{d\Omega} = \frac{r_e^2}{2} [1 + k(1 - \cos\theta)][F(q, Z)]^2 \quad (5)$$

As known, pair production is observed, when the photon energy exceeds a certain threshold energy which is 1022

keV. At this time, pair production cross section was calculated based on Bethe-Heitler formula [20]. The energy absorbed in the phantom as a result of all interactions was recorded and the absorbed dose was calculated as a ratio of the energy to mass. The geometry which was used to perform all experimental measurements were used to calculate absolute dose, output factors, point dose measurements and percent depth dose. Simulated phantom geometry is shown in Fig.1.

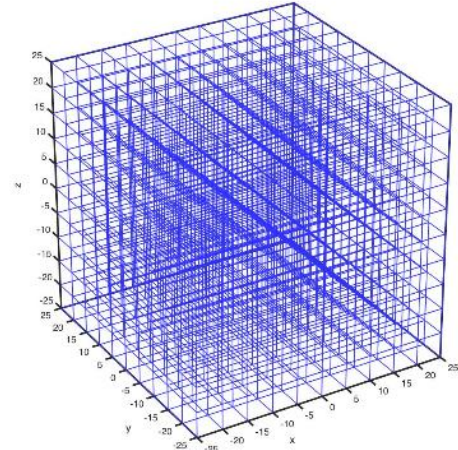


Fig.1. Simulated water phantom geometry

The calculated results through MC-SCAN Monte Carlo dose engine were compared with the experimental results to evaluate MC-SCAN code. MC-SCAN dose calculation photon transport logic was shown in Fig.2.

## 3. Results

### 3.1. Absorbed dose comparison

Before point dose measurements, the absolute dose calibration was done per MU for 10x10 cm<sup>2</sup> field size at 100 cm SSD and 10 cm depth and the same geometry was used for MC-SCAN code. The difference between MC-SCAN (101.08 cGy  $\pm$  0.23) and measured data (100.67 cGy  $\pm$  0.05) for absolute dose is 0.4%. The planned dose with Monte Carlo algorithm through Monaco 5.51 TPS was 80.50 cGy, the measured dose was 79.90 cGy and the calculated dose via MC-SCAN was 78.18 cGy. The difference Monaco TPS vs MC-SCAN is 2.88%, the difference experimental measurement vs MC-SCAN is 2.15%. Finally, the tissue phantom ratio (TPR<sub>20/10</sub>) was compared. The calculated TPR<sub>20/10</sub> via MC-SCAN is 0.68 and the measured one is 0.676. Based on these values, the difference between calculated and measured data is 1.62%.

### 3.2. Output factors

The output factors for 6 MV photon energy was measured/calculated for different field sizes and the difference between the measured and calculated output results were listed in Table-1.

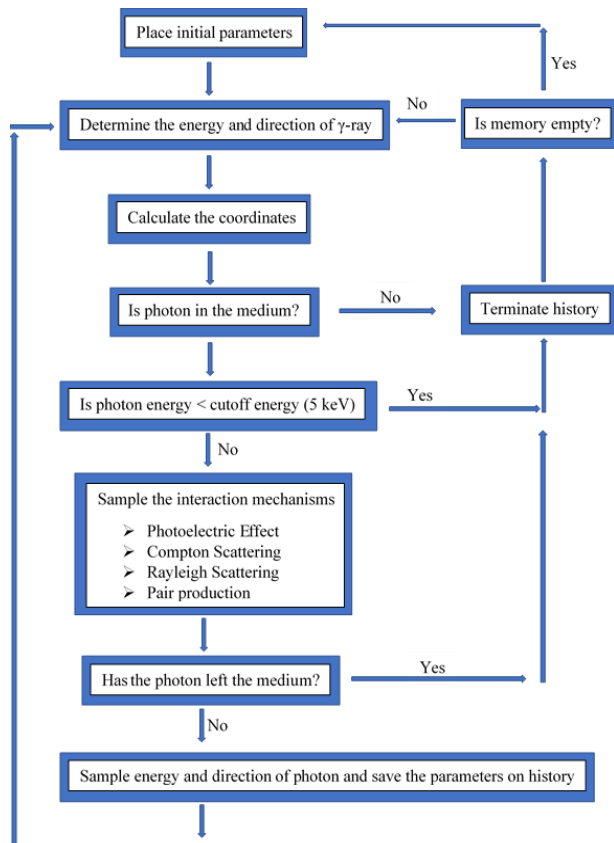


Fig.2. MC-SCAN Monte Carlo code photon transport logic

Table 1. Output factors for 6 MV photon energy

Field Size (cm x cm)	MC-SCAN	Experimental	Difference (%)
2x2	0.734 ± 0.24	0.713 ± 0.003	2.94
4x4	0.861 ± 0.22	0.876 ± 0.004	1.71
5x5	0.904 ± 0.34	0.908 ± 0.004	0.44
10x10	1.000 ± 0.23	1.000 ± 0.005	-
15x15	1.066 ± 0.24	1.051 ± 0.005	1.42
20x20	1.071 ± 0.37	1.083 ± 0.005	1.10
30x30	1.126 ± 0.36	1.115 ± 0.005	0.98
40x40	1.156 ± 0.36	1.113 ± 0.005	3.86

The difference between the calculated output factors via MC-SCAN and experimental values is < 3% for all field sizes except 40x40cm<sup>2</sup> field size. On the other hand, there is a good agreement was observed for both approaches and MC-SCAN code is effective tool to calculate output factors for virtual source model.

### 3.3. Percent depth dose (PDD)

One way to characterize the dose distribution on the central axis is to normalize the dose at a given depth to the dose distribution at the reference depth. On the same ground, PDD was calculated for different field sizes through MC-SCAN and compared with experimental measurement to evaluate the in-house Monte Carlo code. The difference between calculated

PDD and the measured one was < 3% for all field sizes. Additionally, to evaluate whether there is statistically significant difference paired sample t test was applied and  $p < 0.05$  was taken into account. Based on statistical analysis, the significant difference was observed for 10x10 cm<sup>2</sup> field sizes ( $p < 0.05$ ), even though the difference between both approaches is 2.4%. On the other hand, the statistical difference was not significant for 15x15 cm<sup>2</sup>, 20x20 cm<sup>2</sup>, 30x30 cm<sup>2</sup> and 40x 40 cm<sup>2</sup> field sizes ( $p > 0.05$ ). The calculated and measured PDD comparison was shown in Fig.3.

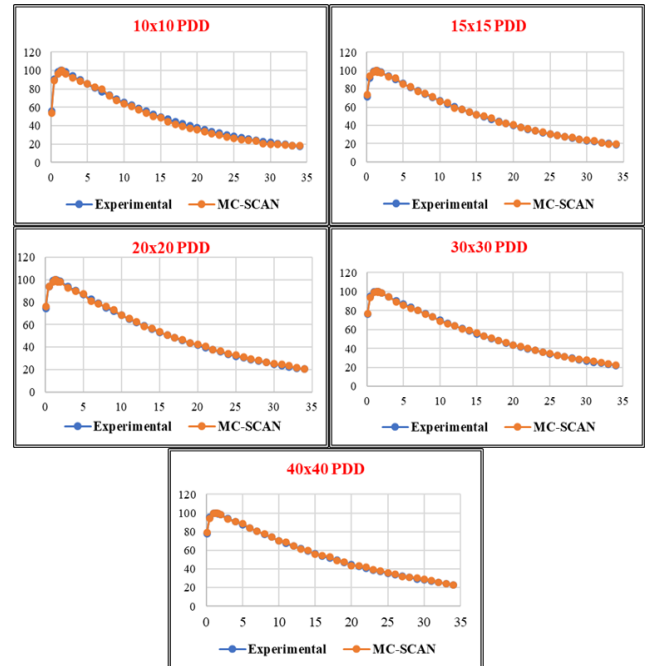


Fig. 3. The calculated and measured PDD

## 4. Conclusions

The in-house Monte Carlo dose calculation engine namely MC-SCAN was developed for this presented study. The MC-SCAN Monte Carlo engine can be used as an alternative tool to simulate virtual source model on Elekta VersaHD LINAC. The difference between experimental measurements for all calculated values via MC-SCAN within < 3%. On the other hand, further investigation needs to be done to improve this algorithm.

## 5. References

- Deng J, Jiang SB, Kapur A, Li J, Pawlicki T, Ma C. Photon beam characterization and modelling for Monte Carlo treatment planning. *Physics in Medicine & Biology*. 2000;45(2):411.
- Ma C-M, Li J, Pawlicki T, Jiang S, Deng J, Lee M, et al. A Monte Carlo dose calculation tool for radiotherapy treatment planning. *Physics in Medicine & Biology*. 2002;47(10):1671.
- Ahnesjö A, Aspradakis MM. Dose calculations for external photon beams in radiotherapy. *Physics in Medicine & Biology*. 1999;44(11):R99.
- Andreo P. Monte Carlo techniques in medical radiation physics. *Physics in Medicine & Biology*. 1991;36(7):861.



5. Liang Y, Muhammad W, Hart GR, Nartowt BJ, Chen ZJ, James BY, et al. A general-purpose Monte Carlo particle transport code based on inverse transform sampling for radiotherapy dose calculation. *Scientific reports*. 2020;10(1):1-18.
6. Brualla L, Rodriguez M, Lallena AM. Monte Carlo systems used for treatment planning and dose verification. *Strahlentherapie und Onkologie*. 2017;193(4):243-59.
7. Spezi E, Lewis G. An overview of Monte Carlo treatment planning for radiotherapy. *Radiation protection dosimetry*. 2008;131(1):123-9.
8. Livingstone A, Crowe S, Sylvander S, Kairn T. Clinical implementation of a Monte Carlo based independent TPS dose checking system. *Physical and Engineering Sciences in Medicine*. 2020;43(3):1113-23.
9. Karbalaee M, Shahbazi-Gahrouei D, Tavakoli M. A Novel GPU-based Fast Monte Carlo Photon Dose Calculating Method for Accurate Radiotherapy Treatment Planning. *Journal of Biomedical Physics & Engineering*. 2020;10(3):329.
10. Ohira S, Takegawa H, Miyazaki M, Koizumi M, Teshima T. Monte Carlo Modeling of the Agility MLC for IMRT and VMAT Calculations. *in vivo*. 2020;34(5):2371-80.
11. Sikora M, Dohm O, Alber M. A virtual photon source model of an Elekta linear accelerator with integrated mini MLC for Monte Carlo based IMRT dose calculation. *Physics in Medicine & Biology*. 2007;52(15):4449.
12. Cashmore J, Golubev S, Dumont JL, Sikora M, Alber M, Ramtoghul M. Validation of a virtual source model for Monte Carlo dose calculations of a flattening filter free linac. *Medical physics*. 2012;39(6Part1):3262-9.
13. Paudel MR, Kim A, Sarfehnia A, Ahmad SB, Beachey DJ, Sahgal A, et al. Experimental evaluation of a GPU-based Monte Carlo dose calculation algorithm in the Monaco treatment planning system. *Journal of applied clinical medical physics*. 2016;17(6):230-41.
14. Li J, Pawlicki T, Deng J, Jiang S, Mok E, Ma C. Validation of a Monte Carlo dose calculation tool for radiotherapy treatment planning. *Physics in Medicine & Biology*. 2000;45(10):2969.
15. Snyder JE, Hyer DE, Flynn RT, Boczkowski A, Wang D. The commissioning and validation of Monaco treatment planning system on an Elekta Versa HD linear accelerator. *Journal of applied clinical medical physics*. 2019;20(1):184-93.
16. Narayanasamy G, Saenz DL, Defoor D, Papanikolaou N, Stathakis S. Dosimetric validation of Monaco treatment planning system on an Elekta Versa HD linear accelerator. *Journal of applied clinical medical physics*. 2017;18(6):123-9.
17. Fraass B, Doppke K, Hunt M, Kutcher G, Starkschall G, Stern R, et al. American Association of Physicists in Medicine Radiation Therapy Committee Task Group 53: quality assurance for clinical radiotherapy treatment planning. *Medical physics*. 1998;25(10):1773-829.
18. Meric N. Calculation of radiation dose to the lens of the eye using Monte Carlo simulation. *Applied Radiation and Isotopes*. 2001;55(4):557-60.
19. Meric M, Bor D, Büget N, Oezkili M. The use of monte carlo technique for the determination of tissue-air ratios (TAR) in diagnostic energy rate. *Physica Medica*. 1998;14(1):3-8.
20. Salvat F, Fernández-Varea J, Sempau J. PENELOPE-2008: a code system for Monte Carlo simulation of electron and photon transport (Issy-les-Moulineaux. France: OECD Nuclear Energy Agency. 2009.

## **CASE STUDY REPORT: ADVANTAGES OF HyperArc™ IN BRAIN RADIOLOGY TREATMENT PLANNING**

Marijus ASTRAUSKAS<sup>1</sup>, Romualdas GRIŠKEVIČIUS<sup>2</sup>, Kęstutis AKELAITIS<sup>3</sup>, Ieva MARKEVIČIENĖ<sup>4</sup>, Jonas VENIUS<sup>5</sup>

<sup>1</sup>Medical physics department, National Cancer Institute; <sup>2</sup>Biomedical physics laboratory, National Cancer Institute  
<sup>1</sup>marijus.astrauskas@nvi.lt; <sup>2</sup>romualdas.griskevicius@nvi.lt; <sup>3</sup>kestutis.akelaitis@nvi.lt; <sup>4</sup>ieva.markeviciene@nvi.lt;  
<sup>5</sup>jonas.venius@nvi.lt

**Abstract:** The goal of this study is to get a better idea of what can be achieved using HyperArc and to evaluate its advantages and disadvantages in comparison to previously planned stereotactic cases in terms of target coverage, conformity, dose gradient and healthy brain dose. 9 patients previously planned for stereotactic radiosurgery, with one or multiple brain metastases were replanned using HyperArc single isocenter approach and compared with dosimetric parameters of the original plan. Results provide better indications for noncoplanar stereotactic treatment options in National Cancer Institute and allow for better patient selection for HyperArc planning.

**Keywords:** treatment, planning, hyperarc, brain, radiosurgery

### **1. Introduction**

Stereotactic radiosurgery (SRS) is now a widely used technique for treating brain metastases. Improvements in diagnostic imaging, linear accelerator technology, patient immobilisation techniques make this an attractive alternative to surgery or whole brain radiotherapy (WBRT) with good local tumor control [1, 2]. This also applies to postresective lesions which can also benefit from high dose single or hypofractionated treatments. The introduction of new generation linear accelerators such as TrueBeam™ STx with 6D treatment couch, on board cone-beam CT, smaller collimation leaves, and flattening filter free beams allow for fast and very precise single fraction high dose delivery. However, treatment planning poses a few challenges, especially when it comes to cases with multiple brain metastases. Finding the best variation of isocentre placement and gantry – collimator – couch angles can be difficult and time consuming. Furthermore, adding couch rotations introduces a new element of inaccuracy and increases treatment duration.

A technique introduced in 2017 by Varian called HyperArc™ (HA) automatically generates the isocentre placement according to the target geometry, as well as gantry, couch and collimator angles. The plan is virtually simulated, to avoid any collisions with the patient during treatment, and optimized for fast automated delivery. Along with the updated stereotactic automatic normal tissue optimisation (NTO) algorithm this becomes an attractive tool for more efficient stereotactic treatment planning and delivery for brain metastases. The purpose of this study was to take existing single fraction brain SRS cases that were planned using conventional VMAT and compare them with those replanned using HA. Replanning was done using two different approaches – a more homogeneous approach (preferred in our clinic) for the original plan and a heterogeneous approach, allowing for higher maximum dose in the target.

### **2. Materials and Methods**

#### **2.1. Patients**

9 patients with 1 - 2 targets (metastasis or post resection irradiation) were selected. 6 of these cases were conventional coplanar VMAT and 3 were noncoplanar VMAT plans. Dose prescription range was 12-24Gy (mean dose – 18.6Gy) as seen in table 1.

#### **2.2 Planning approach**

All plans were made using 0.125cm slice thickness CT images, calculated with 0.125cm resolution calculation grid using AAA 15.5 algorithm. Optimization parameters: aperture shape control – moderate, convergence mode – off, calculation resolution – high, MR level at restart – MR3. Linac used for planning - TrueBeam™ STx, with 6MV flattening filter free beams, Varian HD120 MLC (2.5mm in centre, 5mm in periphery). Plan gross tumor volume GTV was defined by radiation oncologist using registered magnetic

resonance images and 1-2mm margin CTV was created as the primary target volume. Replanning was done using HA automated plan creation tool. The proposed automatic plan isocentre, couch rotations and collimator rotations were used. The summary of plan setup characteristics shown in Table 2 displays the original and HA noncoplanar beam setup. After plan creation the original plan optimisation objectives were exported and imported into the HA plan. The only difference from the original plan was the use of automatic SRS NTO feature with the same priority. In our clinic, a more homogeneous planning approach is preferred by the radiation oncologists, therefore original and the new HA plan had upper target objectives at ~115-120% of the prescribed dose. Then the new plan was revised to see if there was room to reduce the dose for organs at risk. In order to achieve an even better dose falloff, a second heterogeneous HA plan was then created and reoptimised using the same plan objectives, but without the upper target objectives. To better compare the results for the heterogeneous plan a third plan was created using the original plan reoptimized without an upper objective. In summary, three new plans were compared with the original VMAT plan.

**Table 1.** Target characteristics

	Target no.	Target volume, cc	Equivalent sphere size, cm	Dose prescription, Gy
Patient 1	T1	4.7	2.1	20
Patient 2	T2	8.3	2.5	20
Patient 3	T3	4.3	2	18
Patient 4	T4	1	1.2	24
Patient 5	T5	5	2.1	20
Patient 6	T6	7.5	2.4	20
	T7	5.6	2.2	20
Patient 7	T8	10	2.7	12
	T9	7.7	2.5	12
Patient 8	T10	0.3	0.9	20
	T11	1.4	1.4	20
Patient 9	T12	10.6	2.7	18

### 2.3 Plan evaluation

To compare the plans, a few comparison metrics were chosen. Monitor units (MU) to compare the plan complexity and treatment time. Plan quality indices were used to evaluate dosimetric and target coverage characteristics.

Selected quality indices for plan comparison were:

1. RTOG conformity index (CI) -  $CI_{RTOG} = \frac{V_{RI}}{TV}$  (1), where  $V_{RI}$  is the prescription isodose volume, TV is the target volume.
2. Paddik conformity index -  $CI_{Paddik} = \frac{(TV_{PIV})^2}{TV \times V_{RI}}$  (2), where  $TV_{PIV}$  is the target volume that is covered in

the prescription isodose, TV is the target volume,  $V_{RI}$  is volume that receives the prescription isodose.

3. RTOG homogeneity index (HI) -  $HI_{RTOG} = \frac{I_{max}}{RI}$  (3), where  $I_{max}$  is the maximum dose in the target volume, RI is the prescription dose.
4. Coverage index (Q) -  $Q = \frac{I_{min}}{RI}$  (4), where  $I_{min}$  is the minimum dose in the target volume, RI is the prescription dose.
5. Paddik gradient index (GI) -  $GI_{Paddik} = \frac{V_{50\%}}{V_{100\%}}$  (5), where  $V_{50\%}$  is the volume receiving 50% prescription dose and  $V_{100\%}$  is the volume receiving 100% prescription dose.
6. Falloff index -  $FI = \frac{PIV_{50\%}}{TV}$  (6), where  $PIV_{50\%}$  is the volume receiving 50% prescription dose and TV is the target volume.

**Table 2.** Plan setup characteristics

	Number of arcs, degrees		Couch rotation, degrees	
	Original plan	HA plan	Original plan	HA plan
Patient 1	3 (181-330, 330-181, 40-179)	4 (181-179, 180-0, 0-180, 180-0)	0, 0, 270	0, 45, 315, 270
Patient 2	3 (290-179)	4 (180-0, 0-180, 180-0)	0, 0, 0	0, 315, 270, 45
Patient 3	3 (181-179)	3 (180-0, 0-180, 180-0)	0, 0, 0	0, 45, 90
Patient 4	3 (181-179)	3 (180-0, 0-180, 180-0)	0, 0, 0	0, 45, 90
Patient 5	3 (181-179, 179-181, 25-179)	4 (180-0, 0-180, 180-0, 0-180)	0, 0, 90	0, 45, 90, 315
Patient 6	3 (181-179)	4 (180-179, 180-0, 0-180, 180-0)	0, 0, 0	0, 45, 315, 270
	2 (181-179)	4 (180-0, 0-180, 180-0, 0-180)	0, 0	0, 45, 90, 315
Patient 7	3 (181-179)	4 (180-179, 180-0, 0-180, 180-0)	0, 0, 0	0, 45, 315, 270
	4 (0-179)	3 (0-179)	0, 0, 20, 40	0, 45, 90
Patient 8	3 (181-330, 330-181, 40-179)	4 (181-179, 180-0, 0-180, 180-0)	0, 0, 270	0, 45, 315, 270
	3 (290-179)	4 (180-0, 0-180, 180-0)	0, 0, 0	0, 315, 270, 45
Patient 9	3 (181-179)	3 (180-0, 0-180, 180-0)	0, 0, 0	0, 45, 90

For calculating these indices, an additional high resolution evaluation structure – a 1.5cm sphere was created and checked that 50% isodose is inside the structure. These indices were chosen based on recommendations from literature and our own clinical practice [3, 4]. In all original plans the main OAR criteria was local healthy brain dose  $V_{12Gy} < 10cc$  as per clinical protocol. This was evaluated for each individual target by making an additional high resolution

evaluation structure – 1.5cm diameter sphere around each CTV and cropped from GTV. Additionally,  $V10Gy < 12cc$  is also used as brain necrosis risk evaluation factor, therefore it was included into the study as well [5]. The statistical comparison between the two plan sets was made using a paired two tailed Student's t-test in "Microsoft Excel", p value of  $< 0.05$  indicating statistical significance.

For case comparisons, two groups were distinguished. First – comparing the plans that were originally planned using noncoplanar fields, to compare the automatic plan generation with the manually created VMAT plan for quality indices and tissue sparing. Second – to see if there is a benefit to using HA in multiple target cases.

### 3. Results

#### 3.1 Statistical comparison

General comparisons of the plans are presented in Table 3 and 4. In terms of MU, HA plans did produce a higher number of MU, however it was not found to be statistically significant. Looking at quality indices, in terms of conformity and coverage, there were no significant differences between the original and new plans after plan normalization. In terms of homogeneity, comparing the heterogeneous and homogeneous plans against their counterparts, there was no significant difference as well. As expected, significant differences were observed in the dose falloff and healthy brain dose in HA plans, that produce a much steeper dose falloff (due to noncoplanar design), with heterogeneous HA plans exhibiting the steepest falloff. Even comparing the original homogeneous and heterogeneous VMAT plans, there is a marginally significant ( $p=0.057$ ) increase in dose gradient, same being with the falloff index ( $p=0.064$ ), which would indicate that allowing a higher maximum dose in the target, helps to spare normal tissue. We can see this when comparing the healthy brain dose of V12Gy ( $p=0.065$ ) and V10Gy ( $p=0.042$ ) between the original VMAT plans in Table 3. However, the best brain sparing was achieved using heterogeneous HA allowing to significantly improve V12Gy and V10Gy compared to all other modalities.

#### 3.2 Case comparison

The benefit of noncoplanar plans for dose falloff and brain sparing is well known and in simple single target cases it has clear advantages. So, for a further fairer comparison Tables 5 and 6 show the results for the cases where noncoplanar VMAT was used. Compared are the replanned versions with heterogeneous dose and better dose falloff.

Looking at the tables, HA plans still seem better, however the differences now are not as dramatic as when compared to coplanar VMAT plans. Looking at the differences between the original and the HA beam geometry in Fig.1, we see that HA takes advantage of more noncoplanar beams to achieve better dose falloffs at 50% dose.

When comparing the 50% isodose between VMAT and HA plans in Fig.2 it is clear, that more noncoplanar beams give a better dose fall off and smoother dose

distribution in patient 1 and somewhat in patient 9. However, looking at patient 5 (middle), there does not seem to be that much difference. Even though, two more noncoplanar arcs were used in that plan.

**Table 3.** Plan comparison summary, homogeneous

Mean ( $\pm$ SD)	Original plan, homogeneous	HA, homogeneous
MU	5892 ( $\pm$ 1565)	6408 ( $\pm$ 1998)
CIRTOG	1.08 ( $\pm$ 0.15)	1.09 ( $\pm$ 0.14)
CIPaddik	0.9 ( $\pm$ 0.08)	0.9 ( $\pm$ 0.08)
HIRTOG	1.15 ( $\pm$ 0.06)	1.15 ( $\pm$ 0.06)
Coverage, Q	0.91 ( $\pm$ 0.05)	0.93 ( $\pm$ 0.03)
GIPaddik	3.73 ( $\pm$ 0.8)	2.94 ( $\pm$ 0.45)
Falloff	4.07 ( $\pm$ 1.41)	3.23 ( $\pm$ 0.92)
Brain, V12Gy	6.76 ( $\pm$ 2.33)	6.19 ( $\pm$ 2.19)

**Table 4.** Plan comparison summary, heterogeneous

Mean ( $\pm$ SD)	Original plan, heterogeneous	HA, heterogeneous
MU	7263 ( $\pm$ 922)	6999 ( $\pm$ 1150)
CIRTOG	1.08 ( $\pm$ 0.16)	1.08 ( $\pm$ 0.14)
CIPaddik	0.91 ( $\pm$ 0.11)	0.91 ( $\pm$ 0.08)
HIRTOG	1.36 ( $\pm$ 0.09)	1.36 ( $\pm$ 0.12)
Coverage, Q	0.9 ( $\pm$ 0.06)	0.92 ( $\pm$ 0.04)
GIPaddik	3.55 ( $\pm$ 0.72)	2.68 ( $\pm$ 0.36)
Falloff	3.89 ( $\pm$ 1.37)	2.91 ( $\pm$ 0.82)
Brain, V12Gy	6.57 ( $\pm$ 2.41)	6.04 ( $\pm$ 2.32)

**Table 5.** Noncoplanar VMAT vs HA, dose falloff

	GI VMAT	GI HA	FI VMAT	FI HA
Patient 1	2.83	2.60	3.09	2.77
Patient 4	2.54	2.45	2.69	2.64
Patient 9	2.67	2.46	2.62	2.41

**Table 6.** Noncoplanar VMAT vs HA, brain sparing

	V12 VMAT	V12 HA	V10 VMAT	V10 HA
Patient 1	5.12	4.4	7.09	6.12
Patient 4	6.56	6.13	8.62	7.92
Patient 9	9.89	9.92	13.56	13.28

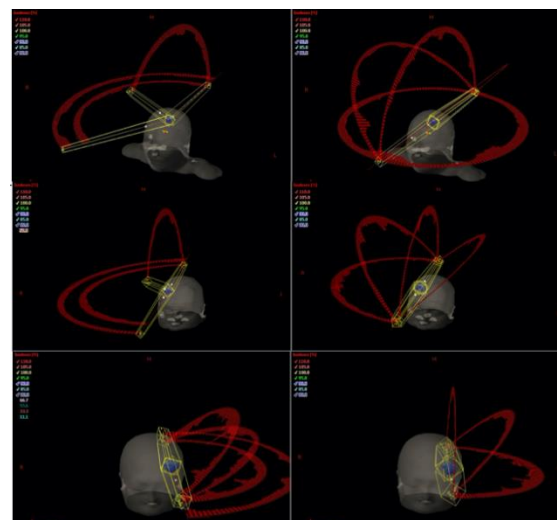


**Fig. 1.** Original VMAT plans (right) vs HA plans (left)

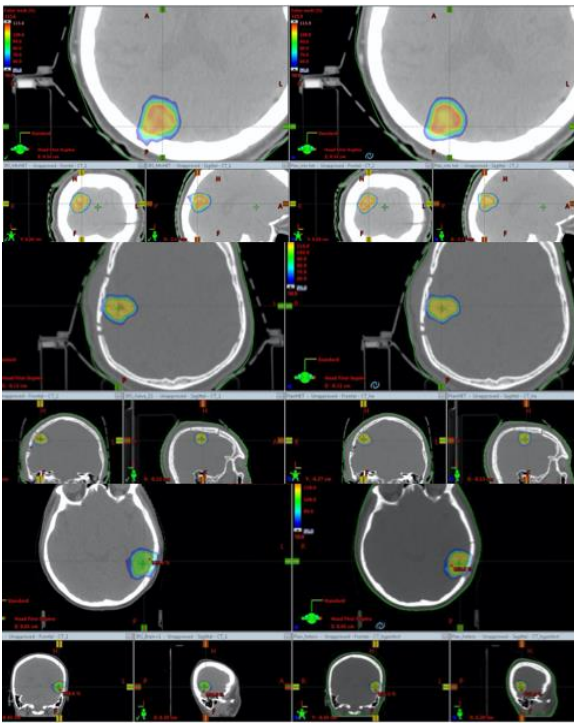


**Fig. 2** Dose differences at 50% isodose VMAT (left) vs HA (right).

Another possible advantage of using HA is planning cases with multiple targets using single isocentre approach. Table 7 shows the results from two cases with multiple targets. First case is patient 6 with two large targets in different parts of the brain and patient 7 with two small metastases in close proximity to each other. The original VMAT plan did not use noncoplanar fields, therefore the differences are much more obvious. In patient 7, since the targets are very close, the brain V12/V10Gy evaluation volume was combined. Figure 3 displays the beam geometry for the plans.

**Table 7.** VMAT Heterogeneous vs HA Heterogeneous

	V12 VMAT	V12 HA	V10 VMAT	V10 HA
Patient 6	8.08	7.56	11.13	10.20
	9.4	7.90	13.35	10.59
Patient 7	4.57	3.71	6.86	5.10

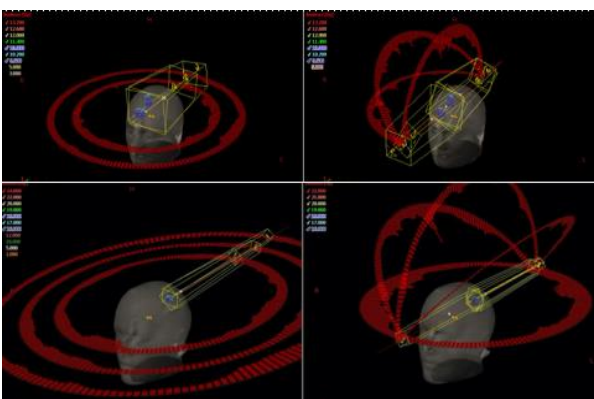


**Fig. 3.** Original VMAT plans (right) vs HA plans (left).

Dose distribution for the plans (Fig. 4.) shows very noticeable differences in dose falloff. Patient 6, having large targets far apart, would have benefited much from a HA plan. However, a two isocentre approach might have been even more beneficial.

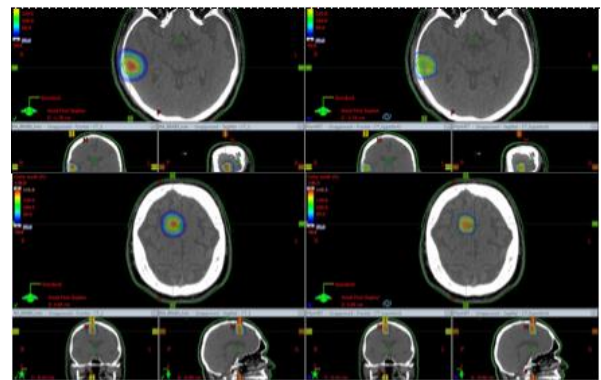


**Fig. 4.** Dose differences at 50% isodose VMAT (left) vs HA (right).

In case of patient 7 (Fig. 5) 50% isodose distribution, the differences are not that pronounced, however still very visible. There are also clear benefits of reduced dose bridging with HA at lower doses.

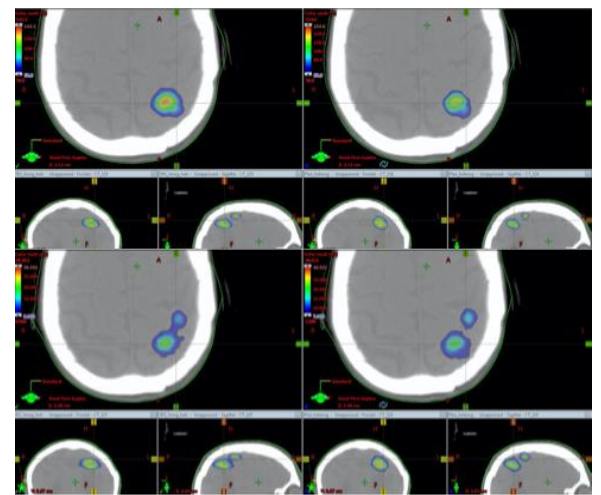


**Fig. 5.** Dose differences at 50% isodose VMAT (left) vs HA (right).

#### 4. Discussion

The aim of this study was to examine the HyperArc planning approach to find out if there are benefits to this new technique. In terms of dose falloff, it is clear that a heterogeneous approach for stereotactic cases benefits the dose falloff regardless of technique used. Noncoplanar plans also further increase the dose falloff and allow for better healthy brain sparing, which is also seen in similar published works on this topic [6, 7]. Not mentioned in the results, but another important benefit was the ease of use and time efficiency of HA planning. Even a less experienced planner can create a good plan using the automated plan creation tool, saving time looking for couch rotation angles, collimator angles and isocentre placement. Since the plan is also virtually simulated, more time is saved by not having to check for collisions before the treatment delivery. However, this might be a problem due to lack of flexibility in the

number of couch angles and number of arcs. The use of automatic SRS NTO should be further studied, since the plans used shell structures in optimisation, therefore the benefits are unclear. However, it does seem to help with dose bridging. Also not mentioned were the plan complexity indices, influencing the QA of the plans, which is a consideration due to higher number of MUs in HA plans. The number of patients is most likely too low to say with confidence that the differences between the plans are significant, especially for noncoplanar VMAT, and further studies should be made. In terms of target conformity and coverage, due to normalizing all plans to the original VMAT plan for most fair comparison of dose falloff, there is also a point to be made, that these metrics could be better, as indicated in published works [8], although most likely at the cost of healthy brain sparing. Despite all this it is clear that HyperArc is a useful tool to have when treating stereotactic brain cases.

### 5. Conclusion

This study showed that HyperArc™ planning solution increased plan quality metrics in all chosen brain SRS cases. HA plans were better than the conventional and noncoplanar VMAT plans, especially in dose falloff and healthy brain sparing. Based on these results, it is suggested to use HA for all brain SRS cases. Based on the plan quality index results from heterogeneous and homogeneous plan comparison it is also recommended to use planning strategies based on a more heterogeneous planning approach.

### 6. References

- [1] Brown PD, Jaeckle K, Ballman KV, et al. Effect of radiosurgery alone vs radiosurgery with whole brain radiation therapy on cognitive function in patients with 1 to 3 brain metastases: a randomized clinical trial. *JAMA*. 2016;316(4):401–409.
- [2] Tsao MN, Rades D, Wirth A, Lo SS, Danielson BL, Gaspar LE, Sperduto PW, Vogelbaum MA, Radawski JD, Wang JZ, Gillin MT, Mohideen N, Hahn CA, Chang EL. Radiotherapeutic and surgical management for newly diagnosed brain metastasis(es): An American Society for Radiation Oncology evidence-based guideline. *Pract Radiat Oncol*. 2012 Jul-Sep;2(3):210-225.
- [3] Shaw E, Kline R, Gillin M, Souhami L, Hirschfeld A, Dinapoli R, et al. Radiation therapy oncology group: Radiosurgery quality assurance guidelines. *Int J Radiat Oncol Biol Phys*. 1993;27:1231–9.
- [4] Paddick I, Lippitz B. A simple dose gradient measurement tool to complement the conformity index. *J Neurosurg*. 2006;105(Suppl):194–201.
- [5] Minniti G, Clarke E, Lanzetta G, et al. Stereotactic radiosurgery for brain metastases: analysis of outcome and risk of brain radionecrosis. *Radiat Oncol*. 2011;6:48–56.
- [6] Ruggero R, Stefania N, Rosario M, Francesco R, Stefanie C, Alba F, Filippo A. Linac-based radiosurgery for multiple brain metastases: Comparison between two mono-isocenter techniques with multiple non-coplanar arcs, *Radiotherapy and Oncology*, 2019;132:70-78.
- [7] Vergalasova I, Liu H, Alonso-Basanta M, Dong L, Li J, Nie K, Shi W, Teo BK, Yu Y, Yue NJ, Zou W, Li T. Multi-Institutional Dosimetric Evaluation of Modern Day Stereotactic Radiosurgery (SRS) Treatment Options for Multiple Brain Metastases. *Front Oncol*. 2019;7:9:483.
- [8] Ohira, S., Ueda, Y., Akino, Y. et al. HyperArc VMAT planning for single and multiple brain metastases stereotactic radiosurgery: a new treatment planning approach. *Radiat Oncol*, 2018;13,13.



## **A SUCCESSFUL PATIENT MANAGEMENT SYSTEM DURING COVID-19 PANDEMIC AND THE IMPACT OF THE RESTRICTIONS IN A RADIATION ONCOLOGY CLINIC IN TURKEY**

Nur KODALOĞLU<sup>1</sup>, Cafer ATAR<sup>1</sup>, Selami KARAHAN<sup>1</sup>

<sup>1</sup>Dr. Abdurrahman Yurtaslan Ankara Oncology Research and Training Hospital

<sup>1</sup>nurkodaloglu@gmail.com

**Abstract:** COVID-19 pandemic created concerns related with infection spread which lead to decrease in the number of patients who apply to the most critical departments, i.e. cardiology, oncology etc. During 2020, a couple of strict new strategies helped us to prevent infection spread in the clinic. Since 11<sup>st</sup> March 2020, the date of the declaration of first COVID-19 patient in the country, besides the applied worldwide known rules, PCR tests 24 hours before the treatments and coming with only one companion lead not to close the clinic.

**Keywords:** Radiotherapy, COVID-19, pandemic, preventive measures, control.

### **1. Introduction**

With the outbreak of severe acute respiratory syndrome coronavirus 2 (SARS-CoV-2), the novel coronavirus 2019 (COVID-19), responsible for the coronavirus disease, has caused disruptions and uncertainties in treatments in many countries. Compared to other populations, oncology patients who are potentially more susceptible, due to immunosuppression, are at risk of severe infection during SARS-CoV-2 outbreaks. After it was announced that the first case was detected in our country on March 11, 2020, we took all the necessary precautions for the pandemic process in our clinic.

### **2. Implemented Measures in the Clinic Related to COVID-19**

A working group on clinical procedures and workflow was established at our hospital during the pandemic. Staff training was also conducted on basic prevention precautions to prevent infection, epidemiological and clinical features of COVID-19 cases and various possible situations. Each training has practiced keeping distance between individuals and limiting the number of people at meetings and conferences. A humane approach was applied to patients, respecting their concerns and values. Priority was given to the

availability of psychological counselling services to patients in need during the epidemic.

Appointment-based medical procedures and visits have been adopted to facilitate patients' access to the hospital or radiotherapy center. Workspaces are divided by function to ensure a smooth workflow in the radiotherapy center and to limit communication.

14 rule directives published by the Ministry of Health have been put into practice (1, 2). Personal protective equipment for all personnel according to their duties; gloves, apron, medical mask (n95/ffp2), goggles, face shields were provided (Fig. 1). Material access points and changing rooms with protective equipment had been created. The rules to be followed while putting on and taking off personal protective equipment had been explained to the personnel.



**Fig. 1.** Personnel with protective equipment (masks, latex gloves, face shields, disposable waterproof isolation gowns and shoe covers).

On 18.03.2020, triage practice was started at the clinic main entrance. Triage nurses were available to assess and assist individuals in the main entrance and reception areas outside the radiotherapy center (Fig. 2). Contact inquiries were made of the patients with fever, cough, respiratory distress, and in contact with people



travelling abroad. All patients and their relatives were required to wear masks in the clinic, and those who did not have a mask were given a mask at the time of triage.



**Fig. 2.** Triage nurses at the main entrance triage area.

Medical personnel are instructed to strictly practice rigorous hand hygiene before and after any contact with patients, before putting on protective equipment, and after removing protective equipment. Health personnel were informed that they should wash their hands after patient examination, pay attention to hand hygiene after contact with contaminated environment and objects, after being exposed to anybody fluid, before meals and after using the toilet. For the purpose of protection, single seat seating arrangement has been changed with 2 meters intervals in the treatment waiting rooms (Fig. 3). Close contact was prevented in examination rooms and waiting areas. Hand hygiene was ensured by placing disinfectants at the entrances of waiting rooms, treatment and planning rooms, locker rooms.



**Fig. 3.** Reorganized treatment waiting rooms and seating areas with 2 meters apart single seats.

Traffic was limited, including the number of patient companions. If there is a patient in need of assistance, the patient is provided to be accompanied by only one person. Only patients and attendants who were not suspected of having SARS-CoV-2 infection could enter the radiotherapy center. Personal protective equipment such as masks, latex gloves, safety glasses or face shields, disposable waterproof isolation gowns and shoe covers are worn when patients with suspected SARS-CoV-2 are taken to infectious disease (pandemic) clinics that provide more detailed assessment and management. Thermometers were distributed to all treatment devices. Before each patient's treatment and planning

procedures, fever, cough, respiratory distress and foreign travel inquiries were made by radiotherapy technicians every day. A patient-specific triage follow-up form was created.

Each patient who has just started the treatment was informed about the pandemic process by the training nurse in the clinical education polyclinic and the possible risks were explained.

The accessories used in the simulation processes were disinfected after each patient. Thermoplastic mask, vacuum bed, etc. accessories made specifically for the patient were disinfected and bagged (Fig. 4).



**Fig. 4.** Thermoplastic masks in bags.

On 23rd March 2020, #stayhome was applied for a limited number of personnel from each field. So, a few number of groups among RTTs were created. Each group of RTTs worked for 2-week-shifts without being in contact with other groups. Besides, radiation oncologists and medical physicists also created different groups with different schedules.

A specific time period was decided for the cleaning of the treatment rooms and the whole clinic.

### 3. Restrictions Around the Country

With the recommendations of the Ministry of Health and the Scientific Committee, on 21st March 2020, it was declared to citizens aged 65 and over, those with a low immune system, chronic lung disease, asthma, COPD, cardiovascular disease, kidney, hypertension and liver disease and those who use drugs that impair their immune system not to leave their residences. They were forbidden to go out on the streets, limiting their walking in the parks and travelling by public transport. On 3rd April 2020, these restrictions had been extended to include teenagers under the age of 20.

On 16th March 2020, education in schools and universities had been suspended and alternative online education became the main educational tool.

To minimize the risk spreading the virus, on 21st March 2020, gathering places such as shopping malls, cinemas, theatres, entertainment venues, wedding/engagement halls, mosques, tea gardens, hairdresser, barber, beauty salons, Turkish baths, saunas, SPAs, condolence houses, sport centers, concert halls, restaurants, internet lounges, coffeehouses, amusement parks, swimming pools, conference centers, scientific organization places, associations etc. were forbidden to enter.

On 1st April 2020, international flights from 70 countries were cancelled.

As the first nationwide restriction, again with the recommendations of the Ministry of Health and the Scientific Committee, curfew restrictions were applied around the country. On 4th April 2020, a curfew was declared between 21:00 and 05:00 on weekdays and all day on weekends. On 3rd May 2020, normalization started.

Due to the rapid increase in the number of COVID-19 positive patients, the second nationwide curfew restrictions applied on 17th November 2020. Weekend

curfew restrictions applied in the whole country. More restrictions applied on different cities depending on the COVID-19 positive patient number in that city.

On 14th April 2021, a curfew was declared between 19:00 and 05:00 on weekdays and all day on weekends.

On 1st June 2021, normalization started.

In our department, there are several machines, used for radiotherapy, as can be seen in both Table 1 and 2. The number of the patients treated with different machines and patients diagnosed COVID-19 positive by months in 2020 and 2021 are given in Table 1 and 2, respectively.

**Table 1.** The number of the patients treated with different machines and diagnosed COVID-19 in 2020.

2020	Jan	Feb	Mar	Apr	May	June	July	Aug	Sep	Oct	Nov	Dec	Total
Cyberknife	36	15	30	13	5	29	31	23	16	10	15	12	235
Tomotherapy HI-Art	19	31	24	14	16	0	14	22	25	19	34	18	236
Varian Trilogy 1	57	68	57	51	35	64	65	57	60	43	61	52	670
Varian Trilogy 2	60	66	61	46	41	71	58	58	68	34	58	39	660
Elekta Synergy Platform	71	58	57	28	35	56	58	31	54	46	41	35	570
IORT Mobetron	0	1	0	0	0	0	0	0	0	0	0	0	1
Nucletron 3D Brachytherapy	16	18	18	12	13	24	20	15	10	14	14	16	190
<b>TOTAL</b>	259	257	247	164	145	244	246	206	233	166	223	172	2562
<b>COVID-19(+)</b>	0	0	2	1	0	1	0	4	8	4	17	8	45

**Table 2.** The number of the patients treated with different machines and diagnosed COVID-19 in 2021.

2021	Jan	Feb	Mar	Apr	May	June	July	Aug	Sep	Oct	Nov	Dec	Total
Cyberknife	17	25	25	30	20	15	11	17					160
Tomotherapy HI-Art	26	25	22	4	7	26	17	25					152
Varian Trilogy 1	51	42	53	41	56	43	35	40					361
Varian Trilogy 2	55	56	59	70	47	54	45	59					445
Elekta Synergy Platform	45	33	50	40	32	47	24	45					316
IORT Mobetron	0	1	0	0	0	0	0	0					0
Nucletron 3D Brachytherapy	18	15	20	15	19	22	22	20					151
<b>TOTAL</b>	212	196	229	200	181	207	154	206					1585
<b>COVID-19(+)</b>	2	1	1	4	1	3	0	1	3				16

#### 4. COVID-19 in Our Clinic

The first COVID-19 positive patient was diagnosed on 27th March 2020 in our clinic. Risk assessment of our personnel in contact with the patient had been made and our personnel hadn't been infected. Besides, since that date, there is no infected personnel from any patient diagnosed COVID-19 before or during their treatments.

Since 18th September 2020, PCR test have been applied to each patient 24 hours before their treatments. Therefore, between 18 September 2020 and 31 December 2020, 523 PCR tests per patient were applied. 21 COVID-19 positive patients were detected 24 hours before their treatments and 24 patients during their treatments (45 patients in total) in that time period. From 18 September 2020 to 20 September 2021, 1987 PCR tests per patient were applied. 14 COVID-19 positive patients were detected 24 hours before their treatments and 2 patients during their treatments (16 patients in total) in 2021.

The total number of patients treated in our clinic between 2003 and 2021, excluding brachytherapy patients, are given in Table 3. As can be seen from Table 3, until 2020, annual number of patients were roughly at least 2500 and above. The lowest number of patients was seen in 2020 due to the pandemic.

The COVID-19 positive personnel in the clinic in 2020 and 2021 are given in Table 4. Among 32 radiation oncologists, 4 of them were infected in 2020 and 1 of them in 2021. Among 19 medical physicists 2 of them were infected in 2020 and none in 2021. Among 46 RTTs, 5 of them were infected in 2020 and 2 of them in 2021. Among 6 nurses, none of them were infected in 2020 and 1 of them in 2021. Among 5 secretaries, 1 of them were infected in 2020 and none of them in 2021. The COVID-19 positive personnel in the clinic were infected from their families or from other contacts apart from the clinic.

**Table 3.** The number of the patients treated between 2003 and 2021.

Year	2003	2004	2005	2006	2007	2008	2009	2010	2011	2012	2013	2014	2015	2016	2017	2018	2019	2020	2021
Number of Patients	2792	3017	3463	3729	3583	2993	3249	3202	3404	2982	2815	2755	2670	2589	2684	2833	3032	2372	1585

**Table 4.** The number of patients diagnosed COVID-19 before and during the treatments in 2020 and 2021.

	2020										2020 Total	2021										2021 Total	Total
	Mar	Apr	May	June	July	Aug	Sep	Oct	Nov	Dec	523 PCR	Jan	Feb	Mar	Apr	May	June	July	Aug	Sep	1464 PCR	1987 PCR	
Before Treatment	0	0	0	0	0	0	1	2	12	6	21	1	1	1	3	1	3	0	1	3	14	35	
During Treatment	2	1	0	1	0	4	7	2	5	2	24	1	0	0	1	0	0	0	0	0	2	26	

**Table 5.** The number of personnel diagnosed COVID-19 in the Radiation Oncology Clinic.

	Radiation Oncologists		Medical Physicists		RTTs		Nurses		Secretary	
	2020	2021	2020	2021	2020	2021	2020	2021	2020	2021
COVID (+)	4	1	2	0	5	2	0	1	1	0
Total number of personnel	32		19		46		6		5	

## 5. Results

Among the number of treated patients from 2003 to 2021, the most dramatic decrease is observed in 2020 with the number 2372 (excluding brachytherapy patients) due to the pandemic (Table 3). Besides, the effect of the governmental restrictions can be seen from Table 1. In April-May and October (2020), the decrease in the number of the treated patients can be seen easily. Both decreases occurred right after the increase in the COVID-19 positive patients in the country and the declaration of curfews. When comparing Table 1 and 2, the effect of fear of infection in 2020 can be easily seen from the low numbers in April and May which increased in 2021.

Among 523 patients (between 18 September 2020 – December 2020), only 45 of them were diagnosed positive (21 before and 24 during their treatments). Beginning from September 2020, the increase of the COVID-19 positive patients in the clinic was correlated with national numbers. This obvious increase led anxiety among patients which resulted skipping their treatments. 1987 PCR tests per patient were applied from 18 September 2020 to 20 September 2021. 14 COVID-19 positive patients were detected before their treatments and 2 patients during their treatments (16 patients in total) in 2021. So, in 2021 roughly one third of the COVID-19 positive patients were detected compared to 2020 due to the rising awareness of self-protection of individuals and the effect of vaccines. Besides, only 5 radiation oncologists (4 in 2020, 1 in 2021), 2 medical physicists

(in 2020), 7 RTTs (5 in 2020, 2 in 2021), 1 nurse (in 2021), 1 secretariat (in 2020) were COVID-19 positive due to the in family contact or contacts from outside the clinic.

## 6. Conclusions

The psychological pressure of the national restrictions caused patients to skip their treatments or initiating new procedures for diagnoses which also lead a decrease in May and September 2020 (145 and 166, respectively). Due to avoiding symptoms and postponing related examines, it is highly expected to face higher grades in the future. Each of the rules applied to cope with pandemic in our clinic seems very effective taking into account such low COVID-19 positive numbers both among patients and staff.

Due to the all precautions implemented in our clinic, none of the treatments were interrupted and our clinic was never under quarantine. Contamination due to the contact both among the patients and among the personnel was never seen because of early detection via PCRs and symptom tracking among all patients.

## 7. References

- Ministry of Health (2020). COVID-19 Yeni Koronavirüs Hastalığı [online]. Website: <https://covid19bilgi.saglik.gov.tr/> tr/ [accessed 17April 2020].
- Ministry of Health (2020). COVID-19 Algoritmalar [online]. Website: <https://covid19bilgi.saglik.gov.tr/tr/algoritmalar> [accessed 17April 2020].

## **RADIOSURGERY DOSE OPTIMIZATION FOR THE PATIENTS WITH CEREBRAL ARTERIOVENOUS MALFORMATIONS AFTER ENDOVASCULAR EMBOLIZATION**

Linās KUDREVČIUS<sup>1,2</sup>, Evelina JASELSKĖ<sup>1,2</sup>, Diana ADLIENĖ<sup>2</sup>

<sup>1</sup> The Hospital of Lithuanian University of Health Sciences Kaunas Clinics; <sup>2</sup> Kaunas University of Technology, Physics department;  
linas.kudrevicius@ktu.edu; evelina.jaselske@ktu.lt; diana.adliene@ktu.lt

**Abstract:** The treatment of patients with relatively rare cerebral arteriovenous malformations (AVMs) requires specific knowledge and high precision of multidisciplinary team. Treatment management consists of microsurgery, endovascular embolization, dosimetry method application and radiosurgery using Gamma knife facility or stereotactic radiotherapy (SRS) with linear accelerator. The overview of AVMs treatments in LUHS Kaunas clinics, Neurosurgery department during the period from 2019-06-11 to 2021-09-01 is presented in results part.

**Keywords:** arteriovenous malformations, radiosurgery, Gamma knife, endovascular embolization, individual dosimetry.

### **1. Introduction**

Cerebral arteriovenous malformation (AVMs) is aberrant blood vessels tangle connecting arteries and veins in the head. This tangle disturbs normal oxygen circulation and blood flow. Any single treatment strategy success for large AVMs (volume >10ml, conventionally nidus diameter >3cm) is limited and related to higher complications after treatment [1]. Individual treatment modality selection often includes microsurgery, endovascular embolization and radiosurgery combinations. Microsurgery can exclude AVMs from blood circulation immediately [2], radiosurgery is very useful when surgical procedures are at high risk related to close critical anatomic structures. If AVMs are formed near functionally important areas, the tactic of endovascular embolization before Gamma knife (GK) radiosurgery [3] is the mostly used alternative to open surgery and is especially preferred for high-flow AVM [4]. Aggregation of two methods derivation can improve treatment efficacy from 30-62% to 68-90%, but an occlusion occurs after 1-3 years [5]. It should be noted that the dose delivered to the target during Gamma knife treatment should be verified and

optimized following individual dosimetry concept for each patient. Treatment volume is the only significant factor for adverse radiation effects in pediatric patients (under 15 years) [6] treated in Gamma knife facility however for elder patients also the neurologic deficits should be taken into account. [7]. According to long term follow-up [8] maximum treatment diameter less than 15 mm and margin dose of more than 20 Gy was associated with better obliteration.

### **2. Materials and methods**

11 AVMs were treated Using Elekta Gamma Knife® Icon™ facility in the Neurosurgery Gamma sector of the Hospital of Lithuanian University of Health Sciences Kaunas Clinics within the period between June, 2019 and September, 2021.

Patients data used in this investigation were depersonalized and agreed by a signature of each patient on their further usage for research purposes.

#### **2.1. AVMs treatment workflow**

Radiosurgery treatment procedure consisted of several steps. In the first step stereotactic Leksell Frame G was fixed to the patient skull by 4 screws using local anesthesia. After this procedure an open MR indicator was placed on the fixated frame and each patient was scanned in MRI unit (Siemens MAGNETOM Avanto 1.5T, in our case) using patient's specific calibrated stereotactic magnetic resonance imaging sequence. TOF-3D multi-slab, proton density-weighted turbo spin echo (PD-TSE) and contrast-enhanced T1-MPRAGE magnetic resonance imaging sequences were generally applied for scanning of AVM patients. Subsequently for MRI scan, stereotactic contrast enhanced angiography procedure was performed by fixing of patient with a frame on the angiography table. An example of stereotactic angiography image set is provided in Fig.1.

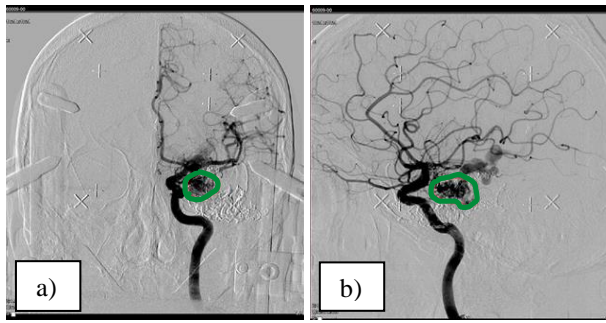


**Fig. 1.** The coronal a) and sagittal b) plane of stereotactic contrast enhanced AVMs angiography; with indicated AVMs location.

All acquired patient's images were sent to treatment planning system equipped with Leksell GammaPlan (11.1.1) software for individual treatment dose planning. Planning was performed by indicating treatment shot locations in stereotactic space coordinate system according to the defined reference points obtained from both sets of images. Shot locations were adjusted according to AVMs locations in each plan without any consideration of margins. Treatment dose was chosen individually for each patient according to the nidus size. Dose selection was based on information provided by other researchers [9-10]. Prescribed irradiation dose was dependent on arteriovenous malformation's size, location, and surrounding critical structures.

## 2.2. Individual dosimetry concept

It is known that endovascular embolization of AVMs is a common solution before Gamma knife treatment. However it may affect energy absorption or scattering processes, also some of in vitro studies were showing negligible dose reduction following beam penetration of embolic agents [11]. Due to this, the only way for the implementation of the precise treatment is proper target visualization.

Some authors have used Onix glue as embolization agent for theoretical dose reduction calculations using CT-images and  $^{60}\text{Co}$  attenuation coefficients [12] and found 0.01-1% dose reduction related to embolization.

In order to assess embolization related dose reduction, combination of patient specific 3D printed AVMs models immersed in VIPAR-type polymer dose gels, manufacturing process of which was described in our previous publications [13-14], were used (Fig.2).

Menox glue was used to recall embolization of AVMs.

Two cases were explored: polymer gels with inserted AVM model: gel with empty AVM model and gel with Menox glue filled vascular model inside. After 24 hours both identically Gamma Knife identically irradiated samples were MRI scanned keeping the same parameters. Optical density of the MRI images was used to identify absorbed dose values in polymerized dose gel.

Dose verification was performed comparing the doses generated by Gammaplan treatment planning system of the facility and doses obtained performing dosimetric evaluation of the polymer gel structures irradiated

according to the real patient's plans (same shape and realized dose).

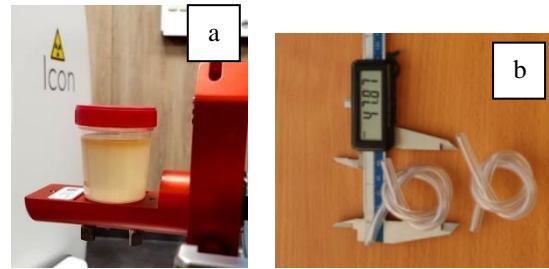


**Fig. 2.** Manufactured VIPAR<sup>nd</sup> dose gel sample a) and 3D printed vascular models b)

## 3. Results

6 of 11 AVMs patients previously had partial vascular embolization and one of them was after multiple embolization procedures, among them 5 male and 1 female patient. Some treatment related parameters are provided in the Table1.

**Table 1.** AVM patients related information.

Parameter	Range or count	Average or percentage
Number of AVM patients	6/11	54%
Age, years	19 - 67	46
ECoG (electrocorticography)	0 - 1	
KPS (Karnofsky Performance Status)	100 - 80	
AVM size, ml	0.10– 1.33	0.82
Prescribed irradiation dose, Gy	18 - 25	22.5
Isodose, Gy	50 - 60	53
Treatment time, min.	21.9 – 83.9	47.7

Control MRI scans and angiography screening were usually performed between 12 to 18 months after the Gamma Knife stereotactic radiosurgery. Positive impact of the embolization on the outcome of Gamma knife treatment can be clearly identified in both, angiography images (Fig.3) and MRI scans (Fig.4) of the treated AVMs patient.

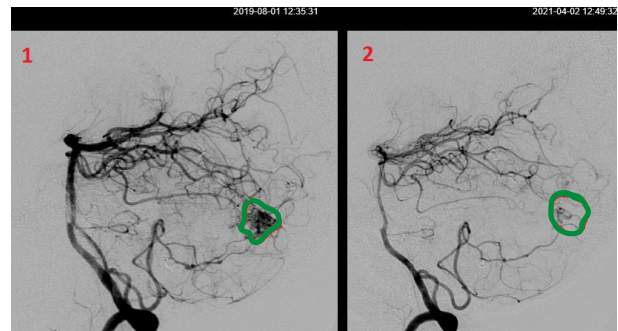


**Fig. 3.** Sagittal plane angiography: 1 – 14 months after embolization, 2 – 19 months after Gamma Knife radiosurgery (0.843 ml, 24@50% isodose)



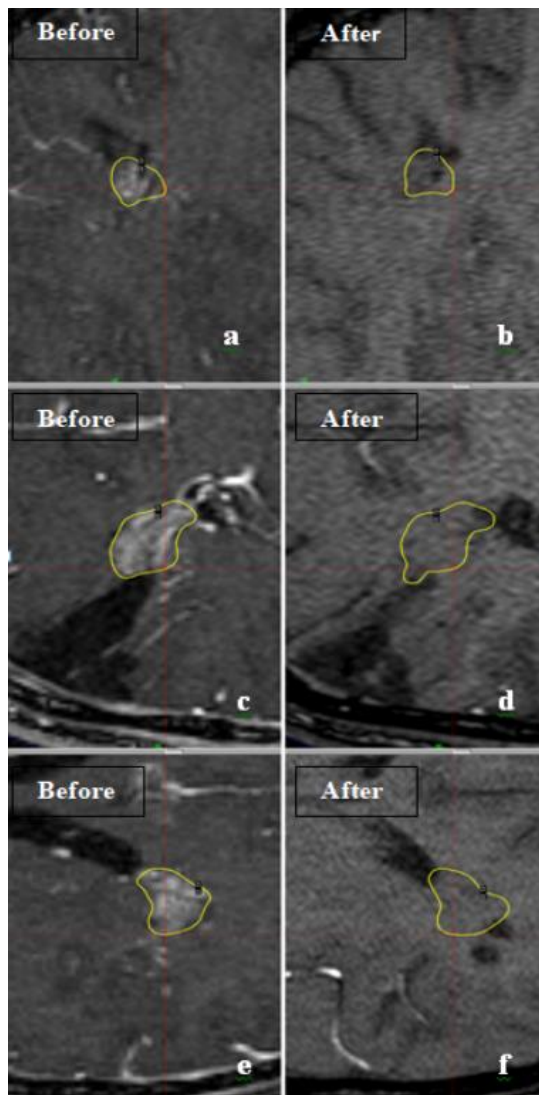


**Fig. 4.** MRI control scans (TOF-3D multi-slab application) , performed 17 month after stereotactic radiosurgery treatment of 1.33 ml AVM with 22 Gy@56% at isodose in Gamma Knife facility. (a,b – sagittal, c,d – coronal, e,f – axial planes)

Identification of nidus is not that complicated in angiography as compared to identification of the smaller arterial feeders, especially in the case if there is more than one of them. If the bigger non-compact AVM nidus with non-single draining vein is detected, partial embolization small feeders is done [15], which not necessarily totally stops blood circulation in AVMs, thus increasing hemorrhage risk.

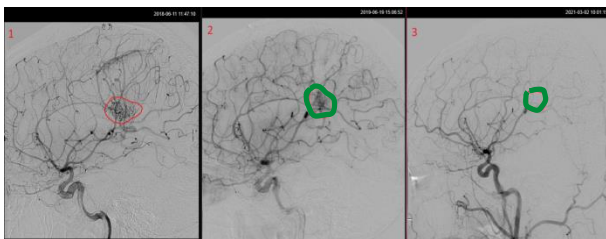


**Fig. 5.** Sagittal plane angiography: 1- Confirmed AVM after haemorrhage in 2018, 2 – 12 months after partial embolization, 3 – 18 months after Gamma Knife radiosurgery

Having similar situation microsurgery is impossible and only repeated embolization or SRS treatment options

exist. An example of successful treatment in similar situation with GK is provided in Fig. 5.

#### 4. Conclusions

All 6 after endovascular embolization GK treated patients were under control for at least 2 years. According to the performed MRI and/or angiography examination results treatment clearly improved the life expectations of 4 patients since arteriovenous malformations were shut down from blood circulation. MRI control scans performed for other two patients indicated remaining gliosis changes a in place of AVMs. Due to very small (0.1 and 0.3 ml) their pre-treatment size it was impossible to confirm or deny relapse.

Application of the proposed individual dosimetry concept allowed for comparison between doses registered in polymer gels with immersed empty 3D printed AVM model and gels with 3D printed AVM model filled with Menox glue. Detectable dose reduction in sample with Menox glue filled vascular model (~1%) was found. This clearly indicated the need for further more detailed investigation related to dose optimization which should be implemented before delivering doses to AVMs patients with installed vascular embolization.

#### Acknowledgements

Funding: This research was supported by the Research and Innovation Fund of Kaunas University of Technology (project grant No.INP2021/11) and the Research Fund of Lithuanian University of Health Sciences (project acronym SMEGENYS/BRAIN).

#### 5. References

1. El-Shehaby AMN, Reda WA, Abdel Karim KM, Emad Eldin RM, Nabeel AM, Tawadros SR. Volume-Staged Gamma Knife Radiosurgery for Large Brain Arteriovenous Malformation. *World Neurosurg.*, 2019. Vol 132, p. 604-612.
2. Hasegawa H, Shunya H, Masahiro S, Masaaki S et al. Long-Term Outcomes of Single-Session Stereotactic Radiosurgery for Cerebellar Arteriovenous Malformation, with a Median Follow-Up of 10 Years, *World Neurosurg.*, 2016. Vol 98, p. 314-322.
3. Lazzaro MA, Badruddin A, Zaidat OO, Darkhabani Z, Pandya DJ, Lynch JR. Endovascular embolization of head and neck tumors. *Front Neurol*, 2011, p. 1-9.
4. Yuki I, Kim RH, Duckwiler G et al. Treatment of brain arteriovenous malformations with high-flow arteriovenous fistulas: risk and complications associated with endovascular embolization in multimodality treatment. *Clinical article. J Neurosurg.*, 2010. Vol 113(4), p. 715-722.
5. Bendszus M, Bartsch AJ, Solymosi L. Endovascular occlusion of aneurysms using a new bioactive coil.
6. A matched pair analysis with bare platinum coils. *Stroke.* 2007. Vol 38(10), p. 2855-2857.
7. Hasegawa T, Kato T, Naito T, et al. Long-Term Outcomes for Pediatric Patients with Brain Arteriovenous Malformations Treated with Gamma Knife Radiosurgery, Part 2: The Incidence of Cyst Formation, Encapsulated Hematoma, and Radiation-Induced Tumor. *World Neurosurg.*, 2019, Vol 126, p. 1526-1536.

8. Hasegawa H, Hanakita S, Shin M, et al. Does Advanced Age Affect the Outcomes of Stereotactic Radiosurgery for Cerebral Arteriovenous Malformation? *World Neurosurg*, 2018, Vol 109, p. 715-723.
9. Hasegawa H, Hanakita S, Shin M, et al. Long-Term Outcomes of Single-Session Stereotactic Radiosurgery for Cerebellar Arteriovenous Malformation, with a Median Follow-Up of 10 Years. *World Neurosurg*, 2017. Vol 98, p. 314-322.
10. Zhu D, Li Z, Zhang Y, et al. Gamma knife surgery with and without embolization for cerebral arteriovenous malformations: A systematic review and meta-analysis. *J Clin Neurosci*, 2018. Vol 56, p. 67-73.
11. Yang W, Luksik AS, Jiang B, et al. Venous Stenosis and Hemorrhage After Radiosurgery for Cerebral Arteriovenous Malformations. *World Neurosurg*, 2019. Vol 122, p.1615
12. Mamalui-Hunter M, Jiang T, Rich KM, Derdeyn CP, Drzymala RE. Effect of liquid embolic agents on Gamma Knife surgery dosimetry for arteriovenous malformations. *Clinical article. J Neurosurg*, 2011;. Vol 115(2), p. 364-370.
13. Schlesinger DJ, Nordström H, Lundin A, Xu Z, Sheehan JP. Dosimetric effects of Onyx embolization on Gamma Knife arteriovenous malformation dose distributions. *J Neurosurg*, 2016. Vol 125 (Suppl 1), p. 114-122.
14. Jaselskė, Evelina; Adlienė, Diana; Rudžianskas, Viktoras; Urbonavičius, Benas Gabrielis; Inčiūra, Artūras. In vivo dose verification method in catheter based high dose rate brachytherapy // *Physica medica. Oxford : Elsevier*. ISSN 1120-1797. eISSN 1724-191X. 2017, vol. 44, p. 1-10. DOI: 10.1016/j.ejmp.2017.11.003.
15. Jaselskė E, Adlienė D, Rudžianskas V, Korobeinikova E, Radžiūnas A. Application of polymer dose gels for millimeter scale target/tumor pretreatment imitation using gamma knife facility//*Nuclear instruments and methods in physics research. Section B: Beam interactions with materials and atoms*. Amsterdam : Elsevier. ISSN 0168-583X. eISSN 1872-9584. 2020, vol. 470, p. 56-60.
16. Chen CJ, Norat P, Ding D, et al. Transvenous embolization of brain arteriovenous malformations: A review of techniques, indications, and outcomes. *Neurosurg Focus*, 2018. Vol 45(1), p. 1-7.



## INCREASING THE ANTITUMOR EFFICACY OF DOXORUBICIN BY HIGH-ENERGY IRRADIATION OF SALINE

Lyudmila ASLAMOVA<sup>1</sup>, Mykhaylo ZABOLOTNYY<sup>2</sup>, Galina DOVBESHKO<sup>3</sup>, Galina SOLYANIK<sup>4</sup>

<sup>1,2</sup>Taras Shevchenko National University of Kyiv, Ukraine;

<sup>3</sup>Institute of Physics of NASU, Kyiv, Ukraine,

<sup>3</sup>R.E. Kavetsky Institute of Experimental Pathology, Oncology and Radiobiology of NASU, Kyiv, Ukraine

<sup>1</sup>aslamova258@gmail.com; <sup>2</sup>fedcba137@ukr.net; <sup>3</sup>matinelli@gmail.com; <sup>4</sup>gsolyanik@gmail.com

**Abstract:** The effect of modification of optical absorption spectra and pharmacological activity of doxorubicin using pre-irradiation of saline with electrons of 1 MeV and an absorbed dose in the range of 10 - 80 kGy was investigated. It was found that the effect of electron irradiation of saline on the spectra of doxorubicin persists for 2-3 months.

**Keywords:** doxorubicin, saline, electron irradiation, carcinoma

### 1. Introduction

Almost all antitumor drugs are characterized by low specificity of their antitumor activity. This is manifested in the fact that the difference between the dose required to suppress the tumor process and the dose that causes significant damage to healthy organs and tissues of the body is quite small. Existing or acquired resistance of malignant tumor to the action of antitumor drugs also significantly worsens the results of treatment of cancer patients [1]. All these facts cause low efficiency of antitumor drug therapy in the treatment of locally advanced and disseminated forms of malignant neoplasms and raise questions about the development of ways to increase it [2]. A promising method of sensitization of antitumor drugs is based on the use of ionizing radiation for the modification of existing antitumor drugs [3]. It was proposed earlier to modify the properties of doxorubicin by pre-irradiation of the solvent - saline. In this case, a possible mechanism for changing the therapeutic activity of drugs may be the action on the molecules of doxorubicin formed by radiolysis of the solvent free radicals and gas bubbles surrounded by a double electric layer.

Given the above, the aim of the study was to study the change in the effectiveness of doxorubicin during pre-irradiation with high-energy electrons of sodium chloride solvent to determine the patterns of radiation methods of modification of existing anticancer drugs.

### 2. Samples and methods of experiment

The study was performed using the antitumor drug doxorubicin (Sigma, USA). Solutions of doxorubicin preparations were made from doxorubicin powder and saline, bringing the concentration of the active drug to 5 mg/ml. FR irradiation was performed with high-energy electrons with an energy of 1 MeV on a resonant linear electron accelerator "Argus". The IR absorption spectra were recorded on a Bruker IFS-66 spectrometer, and the absorption spectra in the visible and UV range were recorded on a Shimadzu UV-260 spectrophotometer with a measurement range of 190-900 nm.

The dose of saline-absorbed radiation ranged from 4 to 80 kGy. The duration of the process of electron irradiation of saline and the value of absorbed doses are given in Table 1.

**Table 1.** Parameters of saline irradiation with high-energy electrons

The fluence of the electron flux, $\text{sm}^{-2}$	Duration of irradiation time, s	Absorbed radiation dose, kGy (I)
$4 \times 10^{13}$	45	4
$6 \times 10^{13}$	60	10
$1 \times 10^{14}$	76	20
$2 \times 10^{14}$	270	35
$4 \times 10^{14}$	520	70
$4 \times 10^{14}$	580	80

To study the pharmacological activity of doxorubicin after its dissolution in sodium chloride irradiated with high-energy electrons, Lewis's lung cancer tumor cells (LLC) were acquired from the National Bank of Cell Lines and Tumor Strains IEPOR. RE. Kavetsky National Academy of Sciences of Ukraine. Cells were maintained

in vitro in RPMI 1640 medium (Sigma, USA) with the addition of 10% fetal calf serum (Sigma, USA) and 40 mg/ml gentamicin. The cytotoxic/cytostatic effect of doxorubicin on LLC cells was used as an indicator of the pharmacological activity of doxorubicin. To do this, tumor cells were seeded in wells of a 96-well plate of 0.1 ml ( $2 \times 10^5$  cells/ml) and incubated for 16 hours. After the incubation period, doxorubicin of various concentrations, either dissolved in irradiated (absorbed dose 40 kGy) or unirradiated saline (positive control) was added to cells. For comparison, LLC were added to irradiated and irradiated saline without doxorubicin. The number of living cells in the wells after 24 hours of incubation was determined by MTT test using a plate reader at a wavelength of 545 nm.

### 3. The results of experiments and their discussion

The results of measurements in the visible and IR regions of the spectra are illustrated by the graphs presented in Figs. 1 and Fig. 2, respectively. The time between irradiation of the samples and registration of their vibrational spectra did not exceed 14-23 days. The measurements showed that the absorption (A) of the samples in this case was constant. The results of the measurements in the visible region of the spectrum are illustrated in Fig. 1, which shows the spectral dependences of the absorption of doxorubicin molecules in unirradiated and irradiated (70 kGy) saline.

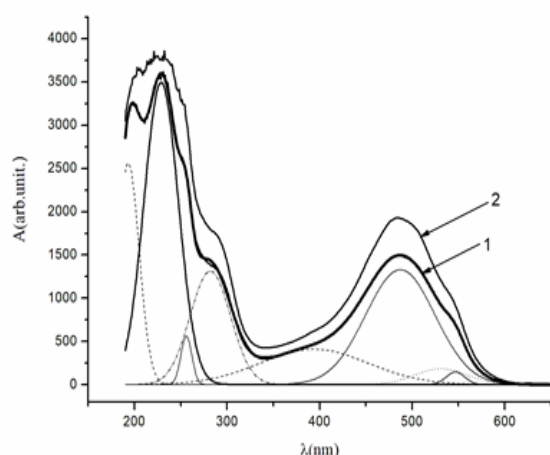


**Fig. 1.** Absorption spectra in the visible region of a doxorubicin solution dissolved in saline solution not irradiated (curve 1) and pre-irradiated (curve 2)

The absorption spectrum of the solution obtained without prior irradiation was analysed using its representation as a composition of Gaussian functions. The graph of the sum of these Gaussian functions conveys all the characteristic features of the experimentally established spectrum (Pearson's pairwise correlation coefficient between them is 0.98). The absorption of radiation in these regions is associated with the excitation of electrons of the s-, p- and n-orbitals of the ground state and the transitions of molecules into the excited state. Therefore, while studying the shift of the positions of the maxima and the change in intensity in this area, conclusions can be drawn about the change in the optical properties of the doxorubicin molecule. The dependence of the positions of the local maxima of the spectra on the value of the

absorbed dose in the optical absorption spectra taken immediately after irradiation of the solvent and the preparation of solutions with doxorubicin are shown in Table 2.

**Table 2.** Dependence of the position of the absorption maxima on the dose in the optical absorption spectra taken immediately after irradiation of the solvent and preparation of solutions with doxorubicin

0 kGy, $\lambda$ (nm)	70 kGy, $\lambda$ (nm)
193,23	192,50
225,86	235,11
256,95	255,24
280,64	291,69
393,33	401,87
486,37	489,76
530,18	529,81
545,21	535,42

Significant dependence on the amount of absorbed dose is also shown by the absorption spectra in the IR range, illustrating the data shown in Fig. 2.

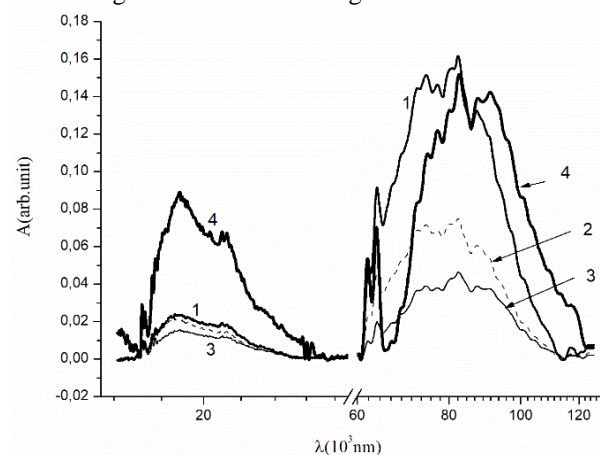


**Fig. 2.** The dependence of the normalized absorption of doxorubicin on the wavelength in the un-irradiated and irradiated saline at different doses of absorbed electron irradiation

Curve 1 describes the absorption spectrum of doxorubicin in non-irradiated saline, curve 2 at  $I = 10$  kGy, curve 3 - 35 kGy, and 4 - 70 kGy. As can be seen from Fig. 2 for the above spectra is characterized by a significant non-monotonic dependence of the configuration of the spectra (the ratio of the amplitudes of high-frequency and low-frequency maxima) from the absorbed dose. This behavior may be due to coagulation (clustering) of babstones, which occurs at high concentrations of babstones (at high levels of radiation). When comparing the dependences of  $A(k)$  for different  $I$ , Pearson's correlation analysis was used. To determine the value of the correlation coefficient between the absorption spectra in the interval [500, 4000], this interval was evenly divided into 3632 points. Pearson correlation coefficients ( $K$ ) were calculated using the obtained data. Calculations showed that  $K(A(0 \text{ kGy}), A(10 \text{ kGy})) = 0.982$ ;  $K(A(0 \text{ kGy}), A(20 \text{ kGy})) = 0.935$ ;  $K(A(0 \text{ kGy}), A(40 \text{ kGy})) = 0.864$ ,  $K(A(0 \text{ kGy}), A(60 \text{ kGy})) = 0.828$ ,  $K(A(0 \text{ kGy}), A(80 \text{ kGy})) = 0.713$ . Thus, the preliminary irradiation of the solvent, without significantly changing the drugs (in all cases, the

correlation coefficient exceeds the critical value), changes some of its properties in the oscillatory range, which significantly depends on the conformational state of the molecules.

Studies of the IR absorption spectra of the samples at small values of the dose absorbed by the solvent (saline) irradiation were performed. The obtained results are illustrated in Fig. 3.

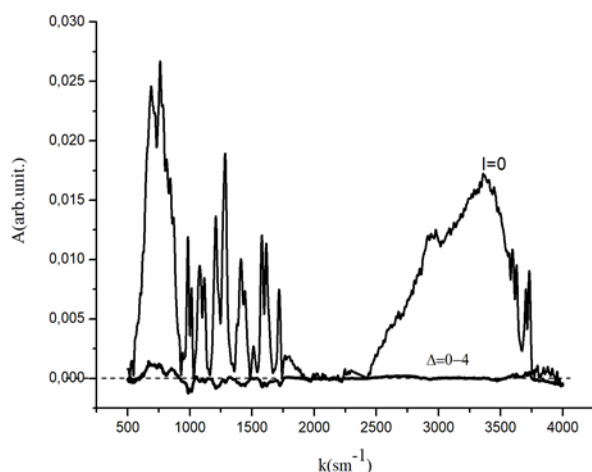


**Fig. 3.** Doxorubicin absorption spectrum in non-irradiated FR and the difference between doxorubicin absorption spectra in non-irradiated and irradiated (4 kGy) saline

Figure 3 shows the absorption spectrum of doxorubicin in the IR range dissolved in non-irradiated saline and the difference between the reduced absorption spectra (same area under the curve) and the absorption spectra in non-irradiated and irradiated saline. From the presented curves it is seen that the radiation-induced changes in the absorption spectra of the samples are close to the magnitude of the noise effects when measuring the absorption spectra of the samples. A similar comparison of doxorubicin absorption spectra in non-irradiated and irradiated solvent at an absorbed dose of 4 kGy was also performed. The obtained data showed that the minimum dose of solvent-absorbed high-energy electron irradiation, at which changes in the conformational states of dissolved doxorubicin are recorded, is 4 kGy. Similar studies were performed to determine the effect of pre-irradiation of the solvent on the absorption of doxorubicin solution in the visible part of the spectrum. Changes in the preliminary irradiation of the saline solution are also recorded in the measurements of absorption in the visible part of the spectrum, illustrating the graphs. 4. Figure 4 shows the differences in the normalized absorption spectra of doxorubicin in unirradiated and irradiated ( $I_1 = 10$ ,  $I_2 = 40$ ,  $I_3 = 80$  kGy) saline.

The graphs of the sum of the Gaussian functions thus obtained describe all the characteristic features of the experimentally established spectra (Pearson's pairwise correlation coefficient between them is 0.98), which made it possible to determine the effect of irradiation on the displacement of the local maxima of absorption spectra. The dependence of the positions of some local maxima of the sectors on the value of the absorbed dose in the optical absorption spectra are shown in Table 3.

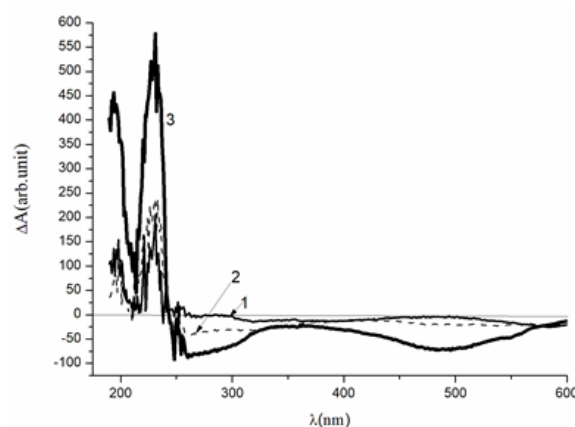


**Fig. 4.** The difference between the absorption spectra  $\Delta_i = A_0 - A_i$  of non-irradiated ( $A_0$ ) and irradiated  $A_i$  ( $i = 1$  is obtained at  $I = 10$  kGy,  $i = 2$ -at  $I = 40$  kGy, and  $= 3 - I = 80$  kGy)

**Table 3.** Dependence of the position of the maximum on the dose in the optical absorption spectra measured immediately after irradiation of the solvent and preparation of solutions with doxorubicin

<b>0 kGy,</b> <b>λ (nm)</b>	225,9	280,6	393,3	486,4	545,2
<b>80 kGy,</b> <b>λ (nm)</b>	235,8	291,6	402,1	489,8	535,9

The biomedical part of the research was conducted according to a standardized method - special studies were conducted to determine the effect of pre-irradiation of saline on the antitumor properties of dissolved doxorubicin. The experiments were performed in vitro using the Lewis Lung Cancer (LLC) malignant cell line. As an indicator of pharmacological activity, cytotoxic/cytostatic effect of aqueous solutions of antitumor drugs (with and without irradiation) against LLC cells in in vitro experiments was used. To do this, tumor cells were seeded in wells of a 96-well plate in 0.1 ml of nutrient medium ( $2 \times 10^5$  cells/ml) and incubated overnight. After that, drugs were added to the cells in 0.1 ml of fresh medium in a wide range of concentrations, which progressively decreased. Fresh medium was added to the control wells in the same volume without the test agent. The number of living cells in the wells after a day of incubation was determined using the MTT test. The research results are illustrated in Fig.5. which shows the dependence of the number (N) of living LLC cells (as a percentage of the corresponding value in the control wells) after 24 hours of incubation on doxorubicin of different concentrations (X), dissolved in unirradiated (1) and irradiated (2) saline.

Incubation of LLC cells for 24 hours in the presence of doxorubicin dissolved in non-irradiated saline leads to a concentration-dependent decrease in the number of living cells (curve 1). This is due either to inhibition of tumor cell proliferation (cytostatic effect) and/or their death (cytotoxic effect) induced by the antitumor drug.

At the same time, doxorubicin dissolved in irradiated saline enhances the cytotoxic/cytostatic effect, which is most pronounced at low concentrations (curve 2): for example, the number of living LLC cells at concentrations below  $3 \mu\text{M}$  decreased by an average of

20% ( $p < 0.05$ ) compared with the action of doxorubicin dissolved in unirradiated saline.

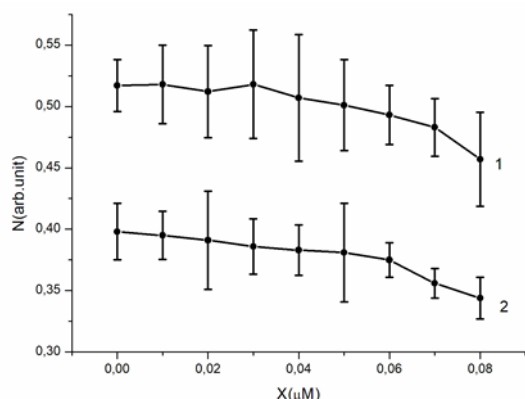


**Fig. 5.** Dependence of the number (N) of live LLC cells (as a percentage of the corresponding value in the control wells) after 24 hours of incubation with doxorubicin at different concentrations (X), dissolved in unirradiated (1) and irradiated (2) saline

Noteworthy is the low variability of cell survival after incubation with doxorubicin on irradiated saline compared to the corresponding values using the irradiated solvent.

Thus, the obtained results confirm the ability of high-energy electron irradiation of the solvent to increase the pharmacological activity of antitumor drugs in the range of low concentrations.

A possible reason for the change in the spectra of doxorubicin solution when using a pre-irradiated solvent is the conformational rearrangements of its molecules caused by interaction with babstones and their clusters, the concentration of which depends on the dose of absorbed radiation. Coagulation of babstones and cluster formation is initiated by force fields formed by double electric layers of babstones. It was taken into account that the ponder motor force between charged babstones of the same name during the implementation of polarization processes may cause mutual attraction of babstones.

#### 4. Conclusions

1. The effect of modification of the pharmacological activity of doxorubicin using pre-irradiation of physiological solution with electrons with an energy of 1 MeV and a dose of absorbed irradiation in the range of 10 - 80 kGy; an explanation of the effect within the model of babstones is offered.
2. The use of pre-irradiated saline to dissolve doxorubicin changes its optical absorption spectrum. The minimum dose of electron irradiation absorbed by saline (1 MeV), at which changes in the spectra of doxorubicin are recorded, is 4 kGy. The effect of electron irradiation of saline on the spectra of doxorubicin persists for 2-3 months.
3. As part of the evaluation of the pharmacological activity of the antitumor drug doxorubicin dissolved in irradiated saline, it was found that it enhances the cytotoxic/cytostatic effect on LLC cells compared to the effect of doxorubicin dissolved in unirradiated saline. The number of live LLC cells under the influence of irradiated saline doxorubicin at concentrations less than 3 μM decreased by an average of 15% compared with the corresponding figure when exposed to doxorubicin without irradiation. It is shown that the modifying effect of irradiation is most pronounced at low concentrations of doxorubicin (<3 μM).

#### 5. References

1. Nurgali K., Jagoe R., Abalo R. Editorial: Adverse Effects of Cancer Chemotherapy: Anything New to Improve Tolerance and Reduce Sequelae. *Front. Pharmacol.* 9, 245, 2018. <https://doi.org/10.3389/fphar.2018.00245>
2. Orel V. B., Zabolotnyy M. A., Orel V. E. Heterogeneity of hypoxia in solid tumours and mechanochemical reactions with oxygen nanobubbles, *Medical Hypotheses* 102, 82-86, 2017. <https://doi.org/10.1016/j.mehy.2017.03.006>
3. Kirsch D., Diehn M., Kesar Wala A. et al. The Future of Radiobiology. *J Natl Cancer Inst.*, 110(4), 329-340, 2018. <https://doi.org/10.1093/jnci/djx231>
4. Aslamova L. I., Zabolotnyy M. A., Dovbeshko G. I. et al. Electron irradiation as a method of increasing efficacy of some water-soluble drugs in oncology, *Proceedings of the 14<sup>th</sup> International Conference "Medical Physics in the Baltic States"*, Kaunas, 151-152, 2019.

## **EXTENDING LAP PRODUCT PORTFOLIO: SOLUTIONS FOR PATIENT QA AND MACHINE QA**

Ramune ULRICH

Sales manager BU Healthcare. LAP GmbH Laser Applikationen  
r.ulrich@lap-laser.com

**Abstract:** LAP’s market-leading laser systems are used for patient positioning in radiation therapy processes worldwide. Since few years already LAP has included QA products into the portfolio for the RT and is further extending this product line by new developments. The very latest solutions for patient QA is RadCalc software for a secondary check of the treatment plan, as well as the fully motorised water phantoms for commissioning and quality assurance – THALES 3D MR SCANNER (for MR-Linacs) and THALES 3D SCANNER (for bore-type Linacs).

**Keywords:** radiotherapy, patient QA, dosimetric verification software, phantom, commissioning, machine QA, MR-Linac

### **1. Introduction**

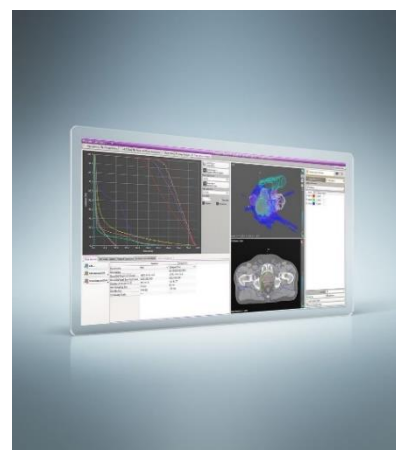
Safety is a priority in radiation therapy. Protecting patients against ionizing radiation to healthy tissue is essential. Every measurement must be as accurate as possible. Various QA processes can produce different results; therefore it is imperative to independently verify calculations a second time. This is exactly what RadCalc does: independently verify dosimetric calculations in an easy-to-use software platform.

Our very latest products are the 2 motorised water phantoms for commissioning and quality assurance of MR-Linac (THALES 3D MR SCANNER) and bore-type Linacs (THALES 3D SCANNER). Developed together with the end-users, these phantoms allows the user to save valuable time with efficient quality assurance and intuitive operation. Below kindly find more detailed elaboration of the features and benefits of the above products.

### **2. RadCalc QA Software – advanced platform for independent and unbiased patient QA**

**RadCalc secondary check software is:**

- **Fast:** a fully automated import and export is much faster when compared to manual data entry and eliminates transcription errors.
- **Independent:** it provides the opportunity to check all results independently from the manufacturer’s TPS. This ensures unbiased third party validation.
- **Accurate:** studies have shown the verification dose to be within  $\pm 3\%$  of the treatment plan dose providing excellent accuracy.
- **Easy to use:** due to its user-friendly interface the software is easy to use. Clear structure, guided menus, sophisticated layout make the recurring tasks simple and time-saving.
- **Powerful:** most common treatment plans can be verified with RadCalc. Comprehensive analytical features provide powerful tools for physicists for plan analysis.



RadCalc includes comprehensive institution and physics data setup, import of radiation therapy plans, automated dosimetric calculations, and export to record and verify systems. RadCalc also provides powerful reporting tools and flexible site licensing.



RadCalc is **modular** as well as **multitasking** and **versatile** software as it supports the following:

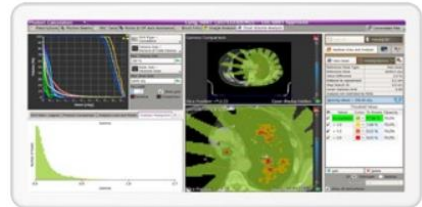
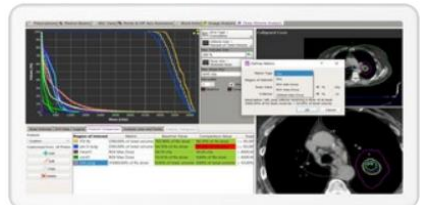
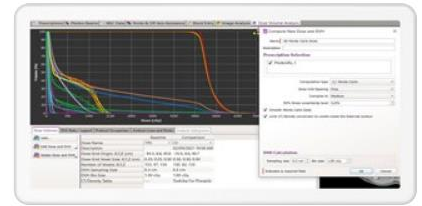
- Modalities: MR-Linacs, Linacs, Halcyon/Ethos, TomoTherapy, CyberKnife, GammaKnife, Cobalt 60, Superficial, and Brachytherapy.
- Treatment techniques: hypofractionation, adaptive radiation therapy, SBS/SRBT, IMRT, VMAT and Brachytherapy techniques.

### 3D functionalities of RadCalc

**3D Calculation Algorithms:** RadCalc provides Collapsed Cone Convolution Superposition and Monte Carlo based algorithm modules, that deliver fast, easy, and accurate 3D Dose Volume verification. RadCalc's 3D Monte Carlo module employs the most established Monte Carlo dose engine available (BEAMnrc), and also utilizes proprietary machine modelling acquired from McGill University.

**DVH Protocols:** Any number of DVH protocols can be defined used from the analysis screen within RadCalc. Using Rules in RadCalc, different DVH protocols can be automatically selected and applied to the specific plan. The software automatically checks whether the DVH objectives are met for critical structures using both the TPS and RadCalc's 3D dose. Analysis reports are automatically attached to the verified plan or to a directory of the choice on the server.

**3D Dose Analysis:** RadCalc provides Percent difference, DVH, Distance to Agreement, Gamma analysis tools to evaluate 3D computations. The functionality includes RadCalcAIR (automated Import & Report) providing a fully automated process for plan import, computations, 3D dose analysis and report generation. RadCalc's fully automated process immediately alerts the plans that fail to pass the pre-set Gamma Analysis acceptance criteria.



RadCalc allows the user to import from radiation TPS, verify and record systems, and/or virtual simulation software through DICOM RT or other proprietary formats. RadCalc provides an export utility that allows users to export treatment plans to a format readable by a record and verify system, what saves re-entry of data, ensures that patient's medical records contain verification results and allows users to export customised plans for special QA processes. Users may export plans and calculations to any record and verify system that accepts DICOM RT or RTP Connect format files.

### 3. THALES 3D MR SCANNER and THALES 3D SCANNER - Motorised water phantoms for commissioning and QA of MR-Linacs/Linacs

THALES 3D MR SCANNER offers comprehensive and efficient commissioning and regular quality assurance of MR-guided Linacs such as ViewRay's MRIdian, while THALES 3D SCANNER – for bore-type Linacs such as VARIAN's Halcyon and Ethos.

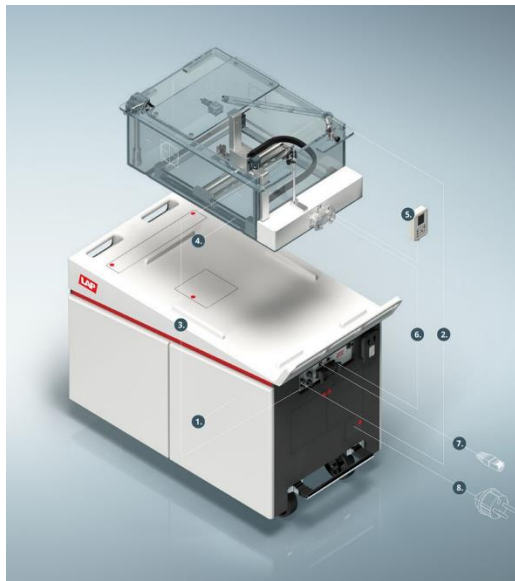


Fig. 1 THALES MR 3D SCANNER for ViewRay's MRIdian



Fig. 2 THALES MR 3D SCANNER VARIAN's Ethos

Both motorised phantoms comprise a carriage system, a water phantom, an integrated electrometer and the THALES software – all-in-one (Fig. 3), saving valuable time with efficient QA and the intuitive operation. From set-up to measurement takes only 15 minutes.



1. Carriage system
2. Extension cable for the reference detector
3. Extension cable for the field detector
4. Water phantom
5. Manual control unit with connection cable
6. Connection cable
7. Network cable
8. Mains power cable

**Fig. 3** THALES MR 3D SCANNER/3D SCANNER components

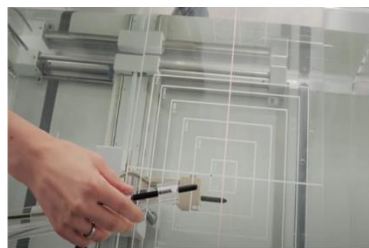
**Easy to use:** the water phantom and the THALES software can be used easily and intuitively ensuring efficient and productive workflows.

**Saves times substantially:** easy and fast set-up of the phantom as well as accelerated workflows, saves valuable time. All the cables and connections are placed conveniently in the carriage system. After connecting the system, filling the water reservoir takes only a few minutes.

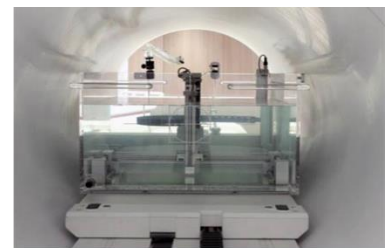
The user can use field detectors from different manufacturers. Field detectors can be installed both horizontally and vertically. The integrated electrometer offers two independent channels with different bias voltages. The water level sensor allows the field detector to be set up correctly, what ensures measurement accuracy. The reference detector is positioned with the help of the positioning plate. After this step, the phantom can be moved into the MR-Linac or Linac. The process for the automatic orientation of the Central Axis (CAX) completes the setup.



- Registration with index bars
- Localize vs. lasers
- Cables connect & water filling



- Adjustment vs. lasers
- Position detector EPOM at water surface
- Reference detector positioned



- Send inside the bore
- Perform CAX corrections

**Fig. 4** Example of the setup of THALES MR 3D SCANNER at ViewRay's MRIdian

User friendly, well-structured and efficient **THALES software** provides high flexibility and portability.

Both integration in clinical network and the direct connection to the phantom are possible. No additional tools are required for the acquisition of data, administration or evaluation. The data archive has an intelligent search function allowing the user to find measurement sequences and generate individual reports.

The THALES software is web-based and optimized for Mozilla Firefox and Google Chrome browsers.



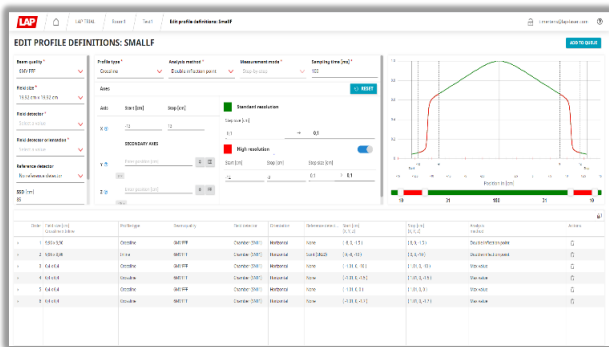


Fig. 5 Workspace for trajectories

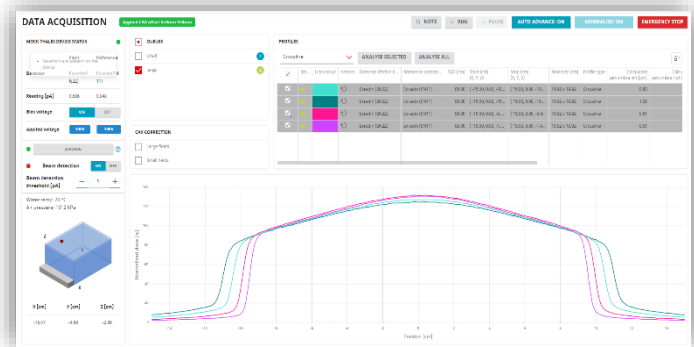


Fig. 6 Workspace for measurements

It also provides special beam analysis methods for large and small field sizes which are used in FFF mode for both transversal and inline measurements.

The software recommends an automatic CAX measurement which combines the diagonal and inline profiles in two different depths with a suggested correction shift.

Users have the option of working with acquired data and filter it by various parameters such as profile type, detectors, acquisition date and many others.

With THALES 3D MR SCANNER/THALES 3D SCANNER the user can acquire data reliably and can perform beam model validation. The THALES software provides comprehensive analysis and comparison tools for the verification of the user's data: Profiles for small and large fields, Percentage Depth Dose, Off-axis fields.

## LAP GmbH Laser Applikationen

Zeppelinstrasse 23, 21337 Lueneburg, Germany

P +49 4131 9511-95 E info@lap-laser.com

www.lap-laser.com, www.radcalc.com

LinkedIn: LAP Laser

YouTube: laplaser



## FORMATION AND INVESTIGATION OF Cu/CuO<sub>x</sub> NANCOMPOMCOSITE FILMS FOR LOW DOSE DOSIMETRY APPLICATION

Džiugilė VALIUKEVIČIUTĖ<sup>1</sup>, Judita PUIŠO<sup>2</sup>, Jurgita LAURIKAITIENĖ<sup>3</sup>, Linas KUDREVIČIUS<sup>4</sup>  
<sup>1, 2, 3, 4</sup> Department of Physics, Kaunas University of Technology, Studentų 50, Kaunas 51368, Lithuania  
<sup>1</sup>dziugile.valiukeviciute@ktu.edu; <sup>2</sup>judita.puiso@ktu.lt; <sup>3</sup>jurgita.laurikaitiene@ktu.lt, <sup>4</sup>linas.kudrevicius@ktu.edu

**Abstract:** Cu/CuO<sub>x</sub> nanoparticles in gelatin and PVP-gelatin composites were formed by reducing method. Transparent Cu/CuO<sub>x</sub> nanoparticles in gelatin and PVP-gelatin films were produced by simple and suitable drying method. Manipulation of the reduction kinetics allows ready control over local surface plasmon resonance of Cu/CuO<sub>x</sub>. The impact of X-ray on Cu/CuO<sub>x</sub> nanoparticles in polymer composite medium was investigated.

**Keywords:** Cu/CuO<sub>x</sub>, nanoparticles, X-ray, mass attenuation coefficient, linear attenuation coefficient, UV-VIS, LSPR

### 1. Introduction

Stable copper oxides (CuO<sub>x</sub>), which consists of two substances, namely cupric oxide (CuO) and cuprous oxide (Cu<sub>2</sub>O), are well-known p-type semiconductors [1]. Due to the natural abundance of copper, CuO<sub>x</sub> was used as a hole transport material in polymer solar cells [1]. It is conductive and light transmittance, non-toxic, low cost and easily manufactured material [1]. Cu composite materials display antiviral, algacide and fungicide properties [2].

The ultrathin CuO<sub>x</sub> films were fabricated via electrochemical deposition [1], magnetron sputtering [2-3], chemical Vapor Deposition (CVD) and physical Vapor Depositions (PVD) techniques [4].

Nanoparticles have been synthesized through several chemical methods such as polyol, reverse micelles, electron beam irradiation, micro-emulsion and wire explosion techniques and in-situ chemical synthesis. However, soluble polymers to form a complex with metal ions, that is important for copper nanoparticles (CuNPs) synthesis, since it prevents the nanoparticles aggregation [5].

Physical and chemical methods used to synthesize polymer nanocomposites, depending on the nanoparticle-polymer interactions. Usage of natural or synthesis biopolymers as stabilizers for the synthesis of

CuNPs has gained momentum because of their availability, biocompatibility and low toxicity. While the as-synthesized colloidal Cu nanocrystals is partially coated with organic ligands in order to prevent aggregation and provide solubility in organic solvents, the metal surface may still interact strongly with solvent molecules and react with dissolved oxygen [6].

The spectra clearly show the disappearance of the Cu surface plasmon peak at approximately 570 nm occurring simultaneously with the appearance of an excitonic peak centered at approximately 715 nm, which corresponds to the first exciton transition for copper oxide [6].

The optical absorption range observed for the Cu/CuO<sub>x</sub> lies between 200 - 730 nm. The spectral region between 500 - 600 nm shows the inter-band transition of Cu(I). The optical absorption between 600 - 730 nm shows the exciton band and the d-d transition of Cu(II) [7].

The LSPR of Cu nanoparticles incorporated to the polymers are around 750 nm, thus an artifact or a step rise occurs. The appearance of artifact around 750 nm is correlated to the change of the range of measurement from visible to infrared IR region [8].

The initial intensity of the copper plasmon was strongly dependent on the properties of the solvent used to form the nanocrystal dispersion; solvents with  $\pi$ -bonds significantly reduced (by >3-fold) the plasmon intensity and this effect was attributed to electron sharing between the solvent and the copper surface. The damped plasmon only recovered to its solvent-independent intensity once the nanocrystal surface oxidized and eliminated the solvent-Cu surface interactions. Solvents without  $\pi$ -bonds induced only a very small damping of the plasmon, and at longer time scales all solvents induced similar changes in the optical properties as oxidation converted the nanocrystals from metallic copper to semiconducting copper oxide.

As the nanocrystals continue to oxidize from metallic Cu to form semiconducting Cu<sub>2</sub>O particles, two additional optical phenomena are observed:

- a shift in the Cu plasmon due to the changing
- around the metal nanocrystal as an oxide shell is generated and replaces the interface between the Cu metal and the organic capping ligands/solvent.
- the eventual attenuation of the plasmon and appearance of an excitonic feature that corresponds to the semiconducting  $Cu_2O$  [6]

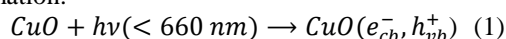
The local plasmon resonance is very sensitive to the electronic properties of the material at the metal surface and, over the course of the oxidation process, the Cu surface initially surrounded by organic molecules with a low dielectric is eventually surrounded with copper oxide (the dielectric constant for  $Cu_2O$  is approximately 7.1) [6].

The increase in the local dielectric constant is expected to yield a measurable red shift, as has been observed for other metal/semiconductor hybrid nanomaterials [6].

The aim of this work was the development and characterization of  $Cu/CuO_x$  nanoparticles enriched radiation sensitive free standing polymer films.

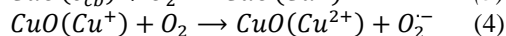
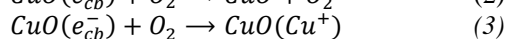
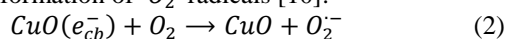
## 2. Theory

Irradiation of  $CuO$  leads to surface oxidative radical formation:

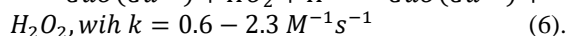
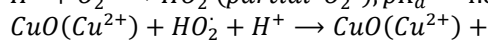
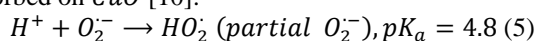


The  $e_{cb}^-$  is produced from  $CuO$  (p-type) with band gap energy of 1.7 eV, a flat band potential of -0.3 V (SCE) ( $pH = 7$ ) and valence band and +1.4 V SCE [reference]

The electron-hole is formed with photon energies exceeding the band-gap  $CuO$ . The excited electron could either react directly with  $O_2$  forming  $O_2^-$  or by reducing  $Cu^{2+}$  lattice to  $Cu^+$  leading to ensuing reaction and formation of  $O_2^-$  radicals [10]:



The equilibrium between  $H^+$  and  $O_2^-$  lead to the formation of the  $HO_2^\cdot$  radical.  $HO_2^\cdot$  generates  $H_2O_2$  adsorbed on  $CuO$  [10]:



Gelatine swells and adsorbs 5–10 times its weight of water to form a gel. Gelatine forms a gel in water at a minimum concentration of 0.5% and at pH range from 4 to 8 [11].

Gelatine is widely used as a food ingredient and a gelling agent forming transparent elastic thermos-reversible gels on cooling below  $\sim 35^\circ\text{C}$ . The chemical structure of gelatine is described by a linear sequence of amino acids. It is always written from the  $-NH_2$  end to the  $-COOH$  end by convention. Gelatine contains relatively high levels of the following amino acids: glycine 26–34%, proline 10–18% and hydroxyproline 7–15%. Other significant amino acids: alanine 8–11%, arginine 8–9%, aspartic acid 6–7% and glutamic acid 10–12%. The water content will vary between 6–9% [11]

dielectric properties of the local environment Two methods are usually explored for preparation of gelatine: the acid and the alkaline processes (in the pre-treatment part) to produce type A and type B gelatines, respectively. In the acid one, pigskin with an isoionic point of  $pH = 7$  to 9 is used. Photographic and pharmaceutical grades of gelatine are often produced from cattle bones and pig skin [11].

## 3. Materials and instruments

### 3.1. Materials

Copper sulphate pentahydrate ( $(CuSO)_4 \cdot 5H_2O$ ;  $\geq 99.5\%$  CAS 7758-99-8), copper nitrate trihydrate ( $(CuNO)_3 \cdot 3H_2O$ ;  $\geq 99\%$ ), were purchased from Sigma – Aldrich. Tri-Sodium citrate dihydrate ( $HOC(COONa)(CH_2COONa)_2 \cdot 2H_2O$ ; 99%) ascorbic acid ( $C_6H_8O_6$  Ph. Eur.), and polyvinyl pyrrolidone (PVP,  $(C_6H_9NO)_n$ ); gelatine ( $C_{102}H_{151}O_{39}N_{31}$ ) were used for  $Cu/CuO_x$  polymer films preparation.

$Cu/CuO_x$  polymer films were prepared by casting copper salt polymer gels in advance. 5 g of copper salt gelatine gels were casted in Petri dishes and dried at room temperature in a dark space. The chemical composition of copper salt gelatine gel is presented in Table 1 and Table 2

**Table 1.** Chemical composition of  $Cu/CuO_x$  gelatine gel

	V11- V12, %	V21- V22, %	V31- V32, V61- V62, %	V41- V4, %	V71- V72, %	V51- V52, %
$CuSO_4$	0.46	0.92	1.38	2.30	0.71	0.92
$C_{102}H_{151}O_{39}N_{39}$	9.58	9.58	9.58	9.58	9.67	9.58
$C_6H_8O_6$	0.02	0.02	0.02	0.02	0.01	0.01
$H_2O$	89.94	89.48	89.02	88.10	89.61	89.49

**Table 2.** Chemical composition of  $Cu/CuO_x$  PVP-gelatine gels

	CuPVP21, %	CuPVP1, %	CuPVP5, %
$Cu(NO_3)_2$	0	0.35	0.35
$CuSO_4$	0.31	0.00	0.00
PVP	0.1	0.19	0.09
$C_{102}H_{151}O_{39}N_{31}$	9.62	9.43	9.26
$H_2O$	89.98	90.02	90.12
$Na_3C_6H_5O_7$	0	0.00	0.19

### 3.2. Irradiation and analytical techniques

$Cu/CuO_x$  gelatine and  $Cu/CuO_x$  PVP gelatine films were irradiated with 6 MeV energy X-ray photons. The irradiation doses varied from 0.01 to 5.00 Gy. Dose values and voltage for sample irradiation were chosen in accordance with the main aim of this research: to investigate the radiation sensitivity of the prepared  $Cu/CuO_x$  containing polymers to low dose irradiation.

Optical properties of experimental samples were investigated using UV-VIS spectrometer Ocean Optics with USB400 (range 190 nm – 900 nm, resolution - 1.5 nm). The mass density of the  $\text{Cu}/\text{CuO}_x$  gelatine and  $\text{Cu}/\text{CuO}_x$  PVP gelatine films was calculated using the data obtained from the mass balance (Cart Scale ( $10 \pm 0.0001$ ) g) and electronic digital Vernier Powerfix G calliper (0-150 mm with accuracy 0.01 mm) and BGF-Technic Werkzeug micrometer (0-25 mm with accuracy 0.001 mm).

### 3.3. Theoretical calculations

The study of theoretical mass attenuation coefficients of the  $\text{Cu}/\text{CuO}_x$  gelatine and  $\text{Cu}/\text{CuO}_x$  PVP gelatine films at 6 MeV were done using WinXCOM web database, which can be used to calculate photon cross sections for scattering, photoelectric absorption and pair production, as well as total attenuation coefficients, for any element, compound or mixture ( $Z \leq 100$ ), at energies from 1 keV to 100 GeV.

## 4. Results

### 4.1. $\text{Cu}/\text{CuO}_x$ gelatine films characterisation

Due to the drying process, the mass of dried  $\text{Cu}/\text{CuO}_x$  gelatin films decreased 88.6 %. The mass density of dried  $\text{Cu}/\text{CuO}_x$  gelatin films varied from 1294 to 1451  $\text{kg/m}^3$  (Table 3). The UV-VIS spectra of  $\text{Cu}/\text{CuO}_x$  gelatine films are presented in Fig. 1. The absorbance band was very weak at that low  $(\text{CuSO}_4)_4 \cdot 5\text{H}_2\text{O}$  and ascorbic acid concentration but in shift of wavelength of absorbance peak is found at 711-730 nm. It is indicating the formation of the  $\text{Cu}/\text{CuO}_x$  nanoparticles medium. X-ray irradiation increased the absorbance band of  $\text{Cu}/\text{CuO}_x$  in some cases up to 55%. Due to finding about the influence of reducer on  $\text{Cu}/\text{CuO}_x$  formation in gelatine medium, ascorbic acid was replaced by PVP. However, PVP can serve as a surface stabilizer, growth modifier, nanoparticle dispersant, and reducing agent.

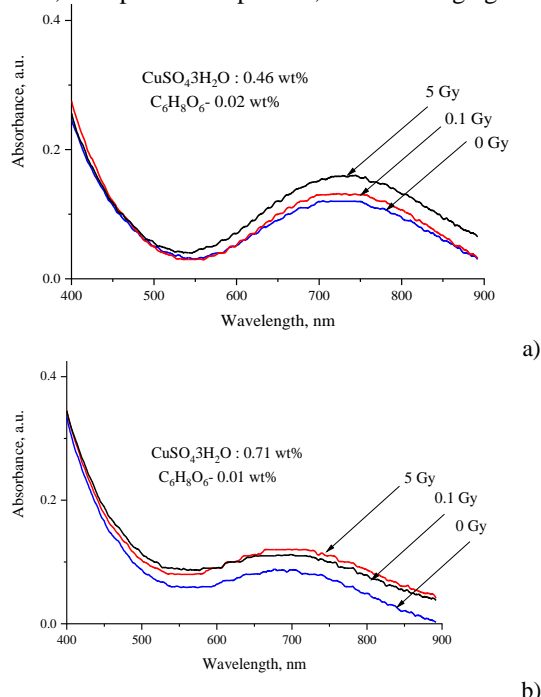


**Fig.1.**  $\text{Cu}/\text{CuO}_x$  nanoparticles on gelatine and  $\text{CuSO}_4$

**Table 3.** Mass density, thickness and LSPR of  $\text{Cu}/\text{CuO}_x$  gelatin films

Sample	t, mm	$\rho$ , $\text{kg/m}^3$	LSPR, nm	$\delta A$ , % after 0.1 Gy	$\delta A$ , % after 5 Gy
V11- V12	0.159	1378	731	11	17
V21- V22	0.155	1294	712	48	55
V31- V32	0.178	1451	718	-	-
V41- V42	0.186	1411	712	14	14
V51- V52	0.180	1311	-	-	-
V61- V62	0.190	1382	721	40	46
V71-V72	0.38	1296	720	6	24

The UV-VIS spectra of  $\text{Cu}/\text{CuO}_x$  gelatin films with PVP additives are presented in Fig. 2. Produced films were lightly blue and transparent. The absorbance  $\text{Cu}/\text{CuO}_x$  band was found at  $\sim 710$  nm, with very low intensity (Fig 2). The influence of X-ray irradiation on  $\text{Cu}/\text{CuO}_x$  formation in PVP-gelatine medium was also insignificant, but an increased absorbance at 400-450 nm was observed. It could be associated with crosslinking of the PVP and sulphur compounds due to X-ray formation.

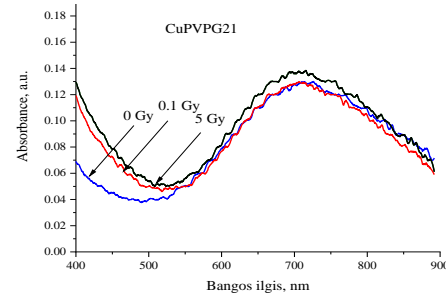


**Fig. 2.**  $\text{Cu}/\text{CuO}_x$  in PVP and gelatine nanocomposites using copper nitrate solution  $\text{CuSO}_4$

The mass density of dried  $\text{Cu}/\text{CuO}_x$  PVP - gelatine films varied from 1245 to 1333  $\text{kg/m}^3$  (Table 3)

**Table 4.** Mass density, thickness and LSPR of  $\text{Cu}/\text{CuO}_x$  gelatin films

Sample	t, mm	$\rho$ , $\text{kg/m}^3$	LSPR, nm	$\delta A$ , % after 0.1 Gy	$\delta A$ , % after 5 Gy
CuPVP G21	0.119	1287	$\sim 710$	-	-
CuPVP G1	0.109	1333	726-729	15.80	18.77
CuPVP G5	0.147	1245	728	33.75	39.84

According to Raman spectroscopy, FTIR spectroscopy and theoretical studies [12, 13], the PVP-metal interaction occurs through the carbonyl oxygen or nitrogen atoms of the repeating unit and the metal surface. To investigate the influence of anions of copper salt on the growth and stability of PVP-gelatine composites,  $\text{Cu}/\text{CuO}_x$  in PVP solution  $(\text{CuSO}_4)_4 \cdot 5\text{H}_2\text{O}$  was changed to  $(\text{CuNO}_3)_3 \cdot 3\text{H}_2\text{O}$ . Produced films using  $(\text{CuNO}_3)_3 \cdot 3\text{H}_2\text{O}$  were also lightly blue and transparent.

UV-VIS spectra of  $\text{Cu}/\text{CuO}_x$  in PVP- gelatine films are provided in Fig.3.

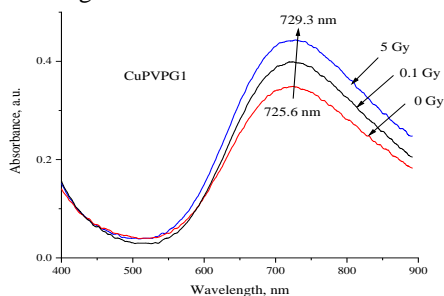


**Fig.3.**  $\text{Cu}/\text{CuO}_x$  in PVP and gelatine nanocomposites using copper nitrate solution  $(\text{CuNO})_3$ .

In comparison with the samples produced using  $(\text{CuSO})_4 \cdot 5\text{H}_2\text{O}$ , the intensity of absorbance was three times higher, thus corresponding to a higher content of nanoparticles in the medium. X-ray irradiation of samples induced a small redshift of absorbance band and increased the intensity by 15.80 % and 30.74 % for 0.1 Gy and 5 Gy of irradiation dose, respectively. The PVP-surface interaction depends on both the metal and solvent being used. The weak reducing ability of PVP is limited by the number of hydroxyl end groups. By adding tri-sodium citrate dehydrate, which is very common reducer and stabilisator for Au and Ag nanoparticles synthesis,  $\text{Cu}/\text{CuO}_x$  in PVP- gelatine films produced are also lightly blue and transparent. The absorbance band of  $\text{Cu}/\text{CuO}_x$  nanoparticles was observed at 726 nm (Fig.3). Increasing the dose of X-ray irradiation induced the redshift from 726 nm to 729 nm and increased the absorbance by 15.80 % and 18.77 % for 0.1 Gy and 5 Gy, respectively.

By adding of trisodium citrate dehydrate as additional reducer to  $(\text{CuNO})_3$  PVP and gelatine solution allow the formation of PVP-gelatine composited with  $\text{Cu}/\text{CuO}_x$  nanoparticles. The absorbance band of  $\text{Cu}/\text{CuO}_x$  was at 728 nm with lower intensity absorbance band (Fig.4). Due to X-ray irradiation the absorbance of  $\text{Cu}/\text{CuO}_x$  band increased by 33.75 % and 39.84 % for 0.1 Gy and 5 Gy.

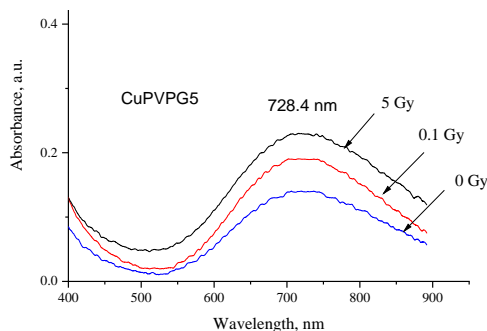


**Fig.4.**  $\text{Cu}/\text{CuO}_x$  in PVP and gelatine nanocomposites with trisodium citrate dehydrate additives and using  $(\text{CuNO})_3$

## 5. Conclusions

$\text{Cu}/\text{CuO}_x$  in gelatine and PVP- gelatine nanocomposites have been produced. Clearly seen plasmon peaks were identified. It was shown that the intensity and position of peaks was changing due to X-ray irradiation. Based on these findings  $\text{Cu}/\text{CuO}_x$  composites were suggested

as the possible candidates for low dose dosimetry applications. However more detailed investigations are needed to have full scope of properties of these composites

## 6. References

1. Miao X., et.al. Room-temperature electrochemical deposition of ultrathin  $\text{CuO}_x$  film as hole transport layer for perovskite solar cells. *Scripta Materialia* 165, 2019. p. 134-139,
2. Castro C., et al. Structure-reactivity relations for DC-magnetron sputtered Cu-layers during E. coli inactivation in the dark and under light. *Journal of Photochemistry and Photobiology A: Chemistry* 216, 2010, p. 205-202.
3. Nejdand B. et al. Cuprous Oxide as a Potential Low-Cost Hole-Transport Material for Stable Perovskite Solar Cells. *ChemSusChem* 9 2016, p. 302-313. doi:
4. Santos-Cruz D., et al.  $\text{CuO}_x$  thin films by direct oxidation of Cu films deposited by physical vapor deposition. *Results in Physics* 7, 2017, p. 4140-4144,
5. Aziz S.B., Morphological and Optical Characteristics of Chitosan(1-x): $\text{CuO}_x$  ( $4 \leq x \leq 12$ ) Based Polymer Nanocomposites: Optical Dielectric Loss as an Alternative Method for Tauc's Model. *Nanomaterials* 7, 2017, p. 444.
6. Walker, K.P..et al. Solvent-Dependent Surface Plasmon Response and Oxidation of Copper Nanocrystals. *J. Phys. Chem. C* 115, 2011, 115, p. 1793-1799.
7. Rtimi S., et al. Effect of light and oxygen on repetitive bacterial inactivation on uniform, adhesive, robust and stable Cu-polyester surfaces. *Journal of Advanced Oxidation Technologies*, 20, 2017, p. 20160178.
8. Biswas A., et al. Tunable multiple plasmon resonance wavelengths response from multicomponent polymer-metal nanocomposite systems. *Appl. Phys. Lett.* 84, 2004, p. 2655
9. Kanninen, P. et al. Influence of ligand structure on the stability and oxidation of copper nanoparticles. *Colloid Interface Sci.* 318, 2008, p. 88 – 95.
10. Goldstein S. et al. D. A mechanistic study of the copper(II)-peptide-catalyzed superoxide dismutation. A pulse radiolysis study. *J. Am. Chem. Soc.* 112 1990, p. 6489-6492
11. Calixto S, et al. Gelatin as a Photosensitive Material. *Molecules*. 23 2018 p. 2064.
12. Borodko Y., et al. Probing the Interaction of Poly(vinylpyrrolidone) with Platinum Nanocrystals by UV-Raman and FTIR. *J. Phys. Chem. B* 110, 2006, 110, p. 23052-23059.
13. Koczur K. M., et al. Polyvinylpyrrolidone (PVP) in nanoparticle synthesis, *Dalton Trans.*, 44, 2015, p. 17883 —17905

## **DEVELOPMENT OF POLYMER GEL BASED EXHALED BREATH BIOMARKERS DETECTION SENSOR FOR COVID-19 MONITORING**

Neringa ŠEPERIENĖ<sup>1</sup>, Ignas PIKAS<sup>2</sup>

<sup>1</sup>MB Hadroneda; <sup>2</sup>Kaunas University of Technology

<sup>1</sup>neringa@brachydose.com; <sup>2</sup>ignas.pikas@ktu.lt

**Abstract:** The pandemics of SARS-CoV-2 left hospitals and health care facilities in extreme need of fast and non-invasive corona illness detection and effective monitoring system. Polymerisable hydrogels such as VIPET, nMAG, nPAG used for radiation detections has showed huge potential for COVID-19 biomarkers detection in exhaled patient's breath. The initial prototype of sensor which showed an accuracy of 98% for detecting common COVID-19 biomarker, acetone, was developed and presented in this paper.

**Keywords:** Hydrogel, COVID-19, biomarker, acetone.

### **1. Introduction**

Due to the severe respiratory syndrome-coronavirus-2 (SARS-CoV-2) pandemics the hospitals and treatment facilities are facing highly increased patient numbers. The World Health Organization reported cases in Italy, Spain, USA and other countries, resulting in overcrowded treatment centres and lack of fast, non-invasive and reliable COVID-19 detection equipment. There is an urgent need to differentiate COVID-19 induced conditions from other respiratory illnesses, as influenza and lungs cancer to increase patients survival rate by 3 times [1,2].

More than 80% of the COVID-19 patients are suffering from respiratory and lungs dysfunction syndrome. One of the most promising methods to monitor the disfunction caused by the illness is to detect biomarkers from patient's exhaled breath [3,4].

The current well-known technologies as serological assays, reverse-transcription polymerase chain reaction and computed tomography exhibit practical limitations and challenges in case of massive and non-invasive testing. Electrochemical conducting polymer based biosensors are considered as potential alternatives due to their functional advantages such as high selectivity, sensitivity, simplicity, rapid detection, flexibility, ease of use. Therefore, CP-based biosensors can serve as multi-sensors, mobile biosensors, and wearable biosensors, facilitating the development of point-of-care

(POC) systems and home-use biosensors for COVID-19 detection [5-7].

However, the application of these biosensors for COVID-19 trigger several challenges related to their degradation, low crystallinity, charge transport properties, and weak interaction with COVID-19 biomarkers [4]. To overcome these challenges, we have studied polymer dose gels as promising sensors to detect biomarkers in exhaled patients' breath. While the most common biomarkers representing COVID-19 are acetone (0.3–1 ppm), isopropanol, isoprene (~105 ppb), hydrogen sulphide (0–1.3 ppm), nitric oxide, ammonia (0.5–2 ppm), hydrogen peroxide, carbon monoxide (0–6 ppm), ethanol and acetaldehyde, the optical properties variation of these biomarkers in gel exposed to exhaled breath could be measured [8-10].

### **2. Materials and methods**

Acetone vapor were chosen for gels exposure and analysis of interaction with monomers. Three sets of hydrogel samples were made. Normoxic nPAG, nMAG and VIPET hydrogels were produced using previously developed recipes [11].

nPAG polymer gels were prepared as follows: gelatin from porcine skin (300 bloom, 5 w/w %, Sigma-Aldrich) was dissolved in half-amount of the total water volume (89 w/w %). The solution was heated up to 40 °C and stirred until the solution became clear. Then acrylamide (3 w/w%, Sigma- Aldrich) and N-N-methylene-bis-acrylamide (3 w/w%, Sigma- Aldrich) were added one by one to the solution. Solution was mixed and cooled down to 38°C. An antioxidant (tetrakis hydroxymethyl phosphonium chloride THPC, 10 mmol/l, Sigma- Aldrich) was added and the solution was stirred.

nMAG gel preparation consisted of firstly dissolving 8 % of gelatin from porcine skin (300 bloom, Sigma-Aldrich) in 86 w/w% of distilled water of high purity (HPLC grade water). When the gelatin was fully inflated by the water, a flask with a gel was heated up to 35°C while stirring by magnetic stirrer. After the gelatin



was fully dissolved, 5 % of methacrylic acid (MAA, Sigma- Aldrich) was added, followed by addition of 2 mM of tetrakis (hydroxymethyl) phosphonium chloride (THPC, Sigma-Aldrich). The mixture was heated up to 45 °C under continuous stirring.

The normoxic VIPET polymer gels were composed of 7 w/w% of gelatin (300 bloom, Sigma- Aldrich), 4 w/w% N-vinylpyrrolidone (VIPE, Sigma-Aldrich), 4% w/w% N-N-methylene-bis-acrylamide (BIS, Sigma- Aldrich), 10 mM of tetrakis (hydroxymethyl) phosphonium chloride (THPC, Sigma-Aldrich) and 89 w/w% of distilled water. The gelatin was added to the distilled water at room temperature (25 °C) and the solution was then heated to 45 °C. Once the temperature was stabilized and the solution was clear, the BIS was added. Heating was achieved through a hot-plate and stirring unit. When the solution became transparent, the mixture was cooled down to approximately 35 °C and VIPE was added. When the constituents were completely dissolved, THPC was added to the solution. Heating and stirring was switched off and the solution was left to settle.

The whole process was conducted in a fume hood under atmospheric conditions. In order to minimize possible oxidation, gels were poured into standard PMMA cuvettes as well as 3D printed sample plates and tightly sealed (fig.1).

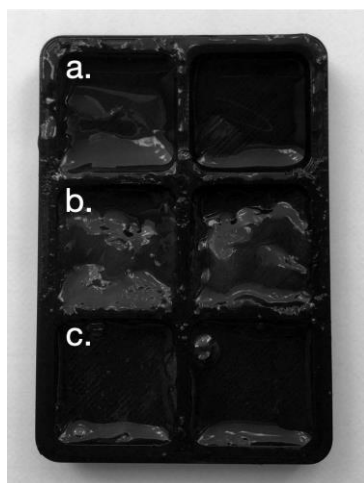


**Fig. 1.** Hydrogel samples in 3D printed plate prepared for acetone vapour exposure: a. VIPET, b. nMAG, c. nPAG

Samples of polymer gels in palate were poured with acetone (Fig. 2), the most common biomarker indicating that the patient's lungs were affected by COVID-19. The flow rate of mixed acetone vapors used in this study (50 - 250 ml/min) was suggested by Koureas et al. [12]. All experiments were conducted at room temperature. Raman spectroscopy was done to investigate polymerization due to acetone exposure and to evaluate the amount of polymerization. Also, absorbance in UV/VIS spectra was measured to explore changes in absorbance peak, construct calibration curve and make the gel easier to fit as sensor.

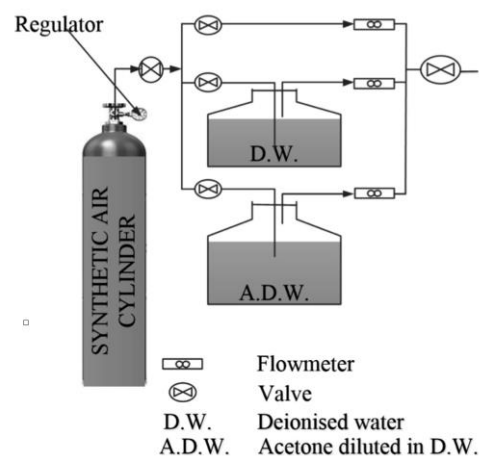


**Fig. 2.** Experimental set for acetone evaporation

### 3. Results and discussion

The aim of the project was to transfer the technology used to make dose hydrogels for radiation detection in medicine to COVID-19 biomarkers detection and make it useful for corona illness monitoring. It was hypothesized that biomarkers of COVID-19 must interact with monomer molecules in hydrogel to initiate polymerizations process. The amount of polymers formed should be detectable via optical methods. The changes in UV/VIS spectra absorbance must be measurable. The final result of the project is initial prototype of COVID-19 biomarkers sensor to detect and monitor the corona illness.

#### 3.1. The research of VIPET gel properties

After the acetone exposure of nPAG, nMAG and VIPET hydrogels, the VIPET gel was selected as most promising to carry on with prototype development. The VIPET gel samples before and after acetone vapor exposure are presented in fig. 3.

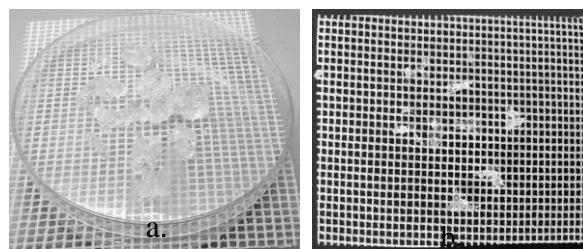


**Fig. 3.** VIPET gel samples: a. before exposure with acetone, b. after exposure with acetone

The measurement of UV/VIS spectroscopy showed that absorbance peak in 300 - 430 nm was increased by 0.4a.u. (fig. 4). Ocean Optics USB 4000 UV/VIS spectrometer was used for gel absorbance spectra research. The gel samples became solid and yellow instead of amorphous transparent structure. Gel samples shrunk by 10 times after acetone exposure.

Gauss function was applied to UV/VIS absorbance spectra of gel to evaluate full width of half maximum (FWHM) representing amount of polymerization. For VIPET gel  $\lambda_{\text{max}} = 349 \text{ nm}$ ,  $\text{FWHM} = 135.8 \text{ nm}$ .

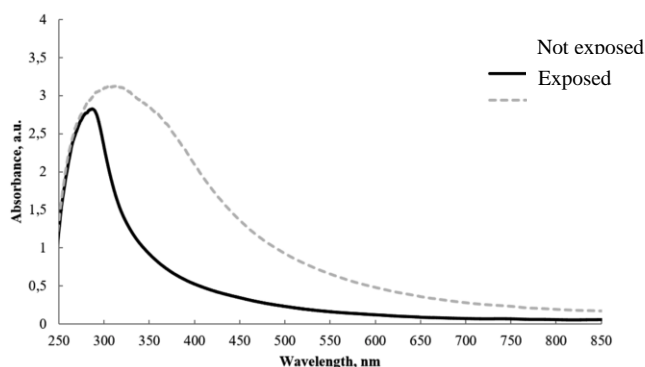


Fig. 4. UV/VIS spectroscopy of acetone exposed VIPET gel

Raman scattering measurements were performed using a Raman microscope inVia (Renishaw). The excitation beam from a diode laser of 532 nm wavelength was focused on the sample using a 20× objective. Laser power at the sample surface was 2 mW. For all measurements, integration time was 10 s. The Raman Stokes signal was dispersed with a diffraction grating (2400 grooves/mm) and data was recorded using a Peltier cooled charge-coupled device (CCD) detector (1024×256 pixels). This system yields a spectral resolution of about 1 cm<sup>-1</sup>. Silicon was used to calibrate the Raman setup in both Raman wavenumber and spectral intensity.

Raman spectra analysis for VIPET hydrogel was performed before the acetone exposure and after the exposure. The intense Raman peaks were seen at: 1115 (C–O stretching), 1259, 1419, 1441, 1650, 1991, 2165, 2315, 2622, 2938, 2989 (attributed to the asymmetric and symmetric C–H stretching), 3191 cm<sup>-1</sup> (N–H stretching and O–H stretching vibrations). 1259 cm<sup>-1</sup> and 1441 cm<sup>-1</sup> are representing acetone related bonds.

### 3.2. Prototype of acetone detection tool

The initial prototype to detect the COVID-19 biomarker, acetone in exhaled patient's breath was constructed of optical scanner module and specially prepared VIPET hydrogel sample. The optical scanner module was made of RGB light source, light collimation and focus to target system, measured data collection and transfers setting. The VIPET hydrogel sample was placed inside the specific tube made to intake exhaled patient's breath. The initial exhaled breath analysis prototype is presented in fig. 5.

The presented prototype operates in this sequence:

1. The patient inflates to intake tube where the exhaled breath travels through hydrogel samples.
2. Polymerization reactions is initiated in gel which leads to change in optical properties.
3. Changes in optical properties are measured by optical scanning system and data are represented on device screen or computer.

The accuracy of acetone detection depends directly on the area of the scanned VIPET gel. The graph representing calibration curve of device and showing the accuracy is presented in fig. 6.

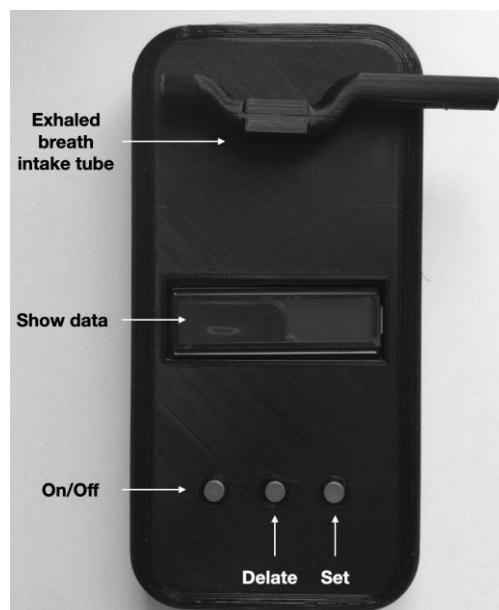


Fig. 5. The initial exhaled breath analysis and acetone detection prototype

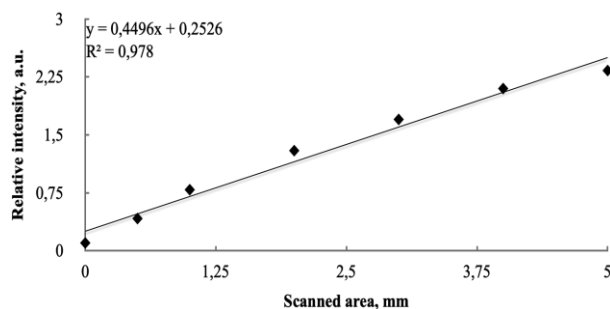


Fig. 6. The calibration curve of prototype

The accuracy of device to detect acetone in exhaled breath is  $R^2 = 0,978$  when the vapor flow is in range 50 - 250 ml/min. This range is close to patients exhaled breath conditions in COVID-19 illness and diabetes cases [7,13].

### 4. Conclusions

Non-invasive exhaled patient's breath analysis has a huge diagnostic and monitoring of COVID-19 potential. From the discovery and validation of biomarkers of corona illness to non-invasive monitoring of treatment progression, a whole realm of analytical possibilities exists. In targeted applications, dedicated sensors are used to monitor a specific compound and thus can be achieved with low-cost optical and polymer gel sensors. The aim of the research and project was to develop the initial prototype sensor by using polymerizable hydrogels in order to avoid charge transport problems in biosensors and weak interaction with COVID-19 biomarkers.

The VIPET hydrogel was seen as promising sensor to detect the most common COVID-19 biomarker - acetone. The accuracy of device for detecting acetone in simulated patients' exhaled breath was close to 98% while evaluating 2 to 5 mm<sup>2</sup> gel samples with optical scanner.

Further development of the prototype will be done with the help of Lithuanian Health Science University bioengineering group. Prototype testing with real patients' exhaled breath samples are planned.

### Acknowledgment

The research was supported by Agency of Science, Technology and Innovation. Lifesaving-innovations: stop COVID-19. Project No. 01.2.1-MITA-T-852-01-0132.

### 5. References

1. Ruszkiewicz D.M., Sanders D., et al. Diagnosis of COVID-19 by analysis of breath with gas chromatography- ion mobility spectrometry - a feasibility study. *EClinicalMedicine*, 2020, p. 2930 100609, DOI:10.1016/j.eclinm.2020.100609.
2. Vinh Van Tran, Nhu Thi Tran. Development strategies of conducting polymer-based electrochemical biosensors for virus biomarkers: Potential for rapid COVID-19 detection. *Biosensors and Bioelectronics*, 2021, p. 182 113192.
3. Sagnik Das, Mrinal Pal. Review—Non-Invasive Monitoring of Human Health by Exhaled Breath Analysis: A Comprehensive Review. *Journal of The Electrochemical Society*, 2020, p. 167 037562 .
4. Khoubnasabjafari M., Jouyban-Gharamaleki V., et al. Exhaled breath condensate as a potential specimen for diagnosing COVID-19. *Bioanalysis*, 2020, ISSN1757-6180, DOI: 10.4155/bio-2020-0083.
5. Ryan DJ, Toomey S, Madden SF, et al. Use of exhaled breath condensate (EBC) in the diagnosis of SARS-COV-2 (COVID-19). *Thorax*, 2021, 76, p. 86–88, DOI:10.1136/thoraxjnl-2020-215705.
6. Usman F., Dennis J.O., et al. Acetone Vapor-Sensing Properties of Chitosan-Polyethylene Glycol Using Surface Plasmon Resonance Technique. *Polymers*, 2020, 12, p. 2586; doi:10.3390/polym12112586.
7. Grassin-Delyle S., Roquencourt C., et al. Metabolomics of exhaled breath in critically ill COVID-19 patients: A pilot study. *EBioMedicine*, 2021, p. 63 103154.
8. Shan B., Broza Y.Y., et al. Multiplexed Nanomaterial-Based Sensor Array for Detection of COVID-19 in Exhaled Breath. *ACS Nano*, 2020, 14, p. 12125–12132, DOI: 10.1021/acsnano.0c05657.
9. Ratiu I. A., Ligor T., et al. Volatile Organic Compounds in Exhaled Breath as Fingerprints of Lung Cancer, Asthma and COPD. *Clinical Medicine*, 2021, p. 10, 32. DOI: 10.3390/jcm10010032.
10. Denis M., VANDEWEERD V., VERBEEKE, LAUDISOIT R. A., REID T., HOBBS E., WYNANTS L., VAN DER VLIET D. COVIPENDIUM: information available to support the development of medical countermeasures and interventions against COVID-19 (Version 2020-10-06). *Transdisciplinary Insights*, 2020, doi.org/10.5281/zenodo.4072014.
11. Vaičiūnaitė, N., Adlienė, D. Optical properties of photon irradiated N-vinylpyrrolidone based polymer gel. *Radiation interaction with materials: fundamentals and applications 2014: 5th international conference*, Kaunas, Lithuania, May 12-15, 2014, Kaunas: Technologija. ISSN 2351-583X. 2014, p. 464-467.
12. Koureas M., Kirgou P. Target Analysis of Volatile Organic Compounds in Exhaled Breath for Lung Cancer Discrimination from Other Pulmonary Diseases and Healthy Persons. *Metabolites*, 2020, p. 10, 317, doi:10.3390/metabo10080317.
13. Koh. H., Chung Mom A.M., et al. Journal of medical virology. Diabetes predicts severity of COVID-19 infection in a retrospective cohort: A mediatory role of the inflammatory biomarker C-reactive protein. 2021, p. 1-10, DOI: 10.1002/jmv.26837.

## DEVELOPMENT OF PATIENT’S BIOMETRIC DATA BASED CT DOSE OPTIMIZATION ALGORITHM

Vijayanand SIVAKUMAR<sup>1</sup>, Diana ADLIENĖ<sup>2</sup>

<sup>1,2</sup>Department of Physics, Kaunas University of Technology

<sup>1</sup>vijayanandphy@gmail.com; <sup>2</sup>diana.adliene@ktu.lt

**Abstract:** An open-source prototype program was developed using MATLAB® for the purpose of optimizing CT examination parameters, based on the biometric data of the patient. The program was tested and presented in front of clinical professionals. The outcomes of the testing and discussion was promising; thus once completely developed, the program has immense potential to be used as a useful research tool by medical physicists during the protocol development phase, in a clinical environment, thereby paving way for optimization of patient dose in CT.

**Keywords:** Computed Tomography, Optimization, CT protocols, Diagnostic Reference Levels, Automatic Exposure Control Systems.

### 1. Introduction

Computed tomography (CT) is one of the clinical imaging techniques that uses X-rays to visualize human anatomy. As CT technology accounts for 60% to 70% of total radiation dose [1], improving the implementation of CT technology, optimizing its use and ensuring patient safety have become the main concerns of researchers and manufacturers. Research involving the influence and quantification of the relationship between CT factors [2-6], automatic exposure control system (AEC) [7-12], CT protocol [13-15], and various strategies for optimizing the patient's dose from CT exposure [16-23], were carefully analysed, and a solution is proposed in the form of a calculation program named – “BioptiDOS”.

### 2. Materials and Methods

In this program, users can simulate different possibilities of dose optimization through the scanner's ATCM system, and consult with clinically approved protocols as well as national, institutional, and local DRL values to ensure that the simulated values are consistent with conventional values. The results of each simulation are stored in a built-in database, and the program refers to this database for continuous

simulation of the same procedure. For the purpose of prototyping, MATLAB® programs were written using MATLAB-R2020b v.9.9.0 (The MathWorks Inc.).

Currently, the prototype program is modelled for SIEMENS Sensation 64 and Sensation 16 scanners, along with their SIEMENS CARE Dose 4D ATCM system. Various exposure patterns of these scanners were obtained using a proprietary software “IndoseCT” developed by Choirul Anam et al. [20], and the empirical equation used in CARE Dose 4D system and derived by McDougall et al. [25], as follows, was used.

$$(mAs_{\text{eff}}/QRM) = e^{(D_{\text{eff}} - D_{\text{Ref}}) \cdot S} \quad (1)$$

The different quantifiers used in this program are, Tube voltage (kV<sub>p</sub>), Tube current (mA), Rotation time (sec), Detector collimation (mm), Slice thickness (mm), Pitch, Computed Tomography Dose Index CTDI (mGy), Dose Length Product DLP (mGy-cm), Anterior – Posterior Length (AP), Lateral length (LAT), Effective diameter (D<sub>eff</sub>), Water Equivalent Diameter (D<sub>w</sub>), Size Specific Dose Estimate SSDE (mGy), Contrast-to-Noise-Ratio (CNR), Relative Dose Factor (RDF), Diagnostic Reference Levels (DRL), and Body Mass Index (BMI). Based on the findings of different researchers and the practices followed by recognized clinical institutions, different recommendations have been generated for a specific procedure. These recommendations have been shown to reduce patient exposure, ensuring patient safety. A set of recommendations were provided for pediatric procedures based on Lateral width and abdominal circumference [25, 27], which is given in Table 1.

The tube current range allowed for body CT procedures, based on Lateral width was proposed by McCollough CH et al. [28] (Table 2),

DRL represent a more general point of reference for a given procedure and the ICRP [22] states that DRL does not define a maximum dose limit or “barrier”, it remains the most important tool for patient dose optimization.

One of the most outstanding aspects of this program is to provide DRL values established for a particular

examination, so that the client become aware of average to realize this, the latest international and national DRL data were collected [29-34]. DRLs information is accessible for both adults and pediatrics, and are assembled for three anatomical premises, head, chest and abdomen. DRL data used in the program are displayed in the Table 3.

**Table 1.** Pediatric protocol recommendations

Phantom	Lateral width (cm)	Effective mAs	kV based on Lateral width	kV based Abdominal circumference
32	≤15	150	80	120
32	16 – 25	175	80	120
32	26 – 35	175	100	120
32	>36	135	120	120
	<b>Pediatric Weight</b>		<b>kV based on Pediatric weight</b>	
16	< 40	-	80/100	80
16	> 40	-	100/120	80

**Table 2.** Maximum and Minimum Tube current range

Lateral width (cm)	Minimum mA	Maximum mA
22.1 – 30	150	280
30.1 – 40	220	500
40.1 – 45	400	720
45.1 – 50+	450	770

resultant dose values for the performed examination and The ICRP reference to existing DRL values allows users to track patient doses and appropriately optimize a given regimen. In order to create a prototype, a MATLAB program based on a simple navigation script was written. The following flowchart describes how the program works.

The workflow of the program involves patient data entry such as one's age, height, weight, etc. The AP and LAT measurements are then carried out manually, from the uploaded scout /Topogram DICOM images. Once the CT protocol is chosen, different age and size-based tube recommendations are displayed, and the user is able to set the preferred tube parameters. Upon this, the result window (Fig. 1) provides a comparison between results, mainly CTDI<sub>vol</sub>, SSDE and CNR values, arising from recommended protocol, kV<sub>p</sub> & mA values and different TCM approaches involving patient's effective diameter (D<sub>eff</sub>) and BMI. It also allows the user to check if these results are in accordance with the Institutional, National and International DRL values for the chosen procedure.

To verify the normal operation of the program, it was tested for a set of 6 pediatric and 3 adult reference patients of various body proportions. The test involves abdomen and head CT examinations in both CTscanners. The results of the verification test are discussed in the following results and discussion section.

**Table 3.** Dose reference levels

Age	Anatomic region	International DRL		National DRL (LT)		CTDI <sub>vol</sub> Alert values (mGy)
		CTDI <sub>vol</sub> (mGy)	DLP (mGy.cm)	CTDI <sub>vol</sub> (mGy)	DLP (mGy.cm)	
ADULT						
	Abdomen	18	665	-	1200	-
	Pelvis	14	525	-	506	50
	AP	15	641	-	-	-
	Head	54	854	-	650	80
	Chest	12	449	-	910	50
	Thoracic	-	-	-	680	
	Cardiac	-	-	-		150
	Lumbar Spine	-	-	-	600	-
	Cervical Spine	-	530	-	-	-
PEDIATRIC						
<= 1 year	Abdomen	5.2	130	-	-	10 (32 cm)
1 – 5 years		7	250	-	-	25 (16 cm)
5 – 10 years		7.8	310	-	-	-
<= 1 year	Head	26	440	-	570	-
1 – 5 years		36	540	-	630	60
5 – 10 years		43	690	-	650	-
<= 1 year	Chest	5.2	130	-	-	10 (32 cm)
1 – 5 years		6	140	-	-	25 (16 cm)
5 – 10 years		6.8	170	-	-	-

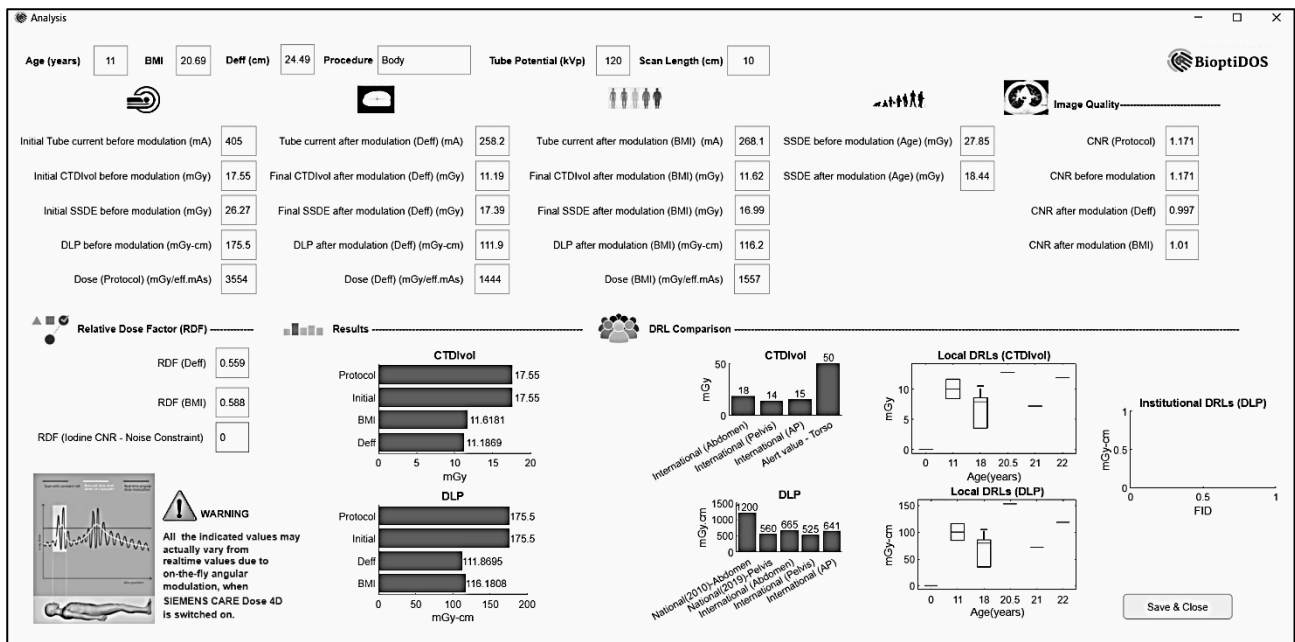


Fig. 1. Results window of the program

### 3. Results and Discussion

Once the input parameters are entered, and the relevant procedure selections are carried out, the program calculates and displays the output figures in a single window, along with the DRLs as shown in the Fig.1.

The correlation between CTDI<sub>vol</sub>, tube potential and current, and patient age, were examined. It was verified that CTDI<sub>vol</sub> increases with increasing phantom size, kV, and tube current. The tube current changes according to the effective diameter of the patient, and the BMI is calculated using the empirical equation applied in CARE dose 4D (equation 1). Obviously, in most cases, changes based on BMI are higher than changes based on difference. The BMI represents the total height and weight of the patient, and D<sub>eff</sub> can be said to consider the longest distance between the patient's AP and LAT measurements. The author supports this claim by stating that BMI considers the attenuation of the patient's tissues, which depends on their physical habits, including thin, normal, obese, underweight, or overweight [16]. Another obvious contrast is the dose of the same patient and the procedure parameters of two different scans. The Sensation 64 dose is less than the Sensation 16 scanner dose, which is not the case. The detector cut-off plays an important role in determining the dose [16]. The program can use factors such as the patient's age, effective diameter, and BMI to calculate the SSDE of the head and body CT procedures. It was found that the SSDE of Sensation 16 is higher than that of Sensation 64 in head and body pediatric procedures.

CNR is used as an indicator of the expected diagnostic image quality. CTDI<sub>vol</sub> and slice thickness can be used to determine CNR, using the formula given in the previous section. The higher the CNR of an image, the better its perceptibility. CNR increases with the increase of CTDI<sub>vol</sub>, but the dose to the patient must be justified. Therefore, understanding the importance of evaluating

pre-modulated CNR for a give slice thickness is essential.

RDF is a quantifier that indicates the radiation dose required/saving when trying to achieve the image quality required by the protocol in case the potential of the tube changes. The RDF quantizer is very useful for understanding the deviation of the amount of radiation stipulated in the agreement and at the same time linking it with the evaluation of the image quality. RDF calculation for the patient is provided in the Table 4.

Table 4. RDF for different patients

Scanner	Region	Patient	Protocol kV	kV used	RDF - Deff	RDF - BMI
Sensation 64	Body	2M	120	80	0.6 (40%)	1.2 (-20%)
		2F	120	80	0.4 (60%)	0.8 (20%)
	Head	1M	120	80	0.35 (65%)	1.32 (-32%)
		5F	120	100	0.74 (26%)	1.21 (-21%)
Sensation 16	Body	2M	120	80	0.7 (30%)	1.5 (-50%)
		2F	120	80	0.5 (50%)	1.0 (0%)
	Head	5F	120	80	0.7 (30%)	1.13 (-13%)

Inferred from Table 4, in the case of BMI-based modulation (expressed as a negative percentage), RDF represents the amount of tube current that is additionally used when using a lower kV. Furthermore, it can be seen that dose savings occurred during D<sub>eff</sub>-based modulation. This shows that, compared to D<sub>eff</sub>, BMI-based tube modulation results in more doses to the patient, and RDF can be used as an effective parameter to assess the deviation between protocol parameters and real-time scan parameters.

In order to investigate the possibility of further improving the prototype program for routine use in clinical environment, and discuss the upcoming implementation plan, professional advice was sought out. The proposed program algorithm was introduced, and discussed with a group of Medical physicist expert from Vilnius University Hospital Santaros Clinics.



#### 4. Conclusions

The purport of this research work was to create an open-source computational program to assist Medical Physicists in optimizing the resultant CT dose by making use of the patient's biometric data. This was successfully achieved by developing a prototype program, with available clinically verified data, and was tested for its basic functionality. Though the program is in its primary stage, it has delivered promising results, which support the conceived idea of having an open access estimator for devising patient-based CT protocols as well as a tool which helps researchers to implement patient's doses optimization in CT examinations.

#### 5. References

- INTERNATIONAL ATOMIC ENERGY AGENCY, *Dose Reduction in CT while Maintaining Diagnostic Confidence: A Feasibility/Demonstration Study*, IAEA-TECDOC 1621, IAEA, Vienna 2009.
- NAGEL H.D, *CT Parameters that Influence the Radiation Dose*. Radiation Dose from Adult and Pediatric Multidetector Computed Tomography. Medical Radiology (Diagnostic Imaging). Springer, Berlin, Heidelberg, pp 51-79, ISBN 978-3-540-68575-3, 2007.
- MCCOLLOUGH CH, LENG S, et al. CT dose index and patient dose: they are not the same thing. *Radiology*.;259(2):311-6, 2011.
- STRAUSS K, et al. Size Specific Dose Estimates in Pediatric and Adult Body CT Examinations, *AAPM Task Group*, 2014.
- BOONE J, et al. Size Specific Dose Estimate Head CT, *AAPM Task Group*, 2019.
- VANO E, et al. ICRP Publication 135: Diagnostic Reference Levels in Medical Imaging. *Ann ICRP*; 46(1):1-144, 2017.
- MARTIN, C J, SOOKPENG S. Setting up computed tomography automatic tube current modulation systems. *Journal of Radiological Protection*, 36(3), R74-R95, 2016.
- SÖDERBERG M. Overview, Practical Tips And Potential Pitfalls Of Using Automatic Exposure Control In Ct: Siemens Care Dose 4D. *Radiation Protection Dosimetry*; 169(1-4):84-91., 2015.
- KEAT N. CT scanner automatic exposure control systems. Available from: doi: 10.13140/RG.2.1.3128.4720, 2005.
- SÖDERBERG M, Automatic exposure control in CT: an investigation between different manufacturers considering radiation dose and image quality, Available from: <http://lup.lub.lu.se/student-papers/record/2157064>, 2008.
- MARTIN C J, SOOKPENG S, Setting up computed tomography automatic tube current modulation systems, *J. Radiol. Prot.* 36 R74, 2016.
- WANG X., et al. Automatic tube potential selection with tube current modulation in coronary CT angiography: Can it achieve consistent image quality among various individuals?. *Experimental and Therapeutic Medicine*, 16, 253-259, 2018.
- TRATTNER S, PEARSON GDN, et al. Standardization and optimization of CT protocols to achieve low dose. *J Am Coll Radiol*.;11(3):271-278, 2014.
- ZHANG, Y, SMITHERMAN C, SAMEI E. Size-specific optimization of CT protocols based on minimum detectability. *Medical Physics*, 44(4), 1301-1311, 2017.
- MCKENNEY SE, SEIBERT JA et al. Methods for CT automatic exposure control protocol translation between scanner platforms. *J Am Coll Radiol*.;11(3):285-91, 2014.
- O'NEILL S, et al. Using body mass index to estimate individualized patient radiation dose in abdominal computed tomography. *European Radiology Experimental*, 2(1), 38, 2018.
- ANAM C, et al. A fully automated calculation of size-specific dose estimates (SSDE) in thoracic and head CT examinations. *Journal of Physics: Conference Series*, 694, 012030, 2016.
- RICCARDI L, et al. Use of radiation dose index monitoring software in a multicenter environment for CT dose optimization. *Radiol med* 123, 944-951, 2018.
- ELLIOT K. FISHMAN, MD, CTisus.com, Available from: <https://www.ctisus.com>, Accessed 17 Mar. 2021.
- ANAM C, et al. Volume computed tomography dose index (CTDI<sub>vol</sub>) and size-specific dose estimate (SSDE) for tube current modulation (TCM) in CT scanning. *Int J Radiat Res.*; 16 (3) :289-297, 2018.
- MUBAROK S et al. Parameter-based estimation of CT dose index and image quality using an in-house android™-based software, *J. Phys.: Conf. Ser.* 694 012037, 2016.
- KATSARI K, et al. Establishing a dose management strategy in Computed Tomography, Proceedings. *EuroSafe Imaging*, ESI-0022, Available from: 10.1594/esi2018/ESI-0022, 2018.
- OSMAN N D, et al. Radiation dose management in CT imaging: Initial experience with commercial dose watch software, *J. Phys.: Conf. Ser.* 1497 012020, 2020.
- SÖDERBERG M, GUNNARSSON M, The effect of different adaptation strengths on image quality and radiation dose using Siemens Care Dose 4D, *Radiation Protection Dosimetry*, Volume 139, Issue 1-3, Pages 173-179, 2010.
- MACDOUGALL RD, et al. Size-based protocol optimization using automatic tube current modulation and automatic kV selection in computed tomography. *J Appl Clin Med Phys.*;17(1):328-341, 2016.
- UT SOUTHWESTERN MEDICAL CENTER, Department of Radiology, Available from: <https://www.utsouthwestern.edu>, Accessed 17 Mar. 2021.
- REID J, et al. Optimization of kVp and mAs for Pediatric Low-Dose Simulated Abdominal CT: Is It Best to Base Parameter Selection on Object Circumference?. *AJR Am J Roentgenol*; 195(4):1015-20, 2010.
- DIEGO L, et al. Tube Potential and CT Radiation Dose Optimization. *American Journal of Roentgenology*, 204(1), W4-W10, 2015.
- MOHAMAD FAWZI AWAD et al, A systematic review on the current status of adult diagnostic reference levels in head, chest and abdominopelvic Computed Tomography, *J. Radiol. Prot.* 40 R71, 2020.
- VASSILEVA, J. et al, A study to establish international diagnostic reference levels for paediatric computed tomography. *Radiation Protection Dosimetry*, 165(1-4), 70-80, 2015.
- EUROPEAN COMMISSION, DDM2 Project Report Part-2, Diagnostic Reference Levels (DRLs) in Europe, Retrieved from: ENER/2010/NUCL/SI2.581237, 2010.
- RADIACINĖS SAUGOS CENTRAS, RSC Annual Report 2012, Retrieved from: <https://www.rsc.lt/index.php/pageid/428>, Vilnius, 2012.
- RADIACINĖS SAUGOS CENTRAS, RSC Annual Report 2015, Retrieved from: <https://www.rsc.lt/index.php/pageid/428>, ISSN 2351-5953, Vilnius, 2015.
- RADIACINĖS SAUGOS CENTRAS, RSC Annual Report 2019, Retrieved from: <https://www.rsc.lt/index.php/pageid/428>, ISSN 2351-5953, Vilnius, 2019.
- VASSILEVA J, REHANI M. Diagnostic Reference Levels. *American Journal of Roentgenology*, 204(1), W1-W3, 2015.

## **HOUSEHOLD SALT (NaCl) FOR OPTICALLY STIMULATED LUMINESCENCE DOSIMETRY: AN OVERVIEW**

Christian BERNHARDSSON<sup>1</sup>, Lovisa WALDNER<sup>2</sup>, Christopher RÄÄF<sup>3</sup>, Aleksandr VODOVATOV<sup>4</sup>

<sup>1,2,3</sup>Lund University, Department of Translational Medicine, Medical Radiation Physics, Malmö, Sweden;

<sup>4</sup>Research Institute of Radiation Hygiene, St Petersburg, Russia

<sup>1</sup>christian.bernhardsson@med.lu.se; <sup>2</sup>lovisa.waldner@med.lu.se; <sup>3</sup>christopher.raaf@med.lu.se;

<sup>4</sup>vodovatoff@gmail.com

**Abstract:** This brief overview of the use of household salt (NaCl) in optically stimulated luminescence (OSL) dosimetry is focusing on the use of NaCl pellets. It is suggested that the most optimal use of household NaCl, in general prospective dosimetry, is to compress the salt grains to pellets and read the radiation induced signal using OSL rather than TL. A summary of the main OSL dosimetric properties is provided for two Swedish household salts, and compared to the OSL properties of 100 different salts from all over the world.

**Keywords:** OSL, NaCl, salt pellet, dosimetry

### **1. Introduction**

Optically stimulated luminescence (OSL) is an increasingly used technique for determining radiation absorbed doses in *e.g.* occupational, environmental, emergency/accident dosimetry and in applications for luminescence dating in geology and archeology. In OSL, luminescence is stimulated from the target sample by a light source. The registered OSL signal is a measure of the absorbed dose from previous radiation exposure of the sample material. In thermoluminescence (TL), or thermally stimulated luminescence, heat is used to stimulate the target sample and the resulting TL signal is a measure of the radiation absorbed dose of the material. Although TL has traditionally been standard for broad range of dosimetry applications, the use of OSL in research and for personal dosimetry has strongly increased during the recent two decades. There are benefits and disadvantages of the TL vs OSL methods. This have been discussed over the years, for example in 2003 [1], where the two debater's main arguments condensed to the principle of the stimulation mode *i.e.* there are advantages and disadvantage with OSL as well as TL, vs the other. Since then there has been a fast development in terms of OSL readers and materials, and the use of the technique is further increasing in various dosimetry applications as well as in luminescence

dating. For personal dosimetry, both OSL and TL will be used for many years to come. However, it has been shown that there are advantages of using OSL as compared to TL when using certain household materials for retrospective dosimetry (*i.e.* luminescence dating and accident dosimetry). This brief overview will focus on one such household material, in particular salt (NaCl) for OSL dosimetry, specifically for prospective dosimetry (pre-manufactured dosimeters) using NaCl pellets.

### **2. Luminescence dosimetry with NaCl**

Research on TL and OSL has a long history. In fact, the TL phenomenon was first observed as early as 1663, although it was not until the 1950s that the research found practical applications [2]. About a decade later it was shown that illumination of radiation exposed salt reduces the intensity of the TL peaks [3], and shortly after that the phenomenon OSL was first mentioned in the literature [4], see *e.g.* Yukihiro & McKeever [5] and references therein for a brief history on TL and OSL. With the advent of compact and optimized OSL/TL readers, analytical grade salt was studied as a dosimeter for applications in luminescence dating [6, 7]. The main results observed were that the OSL response in NaCl, after irradiation, can be measurable and reproduced, and there is no significant short term fading of the OSL signal. Furthermore, and obviously, it was shown that the signal may easily be bleached when the salt is exposed to daylight. At about the same time, household and workplace chemicals (including household salt) were investigated as a dosimeter for retrospective dosimetry *i.e.* accident dosimetry [8]. The results in the latter survey of household and workplace chemicals showed a significantly high OSL signal yield per unit absorbed dose and sample weight for household salt (>99% NaCl), as compared to the other materials investigated, and a fading of only 5% after 2 weeks. Despite these encouraging findings for the use of NaCl

in dosimetry, it would take one more decade before several different groups started to evaluate and use NaCl in various applications for OSL and TL dosimetry.

The first salt application within OSL dosimetry was for retrospective dosimetry (luminescence dating and accident dosimetry) *e.g.* [6-8], using relatively high radiation doses (several Gy) for benchmarking the salts investigated. Later it was shown that household NaCl has a linear dose response also for doses below one gray, with detection limits of about 1 mGy [9-10]. With promising dosimetric properties also in the dose range for occupational radiation protection, research began to evaluate the use of household NaCl for prospective dosimetry *i.e.* pre-prepared dosimeters with salt. One of the first field tests of household NaCl, packed in temporal but dedicated dosimeter holders consisting of NaCl and LiF chips, was carried out in a Chernobyl contaminated village in Belarus [12]. The results showed a good comparison to TLDs of LiF and very good agreement with a handheld NaI(Tl) radiation detector that was used at the same measurement positions as the combined NaCl and LiF dosimeter kits. The same study was repeated during three years with the same results [13]. Approximately at the same time, in-house made NaCl and LiF dosimeters were carried by people living in Chernobyl contaminated villages in Russia [14] and on phantoms in the laboratory [15]. The results from these studies showed a surprisingly good agreement between conventional dosimeters of LiF to OSL materials (NaCl) used in retrospective dosimetry in terms of absorbed dose assessments. This was encouraging for further investigations of NaCl as a dosimeter beyond retrospective purposes.

Therefore, a refined dosimeter dedicated for salt grains was suggested for measurements of personal dose equivalent,  $H_p(10)$  [16]. This dosimeter was tested in the laboratory at different photon energies and incident angles of the radiation field. It was shown that the dosimeter need proper filtration for accurate  $H_p(10)$  dose determinations in order to adjust for the over response at low photon energies (<200 keV) compared with tissue. This was also shown in a parallel study using a different type of a combined NaCl and LiF dosimeter [17]. Furthermore, efforts have also been made to experimentally determine conversion coefficients for NaCl in dosimeter holders, in salt packages, and on physical phantom in different exposure situations [18]. While these studies are supportive for the use of NaCl in OSL dosimetry, it is encouraged to further support these findings with mathematical calculations and simulations.

Although many articles on OSL (and TL) in NaCl refer to its use in retrospective dosimetry applications, the results also apply to OSL dosimetry in general and may be useful for modeling and optimisation of the OSL in NaCl after exposure to ionizing radiation *e.g.* [19-23]. Although more research is needed for understanding the physics of the OSL in various types of NaCl, the well-established advantageous OSL properties of NaCl have encouraged to evaluate the use of the salt from salted snacks and nuts for accident dosimetry [24, 25]. There are also suggestions of using NaCl for mixed neutron-photon fields by using a dedicated dosimeter with a

neutron converter (gadolinium) [26] and by using a specially made NaCl detector and analyzing  $^{24}\text{Na}$  from neutron activation of NaCl [27].

### 3. OSL dosimetry with NaCl pellets

OSL and TL has been investigated for solid dosimeters made from natural calcium fluoride and NaCl powders pressed together ( $\text{CaF}_2\text{:NaCl}$ ) *e.g.* [28]. In that study NaCl pellets were also studied. Although not observed in other studies of NaCl pellets the results from [28] showed that the radiation induced OSL and TL signals were rapidly removed from the pure NaCl pellets by either a pre-heat or a 1 h waiting time. With the intention of using pure household NaCl for prospective dosimetry, a method for producing physically stable NaCl pellets was developed and the OSL dosimetric properties of these pellets were studied using an optimized read-out sequence [29, 30]. These initial studies showed a linear dose response for low doses (from about 5 mGy), low detection limit (<10  $\mu\text{Gy}$ ), and high signal yield per unit absorbed dose and weight. At about the same time, household NaCl pellets were investigated for retrospective TL dosimetry [31]. It was shown that the TL signal was linear over the dose range 0.25 Gy to 20 Gy, and that the fading after 2 weeks was 40%. Recently, the TL properties of NaCl pellets of different thickness (0.1 and 0.3 cm) have been studied for doses from 2 to 10 Gy [32] and NaCl pellets with a thickness of 1 mm in the absorbed dose range of 5 mGy to 5 Gy [33]. Although the studies [32,33] are not directly comparable the conclusion from the first one is that the thinner pellets (0.1 cm) has better TL characteristics than the thicker ones, with 3 times higher TL intensity but with higher fading after 7 days as compared to the 0.3 cm pellets. The study in [33], with even thinner pellets than 0.1 cm, indicates a fading of 20% after 2 weeks and a linear TL signal to dose response in the dose range 5-100 mGy. Although TL dosimetry with NaCl pellets is interesting and may be useful in some situations, the dosimetric properties of household NaCl is greatly improved by using an optimized OSL read protocol with individual single-dose calibration of each pellet. A summary of the comprehensive work made on OSL in NaCl pellets is given in the section below. References therein may be used to fully apply or test the suggested NaCl pellets in various practices.

#### 3.1. Justification for household NaCl pellets in prospective dosimetry

Several researchers have studied NaCl for the use in OSL and TL dosimetry applications. Although there are some difficult issues to overcome in retrospective dosimetry for luminescence dating and accident dosimetry, research in these areas have opened for studies of using NaCl for occupational and environmental dosimetry applications. After it was shown that household NaCl could be used to measure low-doses (<100 mGy), relevant for personal dosimetry [9], efforts have been made to further evaluate the usefulness of household NaCl for prospective OSL

dosimetry applications by compressing the salt to pellets.

Although the main area of use of the suggested dosimeters might be within environmental and accident dosimetry, one promising approach is to apply OSL dosimetry with NaCl pellets within the medical use of ionizing radiation.

According to international guiding documents by *e.g.* IAEA, ICRP and ICRU there are three broad fields for the application of OSL dosimetry. The first is the use of point detectors together with dedicated physical phantoms (CIRS ATOM, Rando, etc.) that allow estimation of organ absorbed doses in different radiosensitive organs/tissues from diagnostics or therapies with ionizing radiation. Estimates or measurements of such radiation absorbed doses are used as a basis for the development and validation of dedicated computational software for patient dose estimation as well as for the optimization of imaging protocols in medical facilities.

The second is the use of point detectors for direct estimation of the entrance surface doses of patients for different diagnostic imaging modalities. IAEA recommends using the entrance surface dose (incident air kerma on the patient body) as one of the main dosimetric quantities for the process of optimization, mainly for the estimation of typical patient doses and for establishing diagnostic reference levels.

The third is the use of point detectors for individual dosimetry of workers, especially those working in highly non-uniform radiation fields (*e.g.* X-ray guided surgery, interventional examinations, nuclear medicine applications).

In many countries, the use of LiF based point detectors is associated with various complications, such as significant costs for the detectors and equipment for annealing and calibration, resource demanding methods for calibration, and significant costs for the lost/damaged detectors. With the one-time use of the in-house made NaCl detectors for OSL, many of these shortcomings can be overcome, with comparable dosimetric properties.

It has been clearly identified that these advantages are important, especially in developing countries that recently or currently started to develop their radiation protection and quality control programs; or, on the contrary, for large countries with significantly varying access and prioritisation to dosimetry services and equipment between different regions (*e.g.* the Russian Federation). As a complement to commercial luminescent dosimeters, or to encourage RP professionals, the NaCl pellets provide an easily accessible tool for accurate dose determinations.

### 3.2. Dosimetric properties of household NaCl pellets

The research group medical radiation physics, Malmö, Lund University, has studied the OSL properties of household NaCl for applications in dosimetry [34, 35] and lately, for optimal use and dosimetry, as pellets [36]. Provided below is a summary of the main dosimetric properties of the suggested household salt pellets for OSL dosimetry.

Common Swedish household salt was investigated for making physically stable NaCl pellets [37]. Using a press tool made in-house, it was suggested to sieve the salt to grains in the size range 100-400  $\mu\text{m}$  and use a compression force of  $3.0 \pm 0.5$  tons applied over the surface of the press tool (distributed over a column of five pellets) for achieving physically stable and rigid pellets. Later it has been suggested to use a commercially available standard desktop table press tool (TDP 0 Desktop Tablet Press, LFA Machines Oxford Ltd) for more convenient production of NaCl pellets with a circular shape of 4 mm in diameter and  $0.8 \pm 0.2$  mm thick (similar size as many LiF chips) [36]: Fig. 1 and 2.

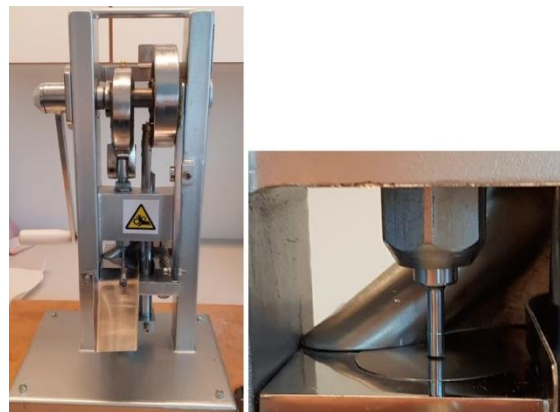


**Fig. 1.** Photograph of the semi-automatic desktop table press for compressing the salt grains to NaCl pellets.

The pellets are intended for one-time use, using a single individual calibration dose (rather than the common SAR protocol that require repeated heating and irradiation of the sample). An optimized readout protocol, using a Risø TL/OSL-DA reader (DTU Physics, Denmark), is provided in [36]. The most relevant dosimetric properties (see below) were studied for two Swedish household salt (Falksalt finkornigt hushållsalt and Falksalt finkornigt medelhavssalt, Salinity AB, Sweden) and one analytical grade salt (Sodium chloride, reagent grade, Scharlau, Scharlab, Spain) [37]. OSL dosimetric properties were also evaluated for 102 household salt from all over the world (including the Swedish salts) to evaluate the global usability of NaCl pellets for OSL dosimetry [36].

A summary of the dosimetric properties, using the suggested NaCl pellets (Fig. 2) are provided below.

**OSL signal to dose response:** the OSL signal is linearly increasing with the absorbed dose, from 0 to 300 mGy [37]. The linearity continues at even higher dose ( $>1$  Gy) and is valid also for the estimated absorbed dose [36]. A pre-established calibration curve for a specific salt may be used, albeit with some precaution, to achieve a fast estimate of the absorbed dose.

**Minimum detectable dose (MDD):** considering the one time use of the NaCl pellets and that they are pre-bleached (emptied of any residual OSL signal in ambient light) the theoretical detection limit, in terms of MDD is low, 5-20  $\mu\text{Gy}$  for the Swedish salts investigated [37]. Studies of the 102 salts from all over the world show MDD in the range from 2 to 1036  $\mu\text{Gy}$ , with a median MDD of 19  $\mu\text{Gy}$ .

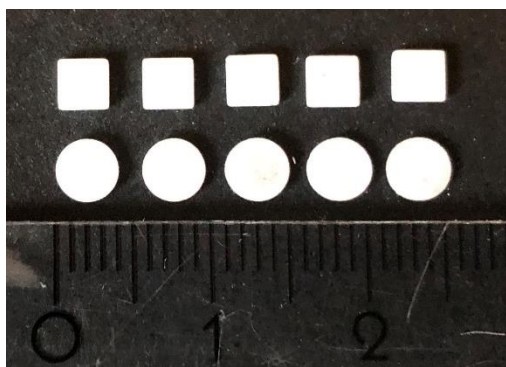


**Fig. 2.** Photo of the NaCl pellets (round in shape) as compared to standrad LiF chips (squared in shape).

**Signal stability over time (fading):** The OSL signal is stable over at least one month after exposure. However, and similar to *e.g.* [22], the estimated dose appears to increase over time. For NaCl pellets, this is an effect of the decrease in signal yield over time when using a single calibration dose [38]. To avoid this problem, the pellets may be stored for a couple of weeks before they are used, for the pellets to age. This is however only a problem when the exposure and readout are separated in time. For extended or chronic exposures the effect of decreasing signal yield from the pellets cannot be seen and no special precautions need to be taken before use.

**Specific luminescence:** The OSL signal normalized to the weight of the pellets and the absorbed dose, ranged from 259 to 576 counts  $\text{mg}^{-1} \text{mGy}^{-1}$  for the two Swedish household salts and one analytical grade salt. This can be compared to the results of the 102 salts investigated, with specific luminescence ranging from 115 to 1950 counts  $\text{mg}^{-1} \text{mGy}^{-1}$ , with a median of 496 counts  $\text{mg}^{-1} \text{mGy}^{-1}$ .

**Reproducibility:** The OSL signal reproducibility is  $<4\%$ , in terms of coefficient of variation for 10 equally treated NaCl pellets, when using a single calibration dose. When only comparing the OSL signals, without any normalization, the reproducibility is around 15%.

**Energy dependence:** The absorbed dose to NaCl pellets has a significant energy dependence at low photon energies, up to a factor of 18 as compared to  $K_{\text{air}}$  and  $H_p(10)$ . Experimentally determined and Monte Carlo calculated energy dependence of NaCl pellets in the energy range 30 keV to 1.25 MeV has been established [39]. The results show that the energy dependence must be accurately compensated for *e.g.* by dosimeter filters or mathematically corrected for in order to achieve accurate dose estimates for dosimetry applications with low photon energies especially.

The suggested NaCl pellets have been thoroughly studied in the laboratory. Several tests have also been carried out in different hospital clinics for occupational and ambient exposure studies [40, 41].

To fully utilize the potential of the NaCl pellets, a dedicated badge with filters correcting for *e.g.* the energy dependence are needed. Depending on the application, the dosimeter may be calibrated to measure either  $H_p(10)$  or  $H^*(10)$ . For some applications where energies  $>200$  keV dominate, a simple badge without filtering may be sufficient. Filters for energy

discrimination or electron detection may also be implemented in a badge. As for readout of the NaCl pellets, a simple dedicated reader would help make the method become more accessible as the number of OSL readers is still limited.

#### 4. Conclusions

The intention with this overview is two-folded: first it is to provide a short introduction to the use of NaCl in OSL dosimetry, secondly it is to show the potential of using NaCl in various dosimetry applications. If using NaCl pellets in OSL dosimetry, as a complement or as a main tool for dosimetry, depending on the situation or application, many issues can be overcome.

In many countries NaCl pellet based dosimeters may serve as a complement to clinical or personal dosimetry, but in case of an accidental radiation exposure event, NaCl pellets may provide additional information for affected individual doses as well as decision making authorities.

In summary, ordinary salt has superior OSL dosimetric properties as compared to many other fortuitous materials close to man. The dosimetric properties are fairly the same for different types of household salt all over the world, although differences may be observed in the OSL decay curves (not yet evaluated). When compressing the salt grains to NaCl pellets the overall handling and dosimetric properties are improved, as compared to using grains of salt. If the NaCl pellets are constructed with the same dimensions as LiF chips they may be directly used in standard dosimetry phantoms etc. A key issue with the suggested NaCl pellets is the same as for commercial alternatives for OSL dosimetry, the pellets must be kept shielded from light exposure. Provided there is an OSL reader available, it is possible to follow the steps in the papers referred to in this overview to achieve NaCl pellet OSL dosimetric properties that are comparable with commercial alternatives but only at a fraction of the cost as compared to commercial luminescent detectors.

#### 5. References

1. McKeever S.W.S. and Moscovitch M. Topics under debate: on the advantages and disadvantages of optically stimulated luminescence dosimetry and thermoluminescence dosimetry. *Radiation Protection Dosimetry*, 104(3):263-270, 2003.
2. Daniels F., Boyd C.A. and Saunders D.F. Thermoluminescence as a research tool. *Science*, 117(3040):343-349, 1953.
3. Stoddard A.E. Effects of illumination upon sodium chloride thermoluminescence. *Physical Review*, 120(1):114-117, 1960.
4. Fowler J.F. Solid state dosimetry. *Physics in Medicine and Biology*, 8(1):1-32, 1963.
5. Yukihiro E.G. and McKeever S.W.S. *Optically stimulated luminescence – fundamentals and applications*. A John Wiley and Sons Ltd, UK. ISBN: 978-0470-69725-2, 362 pp.
6. Bailey R.M., Adamiec G. and Rhodes E.J. OSL properties of NaCl relative to dating and dosimetry. *Radiation Measurements*, 32:717-723, 2000.
7. Zhang J.F., Yan C. and Zhou L.P. Feasibility of optical dating using halite. *Journal of Luminescence*, 114:234-240, 2005.



8. Thomsen K.J., Botter-Jensen L. and Murray A.S. Household and workplace chemicals as retrospective luminescence dosimeters. *Radiation Protection Dosimetry*, 101(1-4):515-518, 2002.
9. Bernhardsson C., Christiansson M., Mattsson S. and Rääf C.L. Household salt as a retrospective dosimeter using optically stimulated luminescence. *Radiation and Environmental Biophysics*, 48:21-28, 2009.
10. Ekendahl D. and Judas L. NaCl as a retrospective and accident dosimeter. *Radiation Protection Dosimetry*, 145(1):36-44, 2011.
11. Timar-Gabor A. and Trandafir O. On optically stimulated luminescence properties of household salt as a retrospective dosimeter. *Radiation Protection Dosimetry*, 155(4):404-409, 2013.
12. Bernhardsson C., Christiansson M., Rääf C. and Mattsson S. OSL in household salt (NaCl) for environmental, occupational and medical dosimetry. Proceedings of the 7<sup>th</sup> International Conference "Medical Physics in the Baltic States", Kaunas, 2009, p. 65-68.
13. Bernhardsson C., Matskevich S., Mattsson S. and Rääf C. Comparative measurements of the external radiation exposure in a <sup>137</sup>Cs contaminated village in Belarus based on optically stimulated luminescence in NaCl and thermoluminescence in LiF. *Health Physics*, 103(6):740-748, 2012.
14. Bernhardsson C., Zvonova I., Rääf C. and Mattsson S. Measurements of long-term external and internal radiation exposure of inhabitants of some villages of the Bryansk region of Russia after the Chernobyl accident. *Science of the Total Environment*, 409:4811-4817, 2011.
15. Ekendahl D., Bulánek B. and Judas L. Comparative measurements of external radiation exposure using mobile phones, dental ceramic, household salt and conventional personal dosimeters. *Radiation Measurements*, 72:60-65, 2015.
16. Ekendahl D., Bulánek B. and Judas L. A low-cost personal dosimeter based on optically stimulated luminescence (OSL) of common household salt (NaCl). *Radiation Measurements*, 85:93-98, 2016.
17. Christiansson M., Bernhardsson C., Geber-Bergstrand T., Mattsson S. and Rääf C. OSL in NaCl vs. TL in LiF for absorbed dose measurements and radiation quality assessment in the photon energy range 20 keV to 1.3 MeV. *Radiation Measurements*, 112:11-15, 2018.
18. Bernhardsson C. Experimental determination of dose conversion coefficients for external radiation exposure with gamma emitting radionuclides. *Radiation Hygiene (Radiat. Hyg.)*, 7(4):125-133, 2014.
19. Polymeris G.S., Kitis G., Kiyak N.G. et al. Dissolution and subsequent re-crystallization as zeroing mechanism, thermal properties and component resolved dose response of salt (NaCl) for retrospective dosimetry. *Applied Radiation and Isotopes*, 69:1255-1262, 2011.
20. Spooner N.A., Smith B.W., Creighton D.F., Questiaux D. and Hunter P.G. Luminescence from NaCl for application to retrospective dosimetry. *Radiation Measurements*, 47:883-889, 2012.
21. Christiansson M., Mattsson S., Bernhardsson C. and Rääf C.L. Optimizing a readout protocol for low dose retrospective OSL-dosimetry using household salt. *Health Physics*, 102(6):631-636, 2012.
22. Biernacka M., Majgier R., Maternicki K., Liang M. and Mandowski A. Peculiarities of optically stimulated luminescence in halite. *Radiation Measurements*, 90:247-251, 2016.
23. Majgier R., Rääf C.L., Mandowski A. and Bernhardsson C. OSL properties in various forms of KCl and NaCl samples after exposure to ionizing radiation. *Radiation Protection Dosimetry*, 184(1):90-97, 2019.
24. Christiansson M., Geber-Bergstrand T., Bernhardsson C., Mattsson S. and Rääf C.L. Retrospective dosimetry using salted snacks and nuts: a feasibility study. *Radiation Protection Dosimetry*, 174(1):1-5, 2017.
25. Maltar-Strmecki N., Vidotto M., Della M.S. et al. Salty crackers as fortuitous dosimeters: a novel PSL method for rapid radiation triage. *Frontiers in Public Health* 9:661376, 2021. doi: 10.3389/fpubh.2021.661376.
26. Mattsson S., Christiansson M. and Bernhardsson C. A passive neutron dosimeter for measurements in mixed neutron-photon radiation fields. Proceedings of the 12<sup>th</sup> International Conference "Medical Physics in the Baltic States", Kaunas, 2015. p. 38-42.
27. Ekendahl D., Rubovic P., Zlebcik P., Huml O. and Mala H. Dosimetry with salt in mixed radiation fields of photons and neutrons. *Radiation Protection Dosimetry*, 178(3):329-332, 2018.
28. Ferreira F.A., Yoshimura E.M., Umisedo N.K. and Nascimento R.P. Correlation of optically and thermally stimulated luminescence of natural fluorite pellets. *Radiation Measurements*, 71:254-257, 2014.
29. Bernhardsson C., Waldner L. and Vodovatov A. Advancements in prospective dosimetry with NaCl read-out by optically stimulated luminescence. Proceedings of the 13<sup>th</sup> International Conference "Medical Physics in the Baltic States", Kaunas, 2017. p. 26-29.
30. Waldner L. NaCl pellets for improved dosimetry. [MSc thesis], Malmö: Lund University, 2017.
31. Elashmawy M. Study of constraints in using household NaCl salt for retrospective dosimetry. *Nuclear Instruments and Methods in Physics Research B*, 423:49-61, 2018.
32. Muhammad Azim M.K., Abdul Sani S.F., Daar E. et al. Luminescence properties of natural dead sea salt pellet dosimetry upon thermal stimulation. *Radiation Physics and Chemistry*, 176:108964, 2020.
33. Ahmad K., Kakahel M.B., Hayat S. et al. Thermoluminescence study of pellets prepared using NaCl from Khewra salt mines in Pakistan. *Radiation and Environmental Biophysics*, 60(2):365-375, 2021.
34. Bernhardsson C. Radiation exposure of human populations in villages in Russia and Belarus by fallout from the Chernobyl reactor. [PhD thesis], Malmö: Lund University, 2011.
35. Christiansson M. Household salt as an emergency radiation dosimeter for retrospective dose assessments using optically stimulated luminescence. [PhD thesis], Malmö: Lund University, 2014.
36. Waldner L. Optically stimulated luminescence dosimetry with NaCl pellets. [PhD thesis], Malmö: Lund University, 2021.
37. Waldner L. and Bernhardsson C. Physical and dosimetric properties of NaCl pellets made in-house for the use in prospective optically stimulated luminescence dosimetry applications. *Radiation Measurements*, 119:52-57, 2018.
38. Waldner L., Rääf C. and Bernhardsson C. NaCl pellets for prospective dosimetry using optically stimulated luminescence: signal integrity and long-term versus short-term exposure. *Radiation and Environmental Biophysics*, 59(4):693-702, 2020.
39. Waldner L., Hinrichsen Y., Herrnsdorf L. and Bernhardsson C. Experimentally determined and Monte Carlo-simulated energy dependence of NaCl pellets read by optically stimulated luminescence for photon beams in the energy range 30 keV to 1.25 MeV. *Radiological Protection*, 40:1321, 2020.
40. Wilke P. Radiation protection measurements in clinical practice – dosimetry with NaCl pellets. [MSc thesis], Malmö: Lund University, 2019.
41. Solak E. A comparison between LiF, Al<sub>2</sub>O<sub>3</sub> and NaCl pellets for luminescence dosimetry based on clinical and laboratory measurements. [MSc thesis], Malmö: Lund University, 2020.



## EVALUATION OF THE IRRADIATION DOSES FROM THE OPERATION OF THE INTENSE FEMTOSECOND LASER

Vytenis BARKAUSKAS<sup>\*1</sup>, Lukas RIMKUS<sup>2</sup>, Jonas REKLAITIS<sup>1</sup>, Artūras PLUKIS<sup>1</sup>, Mikas VENGRIS<sup>2</sup>

<sup>1</sup>Center for Physical Sciences and Technology, Department of Nuclear Research, Vilnius, Lithuania

<sup>2</sup>Vilnius University, Faculty of Physics, Laser Research Centre, Vilnius, Lithuania

\*vytenis.barkauskas@ftmc.lt

**Abstract:** The irradiation doses from the lasers with the high power and high repetition rate dose can accumulate over time and create a hazard which should be evaluated. We propose use of the pre-defined electron temperature scaling for the evaluation of the potential doses. Pilot experimental measurements in the laser laboratory are also presented. Dosimetry issues related with the intense laser pulse-material interaction experiments are identified.

**Keywords:** Femtosecond lasers, Irradiation dose, FLUKA

### 1. Introduction

Powerful femtosecond lasers are used in various fields related with both industrial and medical applications such as material processing, surgeries etc [1, 2]. Irradiances achievable using these lasers may reach  $10^{21}$  W/cm<sup>2</sup>. More simple table-top high frequency femtosecond lasers usually have lower irradiances up to  $10^{17}$  W/cm<sup>2</sup>. When sufficiently intense femtosecond laser pulse interacts with material it produces X-ray. This process is caused by electrons which are torn-off from atoms by laser pulse and later they are decelerated, producing both bremsstrahlung and characteristic fluorescence lines. Energies of the generated X-ray may reach tens or even hundreds of keV. Due to the use of high energy and high repetition-rate source, the X-ray produced may become hazardous from radiation safety point of view. ICRP recommends dose limits to be 20 mSv/y for occupational exposures, averaged over a period of 5 year and 1 mSv/y for the members of the public [3].

Up to now radiation safety and monitoring usually is not evaluated in laboratories which use intense femtosecond lasers. For the table-top laser systems, the range of intensities, which can cause radiological hazard is in between  $10^{14}$  and  $10^{17}$  W/cm<sup>2</sup>. Radiological impact

evaluation of such devices is quite a new topic during the past decade [4, 5, 6].

Precise and correct evaluation of X-ray generation would require characterization of a complex microscopic material-laser interaction, taking into account processes like ionization, electron-phonon heat exchange, phase transition etc. Here we show that dose characterization could be performed using previously defined electron temperature scaling based on both theoretical and experimental evaluations. Maxwell distribution is used to define electron energy. Temperature parameter might be taken from the electron temperature scaling. This leads to a simplification of the radiological hazard evaluation and the reduction of complex physics processes to a phenomenon observed in the conventional X-ray tubes. We show that dose prediction can be rather accurate and this simplified approach could be used for radiological safety evaluation purposes.

### 2. Temperature scalings

Although there are several different electron temperature scalings defining laser-material interaction presented in the articles, we have chosen one which give the highest electron temperatures for given intensity. The empirical scaling given by Beg et al. is the one [7]:

$$T_{hot} = 100 \times I_{17}^{1/3} \quad (1)$$

where  $I_{17}$  is in  $10^{17}$  W/cm<sup>2</sup>.  $T_{hot}$  is electron temperature in keV. Temperature parameter was used to calculate Maxwellian electron energy distribution:

$$p(E) = 2\sqrt{E/\pi} \left(\frac{1}{T}\right)^{3/2} \exp\left(-\frac{E}{T}\right) \quad (2)$$

Maxwellian electron distributions obtained using temperatures for different intensities are given in Fig. 1.

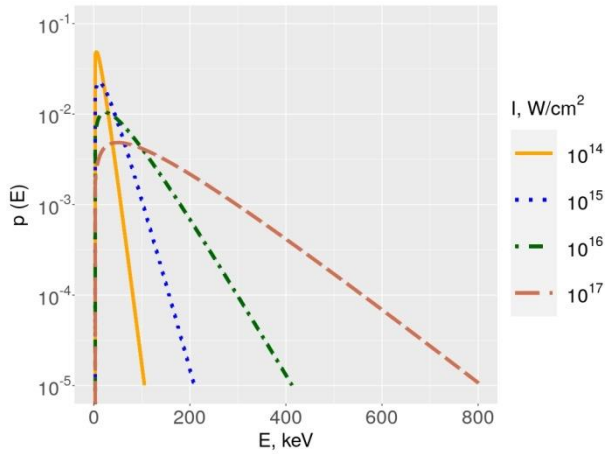


**Fig. 1.** Maxwellian electron distributions obtained using temperatures for different intensities using empirical scaling given by Beg et al [7].

### 3. Methods and models

The FLUKA code was used to calculate the photon spectra and irradiation doses resulting from electron interaction with the target. FLUKA is a code employing Monte Carlo method for calculations of particle transport and interactions [8, 9]. FLUKA gives only averaged single particle (electron) contribution to dose and photon spectrum. To obtain proper estimate of the dose we need two other parameters – number of interacting particles and pulse energy conversion efficiency to bremsstrahlung:

$$D_{total} = D_e \eta_B N_{el} \quad (3)$$

where  $D_{total}$  is total dose,  $D_e$  – dose from single electron,  $\eta_B$  – average bremsstrahlung efficiency in the energy region of interest (above 5 keV), and  $N_{el}$  – number of electrons in the laser pulse-plasma interaction volume. For the dose evaluation a very simple model of electrons interacting with a solid target was created. The target consists of  $1 \times 1 \text{ cm}^2$  area and 0.1 cm thickness plate. Doses were evaluated at a distance of 0.35 meter from the target. As target material also plays an important role for potential dose, we took three different materials with low  $Z$  (Al,  $Z = 13$ ), medium  $Z$  (Cu,  $Z = 29$ ) and high  $Z$  (W,  $Z = 74$ ) for modeling.

CARBIDE laser from Light Conversion was used in the dose measurement experiments. Main laser parameters were: pulse duration 240 fs, wavelength 1030 nm, repetition rate 100 kHz, pulse energy 900  $\mu\text{J}$ . Optimized prepulse-pulse intensity ratio, which results in the highest X-ray intensity and irradiation dose rate was 1/10, time between pulse and prepulse 440 ps. Laser spot at the focus was 26  $\mu\text{m}$  in diameter (FWHM), which gives laser intensity  $4.7 \times 10^{14} \text{ W/cm}^2$ , when pulse energy is 900  $\mu\text{J}$ .

Two types of dosimeters were used for experimental dose measurements. Electronic semiconductor dosimeters (Thermoscientific EPD-N2) were used for dose rate measurements during laser processing. This personal dosimeter detects photons within energy range from 20 keV to 10 MeV. Thermoluminescence dosimeters were used to monitor integral doses at the

different spots in the laboratory during whole experimental session. The same type of dosimeters were used for personal dosimetry. Thermoluminescence dosimeters were capable to measure doses from 0.01 mSv to 10 Sv, in the energy range from 10 keV to 10 MeV. Amptek XR-100CR X-ray spectrometer with Si detector was used to measure spectra of X-ray.

### 4. Results

Equivalent doses from one particle for different intensities and different materials using scaling by Beg et al. [7] were modeled using FLUKA and are given in Fig. 2. Predicted doses show linear temperature dependence. The role of the material (atomic number  $Z$ ) is very important as well: the possible doses could be 3 to 6 times higher in case of W in comparison with Al for the given intensity.

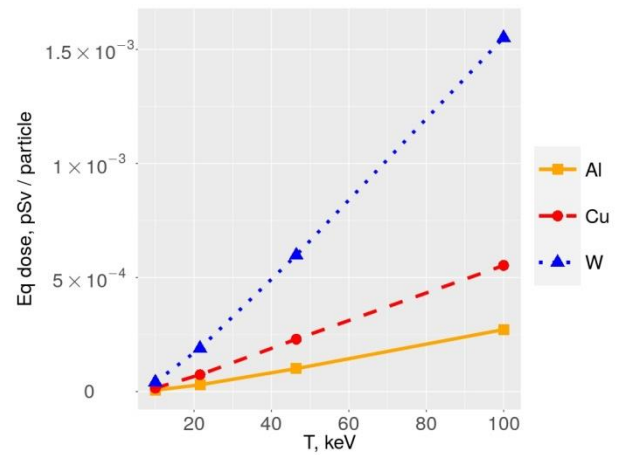


**Fig. 2.** Equivalent doses from one electron for Al, Cu and W.

The spectra of photons emerging from the materials were calculated as well. Modeled spectra are given in Fig. 3. As expected they consist of characteristic lines and bremsstrahlung radiation. Using experimentally determined laser energy conversion efficiencies for  $K\alpha$  lines (varying from  $10^{-6}$  to  $10^{-4}$ ) [10, 11] it is possible evaluate bremsstrahlung efficiency. We can conservatively assume it is higher by one order of magnitude than  $K\alpha$  efficiency. Upper limit for number of interacting electrons is evaluated knowing critical density of the electrons and the focused laser spot size.

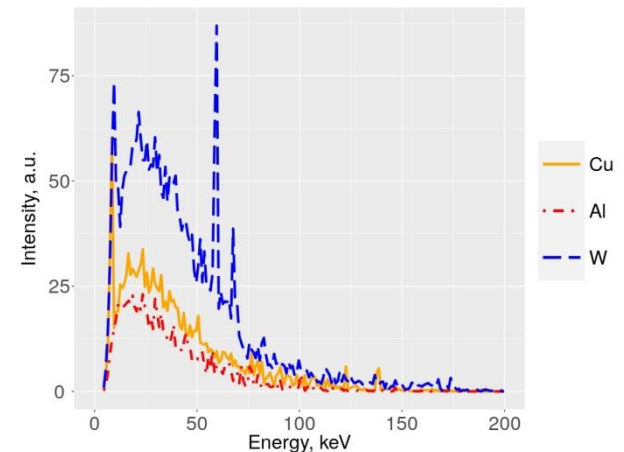


**Fig. 3.** Modeled photon spectra for Al, Cu and W.

Assuming interaction volume of  $100 \mu\text{m}^3$ , electron density  $10^{19} \text{cm}^{-3}$  and total conversion efficiency to bremsstrahlung  $10^{-3}$  we find dose rate from 100 kHz repetition rate at the intensity of  $10^{14} \text{W/cm}^2$  to be 5.5 mSv/h for Cu target at the distance of 35 cm from the target. Doses for Al are lower, while for W it is 15 mSv/h. This is conservative estimate using worst conditions from the radiation protection point of view.

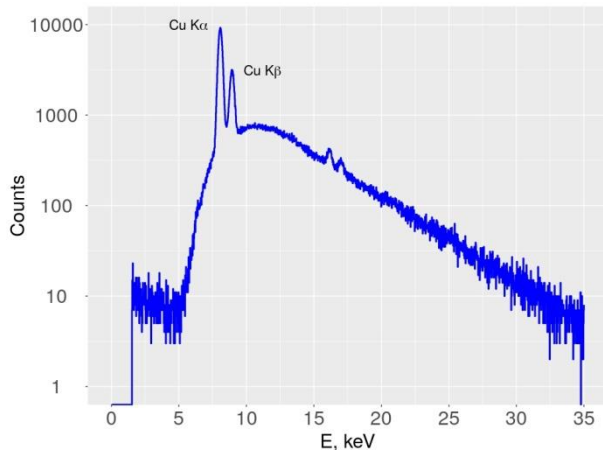


Fig. 4. Measured spectrum of Cu.

Spectra and doses were measured experimentally using laser irradiation described above. Here we present preliminary results only. Measured spectrum of Cu target is given in Fig. 4. Measurements of heavier elements were also performed. Smoothed spectrum of tin, obtained using copper filter to increase resolution [12] is presented in Fig 5. We can clearly identify K line of tin, which proves that electron energies in the focus reach at least 30 keV (K edge energy). Temperature predicted by Beg et al. [7] for highest laser intensity obtained is 17 keV. Part of the electrons in the focus have higher energies than temperature value (See Fig. 1), so our primary analysis show that the prediction given by the scaling is reasonably accurate.

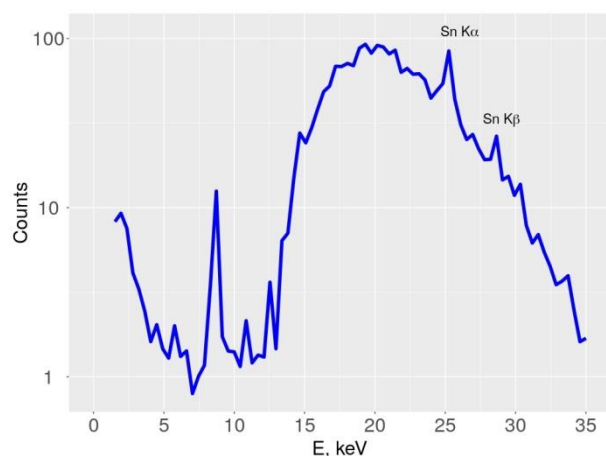


Fig. 5. Measured spectrum of Sn target using Cu filter.

Dose rates were measured using two electronic dosimeters 35 cm away from the laser focal spot. The highest dose rates obtained with dosimeters were 2.4 mSv/h at  $4.7 \times 10^{14} \text{W/cm}^2$  for Cu. Different X-ray

generation intensities and subsequently doses were detected for different materials: dose rates for optimized focusing at highest irradiation intensities were highest for Al, Fe, and Cu (from 1 to 2.4 mSv/h), while other materials gave significantly lower doses (Sn – 0.33 mSv/h, Pb – 0.24 mSv/h). Agreement between modeling and experimental data is reasonably close for low and medium Z. We assume that lower doses for higher Z metals might be attributed to different material properties such as melting point, heat conduction, etc., but this should be investigated more thoroughly.

We used passive thermoluminescence dosimeters to evaluate cumulative dose levels during experimental session. Experiments were performed for 3 weeks (15 days in the lab). The dosimeter closest to the target (30 cm away) measured  $H^*(10)$  dose of 32.4 mSv and  $H'(0.07)$  dose reaching 2.05 Sv during experimental session. Another dosimeter which was behind 3 mm thick iron plate, with the same distance from the target measured 0.04 mSv and 0.33 mSv respectively. Personal dosimeters showed only 0.01 mSv above the background.

Both electronic and thermoluminescence dosimeters have lower energy limits for dose measurement (20 keV and 10 keV respectively). In the spectral measurements we noticed, that most of the energy is contained in the lower energy part of the spectrum, i. e. our dosimeters are not capable to measure significant part of the irradiation dose resulting from low energy X-ray photons. Results of  $H'(0.07)$  dose measurements support this conclusion, as  $H'(0.07)$  dose coefficients are significantly higher in low energy part in comparison with  $H^*(10)$  dose coefficients [13].

## 5. Conclusions

The ionizing radiation created by high intensity femtosecond lasers can cause significant radiological hazard. During laser pulse-material interaction pulse energy is transferred to kinetic motion of the electrons and these electrons drive other processes related with generation of ionizing radiation. We demonstrate that pre-defined electron temperature scaling relating focused beam intensity and generated electron temperature might be used for dose prediction and characterization. Combined dosimetric and X-ray spectral measurements show that dosimeters with 10-20 keV low energy limit are not capable to estimate whole equivalent dose to skin  $H'(0.07)$  near high intensity femtosecond laser. Facilities using high intensity lasers should take measures (e.g. metal plate shielding) to avoid possible irradiation doses.

## Acknowledgements

This research is funded by the European Social Fund under the No 09.3.3-LMT-K-712 “Development of Competences of Scientists, other Researchers and Students through Practical Research Activities” measure.

## 6. References

1. Shuting Lei, Xin Zhao, Xiaoming Yu, Anming Hu, Sinisa Vukelic, Martin B. G. Jun, Hang-Eun Joe, Y. Lawrence Yao, and Yung C. Shin. Ultrafast Laser Applications in Manufacturing Processes: A State-of-the-Art Review. *Journal of Manufacturing Science and Engineering*, 142, 031005, 2020.
2. M. Malinauskas, A. Žukauskas, S. Hasegawa, Y. Hayasaki, V. Mizeikis, R. Buividas, and S. Juodkazis. Ultrafast laser processing of materials: from science to industry. *Light: Science & Applications*, 5(8), 16133, 2016.
3. The 2007 Recommendations of the International Commission on Radiological Protection. ICRP publication 103. *Annals of the ICRP*, 37(2-4), 1–332, 2007.
4. C. Fonseca, C. Mendez, C. Ruiz, F. Fernandez, and L. Roso. High Electron Doses from a GW Laser Interacting with Solid Aluminum Targets. *AIP Conference Proceedings*, 1209(1), 31–34, 2010.
5. M. J. Wesolowski, C. C. Scott, B. Wales, A. Ramadhan, S. Al-Tuairqi, S. N. Wanasundara, K. S. Karim, J. H. Sanderson, C. A. Wesolowski, and P. S. Babyn. X-Ray Dosimetry During Low-Intensity Femtosecond Laser Ablation of Molybdenum in Ambient Conditions. *IEEE Transactions on Nuclear Science*, 64(9):2519–2522, 2017.
6. H. Legall, Ch. Schwanke, S. Pentzien, G. Dittmar, J. Bonse, and J. Krüger. X-ray emission as a potential hazard during ultrashort pulse laser material processing. *Applied Physics A*, 124(6):407, 2018.
7. F. N. Beg, A. R. Bell, A. E. Dangor, C. N. Danson, A. P. Fews, M. E. Glinsky, B. A. Hammel, P. Lee, P. A. Norreys, and M. Tatarakis. A study of picosecond laser–solid interactions up to 1019. *Physics of Plasmas*, 4(2), 447–457, 1997.
8. A. Ferrari, P.R. Sala, A. Fasso, and J. Ranft. FLUKA: A Multi-Particle Transport Code. SLAC-R-773. Technical report, 2005.
9. T.T. Böhlen, F. Cerutti, M.P.W. Chin, A. Fassò, A. Ferrari, P.G. Ortega, A. Mairani, P.R. Sala, G. Smirnov, and V. Vlachoudis. The FLUKA Code: Developments and Challenges for High Energy and Medical Applications. *Nuclear Data Sheets*, 120, 211–214, 2014.
10. C. G. Serbanescu, J. A. Chakera, and R. Fedosejevs. Efficient Ka x-ray source from submillijoule femtosecond laser pulses operated at kilohertz repetition rate. *Review of Scientific Instruments*, 78(10), 103502, 2007.
11. M. Hada and J. Matsuo. Effects of ambient pressure on Cu Ka X-ray radiation with millijoule and high-repetition-rate femtosecond laser. *Applied Physics B*, 99(1), 173–179, 2010.
12. A. Koroliov, J. Reklaitis, K. Varsockaja, D. Germanas, A. Plukis, and V. Remeikis. X-ray pulse emission of alkali metal halide salts irradiated by femtosecond laser pulses. *Applied Physics B*, 126, 144, 2020.
13. ICRP Report No. 74, Conversion Coefficients for use in Radiological Protection against External Radiation, *Ann. ICRP* 26 (1996).

## PERCEPTIONS OF THE RISKS OF RADIODIAGNOSTIC EXAMINATIONS IN POTENTIALLY HIGH-DOSE AND LOW-DOSE PATIENTS

Artem DAVYDOV<sup>1</sup>, Artem BIBLIN<sup>2</sup>, Alexander VODOVATOV<sup>3</sup>, Vladimir SAFRONOV<sup>4</sup>

<sup>123</sup>Research Institute of Radiation Hygiene after P.V. Ramzaev, Saint-Petersburg, Russia

<sup>4</sup>I.M. Sechenov First Moscow State Medical University, Moscow, Russia

<sup>1</sup>[a.davidov@niirg.ru](mailto:a.davidov@niirg.ru), <sup>2</sup>[a.biblin@niirg.ru](mailto:a.biblin@niirg.ru), <sup>3</sup>[a.vodovatov@niirg.ru](mailto:a.vodovatov@niirg.ru), <sup>4</sup>[safronov.w@gmail.com](mailto:safronov.w@gmail.com)

**Abstract:** this article presents the results of a study of patients with potentially high doses and low doses of radiation exposure during radiodiagnostic examinations. It was found that despite the related risk, patients with potentially high doses perceive radiation risks less acutely. This is due to the fact that patients with potentially high doses are much more concerned about the current health problems that cause them to undergo treatment, which makes it difficult for them to risk-communicate and adequately assess the risks of undergoing radiodiagnostic examinations. It is concluded that different risk-communication strategies are needed for high-dose and low-dose patients.

**Keywords:** risk communication, risk perception, radiation

### 1. Introduction

The number of radiological medical examinations has increased in recent years. At the same time, the collective dose and risks to the populations of developed countries are increasing [1,2] and radiation risks communication in the medical field is becoming more relevant. In previous scientific publications, the following is stated: «It is estimated that use of CT may be associated with 1.5% to 2% of all cancers in the United States in the future» [2], «In fact, about 80% of our annual exposure to man-made ionizing radiations (3 mSv) comes from tests and procedures ordered by physicians» [3]. «The 72 million CT scans prescribed in the United States in 2007 were estimated to result in a future health impact of 29,000 excess cancers with a 95% uncertainty range from 15,000 to 45,000 cases» [4]. And some of these statements cause disagreement between expert in the fields since «presenting assessments by quantifying a numeric risk of stochastic disease from relatively low doses of radiation does much more harm than good by fostering misperception and alarm among the lay public, media, and public health communities»[5]. The reasons for the controversy are the scientific uncertainty in the field of radiation safety, the contestability of the LNT [6].

Eventually the doubts reach the patients as well. As Gale et al. well described [3] the range of questions that arise before the laypeople regarding radiation risks: «Understandably, most people have substantial, albeit unrealistic, concerns about the impact of radiation exposure on their health. They are especially focused on the deceptively simple question: What is my risk of cancer? Other important questions, usually after preliminary and contradictory data are released by governments, scientific experts (real and imagined) and the media are: How certain are you of the risk estimate you are telling me? How does this risk compare to other risks in my life? and, Is there anything I can do to avoid or decrease my risk from radiation? (avoid physicians is an easy answer). People need this information for many reasons, but especially for informed decision-making about traveling to Japan, eating sushi in New York, having a CT scan or voting on a proposition for a new nuclear power facility in their country or having a BM transplant».

When it comes to radiological examinations, more efficient communication should be established with the patient in order to avoid rejection of the examination on one hand, and to inform him about the risks and benefits of the procedure on the other hand.

Picano [7] wrote in 2004 that there are 3 risk communication strategies in medicine:

1. the risks should not be mentioned based on the belief that "experts know best". In addition, risk communication is a waste of time and increase the likelihood of refusal of the procedure.
2. Paternalistic approach/understatement of risk often used in radionuclide examinations. Web sites say, "Nuclear medicine exams are safe, with radiation exposure consistent with plain radiography" or "almost always less than conventional radiological exams." But the dose can vary greatly, from very small to very large. «In reality, however, the dose exposure ranges from 50 chest x rays for a thyroid scintigraphy to 4000 chest x rays for a cortical adrenal gland scintigraphy».

3. Full disclosure of complete and detailed descriptions of dose values and risks, using comparisons with other radiation risks.

There are different categories of patients who are exposed to high and low doses of radiation during diagnosis. In some patients, the risks of diagnosis may be comparable to the risks of no treatment, but the patients themselves may not recognize this [8]. This raises questions:

- How to better inform patients during radiological examinations;
- How to better inform different groups of patients.

To answer these questions, we need to understand why the reason for patients consent to radiological examinations should be understood as well as their level of awareness of the risks and benefits of these examinations.

#### The aim of this study is to:

- Compare high-dose groups (potentially the full cycle of undergoing sex reassignment surgery, not just mastectomies) / low-dose groups;
- Determine motive (unreflective habit (don't know risks + "doctors know better") vs consciousness and hopelessness (know risks, but "I have no way out"));
- Investigate distributions, if there is a dependence of anxiety on the amount of exposure.

## 2. Methods

To achieve this objectives, a cross-sectional study was conducted. Using self-administrated questionnaires, two groups of patients were questioned: potential high dose group (99 respondents, ftm-transgenders) and low dose group (41 respondents, plastic surgery patients). All interviewers were patients of the same surgeon, and filled out the questionnaire via Google Forms. Data was collected in the fall of 2019. The following questions were asked:

- risk-communication practices before radiological examinations;
- patient awareness of the risks and benefits of radiological examinations;
- risk perception attitudes.

In the winter of 2020, transgender people were surveyed again, asking them, among other things, about the stages of sex reassignment that they had planned or completed. Of the sent surveys, 87 responses were received.

To compare the differences between the two groups on categorical characteristics, z score test for two population proportions was used. Mann-Whitney test was used to assess differences between two independent samples on quantitatively measured variables (nonparametric test).

## 3. Results and discussion

In the Russian Federation, the law requires a procedure for informing patients about the risks of treatment and diagnosis. All patients must sign an informed consent form. But as can be seen from table 1, the informed consent procedure is not properly conducted. Interestingly, the low-dose group is more attentive to the procedure.

**Table 1.** Risk communication practices

Patients group	Answer (%)		
	Yes	No	Difficult to answer
Did you sign the Informed Consent Form before the examination?			
High dose group	46,9	32,7	20,4
Low dose group	77,5	12,5	10,0
Have you read the contents of?			
High dose group	15,3	66,3	18,4
Low dose group	52,5	37,5	10,0
Did the radiologist inform you before the examination?			
High dose group	39,8	32,7	27,6
Low dose group	24,4	70,7	4,9

As a result, most patients are unaware of the risks and benefits of the radiodiagnostic examination procedure (table 2). High-dose group has fewer "definite answers" to radiation risk communication questions.

**Table 2.** Risk benefit awareness

Patients group	Answer (%)		
	Yes	No	Difficult to answer
Are you aware of the risks of such examinations			
High dose group	48,5	21,6	29,9
Low dose group	41,5	43,9	14,6
Are you aware of the benefits of such examinations			
High dose group	48,5	21,6	29,9
Low dose group	61,5	30,8	7,7

This is because they are more concerned about their current health problems than they are about the radiation risks from radiodiagnostic examinations (table 3).

**Table 3.** Distribution of answers to the question: Which risks are more significant for you: those related to the health problems that you are currently undergoing treatment or those related to exposure to radiation during medical examinations?

Patients group	Answer (%)			
	current health issues	both in equal measure	related to radiation exposure	Difficult to answer
High dose group	69,7	11,1	3,0	16,2
Low dose group	46,3	24,4	7,3	22,0

At the same time, it cannot be said that the high-dose group trusts doctors more and believes in the safety of radiodiagnostic methods - they are rather forced to follow their instructions for treatment (tables 4-5).



**Table 4.** Distribution of answers to the question: Which statement are you more likely to agree with?

1 - Since doctors prescribe radiodiagnostic examinations, then, in general, they are relatively safe and do more good for my health than harm

5 - Doctors are used to prescribing radiodiagnostic examinations, they are so comfortable, they do not think about the long-term consequences for the body

Patients group	Answer (%)					Mean
	1	2	3	4	5	
High dose group	36,4	33,3	15,2	7,1	8,1	2.17
Low dose group	61,0	22,0	2,4	4,9	9,8	1.81

There is a statistically significant difference between the two groups. Using Mann-Whitney statistics, the mean ranks are 75.30 for high dose group and 58.90 for low dose group. The value of  $z$  is -2.311. The value of  $p$  is .021. The result is significant at  $p < 0.05$ .

**Table 5.** Distribution of answers to the question: Which statement are you more likely to agree with?

1 - I agree to radiodiagnostic examinations because I trust doctors

5 - I agree to radiodiagnostic examinations because I have no choice

Patients group	Answer (%)					Mean
	1	2	3	4	5	
High dose group	32,3	18,2	21,2	11,1	17,2	2.63
Low dose group	43,9	14,6	12,2	4,9	24,4	2.51

No statistically significant difference between the two groups. Mann-Whitney statistics. The value of  $z$  is -0.639. Mean ranks are 71.86 for high dose group and 67.21 for low dose group. The value of  $p$  is 0.523. The result is not significant at  $p < 0.05$ .

Up to 30 percent of patients plan to undergo all stages of the process (table 6.), so the dose accumulated during radiodiagnostic procedures will pose significant risks [8]. The risks will be comparable to those of the suits.

**Table 6.** Distribution of answers to the question: What steps do you plan to take (or have you already taken) in sex reassignment surgery?

Operation/group of operations	Percent (number of observations)
mastectomy	96,6 (84)
hysterectomy	88,5 (77)
phalloplasty	19,5 (17)
urethroplasty	23 (20)
metoidioplasty	31 (27)

#### 4. Conclusion

At the moment, in the Russian Federation, the doctor-patient interaction system takes place in a paternalistic format. Patients trust physicians to determine treatment strategies and are not prepared to make joint decisions

where possible, nor do they have the competence to do so.

Studies of the perception of different types of radiation risks show that despite the general wariness of the population's perception of these risks, medical perceptions are moderate, which, combined with a high level of trust in doctors, results in a low outrage effect.

Patients with high hazard are less concerned about the radiation risks of radiodiagnostic examinations because they are highly concerned about health problems. Doses to first patients are higher because their health problems are more serious and require more medical procedures, including radiodiagnostic examinations.

Patients with high hazard are less concerned about the radiation risks of radiodiagnostic examinations because they are highly concerned about health problems.

But objectively, there are different categories of patients - high-dose patients with high risks and low-dose patients with low risks. For different categories of patients, different risk communication strategies should be developed and provided for patients, some to increase outrage, some to decrease, according to the hazard.

#### 5. References

- Onischenko G.G., Popova A.Yu., Romanovich I.K., Vodovatov A.V., Bashketova N.S., Istorik O.A., Chipiga L.A., Shatsky I.G., Sarycheva S.S., Biblin A.M., Repin L.V. Modern principles of the radiation protection from sources of ionizing radiation in medicine. Part 2: radiation risks and development of the system of radiation protection. Radiatsionnaya Gygiena = Radiation Hygiene. 2019;12(2):6-24. (In Russ.) <https://doi.org/10.21514/1998-426X-2019-12-2-6-24>
- Baerlocher, Mark Otto, and Allan S. Detsky. "Discussing radiation risks associated with CT scans with patients." *Jama* 304.19 (2010): 2170-2171.
- Gale R. P., Hoffman F. O. Communicating cancer risk from radiation exposures: nuclear accidents, total body radiation and diagnostic procedures //Bone marrow transplantation. – 2013. – T. 48. – №. 1. – C. 2-3.
- Berrington de Gonza'lez A, Mahesh M, Kim K-P, Bhargavan M, Lewis R, Mettler F, Land C. Projected cancer risks from computed tomographic scans performed in the United States in 2007. *Arch Intern Med* 169:2071–2077; 2009.
- Fellman, A. (2012). Comment on Hoffman et al. Health physics, 102(5), 589-590.
- Tschurlovits, M. (2001). The importance of the Hormesis-LNT controversy for practical radiation protection. In Radiation protection for humans and society in tomorrow's Europe. Joint meeting of OeVS (Oesterreichischer Verband fuer Strahlenschutz) and FS (Fachverband fuer Strahlenschutz). 33. FS annual meeting.
- Picano, E. (2004). Informed consent and communication of risk from radiological and nuclear medicine examinations: how to escape from a communication inferno. *BMJ*, 329(7470), 849–851. doi:10.1136/bmj.329.7470.849
- Safronov V.V., Davydov A.A., Vodovatov A.V., Startseva O.I., Biblin A.M., Repin L.V. Assessment of the medical radiation and non-radiation risks for the patients undergoing the surgical gender reassignment from female to male. Radiatsionnaya Gygiena = Radiation Hygiene. 2020;13(2):99-113. (In Russ.) <https://doi.org/10.21514/1998-426X-2020-13-2-99-113>

## PREDICTION OF DETERMINISTIC SKIN EFFECTS IN PATIENTS UNDERGOING HIGH-DOSES INTERVENTIONAL RADIOLOGY EXAMINATIONS

Svetlana SARYCHEVA<sup>1</sup>, Zumrud VAGIDOVA<sup>2</sup>,

<sup>1,2</sup>Saint-Petersburg Research Institute of Radiation Hygiene after Professor P.V. Ramzaev;

<sup>1</sup>Svetlana2003@mail.ru; <sup>2</sup>Zumrudvagidova@gmail.com

**Abstract:** The study was focused on the assessment of the probability of deterministic skin effects occurrence for patients undergoing hepatic arterial chemoembolization. These procedures can be associated with high patient doses and are frequently performed multiple times for the same patient. The data was collected in three city hospitals from Saint-Petersburg; detailed information about more than 100 procedures was studied. The conversion coefficients from the measured dosimetric values to skin dose and the thresholds values correspond to medically important skin reactions for patient follow-up were proposed.

**Keywords:** interventional radiology, maximum skin dose, deterministic effect

### 1. Introduction

Interventional radiology (IR) is a very important part of modern medicine; however, it can be accompanied by high levels of patient exposure [1, 2]. For radiation protection purposes an estimation of the probability of deterministic effects on the patient's skin in addition to the assessment of stochastic effects for IR procedures is required. [1-5]. This is especially important for periodically repeated procedures when some unwanted tissue reactions have already been reported - therapeutic procedures in the abdomen and pelvic area. [1,3-4]. The maximum skin dose (MSD) - specifically the maximum absorbed dose at the most irradiated area of the skin – is the quantitative characteristic for determining the likelihood of deterministic effects on the skin [2].

There are two main approaches for MSD estimation: it can be measured directly (for example, using radiochromic films) or estimated retrospectively based on other measurable quantities [5]. The basic quantity for MSD assessment is the Cumulative Dose at the reference point (CD) [mGy] - the air kerma accumulated at a specific point representing the location of the patient's skin (on the central ray of the x-ray beam, 15 cm from the

isocenter toward the focal spot) [6]. CD approximates the total radiation dose to the skin, summed over the entire body from all projections. CD was established specifically for the skin dose assessment, however not all angiography units provide this parameter. In this case, the total value of the Dose-Area Product (DAP) [cGy·cm<sup>2</sup> or μGy·m<sup>2</sup>] for MSD estimation is used. DAP is the product of the dose at the center of a certain plane of the X-ray beam (e.g. the surface of the patient) multiplied by the area of the X-ray field at that plane. For assessment of the skin dose by DAP the data about X-ray field size on the patient's body is required. Both modules (DAP and CD) don't consider the beam position changing and don't include tissue backscatter.

Currently, due to the difficulty in MSD assessment, prediction of the possibility of skin reactions after IR procedures based on the trigger levels established by the international organizations CIRSE and IAEA: DAP is greater than 300 Gy·cm<sup>2</sup> or CD is greater than 5 Gy [7, 8]. In theory, these trigger values must correspond to the MSD value of 3 Gy, as recommended by ICRP Publication 85 to determine the need for patient follow-up [1]. This study was focused on the assessment of the probability of deterministic skin effects occurrence for patients undergoing hepatic arterial chemoembolization (HACE). These procedures can be associated with high patient doses and are frequently performed multiple times for the same patient. To predict the possible tissue reactions, the correct predictions and the patient's skin dose assessment are very important. The aim of the study was to analyze the applicability of the existing trigger values for HACE procedures and suggest a new one if necessary.

### 2. Materials and methods

The data were collected in three city hospitals in Saint-Petersburg. The hospitals were equipped with different angiography units: Siemens Artis Zee, Toshiba biplane INFx-8000V/EK, and Philips Allura Xper FD20.

**Table 1.** Parameters of angiography systems, patient cohort, and procedures characteristics.

Angiography system	Patient sample		Geometric parameters of HEPA procedures				Dosimetric parameters	
	Number	Age, year	FOV, cm	SDD, cm	SPD, cm	Projection	DAP, Gy*cm <sup>2</sup>	CD, Gy
Philips Allura Xper	19	60 (33-75)	30*40	(90-100)	(65-70)	PA (0,0)	256/309 (27-776)	1,0/1,2 (0,07-2,8)
Siemens Artis Zee	47	59 (30-85)	30*30	(90-95)	(65-70)	PA (0,0)	118/177 (1-1494)	-
Toshiba INFx	40	57 (39-71)	30*40	(100-105)	(70-75)	PA (0,0)	160/203 (13-957)	0,2/0,4 (0,02-3,3)

All angiography units were used like monoplan systems, have flat-panel detectors, and automatic exposure rate control systems. Patient doses were measured with built-in dose measuring systems with a valid calibration. The total filtrations for angiography units were 3,1 mm Al for Philips Allura Xper FD20, 2,5 mm Al for Siemens Artis Zee and 3,6 mm Al for Toshiba INFx-8000V/EK correspondingly. During the examinations on all systems, the additional filters of 0.1-0.3 mm Cu were automatically inserted into the beam from time to time. Detailed information about more than 100 HACE procedures was obtained. The data about operation technique, physical, technical, geometric, and dosimetric parameters for this type of procedure were observed. The mean characteristics of patient samples and geometrical parameters collected during HACE examinations (source to patient distance [SPD], source to detector distance [SDD], size of field of view [FOV], and projections of radiation field - deviations from direct posterior-anterior (PA) projection) are given in Table 1 as well as the cumulative dosimetric parameters: total DAP and CD. The data are presented in the mean or mean/median format and ranges in parenthesis.

All HACE procedures observed during this study were characterized by similar performance parameters and localization of the radiation field on the patient's body. It was the dominant use of large radiation fields without magnification and PA projection with rare and very small angulations (< 4°). In all cases, femoral artery catheterization was performed. There were slight fluctuations in the location of the radiation field in the area of interest (hepatic artery), and all studies were accompanied by overlapping fields in the central part. The skin dose distribution during high-dose IR examinations as a separate project was studied. To visualize the dose distribution on the patient's skin surface, a series of direct measurements were carried out, using special radiochromic films Gafchromic XR-RV3. The results of this work were already published [9], which shows that almost all IR examinations in the abdominal and pelvic area (except some cases of uterine artery embolization) are accompanied by overlapping fields, this fact is also confirmed by other literature data [10,11].

The total skin dose (TSD) value can be estimated by the CD corrected with the backscatter factor (BSF) or based on the DAP value, considering the radiation field size on the patient's surface (S) and BSF.

TSD can be calculated using Equation (1):

$$TSD = B \cdot CD = B \cdot DAP/S \quad (1)$$

MSD can be taken equal to TSD due to the relatively fixed radiation field for HACE procedures. Thus, the values of the conversion coefficients from the measured values of CD and DAP to MSD can be calculated using the following Equation:

$$K_{DAP} = MSD/DAP = TSD/DAP = BSF/S \quad (2)$$

$$K_{CD} = MSD/CD = BSF \quad (3)$$

Where  $K_{DAP}$  - Conversion coefficient from the measured value of DAP to MSD, mGy/(Gy·cm<sup>2</sup>);

$K_{CD}$  - Conversion coefficient from CD to MSD, rel. unit;

BSF - Backscatter factor, rel. unit;

S - Field size on the patient's entrance plane, cm<sup>2</sup>.

### 3. Results

For MSD assessment based on the DAP or CD values, the large influence size and location of radiation field on the patient's body have. As was mentioned above, the HEPA procedures are carried out with large FOV with a rare decrease and a relatively constant position of the radiation field on the patient's body in the PA projection. Therefore, only BSF and S values are needed to calculate the conversion coefficients from the measured DAP or CD values to MSD using Equation (2) or (3) respectively. BSF is defined as the ratio of a dose on the surface of a phantom to the dose at the same point in space, in the absence of the phantom. Values of BSF were provided by ICRU-74 and IAEA TRS 457, for 21 diagnostic beam qualities with kilovoltages of between 50.0 and 150.0 kV, and different types of filtrations [12,13]. Under the observed HACE procedures conditions, the BSF value was close to 1.4. In the case of stronger filtration (for example with frequent introduction of additional copper filters), BSF can increase up to 1.5 or more. In our calculations, we use the value of 1.4.

The dimensions of the radiation fields on the patient's body were calculated based on the collected geometric parameters of the field sizes on the detector (FOV) and the distances between the source, patient, and detector (shown in Table 1.). The radiation field area on the entrance plane of the patient's body for HACE procedures performed in observed clinics was within 400-500 cm<sup>2</sup>.

Assuming the interventional reference point happens to be on the patient's skin, and the beam does not move a lot during the procedure, the MSD is the CD multiplied by a backscatter factor.

**Table 2.** The conversion coefficient ( $K_{DAP}$ ) from the measured dose area product (DAP) to the maximum skin dose (MSD) for the interventional procedures in the abdominal and pelvic area performing with relatively static radiation field and the two types of trigger values of dose area product (DAP) and cumulative dose (CD) to prevent the deterministic effects in the skin for such examinations.

Field size on the patient entrance plane, cm <sup>2</sup>	$K_{DAP}$ , mGy/(Gy·cm <sup>2</sup> )	Trigger values corresponding to MSD of 3 Gy (normal)		Trigger values corresponding to MSD of 5 Gy (critical)	
		DAP, Gy·cm <sup>2</sup>	CD, Gy	DAP, Gy·cm <sup>2</sup>	CD, Gy
400	3.5	850	2.1	1100	3.6
500	2.8	1400		1750	

According to the equation (3)  $K_{CD} = 1.4$ . Calculating by the Equation (4)  $K_{DAP} = 3.5$  mGy/(Gy·cm<sup>2</sup>) if radiation patient field size is closed to 400 cm<sup>2</sup> and  $K_{DAP} = 2.8$  mGy/(Gy·cm<sup>2</sup>) if field size on the patient surface is around 500 cm<sup>2</sup>.

According to international documents, minimum prompt skin reactions may occur in sensitive patients within hours after an acute MSD exceeding 2 Gy; medically important reactions occur in average patients several weeks later at MSDs exceeding 5 Gy [14].

To determine the necessity of patient's after-care the threshold of 3 Gy is recommended [1]. The thresholds in terms of DAP and CD corresponding to mentioned MSD limits were calculated. The conversion coefficient ( $K_{DAP}$ ) from the measured DAP to MSD and the trigger values of DAP and CD corresponding to the 'normal' MSD of 3 Gy and 'critical' MSD of 5 Gy for different radiation field sizes are given in Table 2.

It can be seen that the received DAP trigger values are significantly higher than 300 Gy·cm<sup>2</sup> and the CD values are conversely below the 5 Gy limit. The problem is that the existing trigger values (DAP > 300 Gy·cm<sup>2</sup>, CD > 5 Gy) has been established for interventional cardiac examinations and are not suitable for IR procedures in the abdominal and pelvic area which are characterized by relatively static and large radiation field.

#### 4. Conclusions

This study was focused on the assessment of the probability of deterministic skin effects occurrence for patients undergoing hepatic arterial chemoembolization (HACE). The possible skin dose distributions during the HACE procedures were studied. Data analysis was carried out for more than 100 procedures performed in 3 clinics. Our own previously obtained film measurements of the skin dose distribution for such examinations were additionally considered.

During the IR procedures performing the total values of DAP and CD are displayed and for MSD assessment in real-time can be used. Now the prediction of the possibility of skin reactions after all IR procedures based on the trigger levels for interventional cardiology: DAP is greater than 300 Gy·cm<sup>2</sup> or CD is greater than 5 Gy. According to the results of our work, those values do not correspond to the threshold for the occurrence of skin reactions after HACE procedures (as well as for other IR procedures performing with large and static radiation fields). The existing trigger levels in terms of DAP value is unreasonably low, while the CD value is too high and makes it possible to miss some cases of skin injuries. In this study, 'normal' and 'critical' thresholds values in terms of DAP and CD correspond to the 3 and 5 Gy of MSD were proposed. MSD of 5 Gy can lead to medically

important skin reactions, which corresponds for HACE procedures to a CD threshold value of 3.6 Gy and DAP more than 1100 Gy·cm<sup>2</sup>.

#### 5. References

1. ICRP. Publication 85. Avoidance of radiation injuries from medical interventional procedures. Ann. ICRP. Vienna, Pergamon Press; 2000; 30(2): 68.
2. Sarycheva S, Golikov V, Kalnicky S. Studies of patient doses in interventional radiological examinations. Radiat Prot Dosimetry. 2010 Apr-May;139(1-3):258-61.
3. Miller DL, Balter S, Cole PE, et al. Radiation doses in interventional radiology procedures: The RAD-IR study: Part II: Skin Dose. J. Vasc. Interv. Radiol. 2003;14: 977-990.
4. Galstyan IA, Nadezhina NM. Local Radiation Injuries as Complications of Medical Radiation Exposure. Meditsinskaya radiologiya i radiatsionnaya bezopasnost = Medical Radiology and Radiation Safety. 2012;57(5): 31-36. (In Russian).
5. Balter S, Fletcher DW, Kuan HM, Miller D, Richter D, Seiss H, et al. Techniques to estimate radiation dose to skin during fluoroscopically guided procedures. J Vasc Interv Radiol. 2001;13: 391-397.
6. International Electrotechnical Commission. Report 60601. Medical electrical equipment—Part 2— 43: particular requirements for the safety of X-ray equipment for interventional procedures. Geneva, Switzerland: IEC, 2000. 60601-2— 43.
7. Stecker MS, Balter S, Towbin RB, Miller DL, Vañó E, Bartal G, Angle JF, Chao CP, Cohen AM, Dixon RG, Gross K, Hartnell GG, Schueler B, Statler JD, de Baère T, Cardella JF; SIR Safety and Health Committee; CIRSE Standards of Practice Committee. Guidelines for patient radiation dose management 2009, J Vasc Interv Radiol 20(7 Suppl) 263-73
8. [https://www.iaea.org/resources/rpop/resources/databa ses -and-learning-systems/safrad](https://www.iaea.org/resources/rpop/resources/databa%20ses%20and%20learning%20systems/safrad)
9. Sarycheva SS. Patients skin dose measurements during interventional radiological examinations using Gafchromic XR-RV3 FILM. Radiatsionnaya Gygiena = Radiation Hygiene, 2019;12(4): 89-95. (In Russian)
10. Neocleous A, Yakoumakis E, Gialousis G, Dimitriadis A, Yakoumakis N, Gargiou E. Dosimetry using Gafchromic XR-RV2 radiochromic films in interventional radiology. Radiation Protection Dosimetry. 2011;147(1-2): P. 78-82.
11. NCRP Report 168. Radiation dose management for fluoroscopically-guided interventional procedures. National Council on Radiological Protection. 2010: 314.
12. ICRU. Publication 74. Patient Dosimetry for X-rays used in medical imaging. Journal of the ICRU. 2005;5(2): 116.
13. IAEA, Dosimetry in Diagnostic Radiology: An International Code of Practice, Technical Reports Series No. 457, IAEA, Vienna (2007).
14. Cousins C, Miller DL, Bernardi G, Rehani MM, Schofield P, Vañó E, Einstein AJ, Geiger B, Heintz P, Padovani R, Sim KH; International Commission on Radiological Protection. ICRP PUBLICATION 120: Radiological protection in cardiology. Ann ICRP. 2013 Feb;42(1):1-125.

## **EARLY EFFECTS OF RADIATION EXPOSURE ON PERIPHERAL BLOOD CELLS AND NORMAL ORGANS OF MICE**

Yuliya DVORNIK<sup>1</sup>, Natalia VEYALKINA<sup>2</sup>, Kseniya FABUSHEVA<sup>3</sup>  
Institute of Radiobiology of the National Academy of Sciences of Belarus  
<sup>1</sup>yvdvornik@gmail.com; <sup>2</sup>veyalkina@mail.ru; <sup>3</sup>fabusheva\_kseniya@mail.ru

**Abstract:** The results demonstrate that the changes in the weight of organs depend on the type of exposure, its duration, and dosage. The spleen is considered to be the most sensitive to radiation exposure and suffers more changes than any other organ compared to control. A single-time exposure to a dose of 10Gy causes the number of peripheral blood leukocytes to decrease ten times as against control. The levels of thrombocytes, erythrocytes, and that of hemoglobin remain within their normal ranges at early stages following the exposure. In a fractional exposure (total of 5 times, 2Gy each), the leukogram changes are much less obvious.

**Keywords:** organ damage, blood cells, fractional exposure, single exposure, weight coefficient

### **1. Introduction**

The studies related to the effects of ionizing radiation on biological objects and humans have increased in numbers over the last few years. For the most part, chest area irradiation cases are associated with radiation therapy of oncological disorders. At the same time, such treatment presents a risk of injuring healthy tissues of the lungs, heart and major vessels exposed to radiation [1]. The present-day level of neoplasm therapy leads to higher survival rates of cancer patients. Nevertheless, what preserves its relevance is the issue related to the long-term effects of radiation developed following the exposure of healthy tissues and organs. Understanding the biological pathways and mechanisms of radiation injury will help to reduce the risk of long-term side effects to human health, which in its turn will lead to more improved cancer therapies in the future. With this regard, the use of animal models, which are similar in cellular responses to humans, can be very helpful in tackling the said issue.

A considerable number of research works over the last decade were aimed at establishing an effective model both for enhancing radiation treatment methods and for reducing the negative consequences of medical

exposures [2-4]. The most common experimental model in radiation-related research is the mouse [5].

Three strains of mice with phenotypic expression of radiation-induced lung injury were studied and analyzed by Jackson et al. [4]. The X-ray source of 320 kV was used to generate the dose rate of 69.2cGy min<sup>-1</sup>. For all strains, the dose was reliably associated with 180-day mortality ( $p < 0.0001$ ). An estimated LD50/180 for C57L/J mice was 11.35Gy, approximately 14.17Gy for CBA/J mice, and 14.10Gy for C57BL/6J mice. The findings showed that the response of some animal models (in particular, C57L/J and CBA/J) could be extrapolated to human lungs to understand the mechanisms of radiation exposure effects.

All the above underlines the relevance and practical significance of the need to investigate the mechanisms of the cellular and subcellular damage development following local irradiation of the chest area.

This study was aimed at exploring the radiation-induced cell and organ damage dynamics resulted from local thorax exposure of laboratory mice and estimating its relevance for the prediction of long-term health effects. Our objective was to assess the health state of mice in the acute post-irradiation period following a single and fractional exposure of the chest area at a dose of 10Gy.

### **2. Materials and methods**

The research animals used in our laboratory experiments were the mice of C57BL/6 strain – physically active animals with smooth and shiny coats and normal visible mucous membranes aged 2.5-3 months at the beginning of our study.

The mice were kept quarantined in the vivarium for two weeks prior to the experiment. On the day of the experiment, additional examination and weighing were carried out. The groups were formed based on the gender and body weight of mice.

All group experiments started at the same time in the morning, taking into account the chronological dependence of physiological and biochemical processes in the body.

The animals were divided into 3 groups ( $N = 30$ ) including a control, single exposure and fractional exposure groups. The mice in group 1 were intact animals subject to all manipulations except for radiation exposure, group 2 was exposed to one-time chest irradiation at a dose of 10Gy, and group 3 was exposed to 2Gy once every 24 h during 5 days straight, with a total radiation dosage to the chest area of 10Gy. Each group of mice consisted of 10 females and 10 males.

The system used for animal irradiation was a biological irradiator X-Rad 320 (Precision X-Ray, USA), with an X-ray tube voltage of 320kV, dose range of 98.8cGy/min, filter No.2 of 1.5mm Al, 0.25mm Cu, 0.75mm Sn, and source to specimen distance of 50cm. The locality of chest area irradiation was achieved by using lead shielding sheets.

The physical condition of animals was being observed during the entire time of the experiments. One and four weeks following the exposure, the animals were submitted to deep anesthesia and decapitated. Blood sampling, isolation and weighing of internal organs were then carried out. A general blood test was made using a Celltac MEK-6318J/K hematology analyzer.

To calculate a post-irradiation weight coefficient, the following equation was used:

$$k = \frac{w_i \cdot 100}{w} \quad (1)$$

where  $w_i$  – weight of  $i$  organ in g,  $w$  – total body weight, g.

Statistical analysis of the data was performed with the Microsoft Office Excel 2013 and STATISTICA 10 tools. An assumed critical level of significance ( $p$ ) in this study was 0.05.

### 3. Results

#### 3.1 Effects on normal tissues and organs

The distribution of the weight coefficient of the four organs in terms of the gender and irradiation modes is shown in Figure 1.

The lung weight coefficient has seen an increase of 20% against control a week after the exposure with a dose of 10Gy, and a 25% increase one month after the exposure. The weight coefficient of the heart was close to the control one week after the exposure, while an increase of 2.9 per cent was observed in this organ the following month. After single-time irradiation, the spleen weight coefficient halved down compared to control. A similar weight coefficient loss was observed both in males and females one week after the exposure.

The spleen contains hematopoietic stem cells. These cells divide more intensively under extreme conditions and therefore deplete. The processes of reparation then start to take place. Fractional irradiation does not show the same sharp decrease as the reparation processes are launched within 24 hours.

After single-time exposure, the weight coefficient of the heart in a male group, when compared to control, decreased by 11.5% during the first week and increased by 1.8% one month following the exposure.

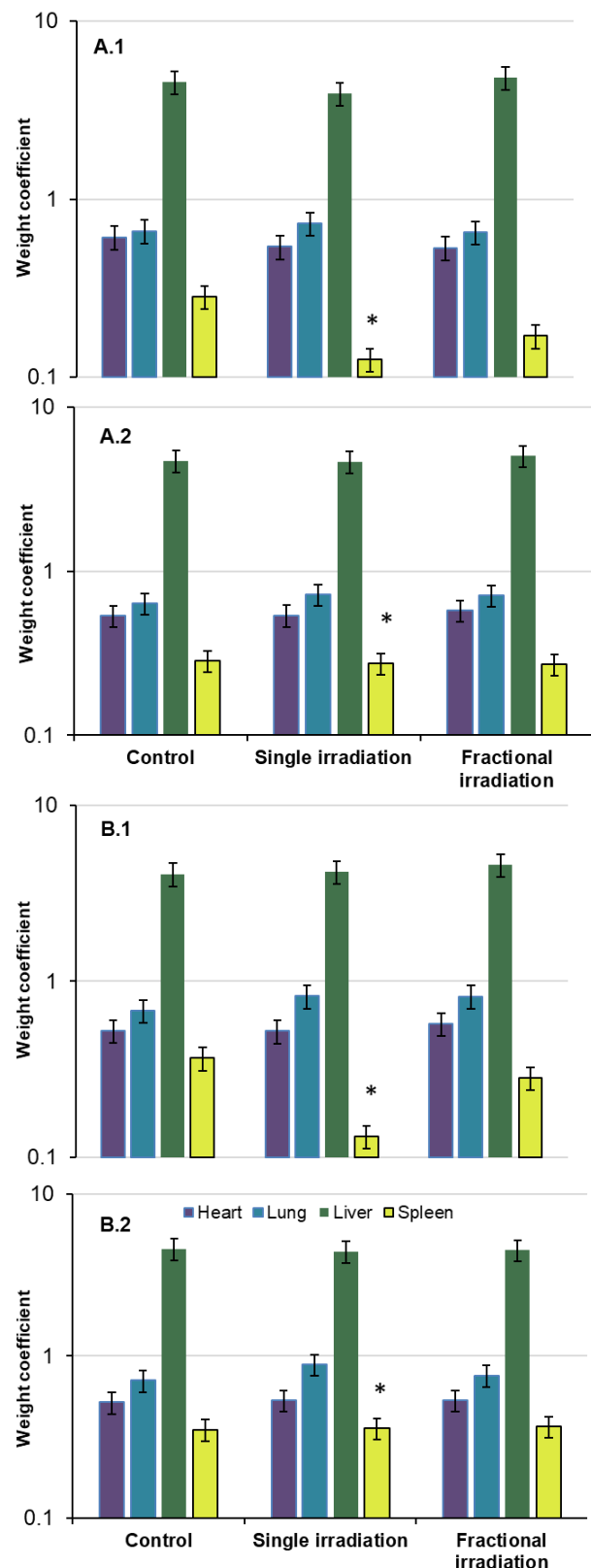


**Fig. 1.** Distribution of organs weight coefficient for male (A) and female (B) mice 1 week (1) and 1 month (2) after exposure. (\*) – statistically significant changes ( $p < 0.05$ ,  $N = 10$ ).

Due to the severe inflammatory response, the lung weight coefficient was 10.6 per cent higher than that in control one week after exposure. Being the main blood-forming organ, the liver is highly exposed to ionizing radiation. Destruction of hematopoietic cells causes a 13.85% decrease of the liver weight coefficient one



week after exposure compared to control. Even so, intensive formation of new blood cells from hematopoietic stem cells leads to a nearly complete recovery of the weight coefficient within one month after the exposure.

Fractional exposure has a long-term but less destructive effect on the four organs. In the male group, the heart weight coefficient decreased by 12.7%, and then increased by 7.1% within, respectively, a week and a month after exposure. The weight coefficient of the lung was 1.6% lower against control a week after irradiation and was 8.3% higher than control after one month following the exposure. The spleen was degraded and its weight coefficient decreased by 39%. One month after exposure, the spleen weight coefficient was 1.4% lower than that in the control group.

In each experimental group, the spleen was clearly the most sensitive to radiation exposure organ, both for male and female mice. Figure 1 demonstrates the significance of changes in the spleen weight coefficients in terms of single-time and repeated fractional exposure.

### 3.2 Effects on peripheral blood cells

Figure 2 demonstrates the leukogram changes in the lab mice 1 week (Fig. 2.A) and 1 month (Fig. 2.B) after irradiation. In a male group, the amount of WBC (leukocytes) decreased by 84% compared to control one week after single-time irradiation. Within a month, the average amount of WBC then slowly recovered up to  $4.86 \pm 0.93 \cdot 10^9$  cells per L (61% of control). One week after fractional exposure, the average amount of WBC decreased by a factor of 3 – from  $5.94 \pm 1.17 \cdot 10^9$  cells per L (control) to  $1.68 \pm 0.66 \cdot 10^9$  cells per L. It then increased to  $4.12 \pm 0.59 \cdot 10^9$  cells per L, or 52% of the control amount.

Single irradiation is characterized by abrupt changes in the leukogram and rapid initiation of repair processes.

In a female group this difference was 93% and 55% one week and one month after the single-time exposure, respectively, compared to control.

A week after fractional exposure the difference between experimental and control groups was 66%, decreasing further down to 50% within the next month.

No sharp decreases in the amount of RBC after irradiation were observed (see Table 1).

**Table 1.** Changes in peripheral blood of mice after irradiation

	RBC	HGB
1 week		
Control	$8.97 \pm 0.15$	$146.6 \pm 1.67$
Single irradiation	$7.04 \pm 0.18$	$116.8 \pm 2.15$
Fractional irradiation	$6.77 \pm 0.17$	$116.0 \pm 1.95$
1 month		
Control	$7.56 \pm 0.79$	$9.31 \pm 0.20$
Single irradiation	$4.12 \pm 0.58$	$8.65 \pm 0.18$
Fractional irradiation	$3.83 \pm 0.37$	$8.54 \pm 0.17$

The general downward trend was observed for RBC (erythrocytes) and HGB (hemoglobin). A week after single irradiation the amount of RBC decreased by 21%. Fractional irradiation caused approximately the same decrease in the amount of RBC. One month later, the

values were again equal and comparable to the control. After exposure to extreme factors such as ionizing radiation, the rate of erythropoiesis increases several times, while the RBC lifespan decreases.

The HGB level after exposure decreased by 20.3%. One week after exposure, the data in group 2 (one-time) and group 3 (fractional) were the same.

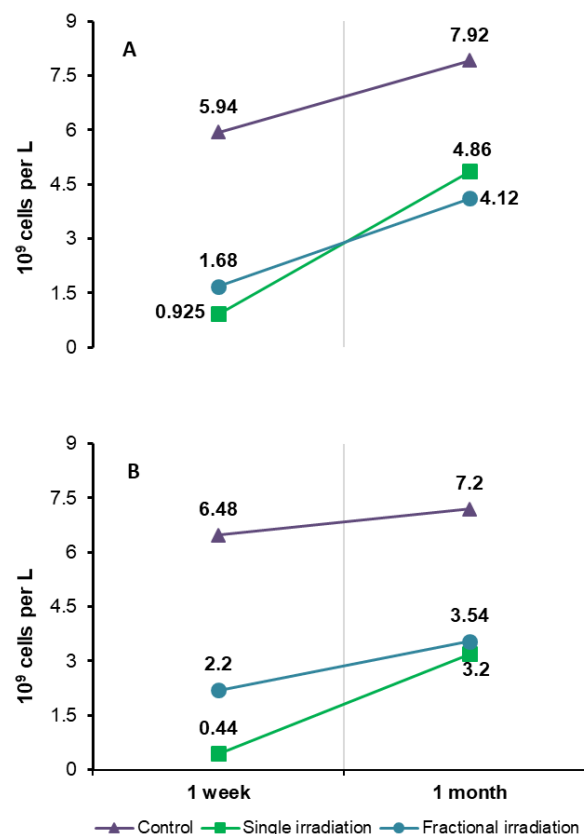


**Fig. 2.** Average amount of WBC 1 week and 1 month after exposure. On the graph: A – male, B – female mice.

### 4. Conclusions

The data analysis presented herein essentially suggests that the effect of ionizing radiation at a dose of 10Gy on the chest area of laboratory mice not only causes destructive changes in animals but can also, over a period of time, trigger recovery processes in the body. The effects of fractional exposure are much less pronounced when compared to single-time local irradiation.

The greater sensitivity of the spleen to ionizing radiation was observed in both male and female groups of mice. The change in the weight of organs shows high dependency on the type of exposure. A one-time exposure (10Gy) causes more visible changes in the weight coefficient of organs compared to fractional exposure (total of 5 times, 2Gy each).

After single irradiation at a dose of 10Gy, the number of peripheral blood leukocytes decreased by a factor of 10. The levels of thrombocytes, erythrocytes and hemoglobin remain within their normal ranges at early stages following the exposure.

## 5. References

1. Michael J. Chen, Paulo E. Novaes, Rafael Gadia, Rodrigo Motta. Guidelines for the treatment of lung cancer using radiotherapy. *Rev. Assoc. Med. Bras.*, 2017, 63(9), 729-732.
2. Thomas J. MacVittie, Ann M. Farese, William Jackson 3<sup>rd</sup>. The hematopoietic syndrome of the acute radiation syndrome in rhesus macaques: a systematic review of the lethal dose response relationship. *Health Phys.*, 2015, 109(5), 342-366.
3. Butterworth KT. Evolution of the supermodel: progress in modelling radiotherapy response in mice. *Clin. Oncol.*, 2019, 31(5), 272-282.
4. Isabel L. Jackson, Pu-Ting Xu, Giao Nguyen, Julian D. Down, Cynthia S. Johnson, et al. Characterization of the dose response relationship for lung injury following acute radiation exposure in three well-established murine strains: developing an interspecies bridge to link animal models with human lung. *Health Phys.*, 2014, 106(1), 45-55.
5. Jacqueline P. Williams, Stephen L. Brown, George E. Georges, Martin Hauer-Jensen, Richard P. Hill, Amy K. Huser, et al. Animal models for medical countermeasures to radiation exposure. *Radiat. Res.*, 2010, 173(4), 557-578.
6. Cheng Zhou, Bleddyn Jones, Mahmoud Moustafa, Christian Schwager, et al. Quantitative assessment of radiation dose and fractionation effects on normal tissue by utilizing a novel lung fibrosis index model. *Radiat. Oncol.*, 2017, 12(1), 172.
7. PRECISION (2021). X-RAD 320 Product Information. Available at: <https://precisionxray.com/x-rad/xrad-320>. Accessed on: 2021-06-25

## OPTIMIZATION OF CONVENTIONAL X-RAY IMAGE ACQUISITION PARAMETERS FOR PELVIC PROCEDURES: A PHANTOM STUDY

Antonio JREIJE<sup>1,2</sup>, Kirill SKOVORODKO<sup>1,3</sup>, Mykolas PAVLAUSKAS<sup>1,4</sup>, Roman MACHNIN<sup>1,4</sup>, Diana ADLIENĖ<sup>2</sup>, Birutė GRICIENĖ<sup>1,4</sup>

<sup>1</sup>Vilnius University Hospital SantarosKlinikos, Vilnius, Lithuania; <sup>2</sup>Department of Physics, Kaunas University of Technology, Kaunas, Lithuania; <sup>3</sup>Center for Physical Sciences and Technology (FTMC), Vilnius, Lithuania; <sup>4</sup>Vilnius University, Faculty of Medicine, Vilnius, Lithuania

antonio.jreije@ktu.edu; kirill.skov@gmail.com; mikas.pavlauskas@gmail.com; roman.machnin@gmail.com; diana.adliene@ktu.edu; birute.griciene@santa.lt

**Abstract:** This study investigated optimization of dose-image quality relationship for pelvic x-ray examinations by varying tube voltage (kV). Patient dose optimization was implemented for three digital radiography systems used for general x-ray examinations (GE Definium, Shimadzu Sonialvision Safire and Siemens Luminos). An anthropomorphic pelvic phantom (CIRS, US) was used to simulate a patient undergoing clinical pelvic X-ray examination. Dose quantities ESD (entrance surface dose), DAP (dose area product) and exposure parameters (kV, mA, mAs) were measured and the impact on the image were evaluated, considering physical CNR (contrast to noise ratio) and observer-based evaluations as image quality metrics. In the case of Definium and Sonialvision Safire, both standard and dose-optimized images were rated as acceptable for clinical use; thus, an increase of 5-10 kV was an effective strategy to reduce patient dose while maintaining image quality. Our results show that the analysis of the images of an anthropomorphic phantom performed using physical and observer evaluations can be an efficient practice for optimizing diagnostic protocols of digital X-ray units.

**Keywords:** digital radiography, dose optimization, radiation exposure, image quality, image evaluation

### 1. Introduction

Medical imaging represents the largest source of radiation exposure from artificial sources. It is a well-established that exposure to high level of ionizing radiation has an adverse effect on human health [1]. Additionally, evidence suggest that pelvis diagnostic examinations may lead to increased risk of cancer to the gonads and other nearby organs [2]. Therefore, due to the large burden of medical radiation sources on the

general population, reduction in patient doses is required to ensure exposure “as low as reasonably achievable” (ALARA) while maintaining adequate diagnostic quality of the acquired images [3].

In order to manage patient exposure in digital radiography, training of personnel in the aspects of patient dose management, continuous collection of patient doses and revision of local DRLs are recommended by ICRP [4]. Moreover, the ICRP recommends the implementation of tools that inform medical physicists and radiologists about doses delivered to patients (i.e. dose area product DAP, exposure index EI, deviation index DI, etc.) [4].

In addition, individual protocol optimization is a key factor for decreasing patient dose. When performing optimization in diagnostic radiology, special attention should be paid to two parameters: patient dose and image quality [5]. The most important goal of exposure optimization is to find parameters that result in an adequate image (i.e. of sufficient diagnostic information), not the best image. However, defining what make up an adequate image for diagnostic purposes might be a challenging task since it depends greatly on the reader experience and the anatomy and physiology being examined. Moreover, it is common for a single hospital to purchase diagnostic units from different manufacturers depending on its need and financial resources. Thus, optimization is necessary for each diagnostic unit as well as for each X-ray protocol.

The aim of this study was to evaluate the effect of exposure parameters on image noise and contrast using an anthropomorphic pelvic phantom and to optimize the diagnostic imaging pelvis protocol of three different digital X-ray machines.

## 2. Materials and Methods

### 2.1. Radiographic equipment

Images were obtained from three digital X-ray equipment (General Electronics, Siemens and Shimatzu) at Vilnius University Hospital Santaros Klinikos, (table 1). Medical physicists of hospital perform regular quality control and assurance testing of X-ray equipments in accordance with the radiation protection act of the Republic of Lithuania [6].

**Table 1.** Radiology equipment information

Department	Manufacturer	Model	Installation year
Pediatric	GE	Definium	2011
Pediatric	Shimatzu	Sonialvision Safire	2011
Radiology	Siemen	Luminos	2018

### 2.2. Radiographic technique

Radiographic images were acquired using a pelvic protocol with an anthropomorphic phantom (CIRS, US) simulating the lower abdomen and pelvis an average size adult male patient (MODEL 801-P). The images were obtained with the phantom placed on the diagnostic table in the supine position (AP anterior-posterior projection) while maintaining a 120 cm source to image detector distance (Fig. 1.).

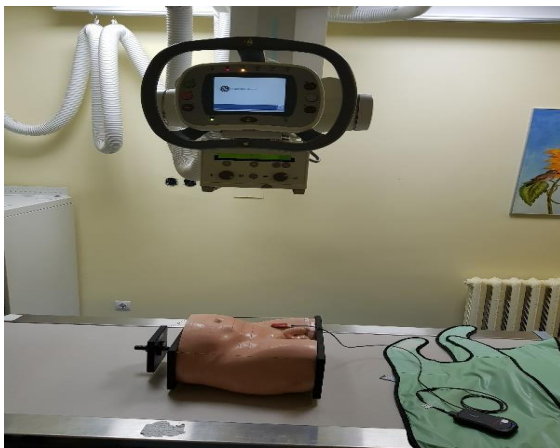


**Fig.1.** Experimental setup for simulating pelvic x-ray examinations with CIRS phantom.

For each X-ray equipment, images of the phantom were obtained using the standard exposure protocol set by the manufacturer. The automatic exposure control (AEC) parameters for each digital system are summarized in table 2. An additional, set of images were acquired in the automatic exposure mode while varying voltage from 65 to 90 keV at 5 keV step interval. In order to compare the performance of all radiology systems, the image quality and delivered dose was evaluated for images obtained using same fixed exposure parameters (80 keV, 10 mAs) for all equipment.

Dose following each exposure was defined as Dose area product (DAP) displayed automatically by each system and measured entrance surface dose (ESD). In order to calculate the ESD, incident air kerma, measured with a solid state sensor (Piranha RTI Dose Probe ®) placed on

the surface of the phantom (Fig. 1.), was multiplied by a backscattering factor corresponding to each beam quality [7].

**Table 2.** Exposure parameters for standard pelvic protocol of a medium size patient.

Equipment	Voltage (kV)	Current (mA)	Current tube product (mAs)
Definium	80	400	18,02
Sonialvision Safire	75	800	20,5
Luminos	77	800	16,2

### 2.3. Objective assessment of image quality

The image quality was quantified by measuring the contrast to noise ratio (CNR) related to the contrast or signal difference between an object of interest and the image background (Fig. 2.) and computed following

$$CNR = \frac{S_1 - S_2}{\sqrt{\frac{\sigma_1^2 + \sigma_2^2}{2}}}$$

where S1 and S2, are the mean pixel values from the region of interest 1 and 2 (ROI1, ROI2) respectively, and  $\sigma_1$  and  $\sigma_2$  are their associated standard deviations. These different parameters were measured using the open source software ImageJ CNR while taking the sacrum and soft tissue as ROI1 and ROI2 respectively for each x-ray image (Fig. 2.).



**Fig. 2.** Regions of interest used to calculate contrast-to-noise ratio (CNR) for pelvic x-ray images.

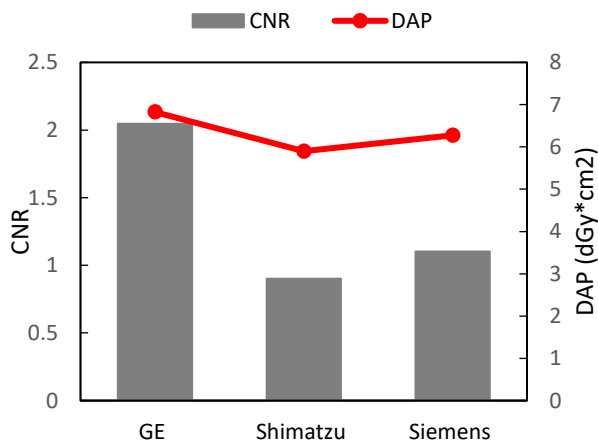
### 2.4. Subjective assessment of image quality

Image quality was assessed independently by two resident radiologists in accordance with guidelines on basic aspects of quality set by the European Commission [8]. For each protocol, the order of the images was randomized and anonymized by stripping of all visible identifying information that might influence observer's assessment including acquisition parameters (keV, mAs, etc). This was done to prevent any biases that could occur due to participants knowledge of the preset acquisition parameters. The evaluation of image quality was based on (a) overall clinical acceptability,

(b) visibility of bone structures against soft tissues and (c) radiographic noise that do not correspond to X-ray attenuation variations of the object. For the subjective assessment, scoring of the questions followed a three-point scale, assigning a score of 1 for unacceptable, 2 for probably acceptable and 3 for fully acceptable. The final quality score for each image consisted of summing the mean score of previously stated questions. All questions were equally weighted while assuming that they are of equal significance to the diagnostic image quality. Interrater agreement was assessed by calculating Cohen's Kappa coefficient using SPSS Statistics (IBM Corp., Armonk, NY, SAD).

### 3. Results and discussion

Due to the variety of digital X-ray units in a single hospital setting, neither radiological examinations nor optimization procedure can be standardized. This study included three radiography equipment from multiple manufacturers (GE, Shimatzu and Siemens). Direct comparison of these three units at a fixed radiation exposure (80 kV, 10 mAs) showed a wide difference in CNR (GE ~2x higher than Shimatzu and Siemens) and exposure dose (DAP ranging from 5.9 and 6.8 dGy\*cm<sup>2</sup>) across all units (Fig.3.). Therefore, optimization should be performed individually for each particular X-ray equipment operating in the clinical setting.



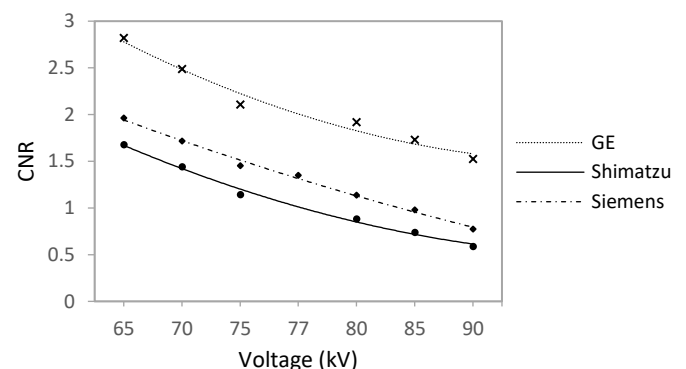
**Fig. 3.** Comparison of image quality (CNR) and dose (DAP) registered for three X-ray units under a fixed pelvic protocol using 80 kV and 10 mAs.

Image quality can be investigated in two ways, objectively based on physical measurements and subjectively through psychophysical assessments [9]. It was previously reported that objective measurements alone are not sufficient to validate the diagnostic benefit of one digital imaging technique over another [9]. The method of choice therefore involves the combination of physical measures and observer performance methods. In this study, investigations of CIRS pelvic phantom images were based on the independent rating of two observers and on measuring the contrast of the sacrum bone against nearby soft tissues (table 3).

**Table 3.** Mean image quality scores across two observers for images taken using different beam quality. R1, Radiologist resident 1; R2, Radiologist resident 2; CoV, Coefficient of variation.

	kV	R1	R2	CoV	Total image score
Siemens Luminos	65	3	3	0	6
	70	3	3	0	6
	75	3	3	0	6
	77	2	3	0.283	5
	81	2	2	0	4
	85	2	2	0	4
	90	1	1	0	2
Shimatzu Sonialvision Safire	65	2.3	2	0.109	4.3
	70	3	3	0	6
	75	3	3	0	6
	80	2.3	3	0.177	5.3
	85	2.3	3	0.177	5.3
	90	2.3	2	0.109	4.3
GE Definium	65	3	3	0	6
	70	3	3	0	6
	75	3	3	0	6
	80	3	3	0	6
	85	3	3	0	6
	90	3	2.7	0.083	5.7

A total of 22 pelvic clinical x-ray images were acquired and analyzed. As expected, radiation dose (ESD and DAP) as well as image quality (CNR) decreased with increasing tube voltage for all X-ray units (Fig. 3. and Fig. 4.). However, percentage change in ESD and DAP was different across each unit. For instance, while increasing the tube voltage by 10 kV from standard value, ESD decreased 18%, 35% and 39% for GE, Shimatzu and Siemens respectively. Overall, ESD and DAP values agreed well in all cases and consequently DAP measurements set by all manufacturers are adequate for estimating patient exposure.



**Fig. 4.** Relationship between tube voltage and image quality (CNR) for the three X-ray equipment.

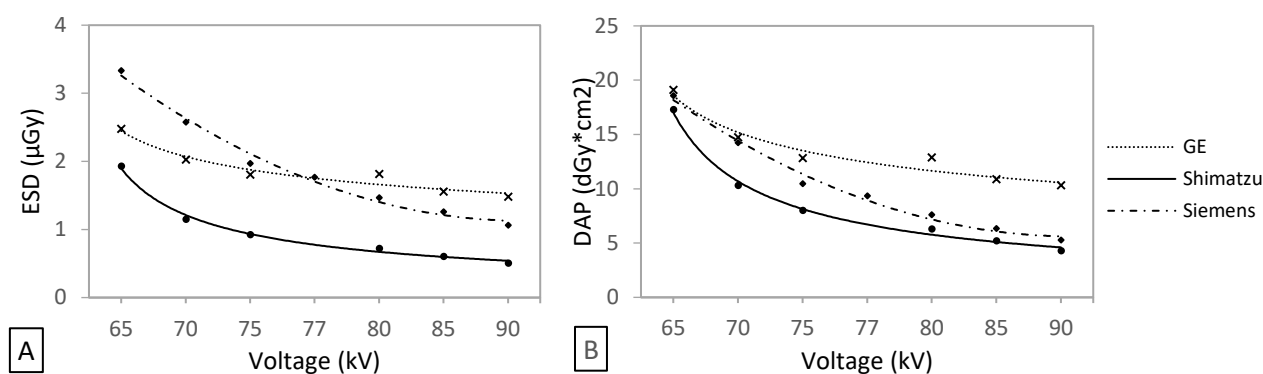


**Fig. 5.** Relationship between tube voltage and delivered dose: (A) ESD measured with the solid detector and (B) DAP automatically registered by each unit.

In order to determine the kV parameter above which the images experience loss of diagnostic information, radiologists rating was compared against physical measurements. There was relatively good agreement between the two radiologists regarding the scoring of image sharpness, noise and diagnostic quality; thus, supporting the validity of our findings (table 3). For GE Definium and Siemens Luminos, the two radiologists agreed on almost all images (except for images obtained at 77 kV and 90 kV for Definium and Luminos respectively). The inter-rater agreement was only moderate in the case of Shimatzu Sonialvision Safire (kappa coefficient = 0.417).

For all X-ray units included in this study, practitioners' ratings of images acquired using standard technical factors were higher in diagnostic quality than those obtained using the dose optimization strategy. For GE and Shimatzu, acquisition done with up to 10 kV above standard protocol were deemed to be of acceptable diagnostic quality. This amount of increase in tube voltage (i.e. +10 kV) appears to be a highly effective dose optimization strategy that decreased ESD by 18% and 35% for GE and Shimatzu respectively (DAP was reduced by 20% and 35% respectively). On the other hand, for Siemens, even the smallest increase in kV above standard voltage resulted in images being rated as suboptimal by both radiologists and thus, optimization is not of clinical benefit. Finally, dose optimization procedure established in this study will be implemented for other digital X-ray units at VUHSK in the near future.

#### 4. Conclusions

This was the first dose optimization study for clinical pelvis protocol at Vilnius University Hospital Santaros Klinikos using a realistic, tissue equivalent anthropomorphic phantom. Optimization strategies can be successful in decreasing radiation doses while maintaining diagnostic image quality in pelvic x-ray examinations performed using digital radiography. The results showed that individual optimization is necessary since technical parameters change between different X-ray units. In this study, optimal exposure parameters were achieved using a combination of physical measurements (CNR, ESD and DAP) which was proven to be key for patient dose optimization and observer-based performance, a method relevant for optimization

based on diagnostic image quality. It should be noted, that the results of investigation performed with anthropomorphic phantom should be validated using clinical images of real patients.

#### Acknowledgment

The authors would like to express their gratitude to the Lithuanian Radiation Protection Center for the possibility of using the pelvic anthropomorphic phantom.

#### 5. References

1. Prasad KN, Cole WC, Hasse GM. Health risks of low dose ionizing radiation in humans: a review. *Exp Biol Med* (Maywood) 2004;229:378–82.
2. United Nations. Report of the United Nations Scientific Committee on the Effects of Atomic Radiation 2010, 57th session: includes scientific report—summary of low-dose radiation effects on health. United Nations Publications website. [unp.un.org/Details.aspx?pid=22259](http://unp.un.org/Details.aspx?pid=22259). Published 2011.
3. International Commission on Radiological Protection. Radiological protection and safety in medicine. ICRP report 73. *Ann ICRP* 1996; 26. doi: 10.1016/s0146-6453(00)89195-2.
4. International Commission on Radiological Protection. Managing Patient Dose in Digital Radiology. Vol. 34. *Ann ICRP*, 2004; 1-74. (ICRP Publication; 93).
5. Andria G, Attivissimo F, Guglielmi G, Lanzolla AML, Maiorana A, Mangiantini M. Towards patient dose optimization in digital radiography. *Meas. J. Int. Meas. Confed.* (2016) <https://doi.org/10.1016/j.measurement.2015.08.015>.
6. Hygiene Standard HN 78:2009 “Quality control requirements and evaluation criteria in medical X-ray diagnostics” adopted by the Order No. V-922 by the Minister of Health Care. 2009.
7. Dosimetry in Diagnostic Radiology: An International Code of Practice. Technical Reports Series No. 457. Vienna: IAEA; 2007.
8. European Commission. European Commission. European guidelines on quality criteria for diagnostic radiographic images. Report EUR 16260. L-2985 Luxembourg: Office for the Official Publications of the European Communities, 1996.



## **FETAL DOSES FOR PREGNANT PATIENTS UNDERGOING CHEST CT EXAMINATIONS**

Larisa CHIPIGA<sup>1</sup>, Aleksandr VODOVATOV<sup>2</sup>, Polina PIVEN<sup>3</sup>, Gleb BERKOVICH<sup>4</sup>, Gennadiy TRUFANOV<sup>5</sup>,  
Irina MASCHENKO<sup>6</sup>, Polina DRUZHININA<sup>7</sup>, Viktor PUZYREV<sup>8</sup>

<sup>1,2,7</sup>Saint-Petersburg Research Institute of Radiation Hygiene after Professor P.V. Ramzaev, St-Petersburg, Russia;

<sup>1</sup>Granov Russian Research Center of Radiology and Surgical Technologies, St-Petersburg, Russia; <sup>1,4,5,6</sup>Almazov National Medical Research Centre, St-Petersburg, Russia; <sup>2,8</sup>St. Petersburg State Pediatric Medical University, St-Petersburg, Russia; <sup>3</sup>Peter the Great Saint-Petersburg Polytechnic University, St-Petersburg, Russia

<sup>1</sup>larisa.chipiga@gmail.com; <sup>2</sup>vodovattoff@gmail.com; <sup>3</sup>polinokp@mail.ru; <sup>4</sup>glebberkovich@gmail.com; <sup>5</sup>trufanovge@mail.ru; <sup>6</sup>mashchenko\_ia@almazovcentre.ru; <sup>7</sup>druzhininapauline@gmail.com; <sup>8</sup>vgpuzyrev@mail.ru

**Abstract:** The aim of this study was to estimate the doses to the fetus from chest CT examinations during the COVID-19 epidemic using NCICT 3.0 and FetalDose software. The absorbed dose in the uterus of the mother and fetal effective dose for the chest CT examinations estimated by NCICT 3.0 were comparable to the fetal absorbed dose estimated by FetalDose and increased with gestational period from 0.07 mGy in the first trimester to 1.5 mGy in the third trimester, depending on the CT model and scan protocol.

**Keywords:** computed tomography, fetal absorbed dose, COVID-19, novel coronavirus infection

### **1. Introduction**

The number of computed tomography (CT) examinations has highly increased in 2020 due to the massive use of this method for the diagnosis of novel coronavirus infection COVID-19, including imaging of pregnant patients [3-4]. CT examinations help in the diagnosis of COVID-19 viral pneumonia, to quickly assess the extent of lung tissue damage and the severity of changes, and to clarify the stage of changes according to patterns specific to novel coronavirus infection. It is possible to quickly route patients and initiate antiviral therapy [5-8] based on CT and clinical data.

The most dangerous effects of ionizing radiation on the fetus are associated with exposure after 3-4 weeks of pregnancy. Fetal absorbed doses exceeding 100 mGy can lead to a significant decrease in intelligence. High sensitivity to exposure is observed during the formation of the central nervous system during 8-15 weeks after conception. Threshold effects also include congenital malformations, growth and developmental delays, and death [9]. Additionally, radiation exposure is associated

**Table 1.** Chest CT protocols for pregnant patients

with an increased risk of developing leukemia and various types of solid cancers [11].

The generally accepted approaches to ensure the radiation protection of pregnant patients [12-13] are:

- justification of X-ray examinations;
- assessment of the absorbed doses in the fetus;

Additional restrictions are introduced in Russian national regulations:

- X-ray examinations should not be performed in the second half of pregnancy, with the exception of cases which require emergency care;

- the absorbed dose limit to the fetus is 100 mGy, in excess of which it is recommended to terminate the pregnancy.

There are no approved methods for assessing the absorbed dose in the fetus in Russian national practice. The lack of reliable national data on fetal radiation doses leads to various kinds of speculation and exaggeration of the negative consequences of CT examinations, including for women with COVID-19.

Hence, the study was aimed at the estimation of the fetal absorbed doses from chest CT examination of pregnant women for diagnostics of the novel coronavirus infection COVID-19. In order to estimate the fetus doses, the parameters of national and foreign chest CT protocols were collected, the absorbed and effective doses in the fetus were estimated using dedicated software, and the conversion coefficients from DLP to the absorbed dose in the mother uterus (fetus) were determined.

### **2. Materials and methods**

#### **2.1. CT protocols**

Data on the chest CT protocols of pregnant patients based on literature sources and collected in medical facilities in St. Petersburg are presented in Table 1.

Nº	Source	CT scanner	kV	mAs	pitch	CTDI <sub>vol</sub> , mGy	Gestation period
Protocols used for chest CT examinations of pregnant patients presented in literature sources (foreign)							
1	H. Liu, et al. 2020 [14]	uCT780, United imaging, China, or Optima 660, GE (64-section multi-detector CT scanner)	120	10-300	1.0875 or 1.375	-	From 20 to 40 weeks
2	Shahir, et al. 2010 [15]	LightSpeed Ultra, LightSpeed Plus, or LightSpeed VCT, GE (8-, 16-, or 64-MDCT scanner)	120-140	150-300	1	-	First, second and third trimesters
3	D. Liu, et al. 2020 [5]	Ingenuity Core 128, Philips	120	-	-	2.3 – 5.8	From 12 to 38 weeks
4	Angle, et al. 2008 [16]	LightSpeed 16, GE	120	100-300	1.375	-	From 5 to 36 weeks
Protocols used for patients with suspected or diagnosed COVID-19 in St. Petersburg, 2020-2021 (national)							
5	-	Ingenuity Core 128, Philips	100	142	1.048	-	All terms
6	-	Somatom Definition AS, Siemens	120	175	-	-	All terms
7	-	Somatom Scope, Siemens	110	75	1.5	-	All terms
8	-	Emotion 16, Siemens	130	60	1.5	-	All terms

## 2.2. Methods for the fetal doses estimation

Calculation of absorbed doses in the mother uterus, as well as the fetal effective dose was performed using the NCICT3.0 software [17-20], based on the family of UF phantoms of women of 8th, 10th, 15th, 20th, 25th, 30th, 35th, 38th weeks of pregnancy [21]. Fetal absorbed doses were estimated using the online calculator FetalDose [22], that is based on a series of hybrid RPI-P3, -P6, and -P9 phantoms (third, sixth, and ninth months of pregnancy, respectively) [23]. Fetal masses for phantoms of pregnant women from NCICT3.0 and FetalDose are presented in Table 2.

The standard scan length in the NCICT 3.0 of 330 mm starting from the clavicle was used as the constant typical scan length, for both calculation methods.

Since the calculation of fetal absorbed doses was performed for the available chest CT protocols (without data on radiation doses for individual patients), the following data processing scheme was used in the study:

- determination of CTDI<sub>vol</sub> and DLP for 32 cm standard phantom in the NCICT 3.0 software for each CT protocol (Table 1) based on the CT model, voltage, mAs, pitch, collimation;
- calculation of the absorbed dose in the mother uterus and the fetal effective dose using NCICT 3.0 and CTDI<sub>vol</sub> for all available gestation periods (8, 10, 15, 20, 25, 30, 35 and 38 weeks);
- calculation of the fetal absorbed dose using online calculator FetalDose, voltage and CTDI<sub>vol</sub> for all pregnancy trimesters.

Statistical data processing was performed using Statistica 10 software. Spearman's correlation analysis was used to determine the relationship between the characteristics; To determine the differences between the samples - the Kruskal-Wallis test with additional pairwise comparison

by the Mann-Whitney test. All differences were considered significant at  $p < 0.05$ .

**Table 2.** Fetal weights in phantoms of pregnant women in NCICT 3.0 and FetalDose.

UF phantoms of pregnant patient NCICT 3.0		RPI phantoms of pregnant patient FetalDose	
Phantom, gestational age	mass, g	Phantom, gestational age	mass, g
UFHF08WK, 8 weeks	3,57	RPI-P3, 3 months	71
UFHF10WK, 10 weeks	21,1		
UFHF15WK, 15 weeks	146	RPI-P6, 6 months	902
UFHF20WK, 20 weeks	467		
UFHF25WK, 25 weeks	984		
UFHF30WK, 30 weeks	1690	RPI-P9, 9 months	2754
UFHF35WK, 35 weeks	2560		
UFHF38WK, 38 weeks	3196		

## 3. Results and discussion

The results of estimation of absorbed dose in the mother uterus and fetal absorbed and effective doses are presented in Fig. 1. The radiation weighting factor for X-ray radiation is 1 so it is possible to compare the absorbed doses in fetus and uterus with the fetal effective dose determined by NCICT 3.0.

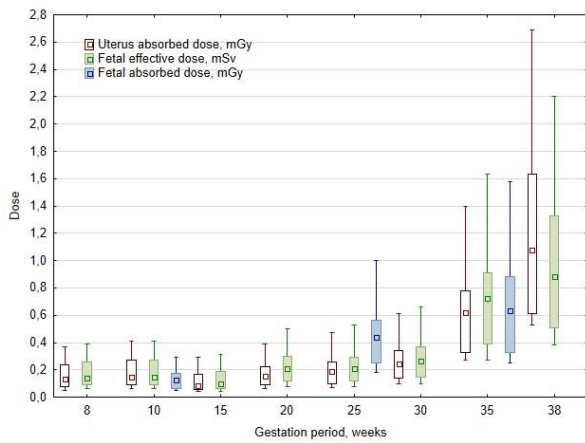


**Fig. 1.** Absorbed dose in mother uterus and fetal effective dose (NCICT 3.0), fetal absorbed dose (FetalDose) for combined sample of CT scanners/protocols for different gestation periods.

There were no significant differences between the samples of absorbed doses in the mother uterus and fetal effective doses estimated using NCICT 3.0, for each gestational period (Mann-Whitney test,  $p > 0.05$ ) according to Fig. 1. Absorbed doses in the mother uterus and fetal effective doses have a significant correlation ( $r = 0.99$ ;  $r^2 = 0.99$ ). This allows using absorbed doses in the mother uterus to assess the fetal doses by software without dedicated pregnant phantoms and with phantoms of different body thickness (for example, XCATdose) [21, 24].

Mass of 3-, 6- and 9-months fetus in FetalDose approximately corresponds to mass of 12, 24 and 36 weeks fetus in NCICT 3.0 (Table 2). Fetal absorbed doses estimated for 3- and 9-months gestation by FetalDose were comparable to both absorbed doses in the mother uterus and fetal effective doses estimated by NCICT 3.0 (significant differences were absent, Mann-Whitney test,  $p > 0.05$ ). The significant difference up to a factor of 1.5 (Mann-Whitney test,  $p < 0.05$ ) were observed between fetal absorbed dose for 6 months of pregnancy by FetalDose and absorbed dose in the uterus for 24 week of pregnancy by NCICT 3.0. That can be explained by differences in the used women models (phantoms). The limited number of phantoms used in the online calculator FetalDose does not allow to use it for more accurate dose estimation.

The median absorbed doses in the mother uterus were approximately constant (0.1 mGy) for a sample of national scanners and 0.25 mGy for a sample of foreign scanners for a range of 1 to 30 weeks (Fig. 2). The absorbed doses begin to increase on average by a factor of two from the 30th week. Median absorbed doses in the uterus for 38 week were 1.6 and 0.6 mGy for samples of foreign and national scanners, respectively; the maximum are 2.7 and 1.0 mGy, respectively. The obtained results demonstrate that the limit for deterministic effects in the fetus (100 mGy) cannot be exceeded even for multiple chest CT examinations. Nevertheless, it is necessary to prognostically assess the fetal absorbed dose before X-ray examination (to assess the potential excess of the 100 mGy) and to estimate real fetal absorbed dose after the examination based on the scan parameters,  $CTDI_{vol}$  or DLP according the national regulations.

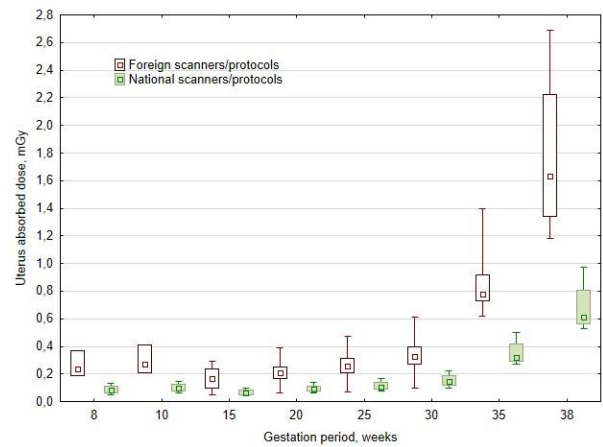


**Fig. 2.** Absorbed doses in the mother uterus estimated by NCICT 3.0 for foreign and national scanners/protocols.

Due to the lack national methods and/or software products for fetal absorbed doses from CT examinations, the conversion coefficients from DLP to fetal absorbed dose (uterus absorbed dose) were estimated using NCICT 3.0. The conversion coefficients are presented in Table 3. They were determined for investigated CT protocol parameters: voltage range presented in Table 1 (100-130 kV), 330 mm scan length starting from the clavicle. These coefficients are developed to provide a quick way to estimate fetal absorbed dose; for a more accurate and correct assessment of fetal dose, it is recommended to use dedicated software, for example, NCICT 3.0 considering the scan length or other CT protocols parameters.

**Table 3.** The conversion coefficients from DLP to the fetal absorbed dose for chest CT examinations.

Gestation period, weeks	$K_{D/DLP}$ , $\mu Gy / (mGy \times cm)$
8	0.41
10	0.46
15	0.33
20	0.44
25	0.54
30	0.71
35	1.46
38	3.1

#### 4. Conclusion

The results of comparison of absorbed doses in the mother uterus, fetal effective and absorbed doses at different gestation periods using NCICT 3.0 and FetalDose indicate that absorbed doses in the uterus and fetal effective doses do not differ significantly for all gestation periods of pregnancy and are approximately at the same level of 0.2 mGy (mSv) for periods of 8-25 weeks, 0.3 mGy (mSv) for 30 weeks, 0.7 mGy (mSv) for 35 weeks, and 1 mGy (mSv) for week 38. The use of the FetalDose is not recommended due to the limited number of phantoms (3 gestation periods) and low accuracy of the absorbed dose estimation.

The limit for the development of fetal deterministic effects (100 mGy) cannot be reached even for multiple (up to 10-15 times) chest CT examinations. Hence, chest CT can be recommended for diagnostics and staging of COVID-19 for pregnant women in the Russian Federation with mandatory assessment of the fetal absorbed dose before and after examination.

The conversion coefficients from DLP to fetal absorbed dose for different gestation periods were determined in the current study. These conversion coefficients can be used in national practice for rough estimation of the fetal dose from chest CT examination of pregnant women. Further study will aim to expand the list of anatomical scan areas with consideration of different CT protocols parameters.

## References

1. Damilakis J. CT Dosimetry: What Has Been Achieved and What Remains to Be Done. *Invest Radiol.* 2021 Jan;56(1):62-68. doi: 10.1097/RLI.0000000000000727. PMID: 32932380
2. Onischenko G.G., Popova A.Yu., Romanovich I.K., Vodovatov A.V., Bashketova N.S., Istorik O.A., Chipiga L.A., Shatsky I.G., Sarycheva S.S., Biblin A.M., Repin L.V. Modern principles of the radiation protection from sources of ionizing radiation in medicine. Part 2: radiation risks and development of the system of radiation protection. *Radiatsionnaya Gygiena = Radiation Hygiene.* 2019;12(2):6-24. (In Russ.) <https://doi.org/10.21514/1998-426X-2019-12-2-6-24>
3. Stopcoronavirus.RF - Online resource. Available at: <https://xn--80aesfpebagmblc0a.xn--p1ai/> Last access: 20.07.2021 r.;
4. Zhao W, Zhong Z, Xie X, Yu Q, Liu J. Relation between chest CT findings and clinical conditions of coronavirus disease (COVID-19) pneumonia: a multicenter study. *AJR* 2020; 214:1072–1077 - Online resource. Available at: <https://www.ajronline.org/doi/abs/10.2214/AJR.20.23288> Last access: 20.07.2021
5. Dehan L. Pregnancy and Perinatal Outcomes of Women with Coronavirus Disease (COVID-19) Pneumonia: A Preliminary Analysis/ L. Dehan, L. Lin, W. Xin [et al] // *AJR* – 2020 – P.P. 127-132.
6. A.V. Vodovatov, Romanovich I.K., Istorik O.A., Eremina L.A., S.P. Morozov, Ryzhov S.A., Berkovich G.V., Kamysanskaya I.G., Trufanov G.E., Chipiga L.A., Druzhinina P.S., Biblin A.M., Akhmatdinov R.R., Basek I.V., Karatetskiy A.A., D. V. Merkulov, Ispravnikova Yu.S., Pritz V.V., Polishchuk N.S., Mukhortova A.N., Pyzyrev V.G. PRERINT - Preliminary assessment of structure and collective dose from CT examinations related to COVID-19 diagnostics in the Russian Federation in March -June 2020. (In Russ)
7. A.V. Vodovatov, Romanovich I.K., Istorik O.A., Eremina L.A., S.P. Morozov, Ryzhov S.A., Berkovich G.V., Kamysanskaya I.G., Trufanov G.E., Chipiga L.A., Druzhinina P.S., Biblin A.M., Akhmatdinov R.R., Basek I.V., Karatetskiy A.A., D. V. Merkulov, Ispravnikova Yu.S., Pritz V.V., Polishchuk N.S., Mukhortova A.N., Pyzyrev V.G. PRERINT - Preliminary assessment of structure and collective dose from CT examinations related to COVID-19 diagnostics in the Russian Federation in March -June 2020. <https://doi.org/10.1101/2020.08.25.20181396>
8. Doll R. Risk of childhood cancer from fetal irradiation/ R. Doll, R. Wakeford // *Drit. J. Radiol.* 70. – 1997 – P.P. 130-139.
9. Emilie Tremblay et al. Quality Initiatives Guidelines for Use of Medical Imaging during Pregnancy and Lactation/Emilie Tremblay, Eric Thérèse, Isabelle Thomassin-Naggara, Isabelle Trop//*Radiographics* - 2012;32(3):897-911pp. doi: 10.1148/rg.323115120
10. ICRP. Recommendations International Commission on Radiation Protection 2007. Publication ICRP No. 103. Transl. from English / Ed. M.F.M. Kiseleva and N.K. Shandaly. M., Ed. LLC PKF "Alana". 2009. - 312p.
11. ICRP (2000) Pregnancy and Medical Radiation. ICRP Publication 84, Annals of the ICRP; 30: P.P. 1– 43.
12. International Atomic Energy Agency. Radiation Protection and Safety of Radiation Sources: International Basic Safety Standards. General safety requirements. IAEA Safety Standards Series No. GSR Part 3. - Vienna: IAEA, 250 p. (2015).
13. International Atomic Energy Agency. Radiation Protection and Safety in Medical Uses of Ionizing Radiation. Specific Safety Guide, №SSG-46. – Vienna: IAEA, 318 p. (2018).
14. Huanhuan L. Clinical and CT imaging features of the COVID-19 pneumonia: Focus on pregnant women and children/ L. Huanhuan, L. Fang, L. Jining [et al] // *Journal of Infection* – 2020 – P.P. 7 – 13.
15. Shahir K. Pulmonary Embolism in Pregnancy: CT Pulmonary Angiography Versus Perfusion Scanning/ K. Shahir, L.R. Goodman, A. Tali [et al] // *AJR*:195 – 2010.
16. Angel E. Radiation dose to the fetus for pregnant patients undergoing multidetector CT imaging: Monte Carlo simulations estimating fetal dose for a range of gestational age and patient size/ E. Angel, C.V. Wellnitz, M.M. Goodsitt [et al] // *Radiology.* 2008;249(1):220-7. DOI:10.1148/radiol.2491071665
17. Lee, C., Kim, K. P., Bolch, W. E., Moroz, B. E., Folio, L. NCICT: a computational solution to estimate organ doses for pediatric and adult patients undergoing CT scans. *J Radiol Prot.* 35(4), 891–909 (2015). doi: 10.1088/0952-4746/35/4/891
18. <https://www.fetaldose.org/calculator/>; Saltybaeva, N., Platon, A., Poletti, P.-A., Hinzpeter, R., Merce, M. S., & Alkadhi, H. (2020). Radiation Dose to the Fetus From Computed Tomography of Pregnant Patients—Development and Validation of a Web-Based Tool. *Investigative Radiology*, 55(12), 762–768. doi:10.1097/rli.0000000000000701
19. Larisa Chipiga, Vladislav Golikov, Aleksandr Vodovatov, Christian Bernhardsson. Comparison of Organ Absorbed Doses in Whole-Body Computed Tomography Scans of Paediatric and Adult Patient Models Estimated by Different Methods. *Radiation Protection Dosimetry*, ncab086, <https://doi.org/10.1093/rpd/ncab086>;
20. Chipiga L.A. A comparison of computational methods for estimation of effective and organ doses to the patients from CT examination. *Radiatsionnaya Gygiena = Radiation Hygiene.* 2017;10(1):56-64. (In Russ.) <https://doi.org/10.21514/1998-426X-2017-10-1-56-64>
21. Chipiga L.A. A comparison of computational methods for estimation of effective and organ doses to the patients from CT examination. *Radiatsionnaya Gygiena = Radiation Hygiene.* 2017;10(1):56-64. (In Russ.) <https://doi.org/10.21514/1998-426X-2017-10-1-56-64>
22. Maynard, M. R., Long, N. S., Moawad, N. S., Shifrin, R. Y., Geyer, A. M., Fong, G., & Bolch, W. E. (2014). The UF Family of hybrid phantoms of the pregnant female for computational radiation dosimetry. *Physics in Medicine and Biology*, 59(15), 4325–4343. doi:10.1088/0031-9155/59/15/4325
23. Xu XG, Taranenko V, Zhang J, et al. A boundary-representation method for designing whole-body radiation dosimetry models: pregnant females at the ends of three gestational periods—RPI-P3, -P6 and -P9. *Phys Med Biol.* 2007;52:7023–7044.
24. Sahbaee P., Segars W.P., Samei E. [Et al.] Patient-based estimation of organ dose for a population of 58 adult patients across 13 protocol categories. *Medical Physics*, 2014, Vol. 41, № 7, pp. 072104-1– 072104-12.

## ASSESSMENT OF EXTREMITY EXPOSURE FOR NUCLEAR MEDICINE PERSONNEL

Inga ANDRIULEVIČIŪTĖ<sup>1,2</sup>, Kirill SKOVORODKO<sup>2,3</sup>, Jurgita LAURIKAITIENĖ<sup>1</sup>, Birutė GRICIENĖ<sup>2,4</sup>

<sup>1</sup>Kaunas University of Technology, Kaunas, Lithuania; <sup>2</sup>Vilnius University Hospital Santaros Klinikos, Vilnius, Lithuania; <sup>3</sup>Center for Physical Sciences and Technology (FTMC), Vilnius, Lithuania; <sup>4</sup>Vilnius University, Faculty of Medicine, Institute of Biomedical Sciences, Vilnius, Lithuania.

<sup>1</sup>inga.andriuleviciute@gmail.com; <sup>2</sup>kirill.skov@gmail.com; <sup>3</sup>jurgita.laurikaitiene@ktu.lt;  
<sup>4</sup>birute.griciene@gmail.com

**Abstract:** The extremity exposure monitoring of nuclear medicine personnel is essential to control exposure in the workplace, to ensure that legal limits are not exceeded, to predict extremity doses and, if possible, to optimize workflow. Distribution of the doses over hand is nonuniform and the obtained doses by  $H_p(0.07)$  passive dosimeter can be significantly lower compared to fingertips. The aim of this study was to assess the extremity exposure of nuclear medicine workers working with  $^{99m}\text{Tc}$  radionuclide.

**Keywords:** nuclear medicine, occupational exposure, hand exposure, thermoluminescence dosimetry.

### 1. Introduction

Rapid development of medical technology and radiopharmacy resulted in significant growth of the nuclear medicine (NM) field and an increased number of NM procedures performed each year. Despite precautions (e.g. shielding, appropriate storage, distance between the sources, administrative procedures, etc.) having been implemented into NM departments, the radionuclide activity that the staff has to deal with is higher due greater number of patients and this might lead to higher annual doses.

The specifics of the work of NM workers include positioning, supervising patients during image acquisition, preparation and administration of radiopharmaceuticals in daily practice. During radiopharmaceutical preparation NM staff hands come into very close contact with the radionuclides leading to higher occupational exposure doses to extremities. According to Radiation Protection Centre, NM workers are one of the most occupationally exposed medical groups in Lithuania, which received the average annual equivalent dose  $H_p(0.07)$  of 17.4 mSv in 2020 [1]. Based on studies [2-3], highest radiation doses in the NM field are received by radiology technologists.

Nowadays, monitoring of NM personnel is performed by wearing a single passive ring dosimeter on the base of the finger of the dominant hand. However, published studies show [2-6] that the most exposed parts of the hand are fingertips. Furthermore, according to ORAMED project [7], which evaluated extremity doses of workers in 32 NM departments in Europe, the doses obtained by the ring dosimeter can be 2-6 times lower compared with the doses of fingertips, leaving a chance of exceeding the recommended annual equivalent dose limit of 500 mSv.

The aim of this study was to evaluate hand doses in different points for radiology technologists of the Nuclear Medicine Department of Vilnius University Hospital Santaros Klinikos working with  $^{99m}\text{Tc}$  radioisotope.

### 2. Materials and methods

#### 2.1. Calibration of dosimeters

For the measurements of hand doses, thermoluminescent dosimeters (TLD-100 (LiF:Mg, Ti)) chips were used. The thickness of these dosimeters was 2 mm, the diameter 4.5 mm. Since the effective atomic number ( $Z_{\text{eff}}$ ) of TLD-100 is 8.14 and it is nearly tissue equivalent, its scattering and absorption properties are similar to those of human tissue ( $Z_{\text{eff}} = 7.42$ ).

TLD-100 chips were calibrated with  $^{99m}\text{Tc}$  source (Fig. 1) in a dose range of (0.5-4) mSv.

The vials (standard 10 mL) were prepared by a radiology technologist in the hot laboratory. The  $^{99m}\text{Tc}$  was extracted from the  $^{99}\text{Mo}/^{99m}\text{Tc}$  generator and was used as  $^{99m}\text{TcO}_4^-$  solution.

The activity meter Veenstra VDC-405 was used for checking of activity (< 3% deviation). The readings of activity meter were verified by the secondary standard chamber Capintec CRC-15R, No. 158488 ( $4\pi$   $\gamma$  ionization chamber) brought to hospitals by the Ionizing

Radiation Metrology Laboratory of the FTMC that is the National Metrology Institute (NMI) in Lithuania.



Fig. 1. Calibration of TLD-100 chips with  $^{99m}\text{Tc}$  source.

Dosimeters were read at Kaunas University of Technology using Rialto TLD system (Fig. 2).



Fig. 2. Rialto TLD system.

## 2.2. Hand dose measurements

Hand dose measurements were performed for radiology technologists of Nuclear Medicine Department who prepare and inject  $^{99m}\text{Tc}$ -labelled radiopharmaceuticals. All dosimeters were put in plastic envelopes to prevent TLDs from contamination, disinfection reasons and were attached to both hands on a palm side at 14 locations (dosimeters No. 1-14, 7 chips on each hand) under disposable gloves (Fig. 3.). Additionally, to evaluate and compare the difference between obtained doses from typical monitoring position (base of a middle finger of the dominant hand) and the most exposed part, dosimeter No. 15 was attached in part of the measurements while working with  $^{99m}\text{Tc}$ .

Each technologist working with  $^{99m}\text{Tc}$  wore dosimeters from 5 to 8 days depending on total radionuclide activity.

Working process was split into two steps: to measure workflow in a hot lab and to administer  $^{99m}\text{Tc}$ -labelled radiopharmaceuticals to patients.

The activity working with  $^{99m}\text{Tc}$  in a hot lab was in a range of 26.80-38.76 GBq (average  $31.99 \pm 4.32$  GBq), for injections 12.01-19.25 GBq (average  $14.54 \pm 4.09$  GBq).

The right hand was the dominant hand of all radiology technologists. The measured doses were normalized per manipulated activity (mSv/GBq).



Fig. 3. TLDs positions on the radiology technologist palms.

## 3. Results

### 3.1. Extremity doses during work with $^{99m}\text{Tc}$

During work with  $^{99m}\text{Tc}$  in a hot lab, it was found that the dominant (right) hand received higher doses by 2.18 times compared with the non-dominant (left) hand and resulted in 0.37 and 0.17 mSv/GBq, respectively. The most exposed parts were the right hand thumb tip 0.73 mSv/GBq, index finger tip 0.52 mSv/GBq and middle finger tip 0.62 mSv/GBq.

The same tendency of dose distribution was also seen in the left hand – the most exposed parts were the tips of the thumb, index finger and middle finger and resulted in average doses of 0.27, 0.37 and 0.21 mSv/GBq, respectively (Fig. 4.).

During preparation of radiopharmaceuticals, the least exposed parts were the left hand palm and wrist and the obtained doses were lower than  $<0.1$  mSv/GBq.

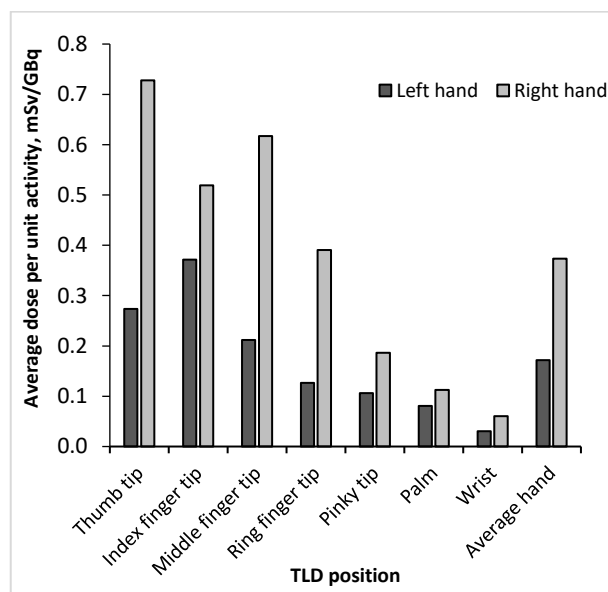
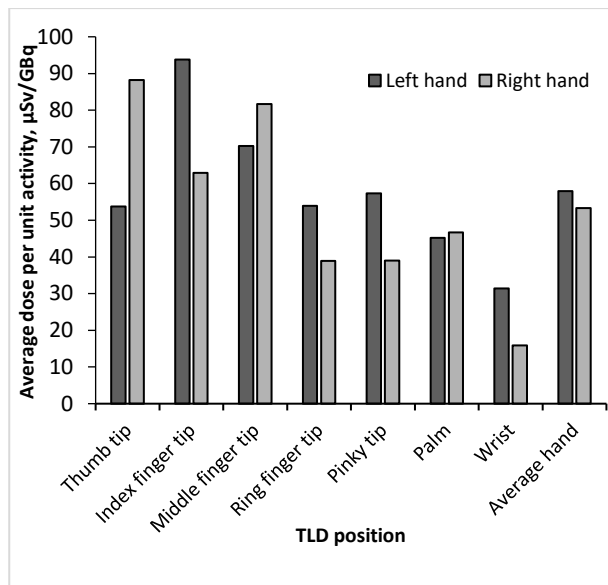


Fig. 4. Hand dose distribution of different TLD positions while working in a hot lab with  $^{99m}\text{Tc}$ .



During  $^{99m}\text{Tc}$  radiopharmaceutical injection to patients, the dose distribution was slightly different compared with the doses obtained while preparing  $^{99m}\text{Tc}$ -labelled radiopharmaceuticals. It was found that the most exposed part was the non-dominant (left) hand index finger tip ( $93.80 \mu\text{Sv/GBq}$ ), however, the difference between average doses of non-dominant and dominant hand were almost the same and resulted in ( $57.94 \pm 14.64$ ) and ( $53.33 \pm 11.87$ )  $\mu\text{Sv/GBq}$ , respectively. Besides doses of the left hand index finger tip, higher average doses per unit activity were also obtained by the right hand thumb tip ( $88.25 \mu\text{Sv/GBq}$ ) and middle finger tip ( $81.67 \mu\text{Sv/GBq}$ ), and the least exposed parts were the left ( $31.39 \mu\text{Sv/GBq}$ ) and right ( $15.90 \mu\text{Sv/GBq}$ ) hand wrists (Fig. 5).



**Fig. 5.** Hand dose distribution of different TLD positions while administering  $^{99m}\text{Tc}$ -labelled radiopharmaceuticals

### 3.2. Doses obtained from typical monitoring position

During 4 measurements performed while working with  $^{99m}\text{Tc}$ , radiology technologists wore an additional dosimeter on typical monitoring position (base of a middle finger of the dominant hand). As seen from Table 1, the maximum dose of fingertip is 2.0-2.4 times higher compared with the doses from typical monitoring position.

**Table 1.** The ratio of maximum hand dose ( $H_p(0.07)_{\text{max}}$ ) and typical monitoring position dose  $H_p(0.07)_{\text{tmp}}$  received during work with  $^{99m}\text{Tc}$ .

No.	$(H_p(0.07)_{\text{max}}, \text{mSv/GBq})$	$H_p(0.07)_{\text{tmp}}, \text{mSv/GBq}$	Ratio, a.u.
1.	0.55	0.23	2.4
2.	0.10	0.05	2.0
3.	0.09	0.04	2.3
4.	0.16	0.07	2.3

### 4. Discussion

Assessment of extremity exposure for NM personnel shows that there is a tendency that the most exposed hand while preparing radiopharmaceuticals is the dominant hand. Similar findings were obtained by other

authors as well (Table 2). Adliene et al. [3], Leide-Svegborn [8] researches reveal that the right hand thumb received the highest doses. Zoccarato et al. [4] also investigated fingertip doses in 4 points (index tip, index base and wrist of the non-dominant hand, and index tip of the dominant hand) and found that the dominant hand is more exposed than the non-dominant hand. However, doses greatly depends on the type of the procedure (radiopharmaceutical preparation, administration, etc.) As it was found in our and Carnicer et al. [7] study, during radiopharmaceutical injection, the most exposed part is index finger tip of non-dominant which could be explained by the fact that the radiology technologists hold the patient's hand directly at the injection site for greater stability.

**Table 2.** Summary of extremity dose results of different studies

Reference	Number of measured locations	Max. dose of fingertip, mSv/GBq (dosimeter position)	Method
This study, 2021	15	1.1 (right hand thumb)	Preparation
		0.114 (left hand index finger tip)	Injection
Adliene et al., 2020 [3]	20	1.93 (right hand thumb)	Preparation and injection
Zoccarato et al. [4]	4	0.067 (right and index finger tip)	Preparation
Carnicer et al., 2011 [7]	22	0.95 (left hand index finger tip)	Injection
Leide-Svegborn, 2011 [8]	11	0.00012 (right hand thumb)	Preparation

### 4. Conclusions

The results of our study showed that the most exposed parts while working with open radioactive sources are fingertips of thumb, index finger and middle finger, thus, monitoring of these points would be the most expedient. Also, it was found that the maximum fingertip doses are 2.0-2.4 times higher compared with the doses from typical monitoring position (base of a middle finger of the dominant hand).

Dose distribution over the hand palm depends on the radionuclide and working procedures, workers' habits, different work approach and optimization means: proper hot lab, shielded syringe, etc. To ensure radiation safety of personnel and keep  $H_p(0.07)$  doses as low as possible, work position rotation (radiopharmaceutical preparation, administration, positioning of the patient for the exam) that is performed in our hospital, is essential. Our study shows that detailed investigation of extremity doses in NM is important to identify the most problematic areas where the doses are highest, to optimize personnel workflow, and to recommend the dosimeter position for routine monitoring for each worker depending on the maximum doses collected by an individual.

## 5. References

1. 2017–2023 metų gyventojų ir darbuotojų, dirbančių su jonizuojančiosios spinduliuotės šaltiniais, apšvitos stebėsenos programos 2020 metų ataskaita. Radiacinės saugos centras, 2021, p. 69.
2. Lee W. J., Choi Y., Ko S., Cha E. S., Kim J., Kim Y. M., Ha Y. W. Projected lifetime cancer risks from occupational radiation exposure among diagnostic medical radiation workers in South Korea. *BMC cancer*, 18(1), 2018, p. 1-10.
3. Adliene D., Gričienė B., Skovorodko K., Laurikaitienė J., Puiso J. Occupational radiation exposure of health professionals and cancer risk assessment for Lithuanian nuclear medicine workers. *Environmental research*, 2020.
4. Zoccarato O., Matheoud R., Zanni D., Vigna L., Campini R., De Crescenzo S., Brambilla M. Extremity doses assessment of nuclear medicine staff involved in  $^{99m}\text{Tc}$ -radiopharmaceuticals preparation: A multicentre study. *Physica Medica*, 32, 2016, p. 230.
5. Sans Merce M., Ruiz N., Barth I., Carnicer A., Donadille L., Ferrari P., Baechler S. Extremity exposure in nuclear medicine: preliminary results of a European study. *Radiation protection dosimetry*, 144(1-4), 2011, p. 515-520.
6. Wrzesień M., Albinia L. Hand exposure of workers in  $^{18}\text{F}$ -FDG production centre. *Journal of Radiological Protection*, 36(4), N67, 2016.
7. Carnicer A., Sans-Merce M., Baechler S., Barth I., Donadille L., Ferrari P., Vanhavere F. Hand exposure in diagnostic nuclear medicine with  $^{18}\text{F}$ - and  $^{99m}\text{Tc}$ -labelled radiopharmaceuticals-Results of the ORAMED project. *Radiation Measurements*, 46(11), p. 1277-1282, 2011.
8. Leide-Svegborn S. External radiation exposure of personnel in nuclear medicine from  $^{18}\text{F}$ ,  $^{99m}\text{Tc}$  and  $^{131}\text{I}$  with special reference to fingers, eyes and thyroid. *Radiation protection dosimetry*, 149(2), 2012, p. 196-206.

## **PET-CT AND OCCUPATIONAL EXPOSURE: COHORT PROFILE UPDATE**

Mikhail V. OSIPOV<sup>1</sup>, Andrey V. VAZHENIN<sup>2</sup>, Daria A. VAZHENINA<sup>2</sup>, Tatyana S. NOVIKOVA<sup>2</sup>, Anna I. KUZNETSOVA<sup>2</sup>, Irina A. AKSENOVA<sup>2</sup>, Mikhail E. SOKOLNIKOV<sup>1</sup>

<sup>1</sup>Southern Urals Biophysics Institute; <sup>2</sup>Chelyabinsk Regional Clinical Center for Oncology and Nuclear Medicine  
<sup>1</sup>ferrum76@mail.ru; <sup>2</sup>2443632@mail.ru;

**Abstract:** The paper describes the results of updated analyses of diagnostic radiation exposure effects on patients examined using PET-CT in Chelyabinsk Regional Clinical Center of Oncology and Nuclear Medicine since 2010 to 2019. Cancer mortality was analyzed in terms of PET-CT number, radiotherapy, occupational exposure and main non-radiation factors: sex, age attained, stage of malignancy and chemotherapy. Logistic regression has been applied to assess the influence of risk factors on cancer death.

**Keywords:** PET-CT, nuclear workers, cancer, medical exposure, radiation risk

### **1. Introduction**

Positron emission tomography (PET) is a modern technique for diagnostic imaging in nuclear medicine that is intended to visualize metabolic processes in malignant tissues. Combined with computed tomography (CT) it substantially enhances the diagnostic results [1]. Although PET-CT procedures usually resulted in a low dose of radiation, repeated diagnostic procedures may increase the diagnostic radiation burden of patients [2]. It is known that external radiation may affect the cancer mortality [3]. In the same time, during the process of cancer diagnostics and treatment, the patient is under the exposure to various risk factors of radiation and non-radiation nature other than PET-CT such as widely used in clinical practice computed tomography (CT) [4], and the exposures that are only specific for oncological patients: radiotherapy and/or chemotherapy. Exposure to man-made radiation other than diagnostic procedures such as occupational ionizing radiation among professionals [5] is also important as an additional risk factor.

The question whether the effects of cumulative exposure to multiple factors are present in the group of oncological patients, and how is the role of diagnostic exposure of oncological patients itself is of concern.

According to that, the objective of the work was to estimate the overall mortality risk related to the exposure to PET-CT among oncological patients in

regard with several confounding factors to understand the role of “pure” PET-CT diagnostic exposure in cancer mortality.

### **2. Material and Methods**

The cohort profile has been updated with new information on vital status and the cause of death, radiotherapy and chemotherapy data.

The information on examinations using hybrid PET-computed tomography (PET-CT) with administered radiopharmaceutical of <sup>18</sup>F-2-fluoro-2-deoxy-d-glucose (FDG) for residents of Ozyorsk District located in the Chelyabinsk Region 15 km far from the first nuclear weapon production complex in the former USSR has been derived from the archive of PET-Center of Chelyabinsk Regional Clinical Center for Oncology and Nuclear Medicine (CRCONM). The data collection process, criteria of inclusion in the cohort and the follow-up conditions, and the dose calculation methodology has been described in details in our previous study [6] using the recommendations [7-8].

In this study vital status information has been updated for patients up to 31.12.2020. The patients with no information on vital status due to migration have been treated as lost to follow-up.

The information on additional CT examinations outside PET-Center of CRCONM has been obtained using the “CT Registry” database [9] which is currently consists of 26,626 individual records.

Cancer death after the 1<sup>st</sup> PET-CT examination was used as the event to be analyzed based on the hypothesis ( $h_i$ ) that exposure to PET confounded by other radiation and non-radiation factors increased the probability of the event occurrence over time.

Binomial odds were calculated as the ratio of probability of an event occurred to the probability of its non-occurrence (1):

$$Odds = P/(1 - P) \quad (1)$$

The logit function was used as the log of the odds ratio (2):

$$OR = \ln(x_i \beta) \quad (2)$$

Multiple logistic regression [10] has been used for statistical modelling a set of multiple parameters  $x_i$  (3):

$$P(y_i \neq 0 | x_i) = \exp(x_i \beta) / 1 + \exp(x_i \beta) \quad (3)$$

The results of fitting the multiple logistic regression model with different parameters  $x_i$  has been tested using likelihood ratio test (LRT). Pseudo  $R^2$  as a coefficient of determination used to assess the dispersion of the dependent variable  $x_i$  described with logistic regression model.

The Wald's Chi-square test for OR estimates ( $\beta$ ) has been performed using 95% level of significance with  $p < 0.05$ . The distribution of the events by follow-up time was presented using Kaplan-Meier survival function.

### 3. Results

#### 3.1 Age and sex distribution

The information from 651 PET-CT protocols of 347 oncological patients examined in the CRCONM in the period since 2010 to 2019 has been used for the analyses. The age and sex distribution among the patients of the study group shown in Fig. 1:

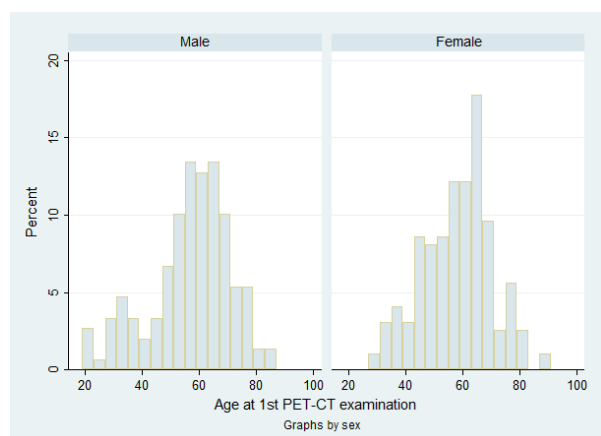


**Fig. 1.** Distribution of the study group by the age at 1<sup>st</sup> PET-CT exposure and sex

In the study group were 42.9% males and 57.1% females at the age from 19 to 91 years to the date of 1<sup>st</sup> PET-CT examination (average  $57.1 \pm 0.7$  years).

Testing the age difference within the study group by sex resulted in the  $(\text{Prob} > F) = 0.35$  that shows no difference between the means of age at 1<sup>st</sup> PET-CT examination among male and female.

#### 3.2 Dosimetry information

35.4% of the study group underwent multiple PET-CT examinations (up to 11 recurrent PET-CT). An additional CT examinations performed outside CRCONM has been accounted using "CT Register" database was 4 (min 1; max 29). The distribution of patients by number of PET-CT, average effective dose

(ED) and administered activity of FDG shown in Table 1.

**Table 1.** The number and the proportion of PET-CT, mean cumulative effective dose from PET-CT examination (ED) and the mean cumulative administered FDG activity (A, mbq)

PET-CT	n	%	ED (std.er)	A, mbq(std.er)
1	225	64.8	22.2 (0.5)	391.2 (5.6)
2	66	19.3	23.1 (0.7)	806.8 (14.9)
3	19	5.2	22.6 (1.4)	1185.8 (36.9)
4-5	22	6.3	24.5 (2.3)	1682.2 (63.7)
6-8	11	3.2	20.6 (1.5)	2599.8 (130.2)
9>	4	1.2	23.0 (4.9)	5678.0 (-)
Total	347	100.0	22.5 (0.4)	660.6 (33.7)

The cumulative effective dose for 1 PET-CT with administered FDG was 23.8 (2.3-71.7) mSv. Mean cumulative effective dose for patients with recurrent PET-CT examinations reached 41.2 mSv. Average cumulative administered FDG activity of 660.6 (594.3-726.9) mBq resulted in average effective dose of 12.5 (11.3-13.8) mSv.

#### 3.3 Information on other risk factors

21.7% of the study group was nuclear workers hired to the "Mayak" nuclear weapon production association (MPA) in the period from 1948 to 2000. The MPA personnel have been potentially exposed to protracted external gamma- and internal alpha ionizing radiation [5].

The distribution of patients by exposure to additional risk factors is shown in Table 2:

**Table 2.** Exposure to additional risk factors

Additional risk factor	n	%
Occupational exposure	75	21.7
CT scans other than CRCONM	268	77.2
Radiotherapy	90	25.9
Chemotherapy	205	59.1
Stage of malignancy (2 > )	277	79.8
Age at 1 <sup>st</sup> PET-CT (> 60 )	167	48.1

The information on stage of MT was available in 96.0%. 87.3% of patients were previously diagnosed with malignant tumor (MT).

#### 3.4 The vital status and survival time

As of 31.12.2020, the number of deaths accumulated through the observation period was 216 (62.2%). 12 patients (3.5%) with no information on the vital status were lost to follow-up.

The proportion of malignant tumours confirmed on autopsy was 94%. Among them, the number of patients died in the first year of follow-up was 90 (41.9%).

The average duration of observation period (time at risk) was  $2.9 \pm 0.13$  years (min 0; max 10). The Kaplan-Meier survival function by the time of follow-up for the study group with known vital status is shown on Fig. 2.

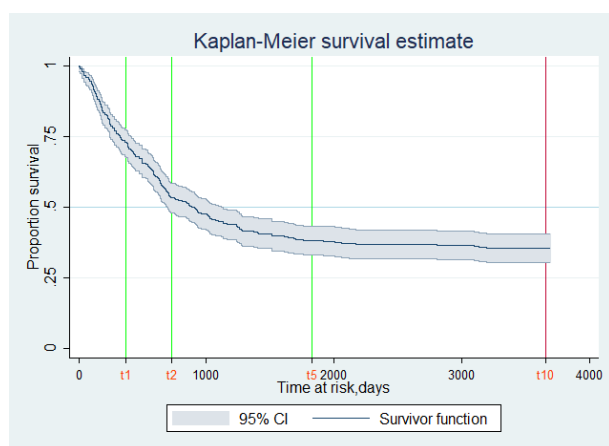


**Fig. 2.** The survivor function of the study group (t1, t2, t5 and t10 ticks equal to 1, 2, 5 and 10 years of follow-up), 95% CI

To the end of follow-up, 50% of the study group survived more than 960 days after the 1<sup>st</sup> PET-CT. Mean time at risk for alive was  $1843.2 \pm 73.4$  days. The proportion of alive to the end of the study was 35.5% at average age at 1<sup>st</sup> PET-CT of  $59.6 \pm 1.4$  ( $56.0 \pm 2.7$  for males and  $61.8 \pm 1.4$  for females).

### 3.5 Results of statistical modelling

The multiple logistic regression model was fitted for 0- and 2 year survivor groups using following parameters: sex male ( $x_1$ ), age 60 at 1<sup>st</sup> PET-CT ( $x_2$ ), malignant tumor stage ( $x_3$ ), occupational exposure ( $x_4$ ), cumulative number of PET-CT ( $x_5$ ), number of CT over than PET-CT ( $x_6$ ), radiotherapy ( $x_7$ ) and chemotherapy ( $x_8$ ) adjusted for the stage of MT. The results are shown in Table 3:

**Table 3.** The results of multiple logistic regression and the OR estimates for 8-parametric model in 0-year and 2-year survivor groups

	0-year (n=335)			2-year (n=179)		
Parameter	OR	Std.er	Wald p	OR	Std.er	Wald p
sex(male) $x_1$	1.41	0.37	1.18	1.35	0.56	0.45
age/60 $x_2$	5.67	3.30	0.003	5.90	5.20	0.04
stage $x_3$	1.04	0.07	0.52	1.10	0.10	0.29
worker $x_4$	1.17	0.39	0.62	1.24	0.63	0.67
PET-CT $x_5$	0.85	0.08	0.08	0.81	0.11	0.12
CT $x_6$	1.11	0.05	0.019	1.41	0.10	0.0001
RT $x_7$	0.79	0.22	0.39	0.90	0.41	0.81
ChT $x_8$	2.28	0.59	0.001	2.30	0.97	0.05
ChT* $x_8$	0.44	0.10	0.001	0.31	0.13	0.006
Prob>Chi <sup>2</sup>	0.001			<0.0001		
Pseudo R <sup>2</sup>	0.06			0.24		

\*adjusted for stage of malignancy

Comparison of two multiparametric models based on pseudo-R<sup>2</sup> estimates showed that 2-year survival model (n=179) was more predictive versus 0-year model (n=335), while low statistical significance level of the OR coefficients was obtained in both models for several parameters.

LRT-test of full model (M1) with 8 parameters ( $x_1 - x_8$ ) versus restricted model (M2) with statistically significant parameters only ( $x_2, x_6, x_8$ ) resulted in the

Prob > Chi<sup>2</sup> = 0.31 that does not allow to reject the assumption that M2 nested in M1.

## 4. Discussion

In this study we analyzed the updated information on the oncological patients who were exposed to low doses of diagnostic radiation during PET-CT examinations performed in the Chelyabinsk Regional Clinical Center of Oncology and Nuclear Medicine with extended follow-up period. Updated vital status and mortality data, and additional information on other risk factors such as radiotherapy and chemotherapy as possible confounders, and the contribution of CT scans performed outside the PET-center accounted using the data of "CT Registry" has been analyzed.

The results of multiparametric analyses showed significant effect of age at 1<sup>st</sup> exposure, cumulative number of CT examinations and chemotherapy in the period after the 1<sup>st</sup> PET-CT examinations among oncological patients. As it in the previous study [6], neither recurrent PET-CT examinations nor the presence of occupational exposure were associated with changes in the mortality.

These results rises the concern on possible effect of cumulative number of CT examinations (OR 1.1-1.4) on the mortality among oncological patients examined with PET-CT. However, an increased risk from multiple CT scans can be substantially biased with the reverse causation (RC) reported in our previous study on cancer mortality among nuclear workers exposed to diagnostic X-ray examinations throughout life [11]. Although the risk of cancer death was dramatically increased (ERR per 1 Gy of X-ray dose was 5.5 for several solid cancers), it can be generally explained by the fact that patients with severe health conditions which is more likely leads to death had more frequent diagnostic examinations, rather than direct effect of exposure to diagnostic ionizing radiation on mortality.

In the same time, radiotherapy that seems to confer higher risks of mortality in cancer patients [12] doesn't show the significant effect on mortality both as independent predictor ( $p=0.48$ ), and included in the multiparametric models ( $p \geq 0.39$ ). Sufficient variability of area exposed to radiation during radiotherapy depending on localization and cancer type can be the source of uncertainties in this case.

The effect of chemotherapy (OR 2.3) which was significant in both survival groups can be explained in conjunction with the stage of malignancy. Although cancer treatment process related with exposure to diagnostic radiation, radiotherapy and chemotherapy (CRT) plays certain role in carcinogenesis [13] and, probably, may lead to shorten the survival time, it should be noticed that severe health conditions require complex anticancer treatment. Started at early stage of malignant process, it is more likely to prevent unfavorable outcome that extend the survival period that may influence on the mortality estimate [14]. This suggestion is consistent with the results of  $x_8$  parameter adjustment for tumour stage 1-2 (OR 0.31-0.44). According to that, chemotherapy administered in the

early period of the development of MT process statistically significantly reduces the chances of mortality in the first decade after the PET-CT diagnostics.

Finally, our findings suggest an appropriateness of ALARA principle [15] in case of recurrent diagnostic exposures of cancer patients using CT. According to that it is advisable to use algorithms for reducing the radiation dose during CT examinations [16], especially in patients undergoing anticancer treatment [17].

## 5. Conclusions

The results of the study based on updated cohort profile data of oncological patients examined with PET-CT showed statistically significant effect of age at first examination, the number of diagnostic CT scans performed, and chemotherapy on the overall mortality within 10 year-period after the 1<sup>st</sup> PET-CT examination. No direct evidence of the “pure” impact of number of PET-CT examinations on the overall mortality adjusted for radiation and non-radiation factors has been found. These results contributes the data of the computed tomography database (CTDB) which is a unique source of information for epidemiological study of low-dose effects of diagnostic exposure among population of Ozyorsk (OCTC study).

## 6. References

1. Beyer T., Townsend D.W., Brun T., Kinahan P.E., Charron M., Roddy R., Jerin J., Young J., Byars L., Nutt R. (2000). A combined PET/CT scanner for clinical oncology. *Journal of Nuclear Medicine*, 41: 1369–1379.
2. Brix G., Nekolla E.A., Borowski M. et al. Radiation risk and protection of patients in clinical SPECT/CT. *Eur J Nucl Med Mol Imaging*. 2014; 41 Suppl 1: S125-136.
3. Rühm W., Harrison R. M. High CT doses return to the agenda. *Radiation and Environmental Biophysics*. 2020; 59: 3–7. DOI: 10.1007/s00411-019-00827-9.
4. Preston D.L., Ron E., Tokuoka S., Funamoto S., Nishi N., Soda M., et al. Solid cancer incidence in atomic bomb survivors: 1958–1998. *Radiat Res*. 2007; 168: 1-64.
5. Romanov S.A., Vasilenko E.K., Khokhryakov V.F., Jacob P. Studies on the Mayak nuclear workers: dosimetry. *Radiat Environ Biophys*. 2002; 41:23–28. DOI 10.1007/s00411-001-0134-3.
6. Osipov, Mikhail V., Vazhenin, Andrey V., Kuznetsova, Anna I., Aksenova, Irina A., Vazhenina, Daria A., Sokolnikov, Mikhail E. (2019) PET-CT in oncological patients with occupational exposure to ionizing radiation. *Medical Physics in the Baltic States* in 2019. Proceedings of the 14th International Conference on Medical Physics. Kaunas, Lithuania, 7-9 November, 2019. P. 164.
7. Basic sanitary rules for radiation safety (OSPORB-99/2010). SP 2.6.1.25 - 10. (in Russian).
8. Radiation Dose to Patients from Radiopharmaceuticals (Addendum to ICRP Publication 53). ICRP Publication 80. Ann. ICRP 28 (3).
9. Osipov Mikhail Viktorovich, Sokolnikov Mikhail Eduardovich, Fomin Evgeny Pavlovich. Database of Computed Tomography of the Ozersk population ("CT Register"). Registration Certificate No. 2020622807, issued on 12.24.2020. Available at [https://new.fips.ru/registers-doc-view/fips\\_servlet?DB=DB&DocNumber=2020622807&typeFile=html](https://new.fips.ru/registers-doc-view/fips_servlet?DB=DB&DocNumber=2020622807&typeFile=html) (Accessed at 12.02.2021). (In Russian).
10. Stata. Stata statistical software: Release 7.0. Stata Corporation, College Station, 2001
11. Osipov M.V., Sokolnikov M.E. (2015). Problems of assessment of carcinogenic risk of medical exposure in a cohort of nuclear personnel. *Medical Radiology and Radiation Safety*. 60 (6): 60 – 66. (in Russian)
12. Boehle A., Katic K., König I.R., Robrahn-Nitschke I., Brandenburg B. (2020). Comparison of outcome endpoints in intermediate- and high-risk prostate cancer after combined-modality radiotherapy. *Brachytherapy*. 19(1):24-32. doi:10.1016/j.brachy.2019.09.001
13. Zhang B, Zhang X, Li M, Kong L, Deng X, Yu J. (2016). How breast cancer chemotherapy increases the risk of leukemia: Thoughts about a case of diffuse large B-cell lymphoma and leukemia after breast cancer chemotherapy. *Cancer Biol Ther*. 17 (2):125-128. doi:10.1080/15384047.2016.1139233
14. Mc Erlain T, Burke A, Branco CM. Life after Cell Death-Survival and Survivorship Following Chemotherapy. *Cancers (Basel)*. 2021 Jun 11;13(12):2942. doi: 10.3390/cancers13122942.
15. ICRP Publication 103. Recommendations of the International Commission on Radiological Protection. Ann. ICRP, 37, No.2 – 4, 2007.
16. Osipov M.V., Lebedev N.I., Fomin E.P. (2015). Radiation Safety of Patients: Reducing the Radiation Dose in Abdominal Multislice Computed Tomography. *Russian Electronic Journal of Radiology*. 5 (2): 47 – 51.
17. Lebedev N.I., Osipov M.V., Sinyak E.V., Fomin E.P. An Algorithm of the Abdominal Multislice CT Study in Cancer Patients undergoing Chemotherapy. *Medical Radiology and Radiation Safety*. 2015; 60 (4): 81-86. (In Russ.)



## **COLOR CHANGES OF DENTAL CERAMICS EXPOSED TO BLEACHING MATERIALS**

Giedrė MORKŪNAITĖ, dr. Rimantas OŽIŪNAS, Vytautas ČEPLAUSKAS  
Lithuanian University of Health Sciences (LSMU) MA Faculty of Odontology Department of Prosthodontics  
m.giedre@yahoo.com

**Abstract.** An aesthetically pleasing smile is an aspiration of patients and dentists and teeth whitening is one of the most conservative procedures, but the effect of bleaching agents on ceramic restorations has not been extensively studied. This study aimed to investigate the effect of hydrogen peroxide and carbamide peroxide on the color ( $\Delta E$ ) of polished and glazed lithium disilicate, leucite-reinforced glass-ceramic and zirconium dioxide ceramics.

**Keywords:** surface roughness, colour stability, bleaching, lithium disilicate, leucite reinforced glass ceramic, zirconium dioxide

### **1. Introduction**

#### **1.1. Ceramics**

Ceramic materials evolved and improved rapidly in terms of their properties and manufacturing methods over the last few decades. Great aesthetics, high fracture strength and optimal biocompatibility are the features that have made ceramic restorations so favoured [1]. There are several types of dental ceramics which are commonly used in a restorative dentistry: Lithium disilicate-reinforced glass ceramics (LS2), Leucite-reinforced glass-ceramics ( $\text{KAlSi}_2\text{O}_6$ ) and Zirconium dioxide based ceramics.

Lithium disilicate (LS2) is a particle-filled glassy material [2], characterised by its high biocompatibility, strength, environmental resistance, durability, great marginal integrity, acid sensitivity, excellent optical properties and its high aesthetics. This ceramics is recommended for the production of single dental crowns, three-unit fixed restorations [1, 3], veneers, inlays and overlays [4-6]. Lithium disilicate can also be used for both anterior and posterior tooth restorations.

Leucite-reinforced glass-ceramics ( $\text{KAlSi}_2\text{O}_6$ ) is composed of irregular-shaped leucite microcrystals accommodated in glass matrix [7]. It is suitable for the production of single tooth restorations - veneers, inlays, overlays, crowns, but it is not strong enough for fixed posterior bridge restorations [8]. Due to the crystalline

structure of this ceramics so called chameleon effect (light scattering) might be observed on restorations. Leucite-reinforced ceramics also have good mechanical resistance, transparency and acid sensitivity [3].

Pure  $\text{ZrO}_2$  has monoclinic structure however due to the heating which is needed to form the product, it becomes tetragonal and later on - cubic. Cooling down initiates the opposite sequence of processes. In order to avoid the fragility of the final product tetragonal phase  $\text{ZrO}_2$  may be stabilized with  $\text{Y}_2\text{O}_3$ , which makes tetragonal phase of  $\text{ZrO}_2$  to metastable. This forms aid to ensure the resistance of the material breakage, as the tetragonal phase can be transformed into a monoclinic phase with increasing the volume up to 4% and creating compressive surface tension [9]. Zirconium restorations are often used due to good biocompatibility, excellent mechanical properties [10], minimal wear of antagonistic teeth [11] and low corrosion potential [12].

#### **1.2. Color and surface of ceramics**

The final color of ceramic restorations not only depends on its base color but it is influenced by the light reflectance from the surface and thickness of the object and cementation process [13].

Smooth surface is essential for longevity of ceramic restoration. Rough surfaces can cause discolouration, secondary caries and soft tissue inflammation due to increased oral microorganisms adhesion to the restoration [14, 15]. Glazing procedure ensures even surface and shine, increases resistance to breakage, closes open pores that occur after the baking step [14] and ensures color stability.

#### **1.3. Teeth bleaching materials**

A teeth whitening is one of the most conservative treatments in aesthetic dentistry. Bleaching is used when extrinsic and intrinsic discoloration occurs. It can be performed in office, at home or it can be combined.

Concentration of bleaching materials can range from 5% to 40% [16]. Hydrogen peroxide (HP), known as a bleaching material, reacts directly with discolorations and releases active carbon molecules to break the double carbon bonds between chromophore molecules, leaving smaller and colourless fragments that are converted into water and carbon dioxide [16-18]. The highest allowed concentration of HP in Europe is 6%. HP concentrations that are higher than 15% does not improve the whitening efficiency and but can lead to changes in enamel hardness and surface morphology [19]. The effectiveness and safety of teeth whitening is also affected by the pH of the whitening material. Alkaline pH of peroxide ensures efficacy of the whitening agent since the pH decreases remarkably after the application on the tooth [20].

Carbamide peroxide (CP) is a compound made of hydrogen peroxide (HP) in conjunction with urea. It is also known under the name “urea hydrogen peroxide” [21]. Contacting with a tooth, it slowly dissociates into HP and urea [22]. Due to a slow decomposition rate, interaction of CP and tooth should be longer as in the case of HP application.

#### 1.4. Ceramics color changes due to the bleaching

Bleaching materials are frequently used for the whitening of combined set of patient's teeth: natural and restored with ceramics.

Ceramics is the most inert of all restorative materials, but its surface layer may be affected due to the contact with the solutions of different pH [23]. Dissolution of alkaline ions and glass can occur due to diffusion of active oxygen and HP. As a result, surface modifications of ceramics can be caused by the reduction of silicon dioxide or potassium peroxide.

Due to the chemical instability of ceramics, endogenous and exogenous color changes may occur [24]. Exogenous changes can also appear due to the surface roughness of the restorative material which can lead to in the increased absorption of pigments from the oral cavity. It was found that application of 16% CP bleaching solution for teeth whitening [3] or teeth whitening supported by LED exposure [25] significantly affects the transparency of lithium disilicate and leucite-reinforced glass-ceramics. This study was performed aiming at the evaluation of the impact of hydrogen peroxide and carbamide peroxide

based bleaching materials on optical properties changes in lithium disilicate, leucite-reinforced glass-ceramics and zirconium dioxide.

## 2. Materials and methods

This study was approved by the Bioethics centre of Lithuanian University of Health Sciences (Nr. BEC-OF-36). Sixty round-shaped disks (ø 11 mm x 2 mm) were produced: twenty lithium disilicate reinforced glass ceramic (Ivoclar Vivadent IPS E.max) samples with and without glaze; twenty leucite reinforced glass ceramic (Ivoclar Vivadent IPS Empress) samples with and without glaze and twenty zirconium dioxide (Dental Direkt BIO ZW ISO) samples with and without glaze. One half of the disks surface was glazed, another one - polished. Samples of glass ceramics were produced in dental laboratory using CAD/CAM and press technologies. Samples of zirconium dioxide were produced using CAD/CAM and synthesis technologies. Glass ceramics samples were first covered with paint (Ivoclar Vivadent IPS E.max essence, Ivoclar Vivadent IPS Empress) and glazing paste (Ivoclar Vivadent IPS E.max, Ivoclar Vivadent IPS Empress) and their surfaces were polished with a „bison” type brush and diamond paste. Lastly the samples were polished with a fluffy brush finalizing preparation of the glazed part of the surface. Zirconium dioxide samples were firstly covered with paint (Ivoclar Vivadent IPS E.max essence) and glazing paste (Ivoclar Vivadent IPS E.max). Lastly their surfaces were polished with a „bison” type brush and diamond paste and then polished with a fluffy brush making glazed part of the surface ready. Another part (polished) of sample's surface was firstly polished with ceramic polishing rubbers (coarse, medium and low roughness) and then with a diamond paste using „bison” type brush. The polished part of the samples was finalized via polishing of samples with a fluffy brush. Polished and glazed ceramics were used to simulate clinical situations and to investigate the impact of different bleaching materials on the optical properties of the differently prepared ceramics surfaces.

Two different bleaching materials were selected for this study. The whole information about materials used in this investigation is provided in Table 1.

**Table 1.** Characteristics of the materials

Material	Title	Concentration	pH	Manufacturer
Lithium disilicate reinforced glass ceramic	IPS e-MAX	-	-	Ivoclar Vivadent AG, Schaan, Liechtenstein H13049
Leucite-reinforced glass ceramic	IPS Empress	-	-	Ivoclar Vivadent AG, Schaan, Liechtenstein H13049
Zirconium dioxide	Dental Direkt BIO ZW ISO	-	-	Dental Direkt GmbH Industriezentrum 106-108 32139 Spenge, Germany
Carbamide peroxide	Philips Zoom NiteWhite	16 %	5,8 - 6,2	Philips Consumer Lifestyle BV, Tussendiepen4, 9206 AD Drachten Netherlands
Hydrogen peroxide	Pola Office+6 %	6 %	9	SDI Limited, Bayswater, Victoria 3153, Australia

Prior to bleaching color of all specimens with and without glaze were determined using a spectrophotometer (VITA Easyshade V; VITA Zahnfabrik). A single tooth color setting mode was selected to obtain CIELAB data (L, a, b), where L - indicates brightness from 0 (black) to 100 (white), a - indicates a point on the red-green color scale, b - indicates a point on the yellow-blue color scale.

The color difference ( $\Delta E$ ) was estimated according to the following formula [3]:

$$\Delta E = \sqrt{(\Delta L)^2 + (\Delta a)^2 + (\Delta b)^2} \quad (1)$$

### 2.1. Bleaching with 16% CP

10 lithium disilicate, 10 leucite-reinforced glass ceramic and 10 zirconium dioxide specimens with and without glaze were bleached with Philips Zoom Nitewhite system with 16% CP. This whitening agent is used to bleach teeth at home during night with individual trays. Bleaching gel was applied in a thin layer as shown in Fig. 1(A) every day and stored for 8 hours per day. The procedure was repeated for 14 days.

After procedure bleaching material was removed with a damp cloth and the sample surface was dried.

### 2.3. Bleaching with 6% HP

10 lithium disilicate, 10 leucite-reinforced glass ceramic and 10 zirconia samples with and without glaze were bleached using Pola Office + 6% system containing 6% of HP. This whitening system is used only in-office. A thin layer of bleaching gel was deposited onto the specimen's surface (Fig. 1(B), and left for 15 minutes). Then the bleaching material was removed with a suction system and HP was reapplied. The total of 4 sessions was applied. After bleaching samples were washed with water and wiped dry.

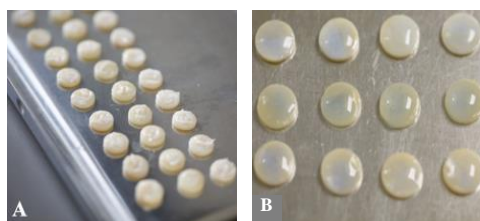


**Fig.1.** Bleaching of samples: A –with 16% CP; B – bleaching with 6% HP

## 2.4. Evaluation of color changes of specimens after bleaching

Color changes ( $\Delta E$ ) in specimens after bleaching were assessed using spectrophotometer VITA Easyshade V. data and applying criteria set by National Bureau of Standards (NBS) provided in the Table 2 [26].

**Table2.** NBS criteria for ( $\Delta E$ ) evaluation

$\Delta E$	NBS Criteria
0-0.5	Trace: remarkably slight alteration
0.5-1.5	Slight: slight alteration
1.5-3	Noticeable: observable alteration
3-6	Appreciable: apparent alteration
6-12	Much: remarkably apparent alteration
12 and more	Very much: alteration to other color

## 2.5. Statistical analysis

Statistical analysis was performed using program package SPSS 21 for Windows. Study data were analysed with descriptive statistics using one-way analysis of variance ANOVA methods. The difference between the variables was considered statistically significant if  $p < 0.05$ . Since the data were normally distributed (Shapiro-Wilk); ANOVA and Tukey HSD were used.

## 3. Results

Calculated color changes ( $\Delta E$ ) of the specimens after bleaching and the mean values  $\pm$  standard deviations are provided in the (Table 3).

The results were evaluated according to the NBS evaluation criteria [26]. Performed investigation revealed, that all restoration ceramics were reacting to the bleaching, however each ceramics responded differently. Notable difference in color changes after bleaching was also observed analysing polished and glazed parts of the same samples.

The highest impact on the color changes had bleaching performed using 16 % carbamide peroxide (CP) solution. Using this material significant difference in color was observed for both polished and glazed ceramics which ranged from noticeable to appreciable (Table 2) when compared to other bleaching materials.

**Table 3.** Color changes in the ceramics after bleaching (mean values  $\pm$  standard deviations)

	16% CP, $\Delta E$	6% HP, $\Delta E$
Polished lithium disilicate	2,9302 $\pm$ 0,43262	1,8930 $\pm$ 0,39954
Glazed lithium disilicate	3,1665 $\pm$ 0,9617	1,8722 $\pm$ 0,43793
Polished leucite-reinforced glass ceramic	4,7045 $\pm$ 0,78505	4,1792 $\pm$ 1,13108
Glazed leucite-reinforced glass ceramic	4,8660 $\pm$ 0,67218	4,0530 $\pm$ 2,10356
Polished zirconium dioxide	4,5187 $\pm$ 1,16461	1,6208 $\pm$ 0,48593
Glazed zirconium dioxide	3,3472 $\pm$ 1,56487	2,1875 $\pm$ 1,86009

#### 4. Conclusions

The impact of bleaching material on the color changes of three types of restoration ceramics (lithium disilicate reinforced glass ceramics, leucite reinforced glass ceramics and zirconium dioxide ceramics) has been investigated applying hydrogen peroxide and carbamide peroxide as bleaching materials.

It was found that each ceramic responded differently to the bleaching procedure and indicated notable color changes depending on ceramics type and its surface preparation (polished or glazed) and also bleaching material used. The later leads to conclusion that more detailed information on optical properties changes after bleaching may be assessed having investigated changes of surface roughness of the ceramics.

In overall, the highest impact on the color changes was found after samples bleaching with 16 % carbamide peroxide (CP) solution.

#### 5. References

1. Mohammadibassir M, et al. Effect of Two Polishing Systems on Surface Roughness, Topography, and Flexural Strength of a Monolithic Lithium Disilicate Ceramic. *Journal of Prosthodontics*, 2019;28: e172-e180.
2. Zarone F, et al. Current status on lithium disilicate and zirconia: a narrative review. *BMC Oral Health*. 2019;19 (1):p. 134.
3. Karci M, Demir N. Effect of Home Bleaching on the Translucency of CAD/CAM Systems. *J Prosthodont*. 2019 Mar; 28(3):310-314.
4. Haralur SB, et al. Effect of hydrothermal aging and beverages on color stability of lithium disilicate and zirconia based ceramics. *Medicina*. 2019;55:749.
5. Azar B, et al. The marginal fit of lithium disilicate crowns: Press vs. CAD/CAM. *Braz Oral Res*. 2018;32:e001.
6. Luciano M, et al. Lithium disilicate posterior overlays: clinical and biomechanical features. *Clin Oral Invest* 24, 841–848 (2020).
7. Fu L, Engqvist H, Xia W. Glass-Ceramics in Dentistry: A Review. *Materials (Basel)*. 2020 Feb 26;13(5):1049
8. Montazerian M, Zanotto ED. Bioactive and inert dental glass-ceramics. *J Biomed Mater Res A*. 2017 Feb;105(2):619-639.
9. Alves LMM, et al. The Wear Performance of Glazed and Polished Full Contour Zirconia. *Braz Dent J*. 2019 Oct 7;30(5):511-518.
10. Colombo M, et al. Color stability of CAD/CAM Zirconia ceramics following exposure to acidic and staining drinks. *J Clin Exp Dent*. 2017 Nov 1;9(11):e1297-e1303.
11. Papageorgiou-Kyran A, Kokoti M, Kontonasaki E, Koidis P. Evaluation of color stability of preshaded and liquid-shaded monolithic zirconia. *J Prosthet Dent*. 2018 Mar;119(3):467-472.
12. Kontonasaki E, Giasimakopoulos P, Rigos AE. Strength and aging resistance of monolithic zirconia: an update to current knowledge. *Jpn Dent Sci Rev*. 2020 Dec;56(1):1-23.
13. Yan J, Kaizer MR, Zhang Y.. Load-bearing capacity of lithium disilicate and ultra-translucent zirconias. *J Mech Behav Biomed Mater*. 2018;88:170–175.
14. Demir N, Karci M, Ozcan M, 2020. Effects of 16% Carbamide Peroxide Bleaching on the Surface Properties of Glazed Glassy Matrix Ceramics. *BioMed Research International* 2020.
15. Tinastepe N, Malkondu O, Iscan I, Kazazoglu E. Effect of home and over the contour bleaching on stainability of CAD/CAM esthetic restorative materials. *J Esthet Restor Dent*. 2021 Mar;33(2):303-313.
16. Kwon SR, Wertz PW. Review of the mechanism of tooth whitening. *J Esthet Restor Dent*. 2015; 27( 5): 240- 257.
17. Lilaj B, et al. Comparison of bleaching products with up to 6% and with more than 6% hydrogen peroxide: whitening efficacy using BI and WID and side effects - an in vitro study. *Front Physiol*. 2019;10:919.
18. Coceska E, et al. Enamel alteration following tooth bleaching and remineralization. *J Microsc*. 2016 Jun;262(3):232-44.
19. Grazioli G, et al. Bleaching and enamel surface interactions resulting from the use of highly-concentrated bleaching gels. *Arch Oral Biol*. 2018 Mar; 87:157-162.
20. Mushashe AM, et al. Effect of different bleaching protocols on whitening efficiency and enamel superficial microhardness. *J Clin Exp Dent*. 2018;10:e772–5.
21. Lima FV, et al. Carbamide peroxide nanoparticles for dental whitening application: Characterization, stability and in vivo/in situ evaluation. *Colloids Surf B Biointerfaces*. 2019 Jul 1;179:326-333.
22. Redha O, et al. Impact of Carbamide Peroxide Whitening Agent on Dentinal Collagen. *J Dent Res*. 2019 Apr;98(4):443-449.
23. Rea FT, et al. Effect of carbamide peroxide bleaching agent on the surface roughness and gloss of a pressable ceramic. *J Esthet Restor Dent*. 2019 Sep;31(5):451-456.
24. Rodrigues CRT, et al. Changes to Glazed Dental Ceramic Shade, Roughness, and Microhardness after Bleaching and Simulated Brushing. *J Prosthodont*. 2019 Jan;28(1):e59-e67.
25. Juntavee N, Juntavee A, Riyaboot K. Color stability of computer-aided design–computer-aided manufacturing of ceramic materials upon light-emitting diode illumination bleaching. *World Journal of Dentistry*. 2017;8, 445–45.
26. Özdaş DÖ, et al. Color Stability of Composites After Short-term Oral Simulation: An *in vitro* Study. *Open Dent J*. 2016 Aug 31;10:431-437.

## **ASSESSMENT OF THE RADIATION RISKS FROM MEDICAL X-RAY EXAMINATIONS CONSIDERING AGE AND GENDER COMPOSITION OF THE PATIENTS**

Vladislav GOLIKOV

St-Petersburg Research Institute of Radiation Hygiene after prof. P.V. Ramzaev  
sg235@rambler.ru

**Abstract:** At the present time, the collective risk from medical exposure in the Russian Federation is estimated by multiplying a collective effective dose by the value of the nominal risk coefficient, while the age composition of patients is significantly different from those for the entire population. The aim of this study was to assess the correction factors that consider the difference in the age and sex distribution of the patients and the entire population for a more correct estimation of collective risks both from selected X-ray examinations and for medical exposure in the Russian Federation as a whole. It is shown that risk estimates for some X-ray examinations calculated using the age and sex dependence of the lifetime detriment-weighted radiation risk coefficients, organ doses and age distribution of patients may differ from such estimates on the base of effective dose and nominal risk coefficients up to order of magnitude.

**Keywords:** medical examinations, patients, radiation risk, nominal risk coefficients, effective dose.

### **1. Introduction**

Bearing in mind the uncertainties associated with risk projection to low doses, the new ICRP Publication 147 [1] concluded that effective dose may be considered as an approximate indicator of potential risk with the additional consideration of variation in the risk with age and sex of a population group.

The age dependence of the lifetime radiation risk is different for different organs. For example, for stomach and thyroid the values of risk significantly decline with the increase in the age. At the same time this relation is less pronounced for the red bone marrow; for the lungs and esophagus maximal risk is observed at the age of 45 and 75, respectively. Hence, for the correct assessment of the collective risk from X-ray examinations it is necessary to know the age and sex distribution of the patient sample. Additionally, radiation risk will vary depending on the irradiated organs, the level of their exposure and the type of X-ray examination.

At the present time the collective risk from medical exposure in the Russian Federation is estimated by multiplying a collective effective dose by the value of the nominal risk coefficient, while the age composition of patients is significantly different from those for the entire population and for different medical examinations in various ways.

The aim of this study was to assess the correction factors that consider the difference in the age and sex distribution of the patients and the entire population for a more correct estimation of collective risks, both from selected X-ray examinations and for all medical exposure in the Russian Federation.

### **2. Materials and methods**

Currently official data on the age and sex distribution of patients in the Russian Federation is not collected; hence European statistical data was used as a basis for the study [2]. The European sex and age distribution of patients were used in accordance with the structure of X-ray examinations in the Russian Federation, represented by the following modalities: fluorography, plain radiography, fluoroscopy, computed tomography, interventional examinations. Data for fluorography was based on the distribution of European patients for chest radiography considering that in the Russian Federation fluorography is performed from the age of 14 years. Plain radiography was represented by the examinations of the skull, chest, cervical spine, thoracic spine, lumbar spine, abdomen and pelvis; computed tomography - examinations of the skull, chest and abdomen; fluoroscopy – Ba follow, Ba meal and Ba enema; interventional examinations – cardiac angiography. According to the data for 2018, X-ray examinations of these anatomic regions within each modality contribute to a collective dose from medical exposure in Russian Federation from 52% (cardiac angiography) to 96% (fluoroscopy) [3]. Figure 1, as an example, presents age distributions of patients averaged by sex undergoing CT examinations of various parts of the body [2].

The dosimetric model for each selected examination was represented by a set of typical physical-technical and geometric parameters collected earlier in the Russian medical facilities [4-10] and adopted from the publications, if necessary [11-14]. The values of organ and effective doses for these examinations were calculated using computer programs PCXMC 2.0 [15] and EDEREX [16] for plain radiography, fluoroscopy and interventional examinations and NCICT 2.01 [17] for computed tomography.

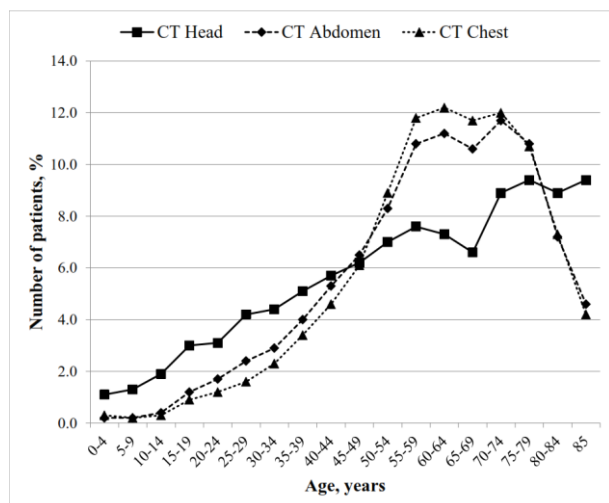


Fig. 1. Age distribution of patients undergoing CT examination [2]

Lifetime detriment-weighted radiation risk of a patient of gender  $G$  and age  $A$  can be estimated based on the absorbed doses in organs and tissues and appropriate risk coefficients for the individual tissues at risk (“gold standard”):

$$R_A^G = \sum_O D_A^G(O) \cdot r_A^G(O) \quad (1)$$

where  $R_A^G$  – is the lifetime detriment-weighted radiation risk of a patient of gender  $G$  and age  $A$  due to the X-ray examination, dimensionless;

$D_A^G(O)$  – is the mean absorbed dose in the organ or tissue  $O$  of a patient of gender  $G$  and age  $A$  due to the X-ray examination, mGy;

$r_A^G(O)$  – is the lifetime detriment-weighted radiation risk coefficient due to exposure of the organ or tissue  $O$  in a patient of gender  $G$  and age  $A$ ,  $\text{mGy}^{-1}$ .

To calculate risks for patients undergoing the above examinations, the values of absorbed doses in organs and the lifetime detriment-weighted radiation risk coefficients normalized per 1 mGy for men and women with 5-year-old age intervals at the time of exposure were used. The risk coefficients were adopted from the existing Russian guidelines [18]. The calculated risks  $R_A^G$  for men and women for 30 most common X-ray examinations for different imaging modalities are presented in [19].

The next step was to calculate the ratios of risks for patients of different age groups estimated using the “gold standard” to the risks for these patients estimated using

effective dose and nominal risk coefficient. The final step was to calculate the correction factors to the risk value based on the effective dose considering the patient distribution by age for the selected X-ray examination using the Equation 2:

$$K_{\text{exam}} = \sum_A \frac{0.5 \cdot [R_A^M + R_A^F]}{5.7 \cdot 10^{-5} \cdot E_A} \cdot f_A(N) \quad (2)$$

where  $R_A^M$  – is the lifetime detriment-weighted radiation risk of a male patient of the age  $A$  due to X-ray examination, dimensionless;

$R_A^F$  – is the lifetime detriment-weighted radiation risk of a female patient of the age  $A$  due to X-ray examination, dimensionless;

$E_A$  – is the effective dose of the patient of the age  $A$  due to X-ray examination, mSv;

$5.7 \cdot 10^{-5} \text{mSv}^{-1}$  – is the nominal risk/detriment coefficient;

$f_A(N)$  – is fraction of patients of the age  $A$  in whole sample of patients for given examination, dimensionless.

### 3. Results and discussion

Typical values of effective doses for the selected X-ray examinations in the Russian Federation are presented in Table 1.

Table 1. Typical values of effective doses (mSv) for the selected X-ray examinations in the Russian Federation

Examination	Age category, years				
	0-4	5-9	10 - 14	15 - 19	Adults
<i>Plain radiography</i>					
Skull	0.04	0.04	0.03	0.05	0.07
Cervical spine	0.08	0.10	0.10	0.13	0.15
Thoracic spine	0.27	0.40	0.45	0.61	0.84
Chest	0.06	0.08	0.08	0.12	0.17
Lumbar spine	0.33	0.52	0.57	1.12	1.90
Abdomen	0.22	0.34	0.45	0.78	1.14
Pelvis	0.21	0.43	0.52	0.61	0.79
<i>Fluorography</i>					
Digital				0.04	0.04
Film				0.37	0.37
<i>Interventional Examination</i>					
Cardiac angiography	5.30	4.60	6.60	13.0	19.0
<i>Fluoroscopy</i>					
Ba meal			0.98	1.29	1.84
Ba follow	0.88	0.74	1.06	3.92	8.00
Ba enema			1.00	4.72	10.4
<i>CT</i>					
Head	1.59	1.63	1.55	2.08	1.90
Chest	2.60	2.77	3.17	4.32	5.16
Abdomen	5.72	5.81	6.32	6.90	7.10

Example of the method of calculation is provided for CT of the abdomen. Results of the calculation of the relation between patient age and life time radiation risk for this examination, based on the “gold standard” and effective dose and nominal risk coefficient are presented on Fig. 2. It is visible, that only for children of both genders, radiation risks estimated using age-specific risk coefficients and corresponding organ doses exceed the risk based on the effective dose. For adult patient that



ratio is less than one. Relevant data for the calculation of the correction factor for this examination and results of calculation are presented in Table 2. Data is presented for 5-year age intervals with corresponding age correction factors for the CT of the abdomen (see Fig. 2). A total value of the correction factor for the CT of the abdomen is calculated as the sum of multiplications of values from columns two and three.

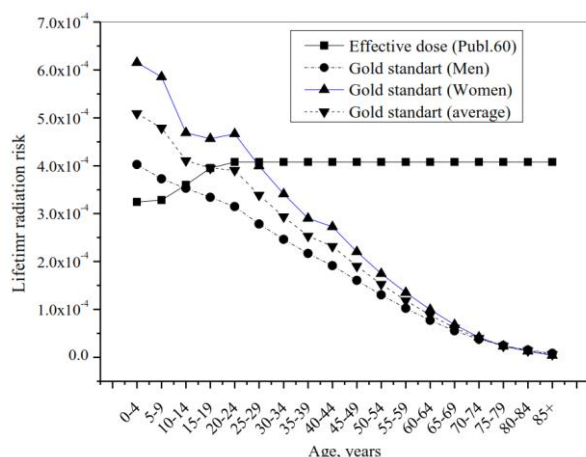


**Fig. 2.** Dependence on the age and sex of patients of the lifetime detriment-weighted radiation risk due to CT of the abdomen calculated for the Russian population according to the "gold standard" and effective dose

**Table 2.** Initial data and the results of calculation of the correction factor for the CT of the abdomen

Patient age group, years	Age correction factor	The fraction of patients of this age group
0-4	1.57	0.002
5-9	1.46	0.002
10-14	1.14	0.004
15-19	1.00	0.012
20-24	0.97	0.017
25-29	0.84	0.024
30-34	0.73	0.029
35-39	0.63	0.040
40-44	0.58	0.053
45-49	0.47	0.065
50-54	0.38	0.083
55-59	0.29	0.11
60-64	0.21	0.11
65-69	0.15	0.11
70-74	0.097	0.12
75-79	0.059	0.11
80-84	0.035	0.072
85+	0.014	0.046
The value of correction factor for total examination		0.29

Hence, collective radiation risk from the CT of the abdomen in the Russian Federation is less than the risk calculated based on the effective dose by the factor of three.

The results of the calculations of the correction factor values for the different imaging modalities, as well as for the separate X-ray examinations are presented in Table 3. Transition from the correction factors for the selected X-ray examinations to the correction factors for the imaging

modalities was performed by weighting the factors for the X-ray examinations by the contribution to the collective dose from the corresponding imaging modalities, based on the state statistical dose data collection [3].

**Table 3.** Correction factors for the risk values calculated using effective doses and nominal risk coefficients

Examination	Correction factor
<i>Fluorography</i>	$K_{FG} = 0.45$
<i>Plain radiography</i>	$K_{PR} = 0.38$
Skull	0.71
Chest	0.51
Cervical spine	0.35
Thoracic spine	0.64
Lumbar spine	0.32
Abdomen	0.30
Pelvis	0.19
<i>Interventional Examinations (IE)</i>	$K_{IE} = 0.40$
Coronary angiography	0.40
<i>CT</i>	$K_{CT} = 0.41$
Head	0.77
Chest	0.33
Abdomen	0.29
<i>Fluoroscopy</i>	$K_{FS} = 0.20$
Ba follow	0.31
Ba meal	0.28
Ba enema	0.09

It is visible, that absolute values of the correction factors for all X-ray examinations are less than one. It can be explained by the age composition of patients shifted towards elderly people with risk coefficient less than nominal that is used for the calculation of the effective dose. Additionally, doses for pediatric patients are commonly significantly lower compared to adults for the majority of X-ray examinations.

Hence, the calculation of the collective risk for the selected X-ray examination considering the age composition of the patients will lead to a conservative estimation of the radiation risk compared to the assessment of the radiation risk when using the effective dose and nominal risk coefficients.

Calculation of the collective risk  $R$  from medical exposure corrected by the age dependent risk coefficients based on the data from the federal statistical forms can be performed using the Equation 3:

$$R = 0.057 \cdot (0.45 \cdot E_{FG}^{coll} + 0.38 \cdot E_{PR}^{coll} + 0.41 \cdot E_{CT}^{coll} + 0.20 \cdot E_{FS}^{coll} + 0.40 \cdot E_{IE}^{coll}) \quad (3)$$

where  $R$  – is the collective lifetime detriment-weighted radiation risk;  $E_{FG}^{coll}, E_{PR}^{coll}, E_{FS}^{coll}, E_{CT}^{coll}, E_{IE}^{coll}$  – are the collective effective doses for different medical technologies, man Sv;  $0.057 \text{ Sv}^{-1}$  – is the nominal risk/detriment coefficient.

Using the presented approach considering the age and gender dependency of the risk coefficients and data on collective effective doses of the corresponding imaging modalities based on the state statistical dose data collection we can show that the collective risk from X-

ray examinations in the Russian Federation in 2018 was lower by the factor of 2.5 compared to the assessment based on the effective dose with nominal risk coefficient. According to the 2018 official data the total collective effective dose from medical exposure of the Russian population was approximately  $8 \cdot 10^4$  man Sv [3]. Just a 10% reduction in the annual collective dose from medical exposure ( $8 \cdot 10^3$  man Sv) will be equivalent to the half of the total collective effective dose of the public in the Russian Federation from the deposition after the Chernobyl accident ( $\sim 1.5 \cdot 10^4$  man Sv). It is also clear that any clarification of the collective dose value due to medical exposure is of great importance in any system of risk management.

#### 4. Conclusion

An approach has been developed that allows in view of the age and sex dependences of the risk coefficients of radiogenic cancer and the age and sex distribution of patients for various X-ray examinations as well to assess the collective radiation risk from both separate X-ray examination and medical exposure as a whole in the Russian Federation.

#### 5. References

1. ICRP, 2021. Use of dose quantities in radiological protection. ICRP Publication 147. Ann. ICRP 50(1).
2. European Commission. Medical Radiation Exposure of the European Population. European Commission. Radiation protection, 2014, № 180, Part 1/2, 181 p.
3. Barkovsky A., Akhmatdinov R., Akhmatdinov R. et al. Radiation doses of the population of the Russian Federation in 2018. Handbook (St. Petersburg: Institute of Radiation Hygiene), 2019, 71p. (in Russian).
4. Golikov V., Balonov M., Kalnitsky S., Sarycheva S. Evaluation of patients doses during interventional radiological examinations. Radiatsionnaya Gygiena = Radiation Hygiene. 2009. Vol. 2, No. 3. p. 26–31 (in Russian).
5. Golikov V., Balonov M., Kalnitsky S., Bratilova A., Sarycheva S., Shatsky I. and Vodovatov A. Exposure levels of patients during radiological examinations in St. Petersburg and the Leningrad region. Radiatsionnaya Gygiena = Radiation Hygiene. 2011. Vol. 4, No. 1. p. 5–13 (in Russian).
6. Bratilova A., Golikov V. and Kalnitsky S. Exposure levels of patients during computed tomography in medical organizations of St. Petersburg and Leningrad region. Radiatsionnaya Gygiena = Radiation Hygiene. 2014. Vol. 7, No. 3. p. 33–38 (in Russian).
7. Balonov M. et al. Modern levels of medical exposure in Russian Federation. Radiatsionnaya Gygiena = Radiation Hygiene. 2015. Vol. 8, No. 3. p. 67–79 (in Russian).
8. Chipiga L. et al. Levels of patient exposure and possible ways of PET diagnostics optimization in Russia. Radiatsionnaya Gygiena = Radiation Hygiene. 2017. Vol. 10, No. 4. p. 31–43 (in Russian).
9. Golikov V.Y., Vodovatov A.V. Estimation of an X-ray machine's workload during routine radiological examinations. Radiatsionnaya Gygiena = Radiation Hygiene. 2015. Vol.8, No.2. p. 6–10 (in Russian).
10. Vodovatov A.V., Golikov V.Y., Kamyshanskaya I.G., Zinkevich K.V., Bernhardsson C. Estimation of the conversion coefficients from dose-area product to effective dose for barium meal examinations for adult patients. Radiatsionnaya Gygiena = Radiation Hygiene. 2018. Vol.11, No.1. p. 93–100. (in Russian).
11. Yakoumakis E. et al. Evaluation of organ and effective doses during paediatric barium meal examinations using PCXMC 2.0 Monte Carlo code. Rad. Prot. Dos. 2015; 163(2): p. 202–209.
12. Damilakis J. et al. Normalized dose data for upper gastrointestinal tract contrast studies performed to infants. Medical Physics 33, 1033 (2006); doi: 10.1118/1.2181297
13. Livingstone R.S., Eapen A., Chiramel G.K. et al. Radiation dose to paediatric patients undergoing fluoroscopic examinations performed using digital imaging system. Radiography (2008) 14, p. 17–23
14. Weir K.A., McMahon S.M., Long G. et al. Radiation doses to children during modified barium swallow studies. Pediatr Radiol (2007) 37:p. 283–290.
15. Tapiovaara, M. and Siiskonen, T. PCXMC—A Monte Carlo Program for Calculating Patient Doses in Medical x-Ray Examinations, second edn. (Helsinki, Finland: Stateilyturvakeskus) (2008) STUK-A 231.
16. Golikov V., Barkovsky A., Wallström E., Cederblad Å. A comparative study of organ doses assessment for patients undergoing conventional X-ray examinations: phantom experiments vs. calculations. Radiation Protection Dosimetry, Vol. 178, Issue 2, 2018, p. 223–234.
17. Lee C. et al. NCICT: a computational solution to estimate organ doses for pediatric and adult patients undergoing CT scans / C. Lee, K.P. Kim, W.E. Bolch et al. // J. Radiol. Prot. – 2015. Vol. 35. – p. 891–909.
18. Methodical Recommendations 2015. Assessment of radiation risks for the patients undergoing diagnostic examinations with the use of ionizing radiation. Methodical Recommendations MR 2.6.1.0098-15 (Moscow: Rospotrebnadzor) p. 34 (in Russian)
19. Methodical Recommendations 2020. Assessment of radiation risks for the patients undergoing diagnostic examinations with the use of ionizing radiation. Methodical Recommendations MR 2.6.1.0215-20 (approved by Head State Sanitary Doctor of the Russian Federation 09/21/2020) (in Russian)

## PREOPERATIONAL ASSESSMENT OF $^{14}\text{C}$ IN THE VICINITY OF THE BELARUSIAN NUCLEAR POWER PLANT

Kristina ERIKSSON STENSTRÖM<sup>1</sup>, Vytenis BARKAUSKAS<sup>2</sup>, Christian BERNHARDSSON<sup>3</sup>, Aliaksandr DVORNIK<sup>4</sup>, Mattias JÖNSSON<sup>5</sup>, Charlotta NILSSON<sup>6</sup>, Mattias OLSSON<sup>7</sup>; Guillaume PÉDEHONTAA-HIAA<sup>8</sup>, Valery RAMZAEV<sup>9</sup>, Christopher RÄÄF<sup>10</sup>, Aleksandr VODOVATOV<sup>11</sup>

<sup>1,6</sup>Lund University, Department of Physics, Division of Nuclear Physics, Lund, Sweden; <sup>2</sup>Center for Physical Sciences and Technology, Department of Nuclear Research, Vilnius, Lithuania; <sup>3,5,8,10</sup>Lund University, Department of Translational Medicine, Medical Radiation Physics, Malmö, Sweden; <sup>4</sup>Institute of Radiobiology of NAS of Belarus, Gomel, Belarus; <sup>7</sup>Lund University, Department of Geology, Lund Sweden; <sup>9,11</sup>Research Institute of Radiation Hygiene, St Petersburg, Russia

<sup>1</sup>kristina.stenstrom@nuclear.lu.se; <sup>2</sup>vytenis.barkauskas@ftmc.lt; <sup>3</sup>christian.bernhardsson@med.lu.se; <sup>4</sup>aadvornik@yandex.ru; <sup>5</sup>mattias.jonsson@med.lu.se; <sup>6</sup>charlotta.nilsson@nuclear.lu.se; <sup>7</sup>mattias.olsson@geol.lu.se; <sup>8</sup>guillaume.pedehontaa-hiaa@med.lu.se; <sup>9</sup>v.ramzaev@mail.ru; <sup>10</sup>christopher.raaf@med.lu.se; <sup>11</sup>vodovattoff@gmail.com

**Abstract:** As part of an independent assessment of the preoperational radiation environment around the Ostrovets nuclear power plant in Belarus, grass and foodstuffs were collected in 2019 for  $^{14}\text{C}$  analysis. The preoperational  $^{14}\text{C}$  specific activities in the Ostrovets region were shown to be similar to that of European data from other uncontaminated sites.

**Keywords:** Nuclear power plant,  $^{14}\text{C}$ , preoperational assessment, Ostrovets, BelNPP

### 1. Introduction

The Belarusian nuclear power plant (BelNPP; N54.76, E26.09) located in the Ostrovets district in the Grodno region, is the first to be operated in Belarus. The nuclear power plant (NPP) is presently equipped with two Russian VVER-1200 reactors (water-water energetic reactors of type AES-2006 from Atomstroyexport). The NPP is located 50 km east of Vilnius, the capital of Lithuania, and the first reactor was officially started for test operation late in year 2020 [1]. As recommended by the IAEA, preoperational studies must be performed prior to start of a new NPP, including mapping the baseline of radiation in the environment [2]. For about one decade the Belarusian state institution Belhydromet (Republican center for hydrometeorology, radioactive contamination control and environmental monitoring) has mapped the radiation environment around BelNPP at defined observation points, some that also include monitoring systems, which comprise the official baseline data. On the initiative of BelNPP, in cooperation with “Russian green cross” and “AEB, Alpha-X91”, a preoperational monitoring programme was started in 2019 focussing on *in situ* and mobile

gamma spectrometry as well as sediment and water sampling along the Viliya river (known as the Neris river on the Lithuanian side) [3]. The survey also included sampling of terrestrial and aquatic vegetation, air and soil for analysis of gamma emitting radionuclides. Samples of water, air and vegetation were collected to determine content of  $^3\text{H}$  and  $^{14}\text{C}$ . Apart from that, radiation baseline assessments have also been carried out in forest ecosystems on the Lithuanian side of the boarder in 2017–2018 [4], including analysis of gamma emitters,  $^3\text{H}$  and  $^{14}\text{C}$ . In 2019 (September and October) a Swedish, Belarusian and Russian research team performed independent baseline measurements around BelNPP, financed by the Swedish Radiation Safety Authority (SSM, SSM project SSM2019-6032). The assessment program included *in situ* gamma spectrometry, soil and grass samplings, measurement of ambient dose rate at 45 sites selected to be evenly distributed (south, west, north) around and within 22 km of BelNPP. Sampling of foodstuff (e.g. fruits, berries, vegetables) and water was carried out around these sites for analysis of gamma emitters,  $^3\text{H}$  and  $^{14}\text{C}$ .

Operational releases of  $^{14}\text{C}$  from NPPs are highly important from a radiological perspective, due to the long physical half-life of  $^{14}\text{C}$  (5740 years), high bioavailability and global circulation of carbon. In fact, the globally dispersed radionuclides  $^3\text{H}$ ,  $^{14}\text{C}$ ,  $^{85}\text{Kr}$  and  $^{129}\text{I}$  – and in particular  $^{14}\text{C}$  – are the main contributors from the nuclear power industry to the overall long-term collective doses (integrated over < 500 years) [5].

In the present paper we report on preoperational measurements of  $^{14}\text{C}$  in samples of grass, apples, potatoes and beetroots. We also summarize typical  $^{14}\text{C}$

levels that have been found in previous preoperational assessments in Belarus and in southern Sweden, and at operational conditions, e.g., around the Ignalina NPP in Lithuania.

## 2. $^{14}\text{C}$ and the nuclear power industry

$^{14}\text{C}$  is a naturally occurring radionuclide that is continuously produced in the upper atmosphere through nuclear reactions between atmospheric oxygen/nitrogen and neutrons (the latter produced from interactions with cosmic radiation). As  $^{14}\text{C}$  is oxidized to  $\text{CO}_2$  and spread throughout the atmosphere,  $^{14}\text{C}$  will be part of the global carbon cycle and is thus incorporated into all living matter.

Anthropogenic  $^{14}\text{C}$  in the environment mainly stems from the extensive testing of nuclear weapons in the mid-20<sup>th</sup> century, as well as the nuclear power industry [5].  $^{14}\text{C}$  is also extensively used as a tracer in various research disciplines and can be formed during operation of various accelerator systems. Locally increased levels of  $^{14}\text{C}$  can therefore be seen in the environment of such facilities and practices [6, 7].

The natural specific activity of carbon in living matter is about  $226 \text{ Bq (kg C)}^{-1}$ , corresponding to a  $^{14}\text{C}/\text{C}$  ratio of about  $10^{-12}$ . An alternative and convenient unitless quantity of expressing post-bomb  $^{14}\text{C}$  levels is fraction Modern,  $\text{F}^{14}\text{C}$  [8, 9]. One advantage of using  $\text{F}^{14}\text{C}$  is that it corrects for isotope fractionation: thus  $\text{F}^{14}\text{C}$  values are directly comparable for different environmental matrixes, whereas specific activity ( $\text{Bq (kg C)}^{-1}$ ) is not [7].

The natural pre-bomb  $\text{F}^{14}\text{C}$  level is  $\sim 1$ , corresponding to about  $226 \text{ Bq (kg C)}^{-1}$ , whereas the maximum  $\text{F}^{14}\text{C}$  resulting from nuclear weapon tests in the 1960s was  $\sim 2$ . Spatial variability in clean air  $^{14}\text{C}$  levels is small in the northern and southern hemisphere, respectively [10]. Since the peak in  $^{14}\text{C}$  activity concentration in 1963,  $\text{F}^{14}\text{C}$  has decreased in an almost exponential fashion due to transfer and mixing with the oceans and biosphere, and due to dilution caused by the increasing  $\text{CO}_2$  concentration resulting from the combustion of fossil fuels (see e.g. [7] and references therein).

In nuclear reactors,  $^{14}\text{C}$  is produced mainly through neutron activation reactions e.g. in nitrogen (e.g.  $^{14}\text{N(n,p)}^{14}\text{C}$ ; high thermal neutron capture cross section of 1.82 b), oxygen (e.g.  $^{17}\text{O(n,\alpha)}^{14}\text{C}$ ; high thermal neutron capture cross section of 0.24 b) and carbon (e.g.  $^{13}\text{C(n,\gamma)}^{14}\text{C}$ ; cross section 0.9 mb) [11]. Nitrogen and oxygen may occur in the fuels, moderators and coolants. The  $^{13}\text{C(n,\gamma)}^{14}\text{C}$  reaction is highly relevant for reactors with graphite moderators. For most reactors, the  $^{14}\text{C}$  released into the environment mainly originates from the coolant/moderator, and airborne releases are dominating over liquid discharges [11]. For all reactor types except Pressurized Water Reactors (PWRs),  $^{14}\text{CO}_2$  is the dominating chemical form of release [12]. According to Zazzeri *et al.* [12], on average 72% of the  $^{14}\text{C}$  releases from PWRs occur as  $^{14}\text{CH}_4$  and the rest as  $^{14}\text{CO}_2$ . The VVER reactors in Ostrovetz are of the PWR type. According to Zazzeri *et al.* [12], VVER reactors have higher emissions of  $^{14}\text{C}$  than other PWR reactors. Details on the  $^{14}\text{C}$  production rates and release rates

from various types of nuclear reactors can be found e.g. in Zazzeri *et al.* [12].

Examples of typical excess concentrations of  $^{14}\text{C}$  in the vicinity of VVER reactors can be found in the literature. Janovics *et al.* [13] report a small excess in  $^{14}\text{CO}_2$  of up to 1.3% above clean air background in annual (year 2000-2009) growth rings of trees located within 1 km of Paks NPP ( $4 \times 500 \text{ MW}_{\text{el}}$ ) in Hungary. Varga *et al.* [14] report that the monitoring stations located  $< 2$  km from Paks NPP show an average  $^{14}\text{CO}_2$  excess of 0.38% whereas the average  $^{14}\text{CO}_2 + ^{14}\text{C}_n\text{H}_m$  excess was 3.11% in years 2015 and 2016.

Jeřkovský *et al.* [15] and Kontul' *et al.* [16] have monitored  $^{14}\text{C}$  in  $\text{CO}_2$  and annual tree rings close to the NPP Jaslovské Bohunice ( $2 \times 440 \text{ MW}_{\text{el}}$ ) in Slovakia. Large variations in  $^{14}\text{C}$  were observed in  $\text{CO}_2$ : up to about 17% above clean air background was occasionally observed, whereas the tree rings and the annual average  $^{14}\text{C}$  levels in air were close to central European background data [15].

An example of a study from other types of PWRs is Dias *et al.* [17] who found up to 22% excess  $^{14}\text{C}$  specific activities in grass samples collected around Angra NPP (one Westinghouse PWR of  $567 \text{ MW}_{\text{el}}$  and one Siemens PWR of  $1350 \text{ MW}_{\text{el}}$ ) in Brazil.

Other types of nuclear reactors, in particular Heavy Water Reactors (HWRs), are known to contribute to significantly higher environmental  $^{14}\text{C}$  concentrations. Milton *et al.* [18] found  $\sim 13 \text{ kBq (kg C)}^{-1}$  in fruits grown in the year of 1996 at  $\sim 1$  km from the large Pickering Nuclear Generating Station (entirely based on HWRs) in Canada, corresponding to a  $\text{F}^{14}\text{C}$  value of  $\sim 58$ . Studies at Pickering in 1998 by Stenström *et al.* [6] showed a  $\text{F}^{14}\text{C}$  value of  $6.84 \pm 0.15$  in grass collected 2 km from the facility, and at a distance of 100 km an excess of 7% was found.

The former NPP in Ignalina (one RBMK-1500 reactor), Lithuania, is located only  $\sim 100$  km NNE of BelNPP, and its environmental impact is therefore of particular interest for preoperational studies of the radiation environment around BelNPP. Graphite moderated reactors like the RBMK has the potential of not only releasing  $^{14}\text{C}$  as gases, but also as graphite particles. Several studies have been performed around Ignalina NPP in the past (e.g. [19, 20]), and a few of these studies have involved some of the authors of the present paper [21-23]. In 2003, an excess  $^{14}\text{C}$  of up to 42% above clean air background was found among various vegetation samples collected within 400 m of the stack of Ignalina NPP [21]. Even higher activity concentrations were found in moss samples, up to  $\sim 20$  times the clean air background ( $4.7 \text{ kBq (kg C)}^{-1}$ ) [21]. In another study conducted between 2001 and 2004,  $\sim 70$  samples of leaves, grass, moss, soil and aquatic plants were collected up to a distance of 32 km from Ignalina NPP [22]. Soil samples collected within 500 m of the NPP showed up to  $\sim 20$  times the clean air background. Moss samples collected within up to  $\sim 4$  km from the NPP showed excess  $^{14}\text{C}$  of up to  $\sim 70\%$ , whereas moss samples collected at longer distances showed no apparent  $^{14}\text{C}$  excess [22].

Chernobyl NPP is located  $\sim 460$  km SE of BelNPP. Studies after the Chernobyl accident in 1986 showed

that  $^{14}\text{C}$  was released in large amounts as  $\text{CO}_2$  as well as graphite particles (see [24] and references therein). The impact from the Chernobyl accident, as well as from normal operation of nearby nuclear reactors (Ignalina NPP, Chernobyl and Smolensk), on the environment in Belarus has been studied by Mikhajlov *et al.* using Liquid Scintillation Counting (LSC) [25]. In 1986,  $\text{F}^{14}\text{C} \sim 2$  was found in grass samples collected near Minsk, and in the Gomel region  $\text{F}^{14}\text{C}$  in grass was as high as up to  $\text{F}^{14}\text{C} \sim 7$  (see [25] and references therein). Vegetation samples collected in 1994–1999 in the Gomel region had  $\text{F}^{14}\text{C}$  up to  $\sim 1.8$  (the highest value in a moss sample) [25]. Chernobyl  $^{14}\text{C}$  was also seen e.g. in a moss sample collected in 1994 in the Volozhin district ( $\text{F}^{14}\text{C} \sim 1.26$ ) [25], which is located  $\sim 80$  km SSE from BelNPP. Close to Ignalina NPP,  $\text{F}^{14}\text{C}$  values of up to  $\sim 1.9$  were found in vegetation collected in 1994 [25], corresponding to a maximum excess of  $\sim 70\%$  compared to central European clean air data ( $\text{F}^{14}\text{C} \sim 1.13$  [26]). Areas remote from Ignalina and Chernobyl showed  $^{14}\text{C}$  levels corresponding to  $\text{F}^{14}\text{C}$  ranging between 0.92 and 1.07 (analytical accuracy and precision not stated in the paper) [25], i.e. close to central European clean air data.

### 3. Materials and methods

Samples of *Poaceae sp.* (grass,  $N=12$ ), *Malus domestica* (apple,  $N=4$ ), *Solanum tuberosum* (potato,  $N=3$ ) and *Beta vulgaris* (beetroot,  $N=1$ ) were collected between 15 and 17 October 2019 at 13 sites close to BelNPP, as described in Table 1 and shown in Figure 1. In total 20 samples were collected, and at several of the sites more than one species were sampled. All sampling sites were located within 22 km of the NPP. The majority of the samples were collected north, west and south of the power plant, covering the area between BelNPP and the Belarusian-Lithuanian border. The area east of the NPP has not yet been included (due to the swampy terrain in the area).

**Table 1.** Sampling sites around BelNPP.

Site	Name	Lat	Long
30	Troshchany	54.924	26.199
31	Barani	54.919	26.111
33	Podol'tsy	54.867	26.087
36	Bystrica	54.796	25.880
37	Zharneli	54.806	25.791
38	Asinovka	54.723	25.780
39	Zacharyski	54.702	25.817
40	Drevenyaki	54.645	25.835
41	Radiuli	54.649	26.074
42	Palushi	54.607	25.875
43	Grodi	54.524	25.885
44	Ostrovets infocentre	54.616	25.982
46	Mikhalishki	54.813	26.158

After collection, the samples were transported to Lund University, Sweden. Single apples, potatoes and beetroots were cut into small pieces prior to drying the samples for several hours in an oven at  $30\text{--}50^\circ\text{C}$  according to the procedures described in Bernhardsson *et al.* [7]. A few strands of each grass sample were also dried prior to being cut into small pieces. A few mg of

each dried sample was taken further to a graphitization process, in which typically 1–2 mg of carbon was extracted from each sample, using the system AGE [27] at the Radiocarbon Dating Laboratory in Lund. The extracted carbon from each sample was pressed into separate aluminium holders, along with graphitized standard samples of known activity and background samples (graphitized  $^{14}\text{C}$ -free fossil material). The  $^{14}\text{C}$  content of the samples were determined from measurements using the Single Stage Accelerator Mass Spectrometry (SSAMS) facility at the Radiocarbon Dating Laboratory at Lund University and subsequent data analysis [28, 29]. Results were expressed as the quantity  $\text{F}^{14}\text{C}$ . Typical analytical uncertainties were  $\sim 0.5\%$  (1 standard deviation). Further details on sample preparation, measurement, analysis and quality assessment can be found in Bernhardsson *et al.* [7], as well as relations between  $\text{F}^{14}\text{C}$  and activity concentrations in various environmental sample types.

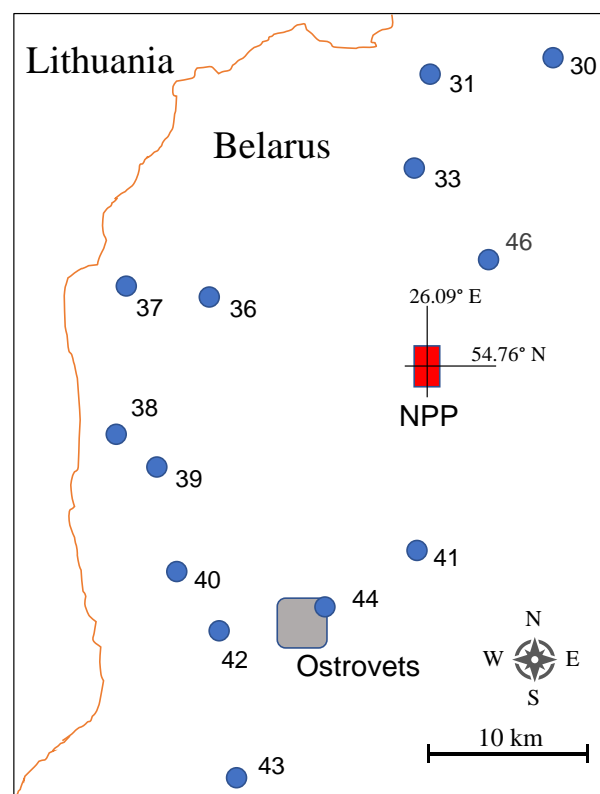


**Fig. 1.** Location of sampling points near the site of the Belarusian NPP.

The obtained results were compared to summer means of clean air  $\text{CO}_2$  data from Sweden (Hyltemossa Research Station,  $N56.10$ ,  $E13.42$ , 46 km NNE of Lund) [30]. Additionally, the data from Belarus was compared to preoperational data from year 2019 for 10 samples of grass, fruits and/or berries collected around the neutron research facility European Spallation Source (ESS;  $N55.73$ ,  $E13.45$ ) [31], which is currently under construction in the outskirts of Lund. The ESS samples were collected between end of August and beginning of October 2019. Data was also compared with the results from preoperational assessments at the Lithuanian-Belarusian border reported by ref [4].



#### 4. Results and discussion

The results of the  $^{14}\text{C}$  analyses of the 20 samples of *Poaceae sp.* (grass), *Malus domestica* (apple), *Solanum tuberosum* (potato) and *Beta vulgaris* (beetroot) are shown in Table 2. The mean of all  $\text{F}^{14}\text{C}$  values was 1.011 (standard deviation (STD): 0.004; standard uncertainty of the mean (SUM): 0.001). The data were normally distributed with no significant outlier. The mean values of the grass and apple samples, respectively, were not significantly different (at the 0.05 level according to an ANOVA test).

**Table 2.**  $\text{F}^{14}\text{C}$  in samples collected around the Belarusian NPP in the Ostrovets district between 15 and 17 October 2019. Uncertainties represent 1 standard deviation.

Site	Species	$\text{F}^{14}\text{C}$
30	<i>Malus domestica</i> (apple)	$1.014 \pm 0.006$
30	<i>Poaceae sp.</i> (grass)	$1.009 \pm 0.006$
31	<i>Solanum tuberosum</i> (potato)	$1.007 \pm 0.006$
31	<i>Poaceae sp.</i> (grass)	$1.014 \pm 0.006$
33	<i>Poaceae sp.</i> (grass)	$1.015 \pm 0.006$
33	<i>Solanum tuberosum</i> (potato)	$1.016 \pm 0.006$
33	<i>Beta vulgaris</i> (beetroot)	$1.003 \pm 0.006$
36	<i>Malus domestica</i> (apple)	$1.009 \pm 0.005$
36	<i>Poaceae sp.</i> (grass)	$1.011 \pm 0.005$
37	<i>Malus domestica</i> (apple)	$1.008 \pm 0.005$
37	<i>Poaceae sp.</i> (grass)	$1.009 \pm 0.005$
38	<i>Poaceae sp.</i> (grass)	$1.013 \pm 0.005$
39	<i>Poaceae sp.</i> (grass)	$1.010 \pm 0.005$
40	<i>Poaceae sp.</i> (grass)	$1.015 \pm 0.005$
41	<i>Poaceae sp.</i> (grass)	$1.007 \pm 0.005$
41	<i>Malus domestica</i> (apple)	$1.009 \pm 0.005$
42	<i>Poaceae sp.</i> (grass)	$1.015 \pm 0.005$
43	<i>Poaceae sp.</i> (grass)	$1.013 \pm 0.005$
44	<i>Poaceae sp.</i> (grass)	$1.007 \pm 0.005$
46	<i>Solanum tuberosum</i> (potato)	$1.008 \pm 0.005$

The mean of the data from the Belarusian samples was identical to the mean of the 10 environmental samples of grass, fruits and/or berries collected in preoperational studies around the ESS facility in Lund the same year: the mean  $\text{F}^{14}\text{C}$  value of all ESS samples was 1.011 (STD: 0.004; SUM: 0.001) [31]. Both data sets, the samples collected around ESS in Sweden and around BelNPP in Belarus, are slightly higher (<0.4% higher, statistically significant at the 0.05 level in a two-sample t test) than  $\text{F}^{14}\text{C}$  data from atmospheric  $\text{CO}_2$  from the ICOS Hyltemossa Research Station (mean  $\text{F}^{14}\text{C}$  for May to August 2019 of 1.007 (STD: 0.003; SUM: 0.001).

Jefanova *et al.* [4] present  $^{14}\text{C}$  data from terrestrial samples collected in 2017–2018 in Lithuania, within the 30-km zone of the BelNPP. LSC measurements provided  $\text{F}^{14}\text{C}$  values in 27 samples of moss, blueberry, rowan, birch and mugwort between  $0.978 \pm 0.013$  and  $1.024 \pm 0.008$ , with an average of 0.993 (STD 0.013; SUM 0.002). As noted by Jefanova *et al.* [4], this is slightly lower (~2%) than Central European clean air data: the average  $\text{F}^{14}\text{C}$  of data corresponding to the growing season of 2017 (May to Aug) was 1.015 (STD 0.002; SUM 0.001) and the corresponding value for 2018 was 1.012 (STD 0.002; SUM 0.001) [26, 32–34]. Jefanova *et al.* [4] speculate that contamination by fossil carbon could cause the offset. Swedish data obtained

from 36 terrestrial samples collected in 2017 in southern Scania region (southern Sweden) as preoperational data for the ESS facility was 1.017 (STD 0.005; SUM 0.001) [7], which is not statistically significantly different from clean air European data. For the 30 Scanian samples collected in 2018 the corresponding average  $\text{F}^{14}\text{C}$  value was 1.016 (STD 0.004; SUM: 0.001), which is only slightly (<0.4%) higher than the average central European data during the growing season. Thus, the Swedish data do not show any general contamination of fossil carbon in the samples analysed.

#### 5. Conclusions

The independent preoperational assessment of  $^{14}\text{C}$  levels in 20 vegetation samples collected in year 2019 within 22 km north, west and south of the Belarusian NPP showed the same mean value as preoperational assessments around the European Spallation Source neutron research facility in Lund, Sweden ( $\text{F}^{14}\text{C}$ =1.011; STD: 0.004; SUM: 0.001). No evidence of  $^{14}\text{C}$  from other present or previous nearby sources or from the Chernobyl accident was apparent in the vegetation samples analysed. In the present study, only samples of grass and foodstuffs were analysed, which reflect the  $^{14}\text{C}$  concentration in atmospheric  $\text{CO}_2$ . It would be of interest to also investigate soil samples to study if any  $^{14}\text{C}$ -containing graphite from the Chernobyl accident or from Ignalina NPP has reached the Ostrovets area.

#### 6. References

1. Belarusian Nuclear Power Plant. Accessed: 2021-08-11. Available from: <https://belaes.by/en/>.
2. IAEA. *Environmental and Source Monitoring for Purposes of Radiation Protection*. Safety Guide RSG1. 8. 2005.
3. *Pre-operational studies in the area of the Belarusian NPP (zero background)*. Express report. Accessed: 2021-08-16. Available from: <https://belaes.by/ru/ekologiya/otchet-po-rezultatam-ekologicheskogo-monitoringa-v-zone-nablyudeniya-belorusskoj-aes.html>. (in Russian).
4. Jefanova, O., Baužienė, I., Lujanienė, G., Švedienė, J., Raudonienė, V., Bridžiuviene, D., Paškevičius, A., et al. *Initiation of radioecological monitoring of forest soils and plants at the Lithuanian border region before the start of the Belarusian nuclear power plant operation*. Environmental Monitoring and Assessment, 192(10): 1–18, 2020.
5. UNSCEAR. *UNSCEAR 2016 Report—Sources, Effects and Risks of Ionizing Radiation*. Report to the General Assembly. Scientific Annexes A, B, C, and D. Available on [unscear.org/unscear/en/publications/2016.html](https://unscear.org/unscear/en/publications/2016.html). (accessed 15 Oct 2017). 2016.
6. Stenström, K., Skog, G., Nilsson, C.M., Hellborg, R., Leide-Svegborn, S., Georgiadou, E., Mattsson, S. *Local variations in  $^{14}\text{C}$  – How is bomb-pulse dating of human tissues and cells affected?* Nuclear Instruments and Methods in Physics Research Section B: Beam Interactions with Materials and Atoms, 268(7–8): 1299–1302, 2010.
7. Bernhardsson, C., Eriksson Stenström, K., Jönsson, M., Mattsson, S., Pedehontaa-Hiaa, G., Rääf, C., Sundin, K., et al. *Assessment of "Zero Point" radiation around the ESS facility*. Report MA RADFYS 2018:01, Report BAR-2018/04. <https://portal.research.lu.se/portal/sv/publications/assessm-ent-of-zero-point-radiation-around-the-ess->



- facility(2153e07c-b465-4191-abc3-dbfcaf28b85b).html. 2018.
8. Reimer, P.J., Brown, T.A., Reimer, R.W. *Discussion: Reporting and calibration of post-bomb  $^{14}\text{C}$  data*. Radiocarbon, 46(3): 1299-1304, 2004.
  9. Eriksson Stenström, K., Skog, G., Georgiadou, E., Genberg, J., Johansson, A. *A guide to radiocarbon units and calculations*. LUNFD6(NFFR-3111)/1-17/(2011). Lund University. Dep of Physics. Div of Nuclear Physics. <http://lup.lub.lu.se/search/ws/files/5555659/2173661.pdf>. 2011.
  10. Hua, Q., Barbetti, M., Rakowski, A.Z. *Atmospheric Radiocarbon for the Period 1950–2010*. Radiocarbon, 55(4): 2059-2072, 2013.
  11. IAEA. *Management of waste containing tritium and carbon-14*. Technical report series no 421. 2004.
  12. Zazzeri, G., Yeomans, E.A., Graven, H. *Global and regional emissions of radiocarbon from nuclear power plants from 1972 to 2016*. Radiocarbon, 60(4): 1067-1081, 2018.
  13. Janovics, R., Kern, Z., Güttler, D., Wacker, L., Barnabás, I., Molnár, M. *Radiocarbon impact on a nearby tree of a light-water VVER-type nuclear power plant, Paks, Hungary*. Radiocarbon, 55(2): 826-832, 2013.
  14. Varga, T., Orsovski, G., Major, I., Veres, M., Bujtás, T., Végh, G., Manga, L., et al. *Advanced atmospheric  $^{14}\text{C}$  monitoring around the Paks Nuclear Power Plant, Hungary*. Journal of Environmental Radioactivity, 213: 106138, 2020.
  15. Jeřkovský, M., Povinec, P.P., Steier, P., Šivo, A., Richtáriková, M., Golser, R. *Retrospective study of  $^{14}\text{C}$  concentration in the vicinity of NPP Jaslovské Bohunice using tree rings and the AMS technique*. Nuclear Instruments and Methods in Physics Research Section B: Beam Interactions with Materials and Atoms, 361: 129-132, 2015.
  16. Kontuľ, I., Povinec, P.P., Šivo, A., Richtáriková, M. *Radiocarbon in the atmosphere around the Bohunice nuclear power plant in Slovakia*. Journal of Radioanalytical and Nuclear Chemistry, 318(3): 2335-2339, 2018.
  17. Dias, C.M., Santos, R.V., Stenstrom, K., Nicoli, I.G., Skog, G., da Silveira Correa, R.  *$^{14}\text{C}$  content in vegetation in the vicinities of Brazilian nuclear power reactors*. J Environ Radioact, 99(7): 1095-101, 2008.
  18. Milton, G.M., Kramer, S.J., Brown, R.M., Repta, C.J.W., King, K.J., Rao, R.R. *Radiocarbon dispersion around Canadian nuclear facilities*. Radiocarbon, 37(2): 485-496, 1995.
  19. Mikhajlov, N.D., Kolkovsky, V.M., Pavlova, I.D. *Radiocarbon distribution in northwest Belarus near the Ignalina nuclear power plant*. Radiocarbon, 41(1): 75-79, 1999.
  20. Ežerinskis, Ž., Šapolaitė, J., Pabedinskas, A., Juodis, L., Garbaras, A., Maceika, E., Druteikienė, R., et al. *Annual variations of  $^{14}\text{C}$  concentration in the tree rings in the vicinity of Ignalina Nuclear Power Plant*. Radiocarbon, 60(4): 1227-1236, 2018.
  21. Magnusson, Å., Stenström, K., Skog, G., Adliene, D., Adlys, G., Hellborg, R., Olariu, A., et al. *Levels of  $^{14}\text{C}$  in the terrestrial environment in the vicinity of two European nuclear power plants*. Radiocarbon, 46(2): 863-868, 2004.
  22. Magnusson, Å., Stenström, K., Adliene, D., Adlys, G., Dias, C., Rääf, C., Skog, G., et al. *Carbon-14 levels in the vicinity of the Lithuanian nuclear power plant Ignalina*. Nuclear Instruments and Methods in Physics Research Section B: Beam Interactions with Materials and Atoms, 259(1): 530-535, 2007.
  23. Adliene, D., Rääf, C., Magnusson, Å., Behring, J., Zakaria, M., Adlys, G., Skog, G., et al. *Assessment of the environmental contamination with long-lived radionuclides around an operating RBMK reactor station*. J Environ Radioact, 90(1): 68-77, 2006.
  24. Buzinny, M. *Radioactive graphite dispersion in the environment in the vicinity of the Chernobyl Nuclear Power Plant*. Radiocarbon, 48(3): 451-458, 2006.
  25. Mikhajlov, N., Kolkovskij, V., Pavlova, I., Luchina, G. *Radiocarbon in elements of the landscape (Belarus)*. Geochronometria: Journal on Methods & Applications of Absolute Chronology, 23, 2004.
  26. Levin, I., Kromer, B. *The tropospheric  $^{14}\text{CO}_2$  level in mid latitudes of the Northern Hemisphere (1959-2003)*. Radiocarbon, 46: 1261-1271, 2004.
  27. Wacker, L., Němec, M., Bourquin, J. *A revolutionary graphitisation system: Fully automated, compact and simple*. Nuclear Instruments and Methods in Physics Research Section B: Beam Interactions with Materials and Atoms, 268(7): 931-934, 2010.
  28. Skog, G., Rundgren, M., Sköld, P. *Status of the Single Stage AMS machine at Lund University after 4 years of operation*. Nuclear Instruments and Methods in Physics Research Section B: Beam Interactions with Materials and Atoms, 268(7-8): 895-897, 2010.
  29. Skog, G. *The single stage AMS machine at Lund University: Status report*. Nuclear Instruments and Methods in Physics Research Section B: Beam Interactions with Materials and Atoms, 259(1): 1-6, 2007.
  30. ICOS. *ICOS ATC  $^{14}\text{C}$  release from Hyltemossa 2016-12-22 – 2019-10-08*. <https://data.icos-cp.eu/portal/>. PID: 11676/WE07MZ3UIYcJau76jaTIW\_Sg. ICOS DATA is licensed under CC4BY (<http://creativecommons.org/licenses/by/4.0/>). 2020.
  31. Bernhardsson, C., Eriksson Stenström, K., Pedehontaa-Hiaa, G., Jönsson, M. *Radiological environmental monitoring at the ESS facility – Annual report 2019*. Report MA RADFYS 2020:03, Report BAR-2020/03. 2020.
  32. Conen, F., Emmenegger, L., Leuenberger, M., Steger, D., Steinbacher, M. *"ICOS RI, 2020. ICOS ATC  $^{14}\text{C}$  Release, Jungfraujoch (10.0 m), 2016-01-04\_2019-08-12"*. [hdl.handle.net/11676/X-IXPKZIO4DWX7wnclQ7akY](https://hdl.handle.net/11676/X-IXPKZIO4DWX7wnclQ7akY); <http://calib.org/CALIBomb/>. 2019.
  33. Levin, I., Kromer, B., Hammer, S. *Atmospheric  $\delta^{14}\text{CO}_2$  trend in Western European background air from 2000 to 2012*. Tellus B: Chemical and Physical Meteorology, 65(1): 20092, 2013.
  34. Hammer, S., Levin, I. *Monthly mean atmospheric  $\delta^{14}\text{CO}_2$  at Jungfraujoch and Schauinsland from 1986 to 2016*. heiDATA: Heidelberg Research Data Repository [Distributor] V2 [Version]. <http://dx.doi.org/10.11588/data/10100>; [www.calibomb.org](http://www.calibomb.org). 2017.

## ACCUMULATION OF $^{137}\text{Cs}$ BY FOREST LICHENS IN THE CHERNOBYL AFFECTED TERRITORIES

Aliaksandr DVORNIK, Veranika SEHLIN

Institute of Radiobiology of the National Academy of Sciences of Belarus, Gomel, Belarus  
aadvornik@gmail.com, seglinv@mail.ru

**Abstract:** The content of cesium-137 in epiphytic and epigeous species of lichens collected in the pinewoods around the Chernobyl Nuclear Power Plant ranges between 5.6 and 268 kBq per kg depending on the sampling site. A high positive correlation is shown between the specific activities of  $^{137}\text{Cs}$  in lichens and its concentrations in pine bark.

**Keywords:** Lichens, accumulation, biomonitoring, radioactive contamination, pine forest

### 1. Introduction

The accident at the Chernobyl Nuclear Power Plant (ChNPP) of 1986 resulted in more than 1.7 million hectares of the forest area of Belarus being contaminated by  $^{137}\text{Cs}$ . The most contaminated forest territories (up to 59.2 MBq m<sup>-2</sup> as of 1986) are located in the 30-km zone around the ChNPP [1].

For a long time now, the properties of lichens as biomonitors have been used to assess radioactivity in the environment [2-4]. Lichens are symbiotic organisms consisting of fungi and algae. The lichen biota is regarded extremely useful for the purposes of radioecological monitoring due to their valuable characteristics: a) widespread occurrence throughout terrestrial ecosystems on a variety of substrates such as stones, trees, soils etc.; b) specific anatomical and morphological structure (i.e. no root system or wax cuticle) that predetermines their ability to accumulate different air pollutants; c) high adsorbing capacity of the entire surface of a vegetative body (thallus) and a long lifespan due to low metabolic activity and slow growth rate during the year [2, 5].

A unique accumulative and adsorbent potential of lichens has predetermined their value for biological monitoring of contaminants in the environment [5-7]. The study of Handley and Overstreet [8] shows that the fixation of radiocesium in lichens does not seem to depend on their physiological activity but occurs mainly in a passive way. Lichens absorb the bulk of radioactive

substances from aerial deposition, but also have the ability to accumulate radionuclides from the substrate (aquatic environment, soil and other surfaces) [9].

In the past 35 years the world has seen at least two large-scale nuclear disasters – Chernobyl and Fukushima Daiichi. Lichens have been successfully tested in some European countries as a tool for assessing cumulative deposition of long-lived radionuclides [10, 11]. The Fukushima Daiichi accident has triggered a new wave of research on the capacity of lichens to absorb and retain radionuclides [12, 13]. The common species of lichens used in such studies are *Cladonia* spp., *Hypogymnia physodes* (L.) Nyl., *Cetraria islandica* (L.) Ach., *Pseudevernia furfuracea* (L.) Zopf, *Parmelia sulcata* Taylor, *Umbilicaria* spp. etc. [14, 15].

The substrate pH, soil structure, snow coverage and other environmental conditions can affect the mobility of radionuclides in the lichen thalli [15, 16]. Some researchers [17, 18] note the concentrations of  $^{137}\text{Cs}$  in individual lichens may increase over time due to the washing of this radionuclide off of the tree crowns. This research paper summarizes the results of our study on  $^{137}\text{Cs}$  accumulation in lichens collected in contaminated pine forests within the 30-km zone around the ChNPP.

### 2. Material and Methods

#### 2.1. Site and sampling description

Three species of epiphytic and epigeous lichens were collected from pinewoods in the three sampling sites inside the 30-km Chernobyl Zone in 2020-2021 (Fig. 1). This choice was driven by the fact that pine trees cover more than 60% of the forestland area in the Belarusian Polesie. The average age of pine trees is 50 ± 5 years. A summarized description of the sampling sites is presented in Table 1.

Air dose measurements were taken using portable dosimeter-radiometers MKS-AT1125A (Atomtex, Belarus) equipped with a scintillation detector NaI (TI). *In situ* measurements were carried out in 5 points in a

square area of 50×50 meters at a height of 1 m above the ground. The measurement uncertainty was up to 15%.

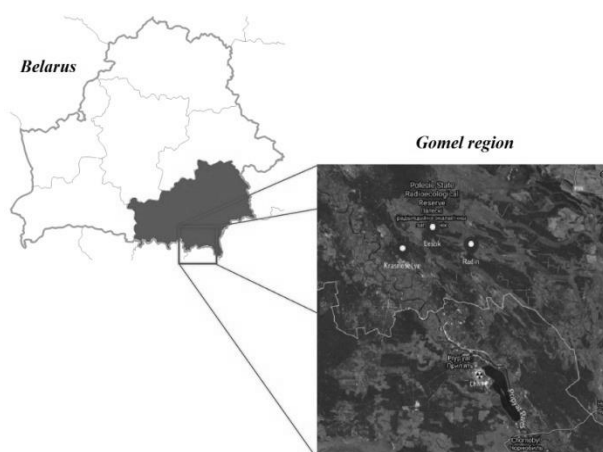


Fig. 1. Location of the sampling sites

Table 1. Characteristics of the sampling sites

Location	Coordinates	$^{137}\text{Cs}$ deposition density, $\text{kBq m}^{-2}$	Gamma-dose rate, $\mu\text{Sv h}^{-1}$
Radin	N 51°34.210' E 30°04.975'	$2599.6 \pm 94.1$	$3.2 \pm 0.3$
Krasnosel'ye	N 51°33.872' E 29°54.453'	$1827.2 \pm 64.4$	$1.7 \pm 0.2$
Lesok	N 51°36.211' E 29°59.054'	$1152.8 \pm 39.3$	$1.3 \pm 0.2$

The samples of lichens were collected in dry weather. At each location, 5 stand-alone upright pine trees with a maximum lichen projective cover were selected. The sampling of epiphytic lichens from a tree stem was done at a height of 1–1.5 m aboveground. Epigeous species were collected from the same trees from the sampling area of 25×25 cm from below the crowns. All sampled thalli were approximately of the same size and age. The lichens collected as samples included the following species: *Hypogymniaphysodes* (L.) Nyl., *Cladonia rangiferina* (L.) Weber ex F.H. Wigg. and *C. arbuscula* (Wallr.) Flot. ( $N = 43$ ).

Radionuclide deposition density in soils was calculated using a composite sample collected from each site. Soil samples were taken to a depth of 20 cm using a core sampler with a diameter of 5 cm. Each soil core was split into layers 1–5 cm deep each (up to maximum depth of 20 cm) using a spatula. Soil samples of the same depth were then mixed together to acquire the site's composite sample.

## 2.2 Sample preparation and activity measurements

The samples were thoroughly cleaned of any left adhering substrate, soil particles and other foreign matter. After cleaning, the samples were first dried at a room temperature and then homogenized. The activity concentrations of  $^{137}\text{Cs}$  were measured in the air-dried samples of two geometries – with a diameter of 11 cm and a height of 8.8 cm (Marinelli beaker, up to 0.5 L in

volume), and with a diameter of 7 cm and a height of 3.2 cm. Each sample was measured three times.

The activity concentration of  $^{137}\text{Cs}$  was measured with a gamma-spectrometer equipped with an HPGe detector (Canberra DSA-LX, USA). The energy resolution of the detector was 1.85 keV for  $^{60}\text{Co}$  at 1.33 MeV. The detection efficiency of spectrum for the energy of 1.33 MeV was 23.5%. Measurement errors ranged from 7 to 10% depending on the sample activity. The specific activity ( $\text{kBq kg}^{-1}$ ) per dry weight was used to estimate the level of radioactivity in samples.

## 2.3 Statistical analysis

Statistical analysis of data was performed with the use of Python libraries for data science such as: NumPy, Matplotlib and Pandas. The data was described in terms of range, mean value, standard error and coefficient of variation. A statistically significant value was  $p < 0.05$ .

## 3. Results and Discussion

### 3.1 Soil deposition density and ambient gamma radiation levels

As shown in Figure 2, the distribution of cesium in the soil profile of the sampling site is relatively similar for all three locations. The soil deposition density ranges from 610.5  $\text{kBq m}^{-2}$  in Lesok to 2902.3  $\text{kBq m}^{-2}$  in Radin.

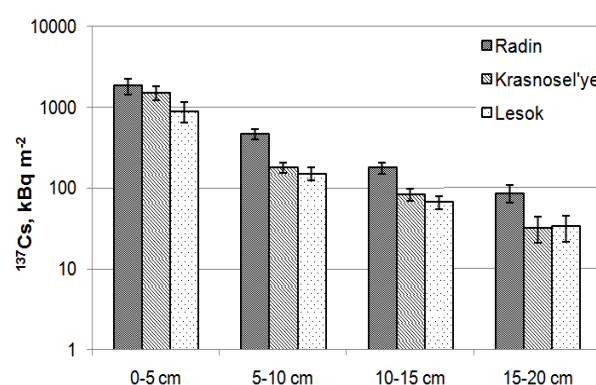


Fig. 2. Vertical distribution of long-lived radionuclides in the soil profile

The activity of radionuclides in soil decreases with depth. The highest concentrations of  $^{137}\text{Cs}$ , as well as of the transuranic elements, are in the top 0–5 cm soil layer. Depending on the site, the fraction of  $^{137}\text{Cs}$  in this layer varies in the range of 58–87%.

The ambient dose rates measured in three locations vary from 1.1  $\mu\text{Sv h}^{-1}$  in Lesok to 3.2  $\mu\text{Sv h}^{-1}$  in Radin. Both of the above parameters are well interrelated and show a positive correlation (Pearson's  $r = 0.86$ ,  $p < 0.01$ ,  $n = 15$ ).

### 3.2 $^{137}\text{Cs}$ activity concentration in the lichen biomass

The values of  $^{137}\text{Cs}$  specific activity in the biomass of *Hypogymnia physodes*, *Cladonia rangiferina* and *C. arbuscula* are given in Table 2. The specific activity of cesium varies considerably (from 5.6 to 268.4  $\text{kBq kg}^{-1}$ ) in the lichens of different taxonomic groups. The highest specific activity was measured in *Hypogymnia*

*physodes* from Radin, and the lowest one in *Cladonia rangiferina* collected in Krasnosel'ye.

**Table 2.** Specific activities of  $^{137}\text{Cs}$  ( $\text{kBq kg}^{-1}$  dry weight)

Location	Species	Specific activity of $^{137}\text{Cs}$ , $\text{kBq kg}^{-1}$	
		mean $\pm$ SE	CV, %
Radin	<i>Hypogymnia physodes</i>	139.7 $\pm$ 34.2	54.7
	<i>Cladonia rangiferina</i>	91.6 $\pm$ 36.4	88.9
Krasnosel'ye	<i>Hypogymnia physodes</i>	23.3 $\pm$ 5.7	73.8
	<i>Cladonia rangiferina</i>	13.1 $\pm$ 3.2	55.0
	<i>Cladonia arbuscula</i>	17.9 $\pm$ 3.3	31.3
Lesok	<i>Hypogymnia physodes</i>	36.6 $\pm$ 2.2	18.6
	<i>Cladonia rangiferina</i>	22.1 $\pm$ 1.6	16.3

The mean values of activity per kg of biomass are  $51.8 \pm 11.2$   $\text{kBq kg}^{-1}$  for *Hypogymnia physodes* and  $42.3 \pm 14.7$   $\text{kBq kg}^{-1}$  for *Cladonia rangiferina*. The mean for *C. arbuscula* is  $17.9 \pm 3.3$   $\text{kBq kg}^{-1}$ . The highest contaminated lichens were collected in the site of Radin. A coefficient of variation for the content of  $^{137}\text{Cs}$  in the lichen biomass varies from 16.3 to 88.9%. The largest variability of values is characteristic to the Radin and Krasnosel'ye locations ranging from 54.7 to 88.8% and from 42.2 to 70.3% respectively. This can be explained by the differences in accumulation capacity of individual lichens, which may be due to the intensified impact of multiple factors such as the soil's physicochemical characteristics, amounts of precipitation, periods of heat and drought in different years etc.

The specific activity of  $^{137}\text{Cs}$  in *Hypogymnia physodes* is significantly higher than that in other lichen species in all sampling sites under similar growth and co-habitat conditions (Fig. 3). The radionuclide content in the biomass of *Hypogymnia physodes* and *Cladonia* lichens from Radin and Krasnosel'ye is not statistically different. According to some studies [14], an additional source of radionuclide contamination in epiphytic lichens may be the water washed out from the trees and shrubs.

### 3.3 Lichens and substrates

The content of  $^{137}\text{Cs}$  in the lichen biomass was compared against its deposition in the substrates, i.e. pine bark and soil. The accumulation of  $^{137}\text{Cs}$  by the biomass of epiphytic lichens is from 3.4 to 12.5 times higher than that by the pine bark.

The Pearson's correlation coefficient shows a strong relationship between cesium specific activity in the biomass of *Hypogymnia physodes* and cesium specific activity in the bark samples ( $r = 0.96$ ,  $p < 0.001$ ). Epiphytic lichens accumulate by up to 12 times more radiocesium than the pine bark. Similar results were reported by Biazrov [14], who found that after 2 years following the ChNPP accident the content of  $^{137}\text{Cs}$  in *Hypogymnia physodes* and *Cladonia* species was several times higher than in the pine bark. The differences in these parameters can be basically explained by the differences in the radionuclide pathways attributable to lichens and trees. While vegetation accumulates radiocesium owing to its active root uptake, lichens absorb and retain radionuclides

from atmospheric depositions [19]. The data analysis shows no strong correlation between the specific activities of  $^{137}\text{Cs}$  in lichens (both epiphytic and epigeous species) and soil deposition density ( $r = 0.25$ ).

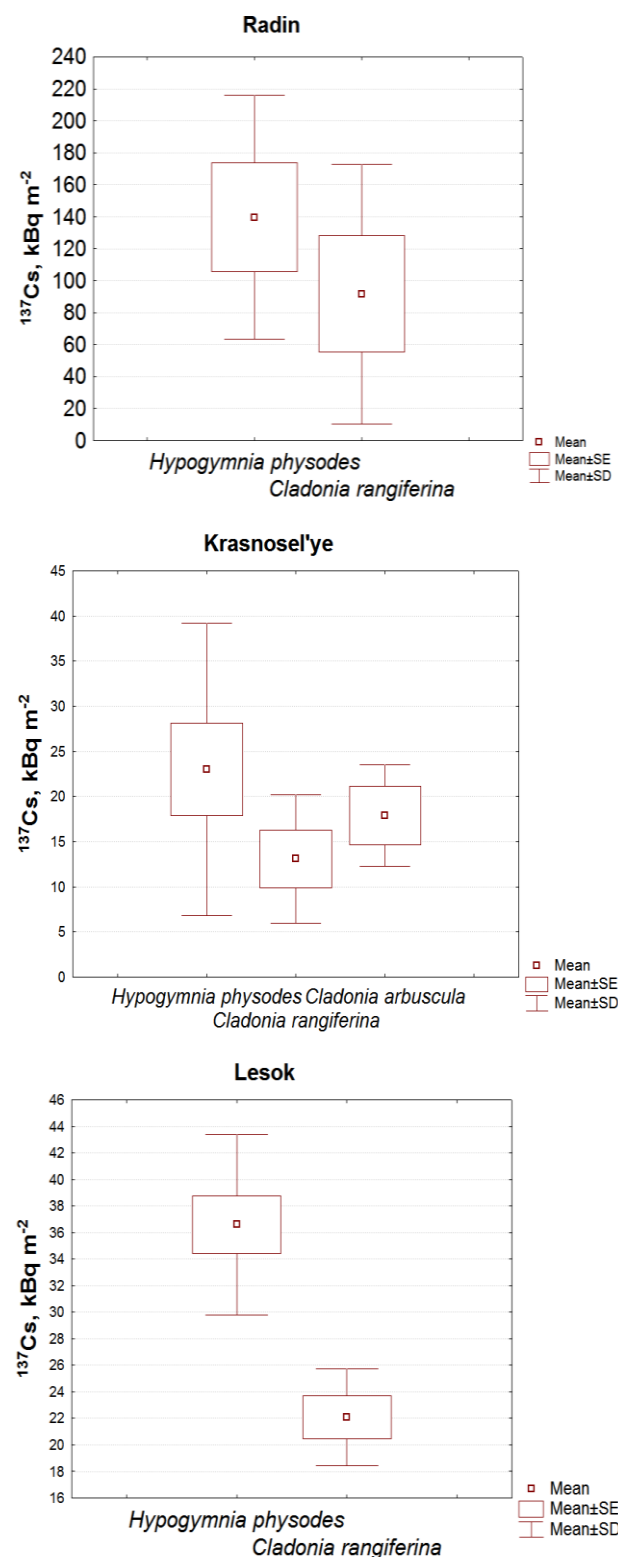


**Fig. 3.** Comparison of  $^{137}\text{Cs}$  content in different types of lichens

#### 4. Conclusion

The scientific data obtained in our study on the concentrations of man-made radionuclides in forest tree lichens is meant to provide important information to make reliable assessments of a radiation situation and the state of individual environmental components in radiation and nuclear emergencies. The study shows a correlation between the accumulation mechanisms of radioactive pollutants in the thalli of lichens of various ecological groups. The specific activity of  $^{137}\text{Cs}$  varies greatly in the lichens of different taxonomic groups. There is no evidence found of the relationship between soil deposition density and  $^{137}\text{Cs}$  activity in the thalli of lichens. Further research is needed to quantify the change in bioavailability of radionuclides for lichens.

#### 5. References

1. Izrael Ya.A., Bogdevich I.M. (eds.). The atlas of recent and predictable aspects of consequences of Chernobyl accident on polluted territories of Russia and Belarus (ARPA Russia-Belarus). Moscow-Minsk: Belkartographia - Foundation "Ionosphere" - NIA-Nature, 2009, 140 p.
2. Seaward M.R.D., Nimis P.L., Scheidegger C., et al. Lichens as Monitors of Radioelements. Monitoring with Lichens – *Monitoring Lichens. NATO Science Series (Series IV: Earth and Environmental Sciences)*, 7, 2002, p. 85–96.
3. Steinnes E., Njaastad O. Use of mosses and lichens for regional mapping of  $^{137}\text{Cs}$  fallout from the Chernobyl accident. *J. Environ. Radioact.*, 21(1), 1993, p. 65–73.
4. Mattsson L.G.  $^{137}\text{Cs}$  in the reindeer lichen *Cladonia alpestris*: deposition, retention and internal distribution, 1961–1970. *Health Phys.*, 28(3), 1975, p. 233–248.
5. Nimis P.L. Radiocesium in plants of forest ecosystems. *Studia Geobotanica*, 15, 1996, p. 3–49.
6. Dohi T., Ohmura Y., Kashiwadani H., et al. Radiocaesium activity concentrations in parmelioid lichens within a 60 km radius of the Fukushima Dai-ichi Nuclear Power Plant. *J. Environ. Radioact.*, 146, 2015, p. 125–133.
7. Nash III T.H. Lichen biology. Cambridge: Cambridge University Press, 1999, 486 p.
8. Handley R., Overstreet R. Uptake of Carrier-free  $^{137}\text{Cs}$  by *Ramalina reticulata*. *Plant Physiology*, 43(9), 1968, p. 1401–1405.
9. Nifontova M.G., Ravinskaya A.P., Shapiro I.A. Bioaccumulation of radionuclides in lichens and mosses. *Sauteria*, 9, 1995, p. 323–329.
10. Puhakainen M., Rahola T., Heikkinen T., et al.  $^{134}\text{Cs}$  and  $^{137}\text{Cs}$  in lichen (*Cladonia stellaris*) in southern Finland. *Boreal Environ. Res.*, 12(1), 2007, p. 29–35.
11. Heinrich G., Oswald K., Müller H.J. Lichens as monitors of radiocesium and radiostrontium in Austria. *J. Environ. Radioact.*, 45(1), 1999, p. 13–27.
12. Ramzaev V.P., Barkovsky A.N., Gromov A.V. Temporal variations of  $^7\text{Be}$ ,  $^{40}\text{K}$ ,  $^{134}\text{Cs}$  and  $^{137}\text{Cs}$  in epiphytic lichens (genus *Usnea*) at the Sakhalin and Kunashir islands after the Fukushima accident. *Radiation Hygiene*, 9(3), 2016, p. 14–27.
13. Conti M.E., Cecchetti G. Biological monitoring: lichens as bioindicators of air pollution assessment – a review. *Environ. Pollut.*, 114, 2001, p. 471–492.
14. Biazrov L. The Radionuclides in Lichen Thalli in Chernobyl and East Urals Areas after Nuclear Accidents. *Phyton*, 34, 1994, p. 85–94.
15. Pinglot J.F., Pourchet M., Lefauconnier B., et al. Accumulation in Svalbard glaciers deduced from ice cores with nuclear tests and Chernobyl reference layers. *Polar Res.*, 18(2), 1999, p. 315–321.
16. Wallace S.H., Shaw S., Morris K., et al. Effect of groundwater pH and ionic strength on strontium sorption in aquifer sediments: implications for  $^{90}\text{Sr}$  mobility at contaminated nuclear sites. *Appl. Geochem.*, 27, 2012, p. 1482–1491.
17. Sloof J.E., Wolterbeek B.Th. Lichens as biomonitors for radiocaesium following the Chernobyl accident. *J. Environ. Radioact.*, 16, 1992, p. 229–242.
18. Heinrich G., Müller H.J., Oswald K. et al. Natural and artificial radionuclides in selected Styrian soils and plants before and after the reactor accident in Chernobyl. *Biochem. Physiol.*, 185, 1989, p. 55–67.
19. Dohi T., Ohmura Y., Yoshimura K., et al. Radiocaesium accumulation capacity of epiphytic lichens and adjacent barks collected at the perimeter boundary site of the Fukushima Dai-ichi Nuclear Power Station. *PLoS One*, 16(5), 2021, e0251828.

## **EVALUATION OF THE REGION-SPECIFIC RISKS OF ACCIDENTAL RADIOACTIVE RELEASES FROM THE EUROPEAN SPALLATION SOURCE**

Guillaume PÉDEHONTAA-HIAA<sup>1,2</sup>, Christian BERNHARDSSON<sup>1</sup>, Vytenis BARKAUSKAS<sup>3</sup>, Andrius PUZAS<sup>3</sup>, Kristina ERIKSSON STENSTRÖM<sup>2</sup>, Christopher RÄÄF<sup>1</sup>, Sören MATTSSON<sup>1</sup>

<sup>1</sup> Lund University, Department of Translational Medicine, Medical Radiation Physics, Malmö, Sweden; <sup>2</sup> Lund University, Department of Physics, Division of Nuclear Physics, Lund, Sweden; <sup>3</sup> Center for Physical Sciences and Technology, Department of Nuclear Research, Vilnius, Lithuania

guillaume.pedehontaa-hiaa@med.lu.se, christian.bernhardsson@med.lu.se, vytenis.barkauskas@ftmc.lt, andrius.puzas@ftmc.lt, kristina.stenstrom@nuclear.lu.se, christopher.raaf@med.lu.se, soeren.mattsson@med.lu.se

**Abstract:** The European Spallation Source (ESS) is a neutron research facility under construction in southern Sweden. The facility will produce a wide range of radionuclides that could be released into the environment. Some radionuclides are of particular concern such as the rare earth gadolinium-148. In this article, the local environment was investigated in terms of food production and rare earth element concentration in soil. The collected data will later be used to model the transfer of radioactive contaminations from the ESS.

**Keywords:** Environmental radiology, Environmental monitoring, Emergency preparedness, Analytical chemistry, ICP-MS

### **1. Introduction**

The European Spallation Source (ESS) is a research facility currently under construction near the city centre of Lund, in south-western Sweden. In the upcoming years, the facility will produce powerful neutron beams for applications e.g. in material science and biology. The neutrons will be produced via spallation, using a 5 MW proton accelerator irradiating a tungsten target. A wide range of radionuclides will be generated as by-products from nuclear reactions in the tungsten target, but also through activation of air, construction details, building materials and surrounding soil.

The experience from operation of high-power spallation sources like ESS is limited and some knowledge gaps exist regarding the consequences of radioactive releases from the facility into the environment. These releases may happen during normal or maintenance operations and also during potential incidents or accidents. Some of the irradiated target material may end up in the soil, water, and plants and eventually reach the human food chain.

The proton irradiation of the tungsten target will generate radio-isotopes of W, Ta, Hf, Lu, Yb, Tm, Er, Ho, Dy, Tb, Gd, Eu, Sm and Pm. A list of the radionuclides that will contribute the most to the radiation exposure of man in case of an accidental release has been established by the regulating authority (the Swedish Radiation Safety Authority, SSM). Among them, the alpha-emitter <sup>148</sup>Gd is of particular concern due to its long physical half-life of 75 years. There are also technical difficulties of its measurement. Moreover, discrepancies exist between models regarding the amounts that will be produced by the ESS. Barkauskas et al. [1] and Kókai et al. [2] estimate its production to be an order of magnitude higher than the estimation of the ESS Preliminary Safety Analysis Report from [3] and Mora et al. [4].

Gadolinium (Gd) belongs to the group of rare earth elements (REEs) which is composed of the scandium, yttrium and the lanthanide series. Its abundance is of 6.1 ppm in surface soils on the Earth's crust [5]. Modern pollution by stable isotopes of Gd comes from several sources. The increasing concentration of Gd in aquatic ecosystems is due to its use in contrast agents injected to patients before Magnetic Resonances Imaging (MRI) examinations. Once excreted by the body, the contrast agents end up in the waste-water system from which they are spread in the environment. Soil contamination occurs in REE mining areas or is due to the use of REEs as fertilisers [6].

Mathematical models are powerful tools to evaluate or anticipate the transfer of radioactive contamination [7]. However, in the case of exotic radionuclides such as <sup>148</sup>Gd, there is a lack of reference values to build such models since it is not found in nature or produced by more conventional nuclear facilities. In the case of the ESS-specific radioactive REEs, one possibility to provide data to such models is the use of data from analogues which can be stable isotopes of the same



elements or of elements with similar chemical properties (e.g. La for Gd). One of the most widely used technique to investigate REEs is inductively coupled plasma mass spectrometry (ICP-MS). Depending on the type of instrument, the technique can determine the concentration of all the stable elements of the REE series or, after sample purification, the isotopic composition of a single element with very low detection limits.

In this study, we investigated the food production around ESS in order to increase the knowledge of the local environment and transfer of REEs from to soil to the human food chain. Soil samples were collected around the ESS, chemically extracted and analysed by ICP-MS to determine their REE levels. The collected data can later be used to build models of radioactive REE transfer in the environment.

## 2. Material and method

### 2.1. Sample selection

Four samples consisting of 20-centimeter-deep top soil cores were selected among a bank of samples previously collected around the facility [8]. The location of the sample sites is presented in Figure 1. A reference sample of estuarine sediment with certified values of REEs (BCR-667, JRC, IRMM) was also analysed for validation purposes.



**Fig. 1.** Maps of the ESS location in the southern Baltic region (top) and of sampling locations around the ESS (bottom)

### 2.2. Pseudo-total extraction

The pseudo-total extractions were performed by mixing 0.25 g of each soil sample with *aqua regia* at 60°C for 6 h. The samples were then centrifuged and filtered. The filtrate was evaporated to dryness at 80°C and redissolved in 2% nitric acid before analysis by ICP-MS.

### 2.3. Sequential extraction

Two sequential extraction procedures were performed based on the methods described by Wiche et al. [9] and Mittermüller et al. [10]. All the required reagents were purchased from VWR.

The selected samples were first extracted sequentially based on Wiche et al. [9] method, composed of 5 different steps: mobile exchangeable soluble materials (1 M ammonium acetate pH = 7), acid soluble elements (1 M acetate buffer pH = 5), element bound to oxidisable matter (acetate buffer pH = 5 + oxygen peroxide at 45°C), non-crystalline fractions, Fe-, Mn-, Al-oxide (0.2 M ammonium oxalate pH = 3.2), crystalline Fe-, Mn-sesquioxides (0.2 M ammonium oxalate + 0.1 M ascorbic acid, 45°C).

Different aliquots of each soil sample were extracted according to the method developed by Mittermüller et al. [10], composed of 4 steps: easily soluble and ion exchangeable (0.05 M calcium nitrate), carbonate bound and mobilised by complexation (0.1 M citric acid), reducible fraction (0.5 M hydroxylamine hydrochloride pH = 2 or 0.1 M nitric acid), acid soluble fraction (1.4 M nitric acid).

Those extraction methods were compared to a pseudo-total extraction with *aqua regia* (*aqua regia* 60°C to dryness and redissolved in 2% nitric acid).

The extracted fractions were diluted 10 to 50 times in 2% nitric acid and measured by ICP-MS on a Bruker Aurora Elite instrument at the Geology Department of Lund University. The instrument was calibrated using a diluted REE solution (Rare earth element mix for ICP, 16 elements, TraceCERT®, Supelco®). The following nuclides were measured:  $^{45}\text{Sc}$ ,  $^{89}\text{Y}$ ,  $^{139}\text{La}$ ,  $^{140}\text{Ce}$ ,  $^{141}\text{Pr}$ ,  $^{146}\text{Nd}$ ,  $^{148}\text{Nd}$ ,  $^{147}\text{Sm}$ ,  $^{153}\text{Eu}$ ,  $^{157}\text{Gd}$ ,  $^{159}\text{Tb}$ ,  $^{163}\text{Dy}$ ,  $^{165}\text{Ho}$ ,  $^{166}\text{Er}$ ,  $^{169}\text{Tm}$ ,  $^{172}\text{Yb}$ ,  $^{175}\text{Lu}$ . The concentration calculations for each element were performed assuming their respective isotopes were present in the sample at their natural abundance.

### 3. Evaluation of the food production around the ESS

After an accidental release, particles of irradiated target material would be deposited on the soil and plants around the ESS. The uptake of these radionuclides by the plants and animals that are part of the food chain could later lead to human contamination. To identify the important transfer pathways, the current food production and the risk groups in case of a severe accident, the area has been surveyed by maps and visits on site. A questionnaire has also been sent to some key persons and organisations that are representative of the farming activities and local population. The questions were related to the food production (e.g. what, how much, where, end consumer), animal husbandry and hunting.

The environment around ESS in the northern part of Lund is dominated by arable lands, which are classified 8-10 on a ten graded scale of the lands yield capacity [11]. These uniquely fertile soils are mainly found in southwest Scania. Although all the local food producers have not been identified, the survey provides a representative picture of what is regularly grown in the area, with the main producers in year 2020 included.

The largest estate is about 1500 ha (1 ha = 10<sup>4</sup> m<sup>2</sup>) of farming land that apply crop rotation of wheat, barley, rape and small amounts of corn. The majority of what is produced is sold as agricultural seeds. Cultivation of sugar beets is planned to replace the corn in the coming years. The second largest farmer in the area operates about 270 ha of fields cultivating various crops, peas and sugar beets that are sold for food production. An additional 43 ha area of farmlands belongs to a third farmer. This land is used for food production and apply crop rotation of similar species. Finally, an apple and pear orchard of about 12 000 trees is distributed over 3.24 ha, plus some 100 trees with pears.

Today, there are a limited number of private dwellings within a radius of about 1.5 to 2.5 km from ESS, with the small village of Östra Odarslöv (18 ha and 70 inhabitants in 2015 [12]) in the northeast direction from ESS. These private dwellings all have garden plots with home-cultivated vegetables and fruits. The residents will be of particular interest in defining the representative group of people around the ESS for whom accurate dose estimates must be made. The area is expanding and more inhabitants are expected in the future when ESS is in operation. A 20 ha area named Science Village is planned to be built in-between the two research activities MAX IV and ESS and will hold facilities such as University departments, guest houses, restaurants and other services. This area will also include a park and about 2 ha of land used for urban community farming. Together with current and future farming in the area, this is important for the next steps: the determination of specific transfer and uptake factors, of the area specific plants and soils, of REEs and in particular gadolinium.

The main identified crops in 2020 were: wheat, barely, rape, malt grains, sugar beets, peas and apples. Limited amount of corn was grown in 2020 but this production will be exchanged to sugar beets in the future. It can be noted that the majority of the agricultural production is currently not sold for food production but as seeds.

Regarding animal product consumption, the interviews revealed the presence of one team of hunters in the area (mainly deer and rabbit hunting). Bees are kept by private owners, at the apple orchard and at the research facility MAX IV for pollination of nearby fields and production of honey. The south-eastern part of the area is used for grazing by cattle.

Based on this survey some key potential pathways for transfer of ESS radioactive material from plant to man have been identified. Table 1 summarises the main foodstuff produced in the area and provides references from the literature that could be used to build transfer models. It is worth noticing that, to our knowledge, the behaviour and concentration of REEs have not been studied in some of the species of interest.

## 4. Experimental results

### 4.1 Pseudo-total extraction

The range of values obtained by pseudo-total extraction of the four ESS soil samples are presented in the Table 2. These results were compared to another available set of topsoil data obtained from forest soil from southern

Sweden by Tyler and Olsson [19] (also presented in Table 2).

**Table 2.** Existing data of REE in foodstuff grown around the ESS facility

Foodstuff grown near ESS	Articles of REE in foodstuff	Reference
Wheat	D'Aquino et al. (2009); Ding et al (2005)	[13], [14]
Barley	Wiche et al. (2017)	[9]
Rapeseed	Wiche et al. (2017), El-Ramady (2008)	[9], [15]
Corn	Wiche et al. (2017); El-Ramady (2008); Diatloff et al. (1995)	[9], [15], [16]
Apples	Sager et al. (2015)	[17]
Honey	Squadrone et al. (2020)	[18]
Green peas	No data	
Sugar beet	No data	

**Table 2.** REE concentration range extracted by *aqua regia* in ESS soil samples (mg kg<sup>-1</sup>) compared to a local forest soil

Element	ESS soil sample (N = 4)	Scanian forest soil Tyler and Olsson [19]
Scandium (Sc)	1.94-3.44	0.92-5.16
Yttrium (Y)	6.57-10.32	4.9-17.6
Lanthanum (La)	13.14-19.03	5.5-33.2
Cerium (Ce)	27.97-39.19	11-68
Praseodymium (Pr)	3.18-4.86	1.3-7.5
Neodymium (Nd)	11.66-18.43	9.3-53
Samarium (Sm)	2.13-3.46	0.9-4.6
Europium (Eu)	0.35-0.57	0.22-0.83
Gadolinium (Gd)	1.95-3.04	1.0-4.8
Terbium (Tb)	0.27-0.42	0.15-0.65
Dysprosium (Dy)	1.29-2.04	0.9-3.7
Holmium (Ho)	0.24-0.38	0.20-0.74
Erbium (Er)	0.66-1.07	0.63-2.2
Thulium (Tm)	0.08-0.14	0.09-0.33
Ytterbium (Yb)	0.51-0.84	0.60-2.3
Lutetium (Lu)	0.07-0.12	0.09-0.34

### 4.2 Sequential extraction

The purpose of extracting REEs sequentially is to obtain more precise information on the fractionation of these elements in the different types of minerals contained in a soil sample. In the different methods, the sample treatment goes from the softest conditions that extract easily soluble or exchange species toward harder conditions able to dissolve crystallised metal oxides for example.

Figure 2 shows the results of the ICP-MS measurements obtained on one of the four samples extracted sequentially by two methods. Each bar represents one REE and each segment represents the amount of REE extracted during a step of the procedure compared to the total amount obtained by pseudo-total extraction. The extraction percentages vary from sample to sample but similar trends were observed on all samples.

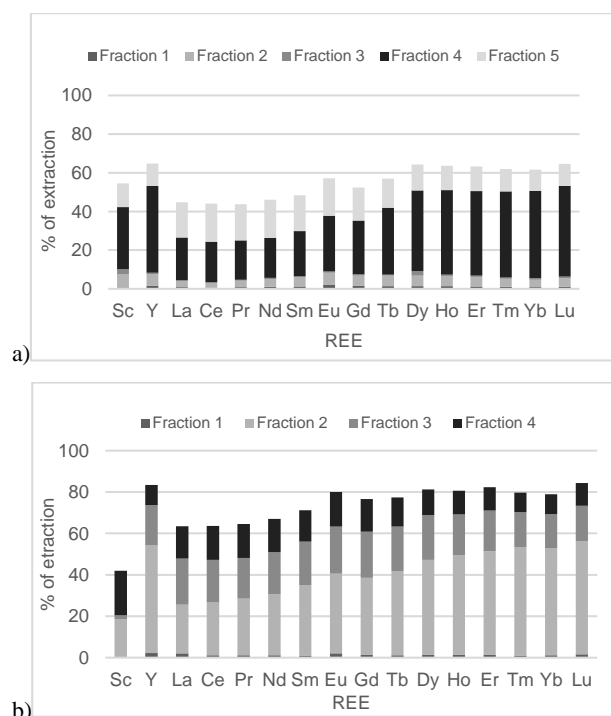


**Fig. 2.** Example of sequential extraction of REE in ESS soil samples according to the methods by a) Wiche et al. [9], and b) Mittermüller et al. [10]

The 5-step method extracted 30 to 60% of the amount of REEs extracted by the pseudo-total extraction which is consistent with results obtained by the authors of the method [9]. Less than 10% of the REE content is extracted by the three first steps. The third step is the most efficient with an increasing from the lighter REEs to the heavier ones (from 20% up to 45%). The last step adds 15 to 20% to the sum.

The 4-step method extracted a more variable amount of REEs going from 35 to 90% depending on the element and sample. The obtained results were occasionally higher than those from the original article [10]. The first step extracted only a few percent of the total amount. The efficiency of the second step increased with the REE weight from 15-25% of La and up to 55% of Lu. The third and fourth steps add additional 5 to 45%.

In both cases, the Sc and Y behaviours differ from the rest of the series with a low extraction yield of Sc (only 10 to 40%) and a high extraction yield of Y (more than 50 to 80%).

## 5. Discussion

All REE concentrations measured in the soils collected around the ESS were in the range observed in the southern Sweden forest soils [19] with the exception of the lowest values of Tm, Yb and Lu which are slightly lower. Since no significant REE excesses were detected in the cultivated soil compared to the forest soil, it seems that the current agricultural practices in the surroundings of the ESS do not increase the REE content of the soils.

The most efficient steps of both REE sequential extraction methods were based on complexing agents, namely oxalates and citric acid. This extraction process can be performed by plants [10]. Thus, a large fraction

of the REE content on the soils near ESS is bioavailable and additional REE released by the facility could also be transferred to plants by the same process. The results obtained indicate that extraction methods based on complexing agents seem to be a very promising way to assess the bioavailable fraction of REEs in soils and thus to produce experimental data to build models that would be specific to the local environment.

The soils around the ESS are not currently presenting anomalous levels of any REEs compared to non-contaminated soils samples. Sequential extraction of REEs could also provide information about the nature of a contamination and its evolution in time by looking at the modification of the REE fractionation in soil. Such experiments could indicate if the contamination is easily soluble or bound to organic materials or certain minerals as it was done with radiocaesium after nuclear accidents [20].

Currently, there is no  $^{148}\text{Gd}$  in the ESS surroundings. However, two isotopes of mass 148 can be found in soil samples: the stable  $^{148}\text{Nd}$  (5.76% natural abundance) and the very long lived  $^{148}\text{Sm}$  ( $t_{1/2} = 7 \times 10^{15}$  y; 11.2% abundance). In case of an accidental release of ESS target material,  $^{148}\text{Gd}$  would be introduced in the local environment together with other shorter lived radionuclides, namely  $^{148\text{m}}\text{Pm}$  ( $t_{1/2} = 41.3$  d) and  $^{148}\text{Eu}$  ( $t_{1/2} = 54.5$  d) as well as other stable isotopes of this mass not included in the modelled target compositions [21]. In the presented REE measurements, the concentration of Nd was calculated based on the  $^{146}\text{Nd}$  signal or based on the  $^{148}\text{Nd}$  signal corrected for  $^{148}\text{Sm}$ . No significant differences were observed between these two calculation methods suggesting that the current levels of  $^{148}\text{Nd}$  and  $^{148}\text{Sm}$  are found at their expected natural abundance in the ESS soils.

## 6. Conclusion

In order to build mathematical models for the transfer of releases of radioactive REEs from the ESS to the local environment, it is necessary to produce additional experimental data. In this work, the plant and animal species that are relevant for transfer to the human food chain were identified.

The current levels of stable REEs in top soils collected around the facility were also investigated. Results of ICP-MS measurements show no current anomalous REE levels compared to forest soils from the same region. It indicates that the REE levels in the area have not been affected by agricultural practices or research and hospital discharges. Additional measurements of neodymium and samarium isotopes seem to confirm that the REEs currently are at their expected natural abundance. Sequential extractions performed on those soil samples revealed that a large fraction of the current REEs is bioavailable since the main extraction mechanism is complexation.

Future work in the scope of the present study will include the measurement of other elements of interest in soil such as tungsten or hafnium. The measurement of traces of REEs and other relevant metals in the locally grown plant species will also contribute to the elaboration of ESS-specific transfer models. The

analysis of artificially contaminated soils and plants will also be considered.

### Acknowledgments

This work was financed by the Swedish Radiation Safety Authority (Strålsäkerhetsmyndigheten), grant SSM2019-1010. The authors also thank Thomas Naeraa (Geology Department, Lund University) for his help with ICP-MS measurements.

### 7. References

1. V. Barkauskas and K. E. Stenström Eriksson, 'Prediction of the radionuclide inventory in the European Spallation Source target using FLUKA', *Nucl. Instrum. Methods Phys. Res. B*, vol. Accepted for publication.
2. Z. Kókai et al., 'Comparison of different target material options for the European Spallation Source based on certain aspects related to the final disposal', *Nuclear Instruments and Methods in Physics Research Section B: Beam Interactions with Materials and Atoms*, vol. 416, pp. 1–8, Feb. 2018, doi: 10.1016/j.nimb.2017.11.027.
3. ESS, 'ESS Preliminary Safety Analysis Report', 2012.
4. T. Mora et al., 'An evaluation of activation and radiation damage effects for the European Spallation Source Target', *Journal of Nuclear Science and Technology*, vol. 55, no. 5, pp. 548–558, May 2018, doi: 10.1080/00223131.2017.1417173.
5. G. Tyler, 'Rare earth elements in soil and plant systems - A review', *Plant Soil*, vol. 267, no. 1, pp. 191–206, Dec. 2004, doi: 10.1007/s11104-005-4888-2.
6. T. Liang, K. Li, and L. Wang, 'State of rare earth elements in different environmental components in mining areas of China', *Environ Monit Assess*, vol. 186, no. 3, pp. 1499–1513, Mar. 2014, doi: 10.1007/s10661-013-3469-8.
7. IAEA, 'Safety Reports Series No.19: Generic Models for Use in Assessing the Impact of Discharges of Radioactive Substances to the Environment', IAEA, Text, Feb. 2019. Accessed: Nov. 02, 2020. Online.. Available: <https://www.iaea.org/publications/6024/generic-models-for-use-in-assessing-the-impact-of-discharges-of-radioactive-substances-to-the-environment>
8. C. Bernhardsson et al., 'Assessment of "Zero Point" radiation around the ESS facility', Lund University, MA RADFYS 2018:01, BAR-2018/04, 2019.
9. O. Wiche, V. Zertani, W. Hentschel, R. Achtziger, and P. Midula, 'Germanium and rare earth elements in topsoil and soil-grown plants on different land use types in the mining area of Freiberg (Germany)', *Journal of Geochemical Exploration*, vol. 175, pp. 120–129, Apr. 2017, doi: 10.1016/j.gexplo.2017.01.008.
10. M. Mittermüller, J. Saatz, and B. Daus, 'A sequential extraction procedure to evaluate the mobilization behavior of rare earth elements in soils and tailings materials', *Chemosphere*, vol. 147, pp. 155–162, Mar. 2016, doi: 10.1016/j.chemosphere.2015.12.101.
11. Länsstyrelse Skåne, 'Lunds kommun'. <https://www.lansstyrelsen.se/skane/besoksmal/kulturmiljoprogram/oversiktliga-beskrivningar/oversiktliga-kommunbeskrivningar/lund.html> (accessed Feb. 16, 2021).
12. 'Småorter; arealer, befolkning', *Statistiska Centralbyrån*. <http://www.scb.se/hitta-statistik/statistik-efter-amne/miljo/markanvandning/smaorter-arealer-befolkning/> (accessed Feb. 16, 2021).
13. L. d'Aquino et al., 'Effect of some rare earth elements on the growth and lanthanide accumulation in different *Trichoderma* strains', *Soil Biology and Biochemistry*, vol. 41, no. 12, pp. 2406–2413, Dec. 2009, doi: 10.1016/j.soilbio.2009.08.012.
14. S. Ding, T. Liang, C. Zhang, J. Yan, and Z. Zhang, 'Accumulation and fractionation of rare earth elements (REEs) in wheat: controlled by phosphate precipitation, cell wall absorption and solution complexation', *J Exp Bot*, vol. 56, no. 420, pp. 2765–2775, Oct. 2005, doi: 10.1093/jxb/eri270.
15. H. El-Ramady, 'Contribution on the bio-actions of rare earth elements in the soil/plant environmentA', Aug. 2008, doi: 10.24355/dbbs.084-200809090200-3.
16. E. Diatloff, F. W. Smith, and C. J. Asher, 'Rare earth elements and plant growth: I. Effects of lanthanum and cerium on root elongation of corn and mungbean.: Journal of Plant Nutrition: Vol 18, No 10', *Journal of Plant Nutrition*, vol. 18, no. 10, 1995, doi: 10.1080/01904169509365037.
17. M. Sager and A. Spornberger, 'Main and trace elements in fruit and leaves of apples grown on various rootstocks.', *Mitteilungen Klosterneuburg, Rebe und Wein, Obstbau und Früchteverwertung*, vol. 65, no. 4, pp. 250–275, 2015.
18. S. Squadrone et al., 'Trace elements and rare earth elements in honeys from the Balkans, Kazakhstan, Italy, South America, and Tanzania', *Environ Sci Pollut Res*, vol. 27, no. 11, pp. 12646–12657, Apr. 2020, doi: 10.1007/s11356-020-07792-7.
19. G. Tyler and T. Olsson, 'Conditions related to solubility of rare and minor elements in forest soils', *Journal of Plant Nutrition and Soil Science*, vol. 165, no. 5, pp. 594–601, 2002, doi: 10.1002/1522-2624(200210)165:5<594::AID-JPLN594>3.0.CO;2-K.
20. K. Fujii, S. Ikeda, A. Akama, M. Komatsu, M. Takahashi, and S. Kaneko, 'Vertical migration of radiocesium and clay mineral composition in five forest soils contaminated by the Fukushima nuclear accident', *Soil Science and Plant Nutrition*, vol. 60, no. 6, pp. 751–764, Nov. 2014, doi: 10.1080/00380768.2014.926781.
21. K. Oishi et al., 'Measurement and analysis of induced activities in concrete irradiated using high-energy neutrons at KENS neutron spallation source facility', *Radiation Protection Dosimetry*, vol. 115, no. 1–4, pp. 623–629, Dec. 2005, doi: 10.1093/rpd/nci165.

## **BACK TO THE FUTURE: THE POSITIVE EDUCATIONAL IMPACT OF COVID-19 PANDEMIC WITH ONLINE LEARNING PROGRAM INTO CLINIC**

Nur KODALOĞLU, Can AZAK, Sezai Güçlü KILIÇOĞLU, Tuğba ULU, Gizem KAVAK EREN, Hasan ÇAMLICALI, Ebru KARAKAYA  
Dr. Abdurrahman Yurtaslan Ankara Oncology Research and Training Hospital  
nurkodaloglu@gmail.com

**Abstract:** COVID-19 pandemic has accelerated online meetings worldwide. In this research, we tried to evaluate the impact of both radiotherapy physics online lectures and the patient related online meetings on residents' education in pandemic period.

**Keywords:** Radiotherapy, COVID-19, pandemic, online education.

### **1. Introduction**

In our Radiation Oncology Clinic, there are 5 residents (2 – 4.5 year-experienced). Since 5th Jan 2021 they (besides many radiation oncologists) attended online radiotherapy physics once a week (20 weeks) for 90 minutes in which the schedule includes not only basic knowledge like atomic structures, radioactivity, interactions with ionizing radiation, radiation dose units, but also details of radiotherapy techniques and related phenomena like LET, RBE, radiotherapy machines (external and superficial), linacs, radiation dosimetry, treatment planning algorithms, 3D-Conformal RT, IMRT, Cranial SRS, SBRT, TBI&TSEI, brachytherapy, nuclear medicine, radiation protection etc. In 9th and 19th weeks they took exams of 40 questions. Besides, they attended national weekly meetings on case based discussions such as gastrointestinal, head and neck, breast, cranial, gynaecology, lung, genitourinary tumors, SBRT, contouring lectures, also with worldwide well known guest lecturers about new technologies and presented articles and seminars.

On the other hand, the flexible shifts of the radiation oncologists lead in the changes of the responsibilities of the residents. These changes also had many advantages and disadvantages to the residents. So, they evaluated the changes marking from 1 to 10 in the survey taking into account before and after the online education period since the beginning of the pandemic.

### **2. Online Radiotherapy Physics Course Content**

Turkish Society for Radiation Oncology organized a 20-week online radiotherapy physics course (1). Residents, specialists or academics were invited to take these lectures. Each lecture was 90 minutes. After the first lecture on 5<sup>th</sup> January 2021, on 9<sup>th</sup> and 19<sup>th</sup> weeks of the schedule, participants took exams of 40 questions. The content of the course can be seen below.

- Historical development of radiotherapy,
- What should a radiation oncologist know about radiation physics?
- How to set up a radiotherapy center?
- Atomic structure and nuclear sciences radioactivity,
- The concept of ionizing radiation and the acquisition of X-rays,
- Interaction of ionizing radiation with matter,
- Radiation dose units,
- Radiation attenuation and LET,
- External radiotherapy devices containing radionuclide,
- Surface X-ray and electron devices,
- Structure of linear accelerators,
- Modern accelerators used in radiotherapy,
- Radiation dosimetry,
- Clinical dosimetry and dosimetry equipment,
- Factors affecting radiation dose distribution: in the device and in the air,
- Factors affecting radiation dose distribution: in the patient,
- Fundamentals of computerized planning,
- Computerized planning software and calculation algorithms,
- 3D-Conformal radiotherapy: basis and treatment planning,
- 3D-Conformal radiotherapy: evaluation of treatment plans,

- IMRT: The foundation and concept of inverse planning,
- IMRT: Dose prescribing and evaluation of treatment plans,
- Cranial SRS,
- SBRT,
- Treatment with electrons,
- TBI & TSEI,
- Fundamentals of brachytherapy physics modern brachytherapy equipment,
- Brachytherapy techniques,
- Brachytherapy: QA and safety,
- Radiation Safety,
- Radiation Accidents,
- Nuclear Medicine Physics and Radionuclides used,
- Radiopharmacy and Theranostic approach,
- Panel: The future of radiotherapy.

### 3. Online Radiation Oncology Course Content

Turkish Society for Radiation Oncology organized another educational programme for cancer types and case meetings for 20 weeks (1). The content of the programme (excluding the monthly invited speakers for specific topics) is given below (1).

- Case Meeting,
- Literature Hour,
- Artificial Intelligence Applications,
- Pediatric Neuro-oncology Course,
- Neurooncology Case Meeting (Adult SNS Tumors),
- Pediatric Wilms, RMS, Neuroblastoma Course,
- Sarcoma Meeting (Soft Tissue Sarcomas),
- Radiobiology Courses (5 weeks),

- Head and Neck Tumors (Nasopharynx and Oropharynx with Cases),
- Urooncology Meeting (Bladder cancer),
- Concomitant Immunotherapy and Radiotherapy,
- Brachytherapy,
- Concurrent Targeted Therapies and Radiotherapy.

Apart from these case councils organized by Turkish Society for Radiation Oncology, there have been many case meetings organized by other organizations and societies i.e. gynaecology, thoracic surgery, urology etc.

A different educational programme was organized to be done in the clinic. Considering each of these different schedules boosted the educational input compared to the years before the pandemic.

### 4. Implementing the Survey

Increasing the both the contents and number of online lectures has made changes (2). To evaluate these changes, we composed a survey. 5 residents took this 10-sentence survey. They marked each sentence considering before and after the online courses. The survey and the marks can be seen in Table 1. They evaluated the change of their knowledge by considering before and after the online lectures via scoring with a minimum of 1 and a maximum of 10.

### 5. Results

The self-evaluation survey results were analyzed by using Wilcoxon test to observe the differences between before and after the online education. Significant differences ( $p < 0.005$ ) were found after the online education period.

**Table 1.** The questions asked to the residents in the survey.

	Before Online Education	After Online Education
There are more external beam radiotherapy devices with different specialties than I thought.	12	41
I have really learned the details about the physical principles on which linac works.	24	42
gained an appreciation of how physics rules play a central role in designing the patient treatment in term of choosing electron, photon or different modalities.	17	43
Visualising beam shaping/modulating devices (jaw, MLCs, wedges, angles etc.) even during contouring.	23	40
Learning the details of the philosophy of physics has broaden our horizons while designing a new research project.	22	37
I realized that I have known very few about radition protection concept previously.	21	44
It created awareness that strict rules of the working mechanism in the brachytherapy operating room should be settled.	20	39
Accesibility and easier contactability with the more experienced oncologists to consult different case scenarios via online meetings.	18	40
Despite the fact that the responsibilities of the residents increased due to decrease in the number of rad.oncologists, online educational systems helped residents to balance both clinical and educational workload.	19	41
I can evaluate treatment plans (DVHs) better.	21	38



## 6. Conclusions

Online education created dramatic contributions on extending the vision of the attendees in terms of both theoretical and practical applications into the clinic. While online meetings facilitate the participation of many people in more meetings in a shorter period, it also increases the interactivity in these meetings. It's also observed that the elderly radiation oncologists overcome their prejudices and reduce their distances from new technologies. Besides, it is stated that they acquire technological habits that cannot be created for other reasons and enjoy the convenience of online meetings (Zoom, Webex etc.)

Contouring courses (mostly on whole weekends) which used to be organized in different cities cost remarkable amounts considering transportation and accommodation taking into account the annual educational schedule. Contouring courses also evolved to a new three step system including pre-course real case contouring assignments, online theoretical information and discussion part during the course and attendee specific contouring assignment feedback discussion after the online session. Hence, not only in terms of saving the costs for the attendees, attendee specific feedbacks and discussions made the new system superior.

For different cancer types, council nights were organized to discuss cases with professors from different fields such as radiation oncology, medical oncology, pathology, surgery, gynaecology, radiology, nuclear medicine etc. During these online councils each attendee (i.e. resident, specialist, academician

etc.) was able to discuss their own cases in details. These interactions with experienced professionals, reduced the problems on making decisions of the participants on difficult cases they face in their daily routines.

Following new techniques and approaches or networking is a remarkable outcome of the traditional congresses. While experienced and respectable names from authorities (AAPM, ESTRO, ASTRO etc.) are invited to such congresses, it is easier to reach more professionals from these organizations more frequently in online trainings and to have chance to discuss with them.

In conclusion, online educational programmes during the pandemic improved not only the interest and updated knowledge in radiation oncology but also interactions among both radiation oncologists and residents.

## 7. References

1. Turkish Society for Radiation Oncology (2021). "Radyoterapi Fiziki Uzaktan Eğitim Programı [online]. Website: [https://www.trod.org.tr/app\\_society\\_educational\\_program?id=1](https://www.trod.org.tr/app_society_educational_program?id=1) [accessed 17 February 2021].
2. Sandhu N, Frank J, Eyben R, Miller J, Obeid J.P, Kastelowitz N, Panjwani N, Soltys S, Bagshaw H.P, Donaldson S.S, Horst K, Beadle B.M, Chang D.T, Gibbs I.C, Pollom E. Virtual Radiation Oncology Clerkship During the COVID-19 Pandemic and Beyond. International Journal of Radiation Oncology Biology Physics, 2020;108: p 444-451.

## IONIZING RADIATION INDUCED COLOUR CHANGES IN HYDROGELS

Aurimas PLAGA, Ignas PIKAS, Judita PUIŠO, Jurgita LAURIKAITIENĖ, Diana ADLIENĖ  
Department of Physics of Kaunas University of Technology  
aurimas.plaga@ktu.edu; ignas.pikas@ktu.edu; diana.adliene@ktu.lt

**Abstract:** It has been determined that the fingertips of nuclear medicine workers receive higher radiation doses than it is measured by worn TLD rings. This increases the potential radiation risks to a worker's wellbeing. There is a need for improving dose assessment capabilities to be able to protect hands of nuclear medicine staff from overexposure. Attaching of standard TLDs to the fingertips may disturb the hand's functionality, thus requiring longer time per procedure which in turn may lead to the higher exposure doses. Attachment of coloured radiation sensitive hydrogel films to the gloves of workers could be an elegant solution of the problem if the hydrogels are sensitive enough to change their colour due to low dose irradiation.

The aim of this work was to explore four different organic dyes admixed to hydrogels and to investigate their response (colour changes) to the irradiation dose.

**Keywords:** nuclear medicine staff, exposure, coloured hydrogels; dosimetry.

### 1. Introduction

Ionizing radiation is commonly used for diagnosis and treatment of various diseases. Nuclear medicine is a field where ionizing radiation from radionuclides/radiopharmaceuticals is used for medical purposes. These radiopharmaceuticals can enter the patient's body through the airways (inhalation), orally (by swallowing) or by administering the required amount via injection, all depending on the organ or anatomical area to be diagnosed [1]. While working with these radioactive substances, it is imperative to reduce the amount of exposure to radiation that nuclear medicine specialists receive during treatment procedures.

The doses accumulated by occupationally exposed workers are limited. Reference dose levels for specialists working with ionizing radiation sources are regulated by national and international legal acts and reference papers. It is established that the exposure of the whole body of a worker may not exceed 20mSv per year, and the exposure of the extremities - 500mSv [2]. A relatively high dose is received by the hands of

specialists working with radiopharmaceuticals. Despite the fact that the exposure levels usually do not exceed the recommended annual limits, the risk of developing radiation-induced cancer still exists and it increases with exposure [3]. This risk can be reduced by optimizing the use of protective measures to shield a physician's hands from ionizing radiation and with precisely monitored exposure.

Normally, the exposure of radiation that a physician receives to his/her extremities is measured using thermoluminescent dosimeters (TLD) built into special rings worn on the middle finger of the hand [4]. This dose has long been considered the standard extremity exposure dose, but recent studies have shown that the dose measured by a dosimetric ring does not correlate to the true dose received by the fingertips. A recent study which was analysing the doses of occupationally exposed workers (2059 TLD measurements) indicated that while Hp(10) doses never exceeded the annual dose limit of 20 mSv as well as doses to hands (measured using TLD rings) never exceeded 500 mSv limit and were showing a decreasing tendency through the years, doses measured at the fingertips were 2-3 times higher than the doses measured using TLD rings [5]. Another study [6] which provided summary of articles focusing on radiopharmaceutical administration also concluded that the finger doses measured at the fingertips were higher when compared to doses measured at the ring position of the finger [6].

Fingertip exposure is also a concern among surgeons, who are exposed to radiation through the required use of intraoperative fluoroscopy. A study found that they are more susceptible to radiation exposure to their fingertips than the rest of the hand [7].

These findings indicate that there is a need for more accurate finger dose measurements which could prevent unnecessary exposure and potential risks to a physician's health. A potential solution for this issue might be application of the coloured hydrogel films containing radiation sensitive dyes for dose registration. These dyes react to ionizing radiation, leading to a change in their colour.

## 2. Coloured hydrogels

There are many kinds of radiation sensitive dyes that might be used in colour hydrogels. Some are based on the fading of colour when exposed to ionizing radiation, such as methylene blue and phenol-endo-2:6-dichlorophenol [8] which are mixed with gelatine or agar to make gel dosimeters.

Other dye-based dosimeters change their colour due to pH changes in gels. An example of such gel is a mixture of agar and chlorine hydrate. When exposed to ionizing radiation, chlorine hydrate splits and forms hydrochloric acid, which can be detected by the use of pH indicators (such as methyl red) that are admixed to the gels [9].

Among the most popular dye-based dosimeters is PRESAGE. PRESAGE is a radiochromic dosimeter that is synthesised using a polyurethane base with a mixture of radiation sensitive leucodyes and radical initiators [10]. It is one of the most popular dye based dosimeters that has a varying effectiveness and sensitivity based on the amount of leucodyes and radical initiators in its formulation [11]. It also has a potential for medical applications, e.g. for dose verification during brachytherapy [12], treatment plan verification for IMRT and VMAT therapy [13] as well as various uses in radiotherapy such as 3D conformal radiotherapy and proton beam therapy [14].

Although a substantial number of dyes are sensitive to ionizing radiation, considerable colour changes often occur at high exposure doses, which are more typical to industrial levels of radiation [15]. Even if the certain dyes, such as leucodyes, already receive extensive attention of researchers, a field of colour-based hydrogels application for dosimetry purposes is still somewhat limited. The examined dyes are not always tested at lower levels of ionizing radiation and comparative analysis of their dose sensitivity is not performed.

The aim of this work was to explore four different organic dyes admixed to hydrogels and to investigate their response (colour changes) to the irradiation dose.

## 3. Materials and methods

Four different organic dyes were used in this work to examine the colour changes induced by ionizing radiation (Fig. 1). To produce the hydrogels, a high-density gelatine "Bloom 250" was used as the structural base for the hydrogel dosimeters. Water and ethanol were used as solvents for the dyes during the hydrogel synthesis.

Each prepared hydrogel was exposed in linear accelerator and their optical properties were measured using a UV-VIS spectrophotometer. Comparison of the results for irradiated and not irradiated hydrogels has been also performed.

### 3.1. Synthesis of Hydrogels

Each coloured hydrogel was synthesised using the same process. A certain amount of gelatine was poured in water and left for 30 minutes to swell. Then 40g of 10% gelatine and water mixture was heated up to 45°C under

continuous stirring with a magnetic stirrer and a certain amount of dye (Carmoisine, Ponceau 4R and Brilliant blue FCF) dissolved in water was added to the water-gelatine mixture continuing to stir. In the case of Xylenol Orange small part of water was replaced by ethanol to improve the solubility of the dye. When the colour of hydrogels solution with dye additives became uniform, warm mixtures were poured into separate PMMA cuvettes creating batches of different samples and left in dark to settle. Chemical content and concentrations of the investigated hydrogels are shown in the Table 2.

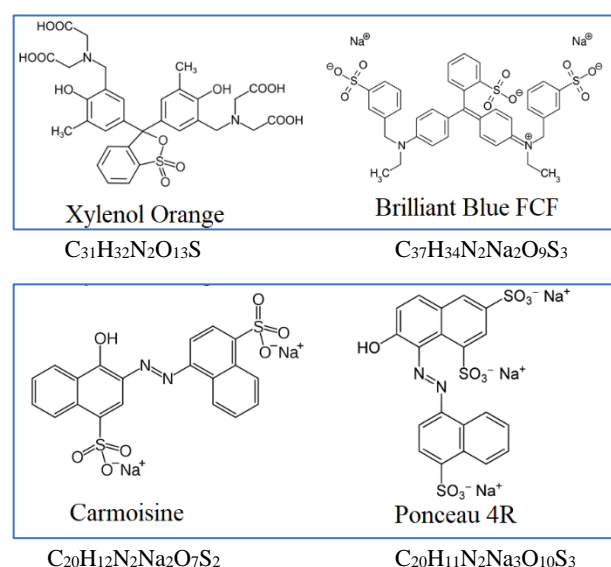


Fig 1. Chemical structure of used organic dyes.

### 3.2. Radiation exposure

Prepared hydrogels were irradiated with doses from the range 0.1-10 Gy in a linear accelerator Clinac DMX (Varian) using 6MeV photon beam [16]. To maintain an irradiation maximum in the centre of the cuvette, a PMMA bolus was used to cover the samples (Fig.2).

Table 2. Percent hydrogel composition

Dye Name	Percent hydrogel composition in one cuvette sample (%)			
	Dye	Gelatine	H <sub>2</sub> O	C <sub>2</sub> H <sub>5</sub> OH
Brilliant Blue FCF (BB)	0.05	9.52	90.43	-
Brilliant Blue FCF (BB2)	0.1	9.09	90.81	-
Carmoisine (BC)	0.05	9.52	90.43	-
Carmoisine (BC2)	0.1	9.09	90.81	-
Ponceau 4R(BS)	0.05	9.52	90.43	-
Ponceau 4R (BS2)	0.1	9.09	90.81	-
Xylenol Orange (XiO)	0.03	9.56	89.03	1.38
Xylenol Orange (XiO2)	0.06	9.15	88.14	2.65
Xylenol Orange (XiO4)	0.12	8.43	86.57	4.88

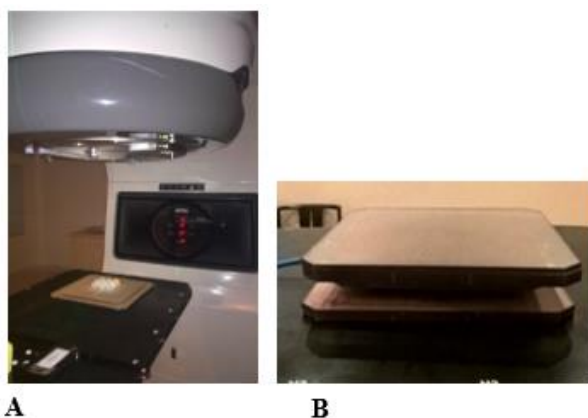


**Fig 2.** Irradiation geometry: A – linear accelerator Clinac DMX (Varian) with samples arranged in the irradiation field; B – PMMA bolus used for covering the experimental samples.

### 3.3. UV-VIS measurements

Radiation sensitivity of colour hydrogels was estimated analysing radiation induced optical characteristics changes of the irradiated samples.

Ocean Optics USB4000 spectrophotometer was used to obtain absorption and transmission spectra (300-900nm) of samples irradiated with certain doses.

Data of measurements were processed using “OceanView” software.

## 4. Results

Light transmittance spectra of each differently irradiated sample were generated to visually depict the effect of ionizing radiation.

In general, a decreasing tendency of light transmission with increased irradiation dose was found in all hydrogels independently from the admixed dye indicating colour changes of hydrogels in the visible range. However, the magnitude of the transmitted light intensity varied depending on the amount and type of dye in the hydrogel and was irradiation dose dependent. An example of transmittance spectra of the samples from one batch (Ponceau 4R), irradiated with different doses is provided in Fig.3.

It should be noted that some results were found to be untrustworthy due to their significant deviations from the measurements results of the total sample group, even after being measured multiple times. These results were not considered for further analysis.

There was substantial difference in dose response found analysing transmitted light intensity changes at a certain wavelength in samples irradiated with small (0-1) Gy and medium (1-10 Gy) doses.

Due to this, two sensitivity curves for each batch of samples were constructed as it is indicated in Fig.4, which depicts obtained results for Ponceu 4R samples. Results of the comparative analysis of each sample batch are provided in Table 3. The radiation sensitivity of irradiated samples containing different concentrations of different dyes varied in a broad range.

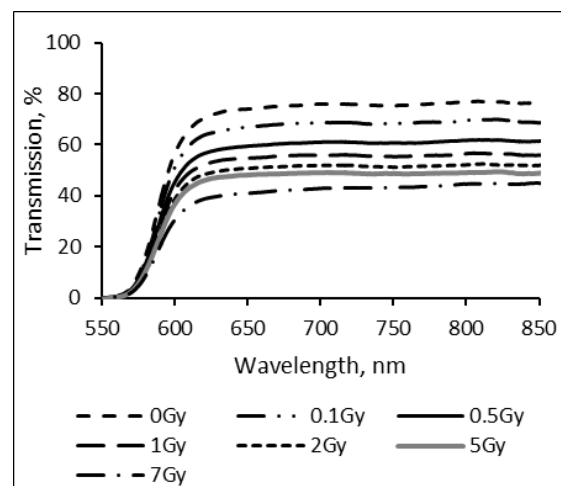


**Fig 3.** Example spectra of Ponceau 4R samples exposed to varying degrees of ionizing radiation (1-7 Gy).

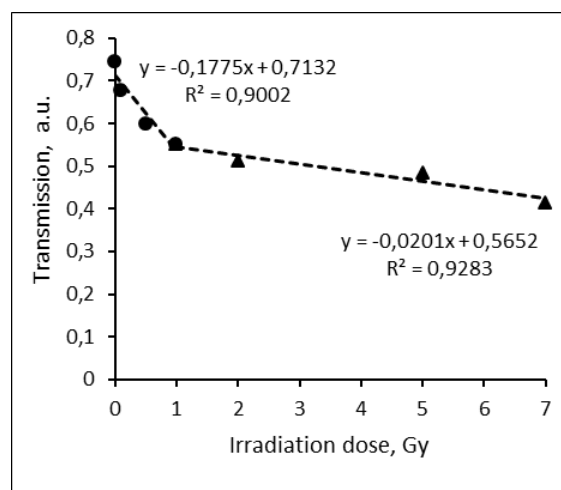


**Fig 4.** Radiation sensitivity variations of Ponceau 4R batch samples obtained analysing transmitted light intensity at 650nm in differently irradiated samples

It is to point out that samples containing higher dye concentration showed smaller differences in the sensitivity of low and middle dose irradiated samples.

The results of the performed investigation have shown that the effect of dye concentration and the exposure dose have a significant impact on the radiation sensitivity of hydrogels containing dyes.

## 5. Discussion

Radiation induced transmitted light intensity changes in hydrogel samples containing different dyes is a result of water radiolysis which occurs when water molecules are exposed to ionizing radiation and dissociate into  $H^+$  and  $OH^-$  radicals. Produced radicals are chemically very reactive and can further recombine producing reactive combinations such as superoxides ( $HO_2$ ), peroxides ( $H_2O_2$ ) or solvated electrons  $e_{aq}^-$  [17]. Produced radicals can react with various functional groups on the organic dyes leading to change in their chemical structure and the degradation of their colour.

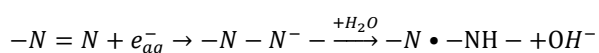
**Table 3.** Relative sensitivity of irradiated samples in low (0-1 Gy) and middle (1-10 Gy) dose ranges.

Dye		Dose ranges					
		0-1 Gy	1-10 Gy	0-1 Gy	1-10 Gy	0-1 Gy	1-10 Gy
Ponceau 4R	Sample	BS		BS2		-	
	Relative sensitivity	0.1775	0.0201	0.0846	0.0196	-	-
Carmoisine	Classification	BC		BC2		-	
	Relative sensitivity	0.1204	0.0154	0.0565	0.0197	-	-
Brilliant Blue FCF	Classification	BB		BB2		-	
	Relative sensitivity	0.0752	0.0114	0.0397	0.0144	-	-
Xylenol Orange	Classification	XiO		XiO2		XiO4	
	Relative sensitivity	0.1114	0.0631	0.0934	0.0701	0.027	0.022

The organic dyes themselves gain the colour through the chromophore and auxochrome functional groups attached to their molecular structure.

Chromophores are molecular regions that reflect light at a certain wavelength of the visible spectrum, giving the molecule colour. Auxochromes are functional groups attached to the chromophore molecule that modify the molecules' ability to absorb light. Unique combinations of chromophore and auxochrome functional groups in a molecule can drastically change the colour of the material [18].

As an example, Ponceau 4R and Carmoisine are both azo - dye compounds with a functional azo - group ( $-N=N-$ ). The azo - group is a chromophore which gives its compounds vivid colours. In the case of Ponceau 4R and Carmoisine dyes the colour is red. These azo - groups, however, can undergo chemical changes when interacting with the products of water radiolysis. As an example, a solvated electron can react with an azo - group, forming a hydrazyl radical and changing the chemical structure of the compound, which also leads to a change of its colour:



Similar changes occur when reactive products of water radiolysis react with other molecular groups of the organic dyes, leading to variation and degradation of their colour [17].

The increased sensitivity of hydrogels containing dyes at lower irradiation doses could be explained by the initial reaction of the organic dyes exposed to ionizing radiation. Water radiolysis starts at the lowest doses and the dissociated radicals start reacting with the dyes. Since the total irradiation dose depends also on irradiation time, with the increasing dose less and less dye molecules are available for further degradation as they've already reacted with the formed radicals. This leads to reduced effectivity of chemical changes in molecular structure which in turn is responsible for reduced transmitted light intensity of irradiated samples.

## 6. Conclusion

Performed investigation has shown a decreasing tendency of the transmitted light intensity in all irradiated hydrogel-dye samples with an increased dose. Comparison of hydrogels sensitivity to the irradiation dose has revealed that hydrogel samples were more sensitive to low dose (0-1 Gy) irradiation. The lowest sensitivity was indicated for Brilliant Blue FCF containing hydrogels, the highest - for Ponceau 4R dye containing hydrogels. The radiation sensitivity of the samples was found to be affected by the amount of dye in the sample and was decreasing as the dye concentration in the sample increased.

Overall, it was shown, that hydrogels with admixed organic dyes may represent dose identification tool which is based on radiation induced colour changes (light intensity changes) of the hydrogels.

## 7. References

1. G. Sgouros, L. Bodei, M. R. McDevitt, and J. R. Nedrow, "Radiopharmaceutical therapy in cancer: clinical advances and challenges," *Nat. Rev. Drug Discov.*, vol. 19, no. 9, pp. 589–608, 2020, doi: 10.1038/s41573-020-0073-9.
2. G. G. Eichholz, "Occupational Radiation Protection: IAEA Safety Standards," *Health Phys.*, vol. 87, no. 6, pp. 673–674, 2004, doi: 10.1097/00004032-200412000-00025.
3. M. H. Nassef and A. A. Kinsara, "Occupational Radiation Dose for Medical Workers at a University Hospital," *J. Taibah Univ. Sci.*, vol. 11, no. 6, pp. 1259–1266, 2017, doi: 10.1016/j.jtusci.2017.01.003.
4. G. S. Pant, S. K. Sharma, and G. K. Rath, "Finger doses for staff handling radiopharmaceuticals in nuclear medicine," *J. Nucl. Med. Technol.*, vol. 34, no. 3, pp. 169–173, 2006.
5. D. Adliene, B. Gričienė, K. Skovorodko, J. Laurikaitienė, and J. Puiso, "Occupational radiation exposure of health professionals and cancer risk assessment for Lithuanian nuclear medicine workers," *Environ. Res.*, vol. 183, no. January, p. 109144, 2020, doi: 10.1016/j.envres.2020.109144.
6. A. Carnicer et al., "Hand exposure in diagnostic nuclear medicine with  $^{18}F$ - and  $^{99m}Tc$ -labelled radiopharmaceuticals - Results of the ORAMED

- project,” *Radiat. Meas.*, vol. 46, no. 11, pp. 1277–1282, 2011, doi: 10.1016/j.radmeas.2011.07.019.
7. M. A. Hafez, R. M. Smith., S. J. Matthews, G. Kalap, and K. P. Sherman, “Radiation exposure to the hands of orthopaedic surgeons: Are we underestimating the risk?,” *Arch. Orthop. Trauma Surg.*, vol. 125, no. 5, pp. 330–335, 2005, doi: 10.1007/s00402-005-0807-5.
8. A. U. SMITH and C. Polge, “Chemical effects of ionizing radiation in some gels,” *Nat. Publ. Gr.*, p. 2, 1950.
9. H. L. Andrews, R. E. Murphy, and E. J. LeBrun, “Gel dosimeter for depth-dose measurements,” *Rev. Sci. Instrum.*, vol. 28, no. 5, pp. 329–332, 1957, doi: 10.1063/1.1715877.
10. J. Adamovics and M. J. Maryanski, “A new approach to radiochromic three-dimensional dosimetry-polyurethane,” *J. Phys. Conf. Ser.*, vol. 3, pp. 172–175, 2004, doi: 10.1088/1742-6596/3/1/020.
11. A. Mostaar, B. Hashemi, M. H. Zahmatkesh, S. M. R. Aghamiri, and S. R. Mahdavi, “A basic dosimetric study of PRESAGE: The effect of different amounts of fabricating components on the sensitivity and stability of the dosimeter,” *Phys. Med. Biol.*, vol. 55, no. 3, pp. 903–912, 2010, doi: 10.1088/0031-9155/55/3/023.
12. A. K. Vidovic et al., “An investigation of a PRESAGE® in vivo dosimeter for brachytherapy,” *Phys. Med. Biol.*, vol. 59, no. 14, pp. 3893–3905, 2014, doi: 10.1088/0031-9155/59/14/3893.
13. J. Jackson, T. Juang, J. Adamovics, and M. Oldham, “An investigation of PRESAGE® 3D dosimetry for IMRT and VMAT radiation therapy treatment verification,” *Phys. Med. Biol.*, vol. 60, no. 6, pp. 2217–2230, 2015, doi: 10.1088/0031-9155/60/6/2217.
14. Q. U. A. Shamsi, S. A. Buzdar, S. Jabeen, and K. Iqbal, “Review on the feasibility of using PRESAGE® dosimeter in various radiotherapy techniques,” *J. Radiother. Pract.*, 2020, doi: 10.1017/S1460396920000163.
15. M. F. Barakat, K. El-Salamawy, M. El-Banna, M. Abdel-Hamid, and A. Abdel-Rehim Taha, “Radiation effects on some dyes in non-aqueous solvents and in some polymeric films,” *Radiat. Phys. Chem.*, vol. 61, no. 2, pp. 129–136, 2001, doi: 10.1016/S0969-806X(01)00181-5.
16. N. Šeperienė, “The development of polymer gels and composites with the enhanced sensitivity to low dose irradiation,” Doctoral dissertation, p. 136, 2018. ISBN 978-609-02-1487-9.
17. M. A. Rauf and S. S. Ashraf, “Radiation induced degradation of dyes-An overview,” *J. Hazard. Mater.*, vol. 166, no. 1, pp. 6–16, 2009, doi: 10.1016/j.jhazmat.2008.11.043.
18. H. G. Kuball, T. Höfer, and S. Kieseewalter, “Chiroptical spectroscopy, general theory,” *Encycl. Spectrosc. Spectrom.*, pp. 217–231, 2016, doi: 10.1016/B978-0-12-409547-2.04980-5.



## **PHANTOM-BASED QUALITY CONTROL MEASUREMENTS FOR THE NEWLY INSTALLED LINEAR ACCELERATOR *HALCYON***

Agnė GIEDRYTĖ<sup>1</sup>, Lamiaa ABDELRAZIK, Marius LAURIKAITIS<sup>2</sup>, Reda ČERAPAITĖ-TRUŠINSKIENĖ<sup>3</sup>,  
Jurgita LAURIKAITIENĖ<sup>1</sup>

<sup>1</sup>Kaunas University of Technology, Kaunas, Lithuania <sup>2</sup>Hospital of Lithuanian University of Health Sciences  
Kaunas Clinics, Oncology Hospital <sup>3</sup>Lithuanian University of Health Sciences

<sup>1</sup>agne.giedryte@ktu.edu; <sup>2</sup>lamiaa4reality@gmail.com; <sup>3</sup>marius@medicinosfizika.lt; <sup>4</sup>redcera@gmail.com

**Abstract:** Image-guided radiotherapy (IGRT) is the one of the ways, ensuring radiation treatment accuracy, due to verification of a patient position and determining an accurate tumour localisation. Analysis of the newly installed linear accelerator *Halcyon* images was performed using treatment planning system *Eclipse*. It was found that image quality control tests used for the daily practice usually are based on the evaluation of constancy measurements, analysing the main parameters of the images quality and calibrating it, if it is needed.

**Keywords:** IGRT, Image quality, Quality assurance, CBCT, *Halcyon*

### **1. Introduction**

Nowadays external beam radiation therapy for a better treatment results could be followed by image-guided radiotherapy (IGRT) [1]. IGRT allows adjustment of patient position, so ensuring a more accurate target irradiation and a better safety of critical organs and healthy tissues. In the last decade, IGRT technology has been improved and spread rapidly, for example, for a lot moving tumours like, lung and prostate cancers [2-3]. Today is widely used cone-beam computed tomography (CBCT) IGRT in a daily clinical practice for the high accuracy patient setup verification and position adjustment. Accuracy assurance is related to the quality of the images, which could be ensured due to periodically done quality control tests (QC): geometric distortion, HU constancy, spatial resolution, uniformity, noise and contrast [4-5]. Due to this reason the aim of this study was to perform quantitative image quality assessment for the cone beam computer tomography imaging.

### **2. Materials and methods**

Linear accelerator (LA) *Halcyon* (Varian Medical Systems, Palo Alto, CA) is radiotherapy equipment,

which was newly installed on April, 2021 in the Hospital of Lithuanian University of Health Sciences Kaunas Clinics, Oncology Hospital, Radiotherapy department.

LA *Halcyon* has MV and kV CBCT imaging systems. It is very important to mention that IGRT for the *Halcyon* is mandatory procedure, i.e. it is impossible to start the treatment procedure without it, while for the standard, open design linear accelerators it could be optional step. It is known, that kV imaging system consists of kV x-ray source with half-bowtie filter and has eleven scanning protocols used in a daily practice for the fixed imaging voltages 80 kV, 100 kV, 125 kV and 140 kV, while mAs settings could be adjustable [6-7].

#### **2.1. Image quality assessment**

Quality control tests (Hounsfield units (HU) accuracy, HU uniformity, signal to noise ratio (SNR), a contrast to noise ratio (CNR), slice thickness, and geometric scaling) were performed using two different phantoms *Quart* and *Gammex 467*.

Phantom *Quart* (model: Quart DVT\_VN CBCT, Quality Assurance In Radiology “QUART” GmbH) usually is used for image quality evaluation of MV/kV CBCT imaging. Phantom *Quart* is a transparent polymethyl methacrylate (PMMA) 160 mm diameter cylinder with visible white cross markers (Fig. 1).

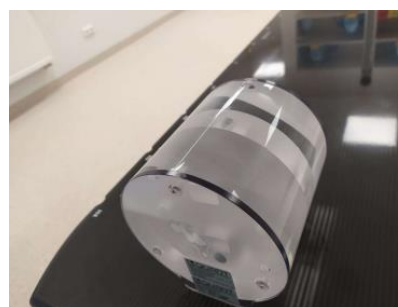


**Fig. 1.** Phantom QUART DVT\_VN

The phantom has two identical modules made of PMMA, also a central module with four different inserts/ holes: two air holes, 1 PTFE (Teflon) hole and 1 Polystyrene hole. (Table 1).

**Table 1.** Materials of the phantom nominal *HU* values [8]

Material types	Nominal <i>HU</i> value
PMMA (Acrylic)	+120
Polystyrene	-35
PTFE (Teflon)	+990
Air	-1000
Water	0

Another phantom used for the quality control was the Tissue Characterization Phantom *Gammex 467*. This phantom consists of 16 holes with 2.8 cm diameter for interchangeable holds for various tissues rods and water substitutes (Fig. 2).

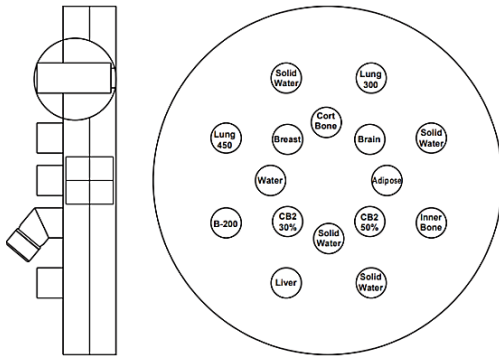


**Fig. 2.** Schematic view and cross-section of the *Gammex 467*

Image quality parameters were analysed and evaluated using treatment planning system (TPS) *Eclipse* (Varian Medical Systems, Palo Alto, CA, USA).

## 2.2. Quality control tests

***HU* accuracy** of CBCT image reconstruction was evaluated by measured *HU* mean values using *QUART* phantom. Different materials (Teflon, 2 Acrylic inserts, Polystyrene and two air holes) were selected for an average *HU* value in the selected region of interests (ROIs) measurements with TPS *Eclipse* (Fig. 3).

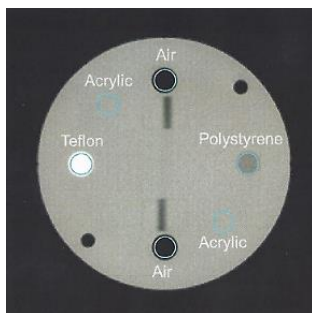


**Fig. 3.** Phantom *QUART* central slice of CBCT image for *HU* accuracy test module (ROIs are shown in circles)

The measured values were compared with nominal values (Table 1). Additionally *HU* accuracy test was done using phantom *Gammex 467* (Fig. 4).

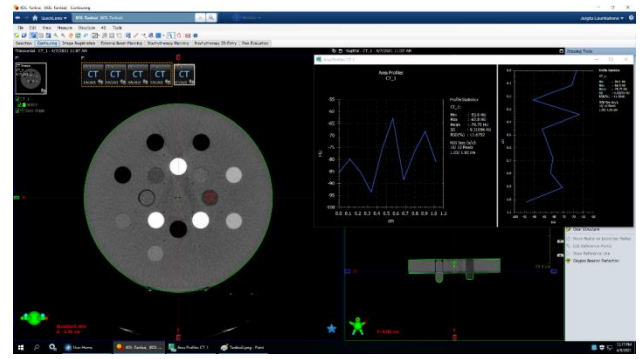


**Fig. 4.** Phantom *Gammex 467* CBCT image for *HU* accuracy test

***HU* uniformity** measurement of CBCT image reconstruction could be measured in one of the two 6 cm thickness homogenous modules, which are located on each side of the central module. Five different ROIs were selected, one at the center and four in a periphery regions (Fig. 5).

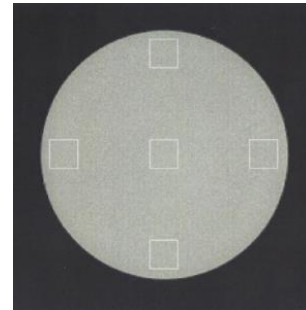


**Fig. 5.** Homogeneous region of CBCT image of phantom *QUART* for *HU* uniformity test module

**Noise** in the image was calculated using the standard deviation of the pixel values divided by the mean values of the ROIs (ROIs usually are selected in homogenous or central slice of the phantom).

**Signal-to-Noise Ratio (SNR).** Noise of the signal could be created due to random scattering effects. SNR is calculated by equation:

$$SNR = \frac{HU \text{ value} + 1000}{\sigma}, \quad (1)$$

where  $\sigma$  refers to a standard deviation.

**Contrast-to-Noise Ratio (CNR)** describes a quality of an image and can be calculated by equation, evaluating the difference of *HU* values between a certain insert and the material surrounding it:

$$CNR = \frac{[abs(HU \text{ insert} - HU \text{ background})]}{\sqrt{\sigma^2 \text{ insert} + \sigma^2 \text{ background}}}, \quad (2)$$

where  $HU_{\text{insert}}$  – mean *HU* values over a ROI in an insert and  $HU_{\text{background}}$  – mean *HU* values over a ROI in the background,  $\sigma_{\text{insert}}$  and  $\sigma_{\text{background}}$  – standard deviation of the *HU* values in the ROI and background.

**Geometric scaling** measurement could be verified measuring the diameter both in vertical and horizontal directions. Typical accuracy for a scaling measurement is 1 %.

**Slice thickness** measurement is usually based on evaluation shape of the tilted structure in a single slice. It can be determined by taking a profile and measuring the full width of half maximum (FWHM) and it can be calculated by equation:

$$S = \tan(\alpha) * FWHM, \quad (3)$$

where  $\alpha$  is angle of the tilted structure in a single constructed slice.

### 3. Results and discussion

Quality control (QC) is an important part of radiotherapy, positioning the patient before the procedure and ensuring accuracy of the treatment. Image quality QC tests used for the daily practice as the CBCT modalities recommendations are based on measurements, evaluating the constancy of these images quality parameters [9]. Due to this reason measurements were performed once per month (for the first two consecutive month: April and May), trying to observe constancy of the measurements.

Regarding *HU* accuracy measurements were measured average *HU* values and were compared with nominal values of the phantom materials/ inserts. Obtained results showed that the highest calculated percentage differences were for Acrylic, Acrylic and Polystyrene 51 %, 42 % and 39 % respectively in measurements which have been done in April, while the lowest percentage was 0.2 % and 0.1 % for air gap regions (Table 2).

**Table 2.** Results of *HU* accuracy values

Materials	Polystyrene	Teflon	Acrylic*	Acrylic*	Air gap 1	Air gap 2
<i>HU<sub>theor</sub></i>	-35	990	120	120	-1000	-1000
Measured <i>HU</i> (April)	-21	1151	170	181	-973	-980
Diff., % (April)	39	16	42	51	3	2
Measured <i>HU</i> (May)	-32	1021	145	159	-986	-996
Diff., % (May)	9	3	21	33	1	0.4

\*Both Acrylic materials were measured in different periphery parts of the *Quart* phantom

Additional measurements were done using phantom *Gammex 467*). The measured results showed that the difference between measured *HU* values and theoretical *HU* values due to a higher density of material had a larger deviations, like bones (Table 3). It means that larger deviation presents a material with a higher density, while smaller deviations were characteristic for the soft tissues (Table 3).

A good agreement was observed evaluating and *HU* uniformity (Table 4). It was found that *HU* values between central and peripheral regions were not exceeding a baseline more than  $\pm 10$  *HU* [10] (Table 4), which usually is dependent on the artefacts, which could

be resulted to a scattering processes and beam hardening.

**Table 3.** Theoretical and measured *HU* values for phantom *Gammex 467* inserts

RMI 467 Gammex	<i>HU</i> Theoretical	<i>HU</i> Measured	Diff.%
LN-300 Lung	-683	-619	-9.4
LN-450 Lung	-565	-464	-17.9
BR-12 Breast	-46	-57	23.1
AP6 Adipose	-105	-104	-0.7
BRN-SR2 Brain	15	18	23.3
CT Solid Water1	6	5	-27.4
LV1 Liver	87	100	14.8
Inner Bone	284	163	-42.5
CB2-30% CaCO <sub>3</sub>	575	292	-49.2
CB2-30% CaCO <sub>3</sub>	1057	651	-38.4
B200 Bone Mineral	309	157	-49.2

**Table 4.** Results of *HU* uniformity test

<i>HU</i> uniformity (April)	<i>HU</i>	Diff, %
ROI periphery 1	188	0.0
ROI periphery 2	186	1.0
ROI periphery 3	189	0.5
ROI periphery 4	191	2.0
ROI (center)	185	2.0
The average value of <i>HU</i> of all ROIs	188	
<i>HU</i> uniformity (May)	<i>HU</i>	Diff, %
ROI periphery 1	183	1.0
ROI periphery 2	185	0.0
ROI periphery 3	190	2.0
ROI periphery 4	188	2.0
ROI (center)	182	2.0
The average value of <i>HU</i> of all ROIs	185	

Evaluating measured SNR and CNR values, which usually are related to a noise and contrast of the image was noticed that it is an indication of the viewed noise in the image and noise respectively. SNR (3.40 (April), 2.90 (May)) and CNR (13.26 (April) and 8.50 (May)) showed that a larger value of SNR is an indication of less viewed noise in the image, as well as a larger value of CNR is an indication of less noise and artefacts in an image (Table 5 and Table 6).

**Table 5.** Signal-to-Noise Ratio (SNR) measurements

Slice No.	1	2	3	4	5	SNR
RSD* % (April)	3.77	3.62	2.96	3.14	3.54	3.40
RSD* % (May)	3.46	2.88	3.48	2.65	2.20	2.90

**Table 6.** Contrasts-to-Noise Ratio (CNR) measurements

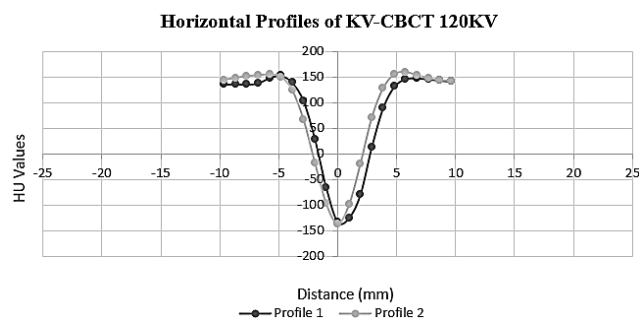
Materials (April)	HU	SD	RSD	CNR
Polystyrene	21.52	11.41	52.99	13.26
PMMA_theor	155.00	11.13	6.58	
Measured	169.19			
Materials (May)	HU	SD	RSD	CNR
Polystyrene	28.43	7.50	21.04	8.50
PMMA_theor	155.00	12.50	7.10	
Measured	151.70			

Regarding slice thickness measurement results summarized in Table 7, trying to get a higher accuracy of the measured slice thickness value, it is recommended to evaluate the result averaging it on both air-gaps profiles (Fig. 6).

**Table 7.** Measurement of slice thickness

Slice Thickness measurement	Profile 1	Profile 2	Average
FWHM, mm (April)	3.33	4.19	3.76
Slice thickness, mm (April)	1.92	2.41	2.17
FWHM, mm (May)	3.40	3.70	3.55
Slice thickness, mm (May)	1.96	2.13	2.05

The calculated by slice thickness (2.17 mm (April) and 2.05 mm (May) showed a good agreement with the value, which is specified by manufacturer of the phantom *Quart* (slice thickness default value has to be equal to 2.00 mm).

**Fig. 6.** Horizontal profiles of kV-CBCT image

The geometric scaling measurements (Table 8), evaluating a phantom diameter measured vertically and horizontally showed that difference is in a recommended limits and is lower than <1% (manufacturer recommendation).

**Table 8.** Measurement of geometric scaling

Geometric Scaling	Horizontal diameter (cm)	Vertical diameter (cm)	Diff. %	Accuracy
April	15.73	15.77	0.25	<1%
May	15.85	15.79	0.37	<1%

## 4. Conclusions

Obtained results of the IGRT quality control tests showed that image quality analysis done once per month, using phantoms *Quart* and *Gammex 467*, for the newly installed LA *Halcyon* image-guided radiotherapy is in the limits of the main requirements.

## 5. References

1. Sadeghi M., Enferadi M., Shirazi A. External and internal radiation therapy: past and future directions // Journal of cancer research and therapeutics, 2010, 6(3), p. 239.
2. Choudhury A., Budgell G., MacKay R., Falk S., Faivre-Finn C., Dubec M., McWilliam A. The future of image-guided radiotherapy // Clinical Oncology, 2017, 29(10), p. 662-666.
3. Pollard J. M., Wen Z., Sadagopan R., Wang J., Ibbott G. S. The future of image-guided radiotherapy will be MR guided // The British journal of radiology, 2017, 90(1073), 20160667.
4. Bamba J., Araki K., Endo A., Okano T. Image quality assessment of three cone beam CT machines using the SEDENTEXCT CT phantom // Dentomaxillofacial Radiology, 2013, 42(8), 20120445.
5. Taneja S., Barbee D. L., Rea A. J., Malin M. CBCT image quality QA: Establishing a quantitative program // Journal of applied clinical medical physics, 2020, 21(11), p. 215-225.
6. Cai B., Laugeman E., Mazur T. R. Park J.C., Henke L.E., Kim H., Li H. Characterization of a prototype rapid kilovoltage x-ray image guidance system designed for a ring shape radiation therapy unit // Medical physics, 2019, 46(3), p. 1355-1370.
7. Kim H., Huq M.S., Lalonde R., Houser C.J., Beriwal S., Heron D. E. Early clinical experience with varian halcyon V2 linear accelerator: Dual-isocenter IMRT planning and delivery with portal dosimetry for gynecological cancer treatments // Journal of applied clinical medical physics, 2019, 20(11), p. 111-120.
8. Peng J., Li H., Laugeman E., Mazur T., Lam D., Li T., Cai B. Long-term Inter-protocol kV CBCT image quality assessment for a ring-gantry linac via automated QA approach // Biomedical physics & engineering express, 2020, 6(1), 015025.
9. Healy B.J., Budanec M., Ourdane B., Peace T., Petrovic B., Sanz D.E., Tuntipumiamorn L. An IAEA survey of radiotherapy practice including quality assurance extent and depth // Acta Oncologica, 2020, 59(5), p. 503-510.
10. Maqbool M. An Introduction to Medical Physics, Biological and Medical Physics, Biomedical Engineering, corrected publication 2018.

## **MEDICAL 3D IMAGE SEGMENTATION IN RADIOTHERAPY TREATMENT FOR A PATIENT WITH HEAD AND NECK TUMOURS**

Mindaugas ILICKAS<sup>1</sup>, Jurgita LAURIKAITIENĖ<sup>1,2</sup>,

<sup>1</sup> Department of Physics, Kaunas University of Technology, Lithuania

<sup>2</sup> Hospital of Lithuanian University of Health Sciences Kaunas Clinics, Oncology Hospital, Radiotherapy  
Department, Kaunas, Lithuania

<sup>1</sup>mindaugas.ilickas@ktu.edu; <sup>2</sup>jurgita.laurikaitiene@ktu.lt

**Abstract:** A handmade personalized 3D phantom produced from reconstructed CT data of a real patient could be used as a low-cost, reusable, and customizable phantom. The phantom assembly was created to mimic the patient's surface shape of the certain region. Two open-source software were used to calculate similarity features. This image analysis approach and the determination of similarity features could be quite accurate and used in a clinical practice.

**Keywords:** segmentation, similarity coefficients, phantom, head and neck tumour

### **1. Introduction**

The number of oncological diseases is increasing every year all over the world. Cancer is the world's second most common cause of death. It is known that one out of six individuals are dying from cancer each year. It is predicted by WHO (World Health Organization) that in the next two decades, the number of cancers in the world will grow by 60% [1].

The treatment/irradiation of head and neck tumours with external radiation therapy is limited by healthy tissues and vital organs near the tumour such as parotid and salivary glands, jaw, spinal cord, larynx, etc. To facilitate the modelling of the treatment and to follow the possible course, medical physicists usually use phantoms. Phantoms are physical or virtual representation of the human body that are used for radiation-sensitive organs and tissues to assess the absorbed dose [2]. Phantoms can differ depending on the size and type of material they are made of, according to the TRS-398 (Technical Report Series) protocol [3]. In general, there are of the most common used types of the phantoms, like water, solid-state, and anthropomorphic phantoms.

This work mostly focuses on anthropomorphic phantoms. Commercial anthropomorphic phantoms are

expensive, so not every hospital or treatment facility can afford them. The solution is a 3D printing technology, which becomes cheaper and accessible to everyone in the last decade. 3D printing materials that may be used and printing settings that impact the characteristics of the printed item are the most essential elements to consider usage of 3D printing phantoms and boluses. Different thermoplastic polymers, such as polylactic acid (PLA), acrylonitrile butadiene styrene (ABS), and high impact polystyrene (HIPS), are tissue-equivalent and have comparable attenuation characteristics to human tissues and/or organs (PLA – thorax and head, ABS – heart, thyroid, HIPS – thorax) [4-5].

The aim of this work is to investigate the similarity of the produced, a low-cost, reusable, homemade customized 3D printed, phantom with patient computed tomography images.

### **2. Materials and Methods**

3D phantom printing was performed using a relatively inexpensive 3D printer, the Zortrax M300 (the price is about 4200\$), which has a large printing volume. An original set of CT scans (CT scanner Siemens Light Speed RT16) in DICOM format depicting an anonymous patient's anatomic region of interest was chosen for 3D printing. A printed phantom of a real patient is shown in Fig. 1.

3D printed patient-specific phantom (phantom-phantom assembly) was connected to a PMMA CT head phantom (16 cm diameter) that was designed to replicate the patient's surface contour in the region of interest. The entire structure was scanned using CT scanner (CT scanner Siemens Light Speed RT16, Erlangen, Germany) and a 3D model of the assembly was reconstructed using open software Blender (blender.org) from CT scans.





**Fig. 1.** The printed phantom is attached to the surface of the PMMA CT Head phantom

Two freely available softwares (*DSCImageCalc v1.2a* [6] and *Project "EvaluateSegmentation"* [7] (written in C++ language)) were selected for the analysis of similarity of 3D phantom CT images.

Software *DSCImageCalc v1.2a* calculates 6 similarity characteristics – Sorensen-Dice Coefficient; Jaccard Coefficient; Proportional Agreement; Cohen's Kappa; Goodman & Kruskal's Gamma; Rogot-Goldberg Agreement.

*Project "EvaluateSegmentation"* calculates 22 different similarity characteristics, which are divided into 6 different groups: 1) based on overlap (Dice Coefficient – DICE, Jaccard Coefficient – JAC, true positive rate (Sensitivity, Recall) – TPR, true negative rate (Specificity) – TNR; false positive rate (Fallout) – FPR, False negative rate (Sensitivity) – FNR; F-Measure – FMS, Global Consistency Error – GCE); 2) based on volume (Volumetric Similarity Coefficient – VS); 3) based on pair counting (Rand Index – IR, Adjusted Rand Index – ARI); 4) based on theoretical information (Mutual Information – MI, Variation of Information – VOI); 5) based on probabilistic data (Interclass correlation – ICC, Probabilistic Distance – PBD, Cohen Kappa – KAP, Area under ROC Curve – AUC) and 6) based on spatial distance (Hausdorff distance – HD, Average distance – AVD, Mahalanobis Distance – MHD).

The software *DSCImageCalc v1.2a* provides a graphical user interface (GUI) for the selection of the files, type of coefficient, colour of the section and to visualisation of the results. A "fuzziness" option allows the software to consider segments where the colours do not fit exactly, but this must be used carefully as it can result analysis of the segment, adding unwanted sections for the image. "For each image analysed, the number of pixels included within the segment, the percentage of the total image, and the position of the calculated centroid, is displayed to help to be sure user that the software has analysed the correct segment" [6]. Also, "after an analysis run, the images are updated to show which parts the software has analysed as part of the segment which the user can check to ensure analysis has proceeded as expected" [6].

Using *Project "EvaluateSegmentation"* there is a mandatory part on the command line which specifies

(shows the location of the images on the computer) the two images to be compared. By default, a fuzzy comparison is performed unless otherwise defined [7].

Medical segmentations are always fuzzy, which means the voxels have a membership rank of  $[0, 1]$ . One way to test fuzzy segmentations is to restrict the chances of receiving binary representations that can be measured as crisp segmentations at a specific value. Thresholding, however, is just a solution that gives a coarse approximation and is not always satisfactory [7]. In addition, the problem of choosing the threshold still exists since the outcomes of the test depend on the selection. This is the impetus to include metrics that can compare fuzzy segmentations without data loss [7].

Using RadiAnt DICOM Viewer 2020.2.3 software DICOM format CT images were converted to .jpg file format, because these programs work only with it. Then with Adobe photoshop 2020 software, areas of interest are marked in the images, and the images are resized to 512x512 pixel size. When using photoshop, threshold values are displayed in interval 0.0-0.99 and an image is obtained. The obtained .jpg format photos are used for image analysis. Using script written in R software from project "EvaluateSegmentation" results the correlation matrix is obtained.

### 3. Results and discussion

The goal of radiation therapy is to irradiate the cancer with the least possible damage to the surrounding organs, which are known as organs at risk (OAR).

It is known that the build-up area for high-energy (MeV) photons forms so called a skin-sparing effect. This is beneficial for treating deep-seated malignancies in the body to minimize unfavourable early and late skin responses. The skin-sparing effect, however, leads to tumour underexposure and a greater risk of recurrence if the tumour is superficial [8]. The use of 3D-printed bolus/compensating structures was investigated in this work to overcome the skin-sparing effect in radiation treatment.

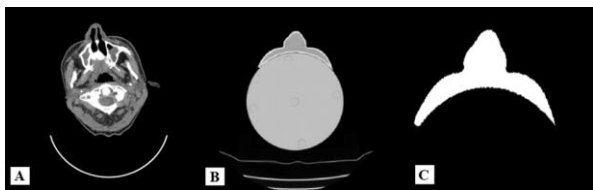
The mistakes introduced at each phase of the 3D printing process, from image segmentation and subsequent changes of the segmented model through printing and post-processing, determine the geometrical correctness and reproducibility of the produced item. Analysing the geometrical accuracy of our patient-specific 3D printed phantom was excellent (using *DSCImageCalc v1.2a* software), which suggests that more detailed analysis is needed (because the results of the software suggest that both images are the same). Dice similarity coefficient, also known as overlap measure between the CT scans of the patient and the phantom, were used to assess the geometric correctness and repeatability of the 3D phantom [9-10]. By appropriately aligning (cropping, rotating zooming images) chosen CT scans obtained for both the patient and the phantom and manually modifying (highlighting) regions of interest on both images (see Fig. 2), reliable DICE assessment has been accomplished (see Table 1).



**Table 1.** Calculated similarity coefficients values with a DSCImageCalc software

Characteristics	Value
Sorensen-Dice Coefficient	1.00
Jaccard Coefficient	1.00
Proportional Agreement	1.00
Cohen's Kappa	1.00
Goodman & Kruskal's Gamma	1.00
Rogot-Goldberg Agreement	1.00

A full overlap between two examined volumes is indicated by a DSCs score of 1. The contours of the patient's skin and/or organs would be properly reproduced by the 3D printed phantom in this scenario. In this work, the similarity of phantom's external shape to the patient's surface was determined by calculating their similarity coefficients using open access software DSCImageCalc and project "EvaluateSegmenation".

**Fig. 2.** CT scan of the patient (A); CT image of the 3D printed phantom positioned on the surface of the CT head phantom (B); CT image overlapping of patient and 3D printed phantom generated using open-source program DSCImageCalc v1.2a (C)

It can be observed that from the Table 1 that the CT images of the 3D printed phantom and the patient are the same (all characteristics are equal to 1), while similarity characteristics values presented in Table 2 are changing and at threshold value (in the most cases) we get the smallest values.

Using a thresholding technique in which all gray levels below the threshold are mapped into black, and those levels above the threshold are mapped into white, or vice versa, features of interest in a picture may also be extracted from their surroundings [11]. However, this method is not without flaws, and it can result in the loss of image signal information and insufficient noise removal [12]. Thresholding at too high-level results in data loss, whereas thresholding at too low level will result in distracting background clutter. Examining the gray level histogram of a given image is a common method of automatically determining a threshold value with which to best perform the segmentation process.

Fig. 3 shows the result of a correlation analysis between the rankings produced by 24 (22 similarity metrics, compilation time and threshold) of the metrics presented in Table 2 when applied to a data set of 10 patient CT and 3D printed phantom CT images.

The pairwise Pearson's correlation coefficients were calculated as well. It was found that analysing the correlation between rankings instead of metric values solves the problem that some of the metrics are similarities and some others are distances and avoids the necessity to convert distances to similarities as well as to normalize metrics to a common range.

**Table 2.** Calculated similarity coefficients values with a project "EvaluateSegmenation" software

Threshold	0.00	0.10	0.20	0.30	0.40	0.50	0.60	0.70	0.80	0.90	0.95	0.99
Dice Coefficient	0.95	0.99	0.99	0.99	0.99	0.75	0.93	0.94	0.95	0.96	0.95	0.81
Jaccard Coefficient	0.91	0.99	0.99	0.99	0.98	0.60	0.87	0.89	0.91	0.92	0.91	0.68
Area under ROC Curve	0.98	1.00	1.00	1.00	0.99	0.92	0.98	0.98	0.99	0.98	0.97	0.87
Cohen Kappa	0.94	0.99	0.99	0.99	0.99	0.75	0.93	0.94	0.95	0.96	0.95	0.81
Rand Index	0.95	0.99	0.99	0.99	0.99	0.97	0.99	0.99	1.00	1.00	1.00	0.99
Adjusted Rand Index	0.90	0.99	0.99	0.99	0.98	0.73	0.93	0.94	0.95	0.95	0.95	0.80
Interclass Correlation	0.95	0.99	0.99	0.99	0.99	0.75	0.93	0.94	0.95	0.96	0.95	0.81
Volumetric Similarity Coefficient	0.97	0.99	1.00	1.00	1.00	0.88	0.97	0.97	0.98	0.99	0.99	0.90
Mutual Information	0.68	0.76	0.76	0.76	0.75	0.11	0.14	0.14	0.14	0.14	0.13	0.08
Hausdorff Distance	140.7	113.4	4.0	4.0	4.0	16.0	39.1	239.2	7.2	9.2	9.2	9.2
Average Hausdorff Distance (in voxel)	0.60	0.01	0.01	0.01	0.01	0.54	1.64	0.85	0.06	0.06	0.07	0.21
Mahanabolis Distance	0.02	0.01	0.01	0.02	0.02	0.14	0.15	0.11	0.07	0.08	0.09	0.12
Variation of Information	0.29	0.06	0.06	0.06	0.07	0.18	0.05	0.04	0.03	0.03	0.04	0.09
Global Consistency Error	0.04	0.01	0.01	0.01	0.01	0.03	0.01	0.00	0.00	0.00	0.00	0.01
Probabilistic Distance	0.00	0.00	0.00	0.00	0.00	0.00	0.00	0.00	0.00	0.00	0.00	0.00
Sensitivity (Recall, true positive rate)	0.99	1.00	1.00	0.99	0.99	0.85	0.96	0.97	0.97	0.96	0.94	0.74
Specificity	0.97	1.00	1.00	1.00	1.00	0.99	1.00	1.00	1.00	1.00	1.00	1.00
Precision	0.92	0.99	0.99	0.99	0.99	0.67	0.90	0.92	0.94	0.95	0.96	0.90
F-Measure	0.95	0.99	0.99	0.99	0.99	0.75	0.93	0.94	0.95	0.96	0.95	0.81
Accuracy	0.98	1.00	1.00	1.00	1.00	0.98	1.00	1.00	1.00	1.00	1.00	0.99

The colour intensity of the cells represents the strength of the correlation.

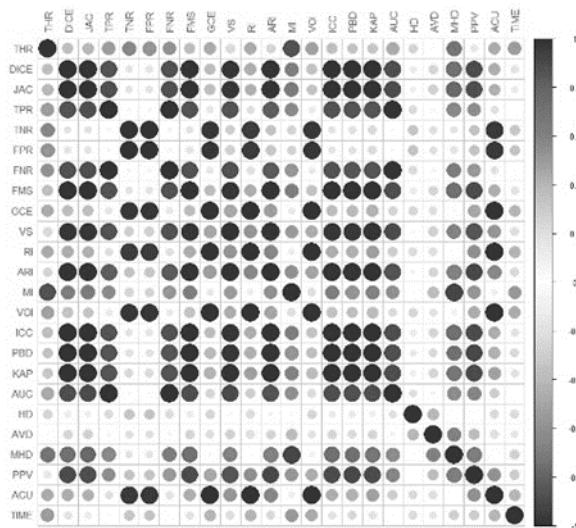


**Fig. 3.** The correlation between the rankings produced by 24 different metrics (22 similarity metrics, compilation time and threshold). The colour intensity of each cell represents the strength of the correlation, where blue denotes direct correlation and red denotes inverse correlation

Based on the connection between the rankings provided by the metrics in Fig. 3, they may be split into two groups: one at the top left, another at the right bottom. Each of these group's measurements have a high association with one another, but no correlation with the other group's metrics. The remaining metrics are somewhat correlated with one another and with the other categories.

The true negatives are mostly included in the definitions of the adjusted rand index (a measure of the similarity between two data clusterings) and the kappa measures, but both conduct chance adjustment, which removes the true negatives impact, i.e., prevents the background's influence dominating the outcome [13]. Also, because they are based on the distances between the foreground voxels, the average distance (AVD) and the Mahalanobis distance (MHD) do not account for real negatives (non-zero voxels). Due to the backdrop (often the greatest part of the segmentation) contributes to the agreement, considering the actual negative in the evaluation has a significant influence on the outcome.

#### 4. Conclusions

Two softwares *DSCImageCalc v1.2a* and *project "EvaluateSegmentation"* were used for 3D printed anthropomorphic phantom evaluating similarity characteristics, which showed that the lowest values of similarity characteristics are obtained at the threshold values (in literature and experimental this value is 0.5). Due to this reason image analysis method and the calculation of similarity characteristics would be quite accurate and could be used in a clinical practice.

#### 5. References

1. World Health Organization. Estimated number of deaths in 2018, worldwide, both sexes, all ages. Access via: [shorturl.at/fpkz8](https://shorturl.at/fpkz8)
2. International atomic energy agency. Technical reports series No 398. Vienna, 2000
3. Physikalisch-technische werkstätten. MP3-T Water Phantom Systez. 2020. Access via: [shorturl.at/tmqv0](https://shorturl.at/tmqv0)
4. Tino R, Yeo A, Leary M, et al. A Systematic Review on 3D-Printed Imaging and Dosimetry Phantoms in Radiation Therapy. *Technol Cancer Res Treat* 2019, 18.
5. Adlienė D., Jaselskė E., Rudžianskas V., Šeperienė N. First approach to ionizing radiation based 3D printing: fabrication of free standing dose gels using high energy gamma photons // *Nuclear instruments in physics research B*, 2018, 435, p. 246-250.
6. Lawton, T. *DSCImageCalc – Software for Determining Similarity Coefficients for the Analysis of Image Segmentations*. *Journal of Open Research Software*, 2017, 5(1), 28.
7. Taha, A. A., & Hanbury, A. Metrics for evaluating 3D medical image segmentation: analysis, selection, and tool. *BMC Medical Imaging*, 2015, 15(1).
8. Wojcicka JB et al. Dosimetric comparison of three different treatment techniques in extensive scalp lesion irradiation. *Radiother Oncol* 2009, 91, 255-260.
9. Taha AA, Hanbury A. Metrics for evaluating 3D medical image segmentation: analysis, selection, and tool. *BMC Med Imaging* 2015, p. 15-29.
10. Zou KH, et al. Statistical validation of image segmentation quality based on a spatial overlap index. *Acad Radiol* 2004. 11(2), p.178-189.
11. T. W. Ridler and S. Calvard. Picture Thresholding Using an Iterative Selection Method. *IEEE Transactions on Systems, Man, and Cybernetics*, 1978, 8(8), p. 630–632.
12. Pandian, D. S. J., et al. Complex threshold method for identifying pixels that contain predominantly noise in magnetic resonance images. *Journal of Magnetic Resonance Imaging*, 2008, 28(3), p. 727–735.
13. Fatourehchi M, et al. Comparison of evaluation metrics in classification applications with imbalanced datasets. In: *ICMLA*. San Diego, CA: 2009. p. 777–82

## **COMPARISON OF EXPERIMENTALLY MEASURED DOSE DEPTH DISTRIBUTIONS WITH MC SIMULATIONS IN ELECTRON-IRRADIATED DOSE GELS**

Aleksandras ŠEVČIK<sup>1</sup>, Diana ADLIENĖ<sup>2</sup>,

<sup>1,2</sup> Department of Physics, Kaunas University of Technology, Kaunas, Lithuania

<sup>1</sup>aleksandras.sevcik@ktu.edu; <sup>2</sup>diana.adliene@ktu.lt

**Abstract:** Polymer gel dosimeters can provide 3D absorbed dose distributions with a good spatial resolution for radiotherapy. During radiation-induced polymerization, attenuation properties of the polymer gels change accordingly so the actual dose distribution pattern may differ, especially along the edges of the polymerized gel structure. Monte Carlo (MC) simulation of 6 MeV electron beam interacting with nMAG normoxic polymer were performed using FLUKA simulation package. The obtained 3D dose distributions were compared with the experimental results. The difference in the dose pattern versus absorbance spectra was assessed.

**Keywords:** polymer gel, dosimetry, Monte Carlo, Fluka

### **1. Introduction**

Electron beams are widely used in radiotherapy because they have superior advantage over photons when treating superficial conditions[1–3]: a rapid dose fall-off beyond the target volume which decreases the probability of healthy tissue complication. This therapy is used to treat various skin cancers[4–6], and may also be used to increase the radiation dose after mastectomy or lumpectomy[7,8]. It is also used in some special cases, such as the management of keloid scars[9]. Currently, treatment-planning algorithms are unable to accurately model electron therapy, including skin collimation, internal collimation, variable-thickness bolus, and so on; hence are unable to fully use existing treatment technology[10]. Furthermore, because of the steep dosage gradient, measuring the electron beam dosimetric properties to get the percentage depth dose for the specific heterogeneous medium using standard dosimetry methods is hard[11].

Treatment planning demands a reliable estimation of the absorbed dose distribution across the tissues of interest. The Monte Carlo simulation of radiation transport is regarded as one of the most accurate methods of calculating radiation therapy doses and is widely used

for electron beam therapy[12–15]. Commonly used codes are BEAMnrc[16], Penelope[17], MCNPX[18], EGSnrc[19], Geant4[20] and some other. The FLUKA code[21] chosen for simulation in this work is more oriented toward ion therapy applications[22], but it has also been validated in electron transport applications in medicine[23]. With the advancement of computational power, Monte Carlo codes have proven to be a valuable tool for obtaining an accurate 3D dose distribution in complex heterogeneous media such as patient-specific body with metal implants[23–25] or organs with tissues that are substantially denser than water, such as the lungs[26].

Another method for obtaining 3D dose distribution is to employ specifically created hydrogels for ionizing-radiation dosimetry, which are made of radiation sensitive polymers that polymerize when exposed to radiation, and the degree of polymerization is dose dependent[27–29]. As a result, the intrinsic spatial resolution of those dosimeters is only constrained by how the dosage information recorded by the medium is transformed to the absorbed dose. Magnetic resonance imaging, optical computed tomography, and X-ray computed tomography are the existing standard procedures for dose quantification[30]. However, these technologies still do not have a wide range of clinical uses. One reason is that polymer gel dosimetry is based on chemical processes that are difficult to assess, such as various degrees of polymerization and their diffusion during and after the irradiation process, which may extend beyond the irradiated field.

Because 3D imaging/dosimetry can surely add value to complex conformal treatment regimens, two of the most prominent 3D dosimetry methods were investigated in this work: Monte Carlo (MC) simulation and polymer gel dosimetry. It should be noted that a correctly verified MC model could assist polymer gel dosimetry by giving reference dose distributions. Both methodologies were used and compared for the 6 MV electron beam on the reference geometry.

## 2. Instruments and methods

### 2.1 Simulation framework and validation

The FLUKA (FLUKtuierende KAskade)[31–33] is a Monte Carlo simulation tool for modeling the interaction of radiation with matter, with applications spanning from high-energy physics to medical and radiation physics, and is used by institutions such as CERN for dosimetry, radioprotection, and beam-machine interaction investigations[34]. The simulation physics setup considers electron, positron, and photon transport, as well as activated Rayleigh scattering and inelastic form factor corrections to Compton scattering and Compton profiles, including multiple scattering and photon polarization for Compton, Rayleigh, and photoelectric effects[35]. The data for pair generation, photoelectric, and total coherent cross-section tabulations are taken from the EPDL97 photon data library [36]. Auxiliary program FLAIR [37] is a user-friendly interface that makes it easy to edit FLUKA input files, execute code, and view output files.

FLUKA's input is a file containing a series of option lines known as "cards" that allow users to specify simulation specifics such as general default values for the selected physics, beam setup and position, geometry creation, transport and scoring parameters. To test the physical setup, the 6 MeV electron beam passing through an infinite cylinder of water was performed, and electrons were scored according to their energy with the aim to determine their averaged range in the medium (Fig 1). It compares favorably with the stated value of the continuous slowing down approximation (CSDA) range in the NIST ESTAR [38], which is 3.052 g/cm<sup>2</sup>. A production threshold and kinetic energy transport cut-off is set to 300 keV since the estimated range of such energy in the water-like media is below 1 mm.

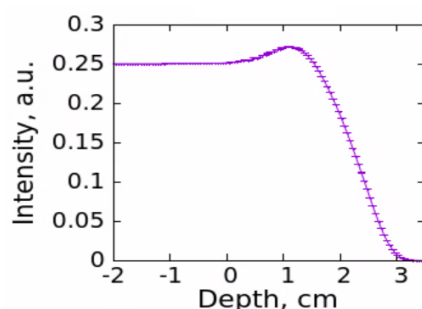


**Fig. 1.** Depth variations of electron beam intensity along cuvette filled with water

The composition of normoxic methacrylic acid was used to model the basis for media. (nMAG) consisting of 5% methacrylic acid (MAA, C<sub>4</sub>H<sub>6</sub>O<sub>2</sub>), 8% gelatin (C<sub>102</sub>H<sub>151</sub>N<sub>31</sub>O<sub>39</sub>), 0.5% of tetrakis-(hydroxymethyl)-phosphonium-chloride (THPC, [(HOCH<sub>2</sub>)<sub>4</sub>PCl]), 86.5% water (H<sub>2</sub>O). The irradiation geometry was built strictly according to the experimental setup (Fig.2).

The FLUKA code estimates the standard deviation of repeated simulation results by calculating the statistical error (type A uncertainty). The simulation was carried out in ten batches, each with 10<sup>7</sup> occurrences. In all

regions of importance, the statistical error was kept under 1%.

### 2.2 Experimental framework

Six standard PMMA cuvettes 12.5x12.5x40.5 mm were filled with nMAG gel consisting of 5% methacrylic acid (MAA, C<sub>4</sub>H<sub>6</sub>O<sub>2</sub>), 8% gelatin (C<sub>102</sub>H<sub>151</sub>N<sub>31</sub>O<sub>39</sub>), 0.5% of tetrakis-(hydroxymethyl)-phosphonium-chloride (THPC, [(HOCH<sub>2</sub>)<sub>4</sub>PCl]), 86.5% water (H<sub>2</sub>O) and irradiated with 6 MeV electron field in the broad beam configuration using Linacs Truebeam 2.7 (Fig.2). The beam was parallelly directed to the bottom of the cuvettes. According to the linacs control system, 1, 2, 3, 4, and 5 Gy doses were delivered with respect to the water medium.



**Fig. 2.** Experimental geometry and the irradiated cuvettes

The optical spectra of the irradiated gels were measured every 0.15 mm along the beam path (Z-axis) using an Ocean Optics 4000 spectrometer. Furthermore, the cuvettes were scanned in transmission mode using Epson V300 scanner, and grayscale images were generated in an uncompressed 16bit 1200 dpi TIFF file. Comparison of the results obtained using the spectrometer and the transmission mode scanner may be useful for future work because the scanner works much faster and is easier to use in a clinical setting. Image analysis software, on the other hand, must be used later to evaluate the scanned data, and a proper data analysis protocol must be applied as well.

## 3. Results and discussion

Fig. 3 depicts the curves derived from measured spectra at the wavelength of 600 nm and from scanning results of the cuvettes filled with gel. It was found that due to the low optical density and low polymerization level, noise was higher at lower doses. More consistent results were observed in the case of spectrometric analysis of irradiated samples as compared with scanned ones.

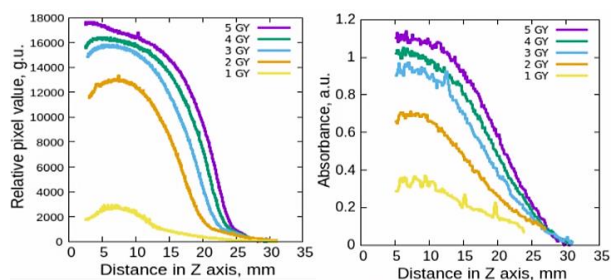


**Fig. 3.** Depth dependent pixel variation in the scanned images of the irradiated samples (left) and in absorbance spectra measured at 600 nm (right)



At various doses, a comparison of relative pixel value versus absorbed dose is shown in Fig.4 - 8. The same pattern of wider shift at higher doses and more noise at lower doses can be seen, but the spectrometer results are unquestionably more accurate and should thus be used in future research.

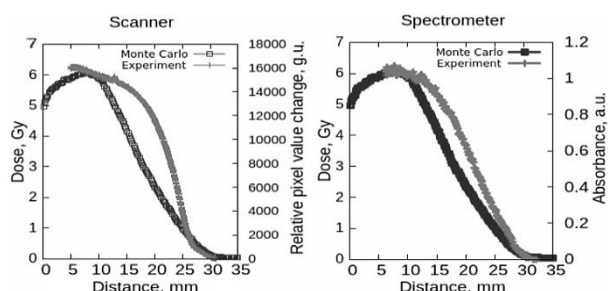


**Fig. 4.** Comparison of 5 Gy simulated absorbed dose pattern and experimental results: versus scanned image pixel values (left) and versus absorption measurements by spectrometer (right)

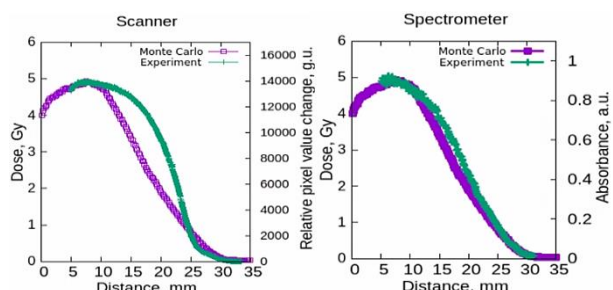


**Fig. 5.** Comparison of 4 Gy simulated absorbed dose pattern and experimental results: versus scanned image pixel values (left) and versus absorption measurements by spectrometer (right)

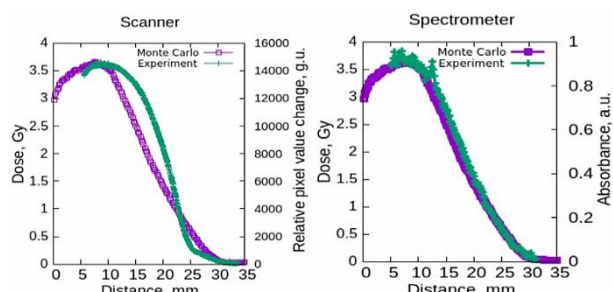


**Fig. 6.** Comparison of 3 Gy simulated absorbed dose pattern and experimental results: versus scanned image pixel values (left) and versus absorption measurements by spectrometer (right)

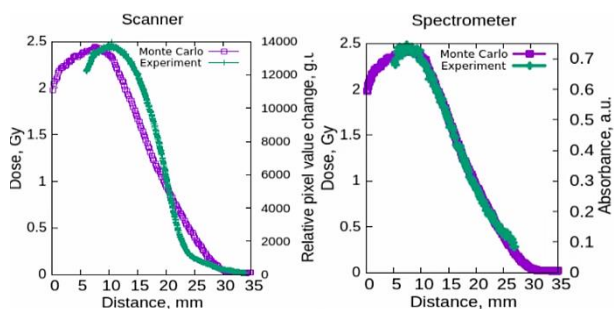


**Fig. 7.** Comparison of 2 Gy simulated absorbed dose pattern and experimental results: versus scanned image pixel values (left) and versus absorption measurements by spectrometer (right)

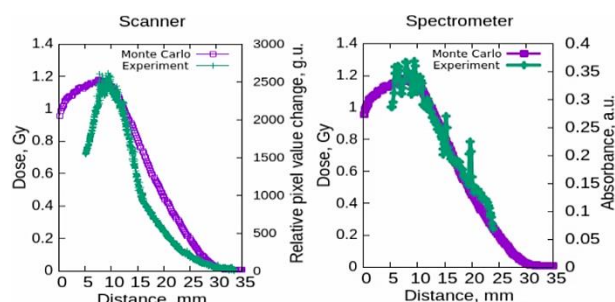


**Fig. 8.** Comparison of 1 Gy simulated absorbed dose pattern and experimental results: versus scanned image pixel values (left) and versus absorption measurements by spectrometer (right)

## 4. Conclusions

The FLUKA simulation package was used to run a Monte Carlo (MC) simulation of a 6 MeV electron beam acting on normoxic polymer gel dosimeters nMAG. The experimental findings were compared to the simulated dosage distribution. The disparity between the dosage pattern and the absorbance spectra was investigated.

This study looked at the difference between simulated dose-depth and experimentally obtained absorbance-depth functions. To begin, instead of using the scanner, the spectrometer should be used because the pixel values obtained by scanning cannot be properly translated to the actual dose shape pattern. Furthermore, it was found that for the 6 MeV electron beam dose around 1 Gy has low polymerization degree, resulting in large noise during spectrometer measurements, whereas polymerization around 2 Gy is strong enough to follow the simulated dose pattern precisely. However, at higher doses (4–5 Gy), we noticed possible oversaturation of the polymer gel, which caused the curve to shift further along the Z-axis. Additional experiments are needed to determine why the shift occurs, such as expansion due to a lack of cuvette capacity, or possible polymerization diffusion, among other possibilities.

## 5. References

- O'Shea TP, Foley MJ, Rajasekar D, Downes PA, van der Putten W, Moore M, et al. Electron beam therapy at extended source-to-surface distance: A Monte Carlo investigation. *J Appl Clin Med Phys* 2008. doi:10.1120/jacmp.v9i4.2811.
- Pashazadeh A, Boese A, Friebe M. Radiation therapy techniques in the treatment of skin cancer: an overview of the current status and outlook. *J Dermatolog Treat* 2019. doi:10.1080/09546634.2019.1573310.
- Sen S, Bandyopadhyay A, Pal JK, Ghosh AK, Deb AR. A dosimetric study of electron beam therapy vs. high-dose-rate mould brachytherapy in adjuvant treatment of non-melanoma skin carcinomas of the head and neck region. *J Contemp Brachytherapy* 2019. doi:10.5114/jcb.2019.90233.
- Newman NB, Patel CG, Ding GX, Zic JA, Zwerner J, Osmundson EC, et al. Prospective observational trial of low-dose skin electron beam therapy in mycosis fungoides using a rotational technique. *J Am Acad Dermatol* 2021. doi:10.1016/j.jaad.2020.12.023.
- Jeans EB, Hu YH, Stish BJ, King B, Davis M, Harmsen WS, et al. Low-Dose Hypofractionated Total Skin Electron Beam Therapy for Adult Cutaneous T-Cell

- Lymphoma. *Pract Radiat Oncol* 2020. doi:10.1016/j.prro.2020.08.001.
6. Chowdhary M, Chhabra AM, Kharod S, Marwaha G. Total Skin Electron Beam Therapy in the Treatment of Mycosis Fungoides: A Review of Conventional and Low-Dose Regimens. *Clin Lymphoma, Myeloma Leuk* 2016. doi:10.1016/j.clml.2016.08.019.
7. Ananthi B, Bhuvana K, Faith R, Selvaluxmy G, Vivekanandan N, Priya I. Conformal electron beam radiotherapy using custom-made step bolus for postmastectomy chest wall irradiation: An institutional experience. *J Cancer Res Ther* 2019. doi:10.4103/jcrt.JCRT\_69\_17.
8. Amin-Zimmerman F, Paris K, Minor GI, Spanos W. Postmastectomy chest wall radiation with electron-beam therapy: Outcomes and complications at the University of Louisville. *Cancer J* 2005. doi:10.1097/00130404-200505000-00006.
9. Rishi KS, Sarkar N, Kesari P, Pathikonda M, Ramachandra P, Donapati PKR, et al. Single Institution Experience of Postoperative Electron Beam Radiation Therapy in the Treatment of Keloids. *Adv Radiat Oncol* 2021. doi:10.1016/j.adro.2020.10.009.
10. Hogstrom KR, Almond PR. Review of electron beam therapy physics. *Phys Med Biol* 2006. doi:10.1088/0031-9155/51/13/R25.
11. Khan FM, Doppke KP, Hogstrom KR, Kutcher GJ, Nath R, Prasad SC, et al. Clinical electron-beam dosimetry: Report of AAPM Radiation Therapy Committee Task Group No. 25. *Med Phys* 1991. doi:10.1118/1.596695.
12. Robatjazi M, Tanha K, Mahdavi SR, Baghani HR, Mirzaei HR, Mousavi M, et al. Monte carlo simulation of electron beams produced by LIAC intraoperative radiation therapy accelerator. *J Biomed Phys Eng* 2018. doi:10.22086/jbpe.v0i0.537.
13. Verhaegen F. Monte Carlo Modeling of External Electron Beams in Radiotherapy. *Monte Carlo Tech. Radiat. Ther.*, 2020. doi:10.1201/b13961-16.
14. Rodrigues A, Sawkey D, Yin FF, Wu Q. A Monte Carlo simulation framework for electron beam dose calculations using Varian phase space files for TrueBeam Linacs. *Med Phys* 2015. doi:10.1118/1.4916896.
15. Cygler JE, Daskalov GM, Chan GH, Ding GX. Evaluation of the first commercial Monte Carlo dose calculation engine for electron beam treatment planning. *Med Phys* 2004. doi:10.1118/1.1633105.
16. Rogers DWO, Walters B, Kawrakow I. BEAMnrc Users Manual. Source 2005.
17. Salvat F, Fern M. PENELOPE – A Code System for Monte Carlo Simulation of Electron and Photon Transport. *Nucl Energy Agency* 2015.
18. Waters LS, McKinney GW, Durkee JW, Fensin ML, Hendricks JS, James MR, et al. The MCNPX Monte Carlo radiation transport code. *AIP Conf. Proc.*, 2007. doi:10.1063/1.2720459.
19. Kawrakow I. Accurate condensed history Monte Carlo simulation of electron transport. I. EGSnrc, the new EGS4 version. *Med Phys* 2000. doi:10.1118/1.598917.
20. Arce P, Bolst D, Bordage MC, Brown JMC, Cirrone P, Cortés-Giraldo MA, et al. Report on G4-Med, a Geant4 benchmarking system for medical physics applications developed by the Geant4 Medical Simulation Benchmarking Group. *Med Phys* 2021. doi:10.1002/mp.14226.
21. Ferrari A, Sala PR, Fassò A, Ranft J. FLUKA: A Multi-Particle Transport Code. 2005.
22. Kozłowska WS, Böhlen TT, Cuccagna C, Ferrari A, Fracchiolla F, Magro G, et al. FLUKA particle therapy tool for Monte Carlo independent calculation of scanned proton and carbon ion beam therapy. *Phys Med Biol* 2019. doi:10.1088/1361-6560/ab02cb.
23. Botta F, Mairani A, Battistoni G, Cremonesi M, Di Dia A, Fassò A, et al. Calculation of electron and isotopes dose point kernels with fluka Monte Carlo code for dosimetry in nuclear medicine therapy. *Med Phys* 2011. doi:10.1118/1.3586038.
24. Sevcik A, Adliene D, Laurikaitiene J, Nedzinskiene R, Masiulyte I. Low energy deposition patterns in irradiated phantom with metal artefacts inside: a comparison between FLUKA Monte Carlo simulation and GafChromic EBT2 film measurements. *Nucl Instruments Methods Phys Res Sect B Beam Interact with Mater Atoms* 2020. doi:10.1016/j.nimb.2020.06.003.
25. Buffard E, Gschwind R, Makovicka L, David C. Monte Carlo calculations of the impact of a hip prosthesis on the dose distribution. *Nucl Instruments Methods Phys Res Sect B Beam Interact with Mater Atoms* 2006. doi:10.1016/j.nimb.2006.05.031.
26. Hasani M, Mohammadi K, Ghorbani M, Gholami S, Knaup C. A Monte Carlo evaluation of dose distribution of commercial treatment planning systems in heterogeneous media. *J Cancer Res Ther* 2019. doi:10.4103/jcrt.JCRT\_1210\_16.
27. Baldock C, De Deene Y, Doran S, Ibbott G, Jirasek A, Lepage M, et al. Polymer gel dosimetry. *Phys Med Biol* 2010. doi:10.1088/0031-9155/55/5/R01.
28. Marrale M, d'Errico F. Hydrogels for Three-Dimensional Ionizing-Radiation Dosimetry. *Gels* 2021. doi:10.3390/gels7020074.
29. Adlienė D, Jaselskė E, Rudžianskas V, Šeperienė N. First approach to ionizing radiation based 3D printing: fabrication of free standing dose gels using high energy gamma photons. *Nucl Instruments Methods Phys Res Sect B Beam Interact with Mater Atoms* 2018. doi:10.1016/j.nimb.2018.01.033.
30. Watanabe Y, Warmington L, Gopishankar N. Three-dimensional radiation dosimetry using polymer gel and solid radiochromic polymer: From basics to clinical applications. *World J Radiol* 2017. doi:10.4329/wjr.v9.i3.112.
31. Ferrari, A. Sala, P.R. Fassò, A. Ranft J. FLUKA: A multi-particle transport code (Program version 2005). *Cern-2005-010* 2005. doi:10.5170/cern-2005-010.
32. Ballarini F, Battistoni G, Campanella M, Carboni M, Cerutti F, Empl A, et al. The FLUKA code: An overview. *J. Phys. Conf. Ser.*, 2006. doi:10.1088/1742-6596/41/1/014.
33. Böhlen TT, Cerutti F, Chin MPW, Fassò A, Ferrari A, Ortega PG, et al. The FLUKA Code: Developments and Challenges for High Energy and Medical Applications 2014. doi:10.1016/j.nds.2014.07.049.
34. Battistoni G, Cerutti F, Chin W, Esposito LS, Fassò A, Ferrari A, et al. Overview of the FLUKA code. *Ann Nucl Energy* 2015;82:10–8. doi:10.1016/j.anucene.2014.11.007.
35. Battistoni G, Cerutti F, Fassò A, Ferrari A, Muraro S, Ranft J, et al. The FLUKA code: Description and benchmarking. *AIP Conf. Proc.*, 2007. doi:10.1063/1.2720455.
36. Ferrari A, Sala PR, Guaraldi R, Padoani F. An improved multiple scattering model for charged particle transport. *Nucl Inst Methods Phys Res B* 1992;71:412–26. doi:10.1016/0168-583X(92)95359-Y.
37. Vlachoudis V. Flair: A powerful but user friendly graphical interface for FLUKA. *Am. Nucl. Soc. - Int. Conf. Math. Comput. Methods React. Phys.* 2009, M C 2009, 2009.
38. Berger MJ, Coursey JS, Zucker MA, Chang J. Stopping-Power and Range Tables for Electrons, Protons, and Helium Ions | NIST. *NIST Stand Ref Database* 124 1998.



## **TLD-100 RESPONSE DEPENDENCE ON VARIOUS FACTORS**

Lijana LILEIKYTĖ, Benas Gabrielis URBONAVIČIUS  
Department of Physics, Kaunas University of Technology  
<sup>1</sup>lijana.lileikyte@ktu.edu

**Abstract:** One of the most mature technologies for dose monitoring is the Thermoluminescent Dosimeters. To be able to use Thermoluminescent Dosimeters (TLDs) for high accuracy measurements, evaluation of their sensitivity in different radiation fields is pertinent. Comprehensive studies on the effects of various influencing factors on TLDs are sparse, thus in this work the dependencies of the Dose Coefficient (C) and Element Correction Coefficient (ECC) on the calibration dose, irradiation angle and dose rate were analyzed. Dosimetric response fading over time was also evaluated.

**Keywords:** Thermoluminescence dosimetry, Element Correction Coefficient, irradiation angle, dose rate, fading.

### **1. Introduction**

Most commonly used thermoluminescent material for dose monitoring is lithium fluoride (LiF) crystals. An example of such dosimeters can be TLD-100, where LiF crystals with titanium and magnesium impurities are used as the sensitive material. LiF is suitable for recording absorbed doses of biological tissue due to it is atomic number  $Z_{\text{LiF}} = 8.2$ , which is near to the average atomic number of biological tissues  $L_{\text{tissues}} = 7.4$  [1]. TLDs can be used for patient in-vivo dosimetry, for example during mammography procedures [2], or for radiotherapy procedures to assure the quality of the treatment. One of such studies was presented in European Medical and Biological Engineering Conference (2017). TLD-100 were used for in vivo dosimetry during a Total Body Irradiation (TBI) for the development of a calculation method to find the doses deposited on the medium of the Dose Area Product (DAP) in various regions of a patient's body [3]. The Imaging and Radiation Oncology Core QA Center in Houston (IROC-H) performs remote dosimetry audits of megavoltage photon and electron beams each year. Both (TLD-100) and optically stimulated luminescent dosimeter (OSLD) system are commissioned for this task. For example, with measurements with TLD, the measurement apparatus includes 3 TLD in an acrylic mini phantom, which are

irradiated by the institution under reference geometry. Dosimetry systems are calibrated based on the signal-to-dose conversion established with reference dosimeters irradiated in a Co-60 beam, using a reference dose of 300 cGy for TLD. This program reports the ratio of the dose detected to the dose reported by the institution. For more than 16,000 TLD results, the average ratio for TLD at the point of dose verification is  $1.000 \pm 1.9 \%$  [4].

Albeit a powerful dosimetric method, several influencing factors must be considered, when using TLDs, such as irradiation angle, dose rate, fading, to name a few. As an example – dose rate should not influence the dosimetric response, but practically it is considered to be not an influencing factor only in a specific dose rate range [5]. Dose rate effects are under investigation to this day. Two unusually long, high temperature anneals at 400°C/2h were applied both - before irradiation and after readout. Selected dose rate range was extremely high, and results showed that TLDs are dose rate independent up to  $4 \cdot 10^9$  Gy/s [6]. Kinetic calculations have predicted the likelihood of dose rate effects based on competition between excitation and trapping rates in TL materials [7]. A definitive conclusion is yet to be drawn, regarding the dose rate affects in specific applications.

Response of TL dosimeters also depends on the angle of incidence of the radiation into the plane of the dosimeter. A set of experiments was performed to investigate the angular and energy dependence of TLDs, intended to be used for in vivo skin dosimetry in dental CBCT. The results showed that, there is no need to apply correction coefficients as the gantry rotates around the patient. However, for higher angles up to 90° a decrease in the response is seen which may necessitate the introduction of specific conversion coefficients. Photon's energy in this study was 80–110 keV [8]. Another study, to determine TLD angular dependence, was performed on 20 cm solid water phantom. The beam field size was adjusted to 10 cm x 10 cm on the phantom surface at 100 cm SSD. The detector was irradiated with 100 MUs and 300 MUs/min at 0°, 25°, 50°, 75°, 285°, 310° and 335° of beam incidence. Result of angular dependence for each detector was compared as a relative surface dose against gantry rotation. Results showed that the incidence

of beam entry angle on the phantom surface has a significant effect on surface dose. The more oblique the beam angle the higher the surface dose. This is due to increase of surface dose deposition by the electrons contamination when the photons striking the beam modifier and also electrons produced from backscattered radiation when photons interact in the phantom. Therefore, application of angular correction factor is recommended [9].

Most common application of TL dosimeters is personnel dosimetry. Regulations require that workers that are exposed to ionizing radiation wear dosimeters so that accumulated doses can be monitored over a preset period. However, irradiated TL dosimeters do not permanently retain 100 % of their trapped charge carriers. This results in a gradual loss of the latent TLD signal with time, which is called fading. Ideally detector should show no fading at room temperature, but practically insignificant fading is considered to be good stability [5]. In one of the studies [10] fading of dosimeters as a function of time was studied. 12 units of TLD-100 dosimeters were irradiated with a 14 mGy dose, and they were stored at a temperature of 20°C. Readings were taken at the post-irradiation time: 3 h, 24 h, 48 h, 120 h, 168 h, 288 h, 720 h. It was observed that the first peak had a higher fading, completely disappearing at the 288 h for the TLD-100. By analyzing the relative intensities, the dosimeters showed a 11 % fading for a period of 3 hours to 48 hours, after this the fading was 15 % between 48 h and 720 h. It was also observed that a non-first order TL glow peak shifts to higher temperatures with decreasing the population of trapping states. In another study [5], the TLD-100 dosimeters were irradiated with a dose of 2 Gy and were studied at different post annealing times for fading. It was seen a decrease in fading with increasing post annealing time. TLDs were irradiated at post annealing time of 24 hours with different doses also. There was no trend of increase or decrease in fading with increasing dose delivered. The average fading after 72 hours for all doses was 20.46 %.

As can be seen – various influencing factors and conditions affects the final dosimetric response of the TL dosimeters. Research regarding these factors are fragmented and does represent only a select range of conditions, which in most cases are beyond the range of possible dose ranges in the external beam radiotherapy. Further described experiments are considering the influencing factors for TLDs in the dose range of external beam radiotherapy.

## 2. Materials and methods

To evaluate the influencing factors of TLDs in the use case of external beam radiotherapy a series of experiments was performed. Selected factors were:

1. Dose Coefficient (C) (sensitivity) dependency on irradiation dose
2. Fading of the dosimetric response over time
3. Dosimetric response angular dependency
4. Dosimetric response dose rate dependency

## 2.1. Equipment and methods

All TL dosimeters were calibrated with linear accelerator Varian Clinac DMX (photon's energy – 6 MeV).

Dimensions of used thermoluminescent dosimeters TLD-100 tablets: diameter ~ 4.50 mm, thickness – 2 mm.

### 2.1.1. Dose Coefficient dependency on irradiation dose

For this evaluation 400 units of TLD-100 were used. 40 dosimeters were assigned to each experimental point (Table 1). Dose rate was 1 Gy/min. Obtained results were also used in the fading effect experiments.

**Table 1.** Experimental groups

Group of higher doses, Gy	Group of smaller doses, Gy
0.5	1
0.6	2
0.7	3
0.8	4
0.9	5

### 2.1.2. Fading of the dosimetric response over time

Dosimetric response fading experiments involved another 100 units of TLD-100 were used. Dosimeters were irradiated together with the Dose coefficient experiment dosimeters, so as to form a baseline values.

Fading was measured twice: after 175 days (5 months and 24 days), and after 270 days (8 months and 27 days) from the day when dosimeters of the first task were read out (baseline values). 5 dosimeters were assigned to each experimental point (Table 1).

### 2.1.3. Dosimetric response angular dependency

For the dosimetric response angular dependency experiments, dosimeters were irradiated at different irradiation angles – 30°, 60°, 85° and 90°. 40 dosimeters were assigned to each experimental point. Calibration dose was 3 Gy and dose rate – 1 Gy/min.

### 2.1.3. Dosimetric response dose rate dependency

For the dose rate effect on dosimetric response, dosimeters were irradiated with different dose rates – 1 Gy/min, 2 Gy/min and 3 Gy/min. 120 units of TLD-100 were used, and 40 dosimeters were assigned to each experimental point. Irradiation dose was 1 Gy.

## 2.2. Dosimeter Read-out Procedure

Rialto thermoluminescent dosimeter reader was used to prepare and read the dosimeters. Rialto TLD scanner uses a step heating cycle [11]. The readout cycle of the dosimeters TLD-100 used in the experiment consists of three main parts:

1. Pre-heat. 10 seconds @ 160°C
2. Readout. 12 seconds @ 300°C
3. Anneal. 40 seconds @ 300°C

An in-house developed software was used for further dosimetric data processing and storage.

### 2.3. Calibration procedure

Thermoluminescent dosimeter does not provide the absolute value of absorbed dose, thus requires calibration. Technical calibration is performed by irradiating a group of TLDs with a known dose and then reading them out. Dose coefficient then can be determined, which can be considered to be a representation of the efficiency (sensitivity) of an individual (or a group) dosimeter. The equation of the dose coefficient  $C$ , which relates the dosimeter response and the calibration dose [1]:

$$C = \frac{\langle TL \rangle}{D} \quad (1)$$

where  $C$  is the dose coefficient;  $\langle TL \rangle$  – average dosimetric response of the calibrated group (or the value of dosimetric response in the case of individual TLD analysis);  $D$  is the absorbed dose used for calibration.

As the efficiency (sensitivity) of individual dosimeters differs, the Element Correction Coefficient ECC is used, which is expressed as the ratio of the mean signal strength  $\langle TL \rangle$  of the calibrated group to the signal strength  $TL_i$  of the individual selected dosimeter [1]:

$$ECC = \frac{\langle TL \rangle}{TL_i} \quad (2)$$

ECCs are then stored with assignments to specific dosimeters, until next calibration is performed.

## 3. Results and Discussion

### 3.1. Dose Coefficient dependency on irradiation dose

After irradiation and readout of the dosimeters, dose coefficients were calculated and the dose coefficient versus calibration dose graph, after  $2\sigma$  rule application with confidence intervals  $\mu \pm \sigma$ , was plotted. Figure 1 shows almost consistent sensitivity in the dose range  $<1.0$  Gy with a maximum variation of 10 %, which is within expected uncertainty levels.

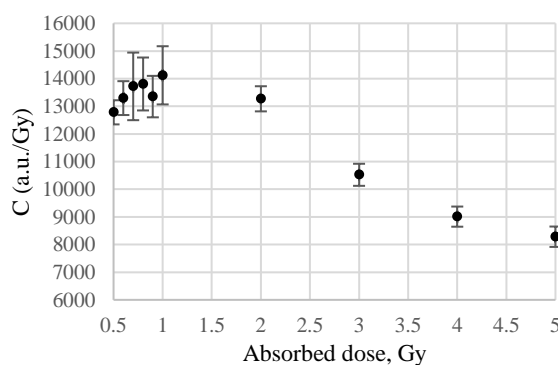


Fig. 1. Dose coefficient versus calibration dose

In higher dose range ( $>1.0$  Gy) the sensitivity decreases almost twofold with increasing dose in the interval 1–5 Gy. Important to note when using such dosimeters in i.e. external beam radiotherapy. It can be recommended to use a center point of measured range of 3 Gy for further dosimeter use in the range of [1-5 Gy].

### 3.2. Fading

Results of fading of the dosimetric response over time are given in Table 2. It can be seen that fading results does not depend on absorbed dose. Also, fading of the response after 175 days and 270 days do not differ significant, even fading results between 175 and 270 days, when absorbed dose was 0.5 Gy, 0.7 Gy and 4 Gy, are negative.

Table 2. Results of fading

Absorbed dose, Gy	Fading after 175 days, %	Fading after 270 days, %	Fading between 175-270 days, %
0.5	18.6	18.3	-0.3
0.6	22.4	24.4	2.5
0.7	27.7	25.7	-2.8
0.8	13.3	24.2	12.5
0.9	16.3	22.9	7.9
1	16.0	16.4	0.5
2	30.4	33.6	4.6
3	24.5	35.0	14.0
4	25.5	10.4	-20.2
5	18.9	19.8	1.0

### 3.3. Dosimetric response angular dependency

ECC and dose coefficient versus irradiation angle graphs, after  $2\sigma$  rule application with confidence intervals  $\mu \pm \sigma$ , were plotted. After  $2\sigma$  rule application, from measurements with irradiation angles  $90^\circ$ ,  $85^\circ$ ,  $60^\circ$ ,  $30^\circ$ , only 32, 33, 30, 35 units of TLDs were analyzed respectively.

From Figure 2 can be seen that if the energy of the photons is relatively high (6 MeV), the energy that is deposited in TLDs does not depend on irradiation angle as it is in diagnostic energy range [8]. In all measurement points maximum variation of the ECC does not exceed 5% and is consistent across measured angle range, with only  $90^\circ$  irradiation angle ECC reaching 7 % variation.

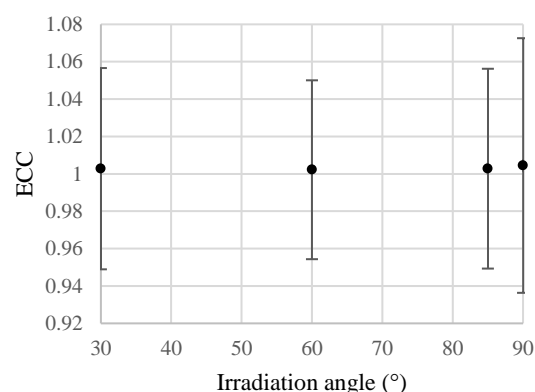
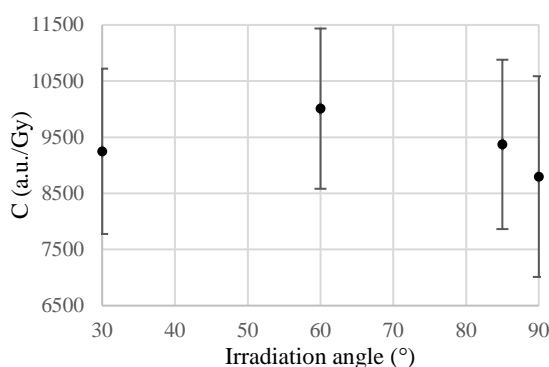


Fig. 2. ECC dependence on irradiation angle

Additionally, for a more detailed analysis, dose coefficient (sensitivity) vs irradiation angle dependency was evaluated.



**Fig. 3.** Dose coefficient dependence on irradiation angle

Figure 3 presents dose coefficient dependence on irradiation angle. At 60 degrees can be seen slightly higher response but it is not statistically significant.

### 3.4. Dosimetric response dose rate dependency

ECC and dose coefficient versus dose rate graphs, after  $2\sigma$  rule application with confidence intervals  $\mu \pm \sigma$ , were plotted. After  $2\sigma$  rule application, from measurements with dose rates 1 Gy/min, 2 Gy/min, 3 Gy/min – 36, 31, 40 units of TLDs were analyzed further respectively. Only from experimental group with dose rate 3 Gy/min none of dosimeters were rejected.

As in the previous set of experiments, after  $2\sigma$  rule application, no significant ECC variation dependence on dose rate can be seen.

TLD response dependence on dose rate can be seen from Figure 4. After  $2\sigma$  rule application, the highest response is seen with dose rate 2 Gy/min. These results are statistically significant and showed that TLDs sensitivity slightly increases with increase of dose rate. The lowest response is with dose rate 1 Gy/min.

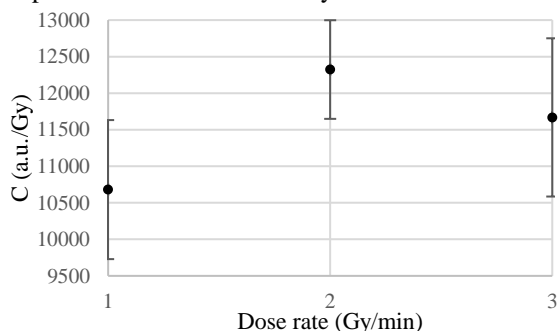


**Fig. 4.** Dose coefficient dependence on dose rate

Recombination processes can be one of the factors that affected these results due to longer irradiation, but still requires further investigation in real-world conditions.

## 4. Conclusions

It was shown that various practical influencing factors are at play when using TLDs in external beam radiotherapy irradiation field.

The sensitivity of dosimeters decreases almost twofold with increasing dose in 1-5 Gy range.

With 6 MeV beams dosimetric response angular dependency is statistically insignificant, thus there is no

need to apply correction coefficients as the irradiation angle changes.

From measurements with dose rates 1, 2, 3 Gy/min, results showed no significant ECC variation dependence on dose rate.

Sensitivity of the used TLD-100 dosimeters is dependent on the irradiation dose rate, being highest at 2 Gy/min, and lowest at 1 Gy/min. This requires further testing to determine the underlying cause.

## References

1. Savva A. Personnel TLD monitors, their calibration and response. Dissertation submitted to the Department of Physics, University of Surrey, [online], 2010.
2. Warren-forward H. M., Duggan L. Towards in vivo TLD dosimetry in mammography. The British Journal of Radiology, 2004.
3. Nolasco A. V., Faria L. O. The use of the TLD-100 for quality assurance in Total Body Irradiation (TBI). In: EMBEC & NBC 2017. Springer, Singapore, 2017. p. 434-437.
4. ALVAREZ, P., et al. TLD and OSLD dosimetry systems for remote audits of radiotherapy external beam calibration. Radiation measurements, 2017, 106: 412-415.
5. Kamil M. U. Effect of Post Annealing Time and Radiation Doses on Fading and Glow Curve Characteristics of Topaz and TLD-100. 2011
6. Adlienė, Diana; Jakštas, Karolis; Urbonavičius, Benas Gabrielis. In vivo TLD dose measurements in catheter-based high-dose-rate brachytherapy // Radiation protection dosimetry. Oxford : Oxford University Press. ISSN 0144-8420. eISSN 1742-3406. 2015, vol. 165, iss. 1-4, p. 477-481. DOI: 10.1093/rpd/ncv054.
7. Karsch L., et al. Dose rate dependence for different dosimeters and detectors: TLD, OSL, EBT films, and diamond detectors. Medical physics, 2012, 39.5: 2447-2455.
8. Adliene, D.; Gričienė, B.; Skovorodko, K.; Laurikaitienė, J.; Puiso, J. Occupational radiation exposure of health professionals and cancer risk assessment for Lithuanian nuclear medicine workers // Environmental research. San Diego, CA : Elsevier. ISSN 0013-9351. eISSN 1096-0953. 2020, vol. 183, art. no. 109144, p. 1-10. DOI: 10.1016/j.envres.2020.109144.
9. Chen R., McKeever S.W.S., Durrani S.A., Solution of the kinetic equations governing trap filling. Consequences concerning dose dependence and dose-rate effects, Phys. Rev. B 24, 1981, 4931-4944.
10. Stratis A., et al. Energy and angular dependence of thermoluminescent detectors in the dental CBCT energy range. Physica Medica: European Journal of Medical Physics, 2014, 30: e95.
11. ABDULLAH, Norhayati, et al. Assessment of surface dose on the ART phantom using three-dimensional conformal breast radiotherapy. J Sains Nucl Malaysia, 2015, 27: 21-8.
12. Fernandez S. D. S., et al. Thermoluminescent characteristics of LiF: Mg, Cu, P and CaSO<sub>4</sub>: Dy for low dose measurement. Applied Radiation and Isotopes, 2016, 111: 50-55.
13. NE Technology. User's Guide to the Rialto TLD Radiotherapy Package. Beenham: NE – Press, 1992.

## **METALLIC ARTIFACTS AND THEIR REDUCTION IN NUCLEAR MAGNETIC RESONANCE IMAGING (AN OVERVIEW)**

Mantas BRUKŠTUS<sup>1</sup>, Diana ADLIENĖ<sup>2</sup>

<sup>1,2</sup>Kaunas University of Technology, faculty of mathematics and natural sciences

<sup>1</sup>mantas.brukstus@ktu.edu; <sup>2</sup>diana.adliene@ktu.lt

**Abstract:** Magnetic resonance imaging (MRI) is a sophisticated diagnostic technology that is utilized in both medicine and dentistry. It is superior to ionizing radiation imaging approaches as it is based on a strong uniform static magnetic field and radiofrequency pulses. Unfortunately, the magnetic field and radiofrequency pulses generated by the magnetic resonance imager interact negatively with metallic implants. As a result, negative effect such as artifact creation occur which leads to uninterpretable MRI images in specific areas of interest. In order to reduce the impact of metallic implants View-Angle Tilting, Multi-Acquisition Variable Resonance Image Combination and Slice Encoding for Metal Artifact Correction artifact reduction techniques were used in conjunction with 8 channel knee coil and in depth analysis of methods was performed.

**Keywords:** Magnetic Resonance Imaging, artifacts, VAT, MAVRIC, SEMAC.

### **1. Introduction**

Magnetic resonance imaging (MRI) is widely used for clinical analysis and evaluation in all clinical fields. However, the presence of metallic objects could possibly render magnetic resonance imaging either unsafe or greatly limit its diagnostic utility. This presents an incredible clinical challenge as there are there a lot of patients with metallic implants which are exactly the population who may need imaging evaluation. For example, over 300,000 spinal fusions were performed in 2007, with failure in as many as 30–40% of subjects. In 2005, there have been 80,000 revision surgeries for total knee and total hip replacements. Metallic implants also are used in surgical reconstruction procedures, wherever patients might need follow-up imaging [1]. In addition, there are a lot of other smaller metallic devices or implants which vary from simple surgical clips to fixation screws or surgical pins that will inevitably complicate imaging techniques. It is very important to note that a lot of implanted

devices are unsafe for MRI. First, ferromagnetic objects will experience robust forces that originate from the static magnetic field. The forces are strongest in regions closest to the magnet where the field strength varies rapidly over a small distance. Unfortunately, the distance over which forces can change from negligible to strong enough to project an object are often small, tens of centimeters [6]. Second, some implants can cause heating because of their interaction with radiofrequency fields. In depth research has characterized MRI safety, and in some cases improved ability to detect unsafe inclusions in human's body, however no current solutions were found that can impact the magnetic resonance imaging safety of ferromagnetic objects that may experience strong magnetic forces, or implants that may cause heating. Although various metals are deemed MRI safe, they will still considerably impede imaging for many reasons. First, fundamentally, no MRI signal can be generated in metals, therefore metal appears dark on MR images. Second, the presence of metal may result in severe variations within the static magnetic field because of the susceptibility variations between metal and surrounding tissue. These field variations depend on the size, form and kind of metal, as well as its orientation within the magnetic field [1, 6].

### **2. Materials and methods**

Experiments were performed on a GE Signa Explorer 1.5 T and GE optima MR360 1.5 T MRI scanners using 8 channel knee coil with MAVRIC and SEMAC software included. Depersonalized patient data was used in this investigation.

### **3. Inhomogeneity of the magnetic field**

Various forces have an effect on the local magnetic field and generate magnetic resonance imaging artifacts. In general, these forces are separated into diamagnetic, paramagnetic, and ferromagnetic. Objects or substances with diamagnetic properties exhibit no intrinsic magnetic moment. Diamagnetism exerts a small

repulsive effect on the local magnetic field. Materials such as soft tissue, water and copper, demonstrate diamagnetism. On a gross scale, the patient's body can be thought of as a large diamagnetic interferent. Paramagnetism features a comparatively small attractive effect on the local magnetic field, and paramagnetic substances have a positive magnetic moment. Materials such as iron ions (eg, hemoglobin breakdown products), oxygen, magnesium, and gadolinium have paramagnetic effects. This is often the primary effect applied with gadolinium-based contrast agents which are used for enhanced imaging quality in MRI diagnostics. Ferromagnetic substances demonstrate a positive magnetic moment, but, in contrast to paramagnetic and diamagnetic materials, they have an incredibly strong positive (attractive) magnetic susceptibility. Examples would include cast-iron and iron alloys (eg, stainless steel), cobalt, and nickel. Ferromagnetic effects are the primary drivers of metal-related artifacts at magnetic resonance imaging [4, 7].

Magnetic field inhomogeneity ( $\psi$ ) can be estimated from the susceptibility distribution ( $\chi$ ) (Eq.1) which shows that the magnitude of ferromagnetic susceptibility is increasing in a very linear relationship with  $B_0$ .

$$\psi(\mathbf{k}) = \frac{\gamma}{2\pi} B_0 \left( \frac{1}{3} - \frac{k_z^2}{kH_k} \right) \hat{\chi}(\mathbf{k}) \quad (1)$$

where  $\gamma/2\pi$  is the gyromagnetic ratio,  $B_0$  is the main magnetic field strength (T),  $\mathbf{k} = [k_x, k_y, k_z]$  denotes the k-space coordinate,  $H$  represents the Hermitian transpose operation, and tilde represents a variable that has undergone three-dimensional Fourier transform. The z-axis is assumed parallel with the bore of the MRI scanner, per usual convention [3].

This indicates that the general degree of artifact will be considerably lower at 1.5 T than at 3.0 T. The improved signal and image quality afforded by a brand new 3.0 T magnet might produce images with so many metallic artifact that the examination will have zero clinical value [3, 7].

#### 4. Imaging mechanisms

Magnetic resonance imaging is enabled by polarizing nuclear spins in a static magnetic field. At macroscopic level, the nuclear spins are collectively referred to as magnetization. The magnetization will be excited, or actively rotated away from the direction of the static magnetic field which is pointing in a transverse direction by a radiofrequency magnetic field. The transverse magnetization then precesses or resonates around the direction of the static field magnetic field, which may generate a radiofrequency signal in a receive coil. The utilization of gradient fields can modify the precession rate as a function of position in an arbitrary direction, which allows image formation in various scan orientations. Most magnetic resonance imaging ways include exciting the magnetization in slices, and forming two dimensional images of every slice. Excitation is achieved by using a slice select gradient that imposes a variation of precession rate (or resonance frequency) in the slice direction (Fig. 1a). Next, a

radiofrequency magnetic field is generated, with a limited bandwidth around the central frequency that is chosen to excite magnetization at a specific position. In magnetic resonance imaging, after the spins within the slice have been excited, the excitation gradient is turned off, and therefore the variation of precession rate within the slice direction is removed [1, 8, 9].

To form two dimensional images, a gradient field may be turned on in a direction inside the plane of the slice, causing a variation of the precession rate (Fig. 1b). The received signal is acquired during this time. The individual frequencies will be assigned to specific image locations using a method referred to as a Fourier transform, with the amplitude of each frequency which corresponds to the strength of the magnetization at a selected position. [1, 8, 9].

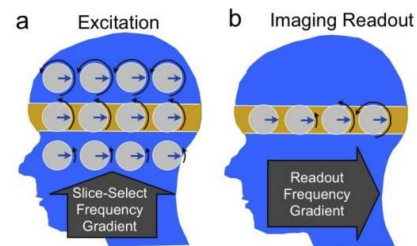


**Fig. 1** Magnetization dynamics throughout slice selection (a) and imaging readout (b). The magnetization precession rate or frequency is indicated by black arrows showing completely different amounts of rotation [1].

#### 5. Image artifacts near metallic implants

The most prominent image artifacts that occur with imaging close to metal arise from the inhomogeneous static magnetic field that causes unpredictable variations within the precession rate across the object. The predominant artifacts that arise in imaging are signal loss thanks to dephasing, failure of fat suppression, and displacement artifacts. Displacement artifacts occur in the slice selection and readout directions and include geometric distortion, signal loss, and signal pile-up. Imaging near metal objects, the magnetic field variations are often very rapid, such that the magnetization inside one imaged voxel precesses at varying rates. This results in dephasing or loss of coherence and signal loss. In images, this manifests as a black area during which there would otherwise be signal. Fortunately, dephasing impacts are often almost entirely avoided by the utilization of spin-echo imaging. Aside from the distortion and dephasing artifacts, an important detrimental effect of imaging near metal is failure of fat suppression. The most common technique of fat suppression is to use chemically selective saturation, often referred to as fat saturation (fat SAT). This method by selection excites fat, exploiting the actual fact that the fat resonance is 220 Hz below that of water at 1.5 T. The frequency shifts close to metallic implants can vary from about 3 to 80 kHz. This will cause massive changes within the fat resonance, easily enough to cause complete failure of fat saturation as a result the saturation pulse completely misses the resonant frequency of fat near metal. Applying the method of selectively exciting a two dimensional slice in magnetic resonance imaging a radiofrequency



magnetic field of finite bandwidth in the presence of a gradient field is used. Because the gradient maps position to resonant frequency, the slice position is decided by constant alteration of the frequency of the radiofrequency field. Variations within the static magnetic field cause an error in the position that is selected. The error can cause a shift in the excited slice, or a curving or “potato-chip” effect. It may also cause the slice to be thicker or thinner than desired and might even lead to splitting of the slice into multiple regions. The general result is that the specified region differs from what was desired, and therefore, the specified slice position no longer represents the position of the image. Although little shifts or curving of the slice might not be noticeable, the thinning and thickening result in clear signal loss or pile-up effect (Fig. 2). Using the radio-tuning analogy, the presence of the metal effectively causes some radio stations to transmit at the incorrect frequency, in order that when you tune to a location you will miss the station you are seeking, hear the wrong station, or hear multiple stations that are being transmitted on identical channel. During image acquisition within the frequency encoding direction, a gradient field is generated to map the position to particular precession rates of the magnetization. The reconstruction inverts this process by localizing and identifying the tones within the signal, with every tone corresponding to a location. However, variations in the static magnetic field cause shifts in these tones, which once more will lead to an error in determining the position from which the signal originates. Like slice distortion, the variations may end up in bulk shifts that may distort the image or, in more extreme cases, signal loss or pile-up effects when the signal is shifted away from a position or when signal from multiple positions is shifted to at least one position. The frequency-encode-direction and slice-direction artifacts are troublesome to separate because both lead to geometric distortion, signal loss, and signal pile-up effects [1, 10].

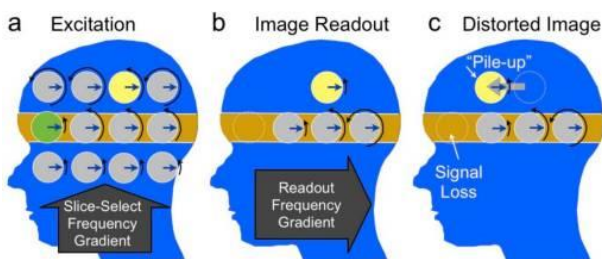


**Fig. 2** The effect of an offset of the resonance frequency or “off-resonance” on slice selection (a); imaging readout (b) and distorted image (c) [1].

## 6. Methods of artifact reduction

In-plane and through-plane artifacts due to displacement include geometric distortion and in more serious cases, signal loss and pile-up artifacts. While optimizing bandwidth is helpful in all situations, there are other options that can further increase image quality. Displacements due to off-resonance are quite predictable if the frequency error is known. In cases with a reasonably smooth frequency error, the geometric distortion can be partially corrected. The primary

assumption of the model is that frequency offset can be resolved by image resolution or in a particular perspective, that one frequency offset is representative for each voxel. The essence of this method is calculation of the frequency offset using field mapping techniques, usually based on multiple echo times. Using this method the image can be distorted in the reconstruction process in order to correct the geometric distortions arising from the frequency offsets [1, 4].

### 6.1. View angle-tilting (VAT)

In a situation where in-plane distortions must be corrected, a method called view-angle tilting (VAT) can be very powerful. VAT takes advantage of the fact that both the slice displacement and in-plane displacement due to off-resonance are well known and have a constant ratio. During the readout, VAT replays the slice-selection gradient that shears the image. As a final result in-plane displacements are canceled exactly so that in-plane displacements are omitted (Fig. 3). However, VAT does not correct the distortion of the slice.

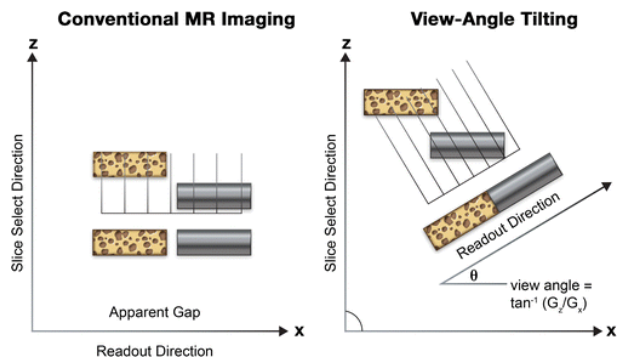


**Fig. 3.** Comparison of image formation in conventional imaging mode with the VAT. (Implementation of VAT mode minimizes in-plane distortions by adding an altered readout gradient, considering the angle  $\theta$ , whereas  $G_x$  = reading gradient,  $G_z$  = concentration gradient,  $\tan$  = tangent) [4]

The alternative view of VAT is based on the fact that the RF excites a certain bandwidth. By replaying the slice selecting gradient, the off-resonance is limited to the RF bandwidth and the in-plane distortion is almost eliminated. However application of VAT is related to the readout length, which is limited by RF excitation (may cause image blurring). This limits the resolution of the SNR or spatial resolution that can be achieved. In order to prevent blurring effect and eliminate residual artifacts from the voxel tilting a high bandwidth readout should be applied when using VAT. The later can be accomplished by spectral-spatial excitation, which excites both a limited and a limited frequency band. As the frequency range is small, this restricts the in-plane artifact. Applying this method the excitation must be performed for different frequencies, which cost scanning time [1, 4, 11].

### 6.2. Multi-acquisition variable resonance image combination (MAVRIC)

Multi-Acquisition Variable Resonance Image Combination (MAVRIC) is a technique used for resolving both in-plane and through-slice displacement

artifacts. MAVRIC uses frequency-selective excitation to cap the range of frequency offsets imaged at one time. This is accompanied by the regular 3D image readout, using a spin echo train. While the frequency range is limited, the in-plane displacement is often limited to about a pixel in this case. MAVRIC avoids the displacement of slice-direction by using phase encoding to resolve them in this direction. The 3D images are replicated for a number of frequencies and are grouped together, usually using a sum-of-squares operation. The merged images have a reduced artifact and provide a signal from a wide array of near-metal frequency offsets. The fundamental concepts of physics behind MAVRIC can be seen in Fig. 4. The key trade-offs for using this method are increased imaging time and increased specific absorption rate (SAR). MAVRIC is more effective at 1.0 T or 1.5 T than 3.0 T or more due to SAR requirements [4, 5, 12, 13].

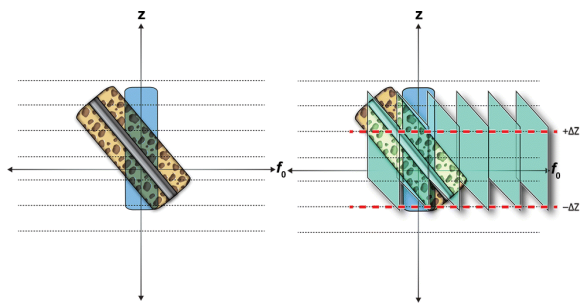


**Fig. 4.** The concept of physics behind MAVRIC[4]: to the left - graphical depiction of a model with a bone (speculated) and a central metal rod (gray) which corresponds to a metallic implant, to the right - depiction of three-dimensional fast spin-echo imaging technique which is used to achieve a range of excited frequencies around the region of interest.

The measurement of SAR in humans is very complicated (and imprecise), involving sophisticated mathematical modelling and computer simulation. Most of commercially available MR scanners have programs that automatically predict SAR values when a particular imaging protocol is chosen and warn the operator if regulatory limits are likely to be surpassed. Radiofrequency injury to patients is the product of increased temperatures in the tissues, not the SAR itself. As a rough estimate, a SAR of 1 W/kg will increase the temperature of the insulated tissue slab by around 1 °C per hour. In addition, some organs (such as the eye and the testis) are highly susceptible to heat-induced damage, while others are not [14, 15].

### 6.3. Slice Encoding for Metal Artifact Correction (SEMAC)

Just like MAVRIC the SEMAC technique corrects metal objects by effective encoding of each excited slice against metal-induced field inhomogeneities. SEMAC has the ability to fix in-plane and through-slice artifacts. Robust slice encoding is accomplished by enhancing the view-angle tilting (VAT) spin-echo (SE) series with additional z-phase encoding (**Fig. 5**). Although the VAT correction gradient suppresses most in-plane distortions,

the z-phase encoding completely resolves distorted excitation profiles that induce through-plane distortions.

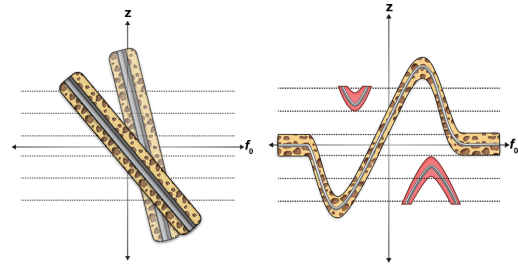


**Fig. 5.** Excitation process (left); Section distortion (right) [4]

By positioning all spins in an area of interest to their actual spatial positions, the through-plane distortions can be resolved by summing up the fixed spins in each voxel (Fig. 8 and 9). The SEMAC method does not need additional hardware and can be implemented on a large base of full-body MRI systems. The effectiveness of the SEMAC technique in the reduction of metal-induced distortions with reasonable scanning times [1, 3, 4, 5, 10].

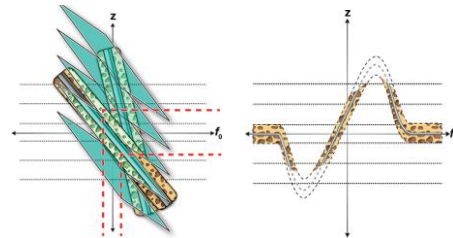


**Fig. 6.** Profile resolution (left); Reconstruction (right)[4]

### 6.3. MAVRIC-SEMAC Hybrid

In certain ways, MAVRIC and SEMAC are very similar. Both are using multiple excitations to excite the overall volume being imaged, and both use 3D spin echo acquisition to overcome the through-plane distortion. In both cases, the residual distortion in the readout direction is pretty much the same, within about a pixel. A hybrid approach has been developed that combines beneficial features of both SEMAC and MAVRIC imaging techniques. SEMAC's slab selectivity was blended with MAVRIC's smooth bin combination and higher spectral SNR technique. Hybrid method typically acquires images with acquisition times ranging roughly from 7 to 12 minutes [1, 5, 16].

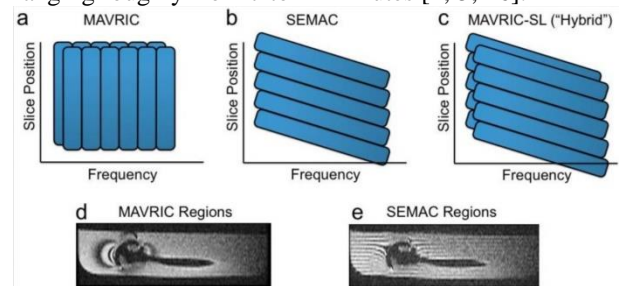


**Fig. 7.** Excited regions: (a) MAVRIC and (b) SEMAC and (c) MAVRIC-SL (Hybrid) [1]

## 7. Results

The comparison of different methods used for metal artifacts suppression in MRI is provided in Table 1 as well as an example of their usage in subjects with complete knee arthroplasty is shown in Fig.8.

**Table 1.** Comparison of effectiveness of VAT, MAVRIC, SEMAC and MAVRIC-SEMAC hybrid methods [1,4, 5]

Method	Advantages	Disadvantages
VAT	<ul style="list-style-type: none"> <li>- Is integrated in almost every diagnostic MRI;</li> <li>- Scans are completed in less than 5 min;</li> <li>- Cancels in-plane displacements at the cost of slightly tilted images.</li> </ul>	<ul style="list-style-type: none"> <li>- Unable to fix through-plane slice distortions, therefore signal pile-up's may occur near metallic implants;</li> <li>- Produces blurring.</li> </ul>
MAVRIC	<ul style="list-style-type: none"> <li>- Excited limited frequency bands;</li> <li>- Using phase encoding avoids slice-direction displacements;</li> <li>- Minimal artifacts, includes signals from offsets near metal.</li> </ul>	<ul style="list-style-type: none"> <li>- Generates a lot of heat (SAR) in metallic implant, which leads to probability of scan inhibition;</li> <li>- Scanning time increases drastically if higher quality is desired &lt;10 min</li> </ul>
SEMAC	<ul style="list-style-type: none"> <li>-Excites limited spatial bands;</li> <li>- Metallic implants can be seen almost clearly without distortion or pile-up artifacts.</li> </ul>	<ul style="list-style-type: none"> <li>- Scanning time varies from 5 to 10min;</li> <li>- Might create “potato-chip” artifact on soft tissues at the cost of better visualisation on prosthesis or implant.</li> </ul>
MAVRIC-SEMAC hybrid	<ul style="list-style-type: none"> <li>-Spatially selective excitation combined with overlapped regions;</li> <li>- Perfectly visible metallic implants and no distortion in surrounding tissues.</li> </ul>	<ul style="list-style-type: none"> <li>- Generates less heat than MAVRIC;</li> <li>- Scanning time is around 10 min</li> </ul>

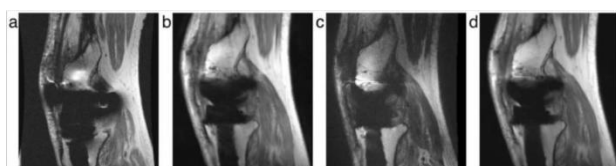


**Fig. 5.** Example images using (a) VAT, (b) SEMAC, (c) MAVRIC and (d) MAVRIC-SEMAC-hybrid technique in subjects with complete knee arthroplasty.

## 8. Conclusions

Characterization of metallic implant by its own susceptibility indicates that the larger susceptibility value and strength of applied magnetic field will cause larger magnetic field inhomogeneity and will create more artifacts when the object is scanned in MRI facility.

Currently used methods for metal artifact reduction are known by their efficacy, e.g. the mostly used (standard) View-angle tilting (VAT) method is effective for the in-plane displacement artifacts. Much better results (correction for both in-plane and through-slice displacements) can be successfully achieved applying multi-spectral imaging methods such as MAVRIC or SEMAC, however at a cost of increased scan time and heat effect (SAR) [1, 4, 12, 13, 15]

## 9. References

- Morelli, J. et al. An Image-based Approach to Understanding the Physics of MR Artifacts *RadioGraphics* (2011) 31:3, 849–866.
- Hargreaves, B. A., et al. Metal-induced artifacts in MRI. *AJR. American journal of roentgenology* (2011), 197(3), 547–555.
- Smith, M. R., et al. Characterizing the limits of MRI near metallic prostheses. *Magnetic resonance in medicine* (2015), 74(6), 1564–1573.
- Talbot, B.S. and Weinberg, E. MR Imaging with Metal-suppression Sequences for Evaluation of Total Joint Arthroplasty. *RadioGraphics* (2016) 36:1, 209–225.
- Filli, L. et al. Material-Dependent Implant Artifact Reduction Using SEMAC-VAT and MAVRIC. A Prospective MRI Phantom Study. *Invest Radiol* (2017); 52: 381–387.
- Smith, M. R., et al. Characterizing the limits of MRI near metallic prostheses. *Magnetic resonance in medicine*(2015), 74(6), 1564–1573.
- Schenck JF. The role of magnetic susceptibility in magnetic resonance imaging: MRI magnetic compatibility of the first and second kinds. *Med Phys* (1996); 23:815–850.
- <https://www.nibib.nih.gov/science-education/science-topics/magnetic-resonance-imaging-mri>
- Lee DH. Mechanisms of contrast enhancement in magnetic resonance imaging. *Can Assoc Radiol J.* (1991) Feb;42(1):6–12. PMID: 2001531.
- Lu, W., et al. SEMAC: Slice Encoding for Metal Artifact Correction in MRI. *Magnetic resonance in medicine* (2009), 62(1), 66–76.
- Butts K, et al. Reduction of blurring in view angle tilting MRI. *Magn Reson Med.* (2005) 53(2):418–24.
- Choi SJ, et al. Metal artifact reduction with MAVRIC SL at 3-T MRI in patients with hip arthroplasty. *Am J Roentgenol.* (2015) 204(1):140–7.
- Koch KM, et al. A multispectral three-dimensional acquisition technique for imaging near metal implants. *Magn Reson Med.* (2009), 61(2):381–90.
- National Electrical Manufacturers Association. NEMA Standards 8-2016. Characterization of the Specific Absorption Rate (SAR) for Magnetic Resonance Imaging Systems. <https://www.nema.org/standards/view/Characterization-of-the-Specific-Absorption-Rate-for-Magnetic-Resonance-Imaging-Systems>.
- Foster KR and Glaser R. Thermal mechanisms of interaction of radio frequency energy with biological systems with relevance to exposure guidelines. *Health Phys* 2007; 92:609–620
- Koch KM, et al. Imaging near metal with a MAVRIC-SEMAC hybrid. *Magn Reson Med.*(2011) ; 65(1):71–82.

## IS IT POSSIBLE TO APPLY A NEW TECHNIQUE WITH AN OLD LINAC? A FEASIBILITY STUDY OF PLDR WITH ELEKTA SYNERGY PLATFORM LINAC

Nur KODALOĞLU

Dr. Abdurrahman Yurtaslan Ankara Oncology Research and Training Hospital  
nurkodaloglu@gmail.com

**Abstract:** Since the beginning of 2000, hyper-radiosensitivity (HRS) cell studies lead to increase in the number of pulse low dose rate (PLDR) or pulsed reduced dose rate (PRDR) applications in radiotherapy especially for radioresistant tumors (1). Therefore, this work investigated the applicability and physical availability of PLDR treatment with an old linac for a regular treatment such as whole cranium irradiation.

**Keywords:** PLDR, Radiotherapy, hyper-radiosensitivity.

### 1. Introduction

Pulse low dose rate (PLDR) or pulsed reduced dose rate (PRDR) is aimed to irradiate patients with radioresistant tumors or recurrent cancers with  $<0.2$  Gy in order to reach higher treatment doses, increase tumor radiosensitivity to this dose rate and achieve rapid recovery of normal tissues. Between 0.2 and 0.8 Gy, tumors cells become more resistant. Therefore, 2 Gy/day is delivered in 10 fractions with 30 minutes between each 20cGy irradiation (approximately 30 minutes in total in a day). The corresponding dose rate is 6.67 cGy/min. In literature (2-4), there are many indications for pulse low dose rate radiotherapy such as the treatment of oesophagus, glial tumors, pancreas, head and neck, prostate, lung, breast cancer, etc. Besides, with the new technologies, apart from conformal RT, IMRT and VMAT can also be applied with PLDR (5). For brain metastasis, whole brain reirradiation is a difficult concern considering neurocognitive functions and quality of life of the patients. In this study, a treatment plan similar to whole brain irradiation was demonstrated. Irradiation of RW3 water equivalent solid phantoms was performed to investigate the applicability of the PLDR technique. Then, a whole brain radiotherapy plan was created for Alderson Rando phantom with both 3D conformal and PLDR treatments. Both plans were irradiated and measured with MOSFET (TN-RD-16) detectors.

### 2. Treatment Planning and Irradiation of the RW3 Solid Phantom

For the first part of this study, the applicability of a whole brain radiotherapy plan on RW3 water equivalent solid phantom ( $30 \times 30 \times 30$  cm<sup>3</sup>) was investigated. For this purpose, a 90° and 270° gantry angles opposed lateral field plan was made with 2x2 cm<sup>2</sup> field. The dose to the isocenter was evaluated as 200 cGy. Related plan data and colored isodoses can be seen in Fig. 1. Then, the plan was irradiated with the linac. To achieve the PLDR dose rates, the dose rate data was set to 500 MU/min. Total dose of 200 cGy was divided in 10 fractions of 20 cGy with 3 minutes between each fraction. Approximately, one fraction which means 20 cGy took 4.1 seconds.

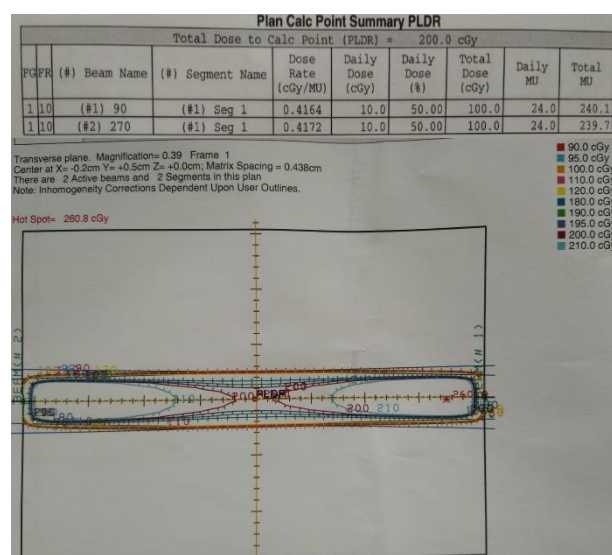


**Fig. 1.** The treatment plan parameter and dose colour wash of the plan.

### 3. Treatment Planning and Irradiation of the Alderson Rando Phantom

For the second part of this study, Alderson Rando phantom whole brain radiotherapy plan was created and



irradiated. CT acquisition of Alderson Rando phantom was made with a CT-simulator. Then, the target organ, brain and the organs at risk, brain stem, eyes, lenses, optic nerves, cochleas, hypophysis, chiasma were contoured. To compare easily with data from the literature, a total dose of 200 cGy to whole brain was planned with opposed lateral fields. MLC apertures of the plan can be seen in Figure 2. Related organ doses of the treatment plan can be seen in Table 1.

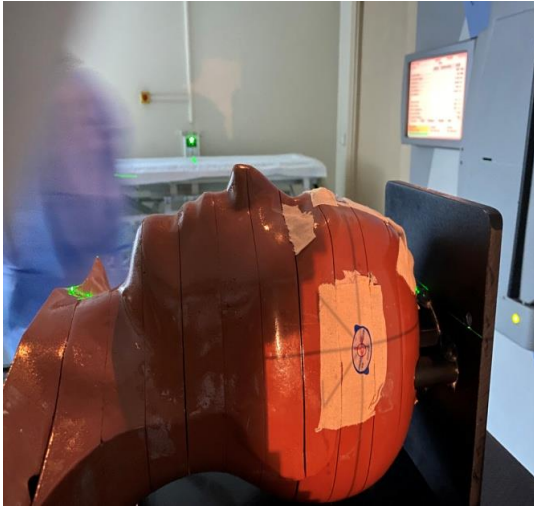


Fig. 2. Whole brain irradiation of Alderson Rando phantom.

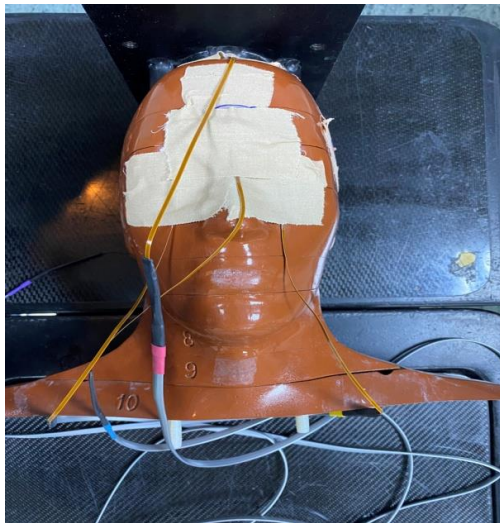


Fig. 3. MOSFET measurements during whole brain irradiation of Alderson Rando Phantom.

To evaluate the applicability of the PLDR technique, same whole brain radiotherapy plan was irradiated both as 3D-conformal plan and as PLDR plan with 10 subfractions of 20 cGy. To compare traditional 3D conformal and PLDR plans, irradiations were measured with MOSFET detectors. 5 MOSFET detectors were placed on right and left lens surfaces, forehead surface, occipital surface and apex surface which can be seen in Fig. 3. Firstly, 3D conformal plan was irradiated and MOSFET detector measurements were recorded. Then, for PLDR measurements, dose rate was set to 500 MU/min and irradiation was done with one fraction of 20 cGy, at an interval of 3 minutes before the next dose, instead of 200 cGy. PLDR MOSFET measurement data were recorded after completing 10 fractions.

Point doses of right and left lenses, right and left lens surfaces, brain stem, right and left brain lobes, right and left cerebellums, forehead surface, occipital surface, apex surface were obtained from the treatment plan to compare with the MOSFET measurements. The results and the percentage errors can be seen in Table 2. As can be seen from the table, a few of the point dose data were obtained for verification, not to be compared with MOSFET measurements. Since MOSFET were not suited for placement in the holes of the Alderson Rando phantom, each point dose data couldn't be compared with the MOSFET measurements.

#### 4. Results

The solid phantom plan was evaluated to deliver 200 cGy to the isocenter of the phantom from 90° and 270° gantry angles with 2x2 cm<sup>2</sup> field. The MUs, cGy/MU and related planning data can be seen in Figure 1. The dose rate was set to 500 MU/min. One fraction of 20 cGy took 4.1 seconds. The interval from the beginning of the first fraction to the next one was 3 minutes. From this simple trial, it was observed that PLDR can be easily applied. Oscillations were observed at the surface doses due to the build-up effect. Measurements could not be taken in the parts of the MOSFETs where it is not possible to place them inside the phantom (Table 2 - NA). In MOSFET measurements, while dose compatibility was observed on the right-left lens (0.11, 0.07 and 0.08, 0.05) and the surface of the head apex (0.02, 0.03), the error percentages increased because the charged particle equilibrium could not occur on the forehead PLDR (0.51) and occipital surfaces (0.91, 0.91).

Table 1. Organ doses of the Alderson Rando Phantom Whole Brain Radiotherapy treatment plan.

ORGANS	MIN. DOSE (cGy)	MAX. DOSE (cGy)	MEAN DOSE (cGy)	TOTAL VOLUME (cc)
Brain	162	228	204	1058.4
Brain stem	20	215	168	22.5
Right eye	11	167	32	8.1
Left eye	11	154	35	8.1
Right lens	11	64	21	0.8
Left lens	0	71	21	0.5
Right optic nerve	33	198	149	2.4
Left optic nerve	31	200	148	2.4
Right cochlea	184	190	187	0.2
Left cochlea	184	190	187	0.2
Hypophysis	196	198	197	0.1
Chiasma	200	202	201	0.5

**Table 2.** Comparison of organ doses in 3D-Conformal and PLDR plans with MOSFET measurements in whole brain irradiation.

ORGANS	TREATMENT PLAN (cGy)	MOSFET (cGy)			
		3D Conformal	% Error	PLDR	% Error
Right Lens	34.43	NA	NA	NA	NA
Left Lens	37.88	NA	NA	NA	NA
Right Lens Surface	17.07	18.9	0.11	18.26	0.07
Left Lens Surface	16.61	15.2	0.08	17.414	0.05
Brain Stem	196.46	NA	NA	NA	NA
Right Brain	202.17	NA	NA	NA	NA
Left Brain	201.41	NA	NA	NA	NA
Right Cerebellum	196.59	NA	NA	NA	NA
Left Cerebellum	197.35	NA	NA	NA	NA
Forehead (surface)	216.82	109	0.5	105.7	0.51
Occipital (surface)	224.57	19.6	0.91	19.8	0.91
Apex (surface)	224.03	219	0.02	231.6	0.03

## 5. Conclusions

As can be seen from the literature, PLDR shows promising results for the treatment of many radioresistant tumors, reirradiations, and increasing tolerance of normal tissues for recovery especially in case of recurrent tumors. This study also showed that PLDR can be easily applied to daily clinic routine considering the 10 fractions of daily dose. It was also easy to control the irradiation in clinic mode and not necessary to switch to the service mode to check the dose rate or any relevant data. On the other hand, for this machine, considering the reirradiations of the palliative or recurrent tumors, PLDR can be applied for whole brain irradiations and patients' cognitive functions follow-ups can be done. In another scenario, prophylactic whole brain irradiations or whole brain irradiations before TBI can be delivered with PLDR to allow faster recovery of normal tissues than classical conformal irradiations.

This study has shown that all brain reirradiations with PLDR can be done safely and effectively.

## 6. References

1. C.-M. Charlie and G. Luxton, "Pulsed reduced dose rate radiation therapy is likely to become the treatment modality of choice for recurrent cancers", *Medical Physics*, Vol. 38, No. 9, 4909-491, 2011
2. Li, Jie; Zhao, Zhenhua; Du, Guobo; Dai, Tangzhi; Zhen, Xuhai; Cai, Hongwei, "Safety and efficacy of pulsed low-dose rate radiotherapy for local recurrent esophageal squamous cell carcinoma after radiotherapy. Study protocol for a prospective multi-center phase II trial", *Medicine*, Vol. 98, No.26, 2019.
3. C. Ma, M. Lin, K. Wei, J. Li, P. Wang, J. Lang, "Pulsed Low-Dose-Rate Radiation Therapy (PLDR) for Recurrent Cancers: Treatment Planning Strategies for IMRT and VMAT", *Int. Journal of Rad. Onc. Bio. Phys.*, Vol.90, No. 1, S941, 2014.
4. Jing Yan, Ju Yang, Yang Yang, Wei Ren, Juan Liu, Shanbao Gao, Shuangshuang Li, Weiwei Kong, Lijing Zhu, Mi Yang, Xiaoping Qian, and Baorui Liu "Use of Pulsed Low-Dose Rate Radiotherapy in Refractory Malignancies", *Transl Oncol.* 175-181, 2018.
5. C Ma, M Lin, L Wang, R Price, "Dosimetric Evaluation for Pulsed Low Dose Rate Radiation Therapy Using RapidArc Delivery Techniques", *Medical Physics*, Vol. 38, No. 6, 3675-3676, 2011.



## PROTOTYPE OF CONTEMPORARY GAMMA SPECTROMETER BASED ON OBSOLETE RADIOMETER

Justas BERESNEVIČIUS, Benas Gabrielis URBONAVIČIUS  
Department of Physics, Kaunas University of Technology, Lithuania;  
justas.beresnevicius@gmail.com;

**Abstract:** Gamma-ray spectroscopy is complicated in nature and requires relatively exotic equipment to perform. The aim of this work is to examine technological solutions for developing prototype of contemporary gamma-ray spectrometer using modern MCA and USB interface with an obsolete scintillating detector. Tests with the developed prototype have shown that it is certainly possible to convert old radiometers to modern gamma-ray spectrometers, yet much calibration and research must be done.

**Keywords:** gamma-ray spectrometer, ionizing radiation, photomultiplier tube, modern solution

### 1. Introduction

To detect gamma radiation, various detectors can be used. For measuring only counts of gamma photons, ionizing chambers like Geiger tube can be brought into scene, but to obtain precise energy of particular gamma photon, detectors like proportional counters, solid-state semiconductor or scintillating ones are great for such use [1]. The latter ones – scintillation detectors, are used since 1944 [2]. They consist of scintillating crystal, photomultiplier tube and signal processing circuit. Various dosimeters or radiometers, like CΠI-88H, are powered by such detector, but at the time they were constructed, it was quite difficult to use the main advantage of scintillating crystal and photomultiplier tube combination. Biggest merit of scintillating crystal and PMT synergy is that output signal amplitude is directly proportional to incident radiation energy [3,4]. Nowadays, with current advancement of technologies and with the right equipment and tools, it is possible to process the same signal from an old radiometer based on scintillation detector, like CΠI-88H, but in modern way. Using present-day multichannel analyser and USB or 3.5 mm audio jack interfaces for signal output allows to convert obsolete radiometers to contemporary gamma-spectrometers.

### 2. Methods

Any gamma spectrometer must have following parts:

- Gamma-ray detector
- High voltage power supply
- Signal amplifiers
- Multichannel analyser

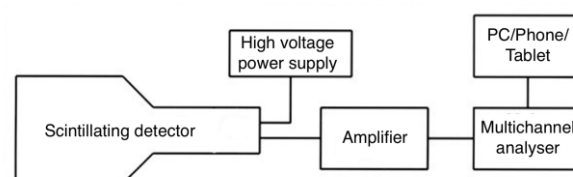


**Fig. 1.** Principal scheme of prototype of gamma spectrometer [4].

In this work, majority of parts were taken from obsolete CΠI-88H radiometer. The main purpose of salvaged device is just to count gamma photons that passed through detector. Since it was fully functional, it was thought that it's possible to avail oneself of high voltage power supply and scintillating detector.

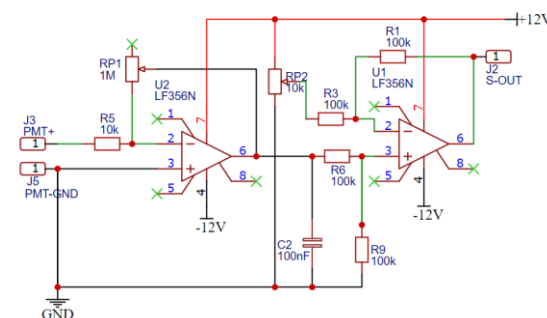


**Fig. 2.** Scheme of primary signal processing

Considering the basis of radiometer, signal processing circuitry is made for different purpose and is not suitable for gamma spectroscopy [4]. The shape of

pulse, does not contain any information about incident radiation energy, it is used just as a count. According to that, first approach to get energy of incident ionizing radiation from radiometer was to design appropriate signal processing circuitry (see fig. 2).

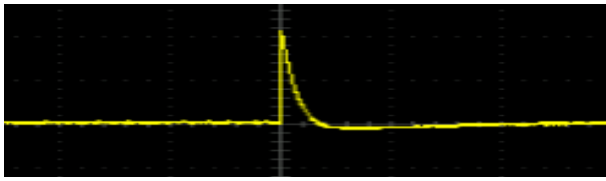


Fig. 3. Expected pulse from PMT

This circuit was hooked up to  $\phi 3y - 85$  photomultiplier tube, which comes as a part of detector from CPII-88H. According to documentation tube's recommended working voltage is 1250V [5]. Since high voltage power supply is used from radiometer, no additional tweaking was needed neither to the voltage divider of PMT, nor to power supply. With this implementation main purpose was to get clean, almost unprocessed pulses of PMT which should look like in fig. 3 where pulse amplitude proportionally corresponds to the energy of incident radiation [6].

Another approach to make scintillating detector from radiometer to work, was to use device named GS-USB-PRO by "Gammaspectacular".



Fig. 4. GS-USB-PRO by "Gammaspectacular"

It was determined as a "Plug'n'Play" solution. GS-USB-PRO has an adjustable high voltage power supply up to 2000V, which allows to power various types of detectors including Geiger and photomultiplier tubes. It also has both USB and 3.5mm audio jack interfaces for pulse/signal output which allows multiplatform use. Most of operating systems are able to recognize this device as an external sound card or if used with audio jack – as a microphone.

Now that new power supply was selected to be used, voltage divider of PMT needed to be checked. It turned out that CPII-88H manufacturers did not correspond to suggested values by  $\phi 3y - 85$  tube makers and resistors values were higher than recommended. This was done as a prevention of overloading original high voltage power supply of radiometer. With GS-USB-PRO recommended resistors are fine to use because it is powerful enough.

When making a new voltage divider, resistors of 1, 1.5 and 2 M $\Omega$  were taken and soldered according to documentation [7]. At this moment decoupling

capacitors were skipped, since the actual pulse from PMT was still unknown.

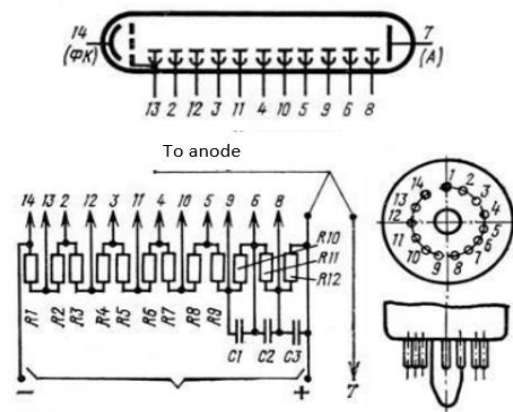


Fig. 5. Voltage divider scheme of  $\phi 3y - 85$

Once this was finished, PMT was just hooked up to high voltage – direct current, where signal comes as an alternating current through the same wire. When pulse reaches the GS-USB-PRO circuitry it is then decoupled using capacitor and processed using LM6142 rail-to-rail amplifier, low/high-pass filters and 16 bits analog to digital converter (ADC). As mentioned before, processed signal can be sent through audio jack and plugged in straight to smartphone or using USB – to computer device.

When the signal reaches chosen device, multichannel analyser software needs to be used. For the machine with Windows operating system, "Theremino MCA" is a great tool.

This software lets to analyse pulse shape, change various parameters such as gain, bin size, sample rate and easily inspect spectrum of performed measurement. Bin was selected as 1x, sampling rate as 192 kHz and audio gain was left default – 1.0.

Before starting any measurement, in the above software, correct input device must be selected.

After that, noise test should be performed, while detector MUST NOT be connected to the GS-USB-PRO [8]. This test listens for all the pulses which are present without PMT plugged in and later filters them out, when the real measurement takes place. When noise test is finished and PMT is connected to GS-USB-PRO, it is necessary to check pulse shape that it looks similar to the one in oscilloscope. Once everything is set, measurement can be performed, yet proper time interval should be considered.

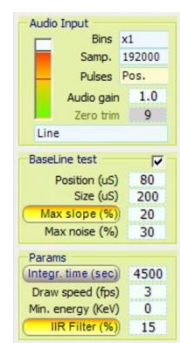


Fig. 6. „Theremino MCA“ software settings

### 3. Results and discussion

With the first approach, before doing any observation, designed scheme was put onto perfboard, the biggest struggle was to put every component in a suitable way that other components pins should not block anything. After everything was soldered, checking that each

wire/track is placed as planned was time consuming. Both problems can be avoided by designing printed circuit board (PCB), but manufacturing PCB on a small scale and just for test is cost inefficient.

When PMT was powered using CPII - 88H radiometer high voltage power supply and oscilloscope was hooked to J2-SOUT pin, it was observed that output signal is very noisy (see fig 7).

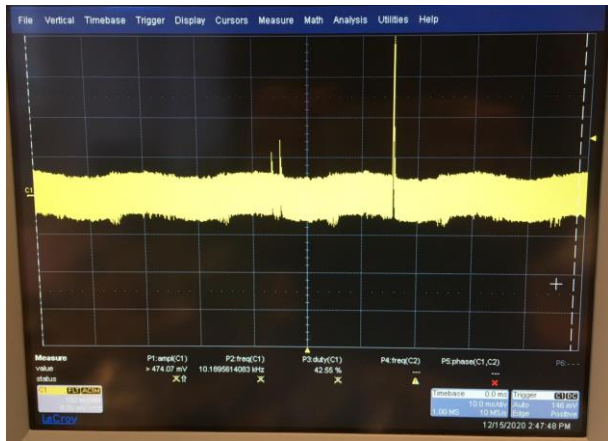


**Fig. 7.** Very noisy signal from PMT when powered with CPII - 88H radiometer high voltage power supply

To filter out this noise some capacitors were added to the output cable, but it did not help. It was determined that this noise comes from high voltage power supply of radiometer and there is no point in continuing this approach.



**Fig. 8.** A -  $\phi 3y - 85$  PMT with initial circuitry; B - with new voltage divider and used shielding

Based on the results of first try, another solution for high voltage power supply was found - GS-USB-PRO. It was a perfect fit for such case.

As mentioned above, since signal processing and high voltage power supply was already present in GS-USB-PRO, all the existing circuitry was taken away.

First thing to test was if signal from PMT is cleaner and it turned out to be true. (see fig 9).

But it was not possible to proceed to next step because no signal was reaching "Theremino" software, which led to conclusion that voltage divider design was poorly chosen and spaces between each other should be wider.

Once replaced – nothing changed. After many hours of debugging it was found that LM6142 rail-to-rail amplifier was broken, since actual pulses from PMT were present. Replacing

LM6142 with new one helped and software started to receive signals.



**Fig. 9.** Clean pulses from PMT when powered from GS-USB-PRO

Pulse shape appeared very clean in software too, which was a good sign (see fig 10).

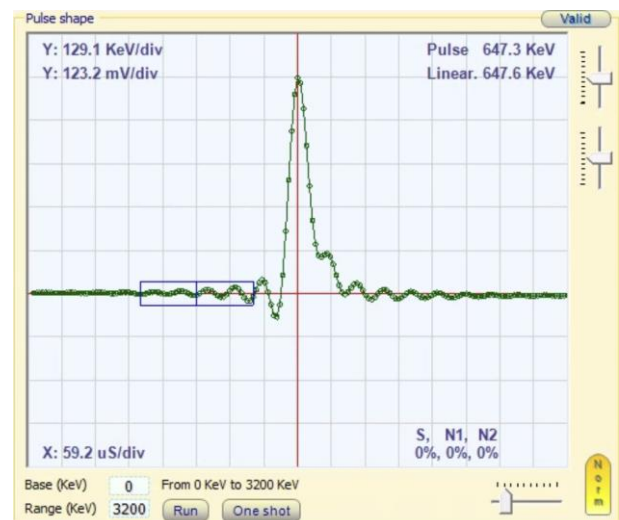


**Fig. 10.** Pulse shape in "Theremino MCA" software

When pulse shape was proved to be acceptable, actual measurements were performed. Each measurement took 600 seconds.

First one was a background radiation check and the second measurement was performed with Co-60 calibrating source from CPII - 88H radiometer, placed near the tip of detector. It must be kept in mind that device was made in 1982 which means the source should have ~0.61% of the activity left and it should be visible in spectrum that it is Cobalt - 60.

**Table 1.** Recommended font types for tables

Measurement	Background	With source
Counts per minute	55.8	82.0
Total pulses	33490	49182

As can be seen from Table 1, total pulses with source are almost 1.5 times higher, which indicates that source is still active and detector is able to detect it.



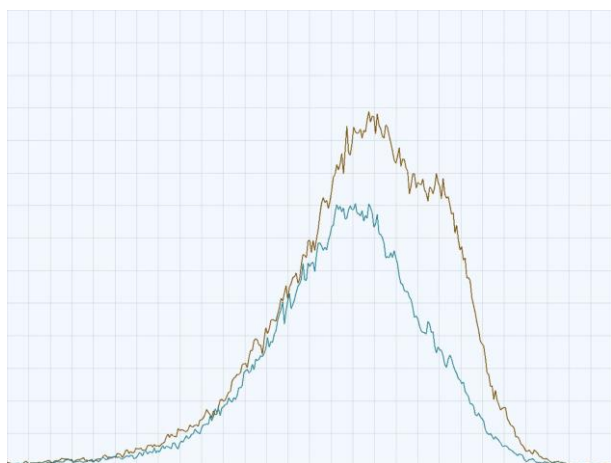


**Fig. 11.** Spectrum of energy levels. Blue-ish line – background; Brown-ish – With source.

From the Fig 11 it is clear that constructed prototype needs more tweaking, because both measurements took same amount of time, yet the counts of energy levels are different across whole interval. Increase only on particular energy level is expected when measuring in the same place just with an ionizing source placed near the detector.

In the measurement with Cs-60 source, there is an increase on the right side of abscissa, which means that detector is able to produce pulse of various energy levels based on the source. Based that it is Cs-60 source, it makes sense to get a peak on the righter side of the spectrum. Considering the results, more tweaking should be done to get more precise results, like adding capacitors to voltage divider or better shielding. Also source from CPII - 88H radiometer must be checked with different detector to make sure that prototype of contemporary gamma spectrometer based on obsolete radiometer shows correct count per minute ratio between background and the source.

#### 4. Conclusions

Developed prototype proved that combination of photomultiplier tube and scintillating crystal is able to transform incident ionizing radiation energy to electric signal and that signal can be processed using amplifiers and contemporary software. Considering the mandatory voltage for PMT, good quality high voltage power

supply must be chosen, which neither produce noise, nor interrupt signal. Power supply of GS-USB-PRO by “Gammaspectacular” proved to be great one for such use and together with “Theremino MCA”, as multichannel analyser, turned out to be in great tandem for analysing spectrum of energy levels. Yet GS-USB-PRO was not a “Plug’n’Play” device, because of the faulty rail-to-rail amplifier.

#### 5. References

1. Lu Lu, Mingzi Sun, Qiuyang Lu, Tong Wu, Bolong Huang, High energy X-ray radiation sensitive scintillating materials for medical imaging, cancer diagnosis and therapy, *Nano Energy*, Volume 79, 2021, 105437
2. QiangYi et al. *Nucl. Instrum. Methods Phys. Res. A* (2013)
3. Grodzicka-Kobylka, M., Moszyński, M., Szczęśniak, T. Silicon photomultipliers in gamma spectroscopy with scintillators. *Nuclear Instruments and Methods in Physics Research Section A: Accelerators, Spectrometers, Detectors and Associated Equipment*. Volume 926, 11 May 2019, Pages 129-147.
4. Puišo, Judita; Laurikaitienė, Jurgita; Adlienė, Diana; Prosyčėvas, Igoris. Liquid radiation detectors based on nanosilver surface plasmon resonance phenomena // *Radiation protection dosimetry*. Oxford : Oxford University Press. ISSN 0144-8420. 2010, Vol. 139, no. 1-3, p. 353-356. DOI: 10.1093/rpd/ncq043.
5. G. F. Knoll. *Radiation Detection and Measurement* (John Wiley & Sons, New York, 2000).
6. Фотоэлектронный умножитель ФЭУ-85. Access via: <https://eandc.ru/pdf/opto/feu-85.pdf>
7. B.K. Lubsandorzhiev, On the history of photomultiplier tube invention, *Nuclear Instruments and Methods in Physics Research Section A: Accelerators, Spectrometers, Detectors and Associated Equipment*, Volume 567, Issue 1, 2006, Pages 236-238.
8. Benjamin Moritz Veit, Active Voltage Dividers for Photomultipliers, 1. March 2019 Access via: [https://indico.cern.ch/event/800973/contributions/3328661/attachments/1804539/2944423/bveit\\_eabi\\_wb\\_active\\_vol tage\\_dividers.pdf](https://indico.cern.ch/event/800973/contributions/3328661/attachments/1804539/2944423/bveit_eabi_wb_active_vol tage_dividers.pdf)
9. M Moszyński, M Szawlowski, M Kapusta, M Balcerzyk, Large area avalanche photodiodes in scintillation and X-rays detection, *Nuclear Instruments and Methods in Physics Research Section A: Accelerators, Spectrometers, Detectors and Associated Equipment*, Volume 485, Issue 3, 2002, Pages 504-521.

## **INVESTIGATION OF LOW TOXICITY DOSE GELS WITH ENHANCED SENSITIVITY**

Mantvydas MERKIS, Ignas PIKAS, Diana ADLIENE  
Physics Department of Kaunas University of Technology, Lithuania  
mantvydas.merkis@ktu.edu

**Abstract:** One of the most perspective gel dosimeters in clinical applications are acrylamide – based. However, acrylamide is likely to be cancerogenic. Sensitivity of gel dosimeters with less toxic alternatives is relatively low. In this work we investigated gel dosimeter with less toxic acrylamide substitute and attempted to modify its composition in order to increase dose sensitivity. Preliminary results are positive – by changing component concentrations, adding co-solvents and selecting optimal fabrication procedures we were able to achieve significantly higher sensitivity.

**Keywords:** Dose gels, polymer gel dosimetry, acrylamide, NIPAM.

### **1. Introduction**

Gel dosimeters have unique capabilities comparing to conventional dosimetry methods. These dosimeters allow to measure dose distribution in three dimensions with high spatial accuracy. Moreover, gel dosimeters are tissue – equivalent in terms of absorption of ionizing radiation [1]. Dose gels could be indispensable tool in verification of novel complex radiotherapy techniques where steep dose gradients are used [2].

The working principle of most of gel dosimeters is based on radiation-induced polymerization of monomers. Due to polymerization, various physical properties of the polymer gel dosimeter are alternated, for example, optical density. Changes of these properties are proportional to the absorbed dose [3].

Although gel dosimeters could be advantageous option, they are rarely used in clinical practice [4]. One of the main drawbacks which limits applicability of gel dosimeters is their toxicity – the most commonly used gel dosimeters contain acrylamide which is neurotoxin and suspected carcinogen. Less toxic gel dosimeters, where acrylamide alternatives are utilized, have lower dose sensitivity [5].

The main objective of this work is to investigate approaches to increase dose sensitivity of low toxicity dose gels.

### **2. Materials and methods**

#### **3.1. Polymer gel formulation**

NIPAM polymer gel dosimeter formulation was selected for the experiments. In this formulation toxic acrylamide is changed with less toxic N-(Isobutoxymethyl) acrylamide. This agent is used as a source of monomers for polymerization reactions. N,N'-Methylene-bis-acrylamide in this formulation is used as crosslinker which is responsible for polymer network formation in the dosimetric gel [6]. In order to maintain spatial integrity of the gel dosimeter gelatin is used. It acts as a scaffold for created polymer chains. Since oxygen inhibits polymerization reactions tetrakis (hydroxymethyl)phosphonium sulfate is used as an oxygen scavenger. The remaining part of the gel constitutes of distilled water that acts as a base agent [4].

**Table 1.** NIPAM polymer gel dosimeter composition [4]

<b>Component</b>	<b>Quantity</b>
N-(Isobutoxymethyl) acrylamide	3wt%
N,N'-Methylene-bis-acrylamide	3wt%
Tetrakis (hydroxymethyl) phosphonium sulfate	10 mM
Gelatin	5wt%
Distilled water	87 wt%

One of the approaches to improve sensitivity of polymer gel dosimeter is to increase amount of N,N'-Methylene-bis-acrylamide crosslinker. However, the problem of this agent is its limited solubility in water - in typical formulations fraction of this crosslinker is limited to 3wt% [7].

In order to improve solubility of N,N'-Methylene-bis-acrylamide crosslinker various co-solvents could be used [7, 8]. In our previous investigations it was determined that acetone demonstrates best solubility enhancing effect. Therefore, part of the water in the gel dosimeter was exchanged with acetone co-solvent (20wt%). This allowed to increase crosslinker fraction from 3wt% to 5wt%. If crosslinker concentration is higher than 5 wt%, particulation of the gel was notified indicating that 5 wt% is solubility limit of the crosslinker. Improved NIPAM polymer gel dosimeter composition is depicted table 2.

**Table 2.** Improved NIPAM polymer gel dosimeter composition

Component	Quantity
N-(Isobutoxymethyl) acrylamide	3 wt%
N,N'-Methylene-bis-acrylamide	5 wt%
Tetrakis (hydroxymethyl) phosphonium sulfate	10 mM
Gelatin	5 wt%
Acetone	20 wt%
Distilled water	65 wt%

### 3.2. Polymer gel fabrication procedure

Additionally, the impact on sensitivity of different fabrication procedures was investigated. Two different fabrication procedures were used - "cold" and "hot". "Hot" fabrication is standard NIPAM polymer gel fabrication procedure, while "cold" procedure is alternative to standard.

During standard ("hot") fabrication procedure the gelatin was soaked in 70% of the distilled water for 15 min at room temperature and after that heated to 50°C with stirring for 10 min until full dissolution. After gelatin dissolution N,N'-Methylene-bis-acrylamide crosslinker was added under continuous stirring. Also, acetone co-solvent was added and mixing continued until dissolution of components. Acquired solution was left to cool down to 37°C with continuous mixing. When required temperature was reached N-(Isobutoxymethyl) acrylamide was added under continuous stirring. After monomer dissolution solution temperature was lowered to 35 °C. Other part of the solution containing tetrakis (hydroxymethyl) phosphonium sulfate and the remaining part of the water at room temperature was added to the main solution and stirred for 2 minutes. When stirring was completed, prepared gel was poured to PMMA cuvettes, sealed with laboratory film and stored away from the sunlight at room temperature for 24 h [9].

Alternative ("cold") fabrication procedure significantly differs from standard fabrication procedure. Firstly, gelatin was soaked for 10 min in 70% of the water and heated to 50°C with continuous stirring until full dissolution. After that, N,N'-Methylene-bis-acrylamide crosslinker was added under mixing. Following crosslinker addition acetone was added with continuous mixing. When constituents fully dissolved, the solution was allowed to cool down to 34 °C. In the meantime

solution containing N-(Isobutoxymethyl) acrylamide, tetrakis (hydroxymethyl) phosphonium sulphate and the remaining part of the water was fabricated at room temperature. Firstly, monomer was added to the water, after that diluted tetrakis (hydroxymethyl) phosphonium sulphate solution was poured with mixing. When required temperature of the main solution was reached, monomer-oxygen scavenger solution was added to the main solution and mixed for 1-2 min. Prepared gel was poured to PMMA cuvettes, sealed with laboratory film and stored away from the sunlight at room temperature for 24 h [10].

### 3.3. Irradiation of samples

Fabricated polymer gel dosimeter samples were irradiated with doses ranging from 0 to 6 Gy with 1 Gy increments to acquire calibration curves. Irradiation was conducted using Varian Clinac DMX linear accelerator in Hospital of Lithuanian University of Health Sciences Kaunas Clinics branch Oncology hospital 24 h after fabrication of gel dosimeters. Energy of irradiation photons – 6 MeV, selected field size - 10x10 cm, source-surface distance - 100 cm, dose rate: 300 cGy/min.

### 3.3. Readout of dose information

Fabricated polymer gel dosimeters were characterized 24 h after irradiation using OceanOptics USB2000+ UV-VIS spectrometer. Absorbance spectrum was acquired. Number of averaged scans - 3, integration time - 100 msec. Measurements were acquired in the middle of each cuvette 3 times and the average was taken. Cuvette influence on acquired results was eliminated by taking reference spectrums with an empty cuvette. From acquired spectral data calibration curves were formed at optimal wavelength where the highest signal amplitude can be achieved with minimal amount of noise.

## 3. Results and discussion

Improved NIPAM polymer gel samples successfully reacted to the irradiation - samples became increasingly white with increasing dose. No inhomogeneities were notified in irradiated gels except in the region near to the sealed entrance of the cuvette where due to poor sealing oxygen inhibited polymerization reactions. Appearance of irradiated samples is depicted below.



**Fig. 1.** Improved NIPAM polymer gel dosimeter samples fabricated using "hot" procedure and irradiated with doses from 1 to 6 Gy.



From photospectrometric measurements of samples fabricated using different procedures significant differences were notified.

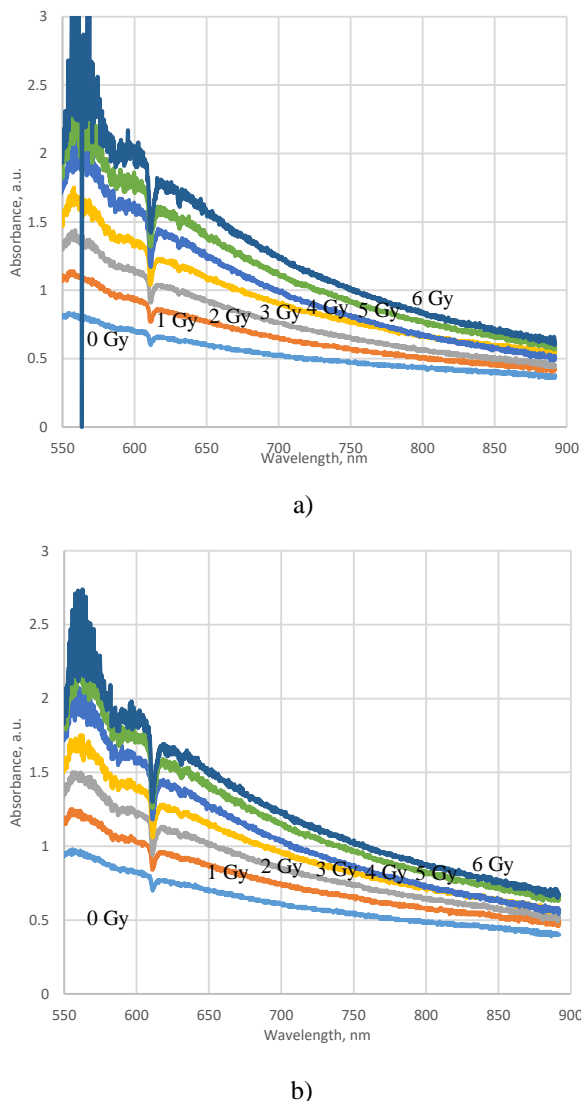


**Fig. 2.** Spectra of improved NIPAM polymer gel dosimeter samples fabricated using “hot” procedure (a) and “cold” procedure (b) on different irradiation doses

From acquired spectra in both cases we can notify slight redshift with increasing irradiation dose that indicates growth of polymer network. Also, increasing extent of polymerization can be notified from increasing absorbance values. Separation between spectra on different doses is higher when samples were fabricated using “hot” procedure indicating acquired better dose sensitivity.

At 611 nm pit can be notified in all acquired spectra. This pit possibly is associated with one of emission wavelengths of fluorescent lamps. Therefore, spectrum subtraction during spectrophotometry measurements was insufficient to effectively eliminate environmental influence.

From measured spectral data calibration points were acquired at optimal wavelength (639 nm) and approximated with first order polynomial to acquire calibration curves.

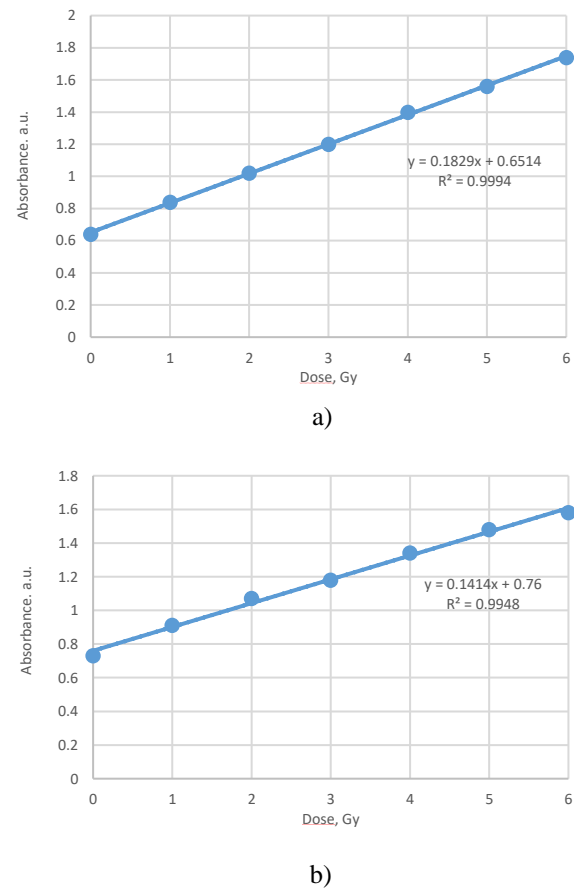


**Fig. 3.** Calibration curves of improved NIPAM polymer gel dosimeter samples fabricated using “hot” procedure (a) and “cold” procedure (b)

Dose response of improved NIPAM polymer gel dosimeter response is almost linear with  $R^2$  higher than 0.99 for both used fabrication procedures.

From acquired calibration curves we can notify that increase of the crosslinker fraction from 3%wt to 5%wt allowed to significantly enhance sensitivity of NIPAM polymer gel dosimeter. When “hot” fabrication procedure was used sensitivity of the gel dosimeter increased from 0.1 (original formulation) to 0.183, therefore 83% enhancement was achieved. When “cold” fabrication procedure was used sensitivity of the gel dosimeter increased from 0.1 to 0.141, thus 41% enhancement was achieved.

Fabrication procedure has significant impact on improved NIPAM polymer gel sensitivity. When “hot” fabrication procedure is used it is possible to achieve approximately 2 times larger sensitivity enhancement comparing to “cold” fabrication procedure. Possible cause of this phenomena – better dissolution and distribution of monomer during “hot” fabrication procedure. When mentioned fabrication procedure is used, monomer is added at 37°C main solution temperature with continuous stirring until full visual dissolution. During “cold” fabrication procedure possibility of full dissolution of monomer is lower because monomer, oxygen scavenger and a part of water are mixed separately from the main solution at lower temperature (room temperature) and only then added to the final solution with mixing for a limited

time (1-2 min). Mixing time is limited because for longer stirring times oxygen scavenger tend to cause sudden solidification of the gel dosimeter. Thus, it becomes impossible to pour dosimetric gel to cuvettes. Moreover, after sudden solidification radiation-induced polymerization process is inhibited completely possibly due to used up oxygen scavenger.

#### 4. Conclusions

Increase amount of the crosslinker by adding co-solvent proved to be a successful approach to improve sensitivity of NIPAM polymer gel dosimeter. Increase of the crosslinker fraction from 3%wt to 5%wt allowed to achieve 83% better sensitivity comparing to the initial case.

Fabrication procedure has significant impact on the sensitivity of the improved NIPAM dose gel. Sensitivity enhancement differs approximately 2 times when different fabrication procedures were utilized.

During further experiments it is planned to investigate improved NIPAM dosimetric gel spatial, temporal, temperature stability and sensitivity influence on irradiation parameters (dose rate, energy).

#### 5. References

1. Baldock, C. Review of gel dosimetry: a personal reflection. In: Journal of Physics: Conference Series. IOP Publishing, 2017. p. 012029.
2. De Deene, Yves; JIRASEK, Andrew. Uncertainty in 3D gel dosimetry. In: Journal of Physics: Conference Series. IOP Publishing, 2015. p. 012008.
3. Baldock, Clive, et al. Polymer gel dosimetry. Physics in Medicine & Biology, 2010, 55.5: R1.
4. Javaheri, Negin, et al. Improvement of sensitivity of X-ray CT reading method for polymer gel in radiation therapy. Reports of Practical Oncology & Radiotherapy, 2020, 25.1: 100-103.
5. Abtahi, Seyed Mohammad Mahdi; Pourghanbari, Mohammad. A new less toxic polymer gel dosimeter: Radiological characteristics and dosimetry properties. Physica Medica, 2018, 53: 137-144.
6. Cheng, Kai-Yuan; HSIEH, Ling-Ling; SHIH, Cheng-Ting. A comprehensive evaluation of NIPAM polymer gel dosimeters on three orthogonal planes and temporal stability analysis. Plos one, 2016, 11.5: e0155797.
7. Rabiah, Khalid A., et al. High dose sensitivity of N-(isobutoxymethyl) acrylamide polymer gel dosimeters with improved monomer solubility using acetone co-solvent. Nuclear Instruments and Methods in Physics Research Section B: Beam Interactions with Materials and Atoms, 2019, 442: 67-72.
8. Moftah, Belal, et al. Novel 3D polymer gel dosimeters based on N-(3-Methoxypropyl) acrylamide (NMPAGAT) for quality assurance in radiation oncology. Radiation Measurements, 2020, 135: 106372.
9. Abtahi, Seyed Mohammad Mahdi; Kargar Shaker Langaroodi, Roghayeh; Akbari, Mohammad Esmail. Dose distribution verification in intraoperative radiation therapy using an N-isopropyl acrylamide-based polymer gel dosimeter. Journal of Radioanalytical & Nuclear Chemistry, 2020, 324.2.
10. Olding, Timothy, et al. Small field dose delivery evaluations using cone beam optical computed tomography-based polymer gel dosimetry. Journal of medical physics/Association of Medical Physicists of India, 2011, 36.1: 3.

## **INVESTIGATION OF EXPOSURE DOSES TO NUCLEAR MEDICINE STAFF WORKING WITH Tc-99m**

Greta VAINIŪTĖ<sup>1</sup>, Laurynas GILYS<sup>1,2</sup>, Lijana LILEIKYTĖ<sup>1</sup>, Diana ADLIENĖ<sup>1</sup>

<sup>1</sup>Physics Department of Kaunas University of Technology, Lithuania

<sup>2</sup>The Hospital of Lithuanian University of Health Sciences, Kaunas, Lithuania  
greta.vainiute@ktu.edu

**Abstract:** Nuclear medicine technologists are experiencing whole body and hands exposure when administering radiopharmaceuticals. It is known that the doses to hands and especially fingertips may even surpass the dose limits which are set by international and national authorities. Due to this dose monitoring of the exposed nuclear medicine workers plays an important role when assuring safe work with radionuclides.

The aim of this work was to investigate the exposure of nuclear medicine staff working with <sup>99m</sup>Tc and to assess correlation between hand doses Hp(0.07) and whole body doses Hp(10) received by the personnel performing daily routine work. For this reason, dynamic Hp(10) dose measurements were performed using POLYMASTER dosimeters during every entire working day of the technologists. Doses to fingertips were measured using TLD dosimeters.

The analysis of the daily whole body dose distributions in dynamics might be a useful tool for the identification of the time period within the day, when the doses were higher than average. This can help identifying the problems the technologist was facing with and undertake the appropriate measures such as retraining of the staff, improvement of the applied methodology. There were no strong correlation between whole-body doses and doses to extremities found.

**Keywords:** nuclear medicine technologists, exposure, whole body dose, dose to extremities, fingertip doses

### **1. Introduction**

When handling unsealed radiation sources such as radiopharmaceuticals personnel is exposed to a higher level of doses. Measurements of the exposure doses by the staff contribute to ensuring radiation safety and health of personnel since radiation exposure is a potential source for the development of the secondary cancer [1]. Nevertheless, in many cases, the estimation

of doses is performed just for following rules and instructions in obedience and not for ensuring the safety and health of the staff. Moreover, it is important to mention that, the dose monitoring of the extremities is difficult because it is hard to determine the most exposed area [2] and ring dosimeter position is not clearly predefined.

<sup>99m</sup>Tc, <sup>131</sup>I, <sup>125</sup>I, <sup>18</sup>F and several other radionuclides are used in various diagnostic and therapeutic procedures. Handling of these materials is a key to higher radiation doses to the extremities of nuclear medicine workers and especially to the finger tips [3].

The results obtained in the ORAMED (Optimization of Radiation Protection of Medical Staff) project [2] which was aimed at investigation of the exposure levels to extremities of the nuclear medicine department staff working with <sup>99m</sup>Tc and <sup>18</sup>F have shown that nearly one of five workers in nuclear medicine's department might receive more than the dose limit for preset for the skin [4]. Measurements were performed fixing 11 TLD's on the operator's hands and it was found that the extremity doses received by the staff during pharmaceuticals preparation in hot lab were higher as compared to the doses received in the radiopharmaceutical administration phase. The recommendations given after the project includes extremity monitoring being a necessity in NM, shielding being an essential, and training and education being a good practice, which is a relevant parameter.

In 2020 Iranian study [5] was conducted with the aim to optimize shielding in NM using MC simulations. It is known, that thicker shields provide higher photon absorption ability due to the higher number of photon interactions with shielding material. The given recommendation is that at the energies >100 keV the required absorption efficiency cannot be achieved using common thyroid shields and aprons since the shielding thickness must be improved. This is valid for NM personnel working with <sup>99m</sup>Tc (E=141 keV) based radiopharmaceuticals.

Performing another study [6], occupational doses of 30 nuclear medicine department workers (including medical physicists, nursing staff and radiologists) were monitored during one-year period. TLD badges were used for Hp(10) dose assessment as well as ring dosimeters were used for the monitoring of the extremities dose. In all cases, extremity doses were below the annual dose limit (500 mSv), and the annual occupational doses were below the dose limit (20 mSv) as well. However the authors have not investigated the doses to fingertips. The average annual values of 1.22 mSv and 0.73 mSv for Hp(10) and 1.23 mSv and 0.72 mSv for Hp (0.07) were found after investigation of doses to 1243 technologists working at 28 different medical centres in Saudi Arabia in the period between 2015-2019 [7].

Measurements of extremity doses by using a ring dosimeter were reported in [3]. It was found that the extremity doses were extremely high and varied within broad interval ranging between 1.5 - 31.9 mSv for the left hand, and between 1.8 - 55.2 mSv for the right hand, while the whole body doses ranged from 36 mSv to 3 mSv. Also, it is mentioned elsewhere [3] that the use of syringe shields can help to reduce the doses by 75 - 85 % [3].

The information provided in such studies can help not only to evaluate the exposure doses received by the staff working in nuclear medicine's field and update the routine procedures and protocols but also to investigate occupational exposure's impact on workers' health and determination of radiation-induced cancer risk. This indicates the necessity to perform complex investigation and analysis of the doses to NM staff (whole body+ extremities) in parallel with occupational dose monitoring.

## 2. Materials and methods

Individual whole-body doses, doses to extremities and fingertip doses of technologists were assessed during entire 2020 in one of the Lithuania's hospitals. 4 technologists were participating in this project.

For the assessment of doses received by NM staff, technologists were wearing usual OSL personal dosimeters (Hp(10) measurements) and additional electronic personal dosimeters (POLYMASTER) for obtaining dynamic dosimetry data measurements; TLD ring was worn on a randomly selected finger. For the assessment of the doses to fingertips TLD's were attached to the fingertips of both hands.

The technologists were directly involved in preparation and administration of the radiopharmaceuticals with  $^{99m}\text{Tc}$  (gamma emitter with a photon energy of 140 keV, with a half-life of 6 hours).

Dose rate ( $\mu\text{Sv/h}$ ) and dose ( $\mu\text{Sv}$ ) were measured with POLYMASTER dosimeter and then later, accumulated dose ( $\mu\text{Sv}$ ) during the working day was calculated for whole-body monitoring. Doses to the fingertips were derived from the fingertip attached TLD's and information obtained from TLD ring dosimeter (for the comparison). Collected data was analyzed and compared to find the correlation between these parameters.

Whole-body and hand exposure (ring) doses of the staff were evaluated once per three months following national regulations [9]. Dynamic data of doses received by technologists during one day were collected upon request during entire working day and dynamic dose maps were created. Doses to fingers were measured upon request (in this case – for research purposes).

## 3. Results and discussion

The dose accumulated during each working day was calculated and used for further analysis. It was found, that the maximum accumulated dose per day does not exceed 6  $\mu\text{Sv}$  for the first technologist (Tech1); ~9  $\mu\text{Sv}$  for the second technologist (Tech2) and 7.6  $\mu\text{Sv}$  for the third technologist (Tech3). However maximum accumulated dose per day of the fourth technologist (Tech4) was almost twice higher - 14.4  $\mu\text{Sv}$  (Fig. 1).

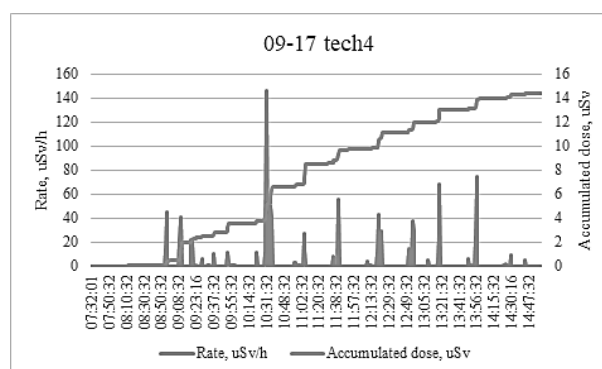


**Fig. 1.** Dynamic dose accumulation map of the technologist (Tech4) measured on September 17, 2020

It must be noted, that dynamic dose accumulation maps were very useful when analyzing work performance of technologists. Usually Hp(10) doses were growing in small steps (~0.37  $\mu\text{Sv}$ ) within a certain time period (according to the preset dosimeter's measurement frequency) which was related to technologist's activity within a period of working day. However in some cases high dose deviations were observed (Fig.2)

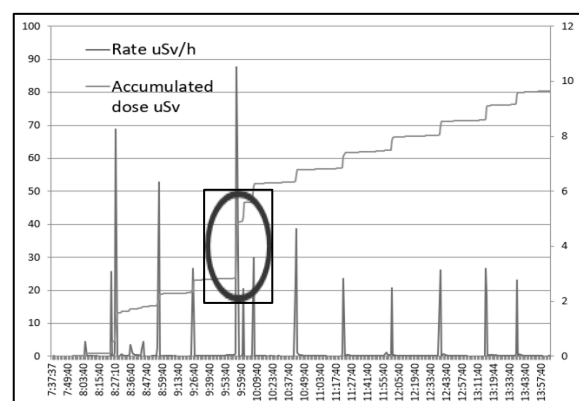


**Fig. 2.** Dynamic dose accumulation map of the technologist (Tech4) measured on November 27, 2020.

During the whole period of study exceptional cases with dose steps, higher than usual, were investigated discussing with the technologists trying to fix the problem and to secure quality of work and radiation protection of staff. In the presented case (Fig.2) it was

found that during injection of  $^{99m}\text{Tc}$  containing radiopharmaceutical to patient Tech4 experienced problems with syringe's fixation to catheter. The cost of this mistake - additional 2.04  $\mu\text{Sv}$  dose to the technician.

The data on average accumulated dose per day (Fig.3) also indicated some tendency of getting higher dose by Tech4. Under such circumstances he was advised to take an additional practical training. This information was considered additionally when analyzing the exposure doses to the fingertips.

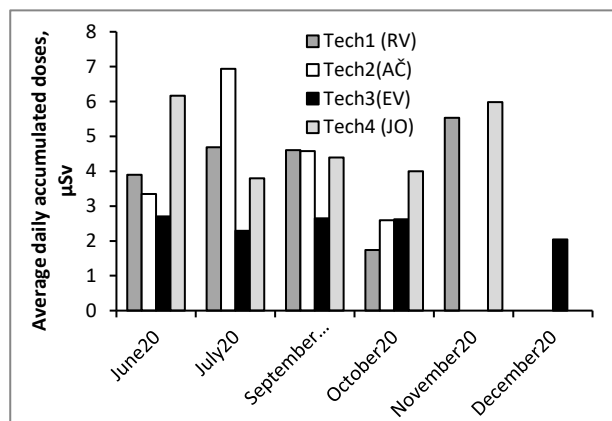


**Fig.3.** Average daily Hp(10) doses accumulated by technologists between June and December 2020

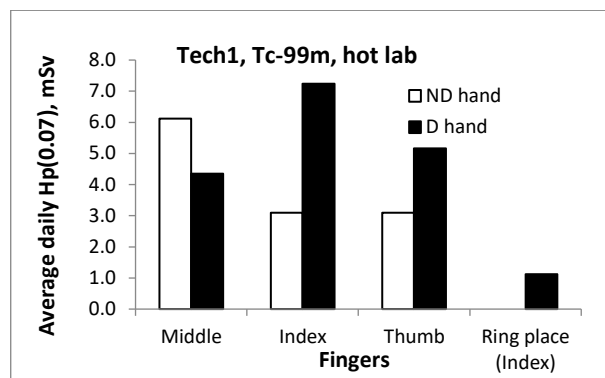
It was to expect that the doses to extremities will be higher performing preparation of radiopharmaceuticals for injections at the hot lab as compared to doses received by injecting of patients. This is due to the fact that radiopharmaceuticals preparation is related to handling of open radiation sources ( $^{99m}\text{Tc}$ ), when the whole body is protected by shielding, but the hands are directly exposed. The results of fingertip dose measurements during preparation of radiopharmaceuticals are provided in Fig.4.

Average daily doses to the fingertips when performing patient's injections with  $^{99m}\text{Tc}$  radiopharmaceuticals for Tech4 are provided in Fig.5 for the comparison.

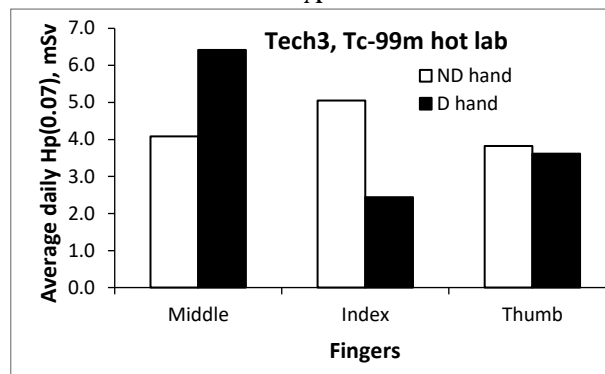
In all cases related to radiopharmaceuticals' preparation doses to different fingers of one individual varied and were different from doses registered with ring dosimeter. This supported the ORAMED [2] suggestions to change the ICRP recommendations regarding wearing of ring dosimeter on distinguished finger. Since there was no strict national regulation how ring dosimeter must be worn, every technologists was wearing the ring dosimeter based on personal convenience.

It should be noted that according the Order V-91 of the Director of Radiation Protection Centre (2020-12-29)[10] a ring dosimeter must be worn on the finger which experiences the highest exposure.

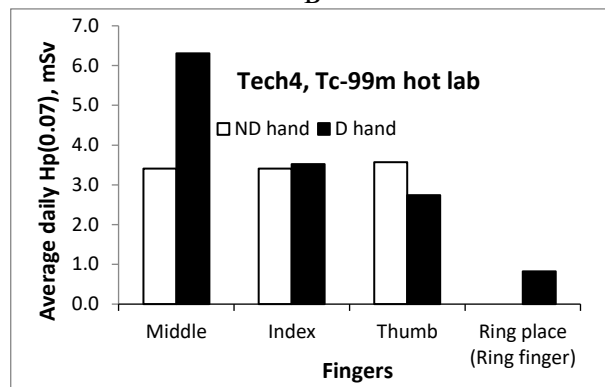
Performed investigation has shown that the highest doses were received by middle finger of the dominant hand of Tech3 and Tech4. They were advised to wear ring dosimeter on a middle finger: Tech3 was already doing this, however Tech 4 was used to wear ring on the ring finger.



A



B



C

**Fig. 4.** Average daily doses to the fingertips when working in hot lab with preparation of  $^{99m}\text{Tc}$  radiopharmaceuticals: A-Tech1; B-Tech3 and C-Tech4.

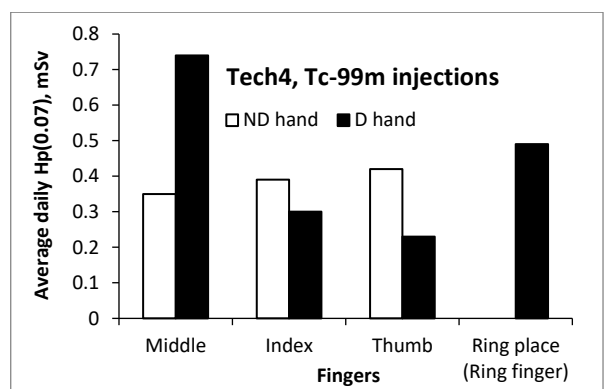


**Fig. 5.** Average daily doses to the fingertips of Tec4 when performing patient's injections with  $^{99m}\text{Tc}$  radiopharmaceuticals.

Data provided in Fig.5 indicated clearly that the average doses to fingertips received performing injections of patients was almost 10 times lower as compared with doses received by fingertips due to preparation of radiopharmaceuticals.

Doses measured at fingertips varied depending on the selected finger, hand and person and were several times higher than doses obtained from ring dosimeter measurements, thus indicating possibility of having higher than recommended exposure to extremities. However the difference between fingertip doses and doses obtained from ring dosimeter measurements was not necessarily factor of 6. (According to international recommendations, ring doses should be multiplied by a factor of 6 in order to estimate doses to fingertips.)

#### 4. Conclusions

Investigation of exposure doses to nuclear medicine department workers (technicians) during administration and preparation of radiopharmaceuticals with  $^{99m}\text{Tc}$  has been performed. Dynamic daily exposure dose maps of whole body exposure were collected and analyzed together with the doses to the hands and fingertips of personnel.

1. Registration of dynamic daily exposure dose maps was found being very practical and suitable for discussions with a staff regarding deviation in registered dose and fixing the occurred problems.
2. It was found that the doses to fingertips were depending on individual's experience, working habits and working conditions. Average daily doses to fingertips were almost 10 times higher when working in hot lab as compared to patients' injection activities. Obtained results allowed to advice technicians regarding the finger on which ring dosimeter should be worn.
3. There was no evident correlation between whole body doses and extremity doses of technicians found.

#### Acknowledgement

This research was supported by the Research and Innovation Fund of Kaunas University of Technology (project grant No. PP54/201) and the Research Fund of Lithuanian University of Health Sciences. Project acronym: BRANDUOLYS-NUCLEUS

#### 5. References

1. Adliene, D., Gričienė, B., Skovorodko, K., Laurikaitienė, J., & Puiso, J. (2020). Occupational radiation exposure of health professionals and cancer risk assessment for Lithuanian nuclear medicine workers. *Environmental research*, 183, 109144.
2. Belgian Nuclear Research Centre (SCK•CEN), Optimization of Radiation Protection of Medical Staff, <http://www.oramed-fp7.eu/en/Presentations>.
3. Tahidul Islam, M., Ferdous, J., Haque, M M Measurement of extremity doses of nuclear energy worker by using ring dosimeter, *Radiation Protection Dosimetry*, Volume 188, Issue 3, March 2020, Pages 271–275,
4. Dehghan, N., Sina, S. Measurement of operational dosimetry quantities for nuclear medicine staff, *Radiation Protection Dosimetry*, Volume 190, Issue 2, June 2020, Pages 119–124,
5. Parvaresh, R., Jalili, M., Haghighparast, A., Khoshgard, K., Eivazi, M. T., & Ghorbani, M. (2020). Evaluations for Determination of Optimum Shields in Nuclear Medicine. *Journal of biomedical physics & engineering*, 10(5), 651.
6. Alkhorayef, M., Mayhoub, F. H., Salah, H., Sulieman, A., Al-Mohammed, H. I., Almuwannis, M., & Bradley, D. A. (2020). Assessment of occupational exposure and radiation risks in nuclear medicine departments. *Radiation Physics and Chemistry*, 170, 108529.
7. Yazeed Alashban, Nasser Shubayr, Occupational Dose Assessment for Nuclear Medicine and Radiotherapy Technologists in Saudi Arabia, *Radiation Protection Dosimetry*, 2021; ncab112,
8. Eckelman, W. C. (2009). Unparalleled contribution of technetium-99m to medicine over 5 decades. *JACC: Cardiovascular Imaging*, 2(3), 364-368.
9. Hygiene Standard, 2018, Hygiene Standard HN 73:2018 Basic Standard of Radiation Protection adopted by the Order No. 663 of the Minister of Health Care (2018).
10. <https://www.e-tar.lt/portal/lt/legalAct/9f6c3bd049de11eb8d9fe110e148c770>



## **DIAGNOSTIC AND CLINICAL GRADE MEDICAL IMAGING DISPLAY PERFORMANCE EVALUATION AND OPTIMIZATION USING QUALITY ASSURANCE PROTOCOLS**

Mindaugas DŽIUGELIS<sup>1</sup>, Leonid KRYNKE<sup>2</sup>  
Vilnius University Hospital Santaros Klinikos  
<sup>1</sup>Mindaugas.Dziugelis@santa.lt; <sup>2</sup>Leonid.Krynke@santa.lt

**Abstract:** In clinical environment, diagnostic displays are important for radiologists. Based on radiographic images, they help to describe patient diagnosis for radiologists or at least give a summary based on which further decisions are made for the patient treatment. Recently released AAPM report No. 270 by the American Association of Physicists in Medicine gives updated requirements for such display evaluation. The purpose of this study was to improve medical display performance and to make it more consistent in clinical practice, which might reduce cases of patient misdiagnosing.

In total, 39 medical monitors were evaluated, and their performance criteria were compared before and after the calibration. Series of medical display performance criteria measurements were performed in three different hospital departments (nuclear medicine, conventional radiology, and computed tomography). To measure the display performance changes, testing patterns and a photometer were used. Measured medical display performance criteria consisted of illuminance, ambient luminance, maximum luminance, as well as luminance response deviation from greyscale display function and backlight uniformity.

**Keywords:** Medical displays, Quality assurance, Performance optimization.

### **1. Introduction**

It is well understood that the fundamental advantage of digitized radiological equipment can only be fulfilled when the primary image analysis also is done in a digital format [1,2]. As new digital image capturing and processing technology advances emerged over time, display imaging technology improved as well. Since medical displays are important, they must have quality assurance programs to monitor its performance criteria. Due to monitor technology changes from CRT to LCD, there was a need to reclassify them as its use became

more specific. AAPM Report No. 270 reclassified monitor quality assurance into 4 categories: diagnostic, modality, clinical, and electronic health record displays [3]. According to the Lithuanian Hygiene Norm HN 78:2009, the American Association of Physicists in Medicine [3], and the European Federation of Organizations for Medical Physics [4], medical physicists should be responsible for daily quality assurance of medical-grade display systems.

This paper provides an overview of the updated recommendations of AAPM Report 270 for a medical physicist to perform quality assurance.

### **2. Display classification**

AAPM Report 270, as mentioned, presents 4 main categories of displays:

1. Diagnostic
2. Modality
3. Clinical specialist (clinical)
4. Electronic health record (EHR) displays.

Diagnostic display type is previously recognized as primary. These displays are used for primary image interpretation and often located in reading rooms, with special lighting conditions.

Modality, clinical and EHR displays were previously (in TG 18 report) classified as secondary display category. As of now, there is a need to reclassify the secondary display class even further.

Modality displays have direct feedback to the operator of the machine modality and are used during medical image acquisition and generation. These displays have a direct impact on image appearance and therefore it is important to ensure that they meet the provided requirements of performance standards.

Clinical displays are used in a clinical environment, such as emergency department, where physicians themselves (if there is an emergency) can review images

for healthcare management decisions. The performance of this display type is important due to the decisions that can be made in clinical environment based on images viewed on these displays. However, based on the fact that these displays are lower quality in general, it is important to evaluate how well according to the recommendations these displays should be performing, whether the quality of such displays affect the smoothness of clinical work.

Electronic Health Record (EHR) displays are used for viewing images, which are obtained over the entire patients health history following the primary interpretation by a radiologist. They may be used in exam room, at a separate workstation where a referring physician is studying photos to better comprehend the diagnosis, or by a surgeon during presurgical planning. Standard consumer-grade screens without specific calibration or brightness settings may be suitable for this purpose in a facility. When poor display performance hinders efficiency or quality care, however, the QA guidelines in Report 270 for luminance performance, grayscale calibration, uniformity, and ambient light are followed.

### 3. Methods

For measurements, a Piranha RTI 657 with LightProbe L100 sensor were used (Fig. 1). X-Rite i1Display Pro monitor calibration device was used for monitor calibration (Fig. 2). Monitors were calibrated using PerfectLum™ 4.0 software. Measurements were performed before and after the calibration and then compared. Both diagnostic (primary) and clinical (secondary) type of displays were measured. While measuring, the conditions of the environment and the monitor settings must be kept identical to the ones used for medical examinations. It is essential to inspect whether the display is clean, as fingerprints and dust residues might affect emitted light optical properties – it can cause distortions or emitted light refraction.

#### 3.1. Illuminance and Ambient Luminance evaluation

In this study illuminance refers to the room's ambient light intensity. This variable, measured by a luxometer in lux units, is significant because it has a direct impact on the monitor's ambient luminance, creating reflections that can significantly influence contrast, luminance response, luminance ratio, and other related factors (fig. 3) [5,6].

The amount of light reflected from the monitor surface is referred to as ambient luminance. It may affect the viewer's ability to detect small visual details, particularly on older monitors and when low contrast differences are present. A photometer is used to measure ambient luminance (unit =  $\text{cd}/\text{m}^2$ ). There are three main types of reflection - specular (produces a distinct reflection from the environment, which is mirror-like, typical for smooth surface screens), diffuse (scatters light uniformly in all directions, such reflection is typical in matt surface screens, usually visible due to light intensity inconsistencies) and haze (might be present in both specular and diffuse reflections. As with

specular reflection, its luminance spikes in the specular direction. However, unlike diffuse reflection, this reflection of the light is proportional to the incident light. Haze reflection occurs as a result of the antiglare matte top layer).



Fig. 1. Piranha RTI 657 with LightProbe L100 sensor and its attachments.



Fig. 2. X-Rite i1Display Pro monitor calibration device.

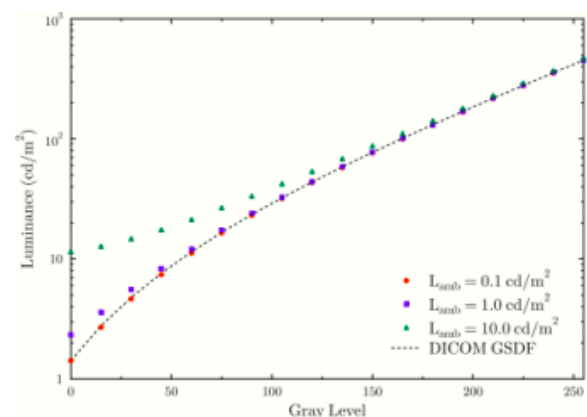


Fig. 3. Effect on display luminance of various ambient light conditions. At darker greyscale points, where display luminance is lower when the ambient light level is much higher, environmental lighting effects are most noticeable in display luminance. The display was calibrated to DICOM GSDF when  $L_{\text{amb}} = 0.1 \text{ cd}/\text{m}^2$  in this case. This shows the importance of environmental conditions when diagnostic images are evaluated – it is impossible to properly calibrate display and see proper images when ambient light is high [3].

#### 3.2. Display Luminance Response and DICOM GSDF

A LightProbe L100 sensor was used to measure a series of steadily increasing grey levels in the luminance response test. It allows to measure distinct grey levels

that are steadily growing over the whole 10-bit gray level range. Equal increments of gradually increasing greyscale brightness of 18 or 52 points, 256 points, and a whole pallet of 1024 points might be checked to determine Luminance Response. The 18-point approach was used in this study.

The luminance response curve, in general, indicates how consistent the contrast change is throughout all of the observed grey levels (as shown in fig. 5). The highest deviation from all points is calculated and expressed as a percentage. The DICOM (Digital Imaging and Communications in Medicine) GSDF (Grayscale Standard Display Function) has been adopted as a standard in measuring luminance response, according to AAPM Report No. 270.

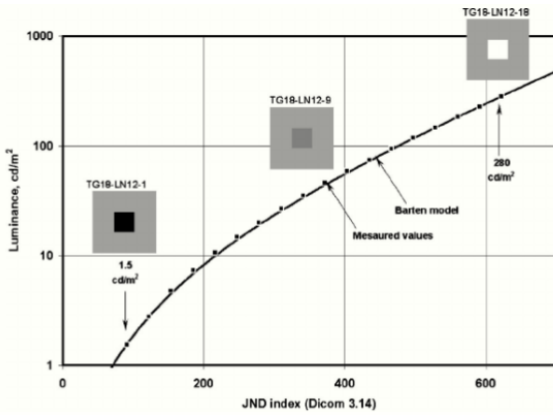


**Fig. 4.** Grayscale Standard Display Function presented as logarithm-of-luminance versus JND-Index [6]. The X-axis shows the JND index, which shows grey levels. Y-axis shows luminance in  $\text{cd/m}^2$ . As the human eye hardly notices dark images, first grayscale levels should increase in wider increments until the grey level becomes bright enough. As a result, curvature in the curve disappears as increments of luminance in grey levels become even.

The luminance response data came from Barten's model, which was based on the human visual system. The square object is displayed in a uniform background (typically at 20 % of maximum luminance). [5].

All obtained luminance values are then converted to just noticeable difference (JND) index  $j$ . The luminance gradient describes the desired JND at the Luminance  $L$ . It is a minimally distinguishable difference, that is visible to an average observer. This conversion thus provides an easy way to compare the calculated values with the intended luminance response. [3]. The coefficients  $a$  to  $m$  and  $A$  to  $I$  for equations are given in table 1.

These are the equations to convert between luminance,  $L$ , and JND index,  $j$  (equation 1 is used when JND indexes are known, equation 2 is used when luminance values in  $\text{cd/m}^2$  for each greyscale value are known) [3]:

$$\log_{10} L(j) = \frac{a + c \cdot \ln(j) + e \cdot \ln^2(j) + g \cdot \ln^3(j) + m \cdot \ln^4(j)}{1 + b \cdot \ln j + d \cdot \ln_2 j + f \cdot \ln_3 j + h \cdot \ln_4 j + k \cdot \ln_5 j} \quad (1)$$

$$j(L) = A + B \cdot \log_{10}(L) + C \cdot \log_2(10(L)) + D \cdot \log_3(10(L)) + E \cdot \log_4(10(L)) + F \cdot \log_5(10(L)) + G \cdot \log_6(10(L)) + H \cdot \log_7(10(L)) + I \cdot \log_8(10(L)) \quad (2)$$

**Table 1.** DICOM GSDF Conversion Coefficients [3].

JND to Luminance		Luminance to JND	
a	-1.3011877	A	71.498068
b	-2.5840191E - 02	B	94.593053
c	8.0242636E - 02	C	41.912053
d	-1.0320229E - 01	D	9.8247004
e	1.3646699E - 01	E	0.28175407
f	2.8745620E - 02	F	-1.1878455
g	-2.5468404E - 02	G	-0.1801434
h	-3.1978977E - 03	H	0.14710899
k	1.2992634E - 04	I	-0.017046845
m	1.3635334E - 03		

After that, mean JND for each GSDF level is measured using the formula [3]:

$$\text{mean} \frac{\Delta JND}{L_{\text{gray level}}} = \frac{j(L'_{\text{max}}) - j(L'_{\text{min}})}{L_{\text{max gray level}} - L_{\text{min gray level}}} \quad (3)$$

Where the denominator is equivalent to the difference of the minimal and maximum gray levels. Because the aim of the GSDF curve is to have an equivalent number of JND indices across each gray level, the average  $\Delta JND/GL$  is the number of JND index that would be present for each gray level on a GSDF capable display. Next in the study, the  $\Delta JND/GL$  across each observed gray level was compared to the mean  $\Delta JND/GL$  to determine the error at each measured phase.

There is an additional parameter to add, which takes into account the contrast threshold model. Equation 4 describes the slope of the luminance response function in the plot of gray level vs. luminance [3]. As observers' eyes cannot detect as sharply differences of contrast in high levels of luminance, the curve of GSDF is not linear. Relative contrast is indicated as  $dL/L$ .

$$\frac{dL}{L} \text{ per } JND = \frac{2(L'_i - L'_{i-1})}{(L'_i + L'_{i-1})(\text{mean} \frac{\Delta JND}{GL})(L_{i \text{ grey level}} - L_{i \text{ grey level}-1})} \quad (4)$$

### 3.3. Display luminance uniformity

Display luminance uniformity shows the display luminance consistency over the entire screen. This is measured using TG18-ULN10 (dark background) and TG18-ULN80 (bright background) test patterns, where luminance is measured in five different screen places using a photometer and after that, the deviation is calculated using the formula:

$$200 \times \frac{L\% \text{ maximum dev.} - L\% \text{ minimum dev.}}{L\% \text{ maximum dev.} + L\% \text{ minimum dev.}} \quad (5)$$

### 3.4. Display Calibration

Since the actual luminance (and thus perceived contrast) characteristics of various LCDs may fluctuate significantly, calibration of these monitors' luminance response is needed to ensure that users' perception of the image is consistent. As previously stated, medical displays must meet the requirements outlined in earlier sections. The luminance response of the screen can be fixed with calibration. The main goal for this is to

ensure the best possible contrast and luminance appearance for radiographic images.

Because LCDs contain a backlight that tends to decrease its luminance output over time, the lowest and maximum luminance ( $L_{\min}$ ,  $L_{\max}$ ) should be established initially when calibrating a display. It usually is measured while determining the contrast ratio. Color displays typically have contrast ratios of 250 to 400, whereas grayscale displays can have contrast ratios of 600 or more when brand new [7]. To properly select the desired maximum luminance, it is essential to note that during calibration, peak luminance might vary according to mathematical calculations applicable to Barten's model [7].  $L_{\min}$  is frequently chosen to be greater than the minimum value for the same reason.

Following the selection of  $L_{\min}$  and  $L_{\max}$  values,  $JND_{\min}$  and  $JND_{\max}$  values are calculated using conversion equation no. 2, which was previously demonstrated with coefficients (see table 1). The difference between  $JND_{\min}$  and  $JND_{\max}$  represents the distribution of each greyscale point. A display with a minimum luminance of 0.5 cd/m<sup>2</sup> and a maximum luminance of 200 cd/m<sup>2</sup> corresponds to 46.6  $JND_{\min}$  and 572.2  $JND_{\max}$ , respectively. The overall JND difference is 525.6, as shown. A full palette of greyscale consists of 256 values because most screens have 8-bit images. The main technical calibration goal is to set luminance levels for each digital driving level (every possible brightness value of, in this case, grey levels, shortened as DDL) input value in such a way that the difference in JND index changes consistently over the DDL range (DDL increment changes in GSDF when the display is calibrated and uncalibrated to DICOM GSDF are shown in GSDF curve example in figure 5). To do so, the total number of JNDs is divided by the total number of DDLs, then subtracted by one. The average number of JNDs per single DDL on the calibrated display is specified below ( $JND_{\text{ave}}$ ). As a result,  $JND_{\text{ave}}$  is equivalent to  $525.6/255 = 2.06$ . The formula is then used to calculate each DDL:

$$JND_{DDL} = JND_{\min} + DDL \times JND_{\text{ave}} \quad (6)$$

Then for each DDL to obtain luminance values, equation no. 1 is used.

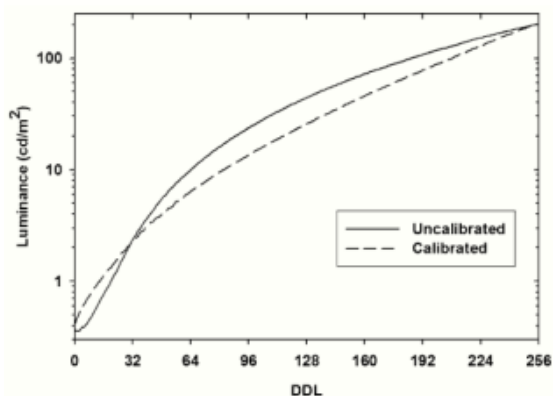


**Fig. 5.** Luminance intensity examples for calibrated and uncalibrated displays for every digital driving level (DDL) of grayscale palette [7].

A look-up table (LUT) must be created after getting JND and luminance values. It's a file that generates new DDL values for each DDL that matches the DICOM GSDF. This file can give instructions to turn input values into specific output values for each DDL using a specific software (e.g., pacsDisplay). The program can then modify the profile of the existing display, resulting in properties that are more likely to comply with the DICOM display standard. This conversion is straightforward, although it isn't without flaws. Overall perceptual contrast is satisfied by 8-bit to 8-bit calibration, but adjacent input pixel values (subpixel red, green, and blue values can be adjusted and manipulated for colored monitors to gain better contrast and more accurate DDL values) remain unchanged; as a result, adjacent input levels drastically change, leaving the monitor with poor contrast and missing grey shades (as transitions might be too drastic in some grey levels). It cannot be an adequate calibration since 8-bit-to-8-bit calibration frequently leads to local contrast loss as well as excessively increased local contrast. It can be stated that grayscale calibration based on the initial luminance measurements at every possible level of LUT value gives the best calibration quality as it is, related to how many points are adjusted for a better match to DICOM GSDF. If every point has been adjusted, the quality of calibration will be the best possible. So, for more precise calibration, each sub-pixel value has to be modified. Commonly, sub-pixel values are adjusted so that all three of them increase at least by 1 level and, therefore, depend on each other. Independent sub-pixel adjustment allows to obtain more than 256 gray values and therefore is called bit stealing, otherwise known as spatial dithering [8, 9].

Monochrome monitors can display 766 gray color tones, while colored monitors can display up to 1786 gray color tones[10,11]. This allows a more accurate match DICOM GSDF model. Compared to the 8-bit palette, there is more choice of possible grey levels to match each grey value for DICOM GSDF after bit stealing. This leads to a possibility to calibrate a monitor that more closely resembles an ideal curve.

With bit stealing, several vendors have used temporal modulation of subpixels to further improve the luminance value distribution throughout all LUT palette levels [8]. Temporal modulation improves the time-averaged luminance output by using fast sequential adjustments in the luminance output of individual subpixels. It works at an undetectable pace for the human eye to notice.

It is important to note that display calibration to DICOM GSDF only ensures that all displays would perform at their best. The overall appearance of medical images can vary depending on different factors like image acquisition parameters (mAs, peak kilovoltage (kVp), etc.) of scanning machine (i.e., CT scanner, X-ray machine, or other modality). Image processing algorithms, which improve over time, are tools that can change display contrast also might help to better visualize medical images along with greyscale transformation mechanisms integrated into PACS program user interface [7].

#### 4. Results

The first criteria measured in medical-grade display evaluation is display luminance. It includes illuminance, ambient luminance, maximum luminance, and luminance response function (otherwise known as Greyscale Standard Display Function). Those parameters are dependant on each other. Suggested limits of monitor luminance levels are published in AAPM's released report TG 270, which set standards for display luminance criteria of primary (mammographic diagnostic and non-mammographic diagnostic) and secondary (modality, clinical, and electronic health record) displays.

Investigated parameters were monitor minimum and maximum illuminance, ambient luminance, luminance response deviation from greyscale display function, monitor backlight uniformity, veiling glare, and noise. In total, 28 diagnostic and 11 clinical displays were evaluated.

**Table 2.** Monitor count of passed acceptance criteria before and after the calibration. Letter C indicates clinical monitor type, D – diagnostic monitor type.

	Before calibration		After calibration	
	C	D	C	D
Illuminance	19 out of 39		19 out of 39	
Ambient light	3 out of 11	5 out of 28	3 out of 11	5 out of 28
L' max	2 out of 11	11 out of 28	4 out of 11	10 out of 28
Luminance response	0 out of 11	13 out of 28	11 out of 11	24 out of 28
Luminance uniformity	37 out of 39			

From all measurements after calibration, four monitors in total (3 from conventional radiology, one from the CT department) failed the luminance response test after calibration, all of them were diagnostic types. These monitors were impossible to calibrate. Part of the reason was that they were very old and worked for a very long time.

One sample t-test was performed for the diagnostic monitors to evaluate whether the true mean from the measured sample exceeds recommended 10% value. The test showed that the true mean deviation of the tested sample values was 6.02% ( $t = -5.4$ ,  $df = 27$ ,  $p = 5.04 \times 10^{-6}$ ). This means that the average DICOM GSDF deviation from all measured diagnostic type monitors was not significantly higher than 10%. After initial measurements, the minimum deviation of diagnostic monitors was 1.4 %, maximum for this type reached 15.1%.

All clinical type monitors passed this criterion; therefore, no statistical analysis was performed, as in such a case, it is evident that the mean DICOM GSDF deviation was lower than 20%. After initial measurements, the minimum deviation of clinical monitors was 2.1%, the maximum for this type reached

18.3%, and the mean deviation of all measured clinical type monitors of this type reached 7.9% deviation.

After comparing clinical type display measured values of DICOM GSDF absolute deviation percentage in just noticeable difference per grey level (JND/GL) before and after calibration using Student Two Sample t-test, the true difference in means was significant with p-value of  $2.128 \times 10^{-9}$ , ( $t = 11.1$ ,  $df = 17.8$ ). Comparing the true difference in means for diagnostic monitor type, Student Two Sample t-test showed significant difference as well ( $t = 4.3$ ,  $df = 28.2$ ,  $p\text{-value} = 0.0002$ ). This indicates that for both clinical and diagnostic monitors, calibration improved DICOM GSDF parameter, according to AAPM recommendations significantly reducing its absolute deviation percentage in just noticeable difference per grey level.

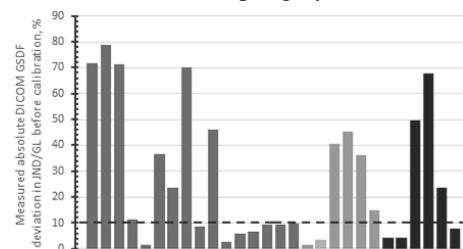


**Fig. 6.** Diagnostic monitor type average luminance response deviation percentage before calibration.

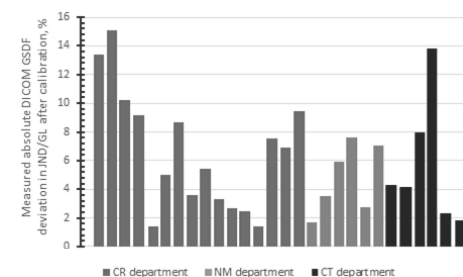


**Fig. 7.** Diagnostic monitor type average luminance response deviation percentage after calibration.

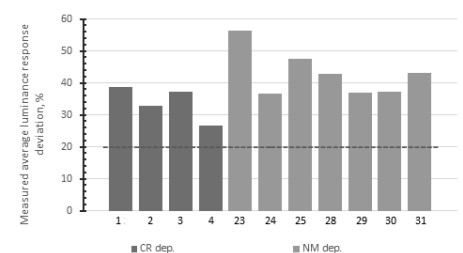


**Fig. 8.** Clinical monitor type average luminance response deviation percentage before calibration.

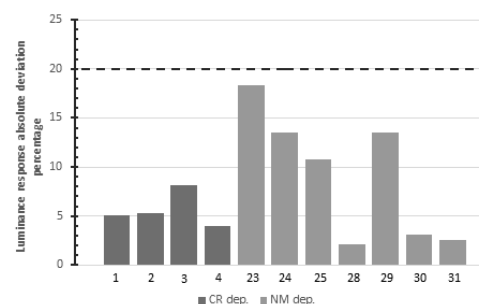


**Fig. 9.** Clinical monitor type average luminance response deviation percentage after calibration.



While comparing the average luminance response deviation percentages per each DDL (as shown in figure 10) for all monitors, it is evident that each DDL error decreased. The most noticeable change (14.8 % improvement) was in the 15th display driving level (DDL 15), where the error was the largest after initial measurements (19.6%). Also, the smallest change (2.1% improvement) was in the 120th display driving level, which after initial measurements had the smallest error from the ideal result (5.3%).

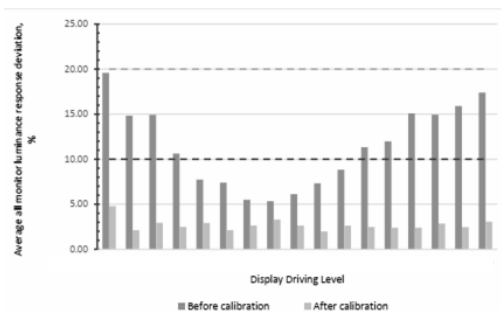


**Fig. 10.** Average all monitor luminance response deviation (measured in percent) per each DDL (display driving level) before and after the calibration. The top dashed line indicates the maximum allowed average error for diagnostic type displays; the lower dashed line indicates the maximum allowed error for the clinical (secondary) type of displays.

## 5. Conclusions

In this work, 39 monitors including 28 diagnostic (primary) and 11 clinical (secondary) type were evaluated, and their performance parameters before and after calibration were compared. Measurements were performed in three different departments (nuclear medicine, conventional radiology, and computed tomography).

It was found that after the calibration the performance of the monitors according to the luminance response criteria has been improved from 33% to 89%, while other parameters were not improved significantly.

When comparing DDL value errors before and after calibration, the largest improvement was in the 15th DDL value - 14.8% decreased error from the GSDF

curve model. The largest errors before calibration were measured at terminal DDL values, which showed the most noticeable improvement after the calibration.

## 6. References

1. Scharitzer M., Prokop M., Weber M., Fuchsiger M., Oschatz E., Schaefer-Prokop C. Detectability of catheters on bedside chest radiographs: comparison between liquid crystal display and high-resolution cathode-ray tube monitors. *Radiology*, 2005. 234, p. 611 - 616.
2. Balassy C., Prokop M., Weber M., Sailer J., Herold C.J., Schaefer-Prokop C. Flat-panel display (LCD) versus high-resolution gray-scale display (CRT) for chest radiography: an observer preference study. *Am J Roentgenol.*, 2005. 184, p.752–756.
3. Bevins N. B., Flynn M. J., Silosky M.S., Marsh R. M., Walz-Flannigan A. I., Badano A. "Display Quality Assurance. The Report of AAPM Task Group 270." American Association of Physicists in Medicine, 2019. 77 p.
4. Gennaro G., Avramova-Cholakova S., Azzalini A., Luisa Chapel M., Chevalier M., Ciraj O., Torresin A. Quality Controls in Digital Mammography protocol of the EFOMP Mammo Working group. *Physica Medica*, 2018. p. 55-64.
5. Ekpo E. U., McEntee M. F. An Evaluation of Performance Characteristics of Primary Display Devices. *Journal of Digital Imaging*, 2015. 29, p. 175–182.
6. Digital Imaging and Communications in Medicine (DICOM) Part 14: Grayscale Standard Display Function, National Electrical Manufacturers Association, 2011.
7. Krupinski E. A. Medical Grade vs Off-the-Shelf Color Displays: Influence on Observer Performance and Visual Search. *Journal of Digital Imaging*, 2008. 22, p. 363–368.
8. Blume H. R., Ho A. M. K., Stevens F., Steven P. M. Practical aspects of grayscale calibration of display systems. *Medical Imaging*, 2001. 4323, p. 28-41.
9. Ogawa E., Shimura K. Appearance matching of radiographic images using lightness index. *Medical Imaging*, 1999. 3663, p. 20-26.
10. Tyler C. W., Chan H., Liu L., McBride B., Kontsevich L. L. Bit stealing: how to get 1786 or more gray levels from an 8-bit color monitor. *Human Vision, Visual Processing, and Digital Display III*, 1992. 1666, p. 1-15.
11. McEntee M. F., Toomey R. J. Display Optimization from a Perception Perspective. *The Handbook of Medical Image Perception and Techniques*, Ch. 30, Cambridge University Press, 2018. p. 452–469.



## APPLICATION OF 3D PRINTED INDIVIDUAL COMPENSATING BOLUS FOR THE VERIFICATION OF SHALLOW HEAD AND NECK CANCER TREATMENT

Kamilė DAMBRAUSKAITĖ<sup>1</sup>, Jurgita LAURIKAITIENĖ<sup>2,3</sup>, Artūras ANDREJAITYS<sup>3</sup>

<sup>1</sup>Kaunas University of Applied Sciences; <sup>2</sup>Kaunas University of Technology, Kaunas, Lithuania; <sup>3</sup>Hospital of Lithuanian University of Health Sciences Kaunas Clinics, Oncology Hospital

<sup>1</sup>kamile.dambrauskaite@go.kauko.lt; <sup>2</sup>jurgita@medicinosfizika.lt

**Abstract:** Bolus is used as an additional body to ensure the delivery of appropriate irradiation dose for shallow tumours. The aim of this study was to apply an individualised 3D printed polylactic acid (PLA) boluses for a simulated case of shallow head and neck cancer on the anthropomorphic phantom “Shane”. Obtained results showed that the 3D minimum dose of the planned tumour volume increased more than 30 % in comparison with a plan without individualised 3D printed bolus. Therefore, 3D printed bolus could be successfully used in clinical practice to provide an adequate superficial tumour irradiation.

**Keywords:** radiation therapy, 3D printing, compensating bolus

### 1. Introduction

Radiotherapy aims at accurately targeting tumours with sufficient dose while preserving as much healthy tissue as possible. Radiotherapy are frequently delivered using photons with energies in the megavoltage (MV) range. The benefit of such beam energies is that the majority of the dose is delivered deeper inside the patient, with maximum dose depths reaching several centimetres below the patient's surface. Because of this effect, radiotherapists may target tumours on organs such as the prostate. On the other hand, larger dose often must be deposited to the near-skin area, for example, in cases of head and neck cancer. Thus, the most important aspects to consider when irradiating surface and shallow tumours are achieving conformal dose distribution in tumour area while protecting healthy tissues. In such clinical cases, one way of solving the issue may be the use of an additional body, also known as a bolus. It provides a water equivalent material with sufficient coverage of the tumour and a uniform dosage delivery. However, the problem is that commercially available boluses made of sheet gels are difficult to apply to certain uneven skin surfaces, such as those of the nose, ears, eyes, and scalp. The air gap between the bolus and

the skin is the most significant problem with these flat boluses, particularly when using a high-energy beam which may reduce the surface dosage [1]. Therefore, the new and relevant technique of three-dimensional (3D) printed patient-specific bolus was suggested to increase the irregular surface dose and improve dose delivery to the tumour in the build-up region.

A lot of studies show successful results for the implementation of 3D printed bolus in radiotherapy treatment. For example, *J. Robar et al.* [2] compared 3D printed polylactic acid (PLA) bolus used for the chest wall radiation therapy with a standard sheet bolus. Analysis of the formed air gaps showed that using a standard sheet bolus, air gaps of >5 mm were formed for ~30% of all irradiated fractions, while 13 % of the patients air gaps were reduced with 3D printed bolus.

*D. Kang et al.* [1] showed, that a low-cost, 3D printed, patient-specific bolus printed of commonly available materials offered a better dose distribution than the one with a standard flat bolus, having better dose coverage to the PTV and dose conformity. 3D surface was created and printed using a cell phone camera for acquiring surface images. Plan with 3D printed bolus showed improved coverage of 95% volume for the PTV (95.65% (3D-printed bolus), while using flat bolus coverage was equal to 88.39%). *K. Fujimoto et al.* [3], reported a shift of the dose distribution towards the surface by 0.3 cm while using 0.5 cm thickness 3D printed bolus in comparison with plan without bolus. The  $d_{max}$  values for the bolus-free and 3D-bolus cases are 0.9 and 0.6 cm, respectively

The most important feature of individualized boluses is that they improve dose homogeneity in the irradiated tumour, especially in the case of shallow tumours. However, when irradiating irregular and curved surfaces of the body or postmastectomy scars, the traditional bolus with a smooth surface can not be fully attached to the skin and an air gaps might be formed in between. It is known, that for air gap of > 5 mm, the surface dose

decreases to ~90% [4,5]. In such cases, patient-specific compensating boluses can be successfully used.

**The aim** of this study was to assess the role of individualised 3D printed PLA compensating bolus in external beam radiotherapy, while imitating treatment of shallow head and neck cancer.

## 2. Materials and methods

**Printing:** Individualized 3D printed polylactic acid (PLA) bolus was used for simulating shallow head and neck cancer irradiation with high-energy photons 6 MeV. Polylactic acid (PLA) material was chosen to print boluses with 90 % infill ratio, due to its properties being similar to soft tissues (78 HU and 1.06 - 1.43 g/cm<sup>3</sup>). The main problem of shallow tumours radiotherapy is insufficient irradiation of the surface and insufficient protection of OARs in the vicinity of the tumour. Due to this, two patient-specific boluses were fabricated and used for imitation of shallow tumour irradiation for head and neck patient/ anthropomorphic phantom Shane (Fig. 1). Three different cases were analysed: 1) without 3D printed PLA bolus; 2) with standard 1 cm thickness 3D printed PLA bolus; 3) with individualised compensating 3D printed PLA bolus.

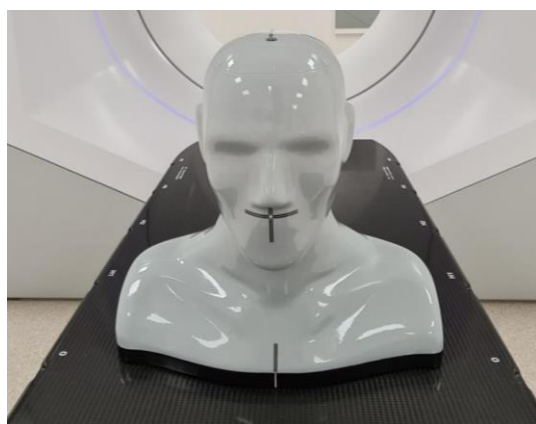


Fig. 1. Anthropomorphic phantom Shane

The main workflow of reconstruction, printing 3D PLA boluses and their use in radiotherapy is presented in Figure 2.

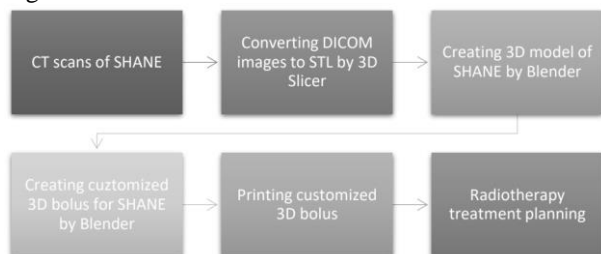


Fig. 2. Workflow for reconstruction and printing 3D PLA boluses

3D printed individualised PLA standard and compensating boluses (Fig. 3) were printed using PLA printing material. It is known, that PLA is tissue-equivalent and mostly similar to water or soft tissues. Also, according to other studies [6] PLA is a non-toxic and does not undergoes any shrinking upon cooling, which ensures that geometrical integrity would be maintained during printing process. Printing was

performed using 3D printer Zortax M300 at Kaunas University of Technology, Department of Physics.

Using the same 3D printing scheme, two boluses were printed: 1) standard 3D printed PLA 1 cm thickness bolus and 2) compensating bolus: the red area of 2.5 cm thickness over the eyeball; the blue area - about 1 cm thickness around the eye region; and remaining part of the bolus is 0.5 cm thickness (Fig. 3).

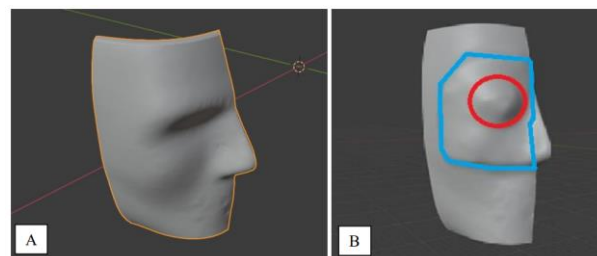


Fig. 3. Image of 3D individualized standard 1 cm thickness (A) and compensating (B) boluses

**Radiotherapy treatment planning:** Dose distribution evaluation for the planning target volume (PTV) and organs at risk (OARs) volume depends on the type and thickness of 3D printed individualised bolus. 3D treatment planning system (TPS) Eclipse (Varian Medical Systems) was used for treatment planning, evaluating effect of used 3D printed boluses.

Three volumetric modulated arc therapy (VMAT) plans were created for the evaluation of dose distribution without bolus and with two different individualised 3D printed boluses. Radiotherapy treatment plans were created, using the same irradiation parameters: triple coplanar clockwise (CW)/counter-clockwise (CCW) arcs, 6 MeV photon energy beams, and were planned for Halcyon 1378 medical linear accelerator. The radiation dose of 66 Gy/33 fractions was prescribed.

Planning target volume (PTV) and all organs at risk (OARs) were delineated imitating nasopharynx cancer case irradiation procedure. All three plans data were compared using isodose distribution and dose volume histograms (DVHs). Using DVHs for the target volume and OARs,  $D_{max}$ ,  $D_{min}$ ,  $D_{mean}$  or certain volume of irradiated structure could be analysed depending on evaluated organ or target.  $D_{max}$ ,  $D_{min}$ ,  $D_{mean}$  represent the maximum, minimum and mean doses for the target or OAR volume, respectively.

## 3. Results

Evaluation of the dose distribution for the phantom Shane imitating shallow tumour irradiation procedure showed insufficient surface dose coverage for VMAT plan with no bolus. The isodose was shifted from the surface to the phantom by 0.6 cm (evaluating minimum recommended 95% coverage of PTV). 3D minimum dose for PTV was equal to 48.2% and 3D mean dose for PTV was equal to 98.9 (Fig. 4). It is important to mention that the minimum successful target coverage ranges from 95% to 107% [7]. This means, that for this case the target is not irradiated sufficiently since the coverage is less than recommended (< 95%).

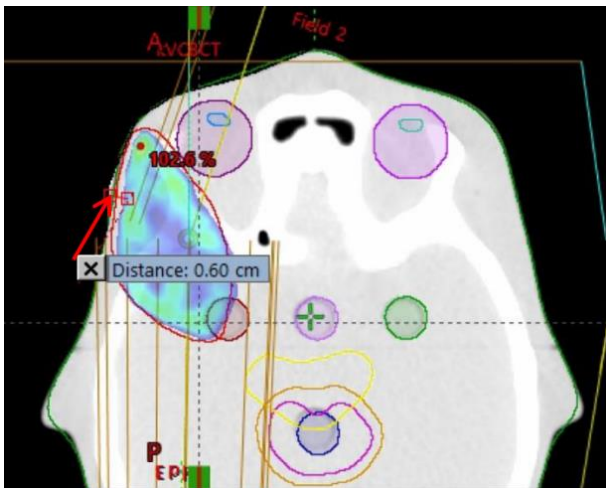


**Fig. 4.** Radiotherapy treatment plan without bolus (red arrow shows the shift of the isodose of 95 % inside the volume of the phantom)

Analysing DVH results, it was observed that 95% (usually only the 95% limit is used for plans evaluation; however, due to VMAT technique ability to ensure higher coverage of the target, it is recommended to also evaluate 98% and 99% dose coverage [8]), 98% and 99% dose coverage of the PTV volume was lower than recommended in this case. According to the DVH of PTV, 95% of the target volume was irradiated with 94.60 % of the prescribed total dose (66 Gy), 98% of PTV volume was covered with 91.40% dose and 99% - 88.00% of prescribed dose. These results also show that the tumour was not irradiated sufficiently when irradiating anthropomorphic phantom Shane without bolus. The same tendency was observed by *S. Kim et al.* In this study, reported  $D_{max}$ ,  $D_{min}$  and  $D_{mean}$  of the target volume were 101.3%, 25.4% and 86.4%, respectively. As a result, the lack of the coverage may lead to disease recurrence. It is known, that after radical treatment of head and neck cancer, about 20–50 % of patients are diagnosed with locoregional recurrence during the first two years [9].



**Fig. 5.** VMAT plan with 3D printed patient-specific bolus

It is important to highlight that formed air gaps in between the phantom and bolus were less than 0.2 cm, thus evaluation of the dose difference resulting from the air gaps was not done. It was found, that using individualised 1 cm thickness 3D printed PLA bolus, the isodose of 95% of coverage was shifted towards the

surface and the 3D minimum dose increased to 74.3% (Fig. 5).

In external radiotherapy, even though technologies have improved for conformal delivery of prescribed dose to the tumour, the healthy tissues are unavoidably irradiated. Because a standard 3D printed bolus does not give significant OAR protection, in order to spare OAR's, 3D printed compensating bolus was used, which give higher OAR protection.

The 3D printed compensating bolus created airgaps up to 0.6 cm in the 0.5 cm thickness region, however this had no effect on the irradiation treatment plan because that zone was not analysed. Air gaps arise because of the thermal action during printing and the temperature difference during cooling. In the eyes and nose region, bolus thickness of 1 cm and 2.5 cm were measured, with created airgaps of up to 0.2 cm, as in the first 3D printed standard bolus.

It was observed, that implementing patient-specific 3D printed compensating bolus increase the 3D minimum dose for PTV to 75.7 % (Fig. 6). Based on the DVH of PTV, 95% of the target volume was irradiated with 95.00 % of the prescribed dose, 98 % of PTV volume was covered with 92.60 % dose and 99% - 90.30 % of prescribed dose. Therefore, results show that using 3D printed compensating bolus can improve superficial tumour irradiation.



**Fig. 6.** VMAT plan with 3D printed patient-specific compensating bolus

On the other hand, even though 3D minimum dose coverage does not differ significantly while using both boluses, isodose distribution shows some important results.

Therefore, the isodose of 52.8 Gy slightly covers the right eyeball in the plan with 3D printed standard bolus. While the plan with 3D compensating bolus, the isodose is shifted away from the right eyeball (Fig. 5 and Fig.6). Therefore, 3D printed compensating bolus can successfully protect the OAR from harmful dose.

According to DVH, maximum dose for 99.4% of right eyeball volume was 60.189 Gy in plan without bolus, whereas with added compensating bolus  $D_{max}$  was 56.138 Gy. 87.8 % of optic nerve volume is irradiated with  $D_{max}$  57.988 Gy and  $D_{max}$  55.523 Gy for the plan with compensating bolus (Fig. 7). 3D maximum dose for right eyeball, optic nerve, midbrain, pons and medulla, optic chiasm and right eye lens were lowered by 5.10 %, 2.70 %, 16.43 %, 12.56 %, 44.81 % and 20.72 %, respectively. According to these results, 3D

printed compensating bolus perfectly fulfils its function by replacing missing tissues and shielding the OAR.

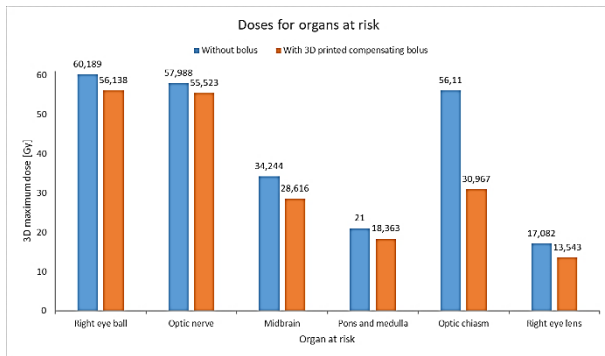


**Fig. 7.** Histogram that shows 3D maximum dose for OAR's for two plans: without bolus and with 3D printed compensating bolus

#### 4. Conclusions

1. Bolus as an additional body is successfully used for shallow tumour irradiation, using high-energy photons. The main problem occurs regarding uneven and/ or concaved surface of patient's body (especially important for head and neck cancer cases), leading to the formation of air gaps between the patient and bolus (up to few cm) that influence dose distribution. This problem could be solved using so called individualised, for example, 3D printed boluses, minimizing air gaps up to 5 mm. Therefore, the efficiency of the treatment procedure could be ensured and probability of disease recurrence reduced.
2. 3D printed individualised polylactic acid (PLA) boluses were reconstructed according to the CT scans of anthropomorphic phantom Shane, using the smallest slice thickness (0.25 cm). Since boluses are usually used to imitate soft tissues, 3D boluses were printed with polylactic acid (PLA) at 90% infill ratio owing to the fact that soft tissues equivalent properties (78 HU and 1.06 - 1.43 g/cm<sup>3</sup>) can be achieved at this infill ratio.
3. Three different cases of treatment planning (without bolus, with standard 3D printed individualised PLA bolus and with compensating 3D printed individualised PLA bolus) were analysed. It was found, that without bolus, the planning target volume (PTV) coverage was insufficient (Dmin (48.2 %)), while coverage of PTV was significantly increased using standard 3D printed PLA bolus (Dmin (74.3 %)) and compensating 3D printed PLA bolus (Dmin (75.7%)). Furthermore, using

compensating bolus, it was observed that doses of organs at risk (OARs) were minimized (right eyeball (5.10 %), optic nerve (2.70 %), midbrain (16.43 %), pons and medulla (12.56 %), optic chiasm (44.81 %) and right eye lens (20.72 %)). Thus, 3D printed individualised standard and compensating boluses could be successfully used in a clinical practice in order to irradiate tumour sufficiently, avoiding possible cancer recurrence.

#### 5. References

1. Kang D., Wang B., Peng Y., Liu X., Deng X. Low-Cost iPhone-Assisted Processing to Obtain Radiotherapy Bolus Using Optical Surface Reconstruction and 3D-Printing. *Scientific Reports*. 2020 Dec 1;10(1).
2. Robar J.L., Moran K., Allan J., Clancey J., Joseph T., Chytko-Praznik K., et al. Inpatient study comparing 3D printed bolus versus standard vinyl gel sheet bolus for postmastectomy chest wall radiation therapy. *Practice in Radiation Oncology*. 2018 Jul 1;8(4):221–9.
3. Fujimoto K., Shiinoki T., Yuasa Y., Hanazawa H., Shibuya K. Efficacy of patient-specific bolus created using three-dimensional printing technique in photon radiotherapy. *Physica Medica*. 2017 Jun 1; 38:1–9.
4. Zhang Y., Han N., Zhang N. Application value of 3D-printed Bolus in radiotherapy after radical mastectomy. 2021 Mar 26.
5. Jreije A.; Keshelava L.; Ilickas M.; Laurikaitiene J.; Urbonavicius B.G.; Gabrielis; Adliene D. Development of patient specific conformal 3D-printed devices for dose verification in radiotherapy // *Applied sciences*. Basel: MDPI. ISSN 2076-3417. 2021, vol. 11, iss. 18, art. no. 8657, p. 1-12.
6. Kim S., Kwak J., Cho B., Song S.Y., Lee S.W., Jeong C. Clinical Implementation of 3D Printing in the Construction of Patient Specific Bolus for Photon Beam Radiotherapy for Mycosis Fungoides. 2017;
7. Atiq M., Atiq A., Iqbal K., Shamsi Q., Andleeb F., Buzdar S.A. Evaluation of dose conformity and coverage of target volume for intensity-modulated radiotherapy of pelvic cancer treatment. *Indian Journal of Cancer*. 2017 Jan 1;54(1):379–84.
8. Palmans H., Andreo P., Huq M.S., Seuntjens J., Christaki K.E., Meghzifene A. Dosimetry of small static fields used in external photon beam radiotherapy: Summary of TRS-483, the IAEA–AAPM international Code of Practice for reference and relative dose determination. *Medical Physics*. 2018 Nov 1;45(11):e1123–45.
9. Rudzianskas V., Kupcinskaite, Noreikiene R. Re-irradiation for Recurrent Head and Neck Cancer. In: *Radiotherapy*. InTech; 2017.



## **MASTER’S PROGRAM IN MEDICAL PHYSICS IN ENGLISH**

Todorka L. DIMITROVA

University of Plovdiv “Paisii Hilendarski”, 24 Tsar Asen St., 4000 Plovdiv, Bulgaria  
tldimitrova@abv.bg

**Abstract:** Medical Physics is an important field of contemporary scientific research, leading to innovative technologies with vast application in medicine. This raises the need for well-educated and trained specialists, as well continuous lifelong learning. In 2012 Medical Physics was recognized as a profession at international level, therefore European countries started to give more attention to the legislation concerning the medical application of ionizing radiation. This way more emphasis was given to Medical Radiation Physics, and it also reflected on educational programs. The number of master programs in Medical Physics increases worldwide. However, they differ not only in every country, but also in every university, depending on available equipment in medical centers, training of lecturers, and how adequately equipped student laboratories are. However, there is a need to define an obligatory set of disciplines by developing a professional profile based on competences. The common efforts of different national and international institutions are needed. The expected result is the modernization and synchronization of education and meeting hospital needs.

**Keywords:** High Education, Master Program, Medical Physics, Medical Physicist

### **1. Introduction**

The participation of qualified experts in Radiation Protection during any activity with ionizing radiation, including medical applications has been requested since 1997 by EC Directive 97/43/Euratom [1]. However, Medical Physics has been recognized as profession only since 2012. It has been included at the International Standard Classification of Occupation under the standard ICSO-08 in both professional directions: Physics and Engineering, and Healthcare.

The trend has been set and recommendations for academic education and training in Medical Physics (MP) has been given by EFOMP and IOMP Policy Statements [2-6]. All of them are applicable only to Medical Physicists working with ionizing radiation.

These recommendations are specific to different areas of Medical Radiation Physics and depend on the national legislation, economy, education, healthcare, etc. IOMP Policy Statement No.2 requires that “The minimum educational qualification for an MP is a university degree (level corresponding to a master’s degree) or equivalent majoring in medical physics or an appropriate science subject.” [6]. This also includes requirements for Professional Training and for Professional Certification.

In Bulgaria, the statute of Medical Radiological Physicists is established via state regulations for standards in Radiotherapy [6] and in Medical Imaging [7], as well via regulation for Radiation Protection in Medical Treatment of the Personnel [8]. Actually, Bachelor’s and Master’s Programs are active at the University of Plovdiv and at the University of Sofia. The Postgraduate Specializations are delivered by the National Center for Radiobiology and Radiation Protection, Ministry of Public Health since 1982 [9].

### **2. Short notes for the Master Programs in Medical Physics in Bulgaria**

The first Master Program in Medical Physics and Radioecology in Bulgaria started at the University of Shumen in 1990. It is not active anymore [10, 11].

A Master Program in Medical Radiation Physics and Technique delivered in English was developed at the University of Plovdiv in 1997 [10, 11]. It was an initiative of Prof. Slavic Tabakov, the president of the International Organization for Medical Physics (IOMP) 2015-2018 and the program was sponsored by an EC TEMPUS Project. An Inter-University Center was created between the University of Plovdiv, the Medical University Plovdiv, and the Technical University Sofia – branch Plovdiv. The project was strongly supported by foreign partners – Kings’ College London (UK), University of Florence (Italy) and University of Dublin (Ireland). The program got accreditation for 5 years from the Institute of Physics and Engineering in Medicine (IPEM), UK. This was the first course in Medical Physics accredited by this institution outside the United Kingdom. After that the education was

delivered in the Bulgarian language. The program was adopted by several foreign universities in Latvia, Lithuania, Estonia, Malaysia, Sudan, and others. The program in Plovdiv ran until 2013. The new government accreditation requested an update of the program. The main problems were related to the big number of external lecturers and lack of elective disciplines. The program was renewed in 2015 while successfully keeping the core courses of the previous program.

The Master Program in Medical Physics at the University of Sofia was opened in 2000. Here one shell mentioned that it differed significantly from its equivalent in the University of Plovdiv.

Today the two Universities – of Sofia and of Plovdiv – became partners in a joint project aiming to develop a new program in Medical Physics delivered in English. The project is called MODERN-A: Modernization in partnership through digitalization of the Academic ecosystem. Several foreign universities are involved as Associated Partners: from UK, France, Spain, Lithuania, Latvia, Greece, and Croatia.

The project is in its beginning and hereby the author expresses her own point of view as a director of the current Master Program in Plovdiv.

### **3. The Need for an update of the Master's Programs in Medical Physics**

Medical Physics is developing very rapidly. The curriculum always tends to be up-to-date, but it never succeeds to follow all trends of science, technology, and the labor market [12-14]. There is always some delay, and no educational program can include the entire related knowledge, nevertheless ensure enough practical training. It needs constant updating.

Medical imaging techniques and radiotherapy equipment offer more and more new diagnostic and therapeutic options. For example, the newest Hybrid/Multimodality Medical Imaging technique combines different techniques in one device, such as PET/MRI, SPECT/CT, PET/CT [15]. A good Medical Physicists should be specialized in at least two different fields.

### **4. The Need for Master Program in Medical Physics delivered in English**

The world is varied, but the diseases are the same. There is a lack of Medical Physicists all over the world. Many countries do not have education in Medical Physics at all, but they need Medical Physicists and therefore educate their own abroad. From another side, many specialists work abroad. For example, a big number of Medical Physicists who graduated in Bulgaria work all over the world in clinics, in the academic field or at some of the international institutions. Nowadays, English is the most recognized language for science communication and technology exchange.

Medical equipment is supplied by leading international companies (Siemens, Varian, Elekta, and others) which also provide technical support.

Medical Physics is international. EFOM, IOMP, IAEA and other international institutions push and support the development of Medical Physics and the establishment

of the professional profile. They issue recommendations and regulations and provide printed materials and post-graduated training.

Maintaining a certain level of performance of Medical Physicists requires their permanent participation in scientific conferences, seminars, webinars, and specialized courses. Therefore, English is the commonly accepted language of Medical Physics.

### **5. The Need for joint Master Programs in Medical Physics**

Education in Medical Physics is not a routine task. It needs theoretically well-prepared lecturers with sufficient experience. The courses should be updated regularly with the newest diagnostic and therapeutic methods applied at hospitals. The best case is when a teacher performs scientific research in the related field. Such specialists are small in numbers in our country. Unfortunately, experts with broad experience are of a certain age and most of them cannot be employed in regular academic positions, according to the new law for academic development. There is an urgent need to educate young people, however this needs time. The statistics shows that over the past decade both universities, the ones in Plovdiv and in Sofia, saw the graduation of 10-15 Master students per year. This type of education is quite expensive and economically not sustainable.

Both universities, in Plovdiv and in Sofia, have well-equipped laboratories in Radiation Physics disciplines – Atomic and Nuclear Physics, Radiation Measurements, Radiation Protection etc. But the practical work in Medical Physics is usually performed at hospitals upon voluntary negotiation. This leads to many difficulties. The medical equipment is extremely expensive, and training cannot be financially supported. Except for doing it at laboratories at the university, students are not permitted to work with ionizing radiation. This difficulty can be overcome through the acquisition of specialized software, for example, simulation systems for treatment planning in Radiotherapy. Due to the small number of students, it's more convenient to purchase such systems via a project in a joint Master Program, as we intend to do. On the other hand, development of a new joint master program would lead to long discussions for defining the core courses, the educational methods etc., and as a result would help clarify the common needs on a national level. In this way the program would become more sustainable.

### **6. The Need for foreign Associated Partners**

There's only so much that a person can do alone. Education needs cooperation, exchange of experience, continuous training of teachers. Foreign Associated Partners could offer their help in preparing/updating courses by providing recommendations and teaching materials, delivering lectures and exchanging scientific visits. This would increase the quality of educational programs on international level. It would bring more visibility for Medical Physics education and the profession itself. A new international network in the field of education and research could be created.



## 7. Challenges for the establishment of a new Master Program in Medical Physics

Creating a new joint Master Program in Medical Physics delivered in English is a big challenge. There are several different aspects, which can go beyond of its direct education purpose.

Being essential for human life and health, Medical Physicists' work is of public importance. There is regulation for Medical Physicists working with ionizing radiation in medicine. But Medical Physicist with Master's and Bachelor's degrees in Bulgaria are neither in the list of regulated professions, nor in the list of professional qualification yet! The specializations (after Master's degree) in Medical Radiological Physics and Medical Sanitary Physics (for Physicists and Engineers) are included as specialists in medicine with no medical education. But they are also not included in the list of regulated professions nor are they in the Directive 2005/36/EO for recognition of the professional qualification. It's a big challenge to approach the public institutions and convince them to change this status.

No University in Bulgaria has accreditation for a doctor degree in Medical Physics! Recently both the universities of Sofia and Plovdiv were recognized as research universities. They perform research in the Medical Physics field as well, but they cannot educate this kind of Ph.D. students. The one and only accredited institution in Bulgaria for Ph.D. degree in Medical Physics is the National Center for Radiobiology and Radiation Protection, Ministry of Public Health. This is an obstacle for academic career development.

There is a huge need for Medical Physicists in Bulgaria. This is obvious from information recently provided by BSBPE (2019). Two years ago, there were 20 departments in Radiotherapy with 81 different devices (linear accelerators, orthovoltage machines, CyberKnives, planning systems etc.) and 61 employed Medical Physicists; 21 Nuclear departments with 28 devices (PET, SPECTS etc.) and 15 employed Medical Physicists; 2478 X ray machines with 7 employed Medical Physicists. The certification of Medical Physics Experts started in 2019 and since then 30 specialists have been certified – 24 in Radiotherapy, 13 in Medical Imaging and 3 in Nuclear Medicine. 7 of them have passed 2 kinds of specializations, and 1 person obtained all 3 kinds of specialization.

Medical Physics needs more publicity. Despite the fact that the profession is crucial for every Medical Imaging and Radiotherapy department, Medical Physicists are invisible. A Medical Physicist works closely with medical doctors but does not have the same level of contact with the patient. Additionally, there is not enough publicly released information for the other branches of Medical Physics, like Medical Sanitary Physics, Medical measurements Nonionizing Radiation in Medicine, etc. This also results in low attraction of students toward academic education in Medical Physics.

## 4. Conclusions

Medical Physics is an important part of contemporary science, technology, and clinical practice. The need for well-educated and trained specialists in this field is

increasing worldwide. There are recommendations from EFOMP, IOMP and IAEA for the grades of education of Medical Specialists. It's included partially at the Bulgarian national legislation and addressed to people working with ionizing radiation. However, an extension toward other, nonionizing methods is needed.

The minimum degree required for working as a Medical Physicist is a Master's one. An update of the educational and training Programs is needed - according to recent technological developments and the current economic and social situation. Master programs in Medical Physics delivered in English would open more possibilities for high performance, work, and achievements of international relevance.

## 5. References

1. European Commission. Council Directive 97/43/EURATOM of 30 June 1997 on health protection of individuals against the dangers of ionizing radiation in relation to medical exposure, Official Journal of the EC, L180, V22, 1997.
2. EFOMP Policy statement No. 1: Medical Physics Education and Training: The Present European Level and Recommendations for its Future Development, 1984.
3. EFOMP Policy statement No. 2: The Roles, Responsibilities and Status of the Clinical Medical Physicist, 1984.
4. EFOMP Policy statement No. 8: Continuing Professional Development for the Medical Physicist, 1998.
5. IOMP Policy Statement No. 1 The Medical Physicist: Role and Responsibilities IOMP Working Group on Policy Statement No. 11 10 August 2010. Approved by the IOMP Council in WC 2012, Beijing, China.
6. IOMP Policy Statement No. 2 Basic Requirements for Education and Training of Medical Physicists. IOMP Working Group on Policy Statement No. 21, 10 August, 2010. Approved by the IOMP Council in WC 2012, Beijing, China.
7. Наредба № 6 от 29 януари 2010 г. за утвърждаване на медицински стандарт „Лъчелечение“. ДВ. бр. 63 от 30.07.2021.
8. Наредба № 9 от 13 юли 2018 г. за утвърждаване на медицински стандарт „Образна диагностика“.
9. Наредба № 2 от 5 февруари 2018 г. за условията и реда за осигуряване на защита на лицата при медицинско обслужване, Министър на здравеопазването, обн. ДВ. бр.13 от 9 Февруари 2018г.
10. L. Litov, T.L. Dimitrova, Education in Medical Physics in Bulgaria. (2010). Medical Physics in the Baltic States 2010, 1, 6-10.
11. T. L. Dimitrova, H. Hristov, E. Milieva. (2011). Medical physics education and training in Bulgaria. "Medical physics – the current status, problems, the way of development. High technologies", First International Workshop, Workshop proceeding, June 02-03, 2011, Kyiv, Ukraine, 24-29.
12. Т. Л. Димитрова. (2014). Примери за добри европейски практики в обучението по медицинска физика. XLII Национална конференция на въпросите на обучението по физика „Световни образователни стандарти, сравнителни измервания и образованието по физика в България“, Стара Загора, 8-11 септември 2014 г., 127-130.
13. Т. Л. Димитрова. (2014). Обучението по медицинска физика в Европа - модерно и актуално. Физика: Методология на обучението, т. 2, кн. 4, 254-261.
14. Т. Л. Димитрова, (2015). „Медицински физик“ - модерна и перспективна професия. Светът на физиката, 1, 44-49.
15. <https://www.ifmp.eu/Plovdiv-page-1.htm>

## CONTENT

Sören Mattsson. Reflections on 60 years of development in medical physics and thoughts about the future .....	3
Carmel J. Caruana. Developing strategic leadership skills is crucial for the future of medical physics .....	9
P.S. Druzhinina, A. Chipiga, A. V. Vodovotov, A.V. Pozdnyakov, Yu. N. Kapyrina, D.O. Ivanov, Yu. V. Petrenko, V.G. Puzyrev. The adjusted effective dose assessment from CT of the chest for pediatric patients: a hospital based study .....	11
Aleksandr Vodovotov, Ivan Romanovich, Sergey Ryzhov, Larisa Chipiga, Gleb Berkovich, Artem Biblin. Assessment of the changes in structure of X-ray diagnostics and collective dose from CT examinations related to Covid-19 in the Russian Federation in 2020.....	15
Leonid Repin, Rustam Akhmatdinov, Artem Biblin. Application of summary measures of population health to radiation risks assessment.....	19
Kirill Skovorodko, Mažena Maciusovič, Marius Burkanas, Sigita Tiškevičius, Laurynas Gilys, Renata Komiagienė, Jonas Venius. Towards harmonization of clinical bone scintigraphy protocol between three different SPECT/CT systems in Lithuania .....	23
Richard Deyhle Jr., Christian Bernhardsson, Lovisa Waldner, Lars E. Olsson, Marie Sydoff. Dosimetry concepts for quality assurance in $\mu$ CT .....	28
Artem Davydov, Dmitri Kononenko, Artem Biblin, Alexander Vodovotov. Perception of medical risks and sociodemographic characteristics of respondents .....	32
Tatjana Vigovska, Katrina Caikovska, Mara Epermane. Estimation method of breast absorbed radiation dose during coronary angiography .....	35
Leonid Krynke, Birutė Gricienė, Antonio Jreije, Laura Bilotaitė. Radiation dose follow-up for common interventional cardiology and radiology procedures.....	39
Ilya Shatskiy, Dmitry Ivanov, Vitaly Reznik, Aleksandr Pozdnyakov, Viktor Puzyrev, Yuliya Kapyrina, Anna Nabieva, Karine Panuntseva, Svetlana Bannova, Yury Petrenko. Relation between the severity of the course of the disease and doses and radiation risk of the chest X-ray and CT examination of children with Covid-19 .....	43
Aurimas Krauleidis, Vanda Andrijaitienė. Gamma spectroscopic analysis of 18 MeV photons activated radioisotopes in Siemens Oncor Impression 3D linac head and its decommissioning experience .....	47
Sumeyra Can, Didem Karacetin, Niyazi Meric. A new monte carlo algorithm to simulate virtual source model on an Elekta Versa HD linac .....	53
Marijus Astrauskas, Romualdas Griškevičius, Kęstutis Akelaitis, Ieva Markevičienė, Jonas Venius. Case study report: advantages of Hyperarc™ in brain radiosurgery treatment planning .....	57
Nur Kodaloğlu, Cafer Atar, Selami Karahan. A successful patient management system during Covid-19 pandemic and the impact of the restrictions in a radiation oncology clinic in Turkey.....	62
Linas Kudrevičius, Evelina Jaselskė, Diana Adlienė. Radiosurgery dose optimization for the patients with cerebral arteriovenous malformations after endovascular embolization.....	66
Lyudmila Aslamova, Mykhaylo Zabolotnyy, Galina Dovbeshko, Galina Solyanik. Increasing the antitumor efficacy of doxorubicin by highenergy irradiation of saline .....	70
Ramune Ulrich. Extending lap product portfolio: Solutions for patient QA and machine QA .....	74

Džiugilė Valiukevičiūtė, Judita Puišo, Jurgita Laurikaitienė, Linas Kudrevičius. Formation and investigation of Cu/CuOx nanocomposite films for low dose dosimetry application .....	78
Neringa Šeperienė, Ignas Pikas. Development of polymer gel based exhaled breath biomarkers detection sensor for Covid-19 monitoring .....	82
Vijayanand Sivakumar, Diana Adlienė. Development of patient's biometric data based CT dose optimization algorithm .....	86
Christian Bernhardsson, Lovisa Waldner, Christopher Rääf, Aleksandr Vodovatov. Household salt (NaCl) for optically stimulated luminescence dosimetry: an overview .....	90
Vytenis Barkauskas, Lukas Rimkus, Jonas Reklaitis, Artūras Plukis, Mikas Vengris. Evaluation of the irradiation doses from the operation of the intense femtosecond laser .....	95
Artem Davydov, Artem Biblin, Alexander Vodovatov, Vladimir Safronov. Perceptions of the risks of radiodiagnostic examinations in potentially high-dose and low-dose patients.....	99
Svetlana Sarycheva, Zmurd Vagidova. Prediction of deterministic skin effects in patients undergoing high-doses interventional radiology examinations.....	102
Yuliya Dvornik, Natalia Veyalkina, Kseniya Fabusheva. Early effects of radiation exposure on peripheral blood cells and normal organs of mice.....	105
Antonio Jreije, Kirill Skovorodko, Mykolas Pavlauskas, Roman Machnin, Diana Adlienė, Birutė Gricienė. Optimization of conventional X-ray image acquisition parameters for pelvic procedures: a phantom study .....	109
Larisa Chipiga, Aleksandr Vodovatov, Polina Piven, Gleb Berkovich, Gennadiy Trufanov, Irina Maschenko, Polina Druzhinina, Viktor Puzyrev. Fetal doses for pregnant patients undergoing chest CT examinations .....	113
Inga Andriulevičiūtė, Kirill Skovorodko, Jurgita Laurikaitienė, Birutė Gricienė. Assessment of extremity exposure for nuclear medicine personnel .....	117
Mikhail V. Osipov, Andrey V. Vazhenin, Daria A. Vazhenina, Tatyana S. Novikova, Anna I. Kuznetsova, Irina A. Aksenova, Mikhail E. Sokolnikov. PET-CT and occupational exposure: cohort profile update..	121
Giedrė Morkūnaitė, Rimantas Ožiušas, Vytautas Čeplauskas. Color changes of dental ceramics exposed to bleaching materials.....	125
Vladislav Golikov. Assessment of the radiation risks from medical X-ray examinations considering age and gender composition of the patients .....	129
Kristina Eriksson Stenström, Vytenis Barkauskas, Christian Bernhardsson, Aliaksandr Dvornik, Mattias Jönsson, Charlotta Nilsson, Mattias Olsson, Guillaume Pédechontaa-Hiaa, Valery Ramzaev, Christopher Rääf, Aleksandr Vodovatov. Preoperational assessment of 14C in the vicinity of the Belarusian nuclear power plant.....	133
Aliaksandr Dvornik, Veranika Sehlín. Accumulation of 137Cs by forest lichens in the chernobyl affected territories .....	138
Guillaume Pédechontaa-Hiaa, Christian Bernhardsson, Vytenis Barkauskas, Andrius Puzas, Kristina Eriksson Stenström, Christopher Rääf, Sören Mattsson. Evaluation of the region-specific risks of accidental radioactive releases from the European Spallation Source.....	142

Nur Kodaloğlu, Can Azak, Sezai Güçlü Kiliçoğlu, Tuğba Ulu, Gizem Kavak Eren, Hasan Çamlicali, Ebru Karakaya. Back to the future: the positive educational impact of Covid-19 pandemic with online learning program into clinic.....	147
Aurimas Plaga, Ignas Pikas, Judita Puišo, Jurgita Laurikaitienė, Diana Adlienė. Ionizing radiation induced colour changes in hydrogels.....	150
Agnė Giedrytė, Lamiaa Abdelrazik, Marius Laurikaitis, Reda Čerapaitė-Trušinskienė, Jurgita Laurikaitienė. Phantom-based quality control measurements for the newly installed linear accelerator halcyon.....	155
Mindaugas Ilickas, Jurgita Laurikaitienė. Medical 3D image segmentation in radiotherapy treatment for a patient with head and neck tumours .....	159
Aleksandras Ševčik, Diana Adlienė. Comparison of experimentally measured dose depth distributions with MC simulations in electron-irradiated dose gels.....	163
Lijana Lileikytė, Benas Gabrielis Urbonavičius. TLD-100 response dependence on various factors .....	167
Mantas Brukštus, Diana Adlienė. Metallic artifacts and their reduction in nuclear magnetic resonance imaging (an overview) .....	171
Nur Kodaloğlu. Is it possible to apply a new technique with an old linac? A feasibility study of PLDR with Elekta Synergy platform linac .....	176
Justas Beresnevičius, Benas Gabrielis Urbonavičius. Prototype of contemporary gamma spectrometer based on obsolete radiometer .....	179
Mantvydas Merkis, Ignas Pikas, Diana Adlienė. Investigation of low toxicity dose gels with enhanced sensitivity .....	183
Greta Vainiūtė, Laurynas Gilys, Lijana Lileikytė, Diana Adlienė. Investigation of exposure doses to nuclear medicine staff working with Tc-99m .....	187
Mindaugas Džiugelis, Leonid Krynke. Diagnostic and clinical grade medical imaging display performance evaluation and optimization using quality assurance protocols .....	191
Kamilė Dambrauskaitė, Jurgita Laurikaitienė, Artūras Andrejaitis. Application of 3D printed individual compensating bolus for the verification of shallow head and neck cancer treatment .....	197
Todorka L. Dimitrova. Master's program in medical physics in english.....	201

## AUTHOR INDEX

- Abdelrazik L. 155  
 Adlienė D. 66, 86, 109, 150, 163, 171, 183, 187  
 Akelaitis K. 57  
 Akhmatdinov R. 19  
 Aksenova I. 121  
 Andrejaitis A. 197  
 Andrijaitienė V. 47  
 Andriulevičiūtė I. 117  
 Aslamova L. 70  
 Astrauskas M. 57  
 Atar C. 62  
 Azak C. 147  
 Bannova S. 43  
 Barkauskas V. 95, 133, 142  
 Beresnevičius J. 179  
 Berkovich G. 15, 113  
 Bernhardsson C. 28, 90, 133, 142  
 Biblin A. 15, 19, 32, 99  
 Bilotaitė L. 39  
 Brukštus M. 171  
 Burkanas M. 23  
 Caikovska K. 35  
 Çamlıcalı H. 147  
 Can S. 53  
 Caruana C. J. 9  
 Chipiga L. 11, 15, 113,  
 Čeplauskas V. 125  
 Čerapaitė-Trušinskienė R. 155,  
 Dambrauskaitė K. 197  
 Davydov A. 32, 99  
 Deyhle R. Jr. 28  
 T. L. Dimitrova 201  
 Dovbeshko G. 70  
 Druzhinina P. 11, 113  
 Dvornik Y. 105  
 Dvornik A. 133, 138  
 Džiugelis M. 191  
 Epermane M. 35  
 Eren G. K. 147  
 Fabusheva K. 105  
 Giedrytė A. 155  
 Gilys L. 23, 187  
 Golikov V. 129  
 Gricienė B. 39, 109, 117,  
 Griškevičius R. 57  
 Ilickas M. 159  
 Ivanov D. O. 11, 43  
 Jaselskė E. 66  
 Jönsson M. 133  
 Jreije A. 39, 109  
 Kapyrina Y. 11, 43  
 Karacetin D. 53  
 Karahan S. 62  
 Karakaya E. 147  
 Kiliçoğlu S.G. 147  
 Kodaloğlu N. 62, 147, 176  
 Komiagienė R. 23  
 Kononenko D. 32  
 Krauleidis A. 47  
 Krynke L. 39, 191  
 Kudrevičius L. 66, 78  
 Kuznetsova A. 121  
 Laurikaitienė J. 78, 117, 150, 155, 159, 197  
 Laurikaitis M. 155  
 Lileikytė L. 167, 187  
 Machnin R. 109  
 Maciusovič M. 23  
 Markevičienė I. 57  
 Maschenko I. 113  
 Mattsson S. 3, 142  
 Meric N. 53  
 Merkis M. 183  
 Morkūnaitė G. 125  
 Nabieva A. 43  
 Nilsson C. 133  
 Novikova T. 121  
 Olsson M. 28, 133  
 Osipov M. 121  
 Ožiūnas R. 125  
 Panuntseva K. 43  
 Pavlauskas M. 109  
 Pédehontaa-Hiaa G. 133, 142  
 Petrenko Y. 11, 43  
 Pikas I. 82, 150, 183  
 Piven P. 113  
 Plaga A. 150  
 Plukis A. 95  
 Pozdnyakov A. 11, 43  
 Puišo J. 78, 150  
 Puzas A. 142  
 Puzyrev V. 11, 43, 113  
 Rääf C. 90, 133, 142  
 Ramzaev V. 133  
 Reklaitis J. 95  
 Repin L. 19  
 Reznik V. 43  
 Rimkus L. 95  
 Ryzhov S. 15  
 Romanovich I. 15  
 Safronov V. 99  
 Sarycheva S. 102  
 Sehlín V. 138  
 Shatskiy I. 43  
 Sivakumar V. 86  
 Skovorodko K. 23, 109, 117  
 Sokolnikov M. 121  
 Solyanik G. 70  
 Stenström K. E. 133, 142  
 Sydoff M. 28  
 Šeperienė N. 82  
 Ševčík A. 163  
 Tiškevičius S. 23  
 Trufanov G. 113  
 Ulrich R. 74  
 Ulu T. 147  
 Urbonavičius B. G. 167, 179  
 Vagidova Z. 102  
 Vainiūtė G. 187  
 Valiukevičiūtė Dž. 78  
 Vazhenin A. 121  
 Vazhenina D. 121  
 Veyalkina N. 105  
 Vengris M. 95  
 Venius J. 23, 57  
 Vigovska T. 35  
 Vodovatov A. 11, 15, 32, 90, 99, 113, 133  
 Waldner L. 28, 90  
 Zabolotnyy M. 70